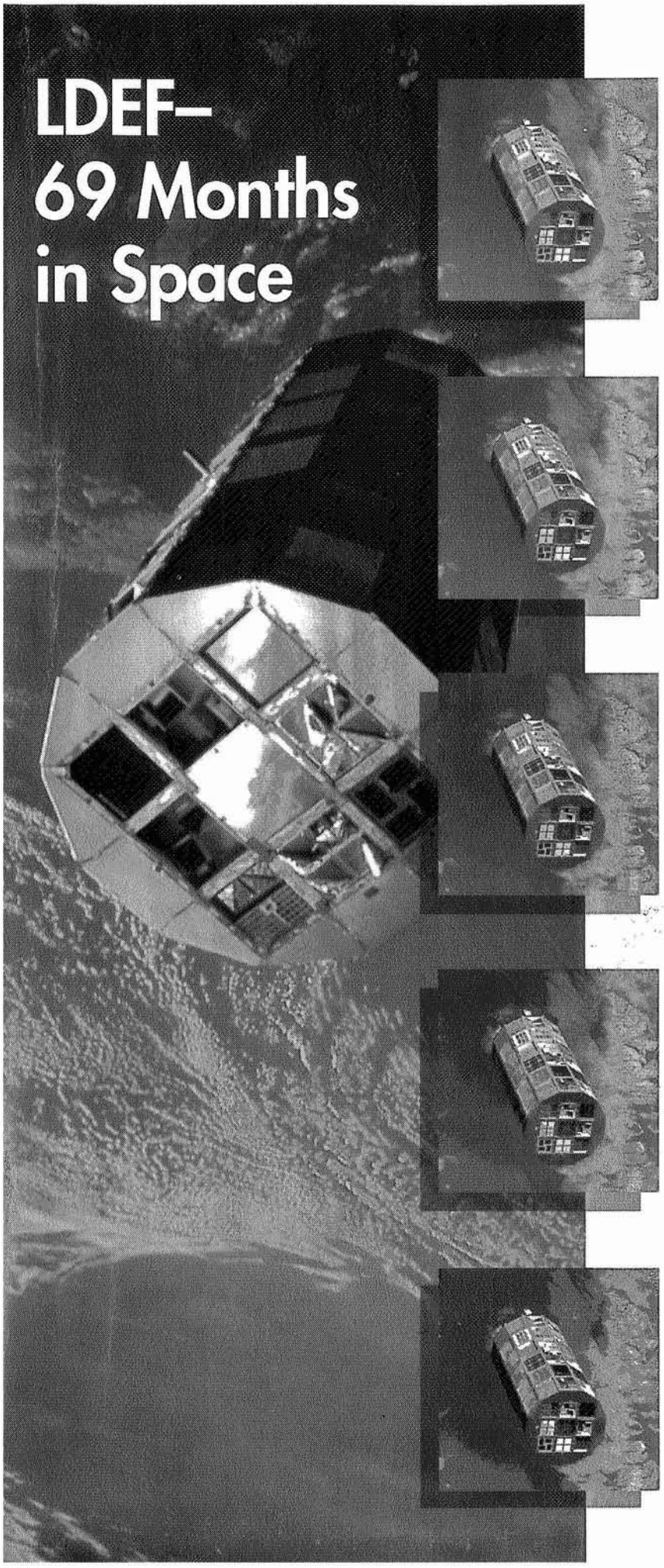

Third Post - Retrieval Symposium

November 8-12, 1993
Williamsburg, Virginia

Sponsors:

LDEF Science Office
NASA Langley Research Center

American Institute of
Aeronautics and Astronautics

NASA Conference Publication 3275
Part 1

National Aeronautics and
Space Administration

American Institute of
Aeronautics and Astronautics

LDEF–
69 Months
in Space

NASA Conference Publication 3275
Part 1

Third
Post - Retrieval
Symposium

Edited by
Arlene S. Levine
NASA Langley Research Center
Hampton, Virginia

Proceedings of a symposium sponsored by the National Aeronautics and Space Administration, Washington, D.C., and the American Institute of Aeronautics and Astronautics, Washington, D.C., and held in Williamsburg, Virginia
November 8-12, 1993

National Aeronautics and
Space Administration

Office of Management

Scientific and Technical
Information Program

1993

The use of trade names of manufacturers in this report does not constitute an official endorsement of such products or manufacturers, either expressed or implied, by the National Aeronautics and Space Administration.

This publication is available from the following sources:

NASA Center for AeroSpace Information
800 Elkridge Landing Road
Linthicum Heights, MD 21090-2934
(301) 621-0390

National Technical Information Service (NTIS)
5285 Port Royal Road
Springfield, VA 22161-2171
(703) 487-4650

FOREWORD

The third LDEF Post-Retrieval Symposium was held at the Williamsburg Lodge in Williamsburg, Virginia, November 8–12, 1993. Approximately 140 papers, posters, and demonstrations were presented. The Symposium represents the transition from focusing solely on a single spacecraft (LDEF) and its exposure to the low Earth orbit, to focusing on a broad approach to study the space environment and its effects. The LDEF program has provided a benchmark and means of comparison for other programs defining the low Earth orbit environment and its effects on spacecraft materials, systems, and structures. This Symposium included the preliminary results of European Retrievable Carrier (EURECA), the Evaluation of Oxygen Interactions with Materials III (EOIM-III) flight experiment, Salyut-7, and future flight experiments.

We have been challenged to design cheaper, better, and longer lasting spacecraft. NASA, other domestic and foreign agencies, and industry have contributed to the experiments and technologies now used to provide more accurate environmental definition and life prediction, lighter, long-lasting materials and structures, and more efficient systems. NASA's mission has always been to disseminate knowledge, and now we have been challenged to see that this knowledge is transformed into relevant technology.

The editor would like to thank all participants at the third Post-Retrieval Symposium for their contributions leading to the transfer of this technology. I would also like to thank all the contributing authors, as well as all those researchers who performed peer reviews of the enclosed papers. A special word of thanks goes to Bland Stein, Don Humes, and Steve Koontz, who reviewed more than their fair share of papers. I would like to thank the Symposium session chairs:

Darrel Tenney, *Opening Session*
Gale Harvey, *Induced Environment*
Alan Dover, *EURECA*
Thomas Parnell and James Adams, *Ionizing Radiation*
Friedrich Hörz, Dale Atkinson, J.A.M. McDonnell, Michael Zolensky, Donald Kessler, Donald Humes, and Jean-Claude Mandeville, *Meteoroid and Debris*
Philip Young, Ann Whitaker, Gary Pippin, James Zwiener, Joan Funk, and Bruce Banks, *Materials*
Steve Koontz and Wayne Stuckey, *EOIM-III*
James Mason, *Systems*
Ranty Liang and William Kinard, *Future Activities*

Many thanks to Susan Hurd (Mason and Hanger) for her patient, gracious, and invaluable editing and to Maureen Sgambelluri (Troy Systems) for her patience and skill in reformatting papers to meet our requirements.

NASA CP-3275 is the third LDEF Post-Retrieval Symposium. The first Symposium, NASA CP-3134, was held in 1991 in Kissimmee, Florida, and the second Symposium, NASA CP-3194, was held in San Diego, California, in 1992. You may request copies of either or both proceedings. For information please contact

Arlene S. Levine
Mail Stop 404
NASA Langley Research Center
Hampton, Virginia 23681-0001
phone: 804 864-3318/fax: 804 864-8094
e-mail: a.s.levine@ larc.nasa.gov

CONTENTS

*Part 2 is presented under separate cover.

PART 3*

EVALUATION OF OXYGEN INTERACTIONS WITH MATERIALS III (EOIM-III)

*Part 3 is presented under separate cover.

SYSTEMS

EXPERIMENTS

omit
vd
p3
9p

AUTHOR INDEX

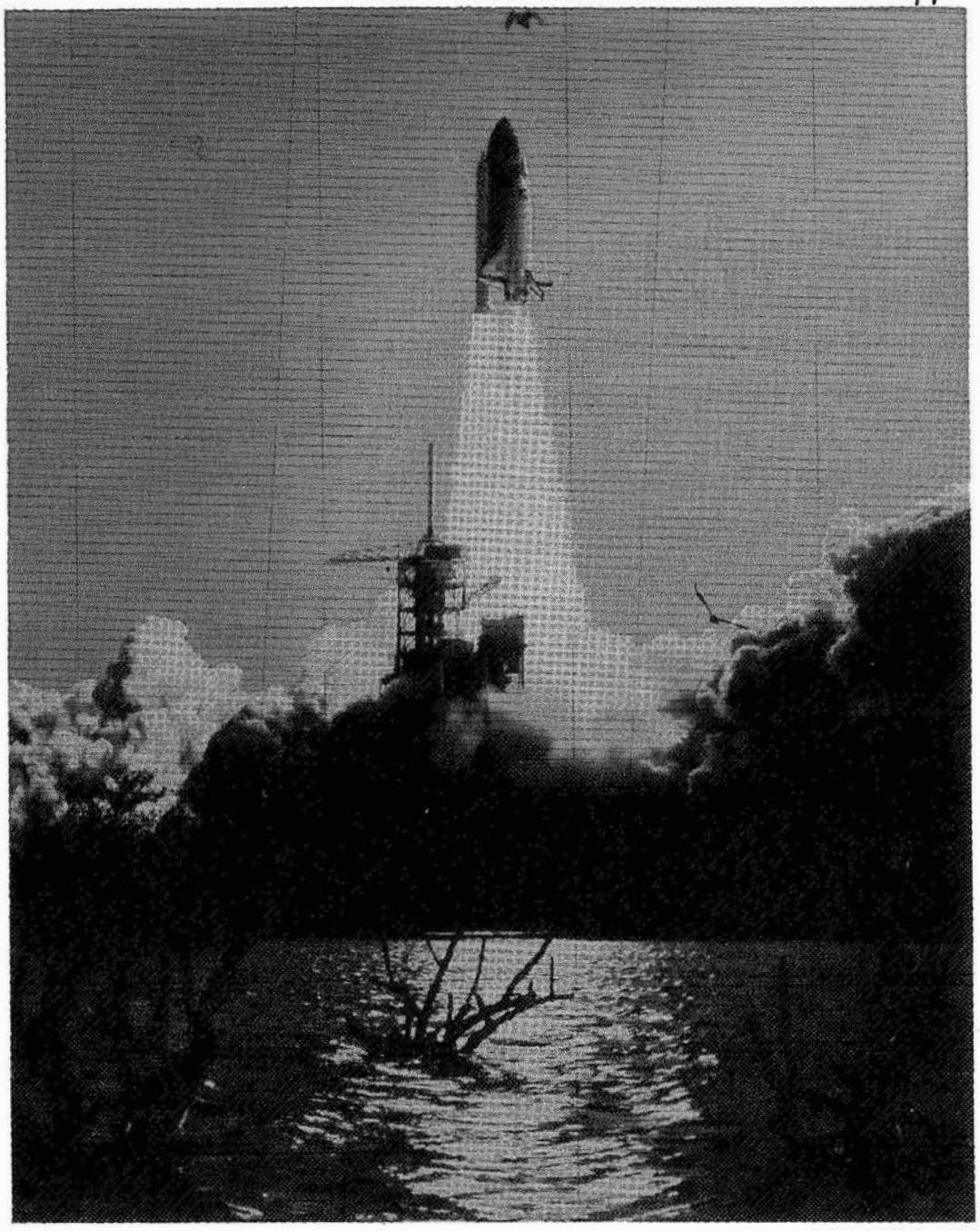

84-5648

AUTHOR INDEX

Part 1 — pages 1—536
Part 2 — pages 537—866
Part 3 — pages 867—1388

C

D

E

F

G

H

I

J

K

L

M

N

O

P

U

V

W

Y

Z

PART 1

NATURAL AND INDUCED ENVIRONMENTS

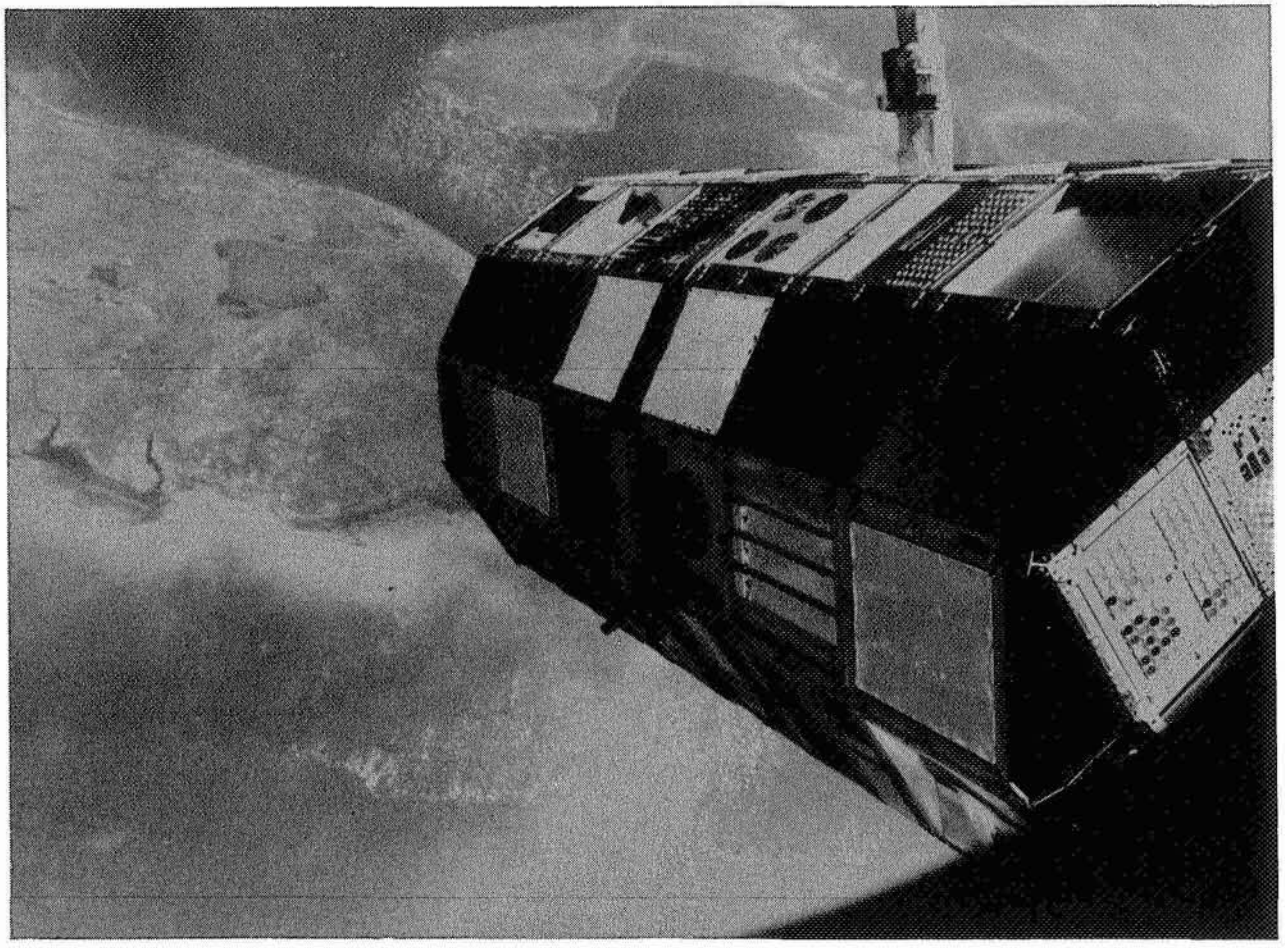

84-04304

LDEF ENVIRONMENT MODELING UPDATES

Tim Gordon
Applied Science Technologies
P.O. Box 621134
Littleton, Colorado 80162
Phone: (303) 973-7708, Fax: (303) 973-7408

Ray Rantanen
ROR Enterprises
2455 W. Summer Ave.
Athol, Idaho 83801
Phone: (208) 623-6376, Fax: (208) 623-6944

Ann Whitaker
NASA, Marshall Space Flight Center
Huntsville, Alabama 35812
Phone: (205) 544- 2510, Fax: (205) 544-5786

ABSTRACT

An updated gas dynamics model for gas interactions around the LDEF is presented that includes improved scattering algorithms. The primary improvement is more accurate predictions of surface fluxes in the wake region. The code used is the Integrated Spacecraft Environments Model (ISEM).

Additionally, initial results of a detailed ISEM prediction model of the Solar Array Passive LDEF Experiment (SAMPLE), A0171, is presented. This model includes details of the A0171 geometry and outgassing characteristics of the many surfaces on the experiment. The detailed model includes the multiple scattering that exists between the ambient atmosphere, LDEF outgassing and atomic oxygen erosion products. Predictions are made for gas densities, surface fluxes and deposition at three different time periods of the LDEF mission.

INTRODUCTION

The objectives of this study were to update the scattering algorithms used in ISEM and to perform more detailed modeling of the AO171 experiment tray. These models were then delivered to NASA, MSFC for use by analysis personnel.

The changes in the scattering algorithms affected, primarily, the wake regions where self scattering is important. This update was initiated after in flight observations of

the Environment Monitor Package,EMP, showed that the wake region wasn't being adequately predicted. The EMP was an instrumented payload deployed from a rocket flight and had a multitude of sensors and objectives(ref.1). Previously ISEM had two scattering algorithms, one for thermal speed collisions and one for collisions with the high speed incoming ambient. These corresponded to a cosine scatter and a cosine to the 20th power scatter. The new center of mass scattering gives nearly the same scattering distributions and ram densities at LEO but does a much more accurate job for low density ambient atmospheres and self scattering in the wake regions behind the spacecraft. Currently the updated scattering algorithms are standard in ISEM (ref. 2).

RESULTS

Updated LDEF Predictions

The fluxes of ambient and contaminant species were predicted in an earlier study (ref. 3). A comparison of some of the previous results with the more recent results are presented to show the influence in the wake regions. The entire set of updated predictions can be found in the final report for the current study (ref. 4).

Figure 1 shows the previous predictions using the old scattering algorithms for the outgassed and erosion products at 463 km. Figure 2 is the same predictions only with the new scattering algorithms. Comparison shows that the surfaces in the wake were influenced the most where the surface flux is near three orders of magnitude greater with the updated scattering algorithms. Surfaces on the ram side show no changes in flux. The same is true for atomic oxygen as can be seen by comparing Figures 3 and 4. It is interesting to note that now the scattered flux of contaminants to the wake surfaces is the same order of magnitude as the scattered atomic oxygen flux at this time in the mission. This same type of increase in the wake flux for the updated algorithm predictions exists for different time periods throughout the mission.

AO171 Experiment Tray Model

The AO171 experiment tray was modeled as a series of six surfaces with the scattering volume surrounding these surfaces as shown in Figure 5. Figure 6 shows the points where the flux to the surfaces was calculated. At these points the flux to both a horizontal and vertical surface was calculated for the different time periods on orbit. Outgassing rates were assigned based on mass loss measurements of some of the post flight samples averaged over time. The actual rate was not considered absolutely necessary for this study since relative differences around the tray were being looked for to explain the different observed discolorations.

Figure 7 shows the flux of atomic oxygen across the tray for flat surfaces. The shadowing of the oxygen by the tray lip is evident in the figure. Figure 8 shows the flux of outgassed products on flat surfaces. The outgassing sources for the six modeled sections of the tray were lumped together as the total outgas plot and separated out for the two tray sections that influenced the modeled point locations the most. See Figure 6 for locations of panels 2 and 5.

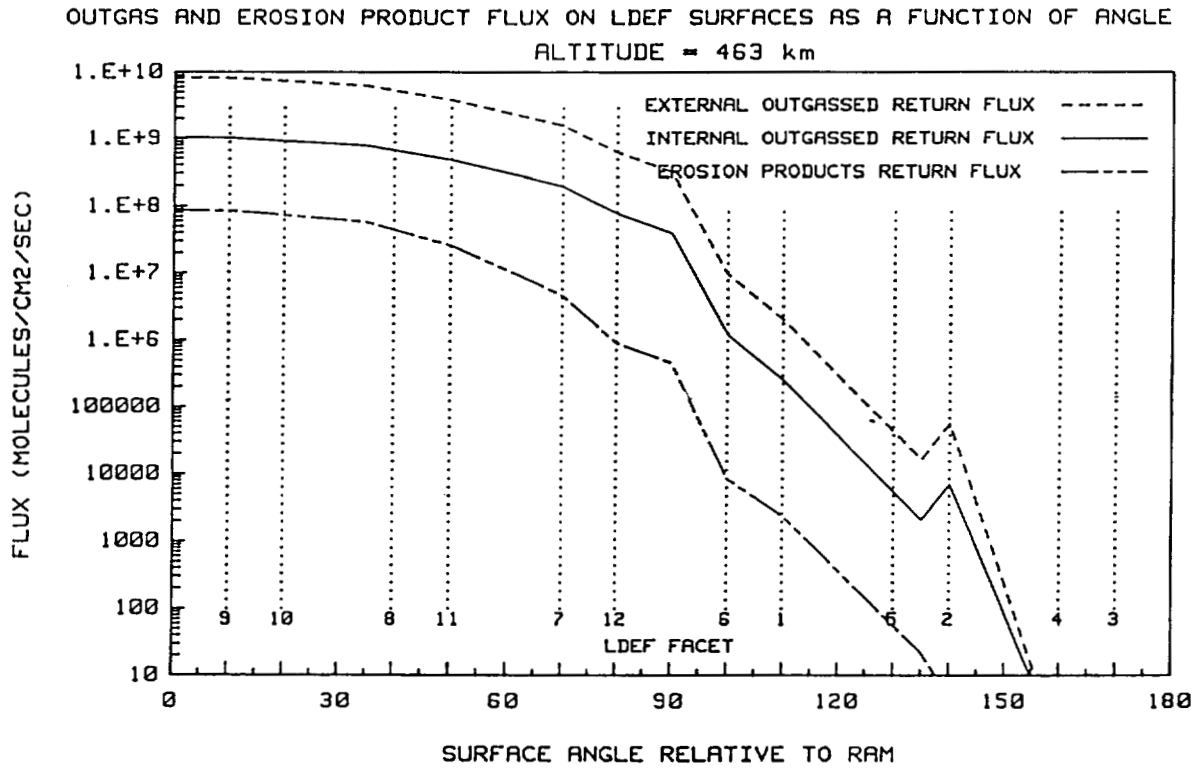

Figure 1. Results Using Old Scattering Algorithm

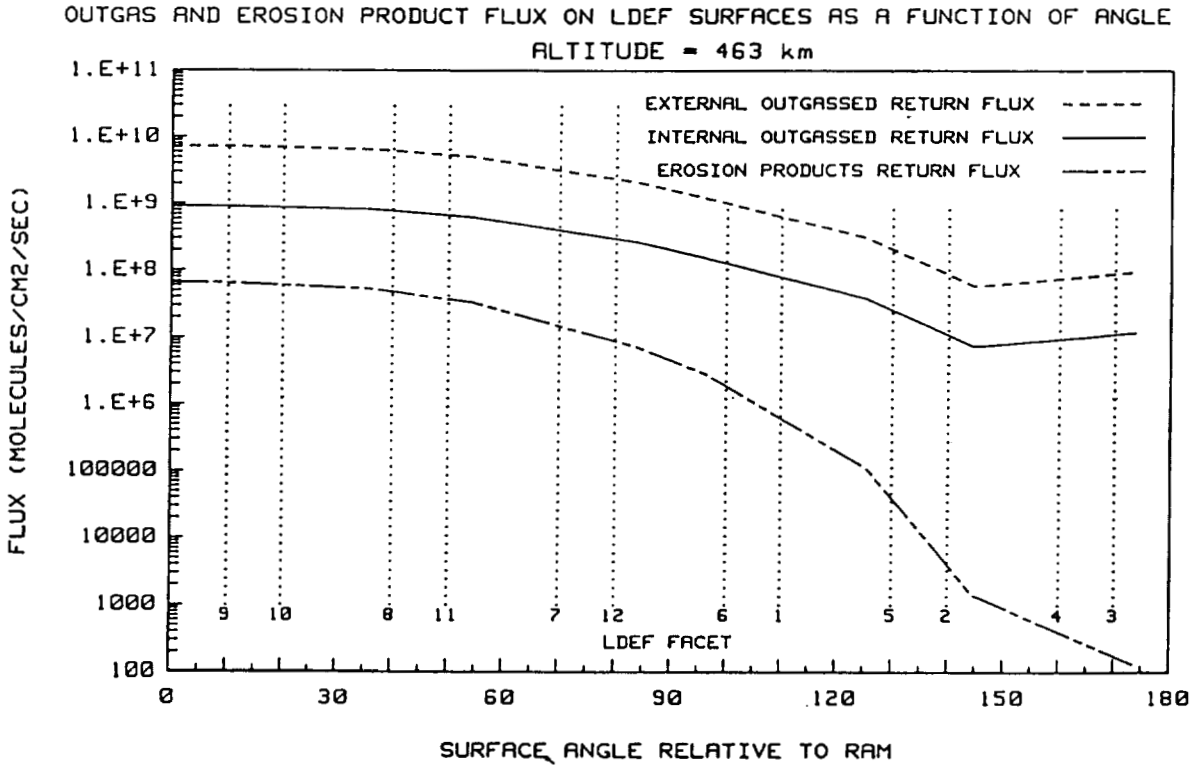

Figure 2. Results Using New Scattering Algorithm

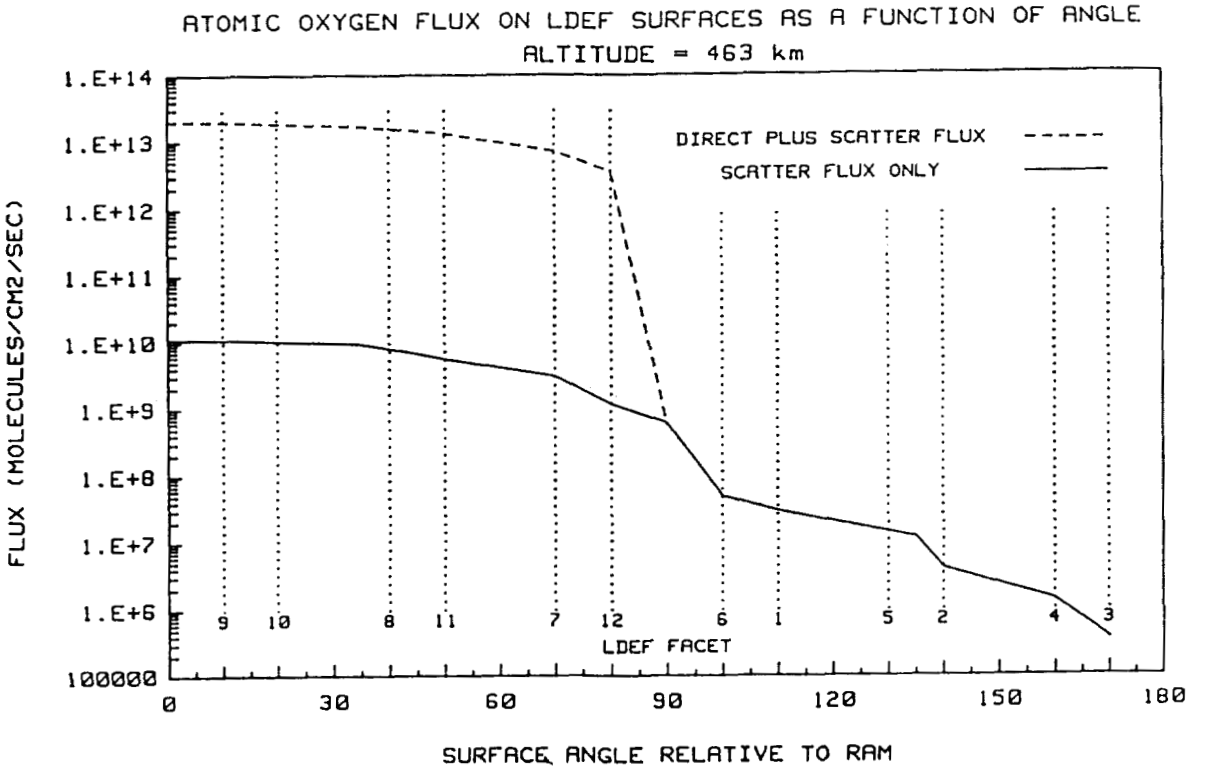

Figure 3. Results For AO Using Old Scattering Algorithm

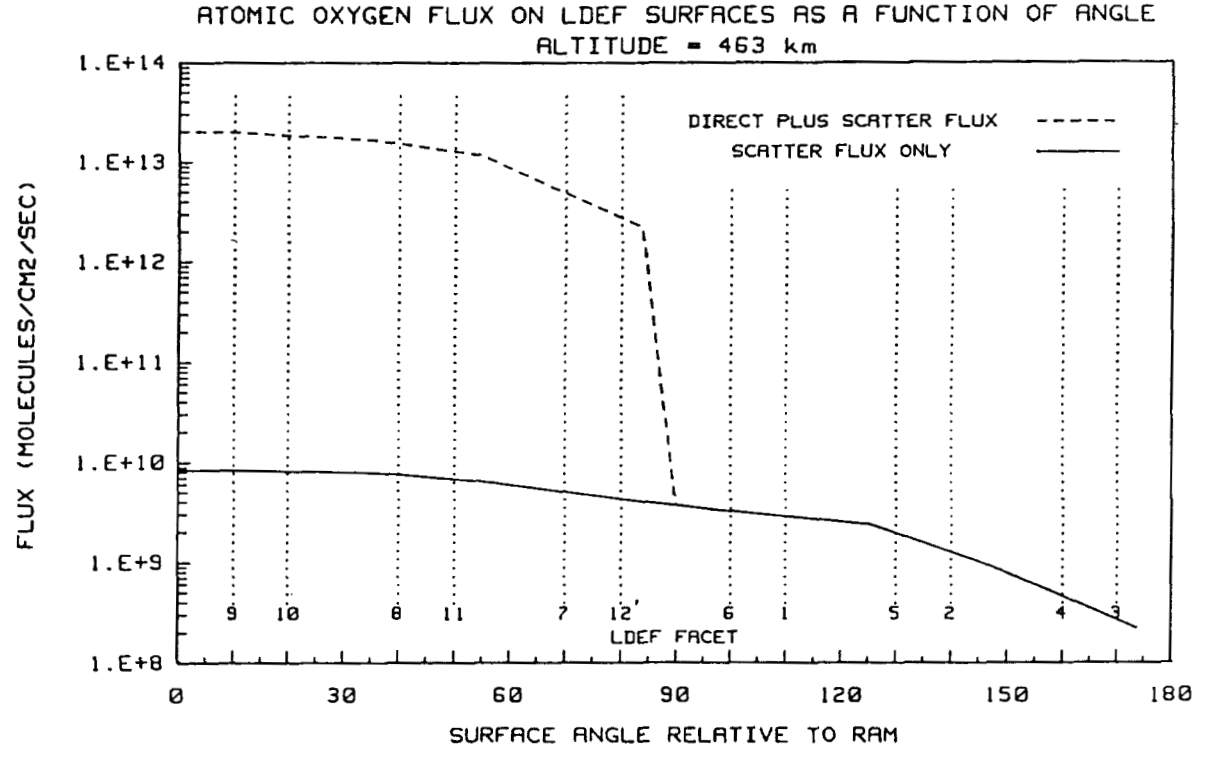

Figure 4. Results For AO Using New Scattering Algorithm

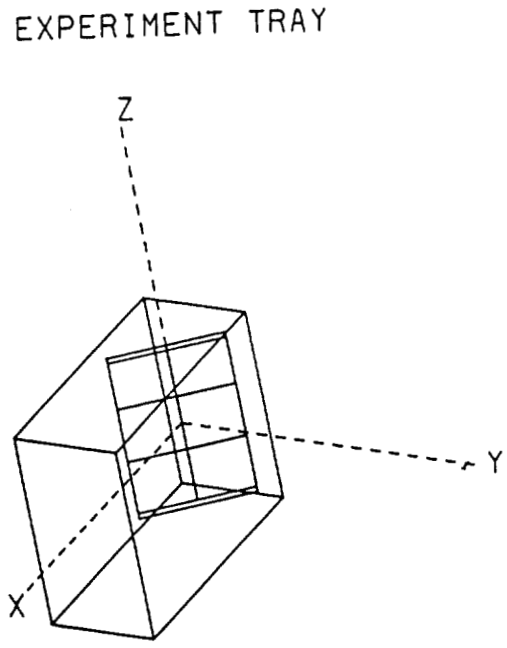

Figure 5. AO171 Experiment Tray Orientation

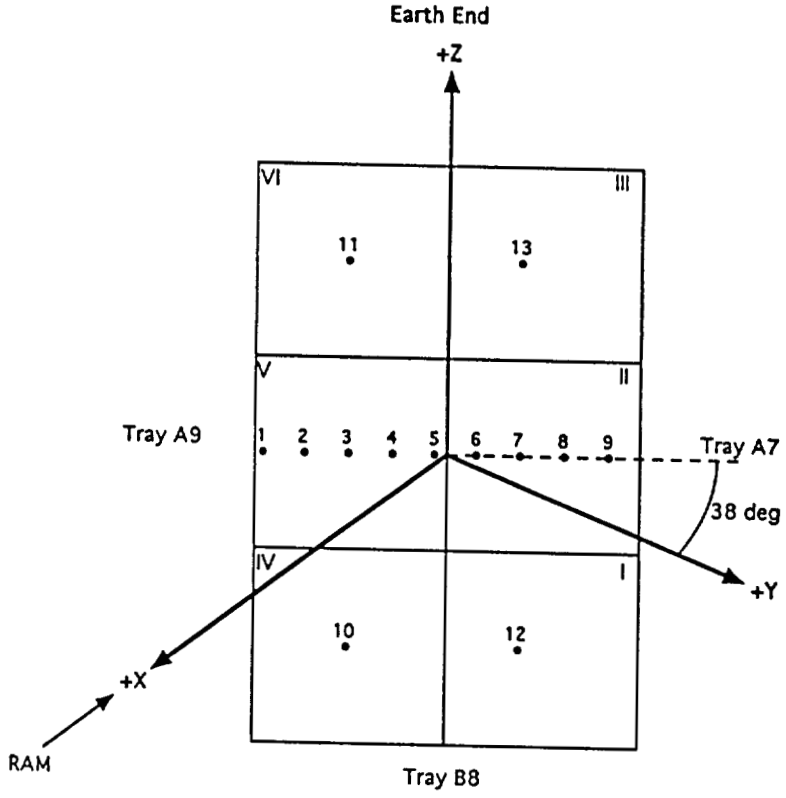

Figure 6. AO171 Model Flux Computation Points

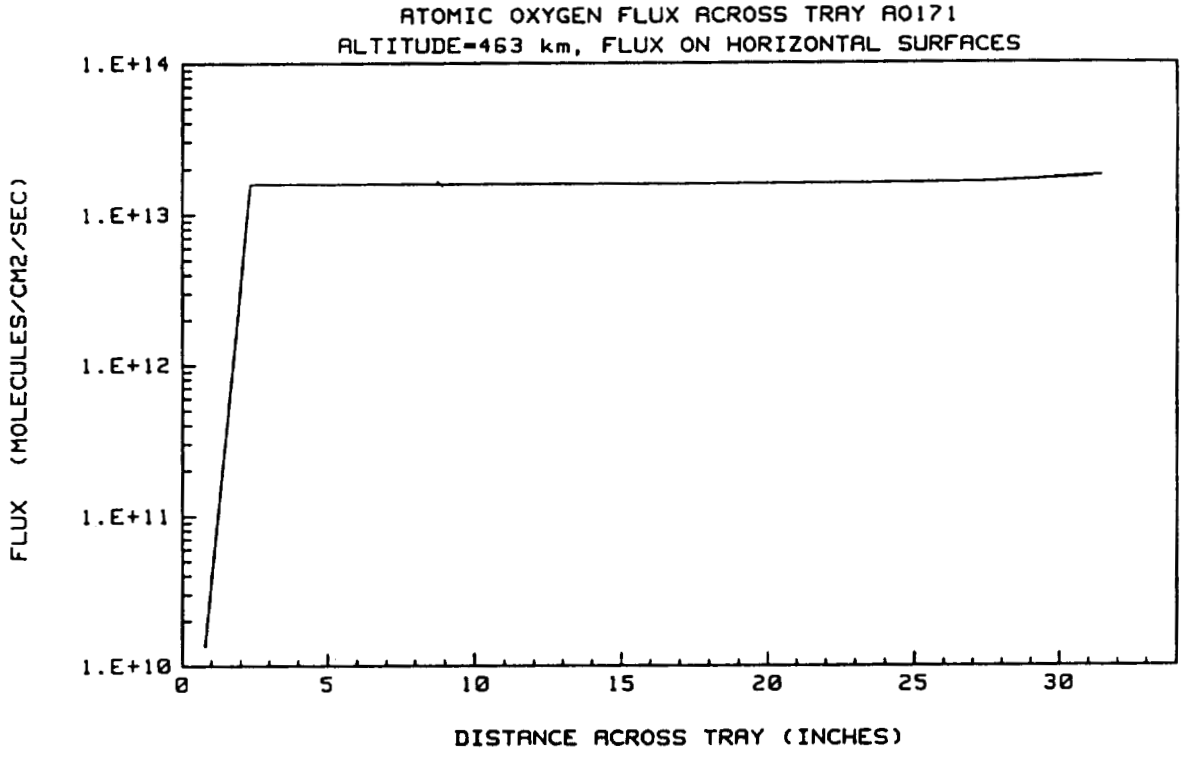

Figure 7. Atomic Oxygen Flux Across Tray

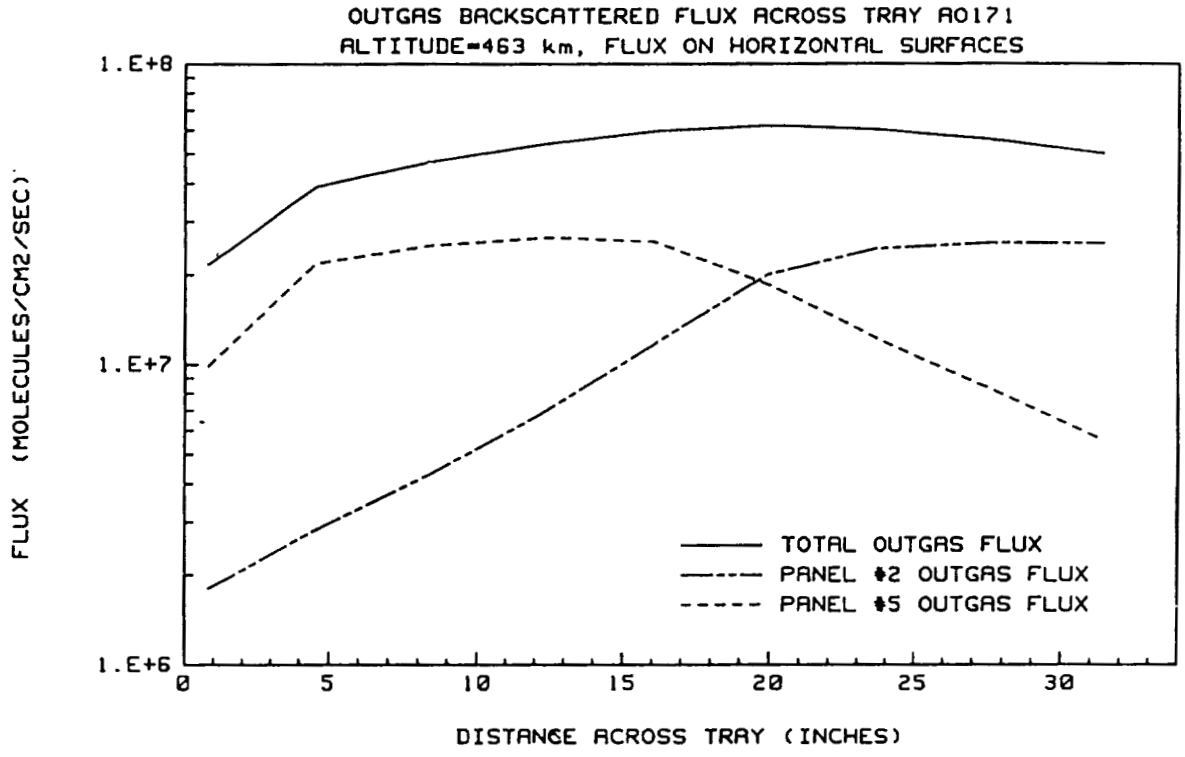

Figure 8. Outgas Backscatter Flux Across Tray

Micro Model

A micro model was utilized to develop fine detail around a sample that was on the tray. For this case a two inch by two inch by one quarter inch thick sample was used and was assigned the outgassing rates measured for RTV 511. It is mounted on a 4 x 4 inch square plate.The modeling volume for scattering was broken down into volumes less than a tenth of an inch in size. Figure 9 shows details of the geometry and the points to which the flux was calculated as a result of outgassing from the small sample and scattering interactions with the ambient. Figure 10 shows flux of atomic oxygen and outgassing downstream relative to the sample. The sharp rise in oxygen near 0.2 inches downstream is a result of shadowing by the sample. This is the region where discoloration is observed near samples on the tray.

CONCLUSIONS

From the results of the three models it appears that the flux of atomic oxygen correlates to the discolorations observed on the experiment. Darker discolorations received the highest atomic oxygen flux. Areas that should have received the same contaminant flux as the darker areas but no atomic oxygen, because of shadowing, were not discolored upon visual inspection.

The source of the contaminant is not clear at this time. The LDEF had outgassing occurring from external surfaces as well as outgassing from internal sources that leaked out and was scattered back to surfaces on the exterior. Similar discolorations were observed on interior surfaces that received atomic oxygen flux through openings to the exterior. This is further supported by the observation of heavy external discoloration near areas that received fluxes of internal outgassing through penetrations to the inside and simultaneous flux of atomic oxygen.

The overall LDEF model that was updated for this study shows that the scattered atomic oxygen flux on the wake surfaces was on the order of 10^{10} $cm^{-2}s^{-1}$ early in the mission while the flux of the ram surfaces was on the order of 10^{13} $cm^{-2}s^{-1}$. The flux of LDEF outgassing at 463 km was 10^8 to 10^9 in the wake region and 10^9 to 10^{10} $cm^{-2}s^{-1}$ on the ram side. Thus the AO scattered flux was comparable to the the scattered outgassed flux in the wake region at 463 km. At 333 km the AO flux was near 10^{15} $cm^{-2}s^{-1}$ on the ram side and 10^{10} $cm^{-2}s^{-1}$ on the wake surfaces. The outgassing scattered back to the surfaces was near 5×10^8 on the ram side and near 10^6 $cm^{-2}s^{-1}$ on the wake surfaces. The relative lower outgassing resulted from the drop in outgassing rates later in the mission.

The tray model showed that the return flux of contaminants to surfaces of the tray that originated from the tray were nearly the same.

The micro model of the nonmetallic sample showed that the atomic oxygen flux occurred about 0.2 inches downstream from the 0.25 inch thick sample. This kind of behavior was observed on the experiment where discolored areas appeared near the downstream side of the materials on the tray. Over the one inch downstream distance the outgas flux from the experiment varied over one order of magnitude.

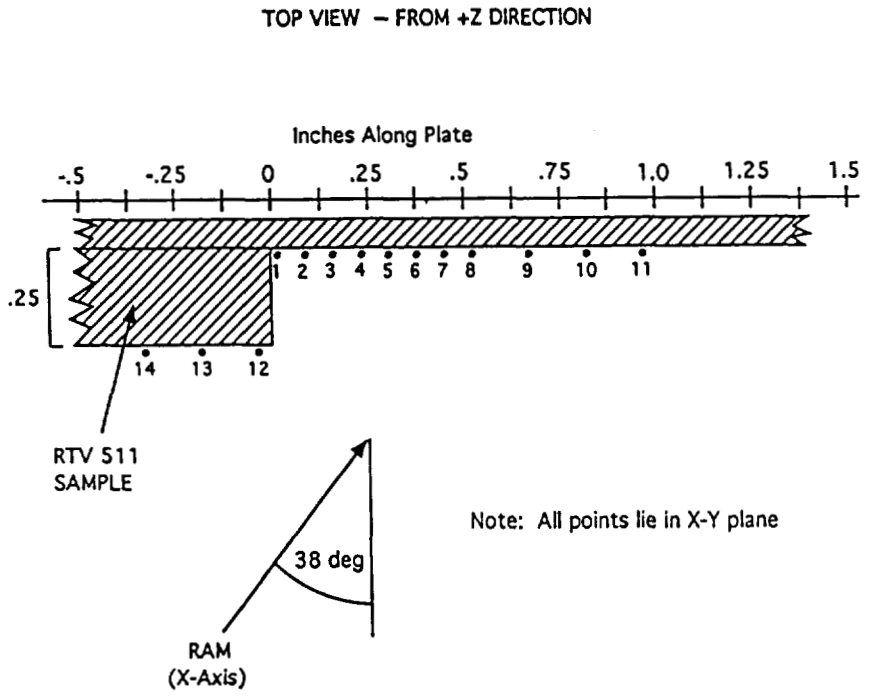

Figure 9. Micro Model Flux Computation Points

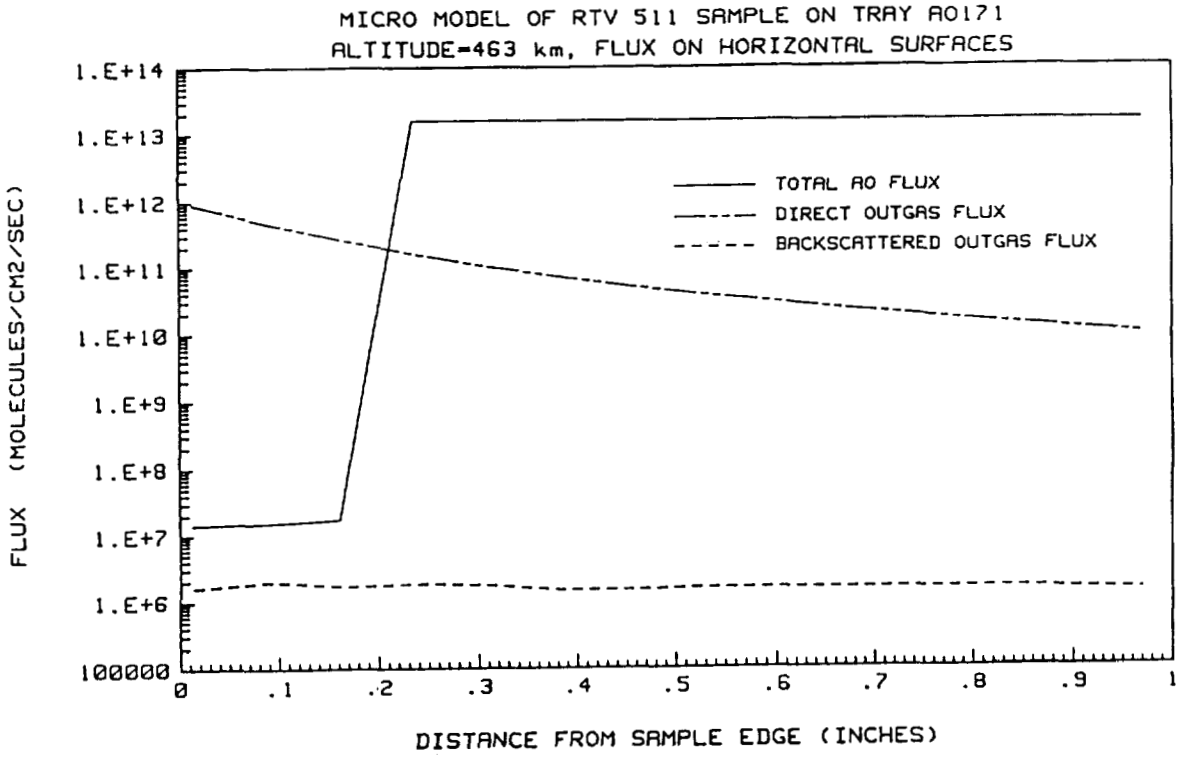

Figure 10. AO and Outgassing Flux

Because no large differences in deposition levels were predicted it is assumed that the pattern of discolorations observed on the experiment correspond to areas of high atomic oxygen flux that fixed the contaminants. Shadowing of the atomic oxygen flux, predicted by the models, corresponds to observations.

RECOMMENDATIONS

It is recommended that some additional modeling be performed to further determine the sources of contaminants. This would include modeling the openings to the interior at the corners of the tray and scattering them back to the surfaces on the tray. The scattering back to surfaces from the large gas cloud that surrounds LDEF can also be included in the tray model and the micro model. However, the flux direction from this large cloud should be very nearly the same as the flux direction of atomic oxygen since the oxygen is one of the prime scatterers of the contaminants.

REFERENCES

1.Erlandson, R.E. and Joyce, P.J., "Observational Plans to Characterize the Contaminant Environment of a Suborbital Vehicle", Proceedings of the Vehicle-Environment Interactions Conference, 11-13 March 1991, John Hopkins University.

2.Gordon, T.D., "Integrated Spacecraft Environments Model User's Guide. Version 5.1", Applied Science Technologies, AST 12.3B, April 1993.

3.Rantanen,R.O. and Gordon, T. D., "LDEF Contamination Modeling" Presented at LDEF Materials Workshop, 19 November 1991.

4.Rantanen, R.O. and Gordon, T. D., "LDEF Experiment AO171 Contamination Modeling", Final Report ROR-MSFC-1-93, 1 October 1993. Delivered to NASA, MSFC.

OUTGASSING PRODUCTS FROM ORBITER TPS MATERIALS

Gale A. Harvey, Tom J. Lash, and J. Richard Rawls
NASA Langley Research Center
Hampton, VA 23681-0001
Phone: 804-864-6742, FAX 804-864-7790

ABSTRACT

The Space Transportation System (STS) orbiters are known to be significant sources of outgassing in low earth orbit (LEO). Infrared and mass spectra of residues and outgassing from orbiter thermal protection tile and an external blanket are presented. Several sources of methyl and phenyl methyl silicones are identified. About fifty pounds of silicones are estimated to be outgassed during an STS mission.

INTRODUCTION

On-orbit contamination of the payload bay was reported for the early shuttle flights (Ref. 1). Several of these measurements showed more than 5 mg/0.1m^2 (5 mg/ft^2) molecular depositions and it was concluded that, "some sensitive experiments would require protective action." Later, many experimenters identified silica films or silicon-rich films on LDEF surfaces and experiments. References 2-9 are a partial list of early reports of atomic silicon or silica (SiO_2) by surface analyses. Reference 10 reports multiple laboratory analyses of the Z306 black paint and primer, used on the LDEF, which show no silicones in the paint or primer. Reference 11 reports that the films on the space exposed surfaces of optical windows in Tray E5 were primarily silica. Reference 11 also reports silicone outgassing in the Payload Changeout Room (PCR) at Kennedy Space Center (KSC). Reference 12 reports silicone residues (chemical reaction products) from the orbiter rewaterproofing compounds and chemical reversion of the Thermal Protection System (TPS) adhesive, RTV 560, caused by the rewaterproofing compound, hexamethyldisilizane (HMDS), Ref.13, used for the LDEF deployment mission. The outgassing of silicones from Atlantis was measured on STS 44 (Ref. 14) and is probably a major source of silicone contamination (up to 26 mg/0.1m^2) seen on attached instruments flown on Atlantis during STS 45 and 46 (Ref. 15). The silicon contamination on attached instruments was reported at two Technical Interchange Meetings (November 1992, Johnson Space Center (JSC) and August 1993, KSC) on STS Payload Contamination.

This paper reports significant outgassing of TPS tile and external flexible insulation blanket (FIB) from the Columbia, at ambient (unheated) temperatures. These outgassing tests indicate that tens of pounds of phenyl methyl silicones are outgassed by the orbiters in LEO during a typical STS mission. Most STS payloads are not adversely affected by this outgassing. However, understanding of the orbiters' outgassing environment is needed for instrument and spacecraft designers and mission operators to minimize contamination of sensitive instruments. High spectral stability optical instruments, low friction mechanical devices, micrometeoroid chemical analyses experiments, and thin film materials are examples of possible contamination sensitive experiments.

CLEANLINESS MEASUREMENTS OF ATLANTIS AND COLUMBIA

Most of the surface chemistry analyses of LDEF which revealed silica films were performed with scanning electron microscopes (Refs. 3-5). However, the silica films can also be detected on suitable substrates by the 10-micron SiO absorption in the infrared spectrum (Ref. 11). A calcium fluoride optical window was flown on STS 46 and the pre- and post-flight IR spectra are shown in Figure 1. The SiO_2 thin glass film absorption is the only contamination indicated by IR spectroscopy. This spectrum and surface analysis of a quartz crystal microbalance housing flown on the same flight indicate quick and nearly complete conversion of silicone contamination to glass films by solar ultraviolet and/or atomic oxygen.

Cleanliness wipes of the orbiter Columbia using twice Soxhlet extracted polyester wipes and analytical grade isopropyl alcohol were performed November 17, 1992. Six wipes were taken in the payload bay and showed about one milligram/0.1m^2 of mostly esters (Table 1). One wipe (#7) of an external FIB

about midway along the fuselage gave 0.35 mg/.1m^2 of NVR that was mostly methyl silicone (Figure 2). These measurements indicate that most of the silicone outgassing of the orbiters is from external surfaces.

Similar wipes reported by a KSC group at the second technical interchange meeting (TIM) on STS payload contamination showed the payload bays of Columbia, Discovery, and Endeavor to generally have less than one mg/0.1m^2 of molecular films and these films were not silicones.

TRANSPORT MECHANISM OF ORBITER OUTGASSING

The long ambient mean-free-path in LEO (~ 2km at 300km altitude, Ref. 16) was cited at the first TIM on STS payload contamination as a reason that outgassing from external orbiter surfaces could not return to the payload bay. In other words, it was alleged there was no transport mechanism for return flux of outgassing from the orbiter. However, Reference 17 reported on-orbit pressures of 10^{-5} to 10^{-6} Torr which correlate to mean-free-paths of 25 to 700 cm (Ref. 16). Reference 18 reports on-orbit pressures in the payload bay for early STS missions of 4.4 x 10^{-4} Torr (mean-free-path ~12 cm) to 8.3 x 10^{-6} Torr (mean-free-path ~620 cm). The microatmosphere (orbiter glow) around an orbiter has been photographed (Ref. 19). The microatmosphere is mostly outgassing H_2O, N_2, and O_2 from adsorbed surfaces and trapped volumes of the orbiter. Thus, there is a transport mechanism for return flux on STS missions.

TPS MATERIALS AND CLEANLINESS

The rewaterproofing compounds immediately react with water to produce silanols which then react to form silicones which can outgas later (Ref. 11). However, other silicon based materials are also used in the orbiter's thermal protection system (Table 2). RTV 577 is a calcium oxide filled (white) phenyl methyl silicone used as a screed or filler between the orbiter body and the TPS. RTV 560 is an iron oxide filled (red) phenyl methyl silicone with high heat conductivity that is used as the TPS adhesive (Ref. 12). The black RTV is a methyl silicone used as gasket material on doors and hatches. The amount of RTV 560/orbiter was calculated by weighing 1 inch square of adhesive from the back of a damaged tile, and an FIB and multiplying by the TPS surface area (1200 m^2) of the orbiter (Ref. 12). A similar mass was estimated from visual inspection for the RTV 577. The amount of black RTV was obtained from the material replacement log for an orbiter refurbishment.

A 1/2 inch cubed section from the back of a 0.025m^2 TPS tile (Fig. 3) was extracted by soaking in analytical grade isopropyl alcohol for 30 minutes. The infrared spectrum of the residue (Fig. 4) is that of phenyl methyl silicone and is identical to that from RTV 560. A similar size section from the interior or core of a tile was also extracted. The infrared spectrum of residue from the core of a tile (Fig. 5) shows the same phenyl methyl silicone and indicates that outgassing from the RTV 560 is absorbed within the tile. A similar amount of debris (0.5 in^3) from an FIB (Fig. 6) removed from Columbia in September 1992 also had phenyl methyl silicone NVR (Fig. 7). However, the non-volatile residue (NVR) from a TPS gap filler was mostly esters .

The TPS tile (Fig. 3) was placed in a high-vacuum chamber (~10^{-7} Torr) and the outgassing at ambient temperature was measured with a mass spectrometer. The chamber background spectrum and the tile outgassing spectrum are shown in Figure 8. The heavy mass fragments are listed in Table 3 and show that the outgassing is phenyl methyl silicone. The absence of mass fragments 147 and 149 shows that the outgassing is not methyl silicone, or alkyl phthalates (the most common NVR on LaRC flight hardware). Similar outgassing measurements of TPS tile (Ref. 20) at Marshal Space Flight Center (MSFC) in 1975 also showed about one gram/0.1m^2 of phenyl methyl silicones.

The FIB from Columbia (Fig. 6) was placed in the same high-vacuum chamber and exposed to high vacuum at ambient temperature (27°C) for 3 days. The mass spectrum of outgassing from the FIB (Fig. 9) is identical to that from the TPS tile. More than 1- 1/2 grams of clear fluid was collected on the scavenger plate maintained at -100°C during this test. This corresponds to about 20 lbs of phenyl methyl silicone outgassing from an orbiter over 3 days in LEO, or an estimated 50 lbs of silicone outgassing over a 9- to 12- day mission. An IR spectrum of the clear fluid is presented as Figure 10. A similar test of a 0.4 m^2 beta

cloth/multilayer insulation blanket flown on EURECA showed no silicone outgassing. Similar outgassing measurements of felt reusable surface insulation (FRSI), Ref. 20, at JSC in 1976 also showed about one gram/0.1m^2 of residue.

Another type of evidence of outgassing of TPS materials is shown in Figures 11 and 12, photographs of black ceramic TPS tiles taken immediately after mission STS-49, the maiden flight of the Endeavor. Figure 11 is a closeup photograph of discolored tiles aft of the nose landing gear door, and Figure 12 is a photograph of heavy outgassing deposits on the elevon leading edge. In most cases the white color results from diffuse scattering of light from glassy deposits. The entire tile surface (black and white, Fig. 5) appears, under a 80X microscope, to be coated with a thin transparent film. Some of the white areas are pits which are partially filled in. The heavy white streams are multiple crazed and fused layers of relatively thick glass deposits. The black ceramic tile are good optical witness plates because of the high contrast and the flat surfaces which aid microscope examination.

A small data base of flight hardware cleanliness measurements has contributed to much confusion in the past regarding outgassing from the orbiters.

Several groups have been extremely helpful to the present study of outgassing of the orbiters. This work would not have been possible without their professional integrity and technical competence. We wish to acknowledge especially Jaime Palou and Frank Jones for their essential contributions.

CONCLUSIONS

Outgassing of large amounts of silicones by the orbiters has been confirmed by several independent measurement techniques (spacecraft and attached instrument glass films and silicone residues, surface wipes, IPA extraction of TPS materials, vacuum outgassing of TPS tile and blanket, and photographs of glassy deposits on TPS tiles). The LDEF and many shuttle attached instruments have experienced depositions of silicones which were converted to glass in LEO. The ubiquitous nature of these silicone-to-glass films strongly indicated sources within the orbiters. Several orbiters' TPS materials have been shown to significantly outgas silicones in LEO. In particular, vacuum outgassing measurements show the TPS adhesive, RTV 560, and the screed filler, RTV 577, can be expected to outgas about 50 lbs of silicones during a typical mission. There was probably even more outgassing of silicones from the Challenger during deployment of LDEF (STS-41C) due to the wide spread reaction with hexamethyldisilizane, the TPS rewaterproofing compound used for that mission.

REFERENCES

1. Ehlers, H. K. F., Jacobs S., and Leger, L. J.: Space Shuttle Contamination Measurements from Flights STS-1 Through STS-4, J. Spacecraft, Vol. 21, 3, pp. 301-308, 1984.

2. Cruther, E. R. and Warner, K. J.: Molecular Films Associated with LDEF, NASA CP-3134, pp. 155-159, 1992.

3. Horz, F. et al.: Preliminary Analysis of LDEF Instrument A0187-1 "Chemistry of Micrometeoroids Experiment", NASA CP-3134, pp. 487-501, 1992.

4. Sachiko, A. et al.: SIMS Chemical Analysis of Extended Impact Features from the Trailing Edge Portion of Experiment A0187-2, NASA CP-3134, pp. 503-516, 1992.

5. Simon, C. G. et al.: Ion Microprobe Elemental Analysis of Impact Features on Interplanetary Dust Experiment Sensor Surfaces, NASA CP-3134, pp. 529-548, 1992.

6. Young, P. R., and Slemp, W. S.: Chemical Characterization of Selected LDEF Polymeric Materials, NASA CP-3134, pp. 687-703, 1992.

7. Blakkolb, B. D. et al.: Long Duration Exposure Facility (LDEF) Preliminary Finding, NASA CP-3134, pp. 737-752, 1992.

8. Hemminger, C. S. and Stucky, W. K.: Space Environmental Effects of Silvered Teflon Thermal Control Surfaces, NASA CP-3134, pp. 831-846, 1992.

9. Levadou, F. et al.: Preliminary Investigations into UHCRE Thermal Control Materials, NASA CP-3134, pp. 875-898, 1992.

10. Golden, J. L.: Z306 Molecular Contamination Ad Hoc Committee Results, NASA CP-3162, pp. 115-140, 1992.

11. Harvey, G. A., "Sources and Transport of Silicone NVR," Proc. of LDEF Materials Workshop, November 1991, NASA CP 3162, pp. 175-184, 1992.

12. Harvey, G. A., "Silazane to Silica," Proc. of Second LDEF Post-Retrieval Symposium, June 1992, NASA CP 3194, Part 3, pp. 797-810, 1993.

13. Hill, W. L.; and Mitchell, S. M., "Certification of Rewaterproofing Agent for Shuttle Thermal Protection Systems," 199th Am. Chem. Soc. Conf., Boston, MA, April 1990.

14. Maag, C. R.; et al., "Result of the Interim Operational Contamination Monitor (IOCM) as Flown on the STS-44 Mission," Final Report, Cal. Tech. J. P. L., 1992.

15. Williams, D.; Maag, C. R.; and Straka, S., In-house communications, Technical Interchange Meetings on STS Payload Contamination, Nov. 1992 and August 1993.

16. Anon., U. S. Standard Atmosphere, 1962, U.S. Government Printing Office, December 1962.

17. Santeler, D. J. et al., "Vacuum Technology and Space Simulation," NASA SP-105, 1966.

18. Scialdone, J. J., "Shuttle Measured Contaminant Environment and Modeling for Payloads," NASA TM 85111, Dec. 1983.

19. Tribble, A. C., "Designing for the Space Environment," Aerospace America pp 26-29, May 1993.

20. Jex, D. C., "The Outgassing Rate for a Shuttle Thermal Protection Surface Using RTV 560 Adhesive," NASA SP-379, pp 321-341, 1975.

21. Visentine, J. T., Richmond, R. G., and Kelso, R. M., "Molecular Outgassing Measurements for an Element of the Shuttle Thermal Protection System," AIAA 11th Thermophysics Conf., San Diego, CA, July 14-16, 1976.

TABLE 1 - CLEANLINESS WIPES OF COLUMBIA (11/17/92)

Wipe #	Location	Evaporation dish	Weighing pan
1	Port sill X775.5	Much fluid and particles	Mostly fluid
2	Sill near monkey fur seal	Some particles, a little fluid	Unmixed fluids
3	PL support equip, B5	Much fluid	Much fluid, fibers
4	PS, B5 cable tray	Mostly particles, some fibers	Fluid, fibers,
5	PS, B5/6, cable tray	Mostly particles, gel	Mostly fluid
6	Avionics shelf, B5	Fluid, fibers, particles	Fluid, fibers, particles
7	Port fwd BLBD exterior	Mostly dust (fine particles)	Mostly particles

Wipe #	Recovered mass(mg)	IR	Comments
1	0.79	Mostly esters	6" x 6" wipe of sill
2	0.17	90% fluorocarbons (Braycote)	
3	2.78	~ 70% HC, 25% CH_3SiO	
4	1.01	Mostly esters	
5	0.62	CH_3SiO and esters	
6	1.11	Mostly esters	
7	0.35	90% CH_3SiO	

TABLE 2-ORBITER TPS SILANES

Compound	~Amount
DMES-dimethylethoxy silane	200 lbs/mission
RTV 560 (red RTV)	1200 lbs
MTMOS-methyltrimethoxy silane	
TEOS-tetraethyl orthosilicate	10 lbs
LUDOX-colloidal silica	2 lbs/mission
MBO 124-085(Scotchguard)	2 lbs
Black RTV	10 lbs/mission
RTV 577 (white RTV)	1200 lbs

TABLE 3 - MASS FRAGMENTS FROM TPS TILE

AMU	Mass Fragments Present
73	$(CH_3)_3Si^+$
78	C_6H6^+
135	$(CH3)_2C_6H_5Si^+$
197	$(CH_3)(C_6H_5)_2Si^+$
	Mass Fragments Missing
147	$(CH_3)_3SiO(CH_3)_2Si^+$
149	alkyl phthalates

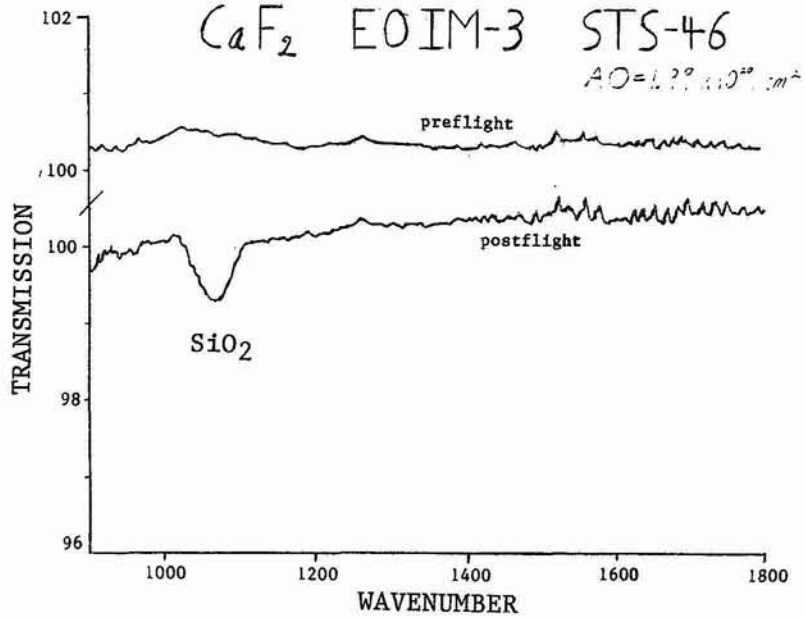

Figure 1. IR spectrum of SiO_2 on CaF_2 window flown on STS-46.

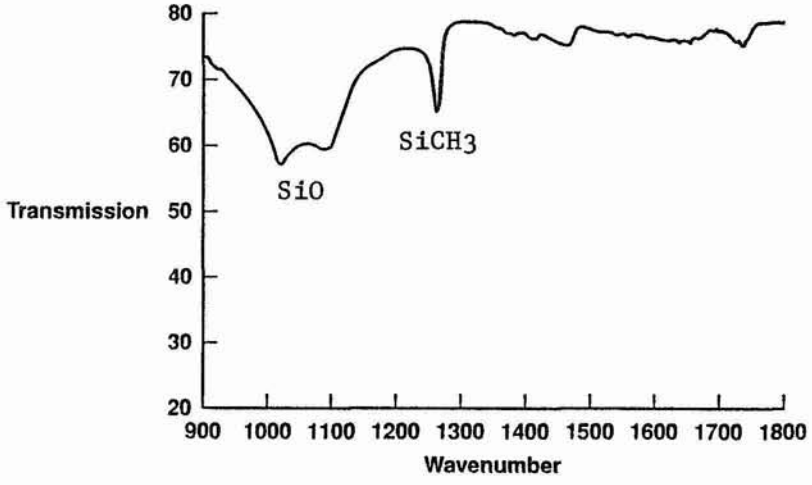

Figure 2. IR spectrum of NVR from Columbia FIB.

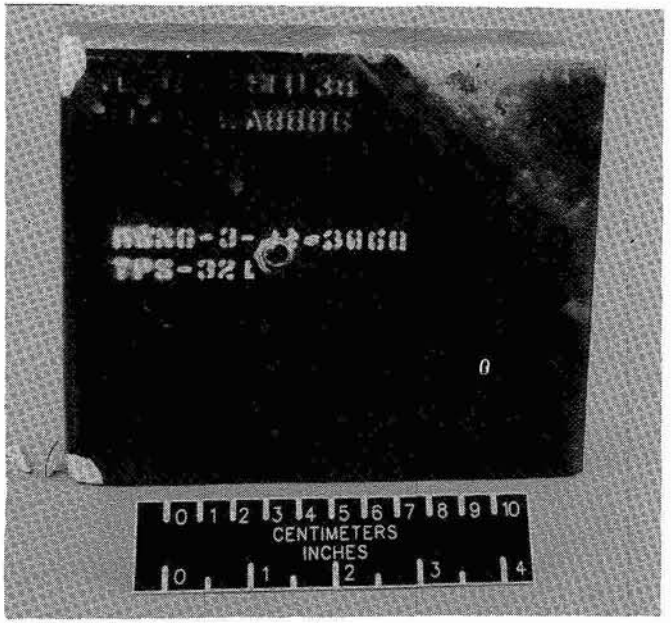

Figure 3. Photograph of a TPS tile.

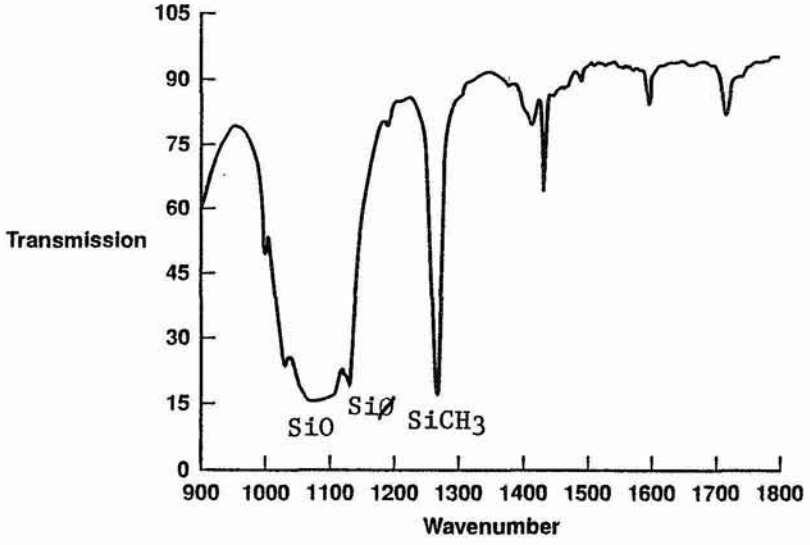

Figure 4. IR spectrum of NVR from back of TPS tile.

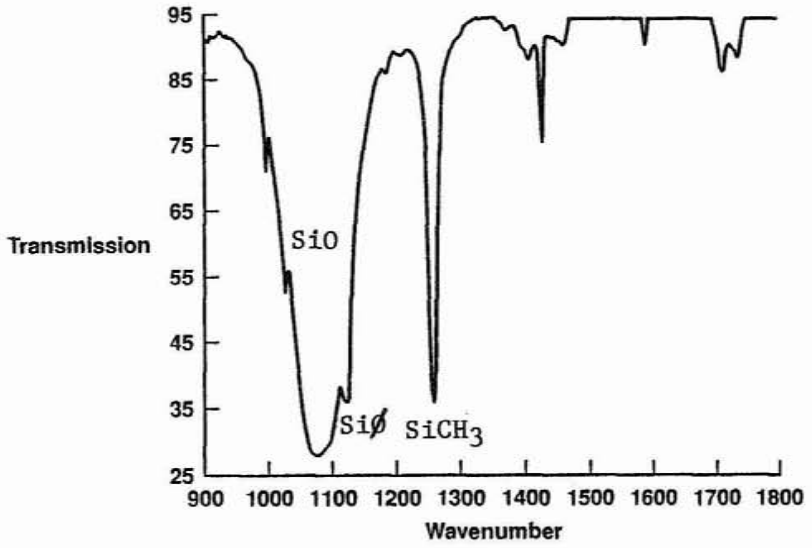

Figure 5. IR spectrum of NVR from core of TPS tile.

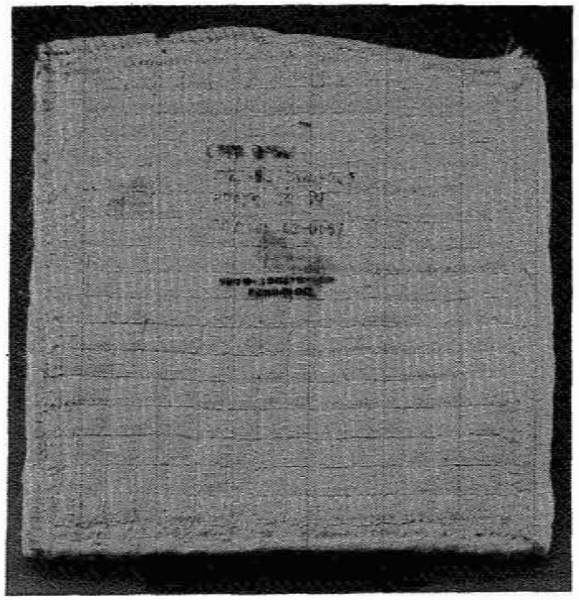

Figure 6. Photograph of FI blanket from Columbia.

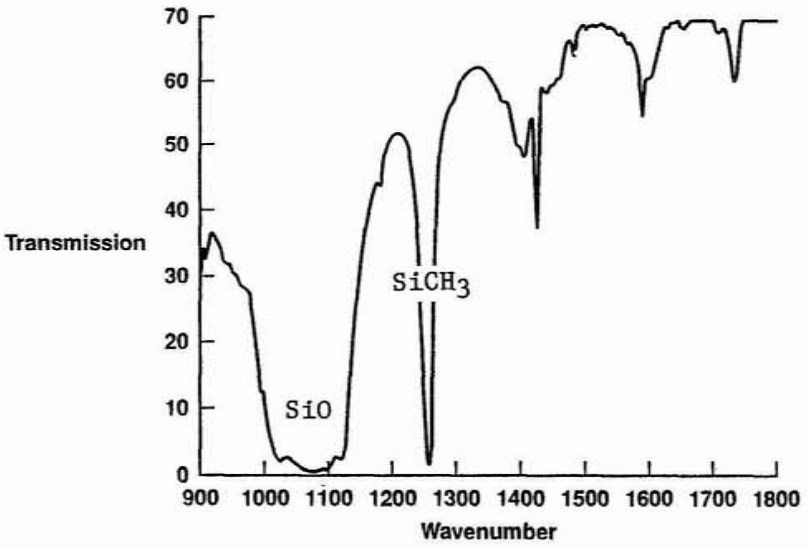

Figure 7. IR spectrum of NVR from FIB debris.

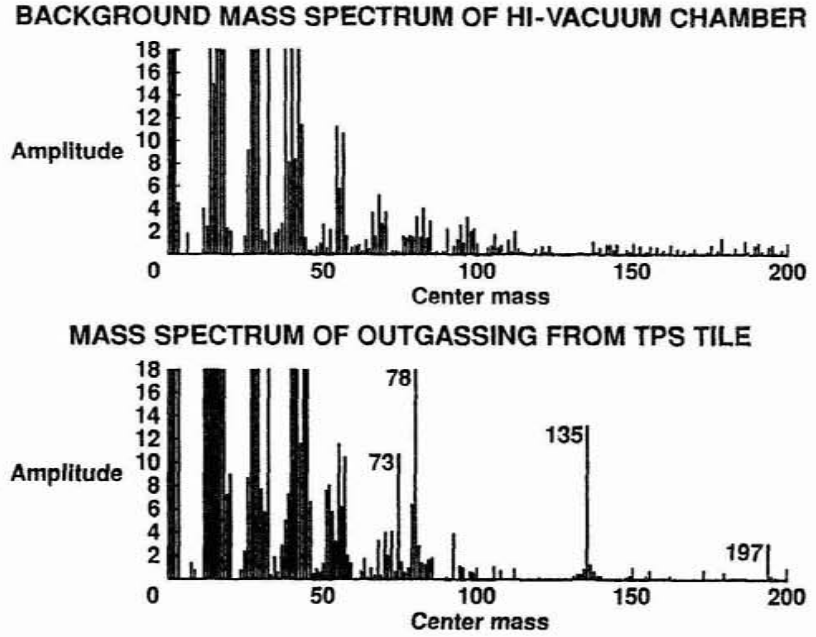

Figure 8. Mass spectrum of outgassing from TPS tile.

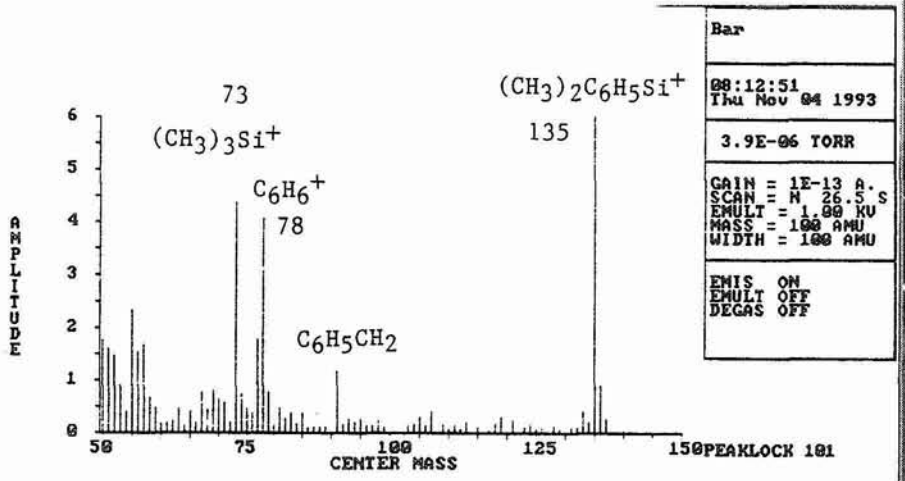

Figure 9. Mass spectrum of outgassing from Columbia FIB.

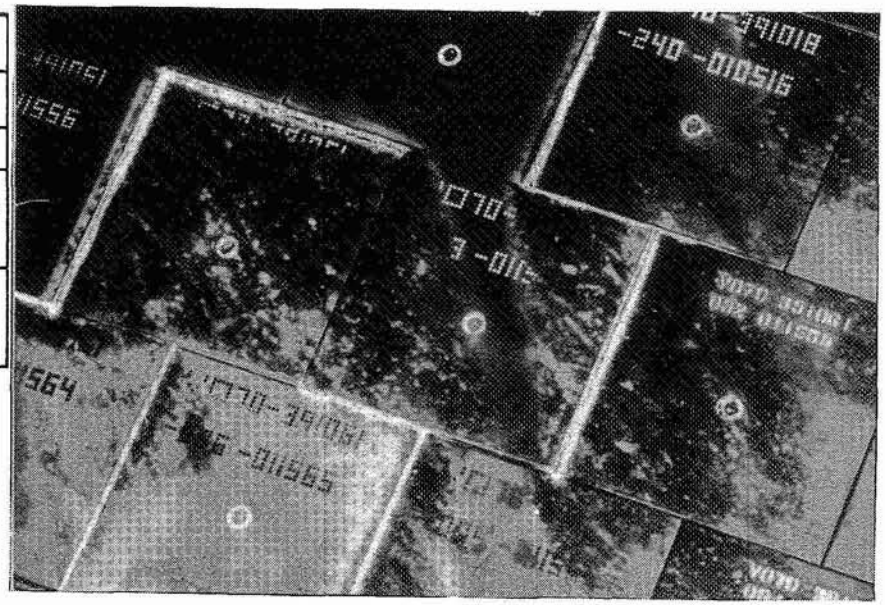

Figure 11. Discolored tile aft of Endeavor Landing Gear door (May 1992).

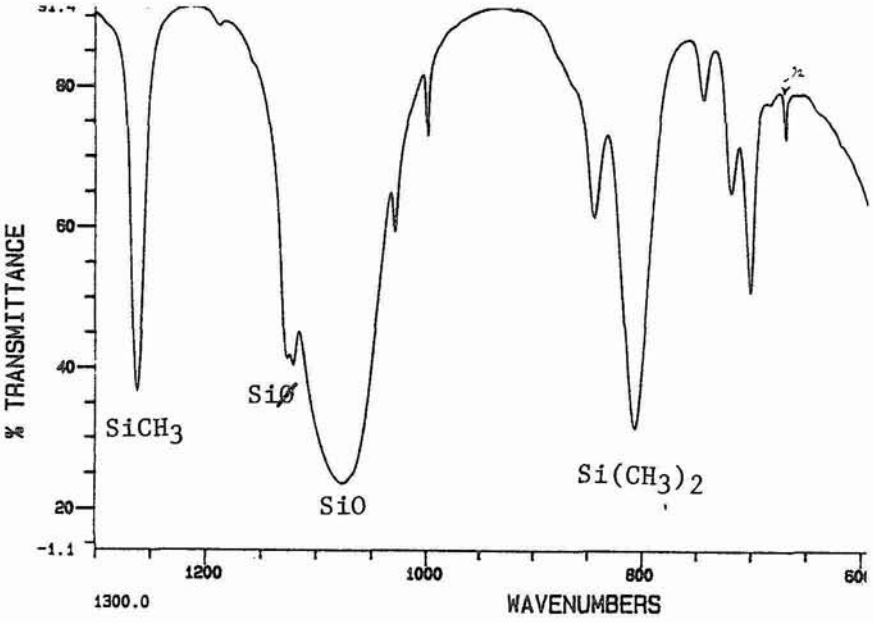

Figure 10. IR spectrum of trapped NVR from Columbia FIB.

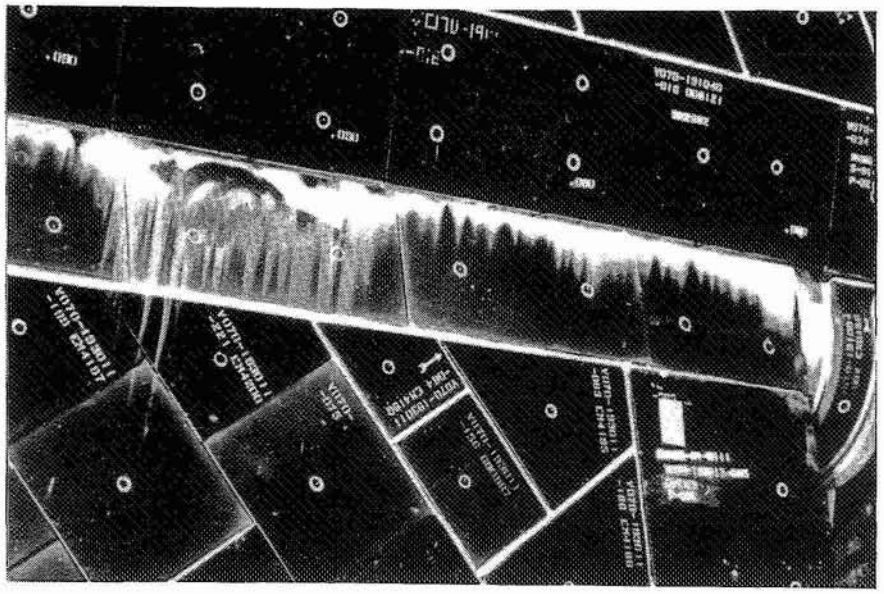

Figure 12. Heavy outgassing deposits on the elevon leading edge of Endeavor (May 1992).

EUROPEAN RETRIEVABLE CARRIER (EURECA)

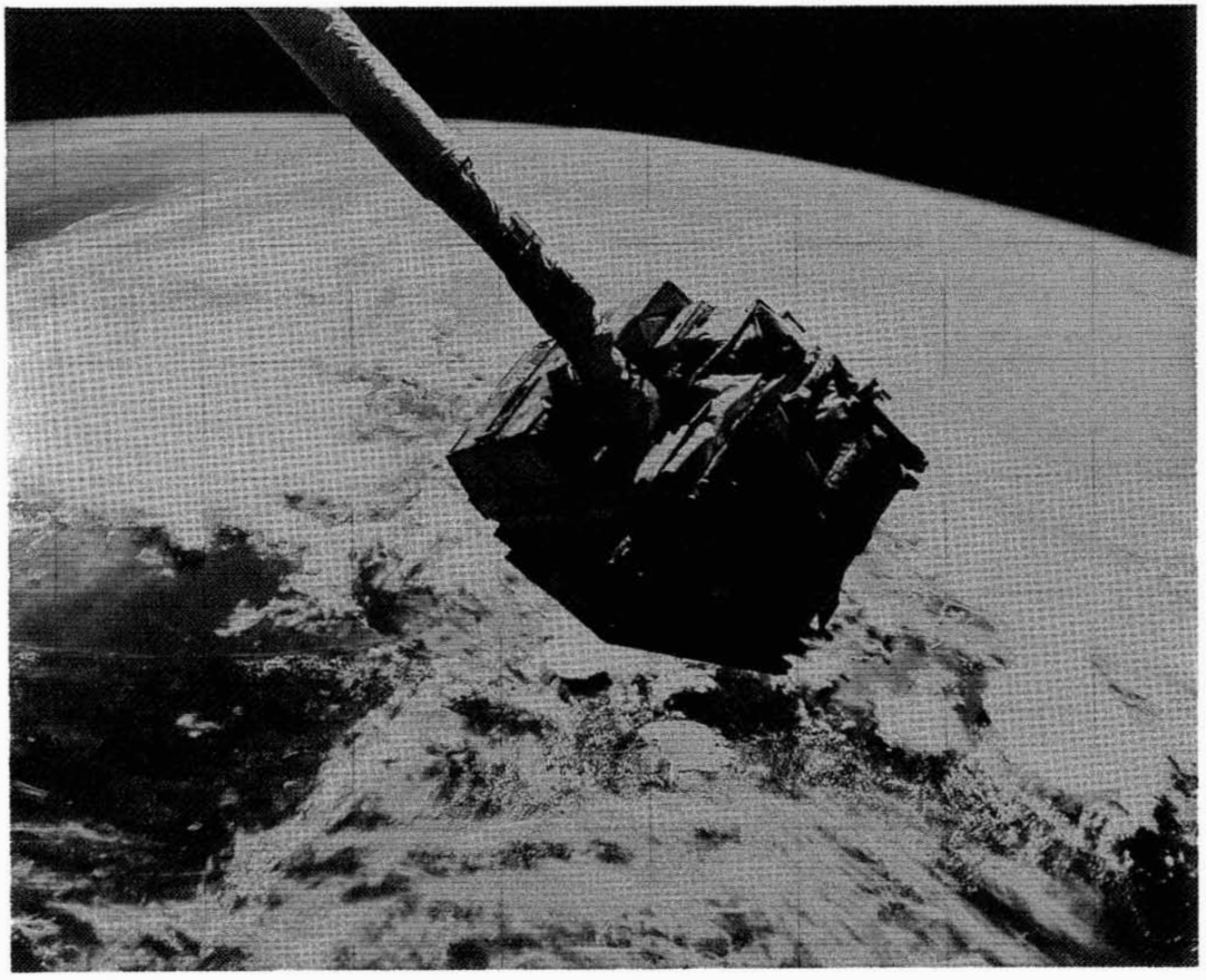

EURECA 11 MONTHS IN ORBIT

INITIAL POST FLIGHT INVESTIGATION RESULTS

Alan Dover, Roberto Aceti and Gerhard Drolshagen
ESA/ESTEC
2200 AG Noordwijk, The Netherlands
Phone 31.17198.3386, Fax 31.17198.4499

SUMMARY

This paper gives a brief overview of the European free flying spacecraft 'EURECA' and the initial post flight investigations following its retrieval in June 1993. EURECA was in low earth orbit for 11 months commencing in August 1992, and is the first spacecraft to be retrieved and returned to earth since the recovery of LDEF.

The primary mission objective of EURECA was the investigation of materials and fluids in a very low micro-gravity environment. In addition other experiments were conducted in space science, technology and space environment disciplines. The European Space Agency (ESA) has taken the initiative in conducting a detailed post-flight investigation to ensure the full exploitation of this unique opportunity.

INTRODUCTION

Ten years ago the ESA identified the need for a retrievable free flying carrier system which would provide flight durations well beyond the 7 to 10 days possible with Spacelab and SPAS. The development of the EUropean REtrievable CArrier (EURECA) was initiated in 1984 with a design and qualification requirement to give a capability for 5 missions of approximately 6 to 9 month's duration. It is Europe's largest and first reusable spacecraft. The second mission is now planned, subject to budget approval, for 1997.

The EURECA programme represents a unique opportunity to undertake a post flight inspection and to compare with the LDEF findings. While this was never a planned goal for the EURECA mission every attempt is being made by the ESA to exploit this opportunity.

EURECA CONFIGURATION

The EURECA flight configuration, often called EURECA-1, consists of the spacecraft and the payload. Figure 1 shows EURECA in its retrieval/launch configuration, with the solar array stowed.

The spacecraft consists of a platform providing accommodation and resources to the payload. The external surface is almost entirely covered by thermal blankets. Exceptions are the radiators and some boxes mounted on the bottom of the spacecraft, which are painted, and the solar array wings. The area of the exposed external surface is about 145 m2, including 99 m2 of solar array's front and rear surfaces.

The overall configuration of the spacecraft was primarily determined for a maximum payload volume, while minimising Shuttle launch costs. This resulted in an optimum spacecraft length to mass ratio. The spacecraft dimensions are 2.3 m (90.55") deep with the solar arrays retracted, and 4.5m (177.16") diameter to fit within the static envelope of the orbiter. With the solar arrays deployed the wing span is 20 m (785.67"). The mass at launch was slightly less than 4500 kg including 660 kg of hydrazine.

A brief description of the EURECA subsystems and payloads is given in the following.

SPACECRAFT

Structure

The structure consists of a framework of high strength carbon fibre struts, joined together at titanium nodal points. The nodal points are designed either to carry directly the loads of heavy equipment or to allow the mounting of secondary structure aluminium plates, called Equipment Support Panels (ESP) where the lighter boxes and instruments are fastened. In the launch configuration three trunnions (two sill and one keel) provide the load carrying interface to the Shuttle.

To assist deployment and retrieval the spacecraft was fitted with a NASA supplied grapple fixture. At the end of the mission there was evidence of a few micro meteoroid impacts.

Thermal Control

The Thermal Control Subsystem (TCS) task is to ensure that the spacecraft equipment and payload instrument interface temperatures are maintained within the allowable limits in all mission phases. This task is performed by using passive and active thermal control means.

Passive thermal control is principally by the use of Multi Layer Insulation (MLI) blankets (see Fig. 2) and finishing materials. The MLI blankets were found after the mission to have provided an ideal medium for the containment of micro meteoroid particles which may be largely unmodified by hitting the spacecraft. Many impacts have been identified and recorded photographically. Analysis of the impacted material within the blankets will commence later this year when the spacecraft has returned to Europe. The EURECA Project has placed all the blankets at the disposal of the micro meteoroid investigation team.

The active thermal control is by a freon cooled loop, principally for the high energy consuming instruments.The cooling loop collects the heat from the most dissipative items and brings it to two space radiators on the ± X sides of the spacecraft. These radiators are both 3.5 m by 1.59 m in size. They form part of the solar array assembly and inspection for micro meteoroid impacts will be part of the solar array inspection in Europe. Heaters are used to compensate the heat leak through the insulation and adjust the temperature of the radiator freon temperature. The heater control is performed by a microprocessor based unit upon the readings of about 250 thermistor.

Electrical Subsystem

The Electrical Power Subsystem (EPS) generates, stores, conditions and distributes the power to the system. The power distribution capability is about 2.5/2.8 kW, where 1000 Watts are dedicated to the payloads. The solar generators are two solar array wings, composed by five panels each generating 2500 watts from solar cells on two identical wings of five panels each. The panels are of a rigid honeycomb structure 3.4 metres by 1.4 metres. The glass covering of the solar cells gives very clear indications where micro meteoroids have impacted. The solar arrays are stowed during lift-off and landing and have the capability to deploy and retract on orbit. During the sunlight phases the charge arrays provide power to the Nickel Cadmium batteries, which in turn release power to the system during the eclipse phases. In the deployed configuration the solar arrays are rigidly attached to the main EURECA body and have no rotational degree of freedom so as to avoid drive mechanisms and any associated μ gravity disturbance to the experiments. It was not possible in the USA to deploy the solar arrays after landing for a full inspection. This awaits a detailed investigation, starting in late October, at the manufacture premises near Amsterdam.

Data Handling

The Data Handling Subsystem (DHS) performs the management, control and monitoring of the EURECA on-board operations, except those relevant to the attitude and thermal control which are performed autonomously. In short, the DHS stores and executes instructions received by telecommand from the EURECA Operations Control Centre (OCC) at ESOC (European Space Operation Centre), Darmstadt, Germany. It also controls the spacecraft and the payload during the non-contact time, and stores the spacecraft housekeeping as well as the payload science data for later transmission to the OCC. To avoid any μ gravity to the experiments by the use of a data tape recorder a magnetic bubble memory with a capability of 128 Mbs was installed.

Attitude Control

The Attitude and Orbit Control Subsystem (AOCS) measures and controls the EURECA attitude and orbit during both orbit transfer manoeuvres and nominal flight operations. The attitude sensors available on-board are optical (three coarse sun sensors (CSS), two fine sun sensors (FSS) and two low altitude conical earth sensors (LACES)) and inertial (three gyro packages containing two gyros each, one accelerometer package). The actuators are three magnetic torque rods, one hydrazine pressurised monopropellant propulsion system, equipped with eight 20 N thrusters and one nitrogen cold gas propulsion system equipped with twelve 20 mN thrusters. The AOCS can operate in several modes. After release from the RMS and before retrieval the spacecraft is in Proximity Operation Mode (POM). The control is performed using gyros as sensors and cold gas thrusters. This mode cannot be maintained for very long because of the gyro drift. The Sun Acquisition Mode (SAM) is used to bring EURECA to the +Z axis sun pointing attitude, with the Y axis in the orbit plane and +X axis towards the northern hemisphere. Sensors used are the six gyros, CSS, FSS and LACES, while the actuators are the hydrazine thrusters. The Earth Acquisition Mode (EAM) is used as preparatory to the orbit transfer manoeuvres. While the +Y axis is always pointing to the centre of the earth, four orientations are possible for the X and Z axes in order to allow in-plane and out-of-plane down manoeuvres. The actuators used are the hydrazine thrusters and the sensors are the gyros, CSS, FSS and LACES. The Orbit Transfer Mode (OTM) is used after the EAM in order to boost the spacecraft in the new orbit. The attitude and sensors of EAM are maintained, while the hydrazine thrusters are used in an off modulation mode during the burn.

During the Operational Mode (OM) the spacecraft +Z axis is sunpointing and the payload is operating under micro gravity conditions. The sensors used are four gyros, FSS and LACES, while the actuators are the magnetic torquers together with the cold gas thrusters. When the micro gravity and attitude pointing requirements are not mandatory, the spacecraft can be operated in Dormant Mode (DM). The attitude is basically the same with reduced accuracy in sun pointing. The sensors are the same as in OM, while the actuators are magnetic torquers, hydrazine thrusters to control rotations around X and Y axes and cold gas around Z axis. If an error occurs in the AOCS which cannot be autonomously recovered, the AOCS configures to Safe Emergency Mode (SEM). Only the CSS and three gyros are used as sensors and hydrazine thrusters in the submode SEM2 and cold gas in the submode SEM1 as actuators.

Microgravity Measurement Subsystem

The Microgravity Measurement Subsystem (MMS) monitors the on-board residual acceleration during the EURECA flight operations in the frequency bandwidth from 0 Hz to 5 Hz and stores the measurement data for later on-ground analysis.

Telemetry

The Telemetry Tracking and Command (TTC) subsystem transfers telemetry data from EURECA to the ground stations and telecommands from the ground stations to EURECA in two ways: via direct RF S-band link during nominal operations and via the Orbiter during deployment and retrieval operations.

INSTRUMENTS

The EURECA-1 payload complement consists of 15 instruments. Except one, mounted on the bottom of the spacecraft, all other instruments are accommodated on the platform top side. Half of the payload complement is dedicated to the microgravity research, including material and life science. The remaining instruments are dedicated to astronomical observation and technology research.
Of direct interest to the study of exposure to the space environment are the following experiments:

TICCE. The Timeband Capture Cell Experiment (TICCE) is designed to study the microparticle population in near-Earth space, typically Earth debris, meteoroids, and cometary dust. TICCE captures micro particles in excess of 3 km/s and stores the debris for retrieval and post mission analysis. Particles detected by the instrument pass through a front foil and into a debris collection substrate positioned 100 nm behind the foil. Each perforation in the foil will have a corresponding debris site on the substrate. Lately it was recognised that additional debris collection techniques were more suitable to the particle sampling. Therefore two additional arrays were added to the four containing the described capture cells. The additional arrays employ new techniques for impact debris collection, like silica aerogel materials and extremely thin aluminium foils, which have been developed by the lesson learnt from the NASA LDEF experience.

EXOBIOLOGY & RADIATION ASSEMBLY (ERA). To study the interaction of cosmic ray particles with biological matter, the synergism of space vacuum and solar UV, and the spectral effectiveness of solar UV on viability should be improved as a result of this instrument.
ERA consists of deployable and fixed experiment trays, and a number of cylindrical stacks, known as Biostacks, containing biological objects such as spores, seeds or eggs alternated with radiation and track detectors.

ATOMIC OXYGEN SAMPLE TRAY (AOST). Two rectangular trays alongside the AOCS sensors and fitted to the +Z sun facing upper surface of the spacecraft. Numerous samples were attached to investigate the effects of UV radiation, AO, and thermal cycling on materials used for thermal control (films,paints and anodisation). Two contamination sensors were also fitted.

DOSIMETER (see later paper)

IN-ORBIT CURING EXPERIMENT (ICE). This is a sample of an Inflatable Space Rigitised Structure (ISRS) material which is a colamination of Kapton and Kelvar with epoxy prepregnated and sewn together. When exposed to radiation the foils cure in a few orbits. The dimensions are 300 mm x 120 mm.

MISSION PROFILE

Launch and Deployment

The EURECA mission started with the STS-46 Atlantis lift-off on July 31st 1992 at 13:56 GMT. The orbit achieved was very close to nominal. The first Orbiter state vector indicated an orbit at an inclination of 28.45 and 425 X 424 km altitude. EURECA was released from the Orbiter on August 2nd, at 7:07 GMT.

Operational Orbit

Immediately after release preparation for the orbit transfer manoeuvres commenced. After two transfer manoeuvres EURECA commenced its operations at an orbit of 508 km. From this point until the descent orbit transfer manoeuvre for retrieval, no orbit maintenance was performed. Therefore the orbit of EURECA was solely determined by the Earth gravity potential, atmospheric drag and the other natural orbit perturbations. The decay of the average altitude axis is plotted in Figure 3 versus the Mission Elapsed Time (MET) in days. The operational mode attitude of EURECA is inertial with the +Z axis pointing to the sun and the Y axis in the orbit plane. The +Y surfaces fly parallel to the velocity vector every orbit at midnight, while the -Y surfaces do it at orbital noon. The above considerations are important to judge the predictions of the meteoroid and debris "frontal" impacts.

Retrieval

The descent orbit transfer manoeuvre preceded by about three weeks the retrieval Shuttle lift-off STS-57 of Endeavour on the 21st June 1993. The orbit eccentricity had been corrected and the spacecraft was placed in a phase repeating parking orbit of 474 km. The rendezvous phase took place at the end of the third flight day. The final approach was manually executed by the Orbiter crew, who took care to minimise any contamination and/or disturbance to the attitude of EURECA by the Orbiter jet plume impingement. After retraction of the appendages, EURECA was grappled and stowed in the cargo bay. The Orbiter extended its mission, due to weather constraints at KSC, landing there on the 1st July 1993.

MISSION FLUX PREDICTIONS

The atomic oxygen prediction analysis was run over the mission duration of 324 days using the three dimensional tool ESABASE . The MSIS-86 reference atmosphere model was used in conjunction with the mean monthly value of the solar F10.7 cm radiation. The value of this parameter is linearly extrapolated between the months in order to obtain a daily figure. A plot of the variation of solar 10.7 cm radiation can be seen in Figure 4.

The mission accumulated AO fluence was calculated for the front and rear of the solar arrays, and to all six faces of the main spacecraft body. It should be noted that the present version of the analysis tool does not take into account the thermal motion effects of the atomic oxygen and also does not include any reflection of scattering. The results are shown in Figure 5.
The accumulated fluence for the solar arrays and the ram direction are as follows:

Solar array front:	1.025×10^{20} atoms / cm^2
Solar array rear:	1.821×10^{20} atoms / cm^2
Ram:	4.911×10^{20} atoms / cm^2

POST FLIGHT ACTIVITIES

Following the landing immediate checks were made to confirm that there were no hydrazine leaks from EURECA propulsion system. These checks indicated a completely sealed system. In addition a ground cable was connected to the Orbiter and charging of the EURECA instrument 'PCF's 'battery was conducted for a period of 4 hours to ensure continued adequate cooling of its samples. The Orbiter was then moved into the Orbiter Processing Facility 7 hours after landing. The cargo bay doors were opened on the 6th July and a full inspection of the upper surface of EURECA was made and a comprehensive photographic survey was taken. On the 7th July access was provided, via a suspended bucket, for the Project to remove the PCF samples. These samples were packed and flown to Europe and handed over to the respective investigators. The spacecraft, along with the Spacehab module and the SHOOT experiment, were removed in one operation from the Orbiter and placed in the Inter Facility Transport Canister. This canister was moved to the Vertical Processing Facility at KSC on the 9th July.

EURECA was lifted out of the canister and placed into its own integration and transportation kit. This provided an opportunity for a full visual and photographic survey of the complete spacecraft. The general conclusion was that a significant change of colour had occurred most pronounced where out-gassing had deposited onto the MLI on the +z surfaces (normal sun facing axis). Areas of paint delamination and many micro meteoroid impacts were clearly visible. All photographs taken are on CD-ROM for detailed examination by the specialists. Numerous specialists participated in this initial inspection at KSC.

On the 14th July, EURECA was moved to Astrotech, Titusville. The first task was to depressurise the propulsion and the cold gas attitude control system and to remove the remaining hydrazine. Tests confirmed that all hydrazine valves were in the closed position. Concerns had been raised, following an in flight anomaly, that the valves might inadvertently open on landing. The pressure was reduced from the helium and nitrogen gas tanks and then the hydrazine was removed. An amount of 323 kg of hydrazine was removed. At launch the tanks had been filled with 660 kg. EURECA was moved into the High Bay on the 6th August for deintegration and preparation for transportation to Europe which took place on the 29 September 1993.

RESULTS OF INITIAL POST FLIGHT ANOMALY INVESTIGATION

Battery capacity measurements were made. The results compared very closely with pre-flight values. Initial calculations show only a 2% reduction in charge capacity at the end of the mission. The uncertainties expressed prior to the launch as to the life capabilities of batteries manufactured in 1985 and removed from cold storage in January 1992 for installation have been answered.

Samples of the freon system have been taken for analysis and the system has been drained for removal of the instruments and the freon pump package. The residual freon accumulator pressure on the spacecraft was 6.1 bars and the loss of freon from the accumulator, since filling 18 months previously, is calculated as being approximately 1.2 litres. This is significantly less than worst case pre-flight estimates. The freon pump operated for just over 4000 hours on orbit and it can be seen that the pumps could have supported a very long mission (qualified for 10000 hours). NASA MSFC plans to perform all post flight inspection activities on the freon pump package, prior to clearance for re flight on a Spacelab mission.

The in-flight anomalies, of progressive loss of power, await to be investigated at Fokker in November. However, based on the limited visibility that exists behind the panels some damage caused by arcing is visible on a number of Wiring Connect Panels (short silver busbars). Inspection of the antennas revealed that on both antennas 1 & 2 the MLI was found to be trapped between the antennae's head and the spacecraft support structure. It is concluded that this trapping was most likely there prior to launch. In addition along the boom of antennae 2 there was interference from the MLI at two positions. The MLI at these two positions could be easily moved but would have put some load on the boom that might have prevented full retraction.

POST FLIGHT INITIAL MATERIAL ASSESSMENT

The ESA material team performed a comprehensive inspection at ASTROTECH, while the carrier was prepared for shipment to Europe and storage. The investigation consisted of four types of survey:

- Visual inspection
- Photographic documentation of the carrier and payload (more than 1000 photos taken)
- Organic contamination (70 wipes taken)
- Thermo-optical properties (100 a/E measurements taken)

In general terms, the most conspicuous visual effects on the EURECA hardware exposed to space are various outgassing deposits present next to venting holes or gaps between blankets in the top and bottom parts of the spacecraft. An example of this was the contamination of some samples on the Atomic Oxygen Sample Tray due to outgassing from the spacecraft at an adjacent thermal blanket joint. In its interiors EURECA is visually clean as in the pre-launch state.

The ß-cloth exposed to space in the top deck of EURECA (+Z face) has turned light brown as a result of possible contamination by Ultra Violet radiation. Organic contamination tests results are not yet available. This change in colour has resulted in an increase of the Solar Absorptance of 0.06 on most of the blankets and up to 0.15 in very contaminated areas. No appreciable change was found in the Normal Emittance values. The FEP tape on the AOCS tower is heavily contaminated; peculiar shadowing effects are visible.

The +X and -X thermal hardware surfaces of the spacecraft are less degraded than the top, as it can be expected from the smaller solar input: the Solar Absorptance has an increase of 0.02 on most of the blankets and up to 0.04 in very contaminated areas closed to blanket gaps. The performance degradation of the ß-cloth on the +Y and -Y surface is similar to the one observed in the top deck. The paint of SCUFF Plate is powdering and peeling, showing signs of Atomic Oxygen degradation.

The EURECA solar arrays will be deployed at the manufacturer premises in mid November. At that point a team led by ESA will execute a detail inspection of the hardware. From the inspections carried out in Astrotech the solar arrays appear to be in general good condition. Several impact features up to 500 µm are visible on the outer panel.The epoxy adhesive used for glass fibre cloth bonding is darkened. The colour of RTV S-691 used for ATOX protection changed from red to brown.

POST FLIGHT IMPACT ANALYSIS

A global optical survey of the outer surfaces of the EURECA main body has been completed. There have been 75 confirmed impact holes in the MLI (>200 μm). 11 impacts were identified in the scuff plates. More details on the impact analysis will be given in separate reports.

FUTURE PLAN FOR INVESTIGATION OF MATERIALS AND MICRO METEOROID AND DEBRIS IMPACTS

From mid November the ESA post flight investigation teams will concentrate their efforts on the solar arrays. ESA plan is to study Atomic Oxygen effects, and changes in material properties in general on all solar arrays components (insulation foil, KAPTON ITO, flex prints, etc.).

Samples of the MLI blankets will be subjected to impact tests to enable the relation of particle size to damage to be determined. The micro-meteoroid team will conduct a global survey on the arrays (front and back), recording features larger than 200 μm.
A more detailed survey will be executed in selected areas. By mid 1994, ESA expects to complete a catalogue with the results of the impact survey and material investigations. It is planned to recover part of the meteoroid or debris trapped in some of the MLI blankets for analysis.

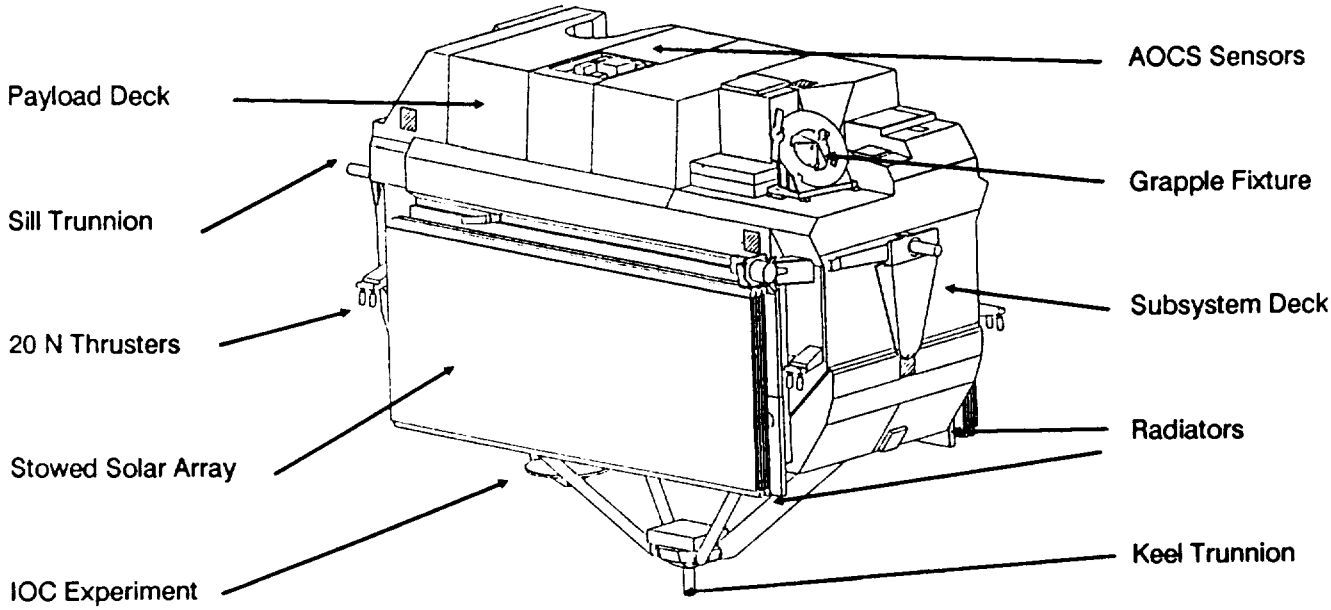

Figure 1. EURECA Configuration

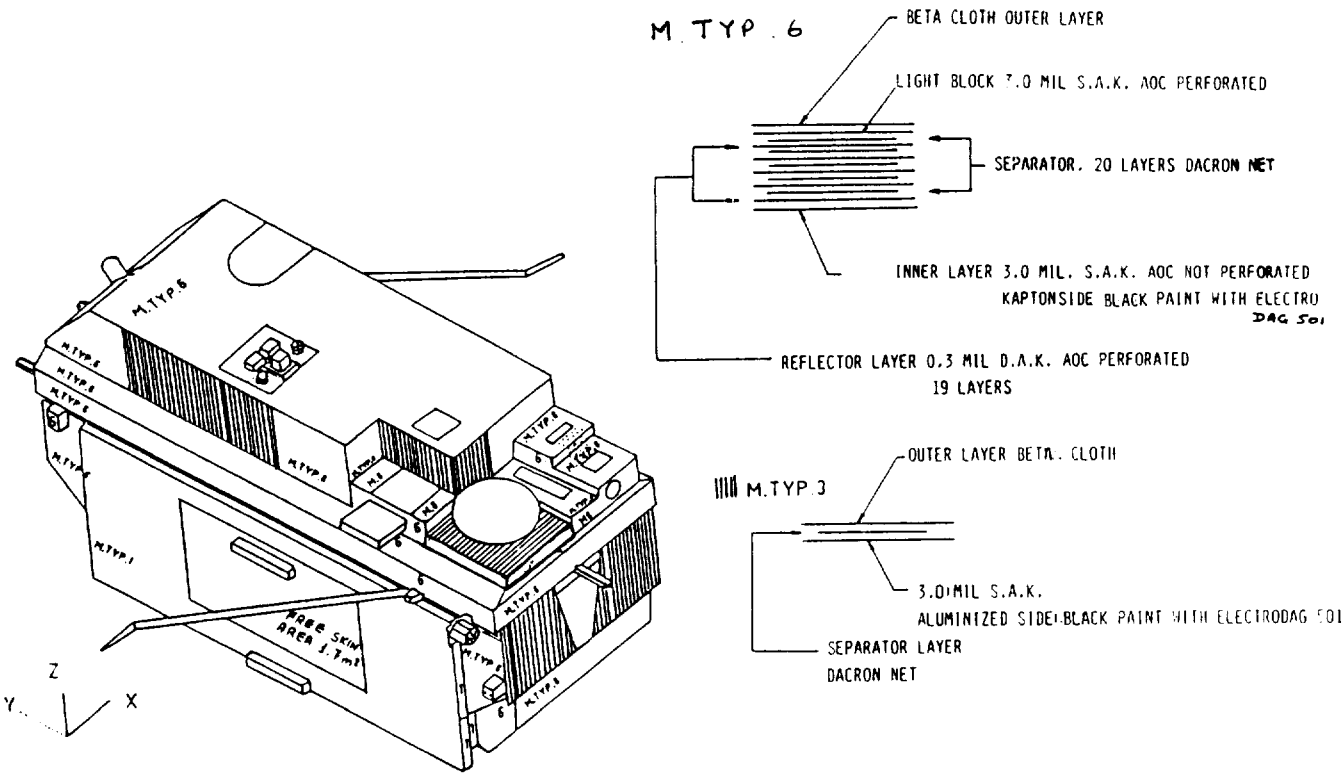

Figure 2. Thermal Blankets

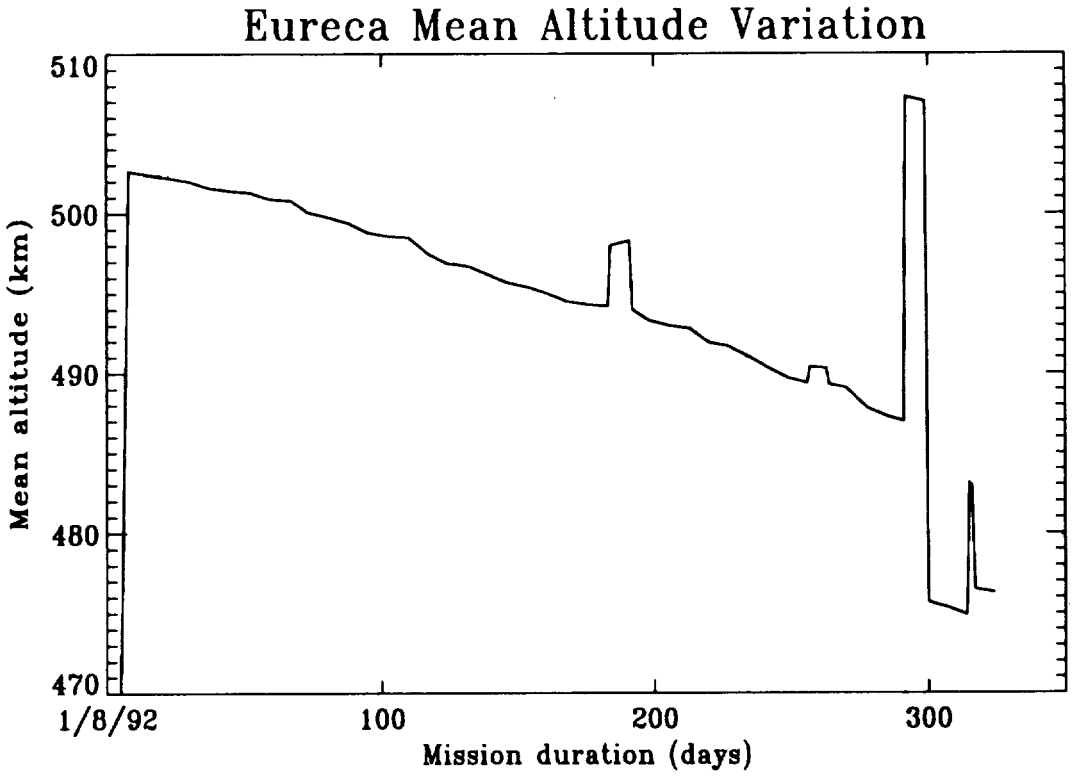

Figure 3. Mean Altitude Variation

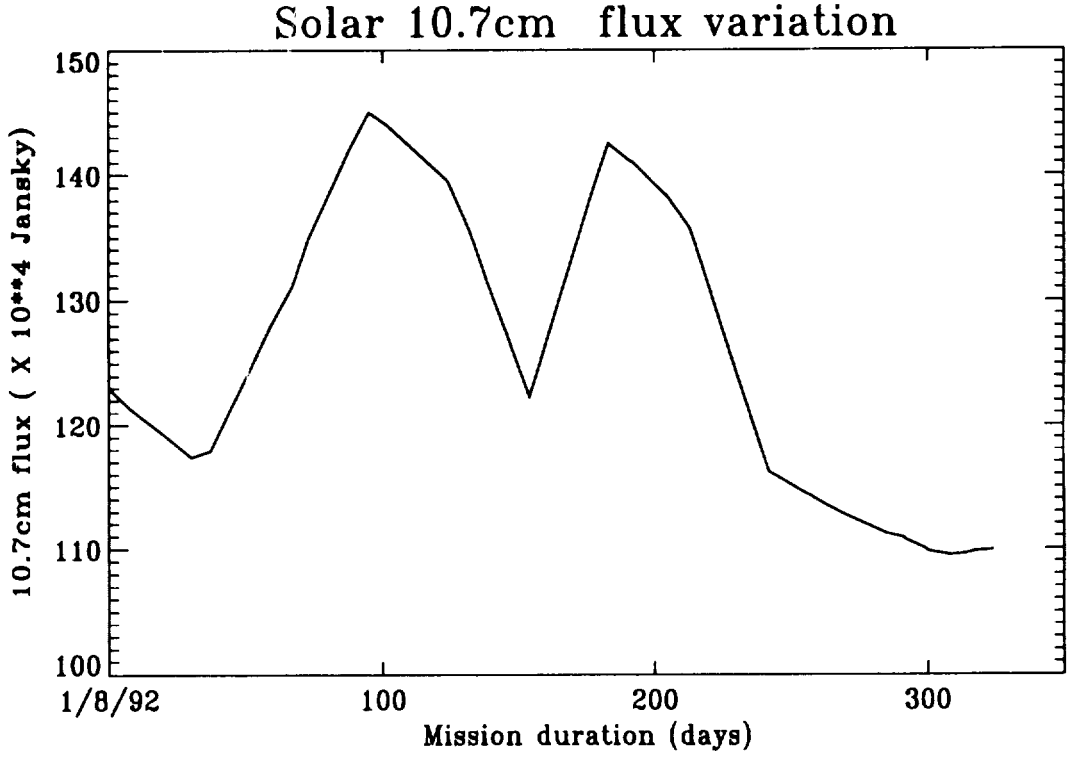

Figure 4. Variation of Solar Radiation During the Mission

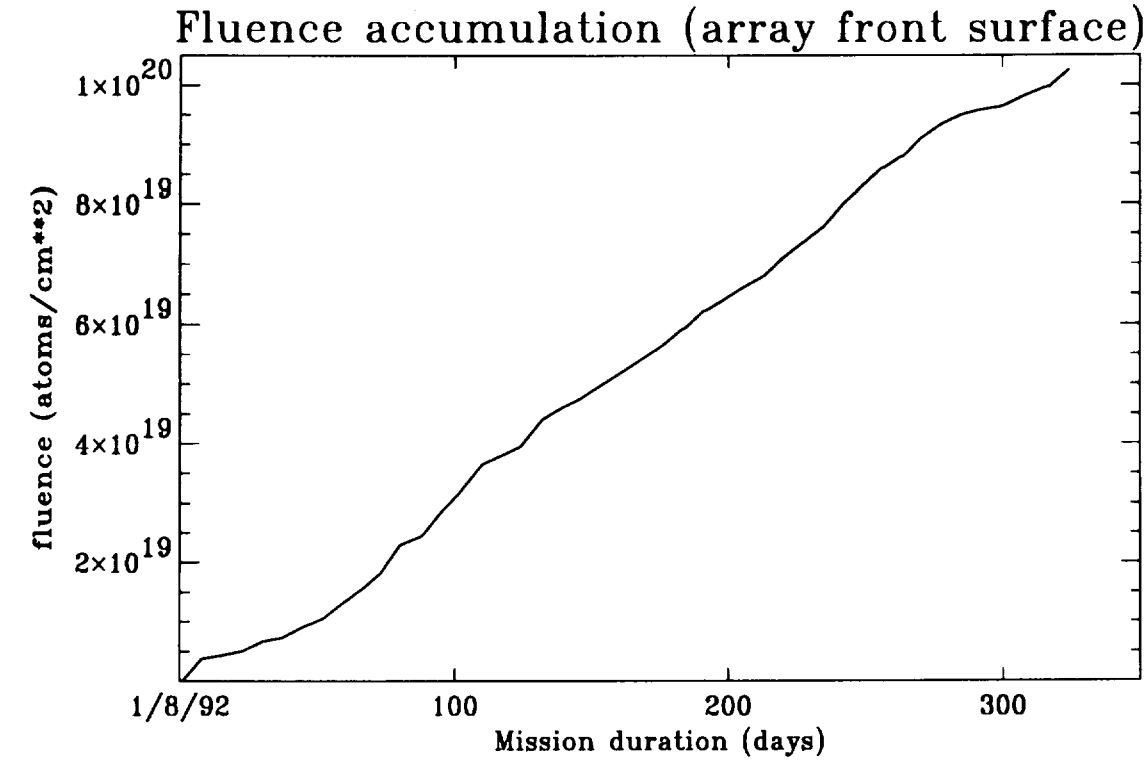

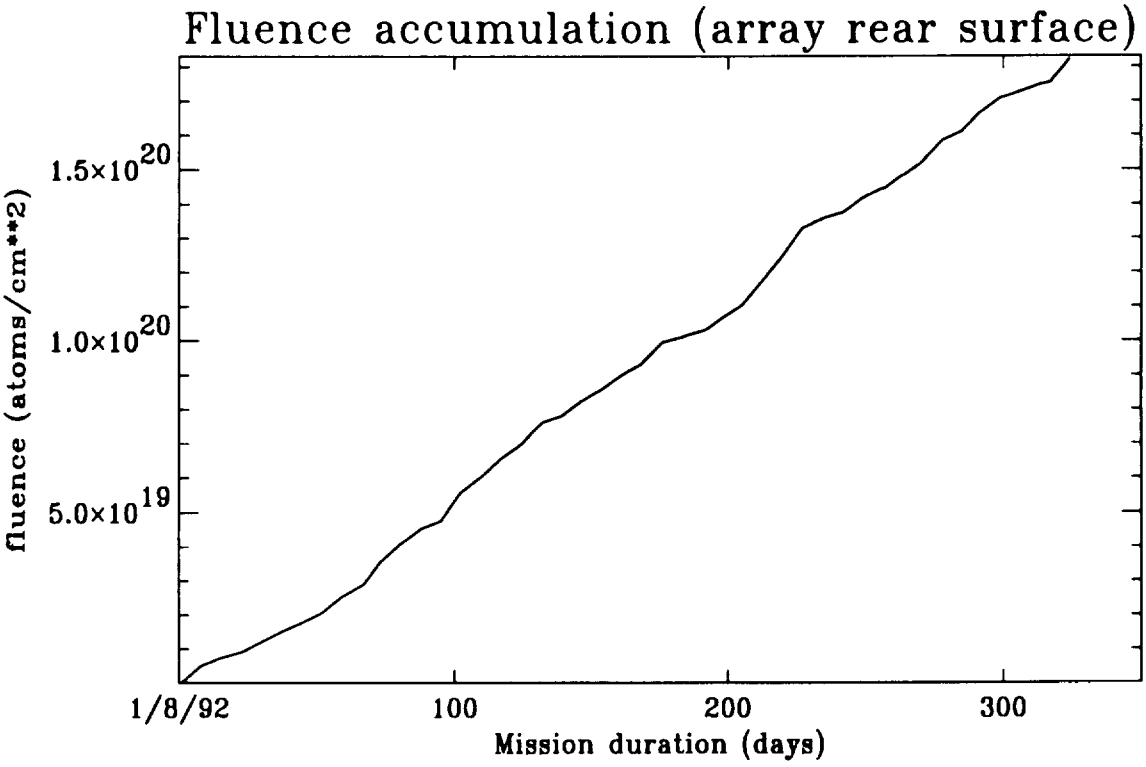

Figure 5. Accumulated Fluence on the Solar Arrays.

//

Dosimetric Results on EURECA

G. Reitz
DLR, Institute for Aerospace Medicine, Radiation Biology
Linder Höhe, 51147 Köln, Germany
Phone: (49) 2203 601 (0) 3137; Fax: (49) 2203 61970

Abstract

Detector packages were exposed on the European Retrievable Carrier (EURECA) as part of the Biostack experiment inside the Exobiology and Radiation Assembly (ERA) and at several locations around EURECA. The packages consist of different plastic nuclear track detectors, nuclear emulsions and thermoluminescence dosimeters (TLDs). Evaluation of these detectors yields data on absorbed dose and particle and LET spectra. Preliminary results of absorbed dose measurements in the EURECA dosimeter packages are reported and compared to results of the LDEF experiments. The highest dose rate measured on EURECA is 63.3 ± 0.4 mGy d^{-1} behind a shielding thickness of 0.09 g cm^{-2} in front of the detector package.

Introduction

The radiation environment in space comprises ionising radiation of all types and energies. Its spectral intensities show a large variability with individual mission profiles and the timing of the mission within the solar cycle. The complexity of an adequate description of the external radiation field in near Earth orbits is matched by the complexity of calculating the transport of the various components through realistic configurations of heterogeneous shielding materials. This transport involves not only attenuation of the separate components, but also, depending on the ratios of the respective free interaction lengths to the absorber thickness, the build-up of some components at the expense of other ones.

At altitudes between 200 and 600 km and at low inclinations the major contribution to the absorbed dose is delivered inside the South Atlantic Anomaly (SAA) by the geomagnetically trapped protons and electrons of the radiation belt. Below shielding thicknesses of 1 g cm^{-2} the contribution from electrons dominates the absorbed dose. The SAA is an area where the radiation belt comes closer to the earth surface due to a displacement of the magnetic dipole axis from the Earth's centre. In this region fluxes are varying extremely rapidly with altitude because of interactions of the charged particles with the nuclei of the upper atmosphere. The flux in the SAA is anisotropic with most of the flux arriving perpendicular to the magnetic field lines. In addition, an energy-dependent east-west anisotropy of the proton flux is observed. Since the westward travelling protons pass a denser atmosphere, more get lost which results in a higher flux coming from the east.

So far, models which are used to describe the radiation environment have a limited capability to predict doses for future missions, especially for those in atmospheric cut-off regions, where particle fluxes drop off rapidly with altitude. For example, radiation levels measured on LDEF are underpredicted by such models /1/. Since available data are limited /e.g. 2-4/, more data are

needed in order to validate shielding and dose calculations and to improve the prediction of doses in future missions.

Since the beginning of manned space flight, the problem of radiation protection from the multiple sources of ionising radiation of the space environment has been a permanent topic of experimental biomedical research in nearly all space flight missions. In the present investigation, the sparsely and the densely ionising components of the radiation field shall be measured with thermoluminescence detectors (TLDs), plastic nuclear track detectors and nuclear emulsions.

In this report, data about absorbed dose measurement with TLDs (TLD 700) will be reported only. The investigation on the other detector types is in progress.

MATERIALS AND METHODS

The experiments on EURECA may be divided into two different experiment sets. The first set comprises nine thin detector units which were attached to the EURECA core facilities and to parts of the platform (Fig. 1). The detector units are covered by a multi-layer insulation (MLI) of 0.08 g cm^{-2} thickness only. Each unit consists of up to nine plastic nuclear track detectors, cellulose nitrate (CN), diallylglycol-carbonate (CR39) and polycarbonate (Lexan) between 0.1 and 0.3 mm thickness and of TLD 600 and TLD 700 lithium fluoride (LiF) chips embedded in a polyethylene foil. In Dos 1 through Dos 3 the TLDs formed the bottom layers and in Dos 4 through Dos 9 the top layers. All packages are equipped with celsi-strip temperature indicators and are wrapped twice in a one-sided aluminized Kapton foil of 25 µm thickness. The temperature of 40° C was exceeded for Dos 1 and Dos 2 only, in which temperatures rose up to 54° C .

The second experiment set was located in the ERA as part of the Biostack experiments (Fig. 2). Each Biostack provides three hermetically sealed cylindrical compartments made of aluminium in which the detector stacks are accommodated. A detector stack consisted of more than 100 layers of nuclear track detectors - partly interspersed with monolayers of biological objects. The top and the bottom of some stacks were formed by two TLD layers.

The doses in the TLD chip were measured with a Harshaw 2800 TLD analyser at standard settings. Calibration was done using a Cs 137 source.

FLIGHT PARAMETERS

EURECA was deployed from the Space Shuttle (flight STS 46) on July 31, 92 at an altitude of 424 km and an inclination of 28°. With its own propulsion system it was transferred to the operational altitude of 508 km, where it remained from Aug. 7, 92 to May 24, 93. It was retrieved at 476 km on June 24, 93 and returned to Earth on July 1, 93. The mission duration was 336 days. During almost the whole mission the EURECA payload was directed towards the sun (+z). This orientation of EURECA is shown on Fig. 3. EURECA was launched at a time when the solar activity was already significantly decreased compared to the maximum solar activity and it decreased further during the mission. On the average, the status of the sun might be comparable to that during the LDEF mission, but this needs detailed investigation.

RESULTS AND DISCUSSION

Table 1 lists the absorbed doses and dose rates obtained from the evaluation of Dos 1 through Dos 9 and table 2 those obtained from the Biostack detector packages. The highest dose rates are measured in Dos 6 through Dos 9 with the highest measurement in Dos 7 with 63.3 ± 0.4 mGy d^{-1}. The ROEU support and the AMF position provide the dosimeter packages with the lowest shielding distribution around them. Shielding thickness in front of the packages was 0.09 g cm^{-2}. The TLDs in Dos 3 formed the bottom layer of the detector package and had an additional shielding by the other detectors of 0.19 g cm^{-2}, and therefore 0.28g cm^{-2} in total. This may explain the by about a factor of 10 lower value than observed in the location AMF (+Z). Dos 2 and Dos 4 and Dos 5 were facing other payloads which certainly results in a higher shielding. The TLDs exposed in the Biostack A4 which faced to -x were shielded by 0.6 g cm^{-2} in this direction . The observed dose rate of 1.25 ± 0.01 mGy d^{-1} is lower than the dose rates obtained for LDEF with 0.7 g cm^{-2} shielding (see table 3 /5/). The shielding thickness in front of TLD layer A4-1 was about 16 g cm^{-2}; also the shielding in y-direction was higher which results in a reduction of the dose by a factor of three. The doses in A2 were expected to be close together with A4-1 dose and lower than all A3 doses, which is actually the case. Measurements in the topmost TLD foils in A1-3 and A3-T-163 agree excellently.

For a promising comparison of the EURECA and LDEF data a mass shielding model is essential. This is planned in co-operation with Rockwell International.

References:

1) Daly EJ and Evans HDR, Problems in radiation environment models at low altitudes, Memorandum ESA/ESTEC/WMA/93-067/ED

2) Benton EV, Parnell TA (1988) Space radiation dosimetry on US and Soviet manned missions. NATO ASI Series A. Life Sciences, Vol. 154, pp 729-794

3) Heinrich W, Wiegel B, Ohrndorf T, Bücker H, Reitz G. and Schott JU, (1989) LET-spectra of cosmic ray nuclei for near earth orbits. Radiat Res 118:63-82

4) Reitz G, Beaujean R, Heckeley N, Obe G, (1993) Dosimetry in the space radiation field, Clin Investig. 71:710-717

5) Reitz G, (1992) Preliminary total dose measurements on LDEF, Adv Space Res. 12 (2)369-(2) 373

Table 1: Dose and dose rates measured in Dos 1 to Dos 9. For the location see fig. 1; the axes given in brackets are the viewing direction of the dosimeter packages.

Dosimeter	Location	Dose [mGy]	Dose Rate [mGy d^{-1}]
Dos 1	ERA (+X)	236 ± 3	0.70 ± 0.01
Dos 2	ERA (+Y)	405 ± 18	1.21 ± 0.05
Dos 3	RITA (+Z)	785 ± 13	2.34 ± 0.04
Dos 4	AMF (+X)	2022 ± 41	6.02 ± 0.12
Dos 5	AMF (+Y)	873 ± 83	2.60 ± 0.25
Dos 6	AMF (+Z)	6372 ± 265	18.96 ± 0.79
Dos 7	ROEU (-X)	21260 ± 1350	63.3 ± 0.4
Dos 8	ROEU (+Y)	4475 ± 116	13.32 ± 0.35
Dos 9	ROEU (+Z)	8109 ± 434	24.1 ± 1.3

Table 2: Dose and dose rates measured in the Biostack units. TLD layers have been positioned in the four Biostack container A1 to A4 in the lower (L), middle (M) and upper (T) compartment of each stack.The number represents the sheet number in the compartment.

Location in Biostack Unit	Dose [mGy]	Dose Rate [mGy d^{-1}]
A1-3	312 ± 12	0.93 ± 0.04
A2-L-1	194 ± 3	0.58 ± 0.01
A2-L-105	163 ± 3	0.49 ± 0.01
A2-T-1	159 ± 2	0.47 ± 0.01
A2-T-91	177 ± 2	0.53 ± 0.01
A3-L-1	209 ± 9	0.62 ± 0.03
A3-L-184	221 ± 11	0.66 ± 0.03
A3-M-1	231 ± 9	0.69 ± 0.03
A3-M-10	237 ± 8	0.71 ± 0.02
A3-T-1	234 ± 8	0.70 ± 0.02
A3-T-163	318 ± 7	0.95 ± 0.02
A4-1	161 ± 3	0.48 ± 0.01
A4-170	421 ± 4	1.25 ± 0.01

Table 3: Doses and dose rates measured in two different locations on LDEF behind different shieldings in front of the dosimeters.

Experiment location	Shielding [g cm^{-2}]	Absorbed dose [Gy]	Dose rate [mGy d^{-1}]
Earth tray (E1)	0.7 12	3.9 ± 0.2 2.2 ± 0.2	1.85 ± 0.09 1.04 ± 0.09
Side tray (S7)	0.7 5 12	4.7 ± 0.3 3.2 ± 0.2 2.5 ± 0.3	2.23 ± 0.14 1.52 ± 0.09 1.19 ± 0.14

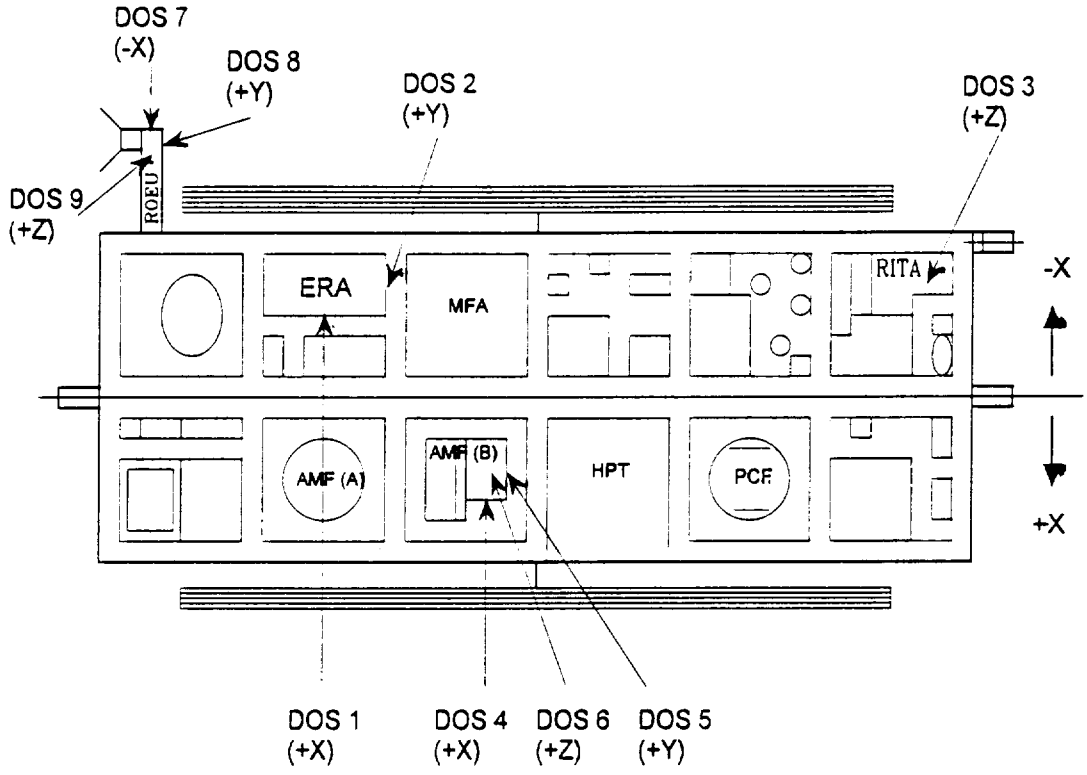

Fig. 1 Distribution of Dos 1 through Dos 9 on EURECA. The axes given in brackets for the single units are the viewing directions of the dosimeter packages. The axes +z are always directed to the sun.

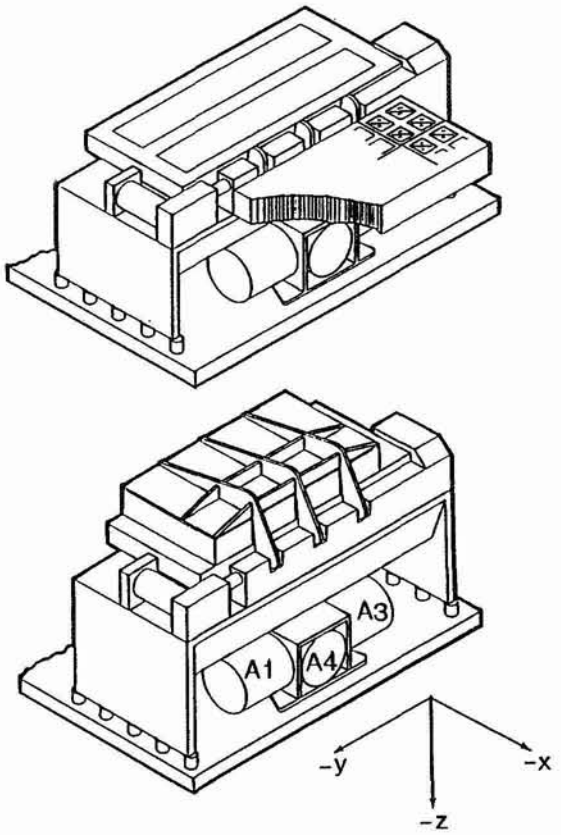

Fig. 2 Location of Biostack experiment units A1 through A4 inside ERA. Unit A4 is directed to -x, unit A1 to -y, unit A3 to +y and unit A2 (not visible, located behind the other Biostacks) to +z.

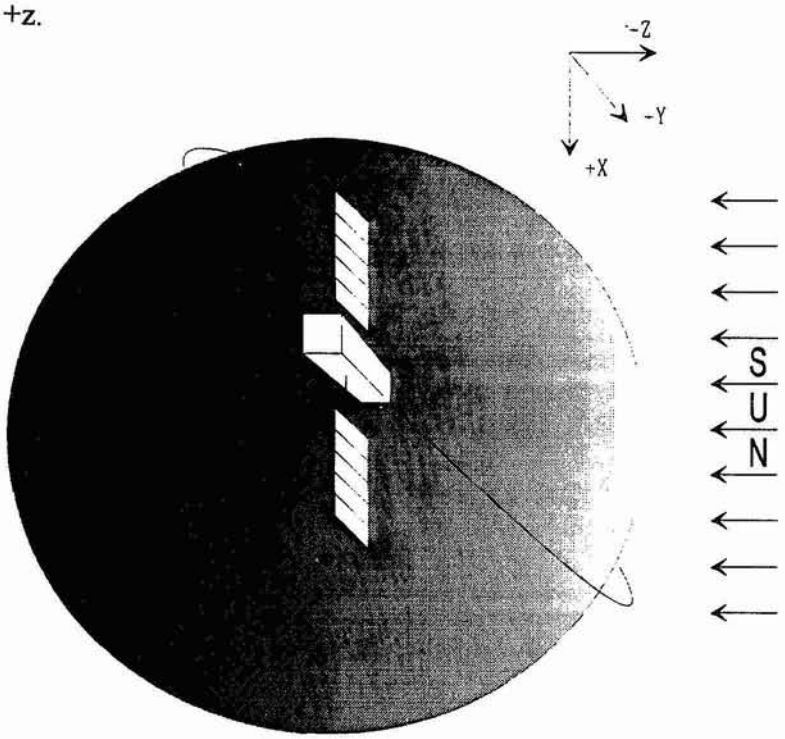

Fig.3 Schematics of the EURECA orbit with its coordinate system. +Z is always directed to the sun; the velocity vector is in direction of Y.

PRELIMINARY RESULTS OF RADIATION MEASUREMENTS ON EURECA*

E.V. Benton and A.L. Frank
Physics Research Laboratory
University of San Francisco
San Francisco, CA 94117-1080, U.S.A.

SUMMARY

The eleven-month duration of the EURECA mission allows long term radiation effects to be studied similarly to those of the Long Duration Exposure Facility (LDEF). Basic data can be generated for projections to crew doses and electronic and computer reliability on spacecraft missions. A radiation experiment has been designed for EURECA which uses passive integrating detectors to measure average radiation levels. The components include a Trackoscope, which employs fourteen plastic nuclear track detector (PNTD) stacks to measure the angular dependence of high LET ($\geq$6 keV/μm) radiation. Also included are TLDs for total absorbed doses, thermal/resonance neutron detectors (TRNDs) for low energy neutron fluences and a thick PNTD stack for depth dependence measurements. LET spectra are derived from the PNTD measurements.

Preliminary TLD results from seven levels within the detector array show that integrated doses inside the flight canister varied from 18.8$\pm$0.6 cGy to 38.9$\pm$1.2 cGy. The TLDs oriented toward the least shielded direction averaged 53% higher in dose than those oriented away from the least shielded direction (minimum shielding toward the least shielded direction varied from 1.13 to 7.9 g/cm^2, Al equivalent). The maximum dose rate on EURECA (1.16 mGy/day) was 37% of the maximum measured on LDEF and dose rates at all depths were less than measured on LDEF. The shielding external to the flight canister covered a greater solid angle about the canister than in the LDEF experiments.

INTRODUCTION

The EURECA mission provided the opportunity for measurements of the space radiation environment in low earth orbit (LEO) over an extended period (11 months). Compared with the LDEF mission, the time period was 16% as long, but the number of orbits was sufficient to obtain an excellent average over the LEO radiation field. In orientation EURECA was in stable alignment with the sun, rather than Earth, which complicates the shielding distribution about the experiments. However, calculations based on environmental radiation models can be made by averaging over shielding for comparisons with the measurements.

*Work partially supported by NASA Grant No. NAG9-235, NASA-Johnson Space Center, Houston, TX 77058

A selection of passive integrating radiation detectors has been flown on the EURECA mission in a sealed aluminum canister. This experiment is similar to the A0015 and P0006 experiments which were flown on LDEF. The EURECA experiment included plastic nuclear track detectors (PNTDs), TLDs and thermal/resonance neutron detectors (TRNDs) to measure total absorbed doses, high LET particle fluences, directionality and shielding depth dependence of the space radiation. A silicon wafer in contact with PNTDs was also included for measurement of the high LET fluences of secondary particles originating in the silicon. The secondary radiation may contribute substantially to electronic microcircuit failures in space.

The radiation detectors in this experiment allow a number of measurements to be made. At present only the TLDs have been read out. Absorbed doses as functions of shielding thickness (due to the Al canister and the composition of the detectors only) are given. The remaining measurements will be reported at a later date.

EXPERIMENT

The EURECA satellite was launched with the STS-46 mission at 8:57 a.m. CDT on July 31, 1992 and returned with the STS-57 mission at 7:52 a.m. CDT on July 1, 1993, for a total duration in space of 335 days. The orbit was 426 km in altitude with an inclination of 28.5°. The flight canister was mounted within the Exobiology Radiation Assembly (discussed below) with open space through an aperture to one side of the canister.

The complement of detectors included in the experiment were a TLD plate, nearest the top of the canister, followed by the Trackoscope and the thick detector stack. The layout is shown in Figure 1. The TLD plate was acrylic, with 16 holes for placement of TLDs: 4 around the center of the plate and 3 at each side.

The Trackoscope base was a truncated cube of acrylic with 14 faces (7 parallel pairs with 6 cm separations). PNTD stacks of 2.86 cm diameter and 0.45 cm thickness were attached to the faces. This arrangement compensates for the directional response of the PNTDs.

The thick detector stack contains layers of TLDs, PNTDs and aluminum, interspersed, and also a silicon wafer, held in place within a polyethylene sheet, and a TRND layer. The thick stack allows a measurement of shielding dependence of absorbed dose and heavy particle LET spectra. A comparison of the LET spectrum adjacent to the Si wafer with that in the near vicinity will yield information about secondary particle production within the wafer. The low energy neutron fluence, to be measured with the TRNDs, is of interest from the standpoint of dosimetry and as a test for the radiation modeling codes. The contents of the detector array are given in Table 1.

There were seven TLD plates included in the detector array with 16 TLD-700 chips ($0.635 \times 0.635 \times 0.089$) in each. After the mission, the TLDs were read out, with controls and ^{137}Cs γ-ray calibration

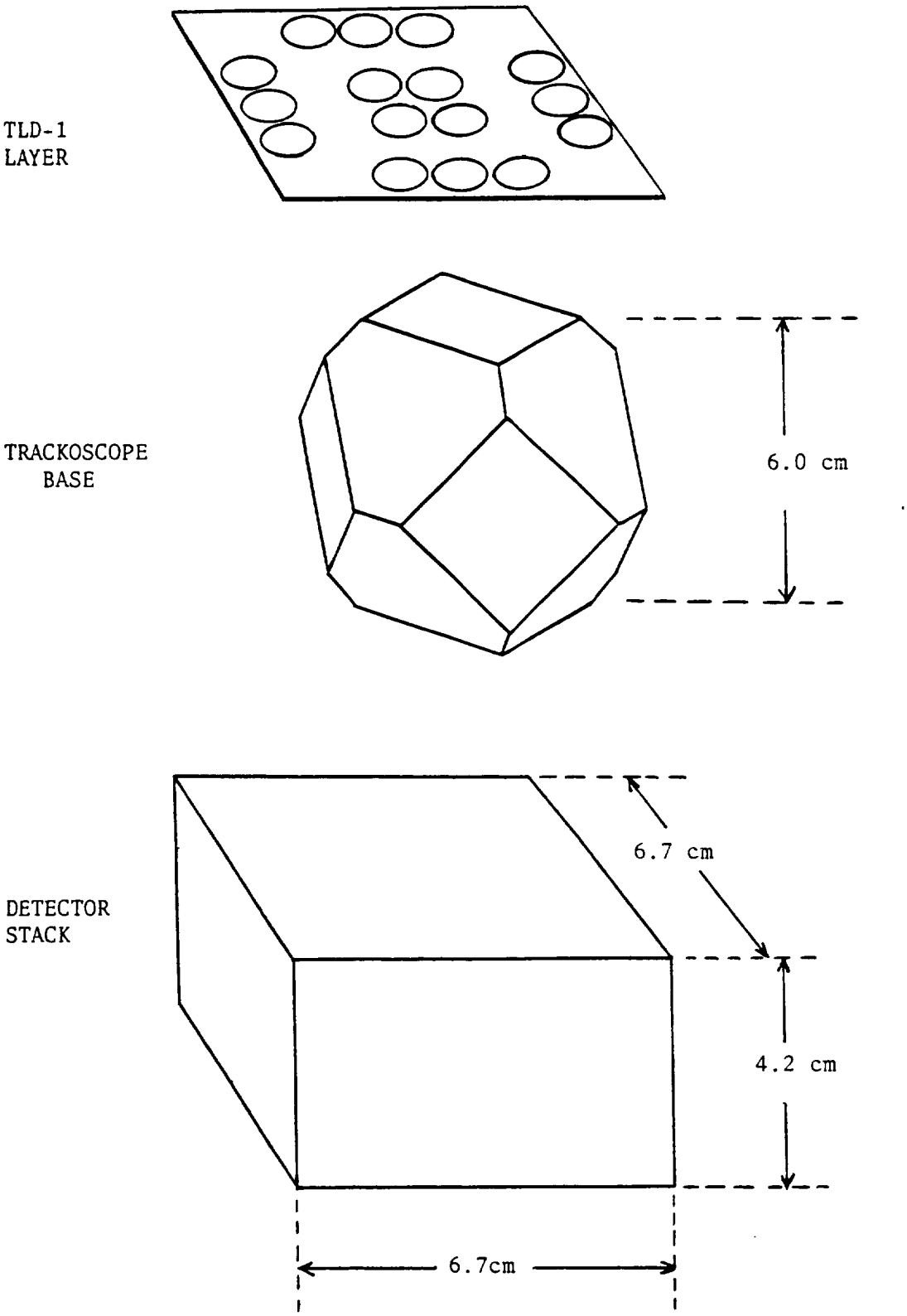

Figure 1: Detector components for EURECA radiation experiment. The Trackoscope base is a truncated cube with 7 pairs of parallel faces. PNTD sub-stacks (2.86 cm diameter × 0.25 cm thick) were placed on each of the 14 faces. The detector stack contained 6 additional TLD layers at various depths.

Table 1: EURECA Detector Assembly.

Material	Layers	Layer Thickness (cm)	Label
TLD (Acrylic)	1	0.165	TLD #1
Trackoscope		6.92	ET-1 – ET-14
Lexan	1	0.025	
TLD (Acrylic)	1	0.165	TLD #2
CR-39 (+PC)*	4	0.060	EUR-1 – EUR-4
Al	1	0.159	
TLD (Acrylic)	1	0.165	TLD #3
CR-39 (+PC)	4	0.060	EUR-5 – EUR-8
Al	1	0.159	
TLD (Acrylic)	1	0.165	TLD #4
CR-39 (+PC)	4	0.060	EUR-9 – EUR-12
Al	1	0.318	
TLD (Acrylic)	1	0.165	TLD #5
CR-39 (+PC)	4	0.060	EUR-13 – EUR-16
Al	1	0.318	
TLD (Acrylic)	1	0.165	TLD #6
CR-39 (+PC)	4	0.060	EUR-17 – EUR-20
Si/Polyethylene	1	0.015	
CR-39	1	0.060	EUR-21
Al	1	0.159	
TLD (Acrylic)	1	0.165	TLD #7
^{6}LiF/CR-39 (Acrylic)	1	0.350	EUR-TRND
Lexan	1	0.025	

*8 μm-thick polycarbonate film was placed between adjacent layers of CR-39

chips, in a Harshaw Model 4000 reader. A pre-readout annealing cycle was used (120°C for 10 sec) to eliminate the low temperature LiF glow peak from the response. A low temperature fading study has shown that this eliminates the need for a fading correction for the EURECA time period. The flight and calibration TLDs were recalibrated together afterward to improve response accuracy.

MEASUREMENTS

The 16 TLD doses in each plate have been averaged into 5 groups: center, left, back, right, front. The measurements are given in Table 2 and Figure 2. The direction of maximum intensity of radiation is seen to be diagonally through the right side and top of the canister. The minimum and maximum doses are 18.8 and 38.9 cGy.

Table 2: TLD Absorbed Doses Measured on EURECA.

TLD PLATE	Absorbed Dose (cGy) Center	Front	Left	Back	Right	Shielding Thickness Al Equiv. (g/cm^2)
1	30.9±0.9	33.9±1.0	28.8±0.9	32.8±1.0	38.9±1.2	0.92
2	22.3±0.7	24.6±0.7	19.7±0.6	25.8±0.8	32.9±1.0	8.30
3	23.2±0.7	24.7±0.7	20.1±0.6	25.4±0.8	31.3±0.9	9.36
4	22.2±0.7	25.2±0.8	20.7±0.6	23.7±0.7	29.7±0.9	10.4
5	22.9±0.7	24.1±0.7	20.1±0.6	24.5±0.7	28.6±0.9	11.9
6	21.1±0.6	22.3±0.7	18.8±0.6	22.8±0.7	29.0±0.9	13.4
7	21.7±0.7	24.1±0.7	19.4±0.6	22.8±0.7	29.6±0.9	14.9

The uncertainty given is standard deviation, σ.
The shielding given is the averaged vertical shielding to the top of the detector array and includes the top of the flight canister. Shielding external to the canister is not given.
Minimum shielding of the side TLDs through the sides of the canister was 1.13 g/cm^2, Al equivalent.

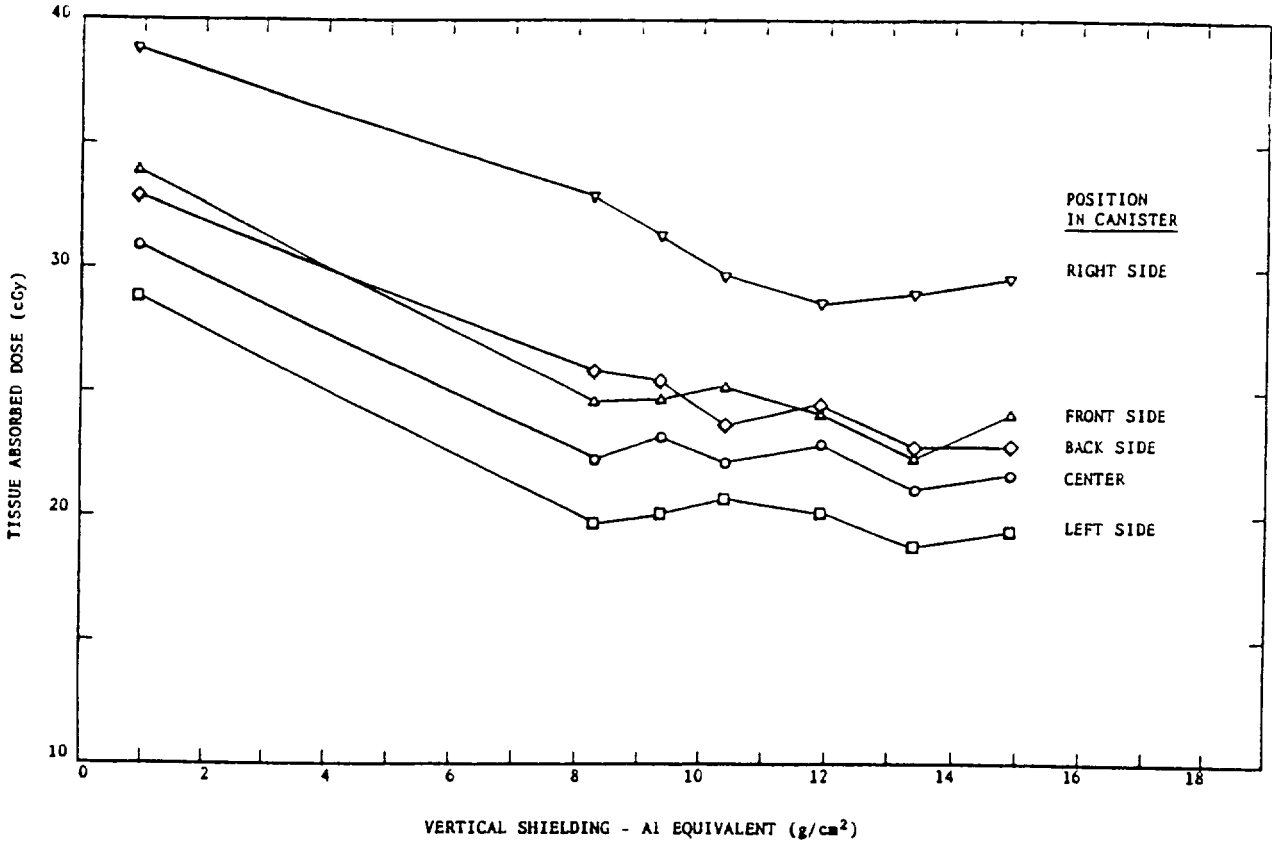

Figure 2: TLD-700 dose as a function of shielding thickness of the LDEF A0015 canister and contents. Shielding is measured vertically to the top of the canister. Minimum external shielding is the right side of the canister.

DISCUSSION

The direction of maximum radiation intensity in the flight canister should correspond to the direction of minimum external shielding. The positions of the Biostack flight canisters, one of which was occupied by the detectors, are shown in Figure 3 relative to the Exobiology Radiation Assembly. It can be seen that one side of the canister is unshielded to space. Also the top of the canister is set back from the side of the assembly so that the top has a significant solid angle open to space. It is also probable that the top of the canister receives a significant fraction of dose through the side of the assembly. This corresponds well to the expected external shielding as projected from the dose distribution.

An accurate solid angle distribution of external shielding about the detector canister will allow the dose measurements to be compared with calculations based on environmental radiation models. A comparison with dose rates measured on LDEF[1] is given in Figure 4. For equivalent shielding, the EURECA dose rates are less than those at all LDEF locations. This is qualitatively consistent with the difference in the external shielding. The LDEF flight canisters (P0006 and A0015) were open to space over an approximately 2π solid angle, while the open solid angle on EURECA was much smaller. Also the different altitudes of EURECA and LDEF contributed to higher LDEF doses. EURECA was launched from STS-46 with a Shuttle altitude of 426 km. LDEF was launched from STS-41C with the Shuttle at an altitude of 478 km. The LDEF altitude decayed, but a higher average trapped proton flux can be expected for this mission. At greater shielding depths the differences are smaller and the EURECA dose rates may be approximately equal to those at the LDEF leading edge.

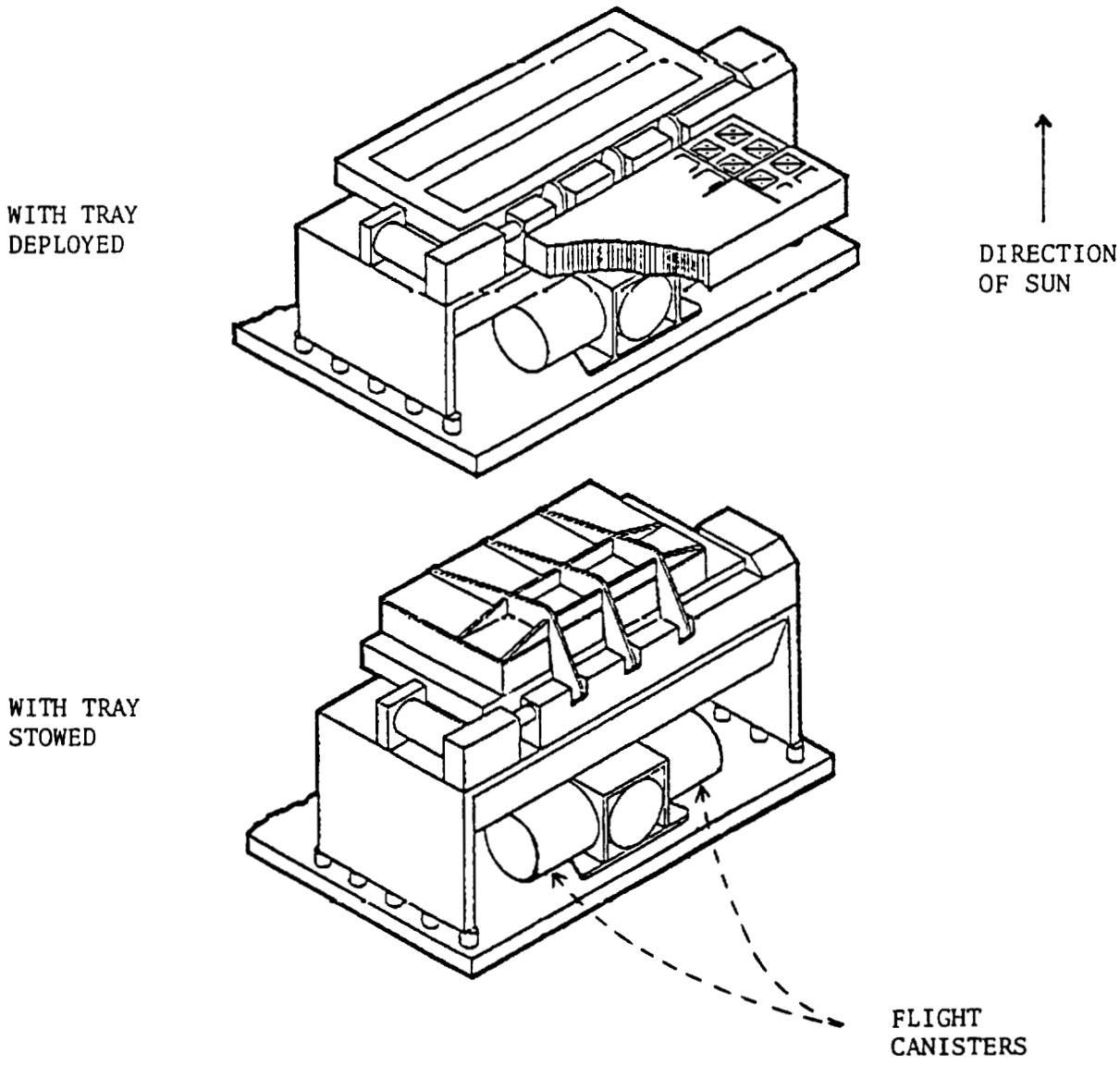

Figure 3: The positions of flight canisters relative to the exobiology radiation assembly on the EURECA satellite.

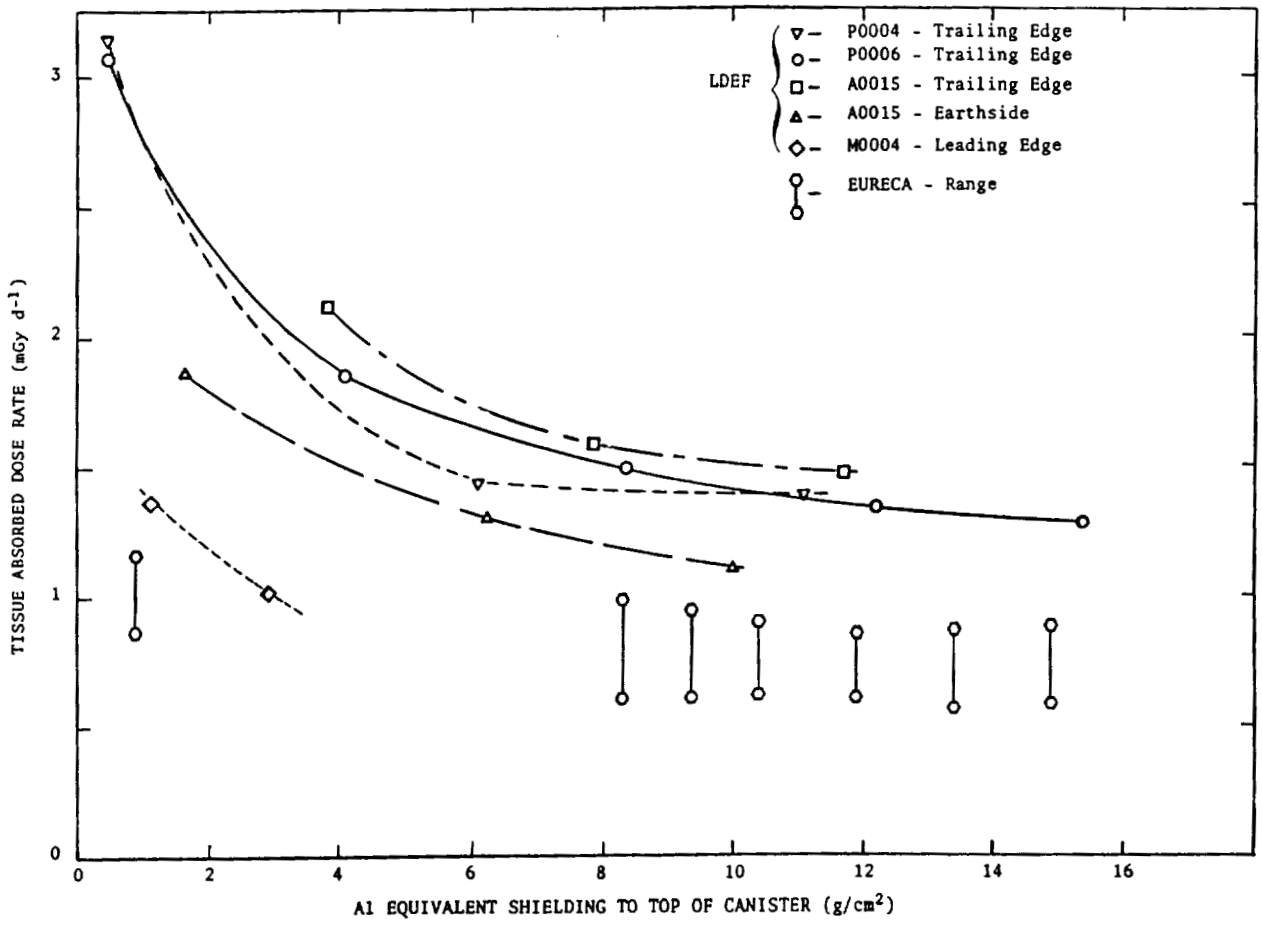

Figure 4: Comparison of LDEF and EURECA TLD-700 dose rates as functions of shielding from the flight canisters and their contents (also thermal blankets on LDEF).

REFERENCES

1. Frank A.L., Benton E.V., Armstrong T.W. and Colborn B.L., "Absorbed dose measurements and predictions on LDEF" *Second Post-Retrieval LDEF Symposium*, NASA-CP 3194, Part 1, pp. 163-170, 1992.

PERFORMANCE CHARACTERIZATIONS OF EURECA RETROREFLECTORS WITH FLUOROPOLYMER-FILLED SiO_x PROTECTIVE COATINGS

Bruce A. Banks
Sharon K. Rutledge
NASA Lewis Research Center
Cleveland, Ohio 44135
Phone: 216/433-2308, Fax: 216/433-2221

Michael Cales
Cleveland State University
Cleveland, Ohio 44115
Phone: 216/433-2308, Fax: 216/433-2221

ABSTRACT

Aluminized corner-cube polymethylmethacrylate retroreflectors were coated with 92% SiO_x-8% fluoropolymer (by volume) and flown on the EURECA spacecraft. The fluoropolymer-filled SiO_x protective coating was found to be durable to atomic oxygen when exposed in a ground-based plasma asher to an anticipated mission fluence of $2x10^{20}$ atoms/cm^2. Unprotected retroreflector surfaces were found to develop highly diffuse reflectance characteristics, thus inhibiting their use for laser retroreflector purposes. A noncontacting retroreflector optical characterization system was constructed and used to measure the optical retroreflection characteristics of the following retroreflector materials: uncoated unexposed, coated unexposed, both uncoated and coated ground laboratory atomic oxygen exposed and coated exposed to space atomic oxygen exposed and coated exposed to space atomic oxygen on the EURECA spacecraft. A comparison of the results of the optical characterizations is presented.

INTRODUCTION

The European Retrievable Carrier (EURECA) Mission included the use of thin, adhesively mounted optical retroreflectors for laser range finding during the retrieval of the EURECA spacecraft. The EURECA spacecraft is a free-flying spacecraft which was launched and retrieved

by the Space Shuttle. The laser retroreflector required durability to atomic oxygen for a fluence in the low 10^{20} atoms/cm^2 range. The acrylic retroreflectors had been used on the Long Duration Exposure Facility (LDEF) and were coated with silicone to prevent optical degradation by atomic oxygen attack (ref. 1, 2). Post-retrieval inspection of the LDEF bicycle reflectors indicated significant degradation in the thin silicone protective coating which had crazed. This allowed atomic oxygen attack of the underlying acrylic corner cube retroreflector. Unprotected polymeric materials are known to be attacked significantly by atomic oxygen producing profusely reflecting surfaces which would not be suitable for laser retroreflector applications (ref. 3, 4). Thus, use of a protective coating applied over the EURECA retroreflector appeared to be a necessity to enable atomic oxygen durability of the specular performance. Ground laboratory and in-space demonstration of SiO_x and fluoropolymer-filled SiO_x protective coatings had demonstrated that such protective coatings should be durable to the anticipated EURECA mission fluence (ref. 4, 5). Thus, the application of an SiO_x or fluoropolymer-filled SiO_x protective coating over the EURECA retroreflector was evaluated and ultimately used in the first functional application in space of such protective coating systems.

APPARATUS AND PROCEDURE

The corner cube retroreflectors used for range finding on the EURECA mission consisted of 15.3 cm x 15.3 cm x 0.22 mm thick sheets of aluminized acrylic reflector material with an adhesive backing for attaching to the EURECA spacecraft. A cross section of the retroreflector configuration for both the uncoated and coated configuration ultimately used is shown in Figure 1. Both approximately 1000Å of SiO_x (where $1.9<x<2.0$) and approximately 1000Å of 8% fluoropolymer-filled SiO_x were evaluated for adhesion to acrylic for retroreflector applications. The fluoropolymer-filled SiO_x was found to be more spall resistant then pure SiO_x coatings; and for this reason, was selected for deposition on the EURECA retroreflectors. Deposition of the 8% fluoropolymer-filled SiO_x coating was accomplished by means of argon ion beam sputter co-deposition from a circular SiO_2 target which had a 5° PTFE Teflon wedge placed on top of it to permit both SiO_x and fluoropolymer scission fragments to deposit on the retroreflector substrates. Deposition of approximately 1000Å was accomplished in approximately 35 minutes of sputter deposition after initial argon ion precleaning. Sputter precleaning was accomplished by a second ion source (designated as 15 cm ion source) as shown in Figure 2. Descriptions of the improved strain-to-failure properties of such fluoropolymer-filled coatings can be found in references 4 and 6. Samples of EURECA retroreflector material were coated with approximately 1000Å of 8% fluoropolymer-filled SiO_x and exposed to atomic oxygen along with uncoated laser retroreflector material in a 13.56 mHz RF plasma asher operated on air to a Kapton effective fluence of $3x10^{20}$ atoms/cm^2. This exposure was performed to evaluate the optical performance of both the protected and unprotected EURECA retroreflector material to the estimated atomic oxygen mission fluence requirement.

Two coated retroreflectors were then provided for attachment to the EURECA spacecraft scuff plate during the spacecraft integration activities. The EURECA spacecraft was deployed from the Space Shuttle Orbiter cargo bay on August 2, 1992, and retrieved after eleven months in space on June 24, 1993, with a total atomic oxygen fluence of $2.3x10^{20}$ atoms/cm^2 exposure to the scuff plate surfaces. The scuff plates containing the two retroreflectors were then removed and post-flight optical characterization was performed at Astrotech Corporation on August 3 and 4, 1993. Figure 3 is a photograph of the EURECA spacecraft showing the retroreflectors on the spacecraft as it is being deployed from the Shuttle bay.

Optical characterization of retroreflector materials cannot be reliably accomplished by conventional diffuse or specular reflection measuring techniques because the specular reflection occurs directly parallel to the incoming illumination. This situation frequently prohibits accurate measurement of the return signal. As a result of this complication, it was necessary to construct an optical measurement system which was specifically designed to measure retroreflectance as opposed to conventional specular or diffuse reflectance. Measurement of the retroreflectance was accomplished by using a 670 nm laser and laser power meter in conjunction with a half-silvered mirror as shown in Figure 4. A sand-blasted fused silica window was used as a light diffuser in front of the laser power meter detector to reduce effects of spatial variations in the output of the laser power meter detector. Such spatial variations occur if a narrow beam laser signal arrives at various locations on the laser power meter detector surface. To prevent the laser power meter from viewing reflected illumination, two welders-glass light-trap surfaces were used to absorb the reflected beam by means of multiple reflections and absorptions. A schematic diagram of the optical characterization apparatus is shown in Figure 4. This measurement system was placed in an opaque black cloth enclosure with a hole in it to allow the exit and return of the laser signal, while preventing stray light detection.

RESULTS AND DISCUSSION

An 8% fluoropolymer-filled SiO_x ($1.9<x<2.0$) protective coating approximately 1000Å thick was found to be durable (based on optical microscope inspections) to atomic oxygen in an RF plasma asher after exposure to a Kapton effective fluence of $3x10^{20}$ atoms/cm^2. In contrast, unprotected EURECA retroreflector samples were significantly attacked by atomic oxygen, resulting in a surface with diffusely scattered light, thus greatly attenuating the intensity of retroreflected light. Figure 5 is a photograph of uncoated and 8% fluoropolymer-filled SiO_x coated EURECA retroreflector materials after exposure to atomic oxygen to a Kapton effective fluence of $3x10^{20}$ atoms/cm^2 in an RF plasma asher operated on air. The photograph shown in Figure 5 was taken by simultaneously illuminating both samples in a direction parallel to the camera viewing direction. Thus the brightness of the sample, as viewed from the direction of the incident light, is a direct indication of the optical performance of the retroreflectors. The uncoated sample appears dark because it diffusely scattered the incident radiation. The bright protected sample appears bright because it confines its reflected radiation to a specular path

parallel to the incident illumination. However, if one views these two samples from a direction other than parallel to the incident illumination, then the atomic oxygen degraded uncoated sample appears much brighter than the protected sample because of significant scattering of the incident illumination from the rough surface of the unprotected sample.

After exposure in space to an atomic oxygen fluence of 2.3×10^{20} atoms/cm^2, the EURECA laser retroreflectors were fully functional, as can be seen in Figure 6. By comparison of Figures 6a and 6b, one can see that the retroreflectors remained capable of returning a bright specular retroreflection signal. Figure 7 shows a close-up photograph of the retroreflector on the left in Figures 6a and 6b. To the unaided eye, the surface of this retroreflector appeared indistinguishable from samples which were not exposed to the space environment. The right retroreflector appeared identical to the left retroreflector except for a small patch 3 cm in diameter where the protective coating had been damaged by abrasion during pre-flight spacecraft integration activities. Apparently, a bolt adjacent to the scuff plate had to be sawed off, causing repeated contact with the retroreflector in this small area. Although this surface-damaged area was then attacked by atomic oxygen, it provided an ideal opportunity to assess the detrimental effects of atomic oxgyen exposure in space to retroreflector material which was not adequately protected.

Optical characterization of the space-exposed retroreflectors required numerous data points to be taken for the various samples at each angle and/or distance because of the great spatial variation in laser retroreflection from the samples. This, in part, is largely due to the fact that the laser beam was approximately 3.5 mm in diameter at 100cm distance, and the corner-cube pattern on the retroreflector material varied in orientation every 4 mm. To average the effects of the spatial variations in retroreflector performance, ten retroreflector measurements were made for each data point averaged and the measurement of the background signal was then subtracted.

Laser retroreflectance characterization of the space-exposed coated EURECA retroreflector materials is shown in Figure 8. This figure compares retroreflectance performance as measured by the optical system shown in Figure 4 for EURECA retroflector material samples that were coated and space-exposed, coated but not exposed, uncoated and unexposed, coated and plasma asher exposed, uncoated and plasma asher exposed, and the matte abraded spot on the space-exposed retroreflector. Because the standard deviation in retroreflectance for the four high absolute-reflectance surfaces was found to be approximately 6% of their reflectance values, one can conclude that the coated and space-exposed retroreflector had an optical performance indistinguishable from coated samples exposed in a plasma asher. However, unexposed samples which were uncoated or coated had reflectances which were 11 or 17% higher respectively. It is obvious from Figure 8 that unprotected retroreflector materials or protected retroreflector materials whose protection has been abraded away both result in severe loss in retroreflection after exposure to atomic oxygen. These quantified results are also qualitatively witnessed in Figure 5, for the laboratory atomic oxygen environment, and Figure 6b, for the space-exposed atomic oxygen environment results. As can be seen in Figure 6b, the right retroreflector does have a dark spot where the abrasion had damaged the optical performance.

The degradation in retroreflected signal versus distance is shown in Figure 9 for various retroreflector surfaces and exposures. As can be seen from Figure 9, based on the 6% uncertainty in the retroreflection signals, all the retroreflector materials whose coatings or exposures have prevented erosion of the surface of the retroreflector have somewhat similar reduction in return signal with distance. However, the uncoated plasma ashed surface had a much more significant loss of return signal with distance than the surfaces of unexposed or protected retroreflector materials. The more rapid loss of retroreflectance with distance of the uncoated plasma ashed surface is a result of the significant diffuse scattering from microscopically roughened acrylic surface.

The optical performance data illustrated in Figures 8 and 9 were for normal-incident laser radiation. In the realistic environment of space, it is unlikely that laser range finding acquisition will occur at normal incidence to the retroreflectors. Thus, it is important that the retroreflectance signal be high even at off-normal incidence to provide a strong return signal. The range finding was successfully accomplished on EURECA, with the retroreflectors providing a bright visual return signal. Figure 10 compares the retroreflectance relative to normal incidence as a function of angle of illumination relative to the surface normal for the various retroreflector surfaces. As can be seen from Figure 10, the EURECA coated and space-exposed retroreflectors had an angular dependence which was indistinguishable from pristine retroreflector surfaces or ones which were coated and exposed to a simulated low Earth orbital environment using RF asher plasma atomic oxygen.

Based on the astronauts' satisfaction with the performance of the retroreflectors, as well as the quantified optical performance shown in Figures 8, 9, and 10, one can conclude that atomic oxygen protection is needed and that 8% fluoropolymer-filled SiO_x protective coatings provide excellent atomic oxygen protection of acrylic retroflector materials for atomic oxygen fluences up to 2.3×10^{20} atoms/cm^2.

SUMMARY

Unprotected acrylic laser retroreflective materials were found to be highly degraded by atomic oxygen produced by ground laboratory RF plasma ashers. Similar optical degradation results were observed for atomic exposure in space on a small portion of a protected EURECA retroreflector which had its protection removed by abrasive damage prior to launch. Thus, it appears that acrylic laser retroreflectors require functional coatings to provide acceptable retroreflectance signals after exposure in low Earth orbit.

A 1000Å sputtered coating of 8% fluoropolymer-filled SiO_x ($1.9<x<2.0$) was found to provide excellent protection of laser retroreflector materials both in ground-based plasma asher tests and in space on the EURECA spacecraft which was exposed to an atomic oxygen fluence of 2.3×10^{20} atoms/cm^2. The optical performance of the protected EURECA retroreflectors was found to be

indistinguishable from protected retroflectors which were exposed to atomic oxygen in an RF plasma asher. The dependence of retroreflectance on distance and angle of arriving illumination was similar for both in-space and ground laboratory atomic oxygen exposed retroreflector samples.

REFERENCES

1. Banks, B. A., Dever, J. A., Gebauer, L., and Hill, C. M.: Atomic Oxygen Interactions with FEP Teflon and Silicones on LDEF. Proceedings of the First LDEF Post-Retrieval Symposium, Kissimmee, FL, June 2-8, 1991.

2. Banks, B. A., Rutledge, S. K., de Groh, K. K., Mirtich, M. J., Gebauer, L., Olle, R., and Hill, C. M.: The Implications of the LDEF Results on Space Station Freedom Power System Materials. Proceedings of the Fifth International Conference on Materials in a Space Environment, Cannes, France, September 16-20, 1991.

3. Lejer, L. J.: Oxygen Atom Reaction with Shuttle Materials at Orbital Altitudes. NASA TM-58246, 1982.

4. Banks, B. A., Mirtich, M. J., Rutledge, S. K., Swec, D. M., and Nahra, H. K.: Ion Beam Sputter-Deposited Thin Film Coatings for Protection of Spacecraft Polymers in Low Earth Orbit. Proceedings of the 23rd Aerospace Sciences Meeting, Sponsored by the American Institute of Aeronautics and Astronautics, Reno, NV, January 14-17, 1985.

5. Rutledge, S. K, and Olle, R. M.: Durability Evaluation of Photovoltaic Blanket Materials Exposed on LDEF Tray S1003. Proceedings of the First LDEF Post-Retrieval Symposium, Kissimmee, FL, June 2-8, 1991.

6. Banks, B. A., Rutledge, S. K., de Groh, K. K., LaMoreaux, C., and Olle, R.: Fluoropolymer Filled SiO_2 Coatings; Properties and Potential Applications. Proceedings of the Society of Vacuum Coaters 35th Annual Technical Conference, Baltimore, MD, March 22-27, 1992.

FIGURES

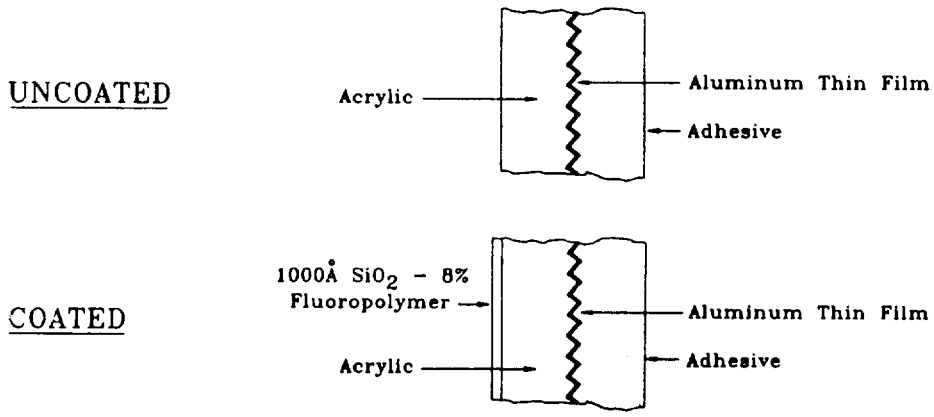

Figure 1. Cross section of uncoated and coated EURECA retroreflector material.

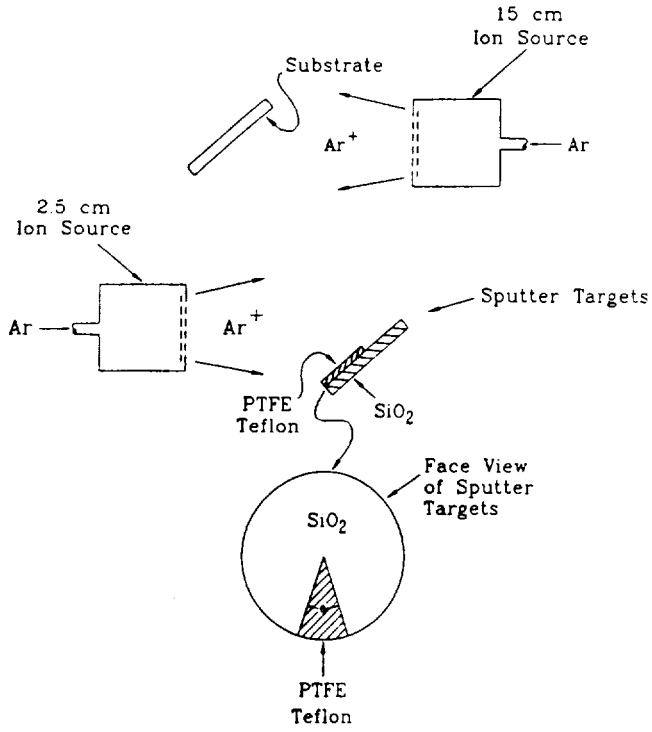

Figure 2. Ion beam sputter coat deposition process for deposition of fluoropolymer-filled SiO_x protective coatings.

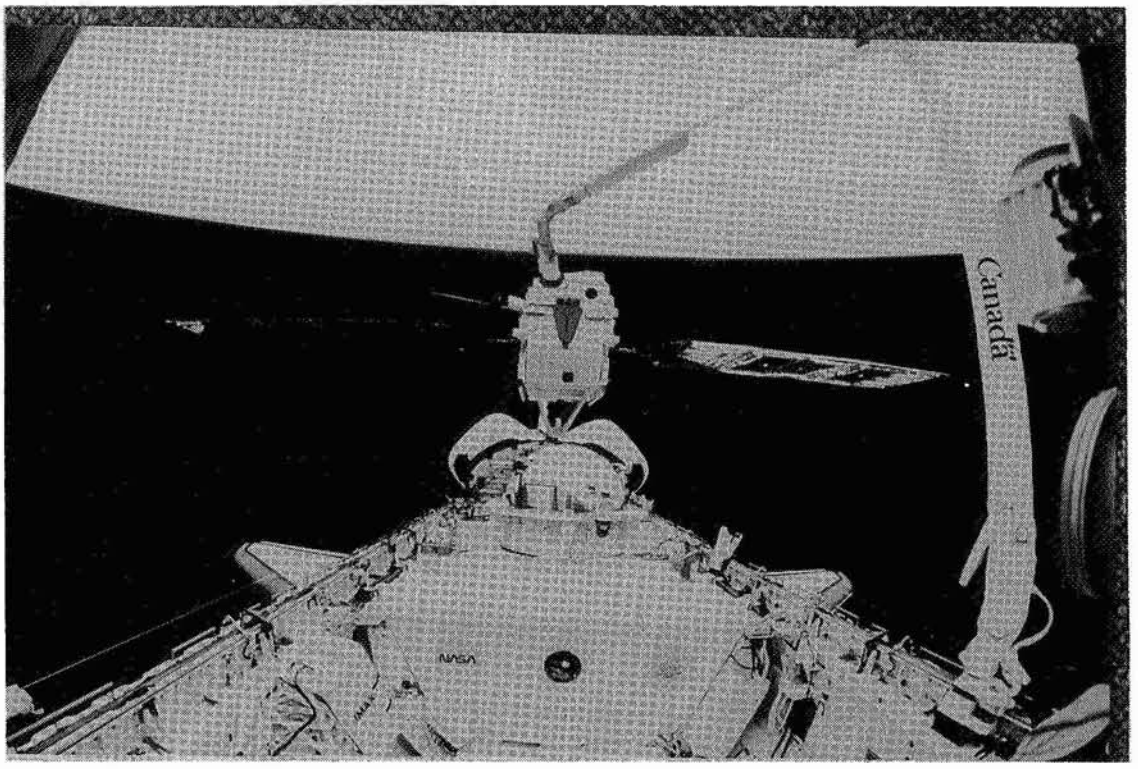

Figure 3. Photograph showing the two laser retroreflectors on the EURECA spacecraft as it is being deployed from the cargo bay of the Space Shuttle on August 2, 1992.

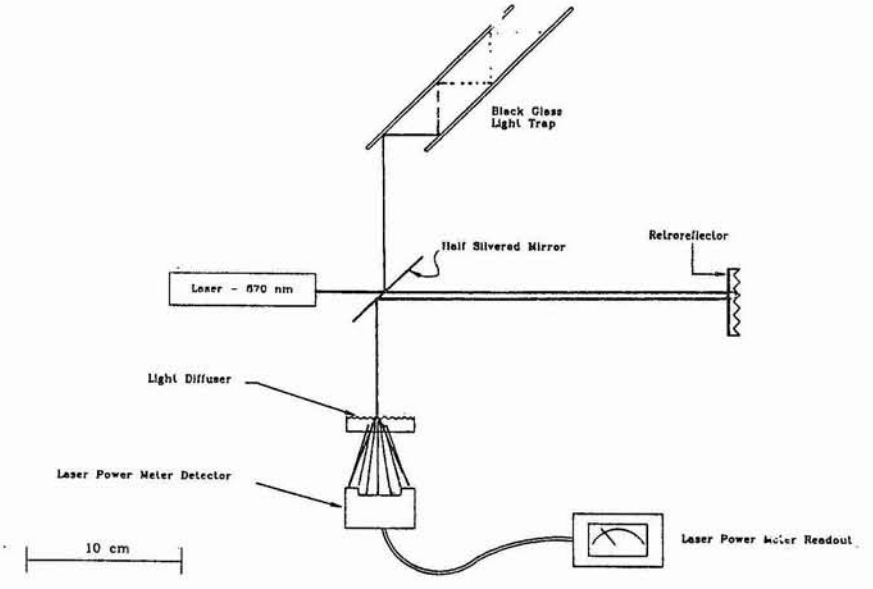

Figure 4. Optical system used to measure the retroreflectance of the EURECA retroreflectors.

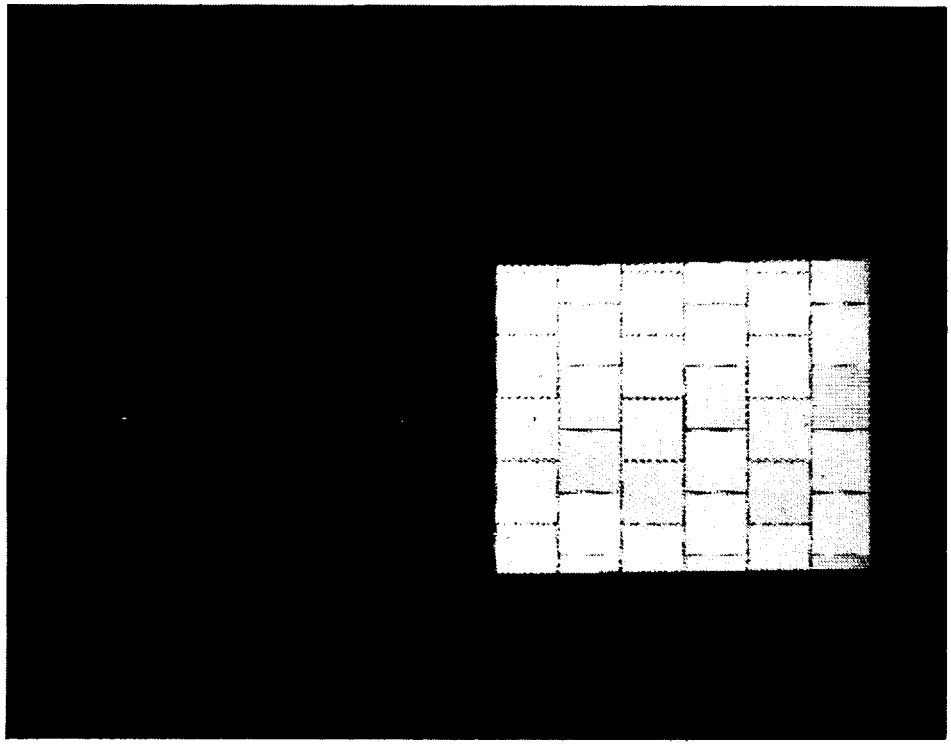

Figure 5. Photograph of uncoated (dark image on the left) and approximately 1000Å thick 8% fluoropolymer-filled SiO_x coated (bright image on the right) EURECA retroreflector samples after exposure to a Kapton effective atomic oxygen fluence of $3x10^{20}$ atoms/cm^2.

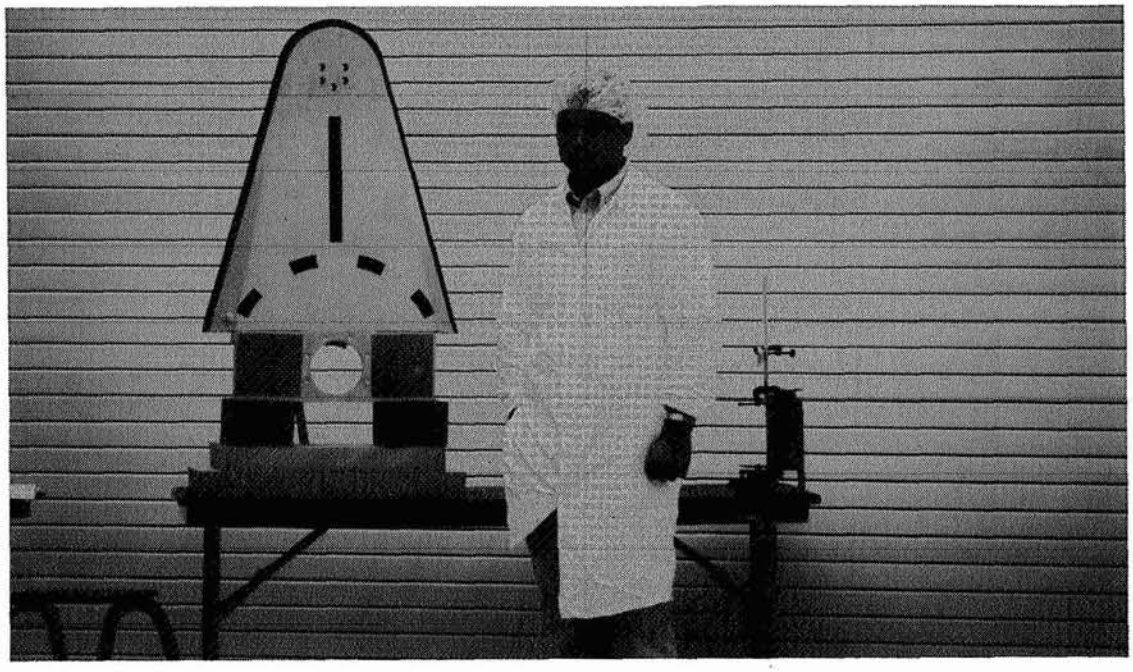

Figure 6a. Photographed with ceiling illumination only.

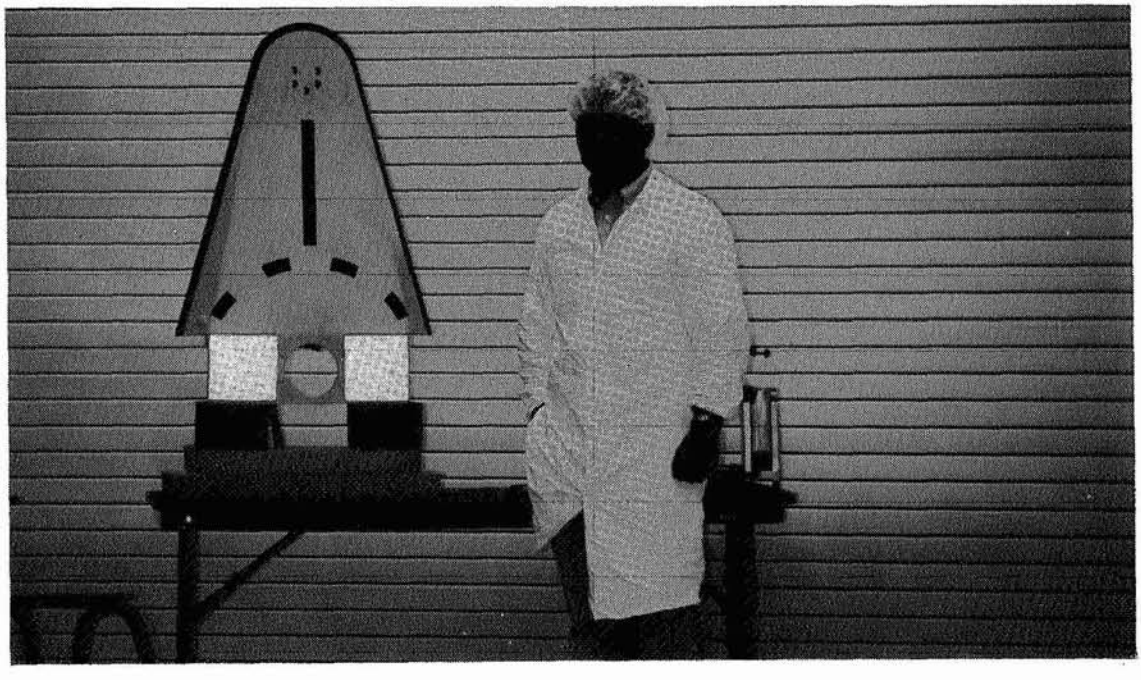

Figure 6b. Photographed with ceiling illumination and incandescent lamp illumination parallel to the camera viewing direction.

Figure 6. Fluoropolymer-filled SiO_x protected EURECA laser reflectors mounted on the EURECA scuff plate after retrieval from in-space exposure.

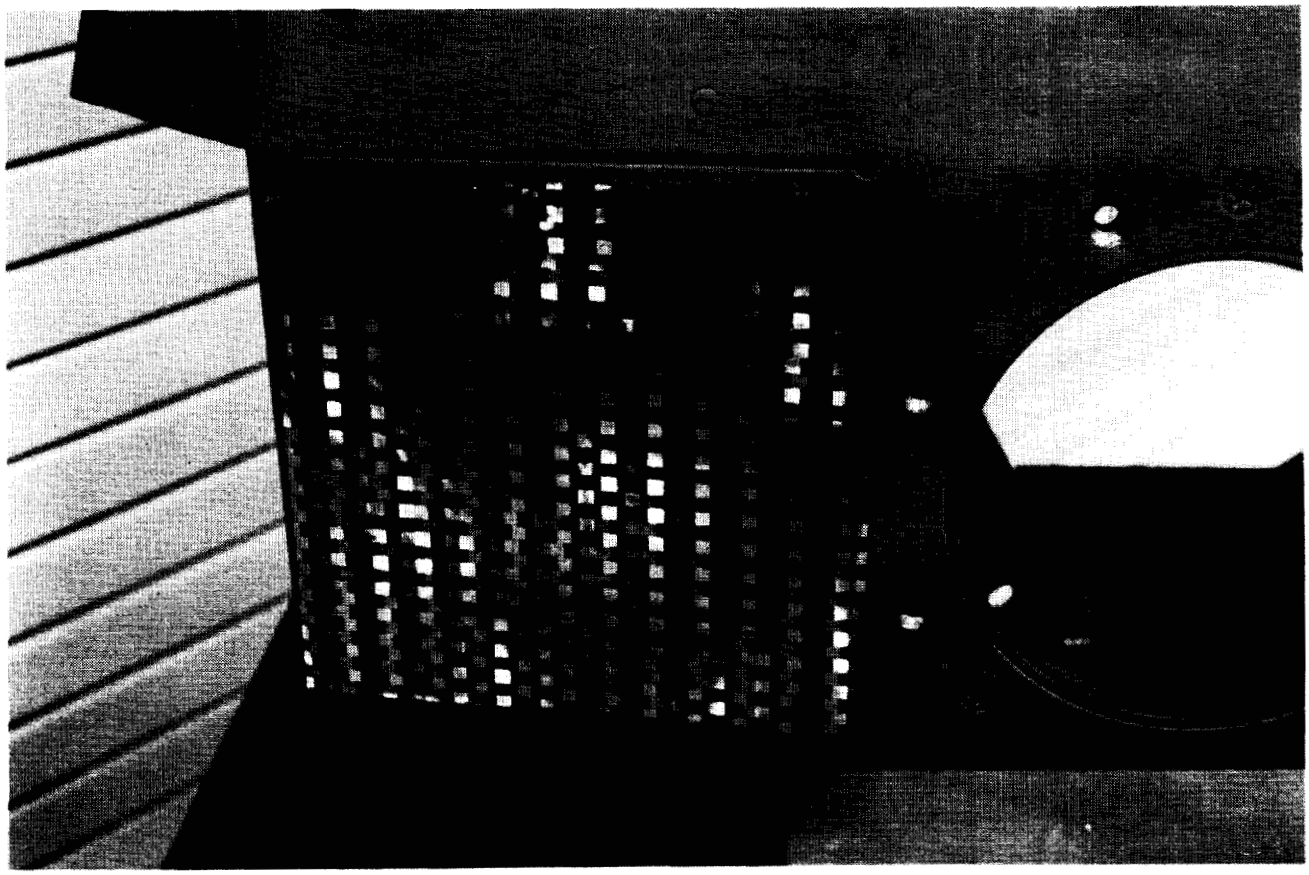

Figure 7. Close-up photograph of left EURECA retroreflector after retrieval from space.

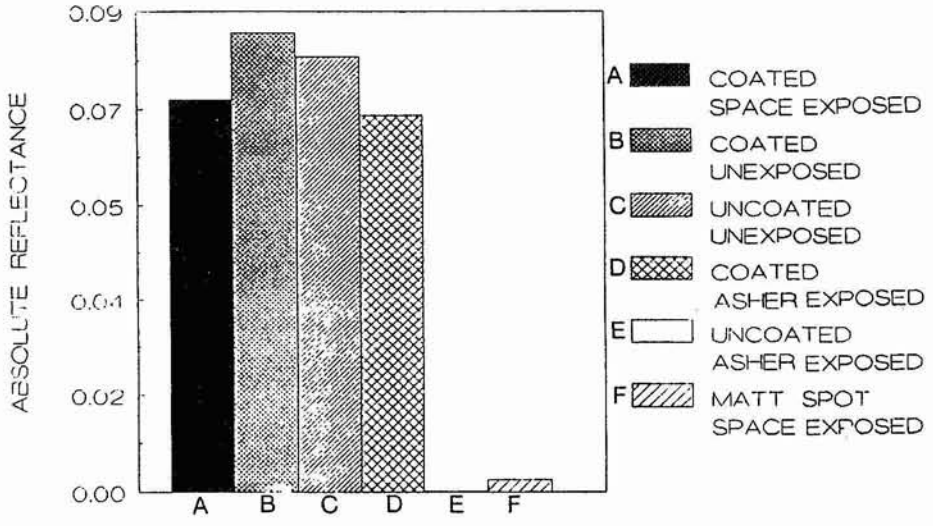

Figure 8. Comparison of optical performance of EURECA retroreflector materials for 670 nm illumination.

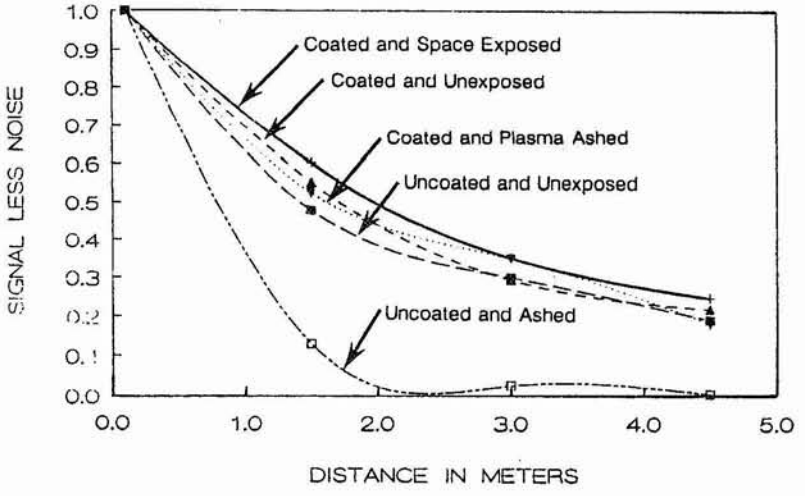

Figure 9. Retroreflector optical performance for coated and space exposed, coated and unexposed, coated and plasma ashed, uncoated and unexposed, and uncoated and plasma ashed retroreflector materials illuminated with 670 nm wavelength light.

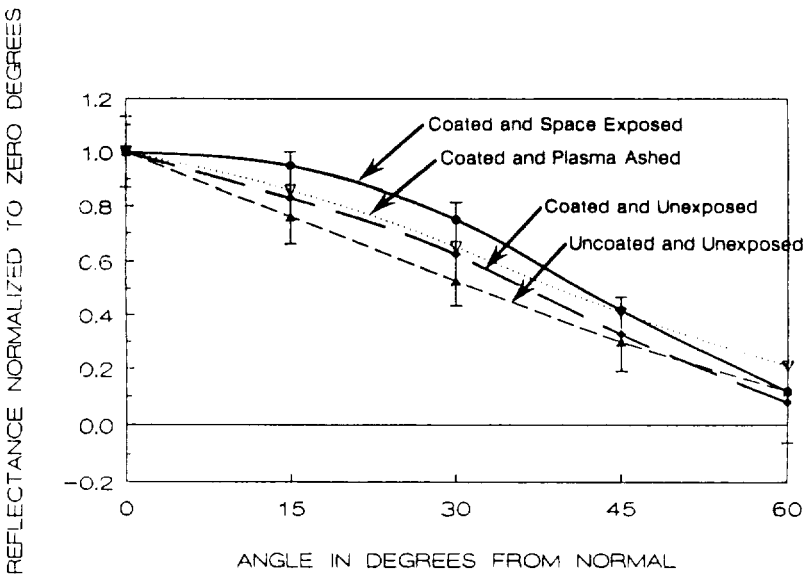

Figure 10. Angular dependence of retroreflectance for coated and space exposed, coated and plasma ashed, coated and unexposed, uncoated and unexposed retroreflector materials illuminated with 670 nm wavelength light.

EFFECT OF THE SPACE ENVIRONMENT ON MATERIALS FLOWN ON THE EURECA/TICCE-HVI EXPERIMENT
- A PRELIMINARY ASSESSMENT -

Carl R. Maag
T & M Engineering
Glendora, CA 91740 USA
Phone: 818-852-9772, Fax: 818-335-9968

William G. Tanner
Baylor University Space Science Laboratory
Waco, TX 76798 USA
Phone: 817-755-3404, Fax: 817-755-3409

Tim J. Stevenson
Mare Crisium
Old Carisbrooke, Isle of Wight, PO30 1NS UK
Phone/Fax: 44-(0)983-822965

Janet Borg
Institut d'Astrophysique Spatiale
91405 Orsay Cedex, France
Phone: 33-1.69.85.86.32, Fax: 1.69.85.86.75

SUMMARY

The primary benefit of accurately quantifying and characterizing the space environmental effects on materials is longer instrument and spacecraft life. Knowledge of the limits of materials allows the designer to optimize the spacecraft design so that the required life is achieved. Materials such as radiator coatings that have excellent durability result in the design of smaller radiators than a radiator coated with a lower durability coating. This may reduce the weight of the spacecraft due to a more optimum design. Another benefit of characterizing materials is the quantification of outgassing properties. Spacecraft which have ultraviolet or visible sensor payloads are susceptible to contamination by outgassed volatile materials. Materials with known outgassing characteristics can be restricted in these spacecraft. Finally, good data on material characteristics improves the ability of analytical models to predict material performance.

A flight experiment was conducted on the European Space Agency's European Retrievable Carrier (EuReCa) as part of the Timeband Capture Cell Experiment (TICCE). Our main objective was to gather additional data on the dust and debris environments, with the focus on understanding growth as a function of size (mass) for hypervelocity particles 1E-06 cm and larger. In addition to enumerating particle impacts, hypervelocity particles were to be captured and returned intact. Measurements were performed post-flight to determine the flux density, diameters, and subsequent effects on various optical, thermal control and structural materials.

In addition to these principal measurements, the experiment also provided a structure and sample holders for the exposure of passive material samples to the space environment, e.g., the effects of thermal cycling, atomic oxygen, etc. Preliminary results are presented, including the techniques used for intact capture of particles.

INTRODUCTION

The space environment is becoming a major concern for many of the space systems presently considered. This concern is due to a combination of fundamental issues. Ultraviolet radiation (UV), electromagnetic waves that have a frequency just above visible light, is present at all orbits. UV heats surface materials at low levels and can also alter the chemical structure of susceptible materials. Atomic oxygen (AO) is present only in low earth orbit (LEO). AO is ionic oxygen atoms travelling at extremely high velocities relative to the spacecraft. The atoms cause erosion of surfaces and oxidation of susceptible materials. AO presents a serious space environment problem in LEO. Although it only affects exterior surfaces, it is a primary concern for thermal control materials and solar array interconnects. Most structural metals (aluminum, magnesium, and titanium) are resistant to the effects of AO exposure. Polymeric/composite materials, to a certain degree, and silver are susceptible to erosion and oxidation due to AO. The erosion products can act as sources of contamination to sensors by increasing the molecular column density in the field-of-view of the sensors.

The debris environment is a dynamic process in which fragmentation due to collisions creates additional objects of different sizes. Some of the small particles are "washed out" by solar pressure and some of the larger particles de-orbit due to aerodynamic drag, if they are in a low orbit. The size distribution as a function of altitude of the total effect is yet unknown but it has been estimated that a uniform increase of at least 2% per year over the entire monitored size range envelopes all uncertainties. Impacts from space debris may cause damage to manned habitable modules, sensors, reflective or refractive optics, etc.

Micrometeoroid and Debris Impact Studies

A large body of experimental data exists concerning hypervelocity impacts. There are several empirical expressions relating the crater volume to the impacting particle size and mass and many previously flown experiments have examined these relationships. It is also well established that a part of the projectile mass is deposited and detectable on the inner surface of the impact crater. Despite being totally disassociated, elements detected from these sites allow coarse categorization of the impacting particle type, particularly with regard to the all important discrimination of space debris.

High purity metallic surfaces have been used for the collection of grains down to submicron sizes [1]. During the impact, a characteristic crater is formed, with rounded habits and a depth to diameter ratio equivalent to the velocity and size of the impacting particle and the encountered metal. During the impact, the particle is destroyed and the remnants are mixed with the target material, concentrating in the bottom of the crater and on the surrounding rims. A major strength of the metallic collectors lies in the fact that analytical techniques can be applied without modification to the craters. Identification of carbon and organic material is quite possible; this is essential for the study of extraterrestrial material (C, H, O, N).

The impact of a hypervelocity projectile (> 3km/s) is a process which subjects both the impactor and the impacted material to a large transient pressure distribution. The resultant stresses cause a large degree of fragmentation, melting, vaporization and ionization (for normal densities). The resulting pressure, however, is directly related to the density relationship between the projectile and target materials. As a consequence, a high density impactor on a low density target will experience the lowest level of damage.

Historically, there have been three different approaches toward achieving the lowest possible target density. The first employs a projectile impinging on a foil or film of moderate density but whose thickness is much less than the particle diameter. This results in the particle experiencing a pressure transient with both a short duration and a greatly reduced destructive effect. A succession of these films, spaced to allow nondestructive energy dissipation between impacts, will reduce the impactor's kinetic energy without allowing its internal energy to rise to the point where complete destruction of the projectile mass will occur. An added advantage to this method is that it yields the possibility of regions within the captured particle where a minimum of thermal modification has taken place [2].

Polymer foams were employed as the primary method of capturing particles with minimum degradation [3]. The manufacture of extremely low bulk density materials is usually achieved by the introduction of voids into the material base. When these low density micropore foams are used, the shock pressures that occur during impact are minimized, which in turn maximizes the probability of survival for the impacting particle.

EURECA EXPERIMENTATION

As a consequence of the experimental data developed during both recent and earlier STS missions and the data expected from this mission, the authors have produced and delivered an experiment for the European Space Agency, European Retrievable Carrier (EuReCa). The Hypervelocity Impact (HVI) experiment was flown as part of the TICCE experiment. The EuReCa payload was launched on the Space Shuttle Atlantis (OV-104) on 31 July 1992, providing a total mission exposure of nearly eleven (11) months in low earth orbit. The TICCE/HVI experiment is shown in Figure 1.

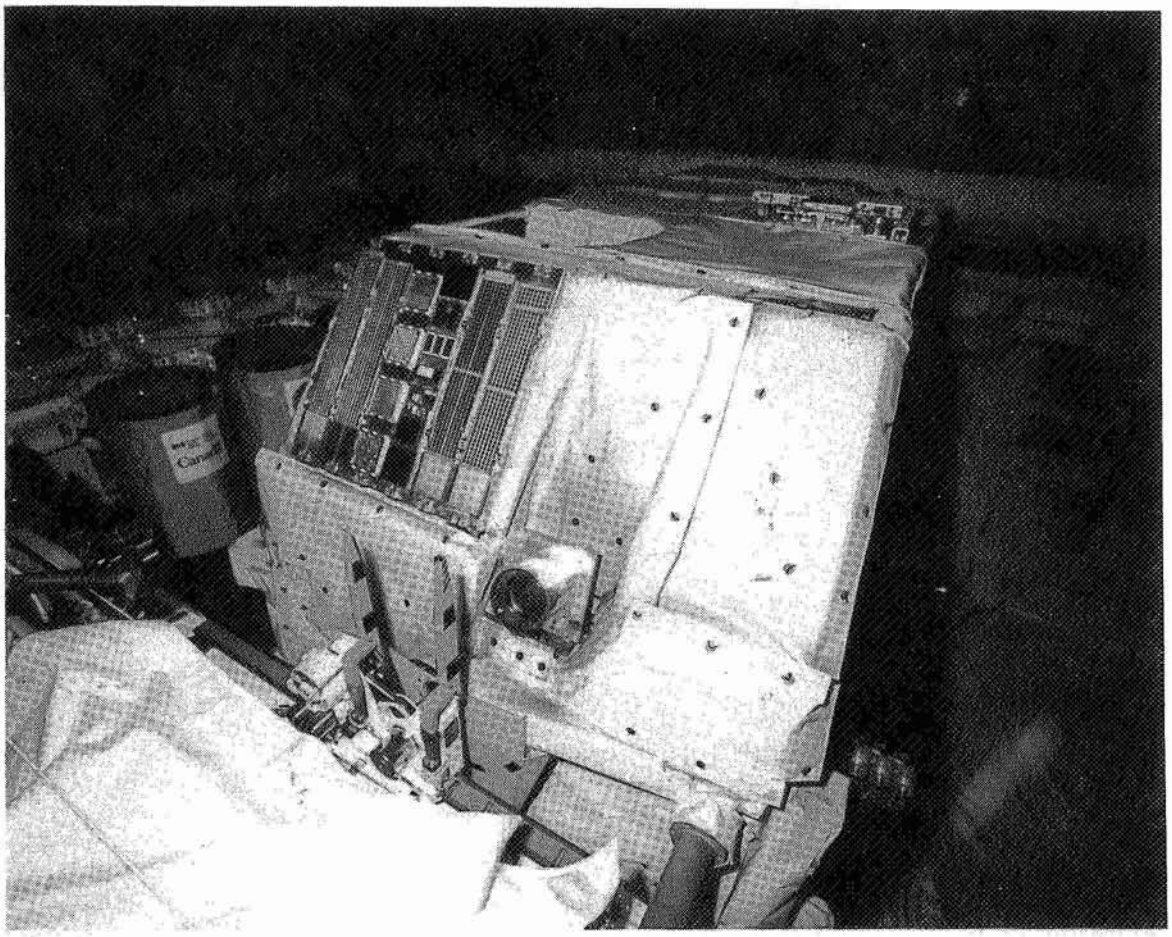

Figure 1. The TICCE/HVI experiment shown mounted to the EuReCa spacecraft.

Objectives of the TICCE/HVI Experiment

The primary objectives of the experiment were to (1) Examine the morphology of primary and secondary hypervelocity impact craters. Primary attention will be paid to craters caused by ejecta during hypervelocity impacts on different substrates; (2) Determine the size distribution of ejecta by means of witness plates and collect fragments of ejecta from craters by means of momentum sensitive micro-pore foam; (3) Assess the directionality of the flux by means of penetration hole alignment of thin films placed above the cells. (4) Capture, intact, the particles which perforated the thin film and entered the cells. Capture medium consisted of both previously flight tested micro-pore foams and Aerogel.

EuReCa 1 Experimental Design

The experiment is comprised of a variety of materials bonded to a large substrate. The design allowed for data to be acquired for both engineering and scientific interests. As previously discussed, the investigators used the numerous techniques to both quantify and understand the effect of the micrometeoroid and debris complex. One of the principal techniques used was the thin film capture cell. The topmost cell (one of two on the experiment) possessed a thin Aluminum film (nominal $t_f < 500$ Å) stacked above a coated substrate. The plane of the film contains 100 cm^2 of impact surface over a Buckbee Mears (90% transmissive) grid which supports the thin film. Each mesh has been covered with an aluminum-coated epoxy layer nominally 5 μm thick to inhibit production of

X-rays by 20kV electrons during laboratory analyses. An estimate of the trajectory of grains within the experiment can be derived from analysis of penetrations made in the thin film and impact sights. Beneath the thin film and above the substrate a network of collimating plates were installed. Each highly polished 0.625 mm thick 3300 aluminum plate was 100 mm long with a height of 8 mm, and possessed slots so that they could interlock with perpendicular plates. These divisions assured that grains whose velocity vectors make a large angle with respect to the surface normal of the 500 Å film would not impinge on another cell, but will impact the witness plates of a specific cell or be stopped by a thin film. The 3300 aluminum witness plates would also record the demise of "barely" penetrating grains. The underside of each thin film will be investigated to assess the constituents of debris clouds deposited on each thin film. The primary function of the 3300 aluminum witness plates near the substrate will be to record the ejecta produced when a hypervelocity grain encounters a semi-infinite stopping plate, viz., the substrate, which has been coated with 2000 Å of Gold. It was not necessary that each portion of the substrate surface be normal to the particle's incident direction. In fact, since the grains which penetrate the film will be directional, the effects of oblique hypervelocity impacts can be examined using the orbital debris and micrometeoroid complex. Angles up to 45° with respect to the substrate surface normal have been accommodated in the design of several of the cells.

Passage of a Particle Through a Thin Film

The pressure an impacting dust grain experiences during a hypervelocity impact can be sufficient to alter the state of matter of the particle. However, very short duration high-pressure pulses can be sustained in large dust grains without fragmentation or complete phase change occurring. In this class of events the cross-sectional area of the impinging dust grain and the thickness of the target are important components of the interaction. The surface area over which a force is administered and the length of time in which the impulse is delivered define the magnitude and the duration of the pressure pulse which gives rise to a sustained shock front in the material. The duration of the shock front will also be determined by the depth of penetration and therefore the thickness of the target, T_f. If one considers the dynamics of an impact event from the perspective of a penetrating particle, the ratio which defines the aspect ratio of the dust grain, i.e., L/D_p, may be investigated to determine the residual length of the particle upon encounter with a thin target. In the case of a thin film penetration event, the ratio of interest is that between the diameter of the dust grain, Dp, and the thickness of the film, T_f. It has been well documented [3] that a projectile with a high aspect ratio will penetrate to a depth defined by the following relationship:

$$p = L \left(\frac{\rho_p}{\rho_T}\right)^{0.5} \tag{1}$$

The penetration depth, p, of a rod into a thin film can be equated with the film thickness, T_f, and the residual length L_R of the penetrating rod can be equated with the residual diameter of the dust grain. The change in the diameter of the dust grain can be roughly estimated to be

$$\frac{L_R}{D_p} \sim 1 - \frac{T_f}{D_p}\left(\frac{\rho_p}{\rho_T}\right)^{0.5} \tag{2}$$

In the case of a ratio of $D_p/T_f = 30$ the residual diameter of the dust grain would be greater than 90% by this estimation. Even though the uneroded nature of the material composing the incident dust grain can only be assessed by other measurement means, the foregoing analogy may serve as a metric for further analysis.

Of particular interest in these investigations is a specific empirical form which relates penetration hole size with the diameter of the penetration hole. This experimentally derived equation for the description of the penetration relationship for iron projectiles impacting aluminum films of various thicknesses was developed by Carey, McDonnell, and Dixon (CMD) [4]. The Carey, McDonnell & Dixon (CMD) empirical equation is being compared with the results of computer simulations of hypervelocity impacts for various velocities of interest for surfaces flown in LEO.

$$\frac{D_h}{D_p} = 1 + 1.5\left(\frac{T_f}{D_p}\right) v\ 0.3\left(\frac{1}{1+\left(\frac{T_f}{D_p}\right)^2 v\ -n}\right);$$

$$n = 1.02 - 4\exp\left(-0.9\ v\ 0.9\right) - 0.003\ (20 - v) \qquad (3)$$

DATA ANALYSIS AND EXPECTED RESULTS

Primary analyses will be performed using a Scanning Electron Microscope (SEM) outfitted with a Princeton Gamma Tech (PGT) elemental analysis system (Beryllium window). Since each unit cell is ~10 mm square, samples will be easily prepared for viewing in the SEM. The SEM is sufficiently large to support the viewing of 5 cm substrate material.

Count of hypervelocity impact craters on the witness plates with diameters larger than 4 μm will be accomplished by the use of SEM photographs. Once digitized by means of a high-resolution optical scanner, these data will be analyzed using a hypervelocity impact morphology system.

Analysis of the substrate will be of particular importance. The same procedure outlined above to analyze the witness plates will be applied to the substrate. Of primary interest will be the recovery of data concerning the affects on the substrate's optical properties, which have been subjected to primary and secondary hypervelocity impacts. Also recoverable from the substrate (and perhaps the witness plates) will be data pertaining to the fragmentation of grains by the thin films.

Principal theoretical analyses will be conducted using hydrocodes to establish the limiting mass which will penetrate all, two, or only one of the thin films. Comparisons of the computational results with experimentally derived parameters will be carried out. Results of both two-dimensional (2D) and three-dimensional (3D) computer simulations of the hypervelocity impact events which penetrate the EuReCa 1 thin films will be reported at a later date. A relationship between the particle diameter, D_p, and the diameter, D_h, of the hole created in a 500 Å aluminum thin film (T_f) and micropore foam (T_m) for relevant particle and target parameters will be derived and will be compared with empirical equations. That relationship will be used to analyze *in situ* data of the thin film experiments flown in LEO, and to determine the size distribution of grains which penetrate the thin films and are captured intact in the micropore foam [2].

Based on the present knowledge of the space debris and micrometeoroid fluxes, all cells should be penetrated by grains with the properties: $m_p = 3.4 \times 10^{-13}$ g; $r_p = 3.8$ g/cm^3; $v_p = 7.00$ km/s; thus, $r_p = 0.3$ μm.

PRELIMINARY RESULTS

Data from the two-dimensional (2D) computer simulations of hypervelocity impact events for the TICCE/HVI thin films conform to a high degree with the Carey, McDonnell, and Dixon (CMD) equation for all densities tested.

Early examination of the aerogel samples flown on the EuReCa TICCE exhibit signs of shrinkage (~ 6 percent in both length and width). Recovery as a function of time will be monitored.

Visual impacts were observed in the deceleration films covering the polymeric foam capture cell experiments. Perforations are visible in all cells. A flux of 10^{-4} impacts/m^2-s (5μm particles) has been calculated for one of the capture cells. Three grains have been removed intact. Work is proceeding to analyze the perforations and remove other grains. The largest impact crater observed

on the HVI plate was elliptical (1.85 x 1.34 mm), with a spall zone of 6.2 mm. Figure 2 shows the impact.

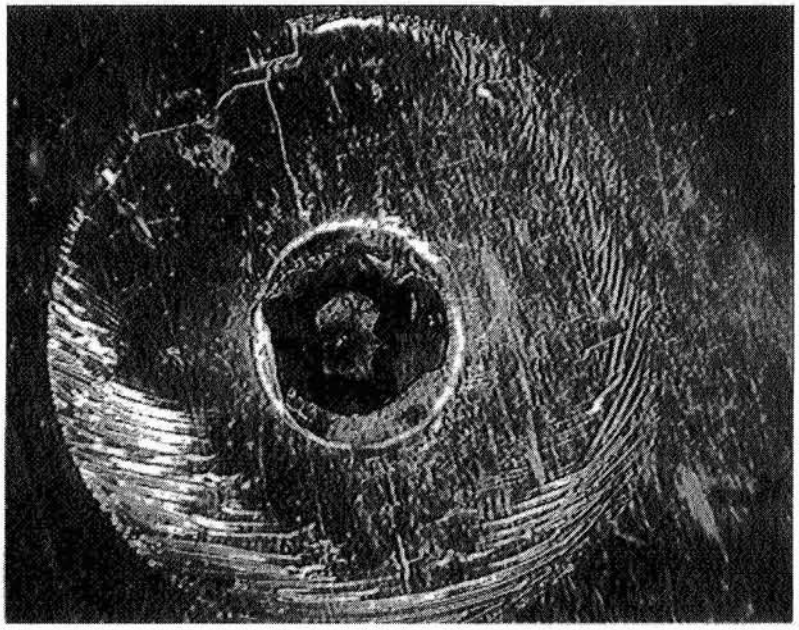

Figure 2. Largest impact observed on the TICCE/HVI experiment.

ACKNOWLEDGEMENT

The authors are indebted to Professor J.A.M. McDonnell for providing space on the TICCE payload to accommodate our experiment.

REFERENCES

1. Bibring, J-P., Borg, J., Langevin, Y., Rosenbaum, B., Salvetat, P. and Surkhov, Y.A., *Lunar and Planetary Sci.* XVI, 55-57, 1985.

2. Tanner, W. G, McDonald, R. A., Alexander, W. M, Maag, C. R., An examination of hypervelocity particle penetration parameters for thin films flown in space, *Intl. Journal of Impact Engineering.*

3. Maag, C. R., Tanner, W. G., Stevenson, T. J., Borg, J., Bibring, J-P, and Alexander, W. M. (1993) Intact capture of hypervelocity impact particles and ejecta, 1st European Conference on Space Debris, esa SD-01.

4. Carey, W. C., McDonnell, J. A. M. and Dixon D. G., An empirical penetration equation for thin metallic films used in capture cell techniques, 85th Proceedings of IAU.

MATERIAL INSPECTION OF EURECA

FIRST FINDINGS AND RECOMMENDATIONS

Marc Van Eesbeek, Michael Froggatt and Georges Gourmelon
ESA/ESTEC
Noordwijk
The Netherlands

ABSTRACT

This paper gives the first results of the Post flight materials investigation on the European Retrievable Carrier (EURECA) after a stay of 11 months in LEO.
The paper will concentrate on the first findings after the visual inspection performed at KSC and Astrotech and give some general design recommendations for potential future Carrier flights.

INTRODUCTION

This materials investigation is part of the more general Post-flight technology Investigations Programme on EURECA initiated by the ESA Technical Directorate and fully supported by the ESA/EURECA project team.

This programme also includes a comprehensive meteoroid and debris investigation, inquiries into anomalies and failures at carrier and experiment level and some basic technology studies (Ref 1).

The material investigation is a joint effort between ESA/ESTEC Materials Division and DASA/ERNO materials specialists and consists of the following main activities :

- Visual inspection shortly after landing at KSC (in OPF and VPF facilities) and during the disassembly of the carrier at Astrotech. More detailed inspections are in the process of being performed at ESTEC and at different Experimenters sites.

- Photographic documentation of carrier and payload during these inspections. At this moment we have in total some 1200 photographs catalogued, 400 taken at KSC, the rest at Astrotech.

- Thermo-optical properties (α_p and ε_n) have been measured on some 100 positions over the spacecraft.

- Organic Contamination is measured using wipes and direct measurements. The analyses first concentrate on IR-spectroscopy and will be followed by more sensitive ESCA and AUGER methods.

- Degradation of material properties due to exposure to the LEO-environment (AO-effects, transmission losses in optics...)

- A database on the above has been developed by DASA/ERNO and contains already results of visual inspection, photographic documentation, α/ε measurements.

FIRST INSPECTION RESULTS

An overall EURECA configuration, experiment description and mission profile are given in Ref.2. A schematic view of the integrated spacecraft can be seen in Fig 1. The solar arrays , located on the +X and -X faces, are deployed to expose the radiator panels.

The majority of the experiments, except for the Inter Orbit Communication Antenna (IOC), are located on the top deck (+Z) either exposed or below the MLI tent. The multi-layer insulation consists of a Beta Cloth top layer and a number of layers of double sided Acrylic coated Aluminised Kapton (typically 20 layers). In order to avoid the contamination and degradation of the Beta Cloth, found during solar simulation testing, it was decided to use a silicone-free version of this material. Only some limited parts of the MLI were still consisting of the original silicone-containing material.

It should be mentioned that even the first thermo-optical measurements were taken only 4 weeks after retrieval and landing of the spacecraft. Some materials are liable to show a significant recovery effect. After UV and particle irradiation tests performed at CERT/DERTS in Toulouse a typical recovery of 0.1 within a few weeks after exposure to air has been found on PSG 120 FD paint. (Ref. 3.)

+Z face (sun-lit top face)

The Beta Cloth over the whole upper area is light brown in colour as a result of possible contamination and UV irradiation, the total solar exposure being ± 5000 e.s.h. This has led to an increase of the Solar Absorptance of 0.07 on most of the blankets and up to 0.26 in very contaminated areas. No appreciable change was found in the Normal Emittance values (see table 1).

There are signs of outgassing from within the spacecraft (see photos 1 to 5). These signs sometimes called "nicotine stains" or brown stains emanate from different unintentional venting holes, e.g. around Attitude and Orbit Control System (AOCS sensors), the Atomic Oxygen Sample Tray (AOST) experiment , Protein Crystallisation Facility (PCF) dome, the Advanced Solar Gallium Arsenide Array (ASGA) , GRAPPLE fixture etc.

The FEP tape (Sheldahl G401905 5 mil Silvered Perforated Teflon type A) on the AOCS sensors tower is heavily contaminated and typical shadowing effects can be seen.

On the Solar Constant and Variability Instrument (SOVA) the aluminised FEP-surface shows non-homogeneous brown stains with a particular pattern, apparently due to temperature gradients on the surface (see photo 6). It is believed that close to tape perforations and tape joints the temperature is higher as a result of the much higher α/ε-ratio and that therefore less condensation and subsequent degradation occurs.

On several optical instruments a degradation of the performances was reported during the flight. Contamination of the front optics was visible and will have contributed to these losses; however, it also appeared that several of the front filters showed failures at interfaces between the different layers. The pure contamination related degradation was highly wavelength dependent (see Fig. 2.).

The amber reflector / orientation patch is blackened as a result of UV irradiation.

The MAP SG11FD white paint on the Solar Spectrum Instrument (SOSP) is slightly tan coloured as a consequence of UV irradiation, resulting in an increase in α of 0.2 and an increase in ε of 0.015.

-Z face (bottom)

There are again signs of outgassing from within the spacecraft. This is very obvious on blankets, around battery boxes and around struts. An increase in α of up to 0.026 was recorded in the contaminated areas. The direct solar irradiation was low since the -Z face was earth oriented during the whole mission, except for a very limited time span, estimated at max 30 hrs, during manoeuvering in the first days of the mission. This could mean that the effect of Albedo UV-radiation in the degradation process cannot be neglected.

The baseplate of the Power Control Unit (PCU), painted in PSG 120 FD, which was recessed approx. 10 cm from the front face of the PCU was degraded (contamination + Albedo UV). The maximum resulting increase in α was 0.13. It is believed that this increase was mainly due to a polymerisation of a contaminant rather than a degradation of the paint itself.

The four keel strut heaters show signs of overheating because of insufficient thermal contact (not bonded by adhesive, maintained by tie-wraps). This is under investigation by DASA/ERNO. Also the heaters from the keel cold gas thrusters show signs of degradation.

On the IOC antenna dish some marks from previous bonding of thermocouples were visible. Marks caused by possible cleaning prior to flight were accentuated by some environmental interactions (UV, Atomic Oxygen ?). Some iridescence on the black thermal blanket was visible as a result of contamination.

+X and -X faces

In general the Beta Cloth is less degraded than on the +Z face (top face), as can be expected from the smaller solar input. This has resulted in an increase of the Solar Absorptance of 0.02 on most of the blankets and up to 0.055 in more contaminated areas (close to ventings).

The EURECA signs (both on -X and +X) show some slight browning of the white paint (PSG120FD), resulting in a $\Delta\alpha$ of +0.07.

The green orientation patch has darkened.

Very prominent degradation of outgassing products is visible on PCF dome where the blanket meets the PSG120FD white paint (see photo 7). Some concentration effect of this degradation is due to multi-reflections in small V-grooves formed between both blanket and dome. The degradation on the top side (+Z) of the dome resulted in an increase in α varying between 0.13 and 0.20, while on the side this increase was limited to 0.04.

The PSG120FD white painted Aluminised Kapton foil from the MLI below the hydrazine thrusters is cracked and peeling due to mechanical and thermal stresses. Also disbonding of folded-over edges on these foils occurred.

The darkening of the MLI in the area of the PCF can be seen in photo 8 where the contrast is obvious between the shaded area below the strut of the payload tent and the exposed area.

+Y face

Here also there are signs of outgassing from within the spacecraft. They are particularly obvious below the Timeband Capture Cell Experiment (TICCE) and behind the Radiofrequency Ion Thruster Assembly (RITA) where there was an unintentional opening in the MLI cover that acted as a chimney (see photo 9). This has resulted in an increase of the Solar Absorptance of 0.06 on most of

the blankets and up to 0.13 in very contaminated areas. No appreciable change was found in the Normal Emittance values (see table1).

The Aluminised FEP (Sheldahl G400900 perforated) on RITA has degraded, due to UV irradiation and Atomic Oxygen attack. Some crazing near perforation holes was visible on the sun-exposed side.
The degradation and splitting of the shrink sleeve surrounding the RF power supply cable of the thruster is mainly resulting from an improper thermal blanket design.

The SCUFF PLATE shows signs of ATOX degradation of the yellow Chemglaze Z853 and the black Z306 paint. The paint is powdering and faded. The paint shows a bad adhesion and is peeling from the substrate (see photo 10).

-Y face

There are signs of outgassing from within the spacecraft. They are particularly obvious behind the Wide Angle Telescope For Cosmic Hard X-rays (WATCH) and on the Freon line MLI, as shown in photo 11.

This has resulted in an increase of the Solar Absorptance of 0.06 on most of the blankets and up to 0.13 in very contaminated areas, similar to the +Y face. No appreciable change was found in the Normal Emittance values.

The GRAPPLE fixture shows signs of UV/ATOX degradation of the grey paint, a blend of Chemglaze black paint TT-C-542 type 2 and a Chemglaze white paint TT-C-542 type 1 (Ref. 4), with a shadowing effect, possibly from the grab arm. The paint is powdering and faded. NASA is investigating if outgassing from the RMS arm has discoloured the GRAPPLE plate.

Inside

The general appearance of the interior of the spacecraft was visibly clean and no apparent problems were noted on painted areas, harness or structure.

The Aluminium tape used to bond cables on the black painted top platform (behind TICCE) has disbonded in some areas.

CONCLUSIONS

Although there is an overall contamination and a noticeable degradation on the +Z face as a result of UV-irradiation, most visual degradation effects are due to venting through apertures from inside the spacecraft, such as e.g. overlaps between thermal blankets. This contamination has polymerised and has darkened under the action of solar Ultraviolet at these vent holes, resulting in the "nicotine stains", very well known from the LDEF after-flight visual inspections.

Also the Earth-facing surfaces showed some brown degradation. These surfaces were sun-lit only during some short manoeuvering periods (total estimated sun exposure < 20hrs). Although the UV in the albedo spectrum is very limited, one cannot exclude this effect totally.

The usefulness of shutters for optical experiments is well demonstrated by the SOSP experiment, where the contamination was confined to the upper side of the shutters rather than on the underlaying optical elements.

RECOMMENDATIONS FOR FUTURE EURECA-FLIGHTS

Since the primary mission objective was microgravity oriented, most of the experiments were built contamination insensitive. There were however some optics on-board that degraded heavily due to deposition and degradation effects. There are some simple measures that can be taken that will reduce the contamination potential for these critical surfaces, namely:

- As far as possible all optical apertures should be within a single plane.
- Use shutters for optical payloads when appropriate.
- No venting shall be allowed in the vicinity or in view of optical apertures, optics and cold surfaces.
- Venting should be directed as much as possible to the wake region.
- Control the thermal blanket design and manufacture to avoid undesired venting due to gaps between different elements. Overlaps, if used, should not be vent openings. It is preferable to have the edges butting to each other and tightly joined.
- A bake should be applied to the carrier, the harness, and the different experiments in order to assure a cleanliness level in conformance with the needs dictated by the most sensitive experiments or sub-systems and to avoid all cross contamination.
- Cleanliness and contamination control specifications (e.g. during manufacturing, testing, handling, packaging, storage) to the appropriate level shall be implemented not only on

optical payloads, but on the whole spacecraft, including the non-sensitive payloads. This also includes a close follow-up by means of Critical Cleanliness Reviews at payload and spacecraft interface levels.

AKNOWLEDGEMENTS

We wish to thank the EURECA project teams and experimenters for the valuable support received during the inspection activities at the different sites.

We also wish to thank the DASA/ERNO materials team, U. Rieck, H. Kersting, B. Schwarz, H.J. Rosik for the cooperative effort in documenting, inspection and photographic data.

We would also like to thank J. Guijt and T. Harper for the various analyses and interesting discussions towards the contamination work performed.

REFERENCES

Ref. 1 ;R. Aceti, G. Drolshagen, L Gerlach, G. Racca. Meteoroid and Debris Investigation on Eureca; ESA/ESTEC. First European Conference on Space Debris. ESA SD-01

Ref. 2. A. Dover, R. Aceti and G. Drolshagen ESA/ESTEC EURECA 11 Months in Orbit - Initial Post Flight Investigation Results . 3rd LDEF Post-Retrieval Symposium, Williamsburg , Virginia, Nov. 1993.

Ref. 3. ESA ESTEC contract 10023/92/NL/NJ
Etude ONERA/CERT/DERTS 439700.

Ref. 4. Private Communication from J. Beaman, Lockheed Engineering and Sciences Company.

TABLE 1. THERMO-OPTICAL VALUES

Face	Material	$\Delta\alpha_p$ Absorptance		$\Delta\varepsilon_n$ Emittance	
		Minimum $\Delta\alpha_p$ Post-flight	Maximum. $\Delta\alpha_p$ Post-flight	Minimum $\Delta\varepsilon_n$ Post-flight	Maximum. $\Delta\varepsilon_n$ Post-flight
+Z	Beta cloth	+ 0.067	+0.26	-0.004	+0.006
+Z	ASTRAL PSG120FD white paint on top of PCF dome	+0.188	+0.198	-0.020	-0.014
+Z	MAP SG11FD white paint on SOSP	+0.127	+0.194	+0.015	----------
+X	Beta cloth	+0.024	+0.052	0	+0.005
+X	ASTRAL PSG120 FD	+0.001	+0.043	-0.001	-0.015
-X	Beta cloth	+0.02	+0.055	-0.010	+0.008
-X	ASTRAL PSG120FD white paint on thruster foils	+0.005	+0.06	-0.005	-0.007
+Y	Beta cloth	+0.06	+0.127	-0.004	-0.003
+Y	Chemglaze Z853 yellow paint on scuff plate	-0.062	----------	+0.007	----------
+Y	Chemglaze Z306 black paint on scuff plate	+0.030	----------	+0.020	----------
-Y	Beta cloth	+0.06	+0.13	-0.008	-0.002
-Y	Chemglaze Z853 yellow paint on scuff plate	-0.072	-0.043	-0.010	+0.020
-Y	Chemglaze Z306 black paint on scuff plate	+0.025	+0.030	+0.037	+0.048
-Z	Beta cloth	+0.012	+0.026	+0.005	+0.006
-Z	ASTRAL PSG120FD	+0.011	+0.131	0	+0.002

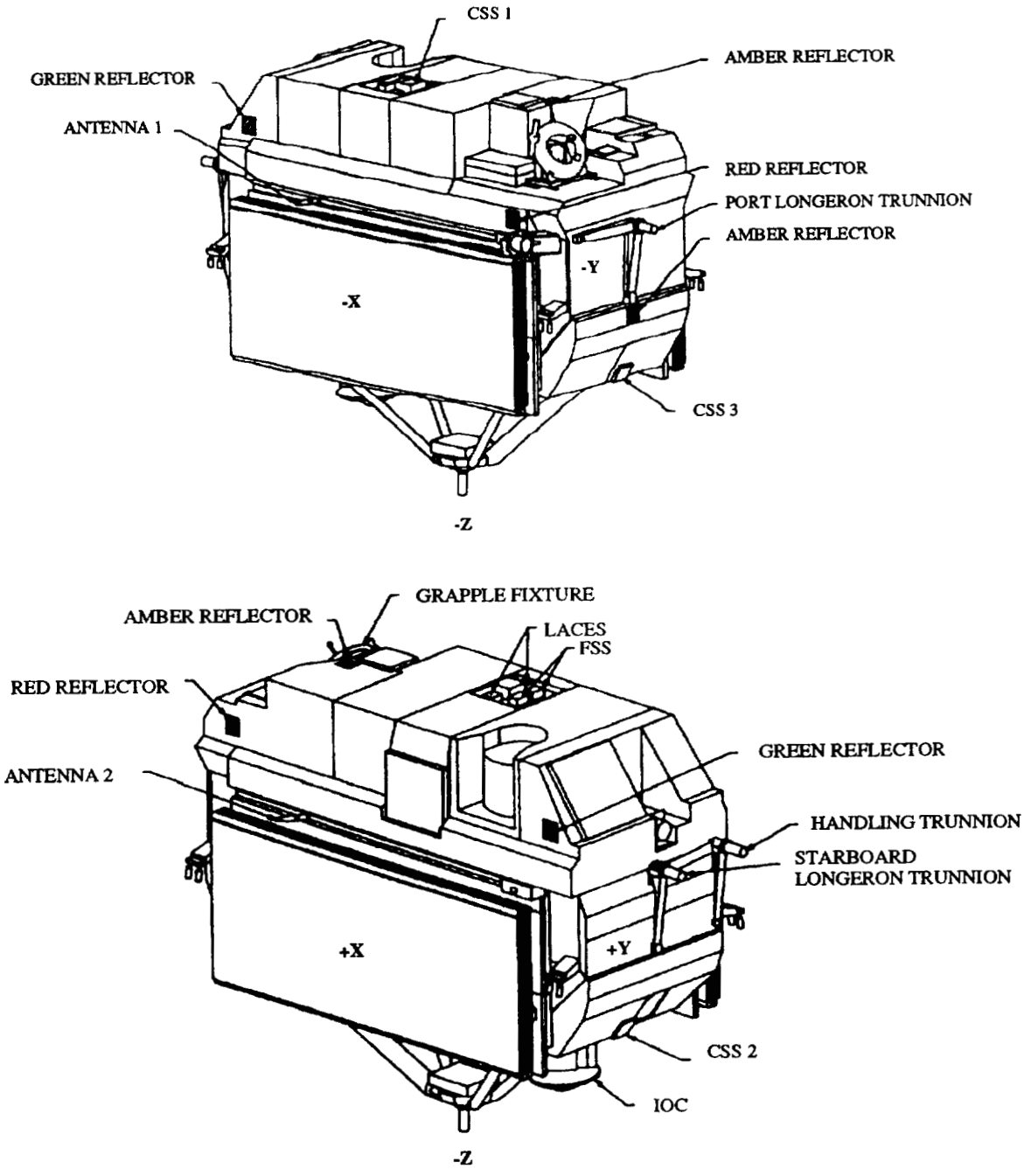

Fig. 1.
Schematic view of EURECA

Fig. 2 BETA CLOTH

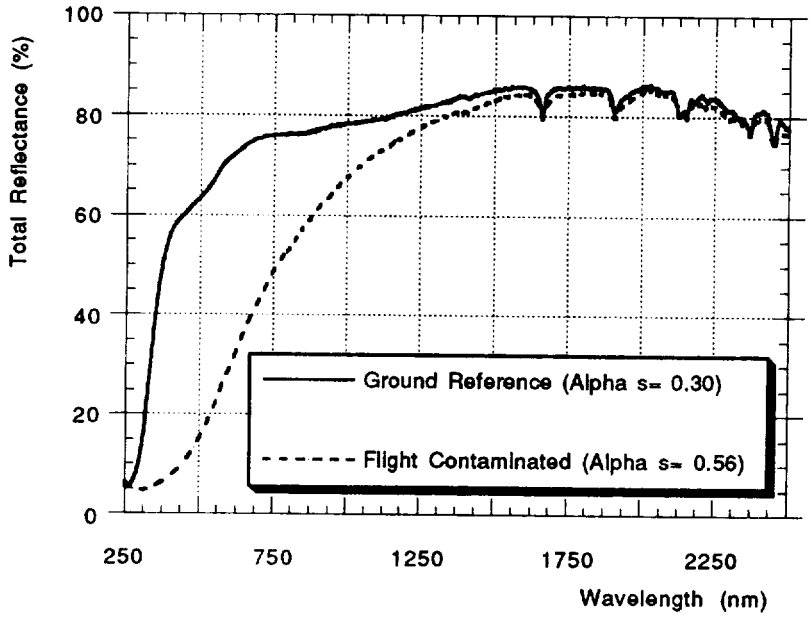

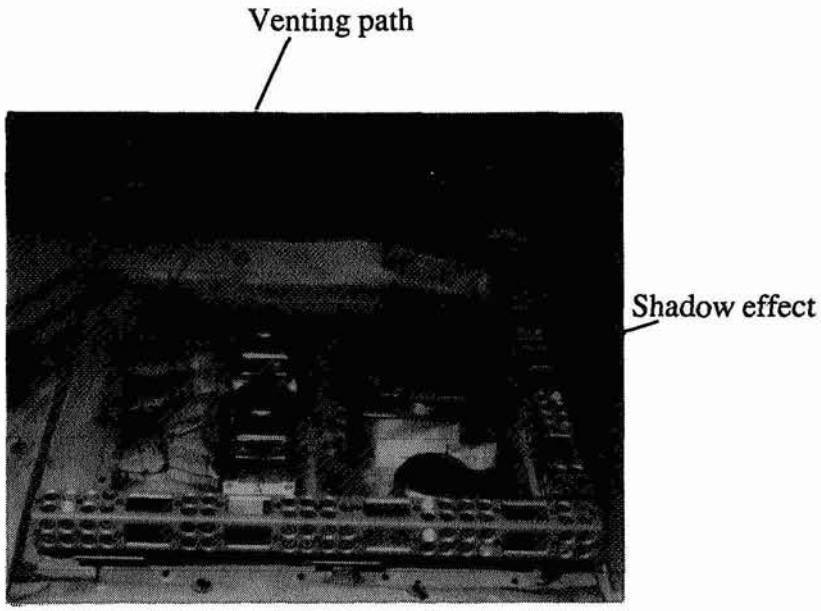

PHOTOGRAPH N° 1. View of AOCS sensor tower showing brown stain in top left-hand corner caused by venting of outgassed materials from within the spacecraft.
(NASA photo)

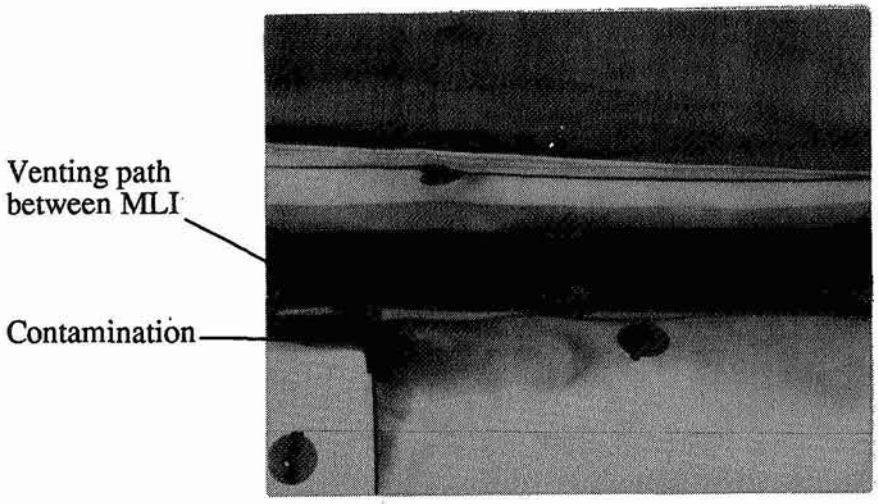

PHOTOGRAPH N° 2. View of venting path between MLI blankets. (NASA photo)

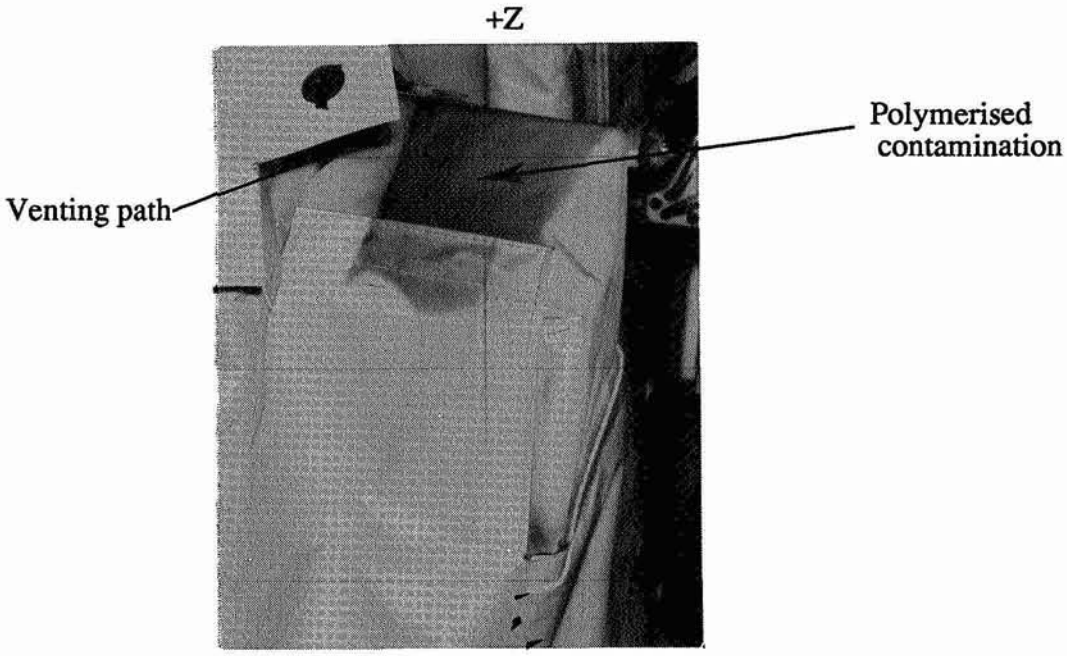

PHOTOGRAPH N° 3. View of brown stain caused by outgassed material being polymerised by UV irradiation after condensing on Beta cloth. (NASA photo)

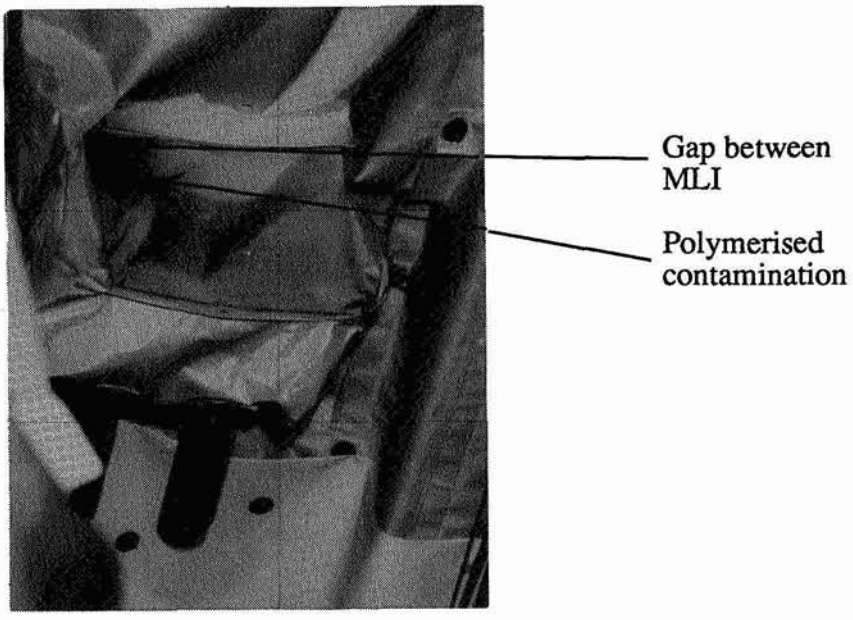

PHOTOGRAPH N° 4. View of brown stain emanating from within the spacecraft. This is typical of the many stains observed around the spacecraft caused by outgassed material venting from between the MLI. (NASA photo)

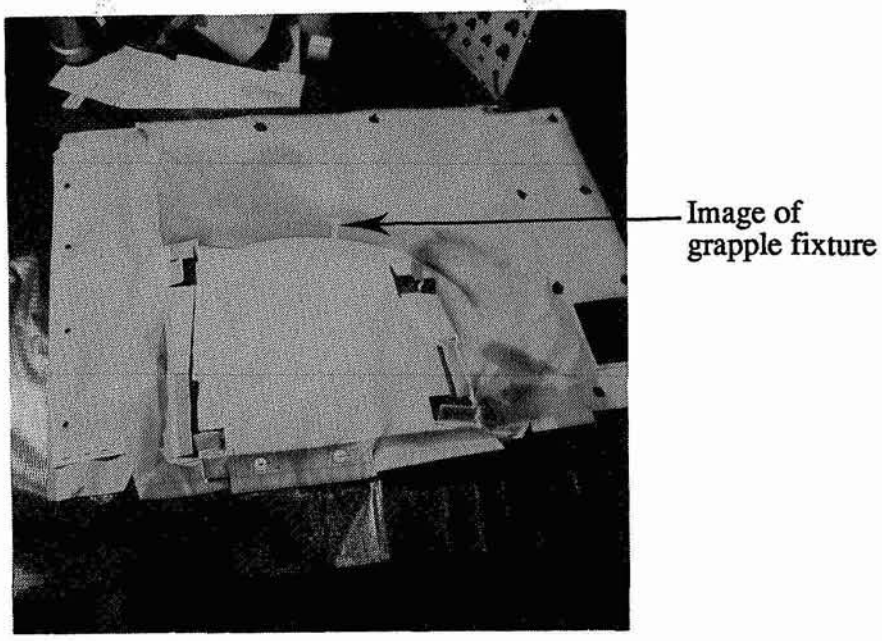

PHOTOGRAPH N° 5. View of UV degradation and outgassed material deposited and polymerised on the MLI surrounding the grapple fixture. Notice the image caused by the shadow of the grapple on the MLI. (DASA ERNO photo)

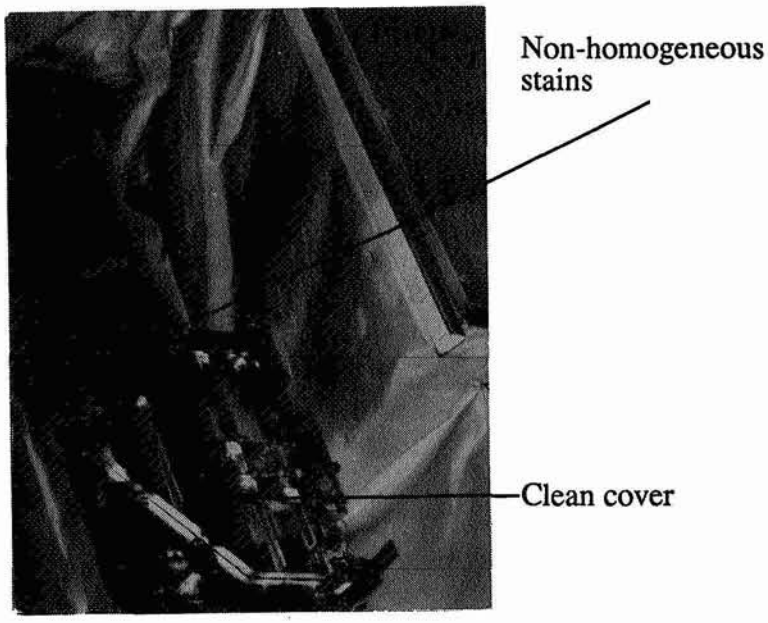

PHOTOGRAPH N° 6. View of SOVA experiment. Notice the non-homogeneous stains on the aluminised FEP tape due to temperature gradients on the surface at perforations and tape joints. (NASA photo)

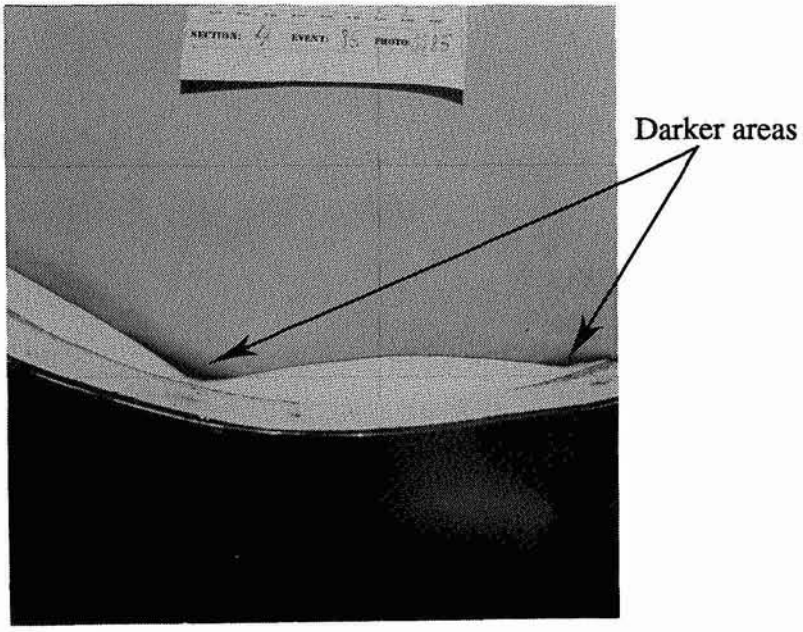

PHOTOGRAPH N° 7. View of UV degradation and outgassed material deposited and polymerised on the interface between the white PSG120FD paint on the PCF dome and the surrounding MLI. Notice darker areas caused by multi reflections in small V-grooves between blanket and dome. (DASA ERNO photo)

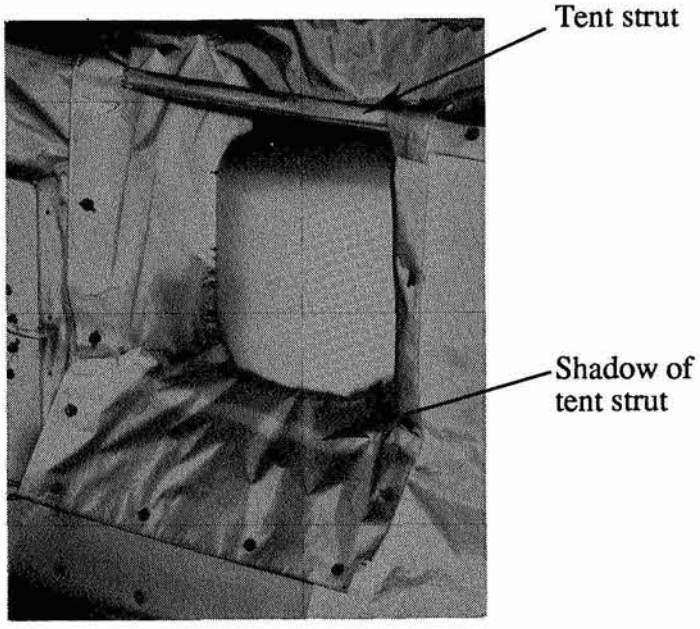

PHOTOGRAPH N° 8. View of PCF dome and the surrounding MLI. Notice the shaded area below the payload tent strut where the Beta cloth is not degraded by UV irradiation or polymerised contaminants. (NASA photo)

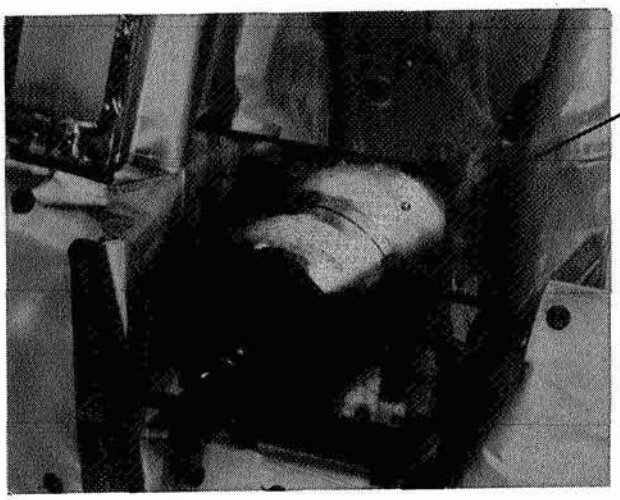

PHOTOGRAPH N° 9. View of RITA. Notice gap behind back plate which provides a chimney for outgassed materials to vent from within the spacecraft. (NASA photo)

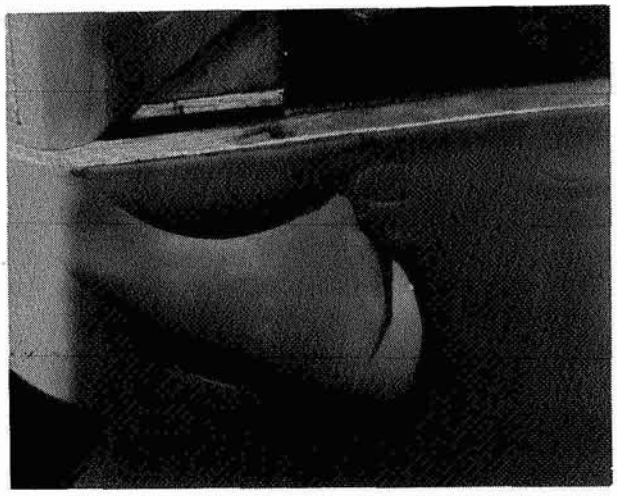

PHOTOGRAPH N° 10. View of Chemglaze Z853 yellow paint peeling from -Y scuff plate. (NASA photo)

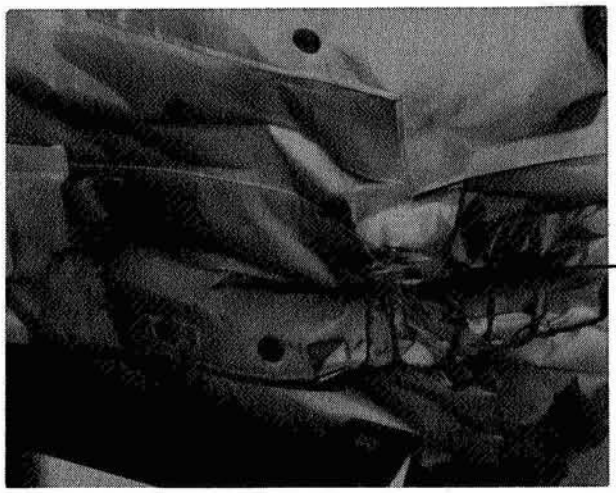

PHOTOGRAPH N° 11. View of outgassed material deposited and polymerised on the Freon pipe MLI. The material has emanated from the gap between the MLI blankets directly above the pipe. (NASA photo)

IONIZING RADIATION

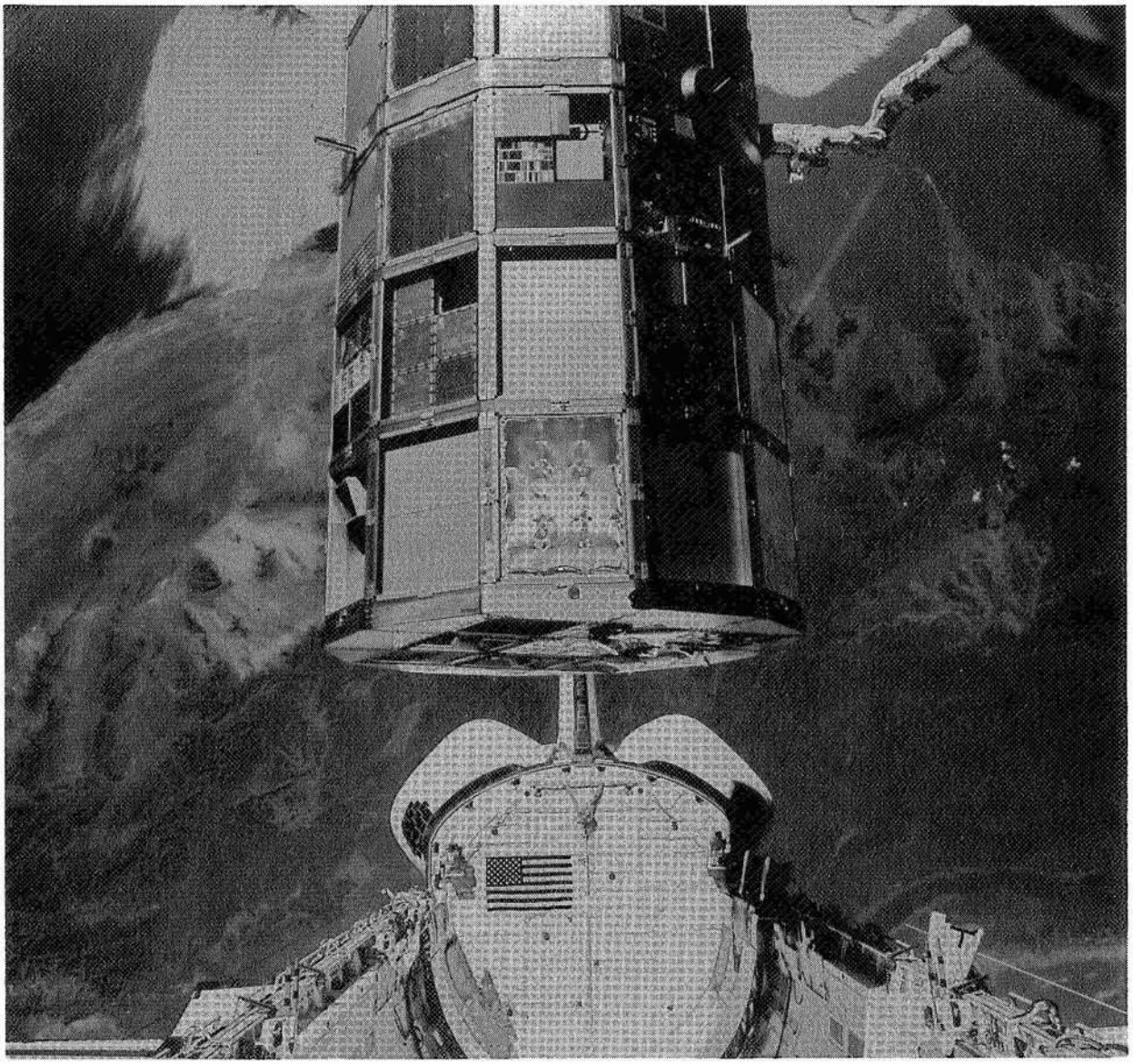

L-90-10473

LDEF CONTRIBUTIONS TO COSMIC RAY AND RADIATION ENVIRONMENTS RESEARCH

Thomas A. Parnell
NASA Marshall Space Flight Center
Huntsville, AL 35812
Phone: 205/544-7690; Fax: 205/544-7754

ABSTRACT

LDEF-1 carried three experiments which are producing significant advances in our knowledge of ultra heavy and anomalous cosmic rays, solar flare particles, and heavy nuclei in the trapped belts. Nine other experiments made measurements on the radiation environments or performed dosmetric monitoring. Data from those experiments, and from measurements of induced radioactivity in LDEF components have significantly improved our knowledge of the LEO radiation environment. Measurements at various locations shielding depths of radiation absorbed dose, linear energy transfer spectra, proton, neutron and heavy ion fluences, and induced radioactivity have been made, and many of these results have been compared to models. This has allowed the assessment of accuracy, and the potential for improvement, of the models. Serendipitous results from the radiation measurements include the discovery of atmospheric ^{7}Be plated on the front surface of LDEF, which has motivated a series of new investigations. A sample of measurements and modeling results will be presented, as well as the status of archiving the measurements and models.

TRAPPED IRON MEASURED ON LDEF

R. Beaujean, D. Jonathal, S. Barz and W. Enge
Institut für Reine und Angewandte Kernphysik
Christian-Albrechts-Universität Kiel, 24118 Kiel, FRG

SUMMARY

Heavy ions far below the cutoff energy were detected on the 28.5° inclination orbit of LDEF in a plastic track detector experiment. The Fe-group particles show a constant energy spectrum at 50≤E≤200 MeV/nuc. The steep energy spectrum of Fe-particles at 20≤E≤50 MeV/nuc and the arrival directions of these ions is consistent with a trapped component incident in the South Atlantic Anomaly at values of L=1.4-1.6.

INTRODUCTION

The objective of experiment M0002-2 was to register heavy cosmic ray nuclei with nuclear charge Z≥3 and to measure the chemical and energy spectra in the energy range from 20 to 1000 MeV/nuc. Two points of great interest were "geomagnetically forbidden" cosmic ray particles and heavy ions of the trapped radiation.

Early measurements at the orbit of Skylab (1) observed steeply falling spectra of nuclei with Z≥8 and 10≤E≤40 MeV/nuc. The steep energy spectra were interpreted as evidence for energetic heavy nuclei in the inner radiation belt. Spacelab-1 measurements (2) reported the registration of oxygen ions in the South Atlantic Anomaly (SAA) and the TRIS data (3) also suggested a steeply falling trapped oxygen component. Finally, in a series of Cosmos flights, it could be proved that oxygen particles were trapped (4). "Geomagnetically forbidden" particles have energies less than the minimum cutoff value required for fully stripped ions to have access to a specific location inside the Earth's magnetic field. Transient magnetic field disturbances and partly ionized particles can produce such a "forbidden" component. SL-1 and SL-3 measurements have detected few iron and sub-iron particles at about 100 MeV/nuc which could only be explained by a strongly reduced ionization state (5,6). All cited experiments (as well as four individual experiments on LDEF) used passive visual track detectors for the registration of the heavy ions. These detectors provide an excellent spatial resolution for the arrival direction of the particles and they have registration thresholds that make the detector system almost insensitive to electrons and protons. No electrical power is needed for the particle registration; however, the detector does not provide information on the arrival time of the particle (special experiment operation (2) can overcome this).

All features of the three axis stabilized Long Duration Exposure Facility (LDEF) which stayed in a circular, 28.5° inclination orbit from April 1984 to January 1990 ($1.8 \cdot 10^8$ s), supported our investigation: a) the low inclination orbit provided a high geomagnetic shielding and thus low energy fully stripped heavy ions had no access to this orbit (the minimum required rigidity is about 3.5 GV); b) 80% of the mission was spent at an altitude greater than 444 km; c) the attitude stabilization provided a fixed orientation during SAA crossings; d) the extremely long-duration flight provided a unique collecting time covering the period of minimum solar modulation.

THE DETECTOR SYSTEM

CR-39 and Kodak CN plastic track detectors from Kiel were exposed on three different positions on LDEF. The Kiel experiment M0002 (on side-tray E6 with an aperture of 1000 cm^2) and two subunits of the Biostack experiment A0015 (DLR Cologne, on side-tray C2 and earth-tray G2, each with an aperture of 48 cm^2) covered an almost omnidirectional field of view. The detector arrangement under thermal covers equivalent to 14 mg/cm^2 is shown in Fig. 1 for the two different types of stacks. Scientific data were accumulated during the whole LDEF mission in latent tracks and revealed in the laboratory by means of chemical etching. After recovery small areas of experiment M0002 were exposed to 200 MeV/nuc Ar^{40} ions at the Saclay accelerator for a post-flight calibration.

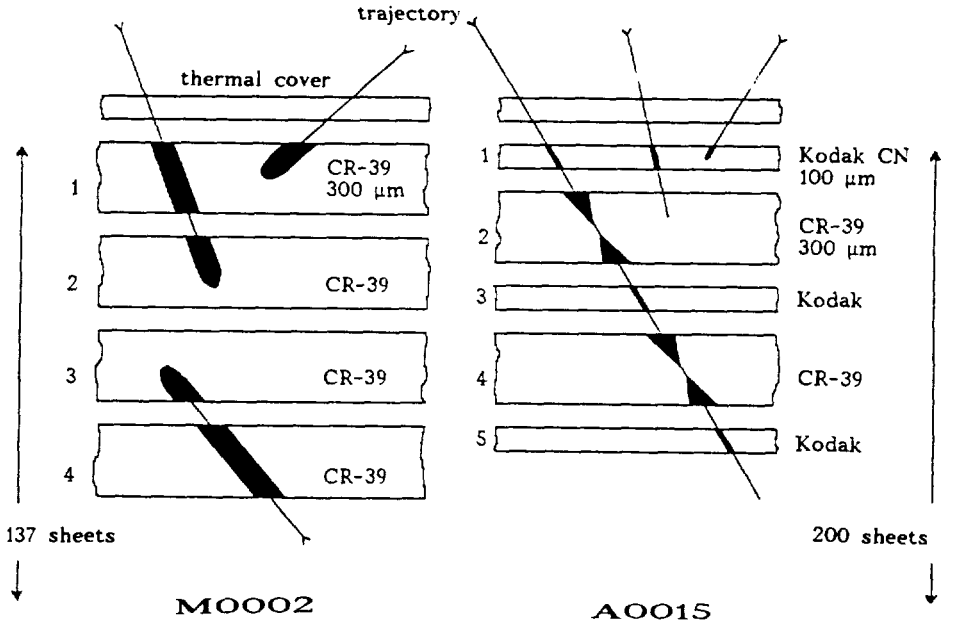

Fig. 1: Side view of the foil arrangement with track images after etching.

Etching of the CR-39 foils was performed at 70° C for 10 hours in 6n NaOH. This treatment was chosen in order to optimize the track size and minimize the number of background tracks (about 1.5 10^5 very small etch pits per cm^2 on the topmost surface and 3.5 10^4 small pits per cm^2 on other surfaces throughout the stack). The Kodak CN foils were etched for 2 hours in 6n NaOH at 50° C.

After etching, the detector foils were scanned and stopping particles were analysed by measuring the arrival direction with respect to the detector foil and the conelength (L) versus residual range (R) dependence. The inflight calibration of the detector response is based on the lack of tracks above the topmost band in the L-R plot (7) which is related to the sudden drop in the elemental abundances above charge Z=26. The edge is allocated to Fe ions and its presence shows that the detector sensitivity did not change seriously during the mission.

Fig. 2b shows the measured charge distribution of 53 particles arriving from unshielded space and stopping in M0002 (CR-39) on 300 cm^2 . The energy range is 50-250 MeV/nuc and the charge resolution deduced from the Fe peak is σ =1.0 charge units. A similar charge distribution was measured

in CR-39 of the A0015 units for the same energy range. The low sensitivity of the CR-39 detector flown on LDEF (which is similar to the CR-39 response on SL-1) is due to the low oxygen concentration within the stack container and causes a decreasing registration probability for ions with decreasing nuclear charge. The response curve of the CR-39 on LDEF as a function of the restricted energy loss is:

$v_S/v_m - 1 = 0.025\ (REL/1000)^{2.6}$ (REL in MeV cm^2 /g, ω_0=200 eV). Low energy particles are studied in the topmost three foils which show a slightly different response. The uncorrected, preliminary charge distribution of particles with E≤50 MeV/nuc is depicted in Fig. 2a (below Z=10 the registration probability is strongly decreased).

The calibration of the Kodak CN, integrated in the A0015 units, is in progress. The preliminary analysis indicates a higher sensitivity compared to the CR-39, and a high registration probability for nuclear charges Z≥ 6 is expected in these foils.

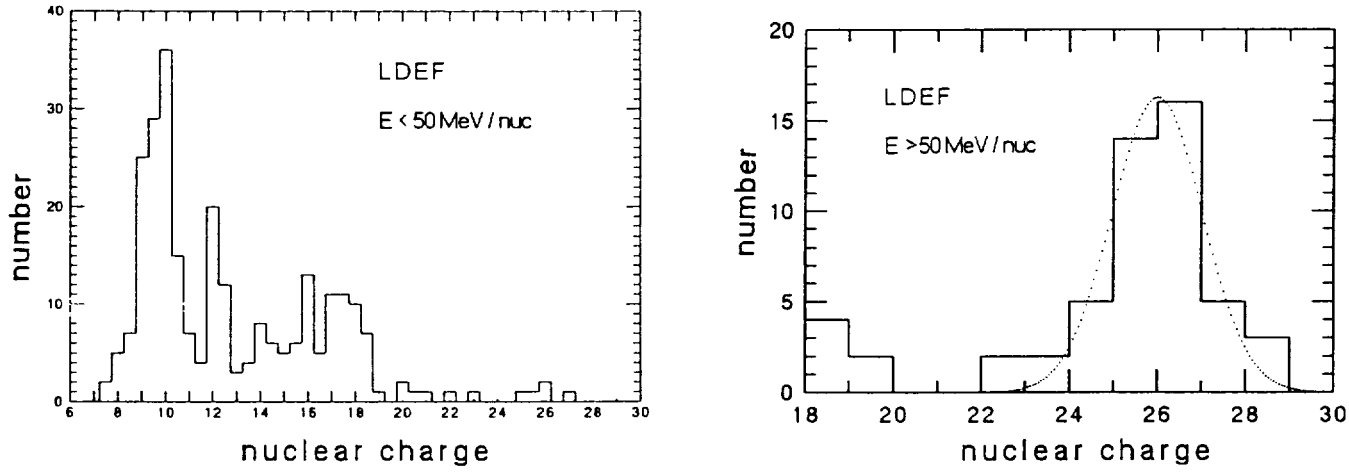

Fig. 2: Measured charge distribution in M0002: a) preliminary spectrum for E≤50 MeV/nuc, b) set of 53 tracks with energies E≥50 MeV/nuc used for the response calibration.

PARTICLE ENERGY SPECTRA

Mission and field of view averaged energy spectra for selected particle groups are shown in Fig. 3. The measurement for Z>6 was calculated from preliminary measurements in Kodak CN; the Ar and Fe results were obtained on 300 cm^2 CR-39 in M0002. The striking feature for the Fe-group is the steeply falling spectrum below 50 MeV/nuc and the plateau up to 200 MeV/nuc where our flux measurement is

in agreement with the results of M0001 (Adams et al., these proceedings). The flux of the Ar-group particles at energies above 50 MeV/nuc was not analysed; however, it is less than the Fe flux at these energies. Preliminary flux calculations for Ne-group particles around 20 MeV/nuc yielded similar flux values and almost the same slope as depicted for Ar. All detected particles have energies well below the cutoff value for the LDEF orbit, assuming fully stripped nuclei.

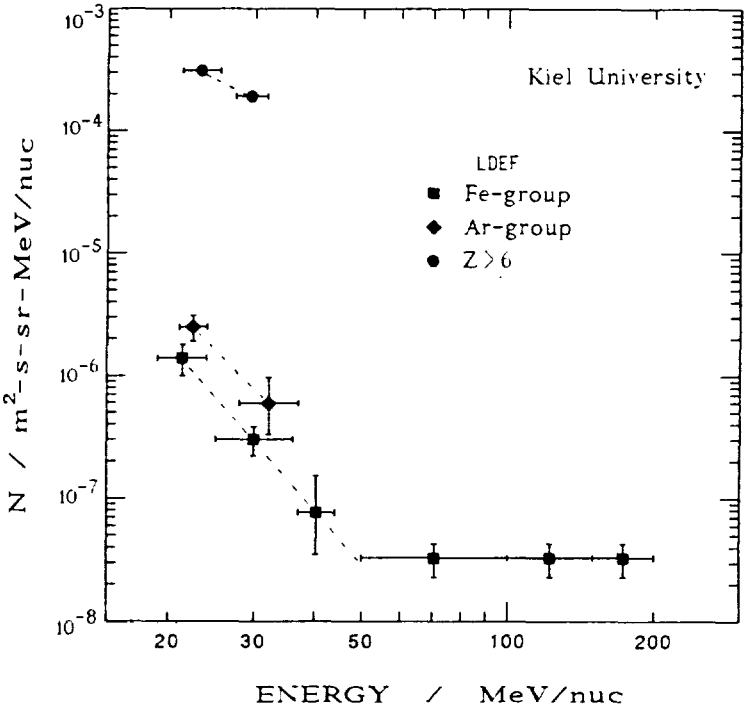

Fig. 3: LDEF mission averaged fluxes for selected charge groups.

PARTICLE ARRIVAL DIRECTIONS

Based on the good spatial resolution of visual track detectors, the arrival directions of the particles were measured with respect to the detector foils. Because LDEF maintained a constant attitude during the mission, the SAA crossings occurred with a known orientation. Thus the trapped heavy ions arrive at characteristic angles, thereby making them distinguishable from other particles.

The particle group Z>6 of Fig. 3, penetrating the topmost Kodak CN foil of A0015 on tray C2 (E≥10 MeV/nuc), has arrival directions as shown in Fig. 4. This highly anisotropic distribution shows the characteristics of a cylindrical geometry. Fig. 5 shows angular distributions from tray E6 for particle groups taken from Fig. 2a (E≤50 MeV/nuc). Again the distributions show the characteristics of a cylindrical geometry but less pronounced. The indicated geographic directions are given as a reference assuming that the LDEF velocity vector is pointing to the east (valid at 28.5° latitude).

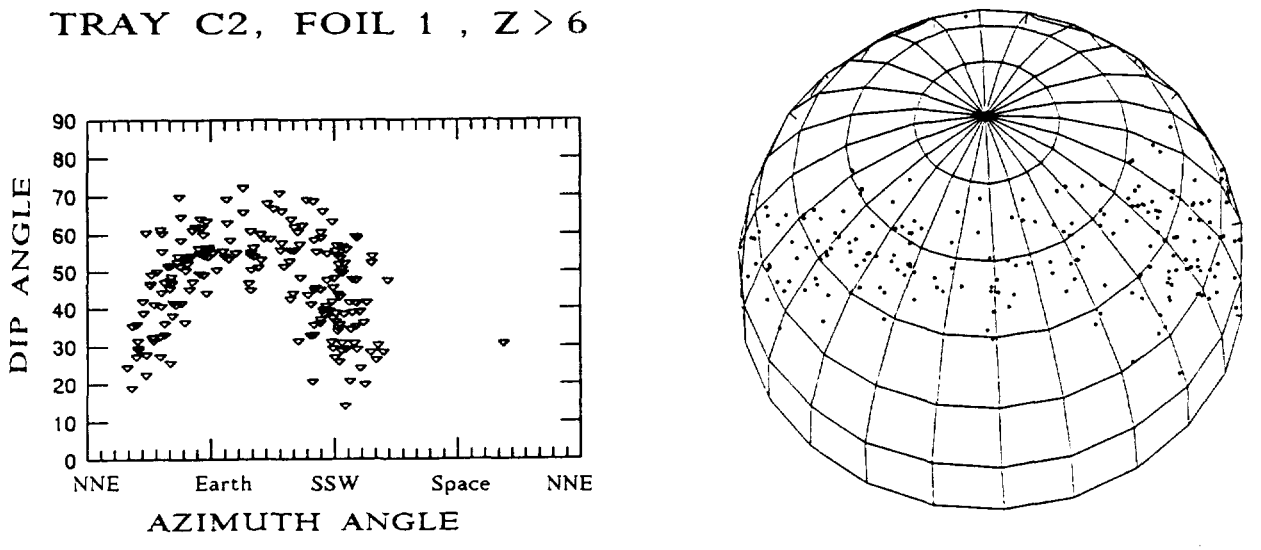

Fig. 4: Arrival directions for particles on tray C2 (Z>6, E>10 MeV/nuc); the pole in the 3D-plot indicates 90° dip angle (vertical incidence).

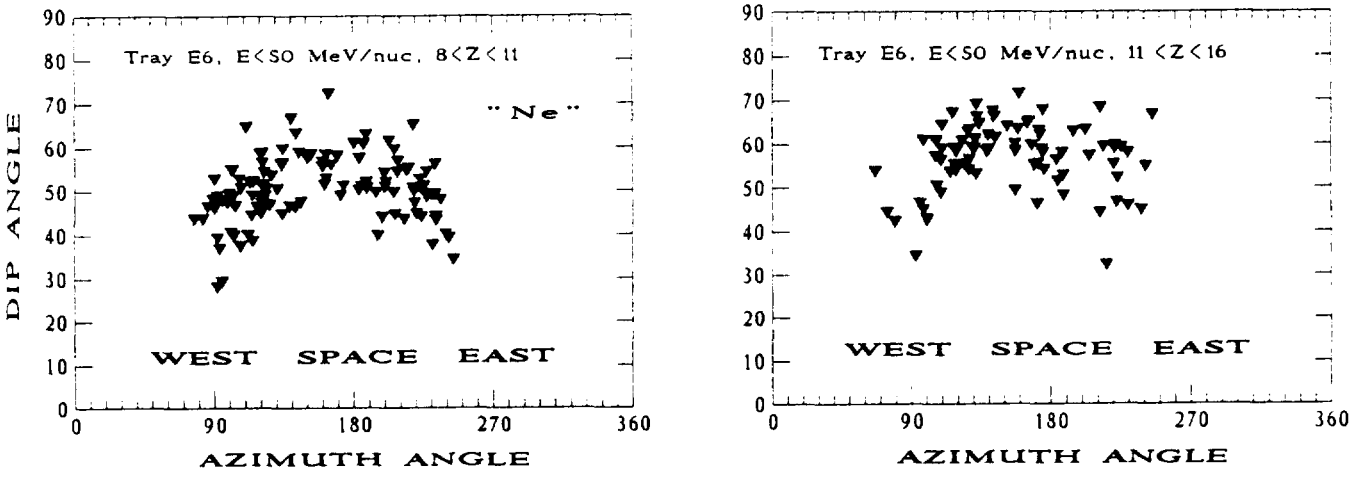

Fig. 5: Arrival directions for particles with E<50 MeV/nuc on tray E6 Azimuth and Dip angles are referred to the detector foil.

The arrival directions of three particle groups are studied in more detail combining measurements on trays E6, C2 and G2 (note the different aperture size). Fig. 6 shows Ar and Fe ions below 50 MeV/nuc; Fig. 7 shows Fe above 50 MeV/nuc (see energy spectra in Fig. 3). The arrival directions in Figs. 6 and 7 are given relative to a plane which is perpendicular to the local vertical with an azimuth angle referring to

the LDEF velocity vector (pointing to the East at 28.5° latitude). The dotted lines define a dip angle of 20° with respect to the detector surface at the three positions (for the earth tray this line is nearly congruent with the shadow of the solid earth).

Although the change of the registration efficiency within the individual fields of view is not yet corrected, one can conclude that up to 200 MeV/nuc the arrival directions show a similar structure (which is discussed in the following chapter), whereas above 200 MeV/nuc all particles arrive from western directions without a pronounced structure. If these particles enter from outside the magnetosphere this distribution can be explained by the fact that the region of the lowest cutoff is the western horizon.

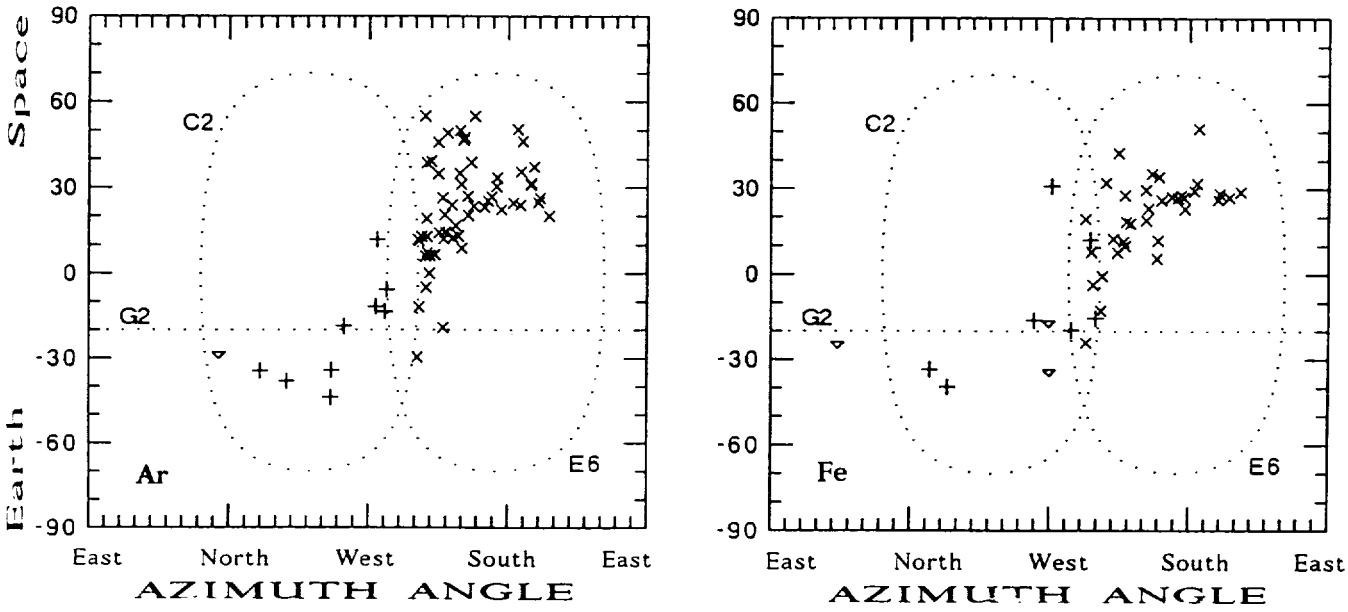

Fig. 6: Arrival direction of Ar- (l) and Fe-group (r) particles with E≤ 50 MeV/nuc.

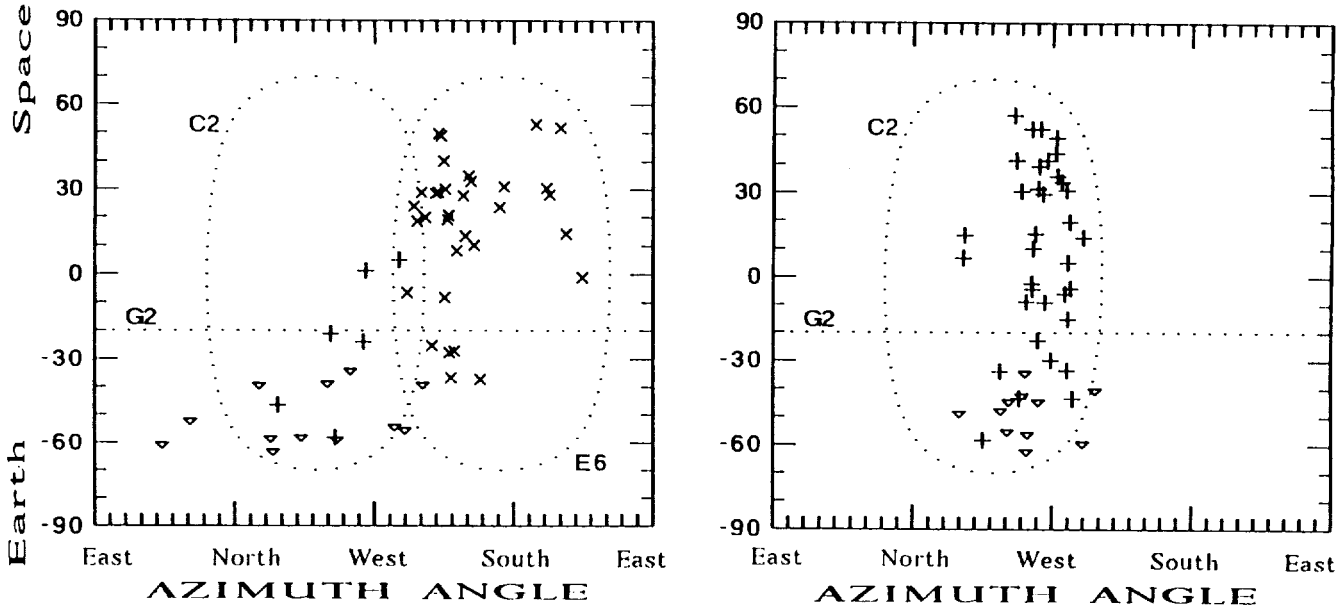

Fig. 7: Arrival direction of Fe-group particles: 50-200 MeV/nuc (left) and 200-400 MeV/nuc. (right, E6 omitted due to limited statistics).

SIMULATION OF TRAPPED PARTICLE ARRIVAL DIRECTIONS

The steep energy spectra below 50 MeV/nuc and the arrival direction distribution are interpreted as evidence for a trapped particle component. To check this interpretation, a Monte-Carlo simulation for the detection of trapped particles (Z>6, Ar and Fe) on the LDEF orbit during SAA crossings was calculated.

As our passive detector system cannot provide the time and orbital position of the particle impact, a geographical region for the particle detection had to be assumed. The basic flux contour lines were adopted from SAA proton measurements at 400 km which

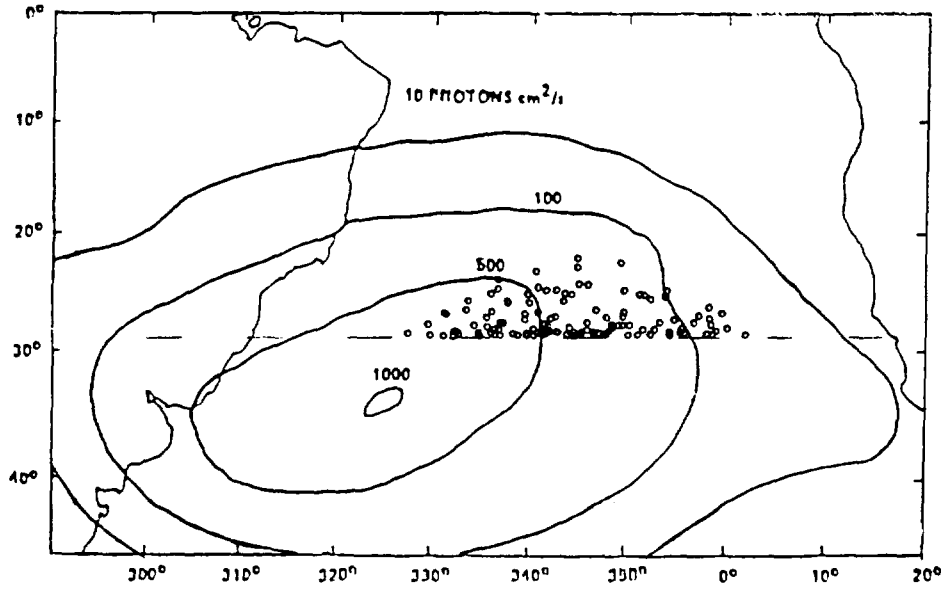

Fig. 8: Monte-Carlo simulation of the geographical distribution for the impact of trapped heavy ions on LDEF (proton contour lines from Watts et al., ref.8).

show a peak flux at 34° S and 35° W. The lateral size of the detection region was assumed to be ±21° longitude and ±13° latitude. Taking random distributed equator crossings of the LDEF orbit (due to the long flight duration), the longitudinal position of the detection region was changed to fit the Monte-Carlo simulation to the measurement.

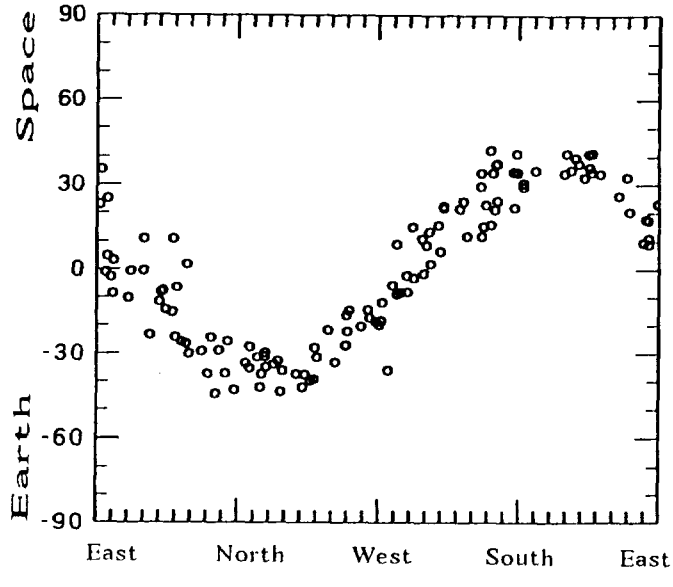

Fig. 9: Simulated arrival directions of trapped heavy ions relative to a horizontal plane (the indicated geographical directions are valid at 28.5° S).

The best fit was achieved when the region was centered at 15° West, yielding the simulated geographical detection distribution shown in Fig. 8. The resulting arrival direction distribution on a horizontal plane on LDEF (Fig. 9) was calculated for 90° pitch angles in the 1985 IGRF field model.

DISCUSSION

All detected particles have energies well below the cut-off value for fully stripped ions to have access to the LDEF orbit. From the energy spectrum and the angular distribution we conclude that two different populations were detected on LDEF.

At energies E>100 MeV/nuc, most of the Fe particles (up to now only these ions were analysed at Kiel above 50 MeV/nuc) seem to originate from outside the magnetosphere. They have to be partly ionized with Q/Z< 0.5 to reach the LDEF orbit. Exact transmission calculations are in progress (taking into account disturbed magnetic conditions) in order to study the origin of these particles. The analysis of M0001 (A.J.Tylka et al., these proceedings) has shown that the features of the Fe data above 200 MeV/nuc can be explained by solar energetic particles from the October 1989 events.

At energies E≤50 MeV/nuc, the features of the detected particles and the Monte-Carlo simulation suggest the registration of a trapped component mirroring at L=1.4-1.6 in the South Atlantic Anomaly. Energy spectra and measured arrival direction distributions of all analysed charge groups on trays E6, C2 and G2 (Z>6 on C2 only) are in agreement with this assumption.

The origin and trapping mechanism of these particles are not clearly identified. Calculations for trapped anomalous cosmic rays (9) predict our results for Argon. However, the detection of trapped anomalous Oxygen and Ne on the LDEF orbit is not predicted in this calculation, and the remaining detected ions are not part of the anomalous component. The comparison of the elemental composition in Fig. 2a with the Galileo results for heavy ions in the October 1989 SEP events (10) indicates that part of the low energy particles on LDEF may originate from these solar events (as well as the Fe component at higher energy, see A.J.Tylka et al., M0001, these proceedings).

The energy spectra of Fig. 3 were calculated as mission time averages for an isotropic flux. However, the angular distributions indicate a highly anisotropic flux and the time intervall of registration may be significantly less than the mission time. Only a small part (1-2%) of the mission time was spent close to the SAA, and the life time of trapped heavy ions originating from SEP events is not considered. In addition, the flux of the trapped anomalous component shows a strong temporal variation correlated with the solar activity cycle (4). Future analysis will take this into consideration.

ACKNOWLEDGEMENTS

We greatly thank B. Filz (AFGL, Bedford, MA) for his invitation to participate in experiment M0002 and G. Reitz (DLR Köln) for the integration of our detector foils in experiment A0015. We thank L. Clark (NASA LaRC, Hampton, VA) for his support during the design phase and the integration at Langley. This work was financially supported by BMFT under grant QV 297 and by DARA under grant OS 9001.

REFERENCES

1. Chan, J.H. and P.B. Price: Composition and Energy Spectra of Heavy Nuclei of Unknown Origin Detected on Skylab, Phys. Rev. Let. Vol 35, 8, 539-542 (1975)

2. Oschlies, K., R. Beaujean and W. Enge: On the Charge State of Anomalous Oxygen, Ap. J., Vol. 345, 776-781 (1989)

3. Adams, J.H., L.P. Beahm and A.J. Tylka: The Charge State of the Anomalous Component: Results of the TRIS Experiment, Ap. J., Vol. 377, 292-305 (1991)

4. Grigorov, N.L., M.A. Kondratyeva, M.I. Panasyuk, Ch.A. Tretyakova, J.H. Adams, J.B. Blake, M. Schulz, R.A. Mewaldt and A.J. Tylka: Evidence for Trapped Anomalous Cosmic Ray Oxygen in the Inner Magnetosphere, Geophy. Res. Lett., Vol. 18, 11, 1959-1962 (1991)

5. Krause, J., R. Beaujean, E. Fischer and W. Enge: CR-39 used for Cosmic Ray Measurement aboard Spacelab-1, Nucl. Tracks Rad. Meas., Vol. 12, Nos. 1-6, 419-422 (1986)

6. Biswas, S., N. Durgaprasad, B. Mitra, R.K. Singh, A. Dutta and J.N. Goswami: Experimental Observation of partially ionized Iron Group (Z=21-26) Ions in the low Energy Galactic Cosmic Rays in Spacelab-3, Proc. 21st Int. CR Conf., Adelaide 1990, Vol. 3, 23-25 (1990)

7. Jonathal, D., R. Beaujean and W. Enge: Heavy Ion Measurement on LDEF, Proc. 2nd LDEF Symposium San Diego 1992, NASA CP 3194, Vol. 1, 239-245 (1993)

8. Watts, J.W., T.A. Parnell, J.H. Derrickson, T.W. Armstrong and E.V. Benton: Prediction of LDEF Ionizing Radiation Environment, Proc. 1st LDEF Symposium Kissimmee 1991, NASA CP 3134, Vol. 1, 213-224 (1991)

9. Tylka, A. J., Spectra and Geographical Distribution of Geomagnetically Trapped Anomalous Cosmic Rays, Proc. 23rd Int. CR Conf., Vol. 3, 436-439 (1993)

10. Garrard, Th. L. and E.C. Stone: Heavy Ions in the October 1989 Solar Flares Observed on the Galileo Spacecraft, Proc. 22nd ICRC, Vol. 3, 331-334 (1991)

CHARACTERISTICS OF LOW ENERGY IONS IN THE HEAVY IONS IN SPACE (HIIS) EXPERIMENT

Thomas Kleis
CSI Institute, George Mason University
Fairfax, VA 22030-4444
Phone: 202/767-2200, Fax: 202/767-6473

Allan J. Tylka, Paul R. Boberg*, James H. Adams, Jr., Lorraine P. Beahm
E.O. Hulburt Center for Space Research, Code 7654, Naval Research Laboratory
Washington, DC 20375-5352
Phone: 202/767-2200, Fax: 202/767-6473

SUMMARY

We present preliminary data on heavy ions ($Z \geq 10$) detected in the topmost Lexan sheets of the track detector stacks of the Heavy Ions in Space (HIIS) experiment (M0001) on LDEF. The energy interval covered by these observations varies with the element, with (for example) Ne observable at 18–100 MeV/nuc and Fe at 45–200 MeV/nuc. All of the observed ions are at energies far below the geomagnetic cutoff for fully-ionized particles at the LDEF orbit. Above 50 MeV/nuc (where most of our observed particles are Fe), the ions arrive primarily from the direction of lowest geomagnetic cutoff. This suggests that these particles originate outside the magnetosphere from a source with a steeply-falling spectrum and may therefore be associated with solar energetic particle (SEP) events. Below 50 MeV/nuc, the distribution of arrival directions suggests that most of the observed heavy ions are trapped in the Earth's magnetic field. Preliminary analysis, however, shows that these trapped heavy ions have a very surprising composition: they include not only Ne and Ar, which are expected from the trapping of anomalous cosmic rays (ACRs), but also Mg and Si, which are not part of the anomalous component. Our preliminary analysis shows that trapped heavy ions at $12 \leq Z \leq 14$ have a steeply-falling spectrum, similar to that reported by the Kiel experiment[1,2,3] on LDEF (M0002) for trapped Ar and Fe at $E < 50$ MeV/nuc. The trapped Mg, Si, and Fe may also be associated with SEP events, but the mechanism by which they have appeared so deep in the inner magnetosphere requires further theoretical investigation.

*NRC Postdoctoral Research Associate

EXPERIMENT DESCRIPTION

The Heavy Ions In Space (HIIS) experiment was mounted on the space-facing end of LDEF, pointing to the zenith. The detector was divided into 8 modules. In each module, the detector contained a main stack (which consisted mostly of CR-39[†] track detector sheets contained in 1 atm of dry air) and a top stack (consisting of 22 5-mil-thick sheets of Lexan[‡], exposed in vacuum under 57 mg/cm^2 of shielding. For a detailed description of the HIIS detector see ref. 4.) Results from the main detector stacks are given by Tylka et al.[5] in these proceedings and in ref. 6. In this paper, we present preliminary results on the lowest-energy heavy ions observed in the HIIS detectors. These data come from several test-etchings of small areas of the top stacks, with each test etching using $\approx 50cm^2$, or roughly 4% of the area of a single module. With these test etchings we have examined approximately 2.5% of the total area available in the top stacks.

In order to reveal stopping ions lighter than the Fe-group, it was necessary to enhance the sensitivity of the Lexan detectors by exposing them to UV radiation prior to etching. This UV exposure, which was done on a machine specifically built for the HIIS Lexan[7], enhanced the visible track formation that occurred during the etching process. Typical processing parameters used in the test-etchings were 4 or 8 days UV exposure followed by etching in 6.25N NaOH at 70°C for 12 hours.

In this analysis, we required that the cosmic-ray track be followed back through at least one sheet above the stopping point, so that every track has at least two measurable etch pits. (This excludes almost entirely elements with atomic number $Z < 10$ from this analysis and also causes the acceptance for Ne (Z=10) to be significantly smaller than that for the heavier registered ions.) For each track we measured the surface ellipse of every etch pit on an image-processing system and the length of the stopping cone on a high precision microscope. We also measured the average post-etch thickness of each sheet. From these measurements, we determined each ion's arrival direction and the v_t/v_b vs. residual range curve, which reveals the ion's atomic number (Z). (See Adams et al.[8] for further details.)

RESULTS FROM A PRELIMINARY CALIBRATION

Because of the various environmental stresses suffered by the Lexan detectors during their extended space-exposure, we have used internal calibrations, based on the observed cosmic-ray tracks. These calibrations used data from tracks that are arriving from above (from space) and from below (i.e., through the side of LDEF). The particles from above are of greater interest for the

[†]CR-39 (Columbia Resin 39) is poly diethylene glycol bis-alyl carbonate and was invented at Pittsburgh Plate Glass's Columbia Resin Laboratory in Barberton, OH.

[‡]Lexan is the tradename for bis-phenol A polycarbonate, as sold by General Electric, Pittsfield, MA. The same polycarbonate is also sold under the tradenames of Tuffak and Rodyne-P.

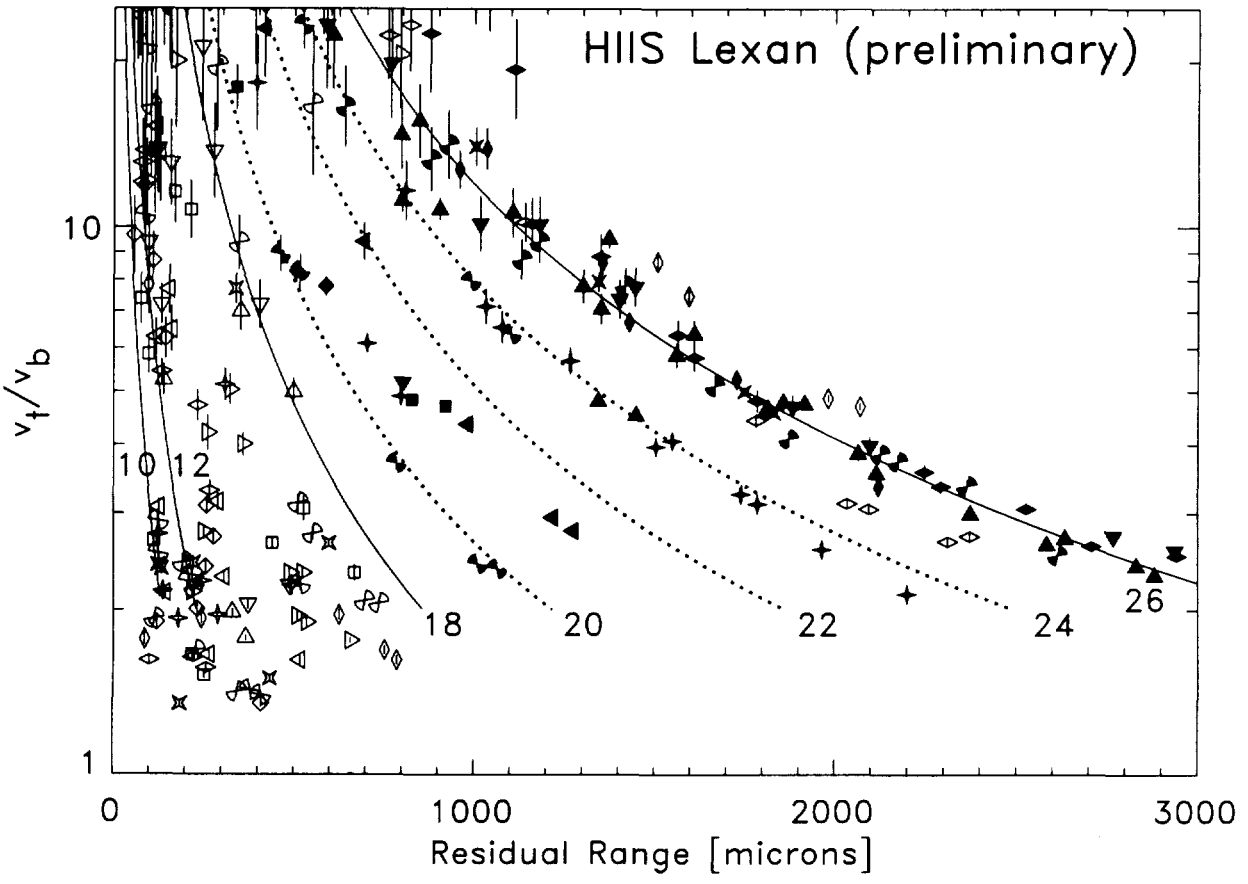

Figure 1: *A typical v_t/v_b vs. residual range plot for particles arriving at the HIIS top stack from above (open symbols) and through the side of LDEF (closed symbols). The curves for Z= 26, 18, 12, 10 (solid) and Z= 24, 22, 20 (dotted) are derived from an internal calibration. The plot shows track data of 77 particles, registered in $\frac{1}{20}$ module area ($\approx 50cm^2$). The lightest detected element's nuclear charge is around $Z \approx 10$.*

analysis because these are the lowest energy particles observable in the HIIS experiment and because they are well below the LDEF orbit's geomagnetic cutoff for fully-ionized particles.

Figure 1 shows a v_t/v_b vs. residual range plot for particles from $\frac{1}{20}$ module area. It shows a strong accumulation of relatively heavily-ionizing particles, which we assume to be Fe (Z=26). Most particles arriving from space, however, have $Z \leq 18$. There are also two visible peaks for very light elements. Using this preliminary calibration, they appear to be Mg (Z=12) and Ne (Z=10).

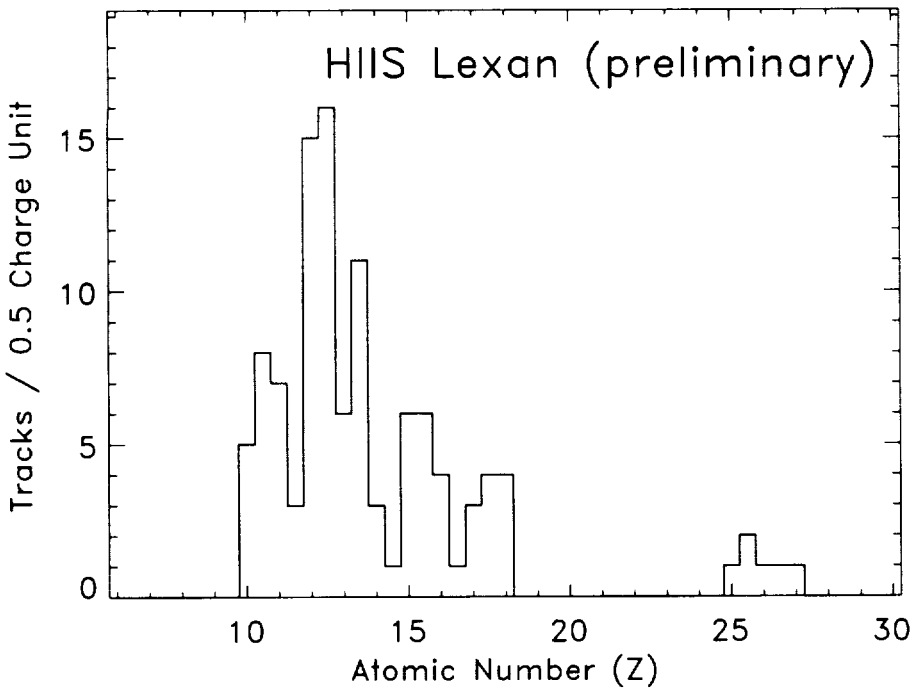

Figure 2: *Preliminary elemental composition of particles registered in the HIIS top stack. The plot includes 109 tracks arriving from space, sampled from test etchings in 2 modules (area* $\approx 150 cm^2$*). The relative abundances have not been corrected for differences in the acceptance.*

A close examination of figure 1 shows some discrepancies between the data and calibration curves, particularly for the lighter elements at $v_t/v_b \geq 5$. Also, the present calibration curves do not extend below $v_t/v_b = 2$, which is critical for identifying the lighter elements. Certainly the analysis of an entire module instead of $\frac{1}{20}$ module area would greatly increase the statistics and thereby improve the accuracy of the internal calibration.

We have used the preliminary calibrations to examine the elemental composition of the ions arriving from above (fig. 2) from three test etchings of material from two different modules. The accumulation of Fe tracks and the relative absence of sub-Fe ($20 < Z < 26$) tracks is clearly seen. There also appear to be charge peaks at Ne (Z=10), Mg (12) and a broad accumulation at $12 < Z \leq 18$. However, given the extended duration of the exposure and complications introduced by partial failure of the HIIS thermal blankets (see Adams et al.[8]), some of this structure may be due to calibration shifts. We emphasize that the composition shown in figure 2 is preliminary. Increased statistics, an improved internal calibration, and comparison with observations of low-energy heavy ions from other LDEF experiments are necessary before any definite conclusions can be drawn about the elemental composition.

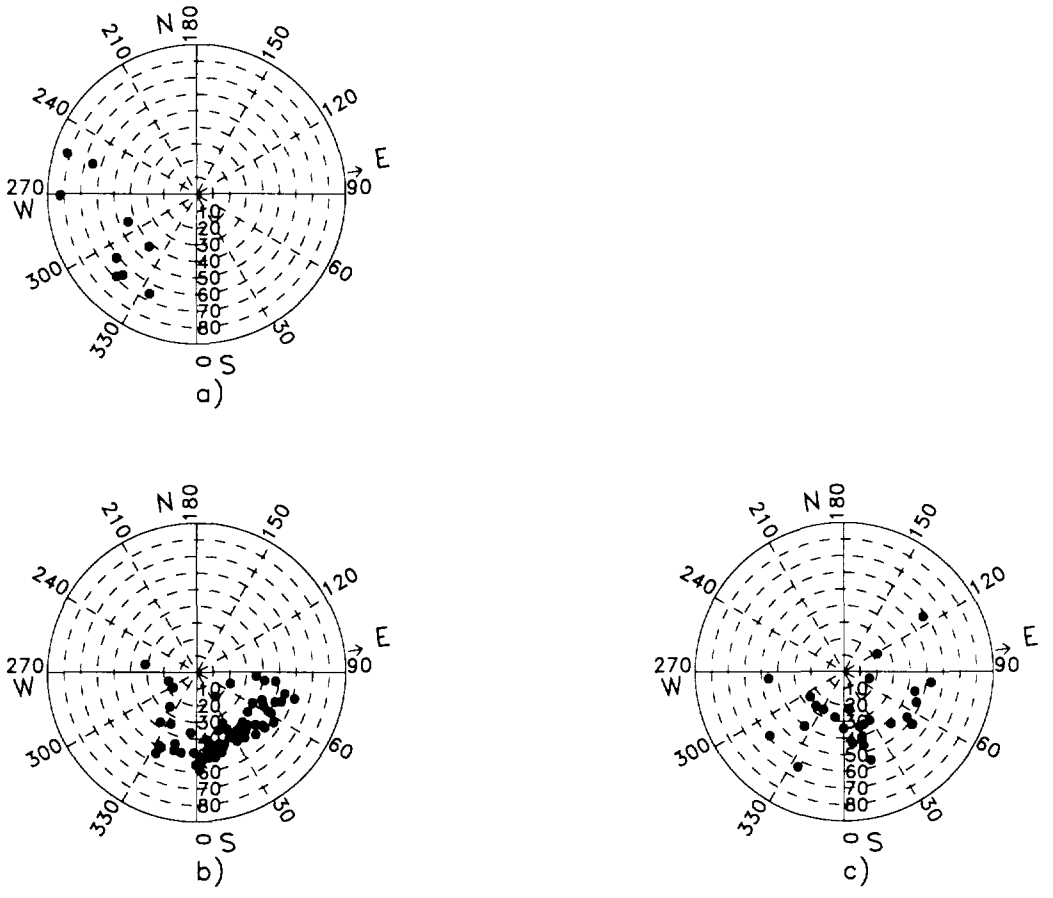

Figure 3: *Arrival directions of particles from above in the HIIS top stack. The radial coordinate is the zenith angle, and the azimuth labels (N,S,E,W) apply at the northern and southern extremes of the orbit, when the satellite is moving due east.*
a: $20 \leq Z \leq 26$, *9 particles sampled from test etchings in 3 modules* ($area \approx 250 cm^2$);
b: $Z \leq 14$, *72 particles sampled from test etchings in 2 modules* ($area \approx 150 cm^2$);
c: $15 \leq Z \leq 20$, *27 particles sampled from test etchings in 2 modules* ($area \approx 150 cm^2$).

PARTICLE ARRIVAL DIRECTIONS

A close look at the arrival directions allows a classification of particles reaching the HIIS top stack. One group arrives from a broad distribution of directions centered about the southwest. For the larger number of particles, however, the arrival direction lies in a tightly clustered band centered around the southeast. Further analysis shows the particles of the Fe-group ($20 \leq Z \leq 26$) arriving mainly from the southwest (fig. 3a). This is the direction of lowest geomagnetic cutoff, which has been associated with SEPs at $E \geq 200$ MeV/nuc[5,6]. We point out that this analysis did not detect Fe-group elements below 45 MeV/nuc. The Kiel experiment[3] on LDEF has also shown particles in

this elemental range at energies $E \geq 50$ MeV/nuc coming from the southwest.

Particles of the group $Z \leq 14$ are clearly arriving from the southeast (fig. 3b). This band of arrival directions coincides very well with the simulated and measured trapped particle distributions of Jonathal et al.[1,2,3]. Both experiments see these trapped particles at energies $E \leq 50$ MeV/nuc.

Compared to particles with $Z \leq 14$, the number of particles in the nuclear charge range $15 \leq Z \leq 20$ is much lower. The angular distribution for these particles (fig. 3c) has equal contributions of particles inside the band centered around southeast and of particles from outside that band. Future measurements will increase the statistics of these distributions so that arrival directions can be examined both for different elements and for different energy intervals.

MISSION-AVERAGED SPECTRA AND FLUXES

We have determined preliminary mission-averaged fluxes for Fe and for the group $12 \leq Z \leq 14$. For Fe we observe a mission-averaged flux of

$$J(50 MeV/nuc \leq E \leq 140 MeV/nuc) \approx 9^{+8}_{-5} \times 10^{-8} [m^2\, s\, sr\, MeV/nuc]^{-1}.$$

This value is in reasonably good agreement with the Kiel data[1] for $20 \leq Z \leq 26$ ions in this energy range.

For $12 \leq Z \leq 14$ we derive a preliminary spectrum (fig. 4). Although our flux calculation is still very preliminary, our data show a steeply falling spectrum similar to the Kiel data[1] for $14 \leq Z \leq 18$.

The averaged flux for particles $12 \leq Z \leq 14$ is

$$J(25 MeV/nuc \leq E \leq 40 MeV/nuc) \approx 3 \pm 2 \times 10^{-6} [m^2\, s\, sr\, MeV/nuc]^{-1}.$$

(Errors given here include statistical and systematic uncertainties, both of which should be reduced by further analysis.)

It should be emphasized that the above flux values are mission-averaged fluxes. That is, the flux has been derived by dividing the fluence collected during the LDEF mission by the total mission time of 5.75 years. We suggest in the next section that the trapped particle fluxes may have substantial temporal variability. In fact, they may be present in the inner magnetosphere only episodically, for days or weeks at a time. If this is indeed the case, then during such periods the actual flux level may be larger by several orders of magnitude. Moreover, the trapped particle flux may also be substantially larger in higher inclination orbits[9].

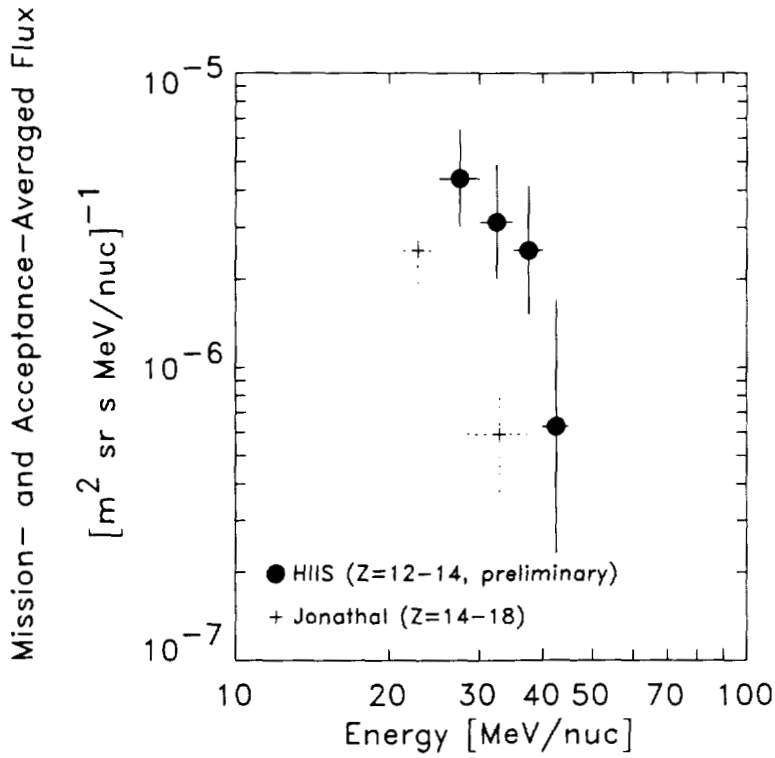

Figure 4: *Preliminary energy spectrum of particles* $12 \leq Z \leq 14$ *compared to data from the Kiel experiment*[1] *on M0002 for* $14 \leq Z \leq 18$.

DISCUSSION

At ~50–200 MeV/nuc, particles of the Fe-group ($20 \leq Z \leq 26$) appear to arrive from the direction of lowest geomagnetic cutoff. It has been shown by Tylka et al.[5] that Fe with mean ionic charge state ≈ 14 from the big SEP events of October 1989 can explain the spectrum and fluence of such ions at $E \geq 200$ MeV/nuc. Further calculations to explore the detection of Fe at energies as low as 50 MeV/nuc are under way. In particular, the SEP event[10] which peaked on 13 March 1989 was smaller and had a steeper spectrum, so that it did not produce measurable fluence above 200 MeV/nuc[§]. But during the declining phase of the particle event, Dst reached −589 nT, the largest geomagnetic disturbance of the whole LDEF mission. There may have been sufficient cutoff suppression to account for the particles arriving from the southwest at 50–200 MeV/nuc.

With increased statistics, we will be able to use the observed sub-Fe/Fe ratio to clarify the source of these particles. In particular, solar energetic particles typically have sub-Fe/Fe ratios of a few percent[11,12], while galactic cosmic rays and albedo have much larger sub-Fe/Fe ratios (see Tylka et al.[5]).

[§]W.F. Dietrich, 1992, private communication.

More interesting than the Fe ions arriving directly from outside the magnetosphere, however, are the trapped heavy ions suggested in the LDEF data. Most of these trapped species have never been observed before at the relatively high energies considered here.

Anomalous cosmic rays (ACRs) were identified by Blake and Friesen[13] in 1977 as a potential source of trapped energetic ions in the inner magnetosphere. [For a recent review of trapped ACRs, see Tylka[14].] ACRs are unique among the energetic heavy ions of the interplanetary medium in that they are singly-ionized[15,16]. Because of this low ionic charge, these ions are able to penetrate deeply into the inner magnetosphere, where the residual atmosphere strips them of their remaining orbital electrons and the ions can become stably trapped. The first conclusive experimental evidence for trapped ACR oxygen was published by Grigorov et al.[17] in 1991, and more recent observations by SAMPEX[18] have confirmed those results. Trapped ACR N and Ne have also been reported[18,20]. Ar is part of the anomalous component[19], and the results from the Kiel M0002 experiment on LDEF may be the first observation of trapped ACR Ar, since theoretical calculations of the geomagnetic distribution of trapped ACR Ar[9] agree well with the geomagnetic distribution inferred from the Kiel data[1].

ACRs have a very unusual elemental composition: according to the Fisk, Kozlovsky, & Ramaty model[15] and to all experimental evidence available to date, ACRs originate as neutral atoms in the local interstellar medium (LISM). Consequently, Mg, Si, and Fe, which have low first ionization potentials and are therefore predominantly ionized in the LISM, are *not* expected to be a significant part of the anomalous component.

Mg, Si, and Fe are abundant, however, in solar energetic particle (SEP) events. How such SEP species may become trapped in the inner magnetosphere requires a more elaborate scenario than that outlined by Blake and Friesen for ACRs. In particular, by combining considerations of (1) geomagnetic access and (2) the adiabatic limit of stable trapping, it can be shown [see, for example, Tylka[14]] that heavy-ion trapping in the Blake-Friesen mechanism requires:

$$Q/Z < 0.12 - 0.15 \qquad (1)$$

where Q and Z are the ion's charge *before* and *after* stripping in the atmosphere, respectively. ACR species (N, O, Ne, Ar) meet this requirement, since Q=+1 before stripping. However, SEP Mg, Si, and Fe do not satisfy this requirement: their observed mean ionic charge states in large, so called 'gradual' SEP events are $< Q > = 10.8$, 11.0, and 14.1, respectively[21,22] (corresponding to a typical plasma temperature of ~2.0 MK in the coronal or solar wind source material). Even taking into account the 'low Q tails' of the charge-state distributions[23,24] gives $Q/Z > 0.25$ for these SEP species.

In the derivation of equation 1, the requirement for geomagnetic access is stated in terms of cutoffs in a quiet magnetosphere. In fact, closer examination shows that it is this geomagnetic access criterion — and not the limit of stable trapping — which ostensibly precludes solar energetic heavy ions from becoming trapped like anomalous cosmic rays. However, during very large geomagnetic storms which sometimes accompany SEP events, there can be very severe cutoff suppression. This suppression gives solar energetic heavy ions access to regions of the inner magnetosphere which they normally cannot reach. (The SEP event peaking on 13 March 1989 may have been just such an occurrence.) Under such conditions, some of heavy ions could reach the

low-altitude mirror points, be stripped of electrons in the residual atmosphere, and become stably trapped, just as ACRs do in geomagnetically-quiet periods. Moreover, large geomagnetic storms can also promote radial diffusion, which would further energize the trapped particles while transporting them even deeper into the magnetosphere. The LDEF data on trapped Fe (and trapped particles of $12 \leq Z \leq 14$, if further data analysis confirms their existence) may be the first experimental evidence for the geomagnetic trapping of high energy solar heavy ions. But detailed theoretical studies are needed to show exactly how these SEP species actually appeared as trapped heavy ions in the low-inclination LDEF orbit.

Thus, it may be that both anomalous cosmic rays and solar energetic particles contribute to the trapped energetic heavy ions observed aboard LDEF. At the energies observed here, the lifetime of these trapped ions, which is limited by energy loss at encounters with the residual atmosphere at low-altitude mirror points, is expected to be on the order of days to weeks. The composition of trapped energetic heavy ions in the inner magnetosphere should therefore show very interesting temporal variation. ACR species (N, O, Ne, and Ar) should be dominant at solar minimum (which can persist for months or years, depending on the solar cycle), when the ACR source flux outside the Earth's magnetosphere is high. Trapped SEP species (such as Mg, Si, and Fe), on the other hand, should appear much more episodically, after a large solar energetic particle event which was coincident with a large geomagnetic disturbance. Moreover, such events are more common at solar maximum. (The LDEF data are unable to address the question of temporal variability directly, since the LDEF experiments have no timing information on when the ions were collected. According to this scenario, however, the trapped ACR species would have been collected primarily during solar minimum at the first half of 1987. The trapped SEP species, on the other hand, would have been collected during the large SEP events and geomagnetic disturbances of 1989.)

If the trapped particle spectrum for Z= 12–14 reported in fig. 4 were a permanent feature of the inner magnetosphere at $L \leq 1.8$, it would be detectable by the HILT[25,26] instrument onboard NASA's SAMPEX satellite at a rate of at least several tens of particles per year. For the same trapped particles the MAST[25,27] instrument onboard SAMPEX would register roughly a few particles per year.

Finally, we note that there have been several reports of far-below cutoff Fe-group ions with a greatly enhanced sub-Fe/Fe ratio[28,29,30]. To date, we have no evidence to support these observations, although further analysis on this question is in progress. See Tylka et al.[5] for further discussion.

CONCLUSIONS

Currently our analysis of the test etchings from the Lexan top stacks shows that HIIS Lexan detects particles $Z \geq 10$ in an energy range E= 20–200 MeV/nuc inside the earth's magnetosphere. The composition suggests a combination of ACRs and SEPs, with important questions regarding the geomagnetic access of solar energetic heavy ions remaining.

Particles of the Fe group in the energy range $45 MeV/nuc \leq E \leq 200 MeV/nuc$ are registered mostly coming from the direction of lowest cutoff. These particles may have been collected during SEP events accompanied by very large geomagnetic cutoff suppression. The examination of the sub-Fe/Fe ratio should help to clarify the source of these ions.

For Fe we estimated the mission-averaged flux to be

$$J(50 MeV/nuc \leq E \leq 140 MeV/nuc) \approx 9^{+8}_{-5} \times 10^{-8} [m^2\, s\, sr\, MeV/nuc]^{-1}.$$

Particles $Z \leq 14$ at $E \leq 50$ MeV/nuc appear to be trapped in the magnetosphere. For particles with Z= 12–14 we find a steeply falling spectrum. The preliminary mission-averaged flux is

$$J(25 MeV/nuc \leq E \leq 40 MeV/nuc) \approx 3 \pm 2 \times 10^{-6} [m^2\, s\, sr\, MeV/nuc]^{-1}.$$

By etching and measuring one complete module, the statistics of the analysis can be increased at least by an order of magnitude. This should allow a better calibration and enable us to derive the elemental composition and energy spectra. With an improved elemental resolution it should be possible to separate the contributions from anomalous cosmic rays and solar energetic particles.

ACKNOWLEDGEMENTS

We thank Don Reames for providing us with data for the March 1989 SEP event. We thank Les Morris of NGDC for magnetometer data and help in interpreting it. We thank Sabine Barz, Rudolf Beaujean, Wolfgang Enge, and Dirk Jonathal for discussions of their observations of stopping heavy ions on LDEF. We thank our student microscopist Kenny Zee for his dedication and hard work. This work was done while Paul R. Boberg held a National Research Council-NRL Research Associateship. This work has been supported by the Office of Naval Research and NASA contract W18409.

REFERENCES

1. Jonathal, D.: Nachweis magnetisch gefangener Schwerionen mit Kernspurdetektoren auf dem Satelliten LDEF. Ph.D. thesis, Institut fuer Kernphysik, Univ. Kiel, Germany, July 1993.

2. Jonathal, D.; Beaujean, R.; and Enge, W.: Trapped Iron Measured on LDEF. Proc. 23rd ICRC (Calgary), vol. 3, 1993, pp. 445–448.

3. Jonathal, D. et al.: Evidence for the Detection of Trapped Iron Nuclei on LDEF. Presented at the Third LDEF Post-Retrieval Symposium, Williamsburg, VA, November 1993 (these proceedings).

4. Adams, J.H. Jr.; Beahm, L.P.; and Tylka, A.J.: Preliminary Results from the Heavy Ions in Space Experiment. Proc. First LDEF Post-Retrieval Symposium, NASA CP-3134, Part 1, 1991, pp. 377–391.

5. Tylka, A.J. et al.: Results from the HIIS Experiment on the Ionic Charge State of Solar Energetic Particles. Presented at the Third LDEF Post-Retrieval Symposium, Williamsburg, VA, November 1993 (these proceedings).

6. Adams, J.H. Jr. et al.: HIIS Observations during the Large Solar Energetic Particle Events of October 1989. Proc. 23rd ICRC (Calgary), vol. 3, 1993, pp. 374–377.

7. Stiller, B.; Adams, J.H. Jr.; and Beahm, L.P.: Ultraviolet Enhancement of Tracks in Lexan with Black Fluorescent Lamps. Nucl. Tracks, vol. 12, 1986, pp. 137–140.

8. Adams, J.H. Jr. et al.: Progress Report on the Heavy Ions in Space (HIIS) Experiment. Proc. Second LDEF Post-Retrieval Symposium, NASA CP-3194, Part 1, 1993, pp. 247–259.

9. Tylka, A.J.: Spectra and Geographical Distribution of Geomagnetically Trapped Anomalous Cosmic Rays. Proc. 23rd ICRC (Calgary), vol. 3, 1993, pp. 436–439.

10. Reeves, G.D. et al.: The Great Solar Energetic Particle Events of 1989 Observed From Geosynchronous Orbit. J. Geophys. Res., vol. 97, 1992, pp. 6219–6226.

11. Mason, G.M.: The Composition of Galactic Cosmic Rays and Solar Energetic Particles. Reviews of Geophysics and Space Physics, vol. 25, 1987, pp. 685–696.

12. Garrard T.L. and Stone E.C.: New SEP-Based Solar Abundances. Proc. 23rd ICRC (Calgary), vol. 3, 1993, pp. 384–387.

13. Blake, J.B. and Friesen, L.M.: A Technique to Determine the Charge State of the Anomalous Low-Energy Cosmic Rays. Proc. 15th ICRC (Plovdiv), vol. 2, 1977, pp. 341–346.

14. Tylka, A.J.: Theoretical Modeling and Interpretation of Trapped Anomalous Cosmic Rays. Proc. 23rd ICRC (Calgary), vol. 5 (Invited, Rapporteur and Highlight Papers), 1994, pp. 465–474.

15. Fisk, L.A.; Kozlovsky, B.; and Ramaty R.: An Interpretation of the Observed Oxygen and Nitrogen Enhancements in Low-Energy Cosmic Rays. Astrophys. J. Letters, vol. 190, 1974, pp. L35–L37.

16. Adams, J.H. Jr. et al.: The Charge State of the Anomalous Component. Astrophys. J. Letters, vol. 375, 1991, pp. L45–L48.

17. Grigorov, N.L. et al.: Evidence for Trapped Anomalous Cosmic Ray Oxygen Ions in the Inner Magnetosphere. Geophys. Res. Letters, vol. 18, 1991, pp. 1959–1962.

18. Cummings, J.R. et al.: New Evidence for Geomagnetically Trapped Anomalous Cosmic Rays. Geophys. Res. Letters, vol. 20, 1993, pp. 2003–2006.

19. Cummings, A.C. and Stone, E.C.: Elemental Composition of the Anomalous Cosmic-Ray Component. Proc. 20th ICRC (Moscow), vol. 3, 1987, pp. 413–416.

20. Bobrovskaya, V.V. et al.: Cosmos Observations of Anomalous Cosmic Ray N and Ne in the Inner Magnetosphere. Proc. 23rd ICRC (Calgary), vol. 3, 1993, pp. 432–435.

21. Luhn, A. et al.: Ionic Charge States of N, Ne, Mg, Si, and S in Solar Energetic Particle Events. Adv. in Space Res., vol. 4, 1984, pp. 161–164.

22. Luhn, A. et al.: The Mean Ionic Charge of Silicon in ^{3}He-Rich Solar Flares. Astrophys. J., vol. 317, 1987, pp. 951–955.

23. Shull, J.M. and Van Steenberg, M.: The Ionization Equilibrium of Astrophysically Abundant Elements. Astrophys. J. Suppl., vol. 48, 1982, pp. 95–107.

24. Arnaud, M. and Raymond, J.: Iron Ionization and Recombination Rates and Ionization Equilibrium. Astrophys. J., vol. 398, 1992, pp. 394–406.

25. Baker, D.N. et al.: An Overview of the Solar, Anomalous and Magnetospheric Particle Explorer (SAMPEX) Mission. IEEE Trans. Geosci. Remote Sensing, vol. 31, 1993, pp. 531–541.

26. Klecker, B. et al.: HILT: A Heavy Ion Large Area Proportional Counter Telescope for Solar and Anomalous Cosmic Rays. IEEE Trans. Geosci. Remote Sensing, vol. 31, 1993, pp. 542–548.

27. Cook, W.R. et al.: MAST: A Mass Spectrometer Telescope for Studies of the Isotopic Composition of Solar, Anomalous, and Galactic Cosmic Ray Nuclei. IEEE Trans. Geosci. Remote Sensing, vol. 31, 1993, pp. 557–564.

28. Biswas, S. et al.: Observation of Low-Energy (30–100 MeV Nucleon^{-1}) Partially Ionized Heavy Ions in Galactic Cosmic Rays. Astrophys. J. Letters, vol. 359, 1990, pp. L5–L9.

29. Biswas, S. et al.: Ratio of Sub-Iron (Sc–Cr) to Iron Ions in Low Energy Galactic Cosmic Rays Inside & Outside of Earth's Magnetosphere. Proc. 22nd ICRC (Dublin), vol. 2, 1991, pp. 308–311.

30. Gargarin, Yu.F. et al.: Sulfur–Nickel Nuclei at Small Energies in Cosmic Rays, Proc. 21st ICRC (Adelaide), vol. 3, 1990, pp. 11–14.

RESULTS FROM THE HEAVY IONS IN SPACE (HIIS) EXPERIMENT ON THE IONIC CHARGE STATE OF SOLAR ENERGETIC PARTICLES

Allan J. Tylka, Paul R. Boberg,[1*] James H. Adams, Jr., and Lorraine P. Beahm
E. O. Hulburt Center for Space Research
Code 7654, Naval Research Laboratory
Washington, DC 20375-5352
Phone: 202/767-2200, Fax: 202/767-6473

Thomas Kleis
CSI Institute, George Mason University
Fairfax, VA 22030-4444
Phone: 202/767-2200, Fax: 202/767-6473

SUMMARY

It has long been known that low-energy solar energetic particles (SEPs) are partially-ionized. For example, in large, so-called "gradual" solar energetic particle events, at ~1 MeV/nucleon the measured mean ionic charge state of Fe ions is $\langle Q \rangle = 14.1 \pm 0.2$, corresponding to a plasma temperature of ~2 MK in the coronal or solar-wind source material. Recent studies, which have greatly clarified the origin of solar energetic particles and their relation to solar flares, suggest that ions in these SEP events are accelerated *not* at a flare site, but by shocks propagating through relatively low-density regions in the interplanetary medium. As a result, the partially-ionized states observed at low energies are expected to continue to higher energies. However, up to now there have been no high-energy measurements of ionic charge states to confirm this notion.

We report here HIIS observations of Fe-group ions at 50-600 MeV/nucleon, at energies and fluences which cannot be explained by fully-ionized galactic cosmic rays, even in the presence of severe geomagnetic cutoff suppression. Above ~200 MeV/nucleon, all features of our data -- fluence, energy spectrum, elemental composition, and arrival directions -- can be explained by the large SEP events of October 1989, *provided* that the mean ionic charge state at these high energies is comparable to the measured value at ~1 MeV/nucleon. By comparing the HIIS observations with measurements in interplanetary space in October 1989, we determine the mean ionic charge state of SEP Fe ions at ~200-600 MeV/nucleon to be $\langle Q \rangle = 13.4 \pm 1.0$, in good agreement with the observed value at ~1 MeV/nucleon. The source of the ions below ~200 MeV/nucleon is not yet clear.

Partially-ionized heavy ions are less effectively deflected by the Earth's magnetic field than fully-ionized cosmic rays and therefore have greatly enhanced access to low-Earth orbit. Moreover, at the high energies observed in HIIS, these ions can penetrate typical amounts of shielding. We discuss the significance of the HIIS results for estimates of the radiation hazard posed by large SEP events to satellites in low-Earth orbit, including the proposed Space Station orbit.

Finally, we comment on previous reports of low-energy below-cutoff Fe-group ions, which some authors have interpreted as evidence for partially-ionized galactic cosmic rays. The LDEF flux levels are much smaller than the corresponding fluxes in these previous reports, implying that the source of these ions has an unusual solar-cycle variation and/or strongly increases with decreasing altitude.

[1*] NRC Postdoctoral Research Associate

INTRODUCTION

Galactic cosmic rays are generally believed to be bare nuclei, fully stripped of all orbital electrons. One of the primary goals of the Heavy Ions in Space (HIIS) experiment is to investigate possible sources of partially-stripped heavy ions. The study of such ions is of astrophysical interest, especially at high energies where the cross-section for electron-stripping greatly exceeds the cross-section for electron pick-up. In this case, a measurement of the mean ionic charge state significantly constrains the amount of matter traversed by the ions, thereby helping to identify their source and the mechanism by which they have been accelerated to high energies. Two well-known sources of partially-ionized heavy ions are anomalous cosmic rays[1] and (at least at low energies) solar energetic particles (SEPs)[2,3,4].

Partially-ionized heavy ions are also of potential practical importance: their lower charge state gives them higher magnetic rigidity than fully-ionized cosmic rays of the same kinetic energy. As a result, partially-ionized heavy ions can penetrate to orbits which are largely shielded from cosmic rays by the Earth's magnetic field. Partially-ionized ions, at least in some orbits and under certain conditions, may thus constitute an important component of the ionizing-radiation environment encountered by humans and hardware in low-Earth orbit.

EXPERIMENT DESCRIPTION

A detailed description of HIIS has been published previously[5,6]. The HIIS detector uses thick stacks of plastic track detectors, mounted on the space-facing end of LDEF, with an unobstructed view of the sky and efficient particle detection down to zenith angles of ~70°. The detectors are completely passive: that is, they provide no information on when individual ions were collected during LDEF's 69 months in space. Conclusions about the origin(s) of ions observed in HIIS must therefore be deduced from other characteristics of the data, such as fluence, energy spectrum, composition, and arrival directions. HIIS is divided into eight modules, each of which consists of a main stack (comprising primarily ~300 10-mil-thick sheets of CR-39[2*] sealed in 1 atm of dry air) and a top stack (consisting of 22 5-mil thick sheets of Lexan[3*], exposed in vacuum.) The collecting power of the total instrument is approximately 2.0 m^2-sr, making HIIS the second-largest cosmic-ray experiment ever flown in space. In this paper, we present data collected from ~60 CR-39 sheets at various depths in the main stack of one module. Preliminary results on low-energy heavy ions from small portions of three top stacks are presented by Kleis et al. in these Proceedings[7].

OBSERVATIONS OF STOPPING HEAVY IONS

We have used a combination of manual and automated scanning to locate stopping tracks in the CR-39 detector sheets. (A detailed description of the detection method, the calibration technique, and track-fitting procedures is given in Ref. 8.) Fig. 1 shows the V_T/V_B vs. residual range measurements from stopping tracks located in CR-39 sheets near the top of one detector module. The strong accumulation

---

[2*] CR-39 is poly diethylene glycol bis-alyl carbonate and was invented at Pittsburgh Plate Glass's Columbia Resin Laboratory in Barberton, OH.

[3*] Lexan is the trade name for bis-phenol A polycarbonate, as sold by General Electric, Pittsfield MA. It is also sold under the tradenames of Tuffak and Rodyne-P.

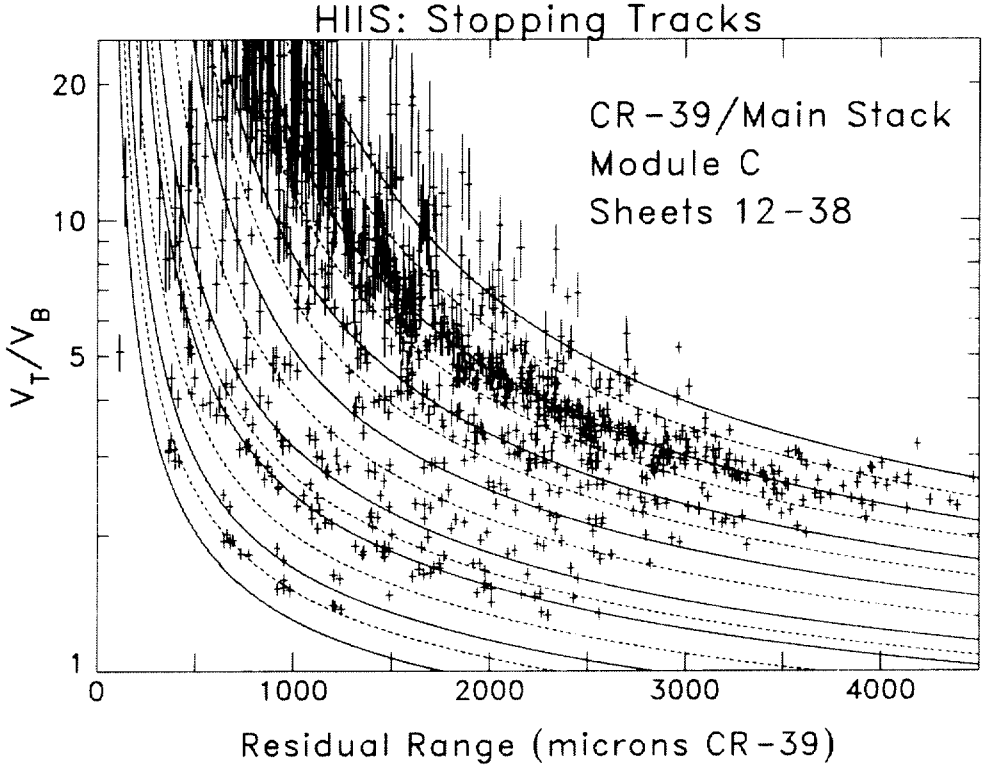

Figure 1: V_T/V_B vs. residual range measurements from stopping tracks found in CR-39 near the top of one module. The plot contains 1028 measurements from 97 cosmic-ray tracks incident upon the detector from space. The response curves are for elements with atomic numbers Z = 14-28, with solid and dashed curves for even and odd elements, respectively.

of tracks was identified as Fe. To derive an internal calibration of the detector we used a subset of these Fe tracks, as well as a few lighter tracks to extend the calibration to $V_T/V_B < 2$. This calibration was then used to generate the elemental response curves shown in Fig. 1.

For each stopping track we typically had ~10 independent V_T/V_B measurements spread over the last ~3500 microns of the particle's range. Each set of V_T/V_B measurements was fitted to the detector response function using a χ^2 minimization to determine the particle's atomic number, Z. Fig. 2 shows the histogram of fitted atomic numbers for particles found throughout the detector stack. The strong Fe peak is clearly seen[4*], and a gaussian fit to this peak gives $\sigma = 0.43 \pm 0.04$ charge units. Fig. 2 is uncorrected for Z-dependent acceptance effects. In particular, our scanning method generally does not find ions at $Z < 14$, and the acceptance increases gradually between Z=14 and Z=20. At larger Z the acceptance is constant to within approximately 15%.

Composition. Fig. 3 examines the composition of the stopping heavy ions in more detail. It shows the sub-Fe to Fe ratio (defined here as $\Sigma(21 < Z < 25)/\Sigma(Z \geq 25)$, because of the detector's modest charge resolution) as observed at various depths in the detector stack. These depths correspond to stopping Fe

---

[4*] In an earlier status report on the HIIS experiment[8] we showed a charge histogram which had a strong peak at Z=25. Those data came from a detector module in which there had been a severe thermal blanket failure, probably near the end of the mission. This failure apparently caused a shift in the detector calibration. The data reported here are from a second module, in which the thermal blanket returned from space nearly intact.

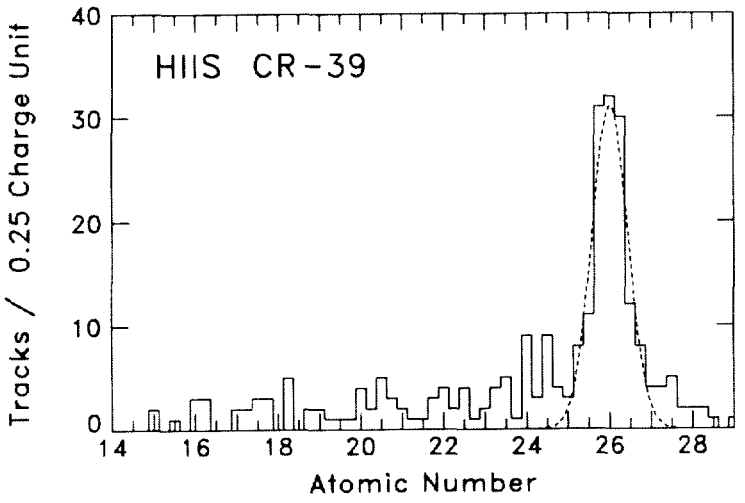

Figure 2: Histogram of fitted atomic numbers. Also shown is a gaussian fit to the Fe peak with σ = 0.43.

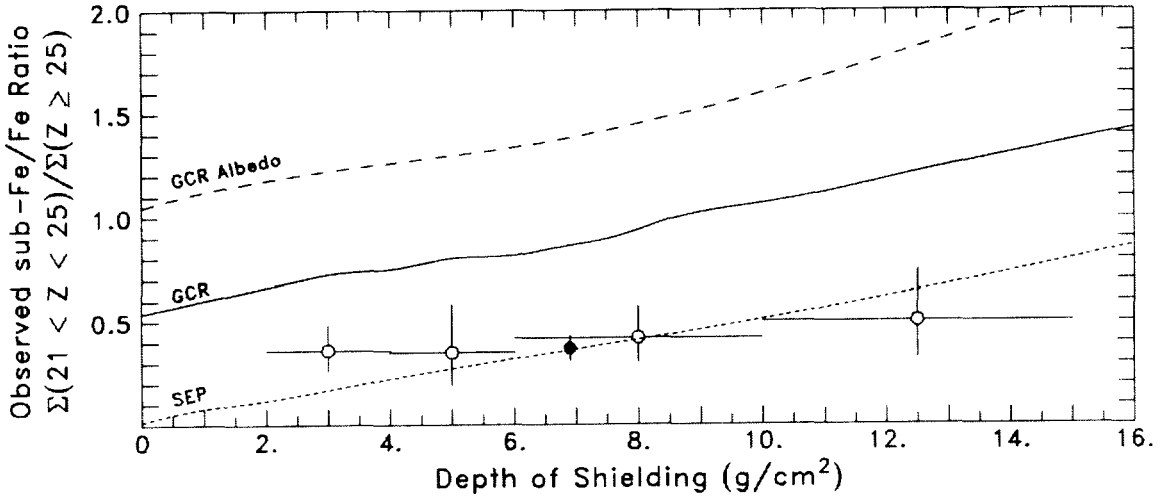

Figure 3: Sub-Fe/Fe ratio of stopping tracks, as observed under various depths of shielding. The open circles are for subsets of the data sample. The filled circle is for the combined dataset of all tracks, with abscissa at the mean shielding depth. The curves show the expected composition for various sources, after taking into account fragmentation in the detector.

ions with incident energies of ~185 - 650 MeV/nucleon at the top of the detector. Small corrections (~5%) have been applied to the measurements, to account for the weak Z-dependence of the detector acceptance.

The composition vs. depth curves in Fig. 3 were calculated by first adjusting the incident spectrum of the hypothetical source (SEPs, galactic cosmic rays (GCRs), or GCR albedo) to match the Fe spectrum in Fig. 5 below. Each hypothetical source was then propagated to various depths in the detector stack using a nuclear transport code[9]. Fig. 3 shows that the observed composition is consistent with an incident source with a very small proportion of sub-Fe ions. In fact, the incident composition is consistent with that of SEPs, with a sub-Fe/Fe ratio of a few percent before fragmentation in the detector. But the observed composition is inconsistent with that expected for GCRs (with an incident sub-Fe/Fe ratio of ~0.5 before additional fragmentation in the detector) or GCR albedo (with even more sub-Fe ions due to fragmentation in the atmosphere before reaching LDEF).

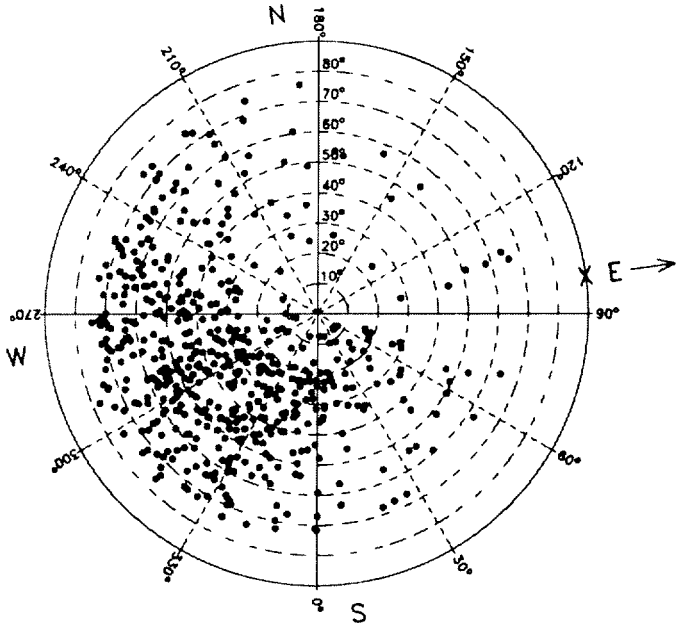

Figure 4: Arrival directions of particles incident from space. The radial coordinate is the zenith angle, and the azimuth angles are as given in the LDEF coordinate system. The small arrow indicates the LDEF velocity vector. The azimuth labels (N,E,S,W) apply at the northern and southern extremes of the orbit, when the satellite is moving due east. This figure contains data from two HIIS modules.

Figure 5: LDEF Fe flux measurements from HIIS (filled circles) and the Kiel[10,11] (open triangle) and Siegen[12] (open circles) experiments. The HIIS data point at 85 MeV/nucleon comes from Kleis et al. measurements[7] in the Lexan top stack. Additional Kiel data points for *trapped* Fe ions below 50 MeV/nucleon are not shown here. The curves show the expected contributions for galactic cosmic rays (GCR) and the solar energetic particle (SEP) events of September-October 1989, as calculated with the indicated values of the mean ionic charge state, <Q>.

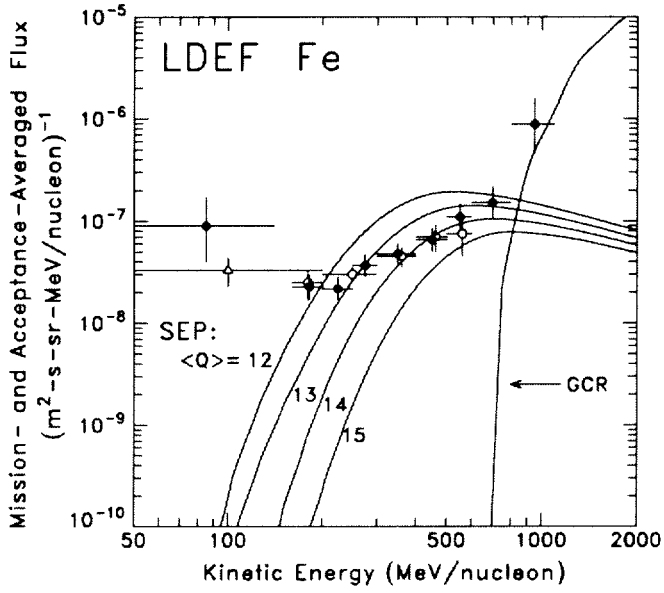

Arrival Directions. Fig. 4 shows the arrival direction distribution of the stopping particles. The distribution is highly anisotropic, with arrival directions centered about the southwest, apparently the direction of lowest geomagnetic cutoff in the LDEF orbit. This distribution suggests that the particles come from a source with a steeply falling spectrum outside the magnetosphere. In fact, the strong azimuthal variation in Fig. 4 is in reasonably good numerical agreement with calculations based on Stormer theory. This angular distribution is dramatically different from what would be expected for geomagnetically-trapped particles in the HIIS detectors[7,10,11].

Iron Flux and Spectrum. Fig. 5 shows our mission- and acceptance-averaged Fe flux measurements at the surface of the satellite, after corrections for energy-loss and fragmentation in the detector. Our flux measurements are in good agreement with those from the Kiel[10,11] and Siegen[12] experiments on LDEF.

The galactic cosmic ray curve (GCR) in Fig. 5 is an absolute prediction, averaged over the solar-cycle variation[13] during the LDEF mission and convoluted with the geomagnetic transmission function[14]. The transmission function we used here took into account cutoff suppression due to geomagnetic storms. This transmission function was calculated using (1) Monte Carlo methods[15,16] to randomly sample HIIS lookout directions and locations along the LDEF orbit; and (2) a trajectory-tracing program[17] to determine whether or not a particle of the specified rigidity had access to HIIS from interplanetary space. The trajectory tracing program incorporated both the International Geomagnetic Reference Field (IGRF)[18] to describe the internal magnetic field of the Earth and the Tysganenko model[19] to describe the contributions from currents in the outer magnetosphere. With this program, we calculated transmission functions for 10 different levels of geomagnetic activity,[5*] corresponding to Kp=0-9. These ten transmission functions were then combined in a weighted average, with relative weights determined from a survey of geomagnetic activity during the LDEF mission.

As an independent check on our cutoff suppression analysis, we also repeated the transmission function calculation using the model of Flueckiger, Smart, and Shea[20] (hereafter FSS). The FSS model gives an analytic expression for the cutoff-suppression at mid- and low-latitudes as a function of *Dst*. This model gives a reasonably good description of cutoff supressions at neutron monitor stations which cover the same rigidity range as LDEF.

At the highest energies (> 800 MeV/nucleon), our Fe flux is consistent with GCRs. Both the trajectory tracings and the FSS model, however, indicate that fully-ionized galactic cosmic rays cannot account for the observed flux at lower energies. In particular, both cutoff suppression calculations indicate that even a geomagnetic storm as severe as *Dst* = -300 nT would not allow fully-stripped Fe ions to reach the LDEF orbit at energies below ~500 MeV/nucleon. During the 6-year LDEF mission, there were only 11 hours during which *Dst* < -300 nT. We calculate that the GCR Fe fluence collected during these 11 hours falls at least 3 orders of magnitude below the observed fluence. Moreover, as already shown in Fig. 3, the observed sub-Fe/Fe ratio is also inconsistent with that of GCRs.

Analysis of Fig. 5 has also led us to reject albedo as a possible source of the observed flux. To match the observed flux and spectrum, $\geq$ 20% of all GCRs would have to pass through $\geq$ 25 g/cm^2 of atmosphere[21]. Such a large pathlength implies a grazing, nearly-horizontal trajectory through the atmosphere, which seems unreasonable for such a large fraction of the incident GCRs. Also, as already shown in Fig. 3, passage through so much atmosphere before reaching LDEF would yield a much larger sub-Fe/Fe ratio than we observe.

[5*] The Tsyganenko model describes the magnetospheric fields using fits to satellite magnetometer data, with 6 sets of fit parameters corresponding to geomagnetic activity levels of Kp = 0,1,2,3,4, and $\geq$5. The magnetometer data used by Tsyganenko were too sparse to provide separate fits to the model parameters at rare, very high levels of geomagnetic disturbance (Kp=6-9). In order to extend the Tsyganenko model to these very large disturbances, we adjusted one key parameter (denoted c_5, which describes the strength of the ring current) in a way which is consistent both with the observed *Dst* values and studies of cutoff suppression at mid- and low-latitude neutron monitor stations. This extension has been tested by comparing it with the measured geomagnetic transmission of solar energetic protons, as deduced from simultaneous observations on GOES-7 (in geosynchronous orbit) and NOAA-10 (in low-Earth orbit) during the large SEP events and geomagnetic disturbances of October 1989. Details of this extension will be published elsewhere (Boberg et al., in preparation).

SOLAR ENERGETIC PARTICLES IN THE HIIS DATA

To further study solar energetic particles in the HIIS data, we obtained a survey[6*] of SEP events during the LDEF mission from the University of Chicago instrument on IMP-8. Preliminary results from this survey show that only 3 events (beginning on 29 September, 19 October, and 24 October 1989) produced significant Fe fluences above 200 MeV/nuc. The time-profile of these events and the accompanying *Dst* variation are shown in Fig. 6. For these three events, the Chicago instrument provided both Fe fluences at 200-400 MeV/nuc and spectral indices. In terms of high-energy heavy-ions, the 24 October 1989 SEP event was the largest that occurred during the LDEF mission. The 19 October 1989 event also contributed a significant fluence to the LDEF observations because of the large geomagnetic storms and cutoff suppression which accompanied it.

For each of these three SEP events we calculated a separate geomagnetic transmission function. To do this we again used trajectory tracings combined with Monte Carlo samplings of HIIS lookout directions and locations along the LDEF orbit: at each rigidity, the value of the transmission function was given by the fraction of trajectory tracings which successfully tracked back to interplanetary space. But because the SEP events were so dynamic, with interplanetary particle fluxes and (generally) geomagnetic activity levels changing by large factors over relatively short times, some additional factors had to be included in the transmission calculations. In particular, we used the actual LDEF orbital trajectory, as reconstructed from orbital elements obtained from US Space Command. Since *Dst* (the geomagnetic index apparently best correlated with cutoff suppression) is available in hourly averages, we then divided the orbital trajectory into one-hour segments. On each segment, we adjusted the ring-current strength parameter (c_5) in the Tsyganenko model to match the observed *Dst*. Also, the number of samplings attempted on each segment was proportional to the SEP fluence outside the magnetosphere at that time[7*] . This fluence-weighting is an important feature of the calculation, since (for example) it ensures that a large geomagnetic disturbance (and hence high transmission) which occurs when the SEP fluence is small contributes to the transmission function only at the appropriate level.

For each SEP event we thus had a transmission function and a measured fluence and spectral index outside the magnetosphere. We used these to calculate the combined contribution of these three SEP events to the HIIS Fe fluxes. In these calculations, we varied the mean ionic charge state <Q>, which we assumed to be the same in all 3 events and independent of energy. Fig. 5 shows the fluxes we calculated for various <Q> values. Clearly, <Q> ~ 13 - 14 gives a good description of the LDEF measurements above ~200 MeV/nucleon.

There is one additional ingredient in the calculations of Fig. 5 which should be noted here. The calculated spectrum depends not only on the *mean* ionic charge value but also the actual *distribution* of ionic charge states. Low-energy ionic charge state observations are not precise enough to measure this distribution directly, so the distribution must be taken from theoretical calculations about the source plasma. These calculations, which determine the distribution corresponding to a specified plasma temperature (and hence <Q> value), take into account the detailed atomic cross-sections for electron stripping and pick-up. For the curves in Fig. 5, we used the theoretical calculations of Arnaud & Raymond[24]. We also tried the calculations of Shull and Van Steenberg[25], which resulted in slightly different normalizations and spectral shapes.

From the HIIS Fe measurements above 200 MeV/nucleon, we determined the best-fit value $<Q> = 13.4 \pm 1.0$. The error bar quoted here comprises statistical and systematic uncertainties

---

6* W.F. Dietrich, 1992, private communication.

7* We used several different interplanetary fluence measurements, including protons from GOES-7, alphas from IMP-8, and (after 19 October 1989) heavy ions from Galileo. These fluence measurements were available in different energy intervals and on various time-scales, ranging from 5-minute to 3-hour averages. Using these different fluences to monitor the SEP's temporal evolution gave transmission calculations which generally agreed to within ~10%.

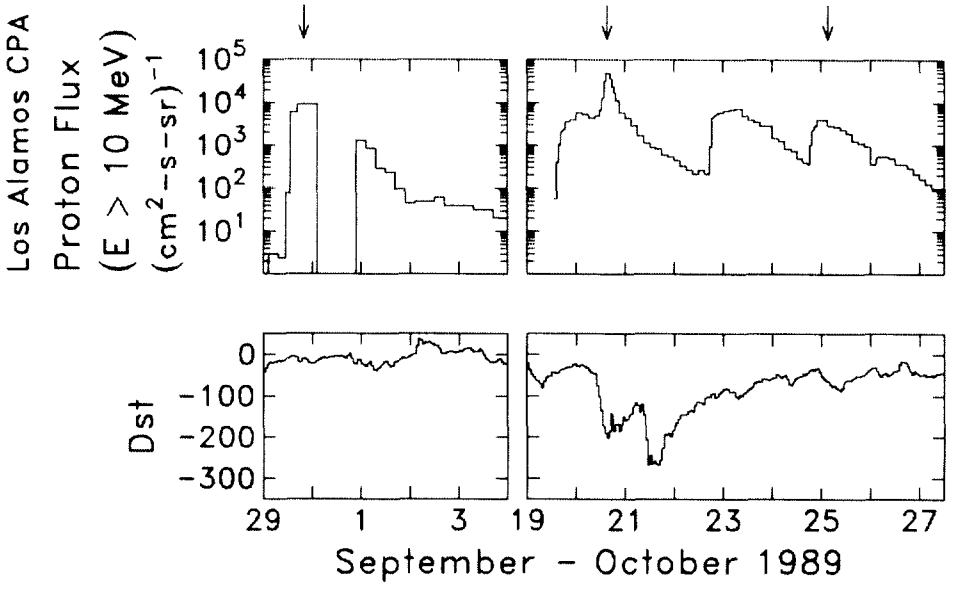

Figure 6: The upper panel shows the time history of the Sept.-Oct. 1989 SEP events, as monitored by >10 MeV proton fluxes from the Los Alamos CPA instrument[22] in geosynchronous orbit. The arrows mark the peaks of the 3 events which produced significant Fe fluence above 200 MeV/nucleon. The lower panel shows the *Dst* history[23] for this same period. There is a gap in the CPA data on 30 Sept. This gap had no impact on our analysis.

including: (1) statistical error in the HIIS measurements (as shown in Fig 5); (2) statistical error in the IMP-8 measurements (provisionally estimated at 20%, pending further analysis); (3) 15% random uncertainty in the transmission calculation (based on comparison of calculated and observed transmission of solar energetic protons in ~60 three-hour intervals during the October 1989 events[8*].) Among sources of systematic error we have considered are (1) 10% systematic error in the HIIS flux measurement, based on track misidentification estimates and uncertainties in calibration and acceptance calculations; (2) systematic uncertainty caused by the choice of either Arnaud & Raymond[24] or Shull & Van Steenberg[25] charge state distributions; and (3) systematic uncertainty in the transmission calculation. In particular, we repeated our transmission calculations using the FSS cutoff suppression model[20]. These results gave a slightly lower best-fit value of <Q> and a somewhat better fit to the observed spectral shape above 200 MeV/nuc. At present, this systematic uncertainty in the transmission calculation is the dominant source of error in our measurement.

There is, however, another potential source of systematic error in our result which we have not yet fully evaluated. This error arises from the possible contribution of additional unidentified sources to our Fe fluxes. Any such additional source will bias our <Q> toward a lower value; an additional source produces excess flux, which falsely implies higher geomagnetic transmission and thus a lower mean charge state. The composition results (Fig. 3) show that, at least on average, albedo does not make a significant contribution to our Fe flux.[9*] Also, the observed arrival direction distribution rules out a significant trapped particle contribution above 200 MeV/nuc. But additional SEP events, which were individually too small to be measured by the IMP-8/Chicago instrument, may contribute to the HIIS flux. Further analysis is required to put quantitative upper limits on the possible contributions of such sources above 200 MeV/nucleon.

[8*] P.R. Boberg et al.: Geomagnetic Transmission During the Solar Energetic Particle Events of October 1989, in preparation.

[9*] Albedo contamination could arise in the Fe spectrum not from fragmentation of heavier ions, but by slowing down in the atmosphere before reaching LDEF.

A striking feature of Fig. 5 is the particle fluxes *below* ~200 MeV/nucleon. Our calculations to date have not been able to explain this data in terms of the SEP fluences and cutoff suppression of October 1989. Also, it is interesting to note that the sub-Fe/Fe ratio in Fig. 3 is somewhat higher than expected at these lower energies. At present, the statistical significance of this sub-Fe excess is only about 2σ, but it may suggest an additional source other than SEPs. Additional composition measurements are critical for understanding the source of these particles.

If the sub-Fe excess is indeed just a statistical fluke, another possibility is that a significant fraction of the fluence below ~200 MeV/nuc may be due to the SEP event of 6-15 March 1989. This event was both smaller and had a steeper spectrum than the events of October 1989. But the largest geomagnetic disturbances of the LDEF mission (including 10 of the 11 hours when $Dst < -300$ nT) occurred during the declining phase of this event. Because of the very large and complex geomagnetic disturbances during this period, modeling the geomagnetic transmission for this event is very challenging. But if this storm did provide access to the LDEF orbit for a significant fluence of SEP Fe ions below 200 MeV/nucleon, it may also be the source of the trapped Fe observed by the Kiel experiment. Such ions could become stripped of their remaining orbital electrons in the residual atmosphere and then become stably-trapped, just as anomalous cosmic rays do. (For further discussion, see Kleis et al[7]. in these Proceedings.)

SIGNIFICANCE OF THE HIIS RESULTS

Origin of Solar Energetic Particle Events. The HIIS results are the first observation of partially-ionized SEPs above ~1 MeV/nucleon. In many analyses[26,27] of SEP data, it has been implicitly assumed that the charge states measured at ~1 MeV/nucleon continue to higher energies. This assumption has been a key ingredient in uncovering patterns of systematic variation in SEP events. The HIIS results therefore validate this otherwise unverified assumption.

The HIIS results show that the mean ionic charge states of SEPs remain essentially unchanged as the particles are accelerated from ambient plasma temperatures up to hundreds of MeV/nucleon. Qualitatively, this observation implies that the acceleration cannot take place in a relatively dense plasma, such as found at the site of a solar flare, in the chromosphere or corona. Our results therefore add another confirmation to the growing consensus[28-31] on the origin of large SEP events in interplanetary shocks driven by coronal mass ejections. Moreover, it should be possible to use the HIIS results to put a stringent upper limit on the amount of matter traversed during the acceleration process and the plasma density in the acceleration region. The high energies investigated here are particularly powerful in such studies, since high energy particles must have longer residence times and hence much longer pathlengths in the acceleration region than low energy particles.

Significance for Radiation Environment Modeling. Partially-ionized heavy ions can penetrate to orbits which are largely shielded from fully-ionized cosmic rays by the Earth's field. This is illustrated in Fig. 7a, which shows the event-averaged integral LET spectrum for the 24 October 1989 SEP event in the LDEF orbit, as deduced from the IMP-8 and HIIS fluence measurements and modeling of the geomagnetic transmission during this period. Note that the spectra are calculated behind 0.25" of aluminum shielding. They are also averaged over all lookout directions and take into account the presence of the solid Earth. The calculation is shown for two different assumptions about the SEP charge state, fully- or partially-ionized. The spectra include all elements[10*] with $Z \leq 28$.

[10*] We used the measured interplanetary fluence and spectra of protons and Fe. For other elements, the Fe spectrum was scaled by the relative abundances given in Ref. 32. In the partially-ionized calculation, we used for these other elements the mean charge states reported in Ref. 3 and the theoretical charge state distributions given in Ref. 25.

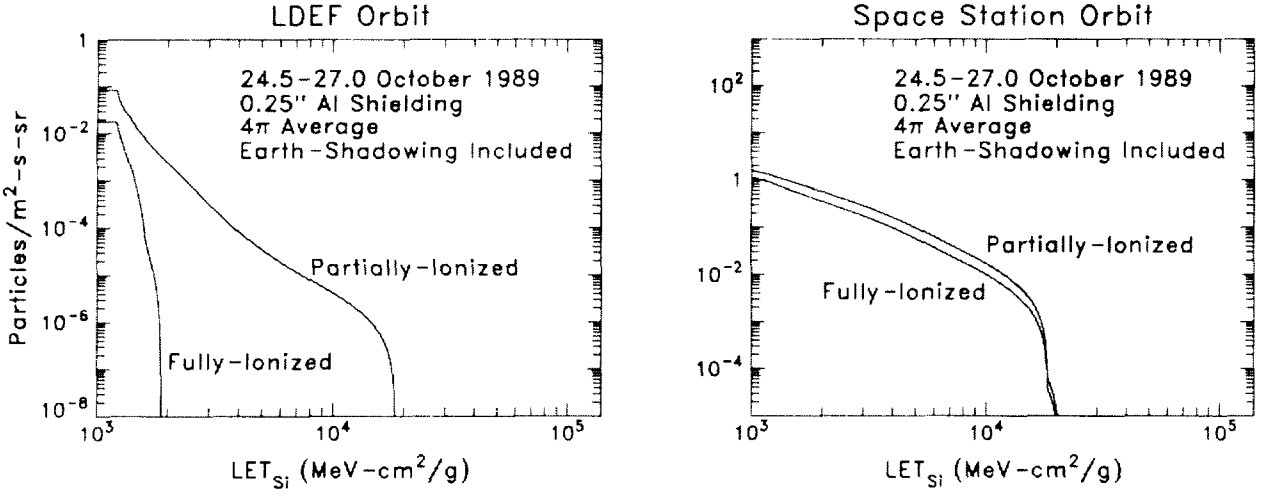

Figure 7: Integral LET spectra in silicon from solar energetic particles, as calculated behind 0.25" of Al shielding, averaged over the period of 24.5-27.0 October 1989. The calculation is shown for two cases, fully- or partially-ionized SEPs. Results are shown in (a) the LDEF orbit and (b) the proposed Space Station orbit. Note the different vertical scales on the two panels. During the peak hour of the event, the flux was larger by roughly an order of magnitude.

It is clear from Fig. 7a that the SEP charge state is an essential ingredient in making a reliable estimate of the radiation hazard posed by this event to systems in the LDEF orbit. Many microelectronic systems start to become vulnerable to upset effects in space at LET ~10^3 MeV-cm^2/g. The partially-ionized SEPs give a flux of particles with LET above this threshold ~5 times higher than fully-ionized SEPs would. At higher LET thresholds, the discrepancy grows by orders of magnitude. At LET ~10^4 MeV-cm^2/g nearly all microelectronic systems become vulnerable. The SEP charge state is therefore crucial in correctly evaluating the reliability of critical systems normally thought to be immune to upset effects in low-inclination orbits.

The single event upset (SEU) rates implied by Fig. 7a are indeed significant. As a specific example, we calculated the SEU rate in a 1-Gbyte solid state recorder which employs the Hitachi 4-Mbit dynamic random access memory (DRAM). Using the methods given in Ref. 33, the partially-ionized LET spectrum in Fig. 7a gave an upset rate of ~ 2 SEU/minute in the 1-Gbyte recorder. This upset rate is sufficiently large that it should be properly taken into account by systems designers.

These results on the mean-ionic charge state of solar energetic particles are ***not*** *included in widely-used space radiation models such as CREME[34]. As a result, the radiation hazard posed by SEPs in low-inclination, low-altitude orbits may be substantially underestimated by these programs.*

Fig. 7b shows the same calculations, but for the 51.6°, 450 km orbit proposed for the Space Station. Because geomagnetic transmission is generally higher in this orbit, the charge state makes relatively little difference to the estimated radiation hazard. Note that Fig. 7b is based on actual fluence data and a detailed geomagnetic transmission calculation for the SEP event with the single-largest fluence of high-energy heavy ions during the entire LDEF mission. It is therefore useful as a reasonable and realistic estimate of the event-averaged radiation hazard posed by large SEPs to the Space Station orbit.

Finally, another important consideration in assessing the radiation hazard is the arrival directions of the solar energetic particles. The calculations in Fig. 7 are averaged over arrival directions. But, as seen in Fig. 4, the SEP flux is highly anisotropic in a low-inclination orbit, with the flux of the highest-LET particles higher from the west than from the east by a factor of ~100. Consequently, the SEP radiation hazard can be reduced significantly by placing the most vulnerable components on the "eastward-looking" side of an orientation-stabilized satellite. In the proposed Space Station orbit, on the other hand, the orbit-averaged east-west asymmetry would be small.

COMPARISON OF LDEF RESULTS TO PREVIOUS REPORTS OF BELOW-CUTOFF Fe-GROUP IONS

Over the years there have been numerous reports[35-40] of below-cutoff Fe-group ions in the inner magnetosphere. These observations were generally made at times free of SEP events, and the arrival directions and collection locations were inconsistent with trapped particles. Some observations also showed a greatly enhanced sub-Fe/Fe ratio[41,42]. These observations comprised just a few tens of ions, but they have nevertheless stimulated much speculation about partially-ionized *galactic* cosmic rays[43,44], suggesting a nearby source of galactic cosmic rays (such as cosmic rays in the first stages of acceleration after encountering the expanding shock from a relatively nearby and recent supernova.)

All of these other experiments were at higher inclinations (ranging from 51.6° - 82°) than LDEF. But most also had some timing information, using either an electronic detector[39] or moving stacks of track detectors[35-38]. In these experiments, it is therefore possible to identify the small subsample of the ions which were collected within ±28.4° latitude. After accounting for the observation time actually spent at these latitudes, the resulting fluxes can be compared to the mission-averaged fluxes on LDEF.

Fig. 8 shows a compilation of all Fe and Fe-group fluxes reported to date from LDEF, including the trapped Fe-group ions from the Kiel experiment[10,11]. Also shown are the fluxes calculated from the results reported by two experiments,[11*] a rotating track-detector apparatus flown[38] on Spacelab-3 and a stack of ionization chambers[39] flown on Cosmos-2022. Because of the latitude cut, these fluxes are based on just *four* identified Fe-group ions. But these four ions were collected in less than two weeks with instruments with smaller geometry factors than those on LDEF. The LDEF experiments should easily have been able to confirm the flux levels implied by these few events. Instead, these fluxes *exceed* the LDEF mission-averaged fluxes by a large factor, even though the LDEF fluxes also contain both SEPs and trapped ions.

One obvious way to reconcile these other observations with the LDEF results is to posit that these below-cutoff ions were present at the reported flux levels for only a small portion of the LDEF mission. Such an explanation is entirely possible, but it would seem to be highly problematical for the notion of a new galactic component. Fig. 9 shows the time periods of the various observations, compared to the solar cycle, as tracked by the Mt. Washington neutron monitor. Note that the LDEF observations span a solar minimum, when solar modulation is most favorable for particles entering the heliosphere from interstellar space. But the other observations were made during periods of higher solar modulation. This too suggests that if the below-cutoff ions really did originate from outside the solar system, the mission-averaged LDEF flux should have been *higher*, not lower.

Taken together, these previous observations of below-cutoff Fe-group ions are almost surely correct, since different groups using different detector techniques at widely separated times report comparable flux levels. But it seems difficult to reconcile the comparison to LDEF results with the notion of a new galactic component.

One additional point may be worth mentioning here. All of the other observations were made at altitudes of 250-370 km. For most of its 69-month mission, LDEF was at 476 km, but the orbit decayed rapidly in the final year. In the last month of the mission, LDEF's altitude fell to ~370 km, and it was finally retrieved at ~330 km. If below cutoff Fe-group ions were collected by LDEF at the previously

---

[11*] Results from two additional experiments are not plotted on Fig. 8. A track detector experiment[35] on Salyut-6 saw a flux level comparable to that shown for Cosmos-2022. But the Salyut-6 detector was exposed *inside* the space station, and the amount of shielding surrounding the apparatus was only poorly known. The energy interval of the observed ions was therefore not well determined, and it is difficult to know where to plot this result on Fig. 8. There is also a report from the Kiel experiment[36] on Spacelab-1, which observed 12 below-cutoff Fe-group ions, but all at high latitudes. From this result we have calculated a 90% C.L. upper limit of 5 x 10^{-6}/m^2-s-sr-MeV/nucleon for Fe-group ions with E = 70-140 MeV/nucleon at LDEF latitudes, and thus consistent with the other measurements.

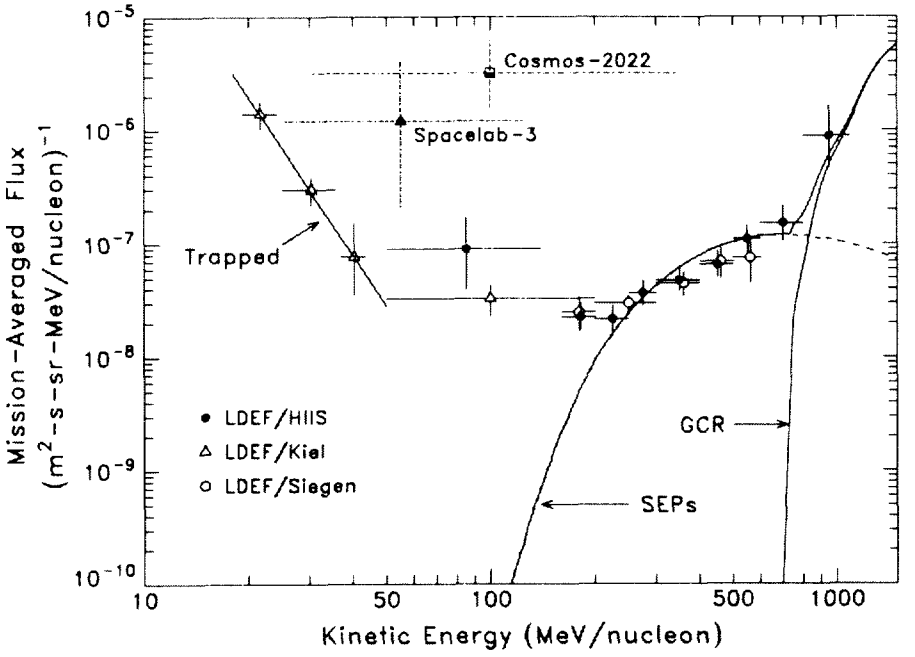

Figure 8: Mission-averaged Fe flux measurements from LDEF. Also shown are fluxes of below-cutoff Fe-group ions observed within ±28.4° latitude by experiments on Spacelab-3 (Ref. 38) and Cosmos-2022 (Ref. 39).

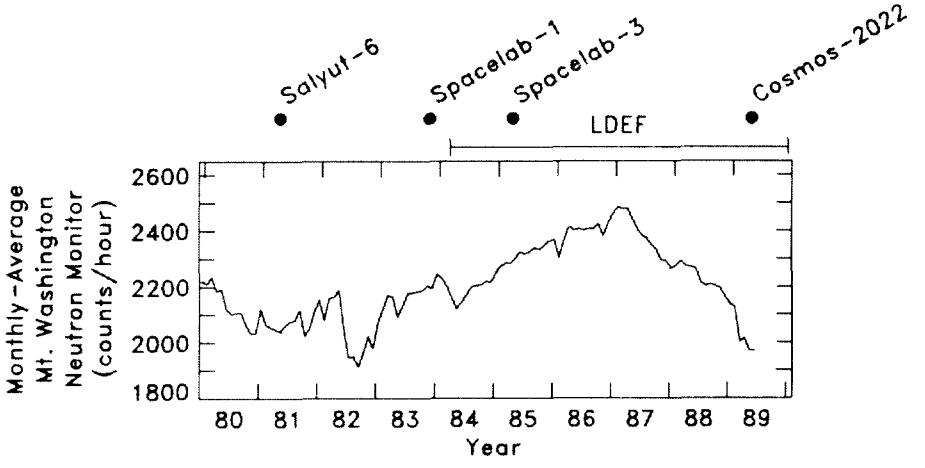

Figure 9: Times of the various observations of below-cutoff Fe-group ions, compared to the solar cycle as shown by the Mt. Washington neutron monitor.

reported flux levels *only during this last month*, the contribution to the *mission-averaged* flux would then be ~3 x 10^{-8}/m^2-s-sr-MeV/nucleon, and hence consistent with the as-of-yet unexplained LDEF flux at ~50-200 MeV/nucleon. But once again, such a steep increase with decreasing altitude seems hard to reconcile with a new galactic component.

In any case, these reports of below-cutoff ions should be confronted soon by new data from the SAMPEX satellite, which has been flying in an 82° orbit at ~600 km since July 1992. If the below-cutoff Fe-group ions are present at the SAMPEX orbit at the flux levels suggested by these earlier observations, the SAMPEX instruments should observe ~100 such ions per year[12*]. If SAMPEX does

[12*] The MAST instrument on SAMPEX has reported one Z = 23 ion collected at 1.45 < L < 2.65 during the first seven months of operation[45].

not confirm the earlier flux levels, a strong altitude dependence may remain as the only way to reconcile all of the observations. Such an altitude dependence would rule out a new galactic component, but it might be explainable in terms of albedo.

CONCLUSIONS

The HIIS detector has observed a large flux of Fe ions at ~200-600 MeV/nucleon which cannot be explained by fully-ionized galactic cosmic rays, even after taking into account occasional severe cutoff suppressions during the LDEF mission. The observed composition of the Fe-group ions also rules out galactic cosmic rays and albedo as their source. But all of the features of the HIIS data in this energy range, including fluence, spectrum, composition, and arrival directions, can be explained by the large solar energetic particle events of October 1989, provided that these SEP ions are partially-ionized. By comparing the HIIS fluxes with interplanetary measurements in October 1989, we determined the mean ionic charge state of SEP Fe ions to be $\langle Q \rangle = 13.4 \pm 1.0$, in good agreement with the value $\langle Q \rangle = 14.1 \pm 0.2$ measured at ~1 MeV/nucleon.

Thus, even at these very high energies, SEP Fe has a mean ionic charge state very similar to that of the source population in the coronal or solar-wind plasma. The acceleration must therefore take place in a very low-density region, and not at the site of a solar flare. The HIIS result is consistent with the notion of SEP acceleration in interplanetary space by shocks driven by coronal mass ejections. With additional theoretical analysis, it should be possible to use the HIIS result to further characterize the region where the acceleration takes place.

The ionic charge state of high energy SEPs is essential for correctly assessing their radiation effects on systems in low-inclination, low-altitude orbits. *It should be a high-priority of the space-environment modeling community to update widely-used programs such as CREME to reflect this new information.*

The source of Fe-group ions at ~50-200 MeV/nucleon is not yet understood. One possible source is the SEP event of 6-15 March 1989. This event did not produce measurable interplanetary Fe fluences above 200 MeV/nucleon, but it was accompanied by the largest geomagnetic disturbances of the LDEF mission. Another possible contributor in this energy range is the unidentified source of below-cutoff ions reported by several earlier experiments. Since these earlier experiments also reported a substantially enhanced sub-Fe/Fe ratio, better composition measurements will be crucial in unraveling this energy range.

LDEF mission-averaged fluxes are far below the flux levels reported in those other observations of below-cutoff Fe-group ions. This is somewhat surprising since (1) the LDEF fluxes also contain both SEPs and trapped ions; and (2) the LDEF observations span the 1987 solar minimum, while the other observations were all made nearer to solar maximum. To reconcile the LDEF and previous observations, the source of these below-cutoff ions must be out-of-phase with the observed solar-cycle variation of other known non-solar cosmic ray sources and/or strongly increase with decreasing altitude. Both of these features would be hard to understand if the source of these below-cutoff ions really were a new component of partially-ionized galactic cosmic rays.

ACKNOWLEDGEMENTS

It is a great pleasure to thank the many individuals who have helped us in this analysis. We thank Bill Dietrich, Tom Garrard, Bob McGuire, Dick Mewaldt, and Don Reames for providing us with the data from their interplanetary instruments, which have been crucial in interpreting the HIIS observations. We also thank Rudolf Beaujean for discussions of the Kiel heavy-ion observations on LDEF. We are grateful to Prof. Erwin Flueckiger and E. Kobel for making available to us their trajectory tracing program. We also thank Don Smart and Peggy Shea for several highly informative discussions of cutoff calculations and the events of October 1989. We are grateful to Dave Evans, Sue Greer, and Ron Zwickl

at NOAA for providing us with the NOAA-10 and GOES-7 proton fluxes. We thank Les Morris of NGDC for magnetometer data and help in interpreting it. We are grateful to Prof. M. Sugiura and Dr. Toyo Kamei of Tokai University for providing us with updated *Dst* values for October 1989. We thank Art Campbell for discussions of SEU effects. AJT thanks Prof. N.L. Grigorov for many helpful discussions of the Cosmos-2022 observations. Finally, we thank our student microscopists Lorie Benning, Rich Witt, and Kenny Zee for their dedication and hard work. This work has been supported by the Office of Naval Research, the NRC Research Associate Program, and NASA contract W18409.

REFERENCES

1. Adams, J.H. Jr. et al.: The Charge State of the Anomalous Component of Cosmic Rays. Astrophys. J. Lett., vol. 375, 1991, pp. L45-L48.
2. Luhn, A. et al.: Ionic Charge States of N, Ne, Mg, Si, and S in Solar Energetic Particle Events. Adv. in Space Res., vol. 4, 1984, pp. 161-164.
3. Luhn, A. et al.: The Mean Ionic Charge State of N, Ne, Mg, Si, and S in Solar Energetic Particle Events. Proc. 19th ICRC (La Jolla), NASA CP-2376, vol. 4, 1985, pp. 241-244.
4. Luhn, A. et al.: The Mean Ionic Charge of Silicon in ^{3}He-Rich Solar Flares. Astrophys. J., vol. 317, 1987, pp. 951-955.
5. Adams, J.H. Jr.; Beahm, L.P.; and Tylka, A.J.: The Heavy Ions in Space Experiment: Preliminary Calibration and Analysis. Proc. 22nd ICRC (Dublin), vol. 2, 1991 pp. 523-526.
6. Adams, J.H.Jr.; Beahm, L.P.; and Tylka, A.J.: Preliminary Results from the Heavy Ions in Space Experiment. Proc. First LDEF Post-Retrieval Symposium, NASA CP-3134, Part 1, 1991, pp. 377-391.
7. Kleis, T. et al.: Characteristics of Low Energy Ions in the Heavy Ions in Space (HIIS) Experiment. Presented at the Third LDEF Post-Retrieval Symposium, Williamsburg, VA, November 1993 (these proceedings).
8. Adams, J.H. Jr. et al.: Progress Report on the Heavy Ions in Space (HIIS) Experiment. Proc. Second LDEF Post-Retrieval Symposium, NASA CP-3194, Part 1, 1993, pp. 247-259.
9. Letaw, J.R: UPROP: A Heavy-Ion Propagation Code, SCC Report 89-02, Severn Communications Corp., Millersvile, MD, 1989. Our version of the UPROP code also includes two recent refinements: improved low-energy heavy-ion spallation cross-sections (Tsao, C.H. et al.: Scaling Algorithm to Calculate Heavy-Ion Spallation Cross Sections, Phys. Rev. C, vol. 47, 1993, pp. 1257-1263) and energy-distributions of projectile fragments (Barghouty, A.F; Tsao, C.H.; and Silberberg, R.: Energy and Momentum Loss in Cosmic Ray Heavy Ion Interactions. Proc. 23nd ICRC (Calgary), vol. 2, 1993, pp. 171-174).
10. Jonathal, D.: Nachweis magnetisch gefangener Schwerionen mit Kernspurdetektoren auf dem Satelliten LDEF. Ph.D. thesis, Institut fuer Kernphysik, Univ. Kiel, Germany, July 1993.
11. Jonathal. D. et al.: Evidence for the Detection of Trapped Iron Nuclei on LDEF. Presented at the Third LDEF Post-Retrieval Symposium, Williamsburg, VA, November 1993 (these proceedings).
12. Wiegel, B. et al.: Measurements of Cosmic ray Nuclei with Energies of Some Hundred MeV/nucleon in the LDEF Mission. Presented at the 1992 COSPAR Conference, Washington DC, 28 August-3 September 1992.
13. Nymmik, R.A. et al.: A Model of Galactic Cosmic Ray Fluxes. Nucl. Tracks. & Radiat. Meas., vol. 20, 1992, pp. 427-429.
14. Adams, J.H. Jr.; Beahm, L.P.; and Tylka, A.J.: The Charge State of the Anomalous Component: Results from the Trapped Ions in Space Experiment. Astrophys. J., vol. 377, 1991, pp. 292-305.
15. Adams, J.H. Jr. et al.: Determining the Charge States of Solar Energetic Ions During Large Geomagnetic Storms. Adv. in Space Res., vol. 13, 1993, pp. 367-370.
16. Boberg, P.R. et al.: The Mean Charge State of Solar Energetic Oxygen at 10 MeV/nucleon. Proc. 23nd ICRC (Calgary), vol. 3, 1993, pp. 396-398.
17. Flueckiger, E.O. et al.: A New Concept for the Simulation and Visualization of Cosmic Ray Particle Transport in the Earth's Magnetosphere. Proc. 22nd ICRC (Dublin), vol. 3, 1991, pp. 648-651.
18. Langel, R. et al.: International Geomagnetic Reference Field, 1991 Revision. J. Geomag. Geoelectr., vol. 43, 1991, pp. 1007-1012.

19. Tsyganenko, N.A.: A Magnetospheric Magnetic Field Model with a Warped Tail Current Sheet. Planet. Space Sci., vol. 37, 1989, pp. 5-20.
20. Flueckiger, E.O.; Smart, D.F., and Shea, M.A.: A Procedure for Estimating the Changes in the Cosmic Ray Cutoff Rigidities and Asymptotic Directions at Low and Middle Latitudes During Periods of Enhanced Geomagnetic Activity. J. Geophys. Res., vol. 91, 1986, pp. 7925-7930.
21. Adams, J.H. Jr.; Beahm, L.P.; and Tylka, A.J.: Observations from LDEF of Heavy Ions Below the Geomagnetic Cutoff. Proc. 22nd ICRC (Dublin), vol. 1, 1991 pp. 619-622.
22. Reeves, G.D. et al.: The Great Solar Energetic Particle Events of 1989 Observed From Geosynchronous Orbit. J. Geophys. Res., vol. 97, 1992, pp. 6219-6226.
23. Coffey, H.E. (ed.): Solar-Geophysical Data, Comprehensive Reports, Number 557, Part I, January 1991, pp. 163-164.
24. Arnaud M. and Raymond, J.: Iron Ionization and Recombination Rates and Ionization Equilibrium. Astrophys. J., vol. 398, 1992, pp. 394-406.
25. Shull, J. M. and Van Steenberg, M.: The Ionization Equilibrium of Astrophysically Abundant Elements. Astrophys. J. Suppl. Series, vol. 48, 1982, pp. 95-107.
26. Breneman, H.H. and Stone, E.C.: Solar Coronal and Photospheric Abundances from Solar Energetic Particle Measurements. Astrophys. J. Lett., vol. 299, 1985, L57-L61.
27. Mazur, J.E. et al.: The Abundances of Hydrogen, Helium, Oxygen, and Iron Accelerated in Large Solar Particle Events. Astrophys. J., vol. 404, 1993, pp. 810-817.
28. Reames, D.V.: Particle Acceleration in Solar Flares: Observations. Presented at the Particle Acceleration in Cosmic Plasmas Workshop, Newark DE, 4-6 December 1991.
29. Kahler, S.W.: Solar Flares and Coronal Mass Ejections. Ann. Rev. Astron. Astrophys., vol. 30, 1992, pp. 113-141.
30. Gosling, J.T.: The Solar Flare Myth. J. Geophys. Res., vol 98, 1993, pp. 18,937-18,949.
31. Gosling, J.T.: New Findings Challenge Beliefs about Solar-Terrestrial Physics. Eos, Transactions Amer. Geophys. Union., vol. 74, 1993, pp. 611-612.
32. Mason, G.M.: The Composition of Galactic Cosmic Rays and Solar Energetic Particles. Rev. Geophysics and Space Physics, vol. 25, 1987, pp. 685-696.
33. Adams, J.H. Jr.: The Variability of Single Event Upset Rates in the Natural Environment. IEEE Trans. Nucl. Science, vol. NS-30, 1983, pp. 4475-4480.
34. Adams, J.H. Jr., Silberberg, R., and Tsao, C.H.: Cosmic Ray Effects on Microelectronics (CREME), Part I. NRL Memorandum Report 4506, 1981; Adams, J.H. Jr., Letaw, J.R., and Smart, D.F.: CREME Part II. NRL Memorandum Report 5099, 1983; Adams, J.H. Jr.: Part IV. NRL Memorandum Report 5901, 1986.
35. Blazh, K. et al.: Flux of Nuclei with Energies of Several Hundreds of MeV/nucleon on the Orbit of the Salyut-6 Station. Cosmic Research, vol. 24, 1986, pp. 604-609.
36. Krause, J.: Magnetisch verbotene Teilchen mittlerer Energie bei der Spacelab 1 Mission, Ph.D. thesis, Institute fuer Kernphysik, Univ. Kiel, FRG, 1986.
37. Biswas, S. et al.: Observation of Low-Energy (30-100 MeV Nucleon^{-1}) Partially Ionized Heavy Ions in Galactic Cosmic Rays. Astrophys. J. Letters, vol. 359, 1990, pp. L5-L9.
38. Dutta, A. et al.: Ionization States of Low-Energy Cosmic Rays: Results from Spacelab 3 Cosmic-Ray Experiment. Astrophys. J., vol. 411, 1993, pp. 418-430.
39. Grigorov, N.L. et al.: Heavy Ions in Cosmic Rays. Sov. J. Nucl. Phys. (Yadernaya Fizica), vol. 53, 1991, pp. 827-834.
40. Gargarin, Yu.F. et al.: Observations of Anomalously High Flux Densities of Low-Energy Heavy Nuclei on the Salyut-6, Salyut-7, and Mir Orbital Stations. JETP Lett., vol. 55, 1992, pp. 88-91.
41. Gargarin, Yu.F. et al.: Sulfur-Nickel Nuclei at Small Energies in Cosmic Rays. Proc. 21st ICRC (Adelaide), vol. 3, 1990, pp. 11-14.
42. Biswas, S. et al.: Ratio of Sub-Iron (Sc-Cr) To Iron Ions in Low Energy Galactic Cosmic Rays Inside & Outside of Earth's Magnetosphere. Proc. 22nd ICRC (Dublin), vol. 2, 1991, pp. 308-311.
43. Mitra, B. et al.: Implications of the Observations of Partially Ionised States in Low Energy Galactic Cosmic Rays. Proc. 22nd ICRC (Dublin), vol. 2, 1991 pp. 312-315.
44. Grigorov, N.L.: Peculiarities of the Proton Energy Spectrum and the Problem of Cosmic Ray Origin. Moscow State University Institute of Nuclear Physics Preprint 92-26/275, 1992.
45. Cummings, J.R. et al.: New Evidence for Geomagnetically Trapped Anomalous Cosmic Rays. Geophysical Research Letters, vol. 20, 1993, pp. 2003-2006.

EARLY RESULTS FROM THE ULTRA HEAVY COSMIC RAY EXPERIMENT

D. O'Sullivan, A. Thompson, J. Bosch, R. Keegan
Dublin Institute for Advanced Studies (DIAS), Ireland
Phone: +353-1-6621333, Fax: +353-1-6621477

K.-P. Wenzel and F. Jansen
Space Science Dept of ESA, ESTEC, Noordwijk, The Netherlands
Phone:+31-1719-83573, Fax: +31-1719-84698

C. Domingo
Universitat Autònoma de Barcelona, Spain
Phone:+34-3-581-1530, Fax: +34-3-581-2155

ABSTRACT

Data extraction and analysis of the LDEF Ultra Heavy Cosmic Ray Experiment is continuing. Almost twice the pre LDEF world sample has been investigated and some details of the charge spectrum in the region from $Z \sim 70$ up to and including the actinides are presented. The early results indicate r process enhancement over solar system source abundances.

INTRODUCTION

Prior to the launch of the LDEF, a number of major experiments designed to study ultra heavy nuclei in Earth orbit had already been completed and the Heavy Nucleus Experiment on HEAO-3[1] along with the Bristol experiment on board Ariel-VI[2] provided most of the data available at that time.

Two important requirements for a successful experiment in the study of charge spectra are good charge resolution and a sufficiently large sample of data. The Dublin-ESTEC experiment has collected almost fifteen times the combined (HEAO-3 + Ariel-VI) data set and there are indications that the charge resolution is at least as good, if not better than planned. To put things further in perspective, the total number of actinides ($Z \geq 87$) observed in these earlier experiments combined was 3, whereas preliminary results for the Dublin-ESTEC experiment indicate a total of $\sim 70 \pm 15$ actinides in the sample obtained.

Astrophysical Significance of Ultra Heavy Nuclei

Ultra heavy nuclei are synthesised by the neutron capture process. This reaction is characterised by two distinct types which depend on the rate at which capture takes place, namely the slow (s) and rapid (r) processes. The contribution of each process to the abundance of nuclei with $Z > 30$ varies widely from element to element. Accordingly, a detailed knowledge of relative abundances can provide evidence for either s or r process domination in a given charge region. The key to solving some problems associated with cosmic ray origin and acceleration is the fact that the s and r processes occur in quite different astrophysical environments so that the measured abundance should reflect different nucleosynthesis histories and provide information on the source of ultra heavy nuclei. The r-process is usually associated with supernova explosions, whereas the s-process is believed to take place in normal stars at an advanced stage of evolution.

To extract the interesting astrophysical implications from data measured in Earth orbit they are usually compared with values derived from models based on particular types of source abundances which have been corrected for fractionation and propagation through the Galaxy. The effect of the first ionisation potential (FIP)[3] of each element in determining its likelihood of being ionised and accelerated as part of the galactic cosmic ray flux is now well established and is also taken into account in these models. The HEAO-3 and Ariel-VI groups used the standard leaky box model of propagation along with the rigidity dependent path length distribution of Ormes and Protheroe[4] and the semiempirical fragmentation cross sections of Silberberg and Tsao[5] which are assumed to be independent of energy above $\sim$ 1GeV/N. The main conclusions drawn by the HEAO-3 and Ariel-VI groups were that (i) for the $33 \leq Z \leq 60$ charge region the observed abundances agree well with solar system source material with FIP fractionation with a slight enrichment of r-process material compared to the accepted solar system mixture, (ii) $Pt(Z = 78)$ and its secondaries are best fitted by a predominantly r-process source with FIP fractionation. It may seem strange that cosmic rays should be richer in r-process material at the upper end of the periodic table than in the region below $Nd(Z = 60)$ but there are r-process conditions which synthesise only nuclei with $Z > 60$.

Experiment Design

Details of the Dublin-ESTEC experiment designed to investigate cosmic ray nuclei with $Z > 65$ are given in several papers. A total of 192 detector stacks, comprised mainly of lexan polycarbonate, were mounted in sets of four within cylindrical eccofoam moulds which were then inserted into 48 separate aluminium pressure vessels (1 atm of dry air). Following recovery of the LDEF after 69 months in space the gas pressure in all cylinders was checked and it was found that no leakage had occurred.

The experiment thermal design was extremely successful and resulted in an average detector stack temperature below $0°C$ with a mean maximum spread of $\pm 10°C$. The corresponding charge shifts were $\pm 0.8e$ for uranium and $\pm 0.6e$ for the Pt-Pb region.

A very fortuitous aspect of the life time of the Dublin-ESTEC experiment was the close parallel with the life time of the facility at the Berkeley Bevalac for accelerating ultra heavy nuclei such as uranium and gold. The facility started in time for pre-flight calibration before launch in 1984 and survived long enough to allow post flight calibration of the detectors before it closed down in February 1993, much to the regret of the cosmic ray community. Analysis of the pre and post flight data has shown that the strict control of detector environment throughout the mission has resulted in no observable degradation of latent image[6].

Locating and Identifying Ultra Heavy Cosmic Ray Nuclei in the Lexan Polycarbonate Stacks

Locating the ultra heavy nuclei is straightforward. Because of the orbital inclination only high energy ($E \geq 2GeV/N$) particles reach the detectors. The ionisation threshold for lexan is such that at these energies only particles with $Z \geq 65$ register and there is no significant background from lighter nuclei (a major consideration when you spend almost 5 years in space !) Approximately 2500 particles with $Z > 65$ have been located.

Following carefully controlled etching of 20 plates from the top of each stack and a similar number from the bottom, a set of the 40 etch rate values V_t were determined for each ultra heavy candidate. Charge identification is based on measurement of (i) G, the fractional etch rate gradient; $G = \frac{1}{S}\frac{dS}{dX}$ where $S = \frac{V_t}{V_g}$, V_g is the bulk etch rate and X is the path length and (ii) the effective reduced etch rate S_{eff}. S is related to a restricted energy loss function through $S = g(REL)^h$ where g and h are determined from our U($\sim 950MeV/N$) and Au($\sim 1150MeV/N$) calibrations at the Bevalac. Typical S versus path length plots are shown in references 7 and 8.

The Preliminary Charge Spectrum Results and Discussion

The preliminary charge spectrum, based on approximately 15% ($\sim$ 450 events) of the total sample, is shown in Fig 1. The presence of nuclei beyond the actinide gap is significant and in view of the modest charge spread ($\sim 1e$) expected from statistical errors and temperature excursions we are confident even at this early stage that the Dublin-ESTEC experiment is capable of providing the first statistically significant sample of cosmic ray nuclei with $Z > 87$ with good charge resolution. How 'good' this resolution will eventually be remains to be seen, but at present we have no reason to believe that it will not be well within the design target of $< 1.5e$, and probably better for a sample of events with appropriate path lengths and geometry.

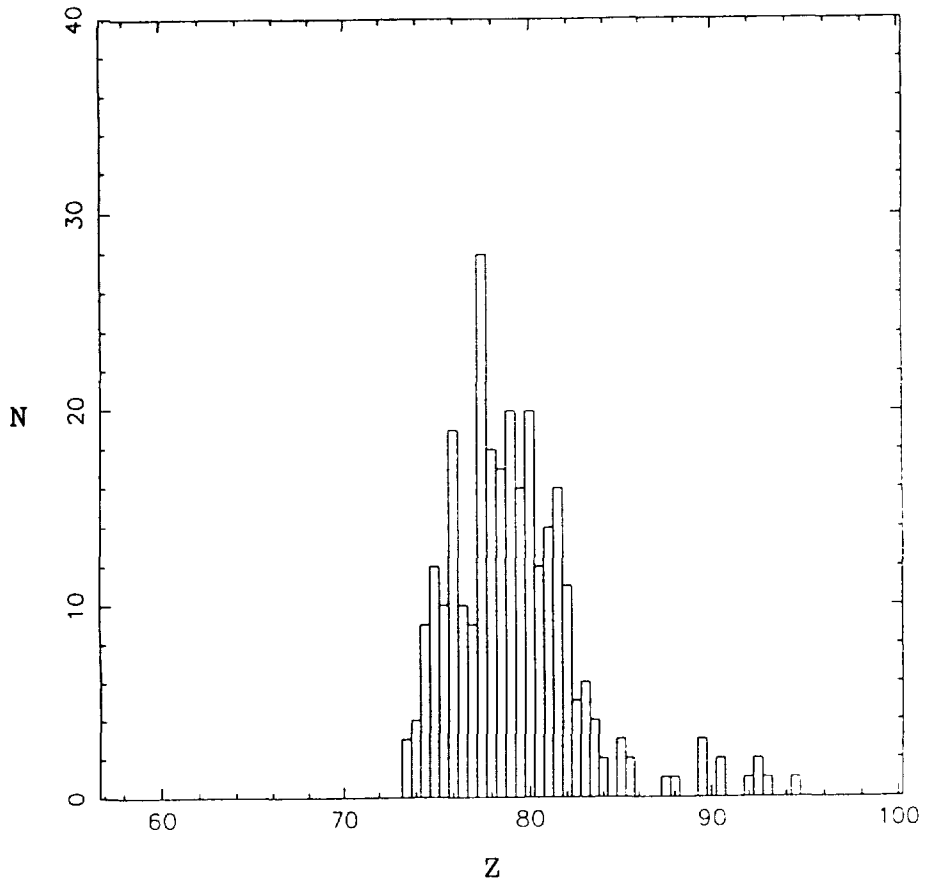

Figure 1: A preliminary charge spectrum for nuclei with $Z > 70$ based on ≈ 450 nuclei ($\approx 15\%$ of total sample) from the Dublin-ESTEC experiment.

Selection from stacks with the smallest temperature excursions will also help and the possibility of obtaining abundance ratios for charge groups (and even a Th/U value) in this region looks promising. The ratio of $(Z \geq 88)/(74 \leq Z \leq 87)$ from Fig 1 is 0.031 ± 0.009 compared with 0.025 ± 0.015 for the combined HEAO-3+Ariel-VI data. It should be emphasised however that this early value from the Dublin-ESTEC experiment should be taken as a lower value since no correction has yet been applied for any differences that may exist in the fragmentation cross-section of actinides as opposed to those for nuclei in the $74 \leq Z \leq 87$ charge region[9]. The relative significance of fission and electromagnetic interactions at high energies for both of these groups of nuclei will be the subject of future investigations. Our initial method of scanning, while efficient at locating those nuclei which survive $\frac{2}{3}$ of their trajectory through the stacks, does not pick up those which interact and lose sufficient charge to fall below threshold ($Z \sim 65$), as would occur in fission for example. We would expect this effect to be highest for the actinide elements. We hope to tackle this problem shortly. Further

down the charge scale we note that the spectrum peaks around $Z = 77.5$, indicating the presence of predominantly r-process nuclei such as osmium and platinum, while Pb (predominantly s-process) is not very dominant.

Within another year we hope to have completed measurements on a total of 1000 ultra heavy nuclei and will have had the opportunity to consider any systematic effects which may exist before trying any serious deconvolution of the spectral peaks. The overall situation at present certainly gives good reason for optimism.

REFERENCES

1. W.R. Binns, T.L. Garrard, P.S. Gibner, M.H. Israel, M.P. Kertzmann, J. Klarmann, B.J. Newport, E.C. Stone and C.J. Waddington, *The Astrophysical Journal*, (1989), **346**, 997-1009

2. P.H. Fowler, R.N.F. Walker, M.R.W. Masheder, R.T. Moses, A. Worley and A.M. Gay, *The Astrophysical Journal*, (1987), **314**, 739-746

3. J.R. Letaw, R. Silberberg and C.H. Tsao, *Ap. J.*, (1984), **279**, 144

4. J.F. Ormes and R.J. Protheroe, *Ap. J.*, (1983), **272**, 756

5. R. Silberberg and C.H. Tsao, *Ap. J. Suppl.*, (1973), **25**, 315

6. A. Thompson, D. O'Sullivan, K-P Wenzel, J. Bosch, R. Keegan, C. Domingo, J. Daly and A. Smit, *Proc 22nd ICRC*, (1991), **2**, 543, (Dublin)

7. D. O'Sullivan, A. Thompson, J. Bosch, R. Keegan, K-P Wenzel, F. Jansen, C. Domingo, *Adv. Sp. Res.*, (1993), to be published.

8. A. Thompson, D. O'Sullivan, J. Bosch, R. Keegan, K-P Wenzel, F. Jansen and C. Domingo, *Proc Second LDEF Post-Retrieval Symposium*, (1992), **1**, 261, (San Diego)

9. L.Y. Geer, J. Klarmann, B.S. Nilsen, C.J. Waddington, W.R. Binns, J.R. Cummings and T.L. Garrard, *Proc 23rd ICRC*, (1993), **2**, 191, (Calgary)

ABSORBED DOSE AND LET SPECTRA MEASUREMENTS ON LDEF*

E. V. Benton, I. Csige, A. L. Frank, E. R. Benton, and L. A. Frigo
Physics Research Laboratory
University of San Francisco
San Francisco, CA 94117-1080, U.S.A.

T. A. Parnell, J. Watts, and A. Harmon
NASA Marshall Space Flight Center
Huntsville, AL 35812, U.S.A.

Summary

Total absorbed doses measured with TLDs, linear energy transfer (LET) spectra measured with plastic track detectors, and low energy neutrons measured on LDEF have been compared with model calculations. The total absorbed doses measured in TLDs were higher than predicted in the calculations of Armstrong *et al.* and differ from the calculations of Atwell *et al.*

LDEF LET spectra are dependent on detector orientation, shielding and experiment location. These factors need to be taken into account when modeling the LDEF LET spectra. LET spectra measured with plastic nuclear track detectors (PNTDs) also deviate significantly from calculations especially for high LET particles ($LET_\infty \cdot H_2O > 100 keV/\mu m$). Modeling efforts to date do not include the contribution of proton induced secondaries.

Analysis of polycarbonate PNTDs from the West-side of LDEF has revealed a very high fluence of tracks ($>1 \times 10^7$ tracks/cm^2 under 2 gm/cm^2 shielding). Fluence drops off rapidly as shielding depth increases. Tracks only form in the region of the detector closest to the surface, not in the bulk of the detector. To date no adequate explanation for this observation has been found.

We plan to measure range distribution of very high LET ($LET_\infty \cdot H_2O > 500$ keV/μm) secondary particles produced in silicon wafer by high energy primary cosmic ray particles. Refinements of experimental techniques and model calculations are also being carried out in order to understand existing discrepancies between experimental measurements and calculations.

*Work supported by NASA under NAG8-282, Marshall Space Flight Center, Huntsville, AL 35812

INTRODUCTION

LDEF provided a unique opportunity to measure the space radiation environment in low Earth orbit. Since the spacecraft was gravity gradient stabilized, it was possible to measure total absorbed dose and LET spectra as functions of experiment location and orientation. The East/West trapped proton anisotropy in the South Atlantic Anomaly (SAA) was measured. An important result was the confirmation of the importance of contributions to LET spectra made by proton-induced elastic and inelastic secondaries.

A variety of passive radiation detectors were included in various LDEF experiments. Thermoluminescent Detectors (TLDs) were used to measure total absorbed dose. CR-39, polycarbonate and polyester Plastic Nuclear Track Detectors (PNTDs) were used to measure LET spectra and total track density. Fission foil/mica and ^{6}LiF/CR-39 detectors were used to measure the neutron environment. Figure 1 shows the location of experiments to measure ionizing radiation on LDEF and the orientation of LDEF relative to the East/West trapped proton anisotropy. Thin stacks of TLDs and PNTDs were included in the M0004 experiment located near the East (leading) edge and the P0004 experiment located near the West (trailing) edge of LDEF. Thick stacks of TLDs and PNTDs, interspersed with layers of Al degrader, were included in the A0015 and P0006 experiments located on the West side and the A0015 experiment located on the Earth-facing end of LDEF. Thermal and Resonance Neutron Detectors (TRNDs) were also included in the P0006 and A0015 experiments.

One of the primary objectives of the ionizing radiation measurements made on LDEF is the comparison of measurements with computer models of the space radiation environment. Comparisons of total absorbed dose measurements in TLDs have been compared with two sets of computer generated estimates. LET spectra has been measured at a variety of locations and shielding depths on LDEF. Comparison of measured LET spectra with pre-recovery estimates have highlighted the deficiencies in the calculations especially as they pertain to the contribution of proton-induced secondaries to the LET spectra above 100 keV/μm.

TOTAL ABSORBED DOSE: COMPARISON OF MEASUREMENTS AND CALCULATIONS

Total absorbed dose was measured using TLDs in several experiments flown on LDEF. The purpose of these measurements was to determine the dose exposure of LDEF as functions of experiment location and shielding depth. These measurements are being used in refining models of the ionizing radiation environment in low Earth orbit and in refining methods of calculating dose inside spacecraft. Total absorbed dose was measured in four experiment locations (Figure 1), M0004 East-facing leading edge, P0004 and P0006 West-facing trailing edge and A0015 Earth-facing end. The read out and analysis of TLD measurement data has been completed[1]. Comparisons have been made between these measurements and model calculations generated by Armstrong *et al.*[2] and Atwell *et al.*[3].

The original set of dose calculations were performed by Armstrong, Colborn and Watts[2]. They are based on the calculations of Watts[4] for the trapped proton exposure, a detailed three dimensional

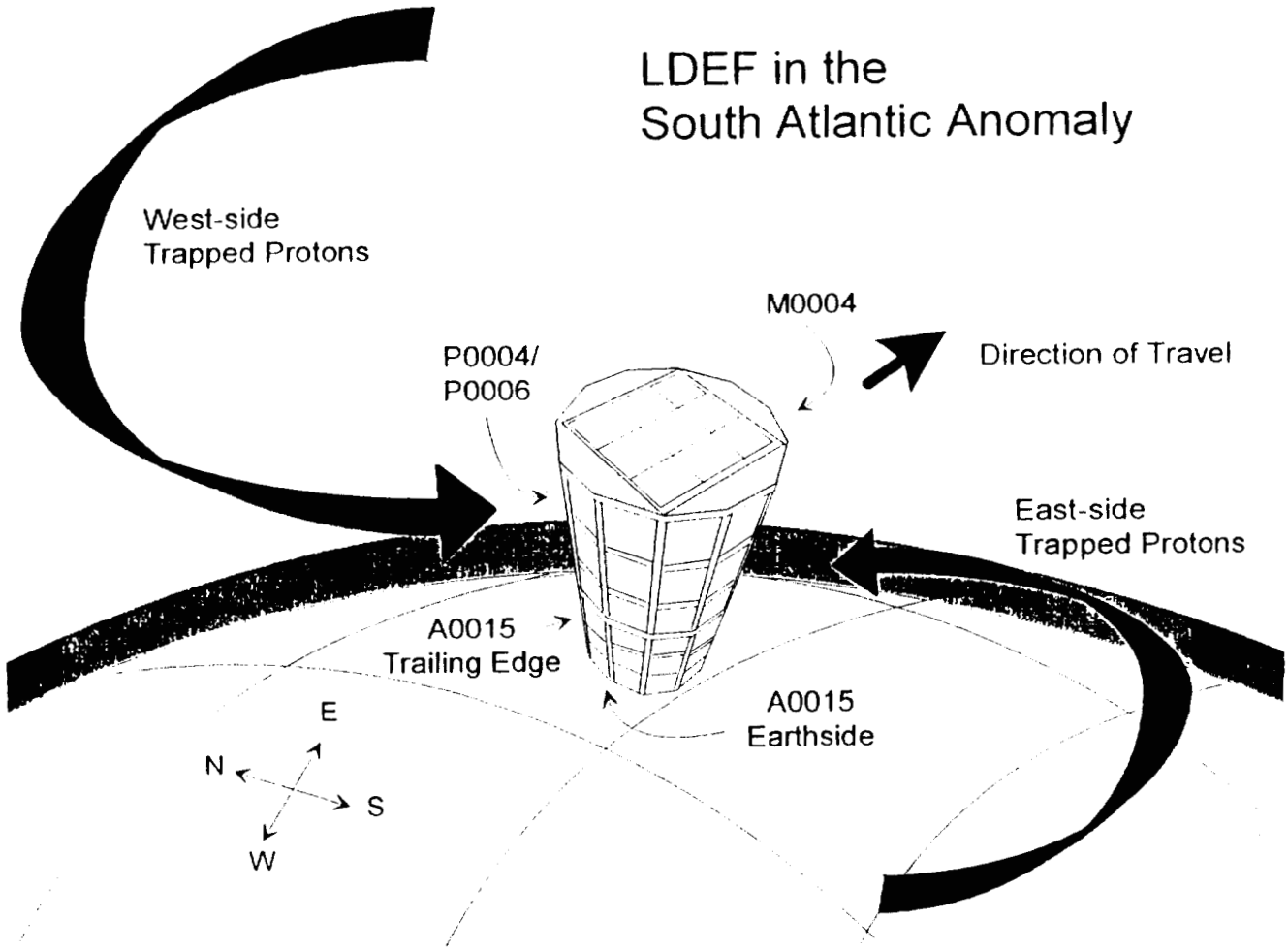

Figure 1: Location of experiments containing radiation detectors on LDEF, relative to the East/West proton anisotropy in the South Atlantic Anomaly.

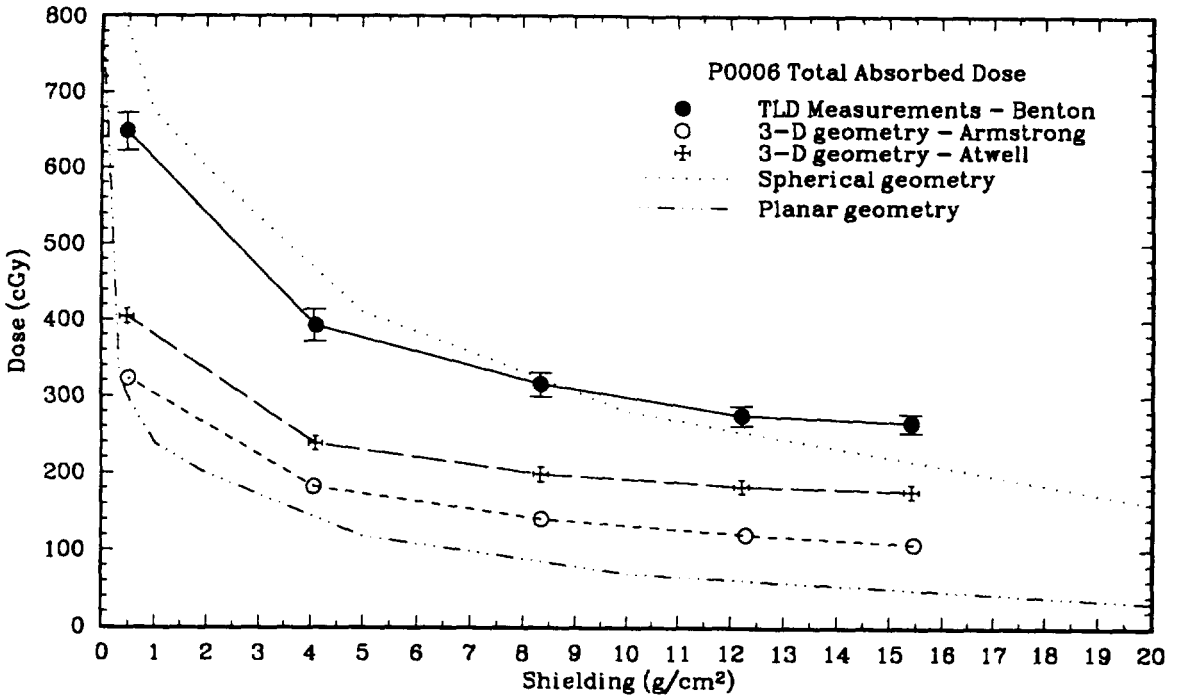

Figure 2: P0006 Total Absorbed Dose: comparison of measurements and calculations.

geometry/mass model developed by Colborn and Armstrong[5] and the transport code of Burrell[6]. The proton exposure model is based on the AP8 omnidirectional proton flux model[7]. Atmospheric height, solar cycle information and a model of the trapped proton anisotropy were included in the calculations.

A second set of calculations were made by Atwell, Badhwar, Hardy and Weyland[3] at JSC. These are considered to be preliminary calculations. The proton flux is based on the AP8 omnidirectional proton flux model[7] and a vector flux model of Kern[8]. Atmospheric scale height and solar cycle were modeled, but the trapped proton anisotropy was not included in the calculations. A simple mass model of the LDEF was used to model the distribution of shielding.

Figure 2 is a comparison of TLD measurements and calculations of absorbed dose in the P0006 experiment. Both sets of model calculations lie below measured values. The largest discrepancy is for the least shielded point (~0.5 g/cm^2) where the calculations fall below measurements by nearly a factor of two. Also plotted in Figure 2 are the pre-recovery estimates of total absorbed dose using planar and spherical geometry models. The spherical geometry model provides the closest agreement with measured values. Figure 3 compares measured absorbed doses from TLDs with calculations for the P0004 experiment as a function of shielding depth. Like Figure 2, both sets of calculations fall below the measured values and the biggest difference is for the least shielded point.

Figure 4 shows a comparison of dose measured in TLDs with calculations as a function of shielding for the M0004 experiment on the leading (East) edge of LDEF. The smaller measured and calculated

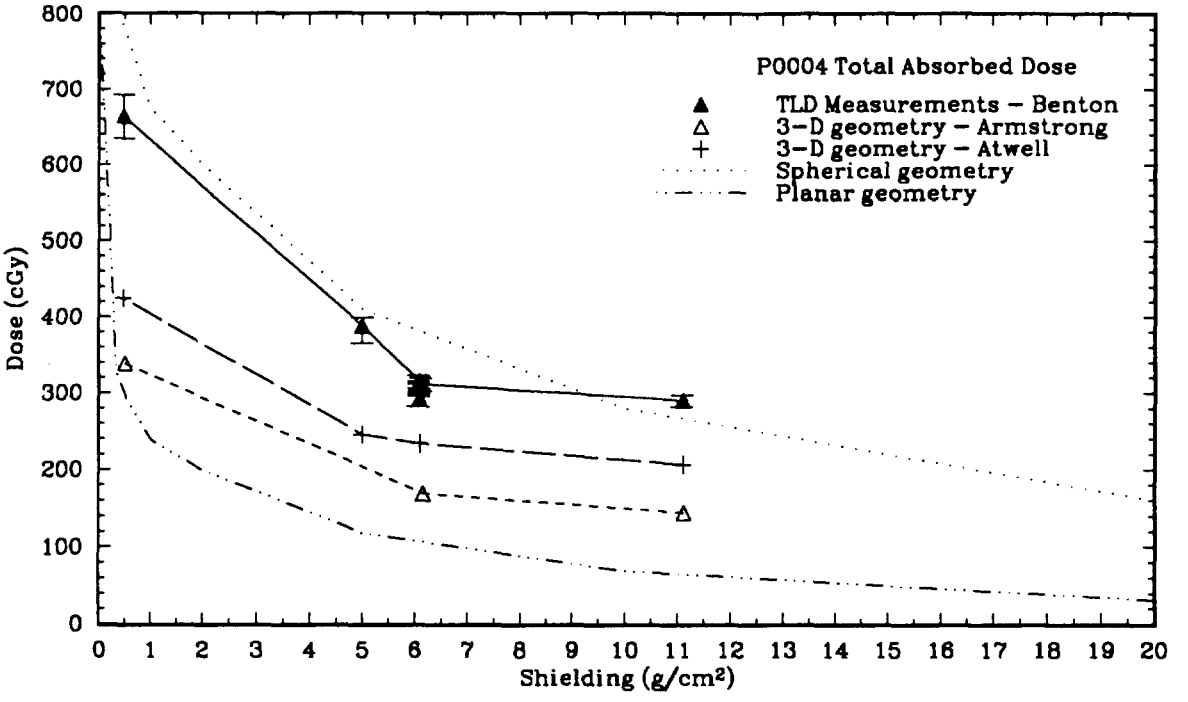

Figure 3: P0004 Total Absorbed Dose: comparison of measurements and calculations.

doses of M0004 as compared with P0006 and P0004 show the effect of the East/West trapped proton anisotropy. The largest difference can be seen for the low shielding point (0.5–1.0 g/cm^2) where the dose on the West side exceeds that of the East side by about a factor of three. The calculations of Armstrong show a ~1.5 times greater dose on the West side as compared to the East side under ~1.5 g/cm^2. Atwell's calculations show little difference between doses (300 cGy Earth-side, 350 cGy West side) between East and West due to the fact that the East/West proton anisotropy was not accounted for in the calculations. Figure 5 is a comparison of total absorbed dose measurements in TLDs from this laboratory (USF) and DLR and with the calculations of Armstrong and Atwell. There is close agreement between the two sets of measurements. The Atwell calculations lie quite close to the DLR measurements, but fall below the USF measurements while Armstrong's calculations fall below both sets of measurements.

The calculations of Armstrong are consistently lower than measurement of dose by approximately a factor of two. This would seem to indicate that there is a systematic omission in the model. The calculations of Atwell fall on both sides of the measurements. There is close agreement with measured doses on the Earth side. Atwell's calculations exceed the measurements of the East side and fall below measurements made on the West side. One difference between the two sets of calculations is the vector flux model used. The Armstrong calculations are based on a vector flux model of Watts[4] and a comparatively high atmospheric scale height. The Atwell calculations are based on a newer vector flux model being developed by Kern[8] at JSC which uses a lower atmospheric scale height. Discrepancy between measurements and Armstrong's calculations might also be due to inadequacies in the trapped proton anisotropy model. While a ratio of 1.5 was calculated between doses on the West and East sides and agreed well with the measured ratio, the measured ratio only included the shielding of the experiment

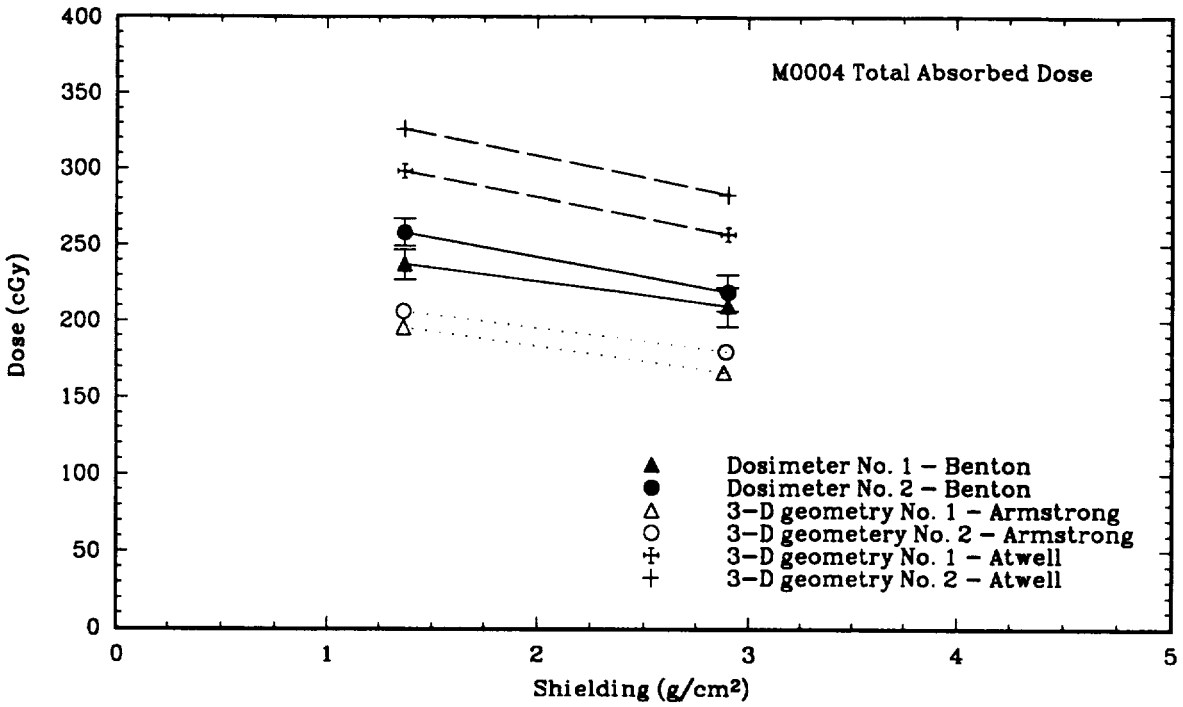

Figure 4: M0004 Total Absorbed Dose: comparison of measurements and calculations.

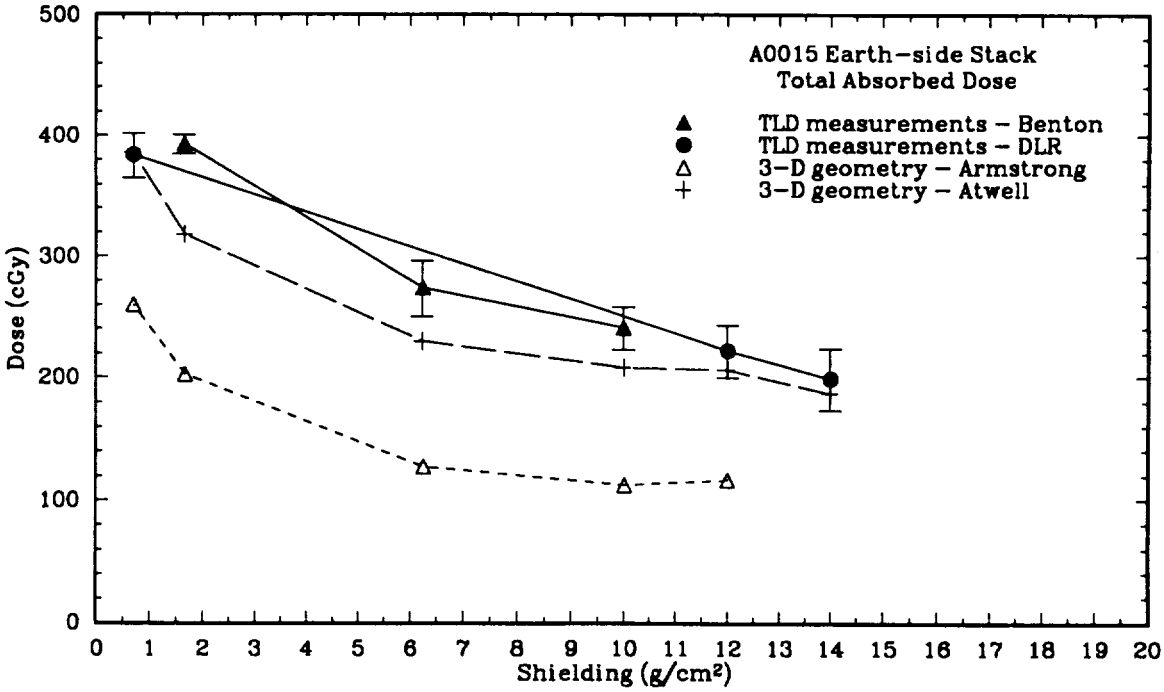

Figure 5: A0015 Total Absorbed Dose: comparison of measurements and calculations.

itself and not the shielding of the entire spacecraft, making the validity of this comparison questionable. The ratio of measurements of induced radioactivity on the West and East sides of the spacecraft is closer to a factor of three. Refinements are expected to be made to both models and new sets of calculations will soon be published.

LET SPECTRA AND FLUENCE MEASUREMENTS WITH CR-39 PNTDS

Measurements of nuclear particle tracks in CR-39 PNTDs provide fluence, flux, dose and dose equivalent LET spectra for different LDEF experiments. LET spectra are useful in refinement of models of both trapped proton and GCR environments in LEO and in development of calculational methods of determining LET spectra. LET spectra, as measured on LDEF, are dependent on detector orientation, shielding, and experiment location. These three factors must be taken into account in any effort to model LDEF LET spectra. The importance of the contribution of proton-induced short range elastic and inelastic secondaries to the LET spectrum has been confirmed. This is seen as an increase in the fluence of high LET (>100 keV/μm) particles and is presently not included in the calculational models.

Due to both the directional sensitivity of the CR-39 detectors and the fixed orientation of LDEF relative to the Earth, track density and LET spectra are dependent on detector orientation. This fact, together with experiment location can be used to measure particular features of the trapped proton environment, such as East/West trapped proton anisotropy. A0015 and P0006 stacks were on the West-side oriented perpendicular to the direction of maximum proton flux, while the M0004 experiment was located on the East-side. Directional sensitivity and the dependence on orientation of the detectors can be illustrated by looking at LET spectra measured in the four side-stacks of the P0006 experiment. Figure 6 shows the orientation of the P0006 stack relative to the Earth. Perpendicular to the main stack were four side stacks labeled A through D. Figure 7 shows total track density plots for the four side stacks. Higher track density is seen near the West end of the detectors than near the East end. Side stack D which faced North and toward space, shows the greatest track density.

Spacecraft shielding affects the LET spectra in two ways: it attenuates the flux of incoming primary protons and galactic cosmic rays and it increases the cross section for the production of secondaries. The contribution to the LET spectra from proton-induced short range elastic and inelastic secondaries was first measured by this laboratory over 20 years ago as part of the investigation into radiation exposure of Biosatellite III[9]. Additional measurements of secondary tracks have not been carried out until LDEF and the contribution of secondaries to the LET spectra has not been sufficiently taken into account in any of the current calculational models. LET spectra were measured under two shielding depths in the A0015 West-side stack[10]. Similar measurements were made in a stack exposed to 154 MeV protons. The LET of 154 MeV protons is below that for track registration, indicating that all the tracks seen in these proton exposures were the result of inelastic and elastic collisions. The similarity in slopes of the differential LET spectra suggests that a significant fraction of tracks measured in the LDEF CR-39 PNTD layers were the result of secondaries. The details of these measurements and plots of the resulting LET spectra may be found in reference 10.

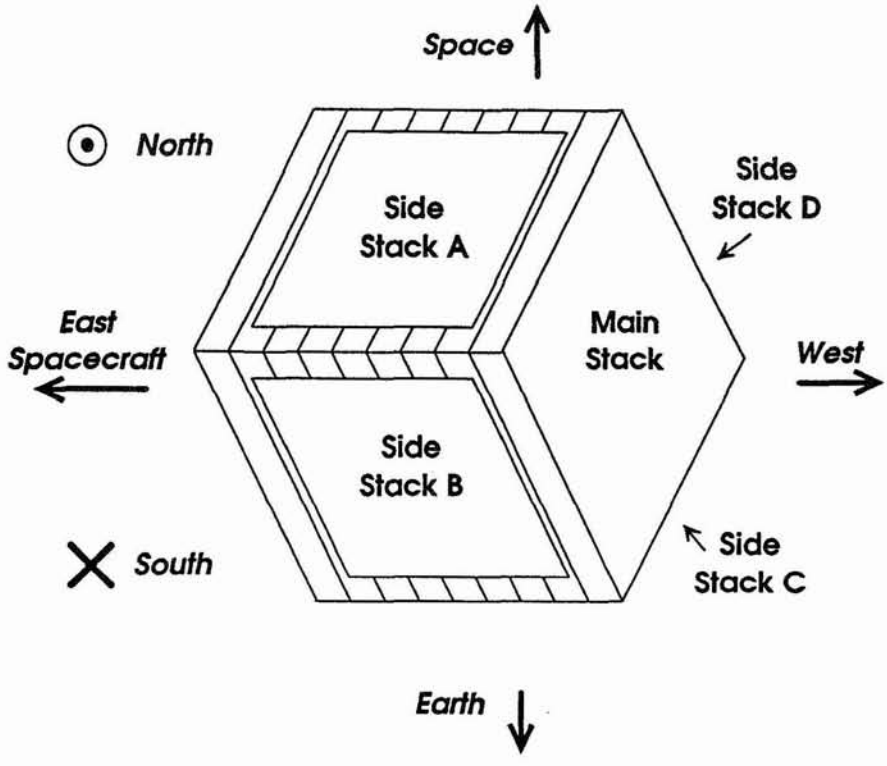

Figure 6: Orientation of side stacks in LDEF P0006 experiment relative to the spacecraft.

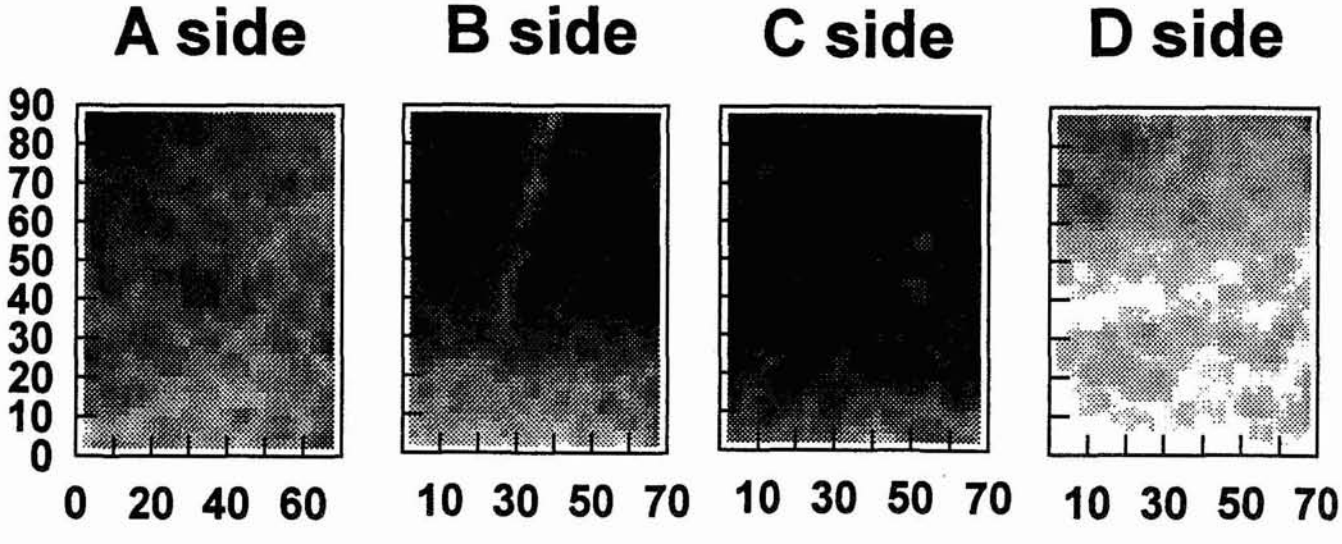

Figure 7: Track Density plots for P0006 side stacks. The darkest region corresponds to a track density $<5 \times 10^5$ tracks/cm^2, while the lightest region corresponds to a density $>9 \times 10^5$ tracks/cm^2.

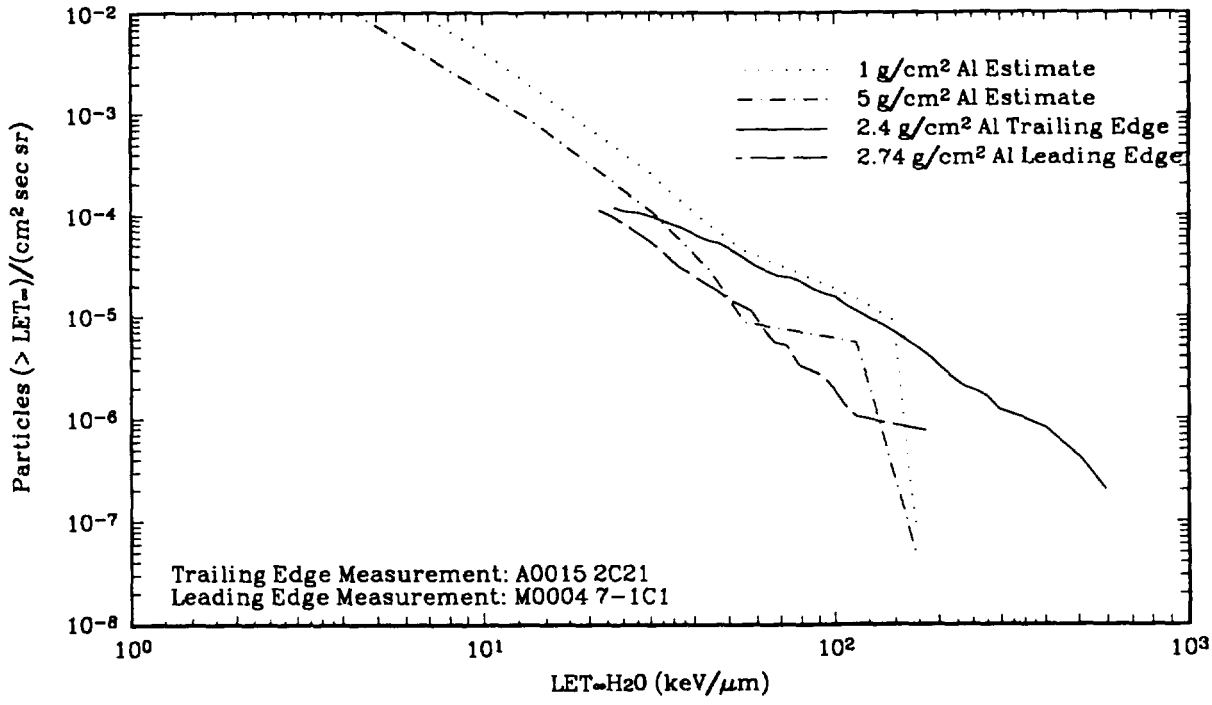

Figure 8: LET Spectra measured on East and West sides of LDEF and LDEF pre-recovery estimate LET spectra for 1 and 5 g/cm^2.

The dependence on detector location of the LET spectra may be seen in a comparison of LET spectra measured on the East and West sides of LDEF. Figure 8 shows LET spectra measured in the M0004 experiment on the East (leading) edge of LDEF and in the A0015 experiment on the West (trailing) edge under similar shielding between 2.4 and 2.6 g/cm^2. The two curves converge at lower LETs ($\sim$20 keV/μm), indicating perhaps that the difference in proton fluences of about 1.5 MeV in energy at the two locations is less than the difference in the higher LET secondary particle fluences. For higher LETs, the West-side curve lies above the curve measured on the East-side, illustrating the effect of the trapped proton anisotropy in the South Atlantic Anomaly. Most of the flux between 20 and 100 keV/μm is the result of trapped primary protons and elastic proton secondaries. Above 100 keV/μm, inelastic collisions between incident trapped protons and carbon and oxygen nuclei of the stopping material make a contribution.

Figure 8 also shows two LET spectra calculated using the CREME code from the LDEF pre-recovery estimates[11] under 1 and 5 g/cm^2. These calculated spectra do not take the contribution of secondaries produced by collisions with high energy trapped primary protons into account. At $\sim$150 keV/μm, the two calculated curves quickly drop off in the region of relativistic Fe due to the geomagnetic cutoff. The measured curves continue to high LETs and fall off much more gradually, illustrating the need to integrate the contribution of secondaries into the calculational models. Calibrations of CR-39 PNTDs are still in progress and future LET spectra curves may show an increase in integral fluence and flux. However this change would have little effect on the dose or dose equivalent derived from the spectra.

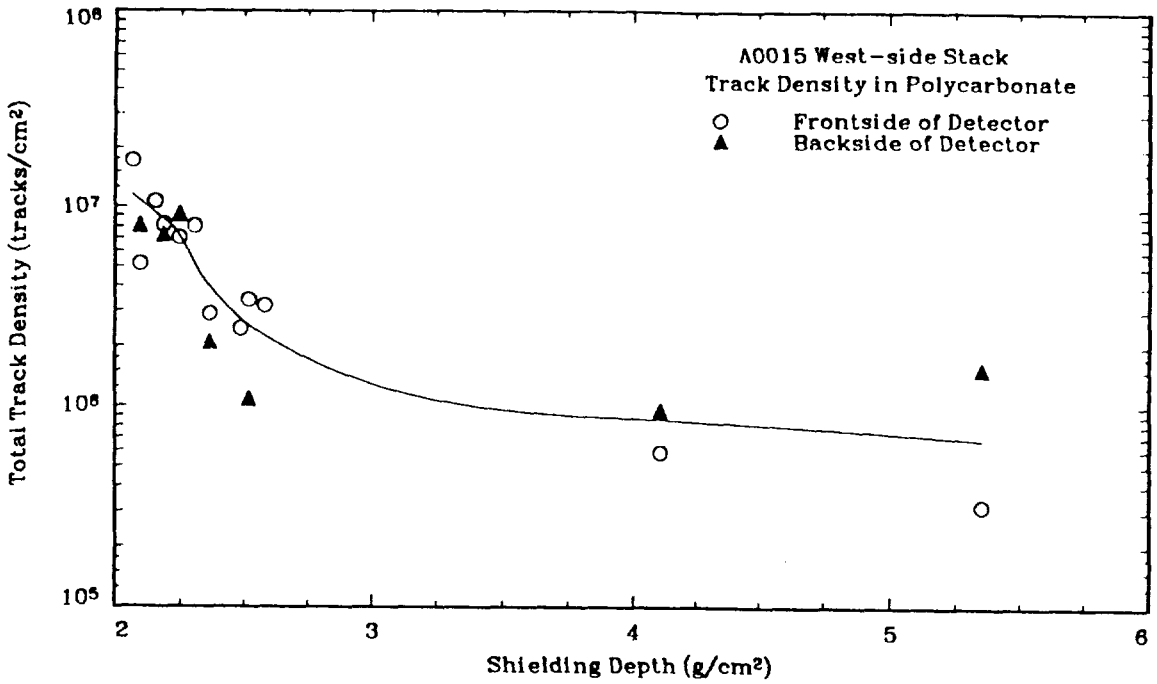

Figure 9: Track densities measured in A0015 West-side polycarbonate PNTDs as a function of shielding depth.

HIGH TRACK DENSITIES IN A0015 POLYCARBONATE PNTDS

Analysis of Sheffield and Tuffak polycarbonate (PC) PNTD layers from the A0015 West-side stack has revealed a much higher than expected track density. A track density of $> 10^7$ tracks/cm^2 was counted on the least shielded PC layer (2.0 g/cm^2). This is far higher than expected considering that the threshold for track registration in PC is usually accepted to be $\sim$250 keV/μm. By comparison, the track density measured in the CR-39 layer closest in the A0015 West-side stack (2.6 g/cm^2) was $\sim 1.1 \times 10^5$ tracks/cm^2. Track densities were counted on the front and back surfaces of each PC layer. Figure 9 shows track density in PC as a function of shielding depth. The track density can be seen to decrease with increasing shielding.

The Sheffield and Tuffak PC layers involved in this analysis were processed for only a short time and a layer of $\sim$2.5 μm thickness was removed from each surface. Figures 10 and 11 are photomicrographs of two of the PC layers showing the high densities of tracks. Most of the tracks are small and over-etched, indicating that the ranges of the particles which made them are less than 2.5 μm. Because the removed layer was so small, the resulting tracks were too small to accurately measure and only track densities were measured. Additional chemical processing enlarged the tracks, but did not uncover any new tracks, indicating that the latent tracks are present only in the few microns beneath the pre-etch surface.

To date, the origin of these tracks is unknown, but several possible causes have been eliminated. One possibility was that the material was irradiated at the time of manufacture. This can be discounted because high track densities are seen in both Tuffak and Sheffield PNTDs, polycarbonates made by

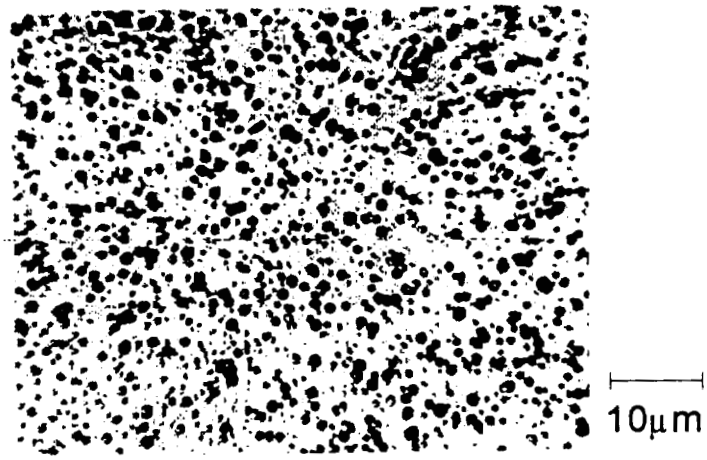

Figure 10: Photomicrograph of PC layer under 2.063 g/cm^2 from the A0015 West-side stack. The track density is $\sim 1.72 \times 10^7$ tracks/cm^2.

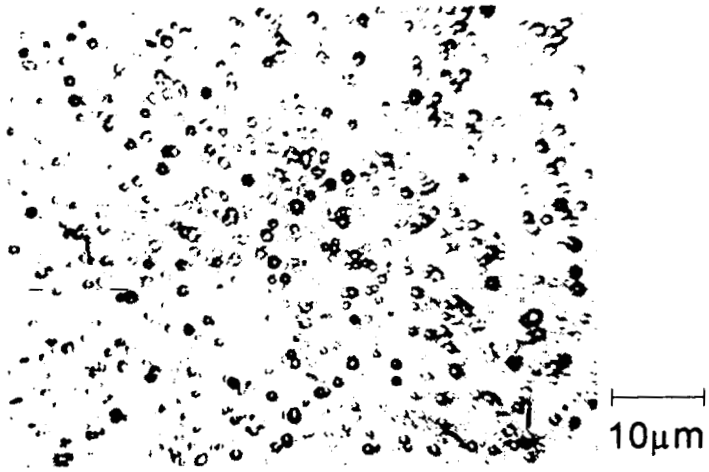

Figure 11: Photomicrograph of PC layer under 2.485 g/cm^2 from the A0015 West-side stack. The track density is $\sim 8.13 \times 10^6$ tracks/cm^2.

different manufacturers. Since track density is seen to attenuate as a function of shielding depth in the stack, exposure must have taken place while the experiment was assembled. Another possibility is that what is being seen are not tracks, but an effect caused by detector handling or chemical processing. This possibility has also been ruled out since these high track densities were counted in detectors which were processed separately. In addition, this effect was not seen in unexposed control detectors processed under the same conditions.

Since the detectors were near the fission foil/mica and ^{6}LiF/CR-39 neutron detectors, it was suggested that the track must be from α-particles from these sources. This possibility has been eliminated due to the fact that the range of α-particles from these sources is too short to form tracks in all the PC layers. This high track density was not seen near the activation foils contained in the P0006 and A0015 Earth-side stacks. If the tracks were from ^{6}Li α-particles, a pattern of track density would be seen due to the placement of the ^{6}LiF chips in the experiment. No such pattern was seen.

It is possible that the tracks are from proton-induced secondaries. To test this hypothesis, a stack of Sheffield and Tuffak PC PNTDs was exposed to a beam of 154 MeV protons at the Harvard Cyclotron. While a small number of recoil tracks were detected, the density was far lower than the density of secondaries counted in the CR-39 PNTDs and could not account for the high track densities seen in the A0015 PC layers. In addition, if these tracks were from proton induced secondaries, a similar high track density should have been counted in the more sensitive CR-39 layers in the A0015 West-side stack. A similar argument can be used to dismiss the possibility that the tracks were from stopping protons or from low energy (trapped or anomalous) α-particles.

One conclusion that can be drawn from the analysis of the A0015 West-side PC layers is that the sensitivity of the material is not constant, but varies as a function of detector thickness. Since high track densities can be counted through many layers of PC on both the front and back surfaces of the detector and since these tracks only appear in the $\sim$3 μm region directly beneath the pre-etch surface and no deeper, it can be concluded that this outer-most region of the PC layer is more sensitive than the rest of the layer. This opens up a number of possibilities including the possibility that this region of the detector is even more sensitive than CR-39 and that the tracks being seen are from primary protons of energy greater than 16 MeV, the highest proton energy detectable in CR-39, but lower than the 154 MeV of the Harvard Cyclotron proton exposures. Similar analysis of Tuffak, Sheffield and Lexan PC is being carried out for other experiments containing PC on LDEF. Ground based experiments are also underway to try and reproduce the results seen in the A0015 West-side polycarbonate PNTDs.

DISCUSSION AND CONCLUSIONS

The LDEF mission provided an unprecedented opportunity to measure the ionizing radiation environment in low Earth orbit due to a number of unique aspects including the fixed orientation of the spacecraft with respect to the Earth and the 5.8 year duration. Measurements of the ionizing radiation exposure of LDEF made with CR-39 and PC PNTDs and with TLDs are useful in refining methods of calculating radiation transport and exposure in spacecraft. These measurements can also be used to

further develop models of the space radiation environment. Integrated doses and linear energy transfer (LET) spectra were measured as functions of spacecraft shielding, orientation and location in TLDs and PNTDs. Total absorbed doses in TLDs have been measured as a function of shielding depth and detector location for several LDEF experiments and comparisons have been made with two preliminary sets of calculated doses. The trapped proton anisotropy in the South Atlantic Anomaly was measured with both TLDs and PNTDs and a ratio of $\sim$1.5 was found between measured doses on the spacecraft's West and East sides under similar experiment shielding. The contribution of proton-induced short range secondaries to the LET spectra, especially at higher LETs (>100 keV/μm), was measured. Unusually high track densities in excess of 10^7 tracks/cm^2 have been counted in polycarbonate PNTD layers from the West-side of the spacecraft. No explanation for these high track densities has yet been found.

Future work on the analysis of LDEF radiation detectors will include investigation of the high track densities measured in polycarbonate, and accelerator exposures to protons and α-particles will be carried out in order to reproduce these track densities. LET spectra will be measured in polycarbonate PNTDs in order to accurately measure the high LET region (>250 keV/μm). Comparisons will be made between the high LET measurements in polycarbonate and those previously measured in CR-39 PNTDs. A new method to measure very short range particles that stop within the removed bulk etch layer is being developed. This technique will measure the contribution of short range particles (2-10 μm) to the LET spectra. Measurements will be made of high LET ($LET_{\infty}\cdot H_2O$>500 keV/μm) secondary particles produced in silicon wafers by high energy primary cosmic rays in the P0006 experiment. Dose and LET spectra measurements will be compared with model calculations. A comparison of measured LET spectra with model calculations that include the contribution of secondaries is of special interest.

REFERENCES

1. Frank, A. L.,; Benton, E. V., Armstrong, T. W., and Colborn, B. L., "Absorbed Dose Measurements and Predictions on LDEF." *Second LDEF Post-Retrieval Symposium*, NASA CP-3194, Part 1, 1993.

2. Armstrong, T. W.; and Colborn, B. L. "Radiation Model Predictions and Validation Using LDEF DATA." *Second LDEF Post-Retrieval Symposium*, NASA CP-3194, Part 1, 1993.

3. Atwell, W., 1993, private communication.

4. Watts, J. W., Armstrong, T. W., and Colborn, B. L., "Revised Prediction of LDEF Exposure to Trapped Protons." *Second LDEF Post-Retrieval Symposium*, NASA CP-3194, Part 1, 1993.

5. Colborn, B. L., and Armstrong, T. W., "Development and Application of a 3-D Geometry/Mass Model for LDEF Satellite Ionizing Radiation Assessments." *Second LDEF Post-Retrieval Symposium*, NASA CP-3194, Part 1, 1993.

6. Burrell, M. O., "The Calculation of Proton Penetration and Dose Rates." George C. Marshall Space Flight Center, Huntsville, AL., NASA TM X-53063, August 1964.

7. Sawyer, D. W., and Vette, J. I., "AP-8 Trapped Proton Environment Model for Solar Maximum and Solar Minimum." National Space Science Data Center, Goddard Space Flight Center, NSSDC/WDC-A-R&S 76-06, December 1976.

8. Kern, J. W., 1993, private communication.

9. Benton, E. V.; Curtis, S. B., Henke, R. P., and Tobias, C. A. "Comparison of Measured and Calculated High-LET Nuclear Recoil Particle Exposure on Biosatellite III." *Health Physics*, Vol. 23, 1972, pp/ 149-157.

10. Benton, E. R., Csige, I., Benton, E. V., and Frigo, L. A., "Contribution of Proton-induced Short Range Secondaries to the LET Spectra on LDEF," *Third LDEF Post-Retrieval Symposium*, NASA CP-3275, 1995.

11. Benton, E. V.; Heinrich, W., Parnell, T. A., Armstrong, T. W., Derrickson, J. H., Fishman, G. J., Frank, A. L., Watts, J. W., and Wiegel, B., "Ionizing radiation exposure of LDEF: Pre-recovery estimates." *Nuclear Tracks and Radiation Measurements*, Vol. 20, No. 1 1992, pp/ 75-100.

FISSION FOIL MEASUREMENTS OF NEUTRON AND PROTON FLUENCES IN THE A0015 EXPERIMENT*

A.L. Frank and E.V. Benton
Eril Research, Inc.
P. O. Box 150788
San Rafael, CA 94915-0788, U.S.A.

T. W. Armstrong and B.L. Colborn
Science Applications International Corporation
Route 2, Prospect, TN 38477, U.S.A.

SUMMARY

Results are given from sets of fission foil detectors (FFDs) (^{181}Ta, ^{209}Bi, ^{232}Th, ^{238}U) which were included in the A0015 experiment to measure combined proton/neutron fluences. Use has been made of recent FFD high energy proton calibrations for improved accuracy of response. Comparisons of track density measurements have been made with the predictions of environmental modeling based on simple 1-D (slab) geometry. At 1 g/cm^2 (trailing edge) the calculations were ~25% lower than measurements; at 13 g/cm^2 (Earthside) calculations were more than a factor of 2 lower. A future 3-D modeling of the experiment is needed for a more meaningful comparison. Approximate mission proton doses and neutron dose equivalents were found. At Earthside (13 g/cm^2) the dose was 171 rad and dose equivalent was 82 rem. At the trailing edge (1 g/cm^2) dose was 315 rad and dose equivalent was 33 rem. The proton doses are less than expected from TLD doses by 16% and 37%, respectively. These differences can be explained by uncertainties in the proton and neutron spectra and in the method used to separate proton and neutron contributions to the measurements.

INTRODUCTION

The A0015 radiation experiment consisted of sets of passive integrating detectors which were contained in three different sealed canisters on the LDEF satellite. Canisters #1 and #2 (at the Earth end and near the trailing edge of LDEF, respectively) were filled with the detectors while Canister #3 (near the trailing edge) was only partially filled. Both #1 and #2 carried a selection of FFDs. The FFDs consist of heavy metal foils in contact with muscovite mica films. The foil types included ^{181}Ta, ^{209}Bi, ^{232}Th and ^{238}U.

*Work partially supported by NASA Contract No. NAS8-38610, Marshall Space Flight Center, Huntsville, AL 35812

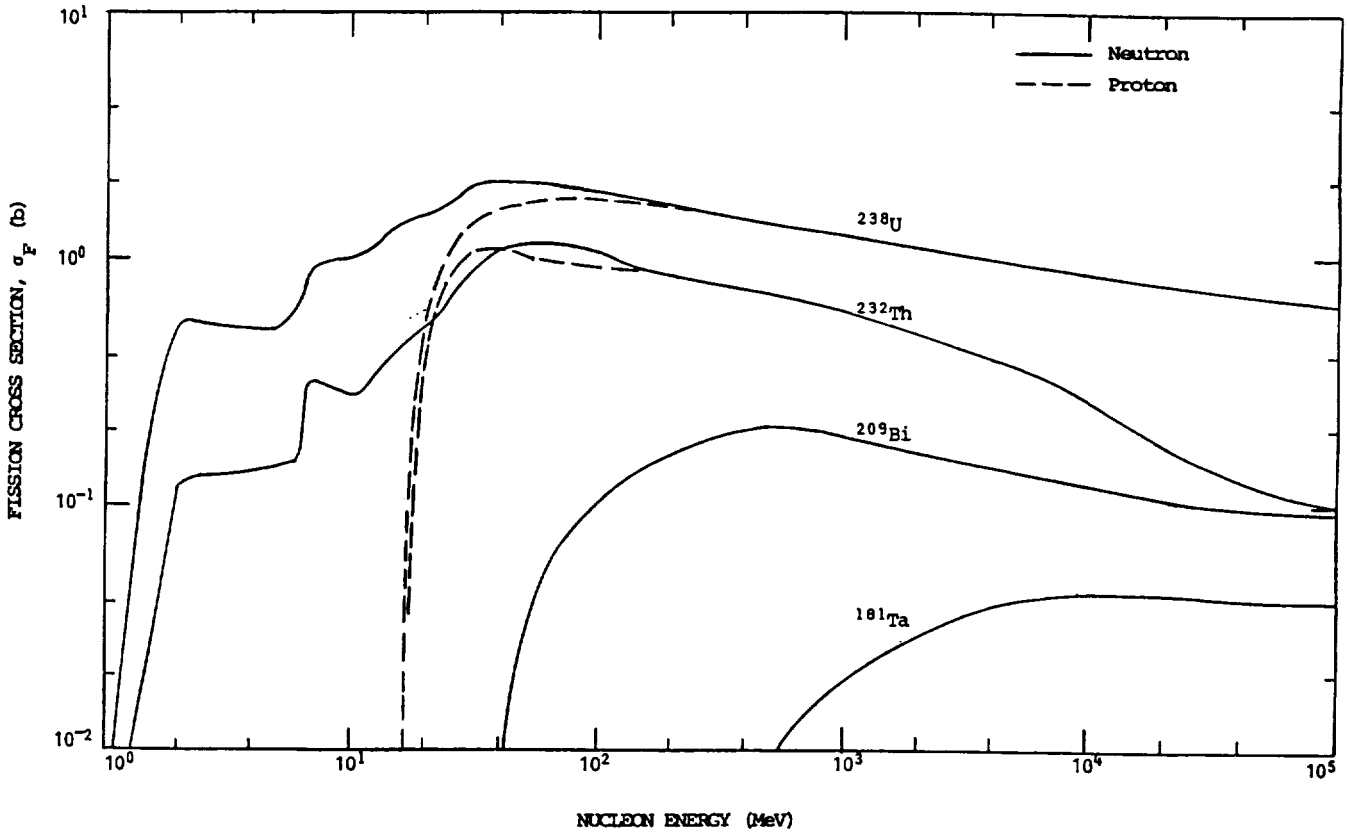

Figure 1: Fission cross sections for neutrons and protons incident on heavy metal foils.

Heavy metal nuclei have significant cross sections for fission when irradiated with neutrons and protons. Each isotope is characterized by threshold energies for the fission reactions and particular energy-dependent cross sections. In the FFDs, fission fragments produced by the reactions are emitted from the foils and create latent particle tracks in the adjacent mica films. When the films are processed, surface tracks are formed which can be optically counted. The track densities are indications of the fluences and spectra of neutrons and/or protons.

FFDs have previously been used for spaceflight measurements[4, 2, 3, 6, 5]. In cases where the proton contribution to track densities can be subtracted out, the FFDs can be used as high energy (>1 MeV) neutron dosimeters. These detectors have been calibrated with neutrons of energies up to ~15 MeV and found to have efficiencies $\epsilon = 1.16 \times 10^{-5}$ tracks/neutron barn[8]. More recently, calibrations have been performed with high energy protons. At high energies, either proton or neutron calibrations are sufficient since the cross section data, plotted in Figure 1[7, 10, 9], show that the proton and neutron fission cross sections are approximately equal.

Detector efficiencies, plotted in Figure 2, have been found for the four FFD types by combining low

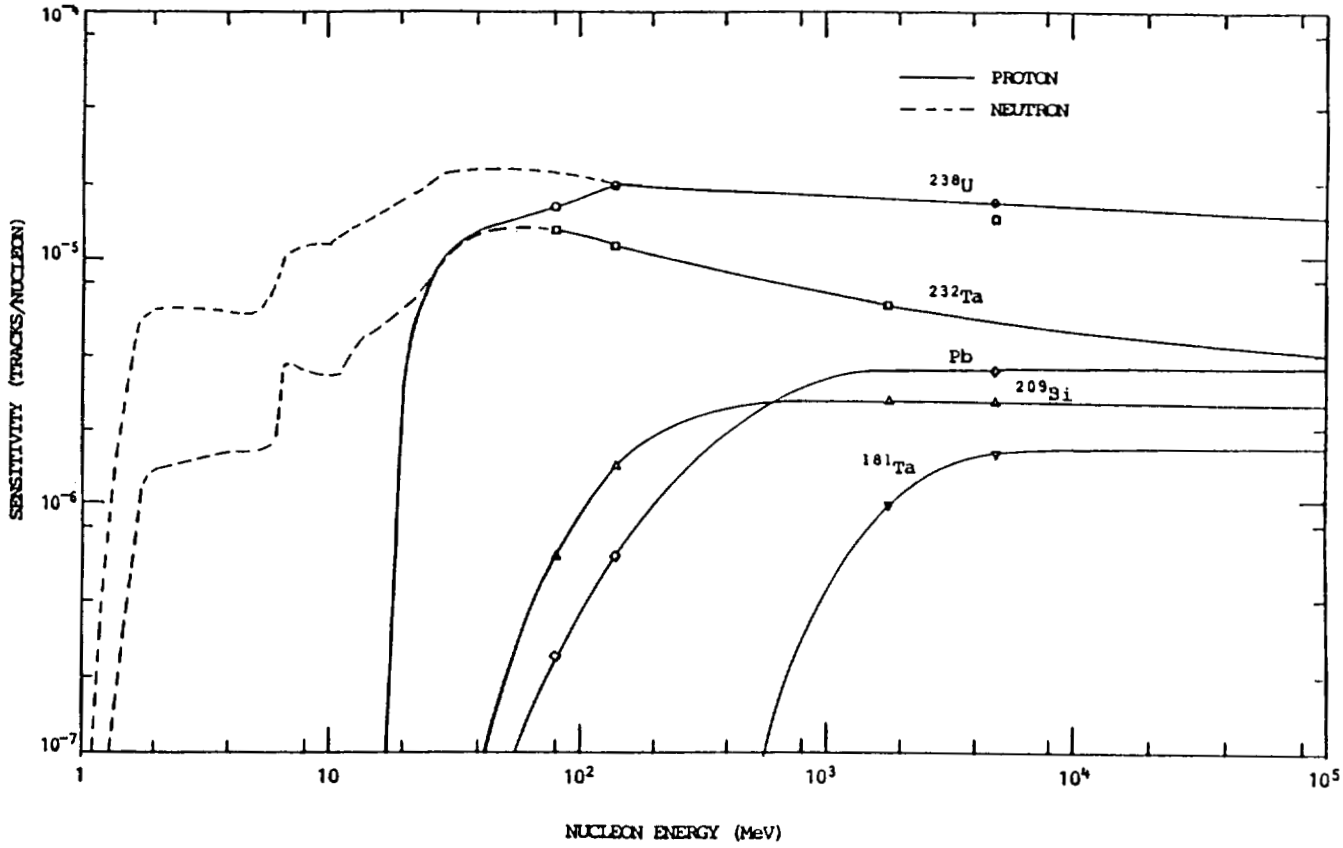

Figure 2: Sensitivities of fission foil detectors to neutrons and protons.

energy neutron and high energy proton calibrations with the published fission cross sections to cover the energy region from 1 MeV to 100 GeV. Armstrong and Colborn[1] have shown that the energy range of interest in space applications extends to 100 GeV for proton/neutron spectra.

The FFD efficiencies $\epsilon(E)$, together with calculated proton or neutron energy spectra, $N(E)$, are used to generate predicted track densities. These values are then compared with measured track densities, for an evaluation of the calculated spectra and determination of LDEF fluences and doses.

EXPERIMENT

The aluminum canisters containing the A0015 detectors had acrylic liners with inner dimensions of 9.7 cm diameter by 8.6 cm depth. The detectors were 7 cm $\times$ 7 cm in dimension (with corners clipped)

Table 1: Shielding of LDEF A0015 Fission Foil Detectors.

Canister	Plate	Min. Vertical Shielding (g/cm^2) Al Equivalent	Min.-Max. Horizontal Shielding (g/cm^2) Al Equivalent
#1	^{209}Bi	12.7	2.75 - 10.0
	^{181}Ta	13.1	2.70 - 22.6
	^{232}Th	13.4	1.87 - 8.92
	^{238}U	13.6	1.87 - 13.4
#2	^{209}Bi	1.65	2.75 - 10.0
	^{181}Ta	1.42	2.70 - 22.6
	^{232}Th	1.20	1.87 - 8.92
	^{238}U	0.97	1.87 - 13.4

Canister #1 was located on the Earthside end of LDEF and Canister #2 near the trailing edge (Tray C2).

and were stacked through the depth of the canisters. The FFDs were contained in cutouts in acrylic plates. The shielding of the FFDs is given in Table 1. The aluminum equivalent values are given but most of the volume of the canisters was filled with plastics (polycarbonate, acrylic and CR-39). This has a significant effect on the scattering of neutrons in the vicinities of the FFDs. FFDs are at one end of the detector arrays and, from the shielding in Table 1, it is seen that the FFDs were oriented toward space in Canister #2 (trailing edge) but away from space in Canister #1 (Earthside). There were 6-10 cm^2 of each of the four foil types in each canister.

After the return of LDEF, the FFDs were removed from the canisters and disassembled. The mica films were processed in 50% HF solution at 21°C for 1.25 hr in order to delineate the fission fragment tracks for counting. The mica was given a pre-flight processing for 3 hr to enlarge the fossil tracks. The films were then counted under an optical microscope at 200×.

MEASUREMENTS

The average track densities from the mica films are given in Table 2. The standard deviations given are due to counting statistics. In addition, there were differences of up to 16% from the mean in track densities across the detector layers in Canister #1 and up to 37% in Canister #2 which seem to have been due mainly to shielding differences through the sides of the canisters. The larger gradients in track densities in Canister #2 would be expected near the trailing edge of LDEF and under smaller shielding.

It is of interest to note that the track density ratios between Canisters #1 and #2 change very little for the four foil types. Since the foils have different threshold energies one can conclude that the ratios of high energy to low energy nucleons are equal to within a few percent for the two FFD positions.

Table 2: Average Track Densities from the LDEF A0015 Fission Foil Detectors.

	Measured Track Density (cm^2)	Calculated Track Density (cm^2)
Canister #1		
^{181}Ta	131 ± 4	51.8
^{209}Bi	2340 ± 47	103
^{232}Th	23880 ± 240	9870
^{238}U	34490 ± 500*	18800
Canister #2		
^{181}Ta	148 ± 5	49.0
^{209}Bi	2825 ± 5	2030
^{232}Th	27030 ± 315	20300
^{238}U	39490 ± 500	34600

*Corrected for spontaneous fission background and surface oxidation of foils.
Canister #1 – Earthside
Canister #2 – Trailing Edge
The calculated track densities are based on proton and neutron spectra derived from primary/secondary particle propagation in a simple slab (one-dimensional) shield.

CALCULATIONS

Numerical integrations were carried out, as discussed above, to calculate theoretical track densities for comparison with measurements. These results are approximate since the simple slab geometry models developed by Armstrong and Colborn[1] were used to propagate the incident particles through shielding. Secondary particles are included in the calculations.

The equation for numerical integration is

$$D_c = \sum_{E_{min}}^{E_{max}} \epsilon_p(E) N_p(E) + \sum_{E_{min}}^{E_{max}} \epsilon_n(E) N_n(E) \quad (1)$$

where ϵ_p and ϵ_n are the detector efficiencies for protons and neutrons, respectively (Figure 2), and N_p and N_n are the calculated proton and neutron spectra in the vicinity of the FFDs. An example of the proton and neutron spectra for a slab thickness of 10 g/cm^2 Al is given in Figure 3.

The calculated track densities for each of the four FFD types as functions of slab thickness are plotted in Figure 4 with the measurements. Values corresponding to the vertical shielding of the FFDs in Table 1 are given in Table 3 along with the measurements. There is better agreement between calculation and measurement for Canister #2, where the shielding is small. For thicker shielding the slab calculations fall well under the canister measurements because of the large difference in shielding from the sides.

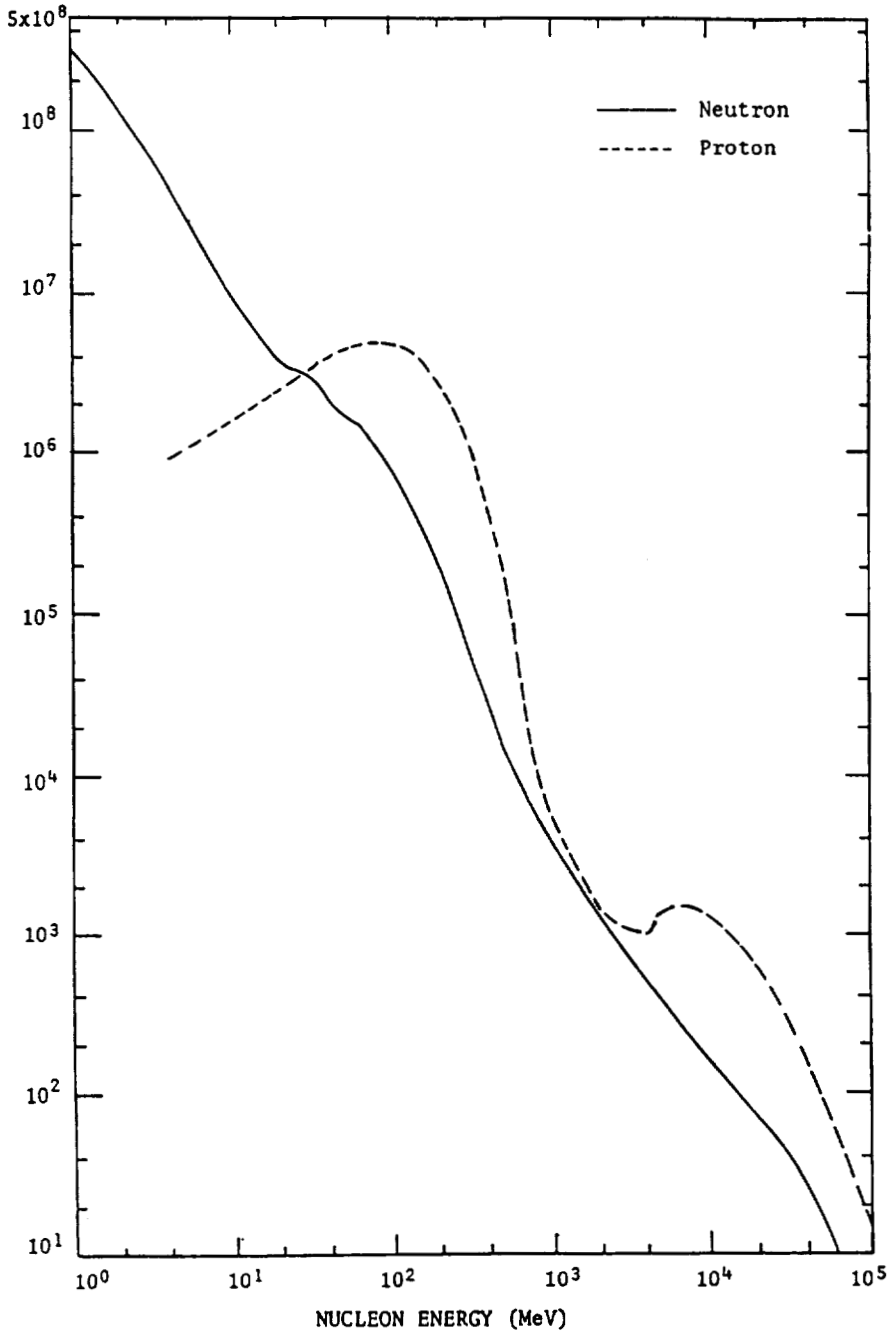

Figure 3: Differential spectra of neutrons and protons accumulated during the total LDEF mission under 10 g/cm^2 Al. from data by Armstrong and Colborn (1990). Summations and extrapolations by the authors.

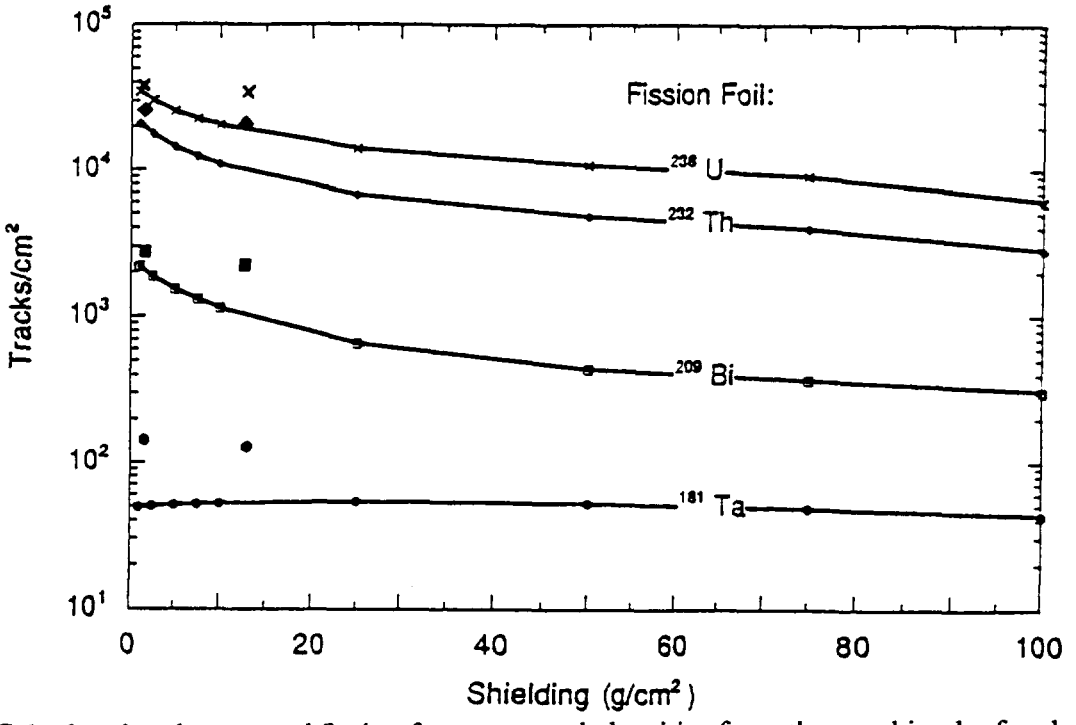

Figure 4: Calculated and measured fission fragment track densities from the combined p,f and n,f reactions in the A0015 fission foil detectors on LDEF. The calculations are based on a simple 1-D (slab) geometry (Armstrong and Colborn, 1990). The measured values lie at approximately 1 and 13 g/cm^2.

The calculations for Canister #2 are low by 67, 28, 25 and 12% for ^{181}Ta, ^{209}Bi, ^{232}Th and ^{238}U, respectively. The higher the energy threshold, the greater the deviation. This suggests that the calculated proton and neutron energy spectra may be deficient at higher energies.

The proton absorbed doses and the neutron dose equivalents have been approximated for the FFD measurements by scaling the calculated proton and neutron track densities to the total measured values. The proton dose, in rad, is given by

$$D = 1.602 \times 10^{-8} \sum_{E_1}^{E_2} N(E) \frac{dE}{dx} \tag{2}$$

where E_1 and E_2 are 10 MeV and 100 GeV, the energy end points in this study. $N(E)$ is the differential proton spectrum in cm^{-2} MeV^{-1} and $\frac{dE}{dx}$ is the energy absorption of protons in tissue in MeV cm^2 g^{-1}.

The dose equivalent for neutrons, in rem, is given by

$$DE = 10^{-3} \sum_{E_1}^{E_2} d(E) n(E) \tag{3}$$

where E_1 and E_2 are 1 MeV and 60 GeV, $d(E)$ is the dose equivalent conversion factor in rem cm^2 and $n(E)$ is the differential neutron spectrum in cm^2 MeV^{-1}. The d values were taken from NCRP (1971) up to 500 MeV and extended to 60 GeV from that energy.

Table 3: High Energy Proton and Neutron Doses for the A0015 Fission Foil Detectors.

Canister	Position	Shielding (g/cm^2) Al Equivalent	Proton Dose (rad)	Neutron Dose (rem)	TLD Proton Dose (rad)
1	Earthside	13.2	171	82	200
2	Trailing Edge	1.3	315	33	500

The doses were determined by scaling calculated values of proton and neutron induced track densities to total measured values.
The doses correspond to proton energies of 10 MeV to 100 GeV and neutron energies of 1 MeV to 60 GeV.

The doses are given in Table 3. The proton doses can be compared to measured TLD doses in the same canisters. Extrapolating from the shielding dose distribution measured with TLDs, we would expect about 225 rad in Canister #1 and 550 rad in Canister #2. About 90% of these doses would be due to protons in the energy range of the FFDs. The TLD proton doses are therefore about a factor of 1.2 higher in Canister #1 and 1.6 higher in Canister #2. Given the approximations involved in the slab calculations of proton and neutron spectra and simple scaling of track densities to get measured proton doses, these differences are within expectations.

DISCUSSION

A comparison has been made between fission foil detector measurements (track densities) induced by proton/neutron fluences encountered on LDEF and predicted track densities based on calculated proton and neutron spectra. The calculations employed a simple slab geometry[1]. The predicted track densities on the detectors were less than measurements by ~25% at 1 g/cm^2 shielding (trailing edge) and more than a factor of 2 at 13 g/cm^2 (Earthside). The differences are primarily due to the slab geometry approximation of actual spaceflight conditions. Future calculations based on a geometrical model of the A0015 experiment are needed for a more accurate test for the radiation modeling code.

The proton doses derived by combining measurements and calculations were 16% and 37% less than TLD doses measured in the flight canisters, when extrapolated to equivalent shielding. The differences can be explained by the approximations involved in the calculations.

In Table 4 the A0015 neutron dose equivalent rates are compared with measurements from other spaceflights. The LDEF rates are seen to be higher than all other measurements, by factors of approximately 6 to 40. The primary reason for the large differences is in the greater LDEF flight altitude, with higher primary proton and secondary neutron fluxes. Shielding differences may also play a significant role.

Table 4: Spaceflight High Energy (>1 MeV) Neutron Measured Comparisons.

Space flight	Experiment	Shielding	Altitude (km)	Inclination	Dose Equiv. Rate (mrem/d)
LDEF	A0015	1 g/cm^2	478	28.5°	16
	A0015	13 g/cm^2			39
	P0006	17 g/cm^2			33
STS-9(SL-1)	VFI	Pallet	241	57°	4.2
STS-51F(SL-2)	VFI	Pallet	322/304	49.5°	4.0
STS-3		Locker	280	40.3°	0.95
STS-4		Locker	297	28.5°	1.3
STS-5		Locker	284	28.5°	2.2
STS-6		Locker	293	25.5°	1.3
Cosmos 936	Inside Spacecraft		419/224	62.8°	6.8
Cosmos 1129	Inside Spacecraft		394/226	62.8°	6.8
Cosmos 2044	Outside Spacecraft		294/216	82.3°	3.3

Due to approximations made in separating neutron and proton contributions to the fission foil detector measurements, the accuracy of neutron dose equivalents is estimated to be within a factor of 3.

REFERENCES

1. Armstrong T.W. and B.L. Colborn, *Scoping estimates of the LDEF satellite induced radioactivity,* SAIC, Report No. SAIC-90/1462, 1990.

2. Benton E.V., R.M. Cassou, A.L. Frank, R.P. Henke and D.D. Peterson, "Space radiation on board Cosmos 936–U.S. portion of experiment K206," *Final Reports of U.S. Plant and Radiation Experiments Flown on the Soviet Satellite Cosmos 936,* (S.N. Rosenzweig and K.A. Souza, eds.). NASA TM 78526, 1978.

3. Benton E.V., R.P. Henke, A.L. Frank, C.S. Johnson, R.M. Cassou, M.T. Tran and E. Etter, "Space radiation dosimetry aboard Cosmos 1129–U.S. portion of experiment K309," *Final Reports of U.S. Plant and Radiation Experiments Flown on the Soviet Satellite Cosmos 1129* (M.R. Heinrich and K.A. Souza, eds.) NASA TM 81288, 1981.

4. Benton E.V., R.P. Henke, A.L. Frank, R.M. Cassou, C.S. Johnson and M.T. Tran, *Final Dosimetry Reports for STS-3, STS- 4, STS-5, STS-6, TR-54, -56, -57, -58,* University of San Francisco Physics Research Laboratory, 1982-1983.

5. Dudkin V.E., Yu.V. Potapov, A.B. Akopova, L.V. Melkumyan, Sh.B. Rshtuni, E.V. Benton and A.L. Frank, "Neutron fluences and energy spectra in the Cosmos-2044 Biosatellite orbit," *Nucl. Tracks Radiat. Meas.*, Vol. 20, No. 1, pp. 139-141, 1992.

6. Frank A.L., E.V. Benton, E.R. Benton, V.E. Dudkin and A.M. Marenny, *Radiation experiments on Cosmos 2044: K-7-41, Parts A,B,C,D,E,* TR-76, University of San Francisco Physics Research Lab, 1990.

7. Lomanov M.F., G.G. Shimchuk and R.M. Yakovlev, "Solid state detectors of fission fragments for the REM dose measurement of mixed proton and neutron radiation," *Hlth. Phys.* Vol. 37, pp.677-686, 1979.

8. Pretre S., E. Tochilin and N. Goldstein, "A standardized method for making neutron fluence measurements by fission fragment tracks in plastics," *Proc. 1st International Congress on Radiation Protection*, Rome, 1968.

9. Stehn J.R., M.D. Goldberg, R. Wiener-Chasmon, S.F. Mughabghab, B.A. Magurno and V.M. May, *Neutron Cross Sections* Vol.III, BNL 325, 1965.

10. Wollenberg H.A. and A.R. Smith, *Energy and flux determinations of high energy nucleons,* UCRL 19364, 1969.

MEASUREMENT OF TRAPPED PROTON FLUENCES IN MAIN STACK OF P0006 EXPERIMENT*

N. Nefedov, I. Csige, E. V. Benton, R. P. Henke, E. R. Benton and L. A. Frigo
Physics Research Laboratory
University of San Francisco
San Francisco, CA 94117-1080 U.S.A.

SUMMARY

We have measured directional distribution and Eastward directed mission fluence of trapped protons at two different energies with plastic nuclear track detectors (CR-39 with DOP) in the main stack of the P0006 experiment on LDEF. Results show arriving directions of trapped protons have very high anisotropy with most protons arriving from the West direction. Selecting these particles we have determined the mission fluence of Eastward directed trapped protons. We found experimental fluences are slightly higher than results of the model calculations of Armstrong and Colborn.

INTRODUCTION

The Long Duration Exposure Facility (LDEF) was flown in space for almost six years in low Earth orbit and low inclination. Pre-recovery estimates show that 95% of the charge particle exposure for the LDEF orbit is from trapped protons[1]. Almost all proton fluence was accumulated in the South Atlantic Anomaly (SAA).

The trapped proton fluence in the SAA is highly anisotropic. This anisotropy has not been an important practical consideration for most previous missions because the varying spacecraft attitude during passage through the radiation belt averages out anisotropy effects over many orbits. However, for the fixed orientation of LDEF and for other planned missions (e.g. space station), where the spacecraft will be gravity-gradient stabilized, the cumulative proton exposure will remain anisotropic, and will result in a highly non-uniform dose distribution around the spacecraft.

The current theoretical models describing the proton radiation environment have a large uncertainty[2] and therefore their experimental verification is of great importance.

In the present paper, we introduce experimental data of measurement, directional distribution and mission fluence of Eastward directed trapped protons using plastic nuclear track detectors (PNTDs) included in the P0006 experiment flown on LDEF.

*Work supported by NASA under NAG8-282, Marshall Space Flight Center, Huntsville, AL 35812

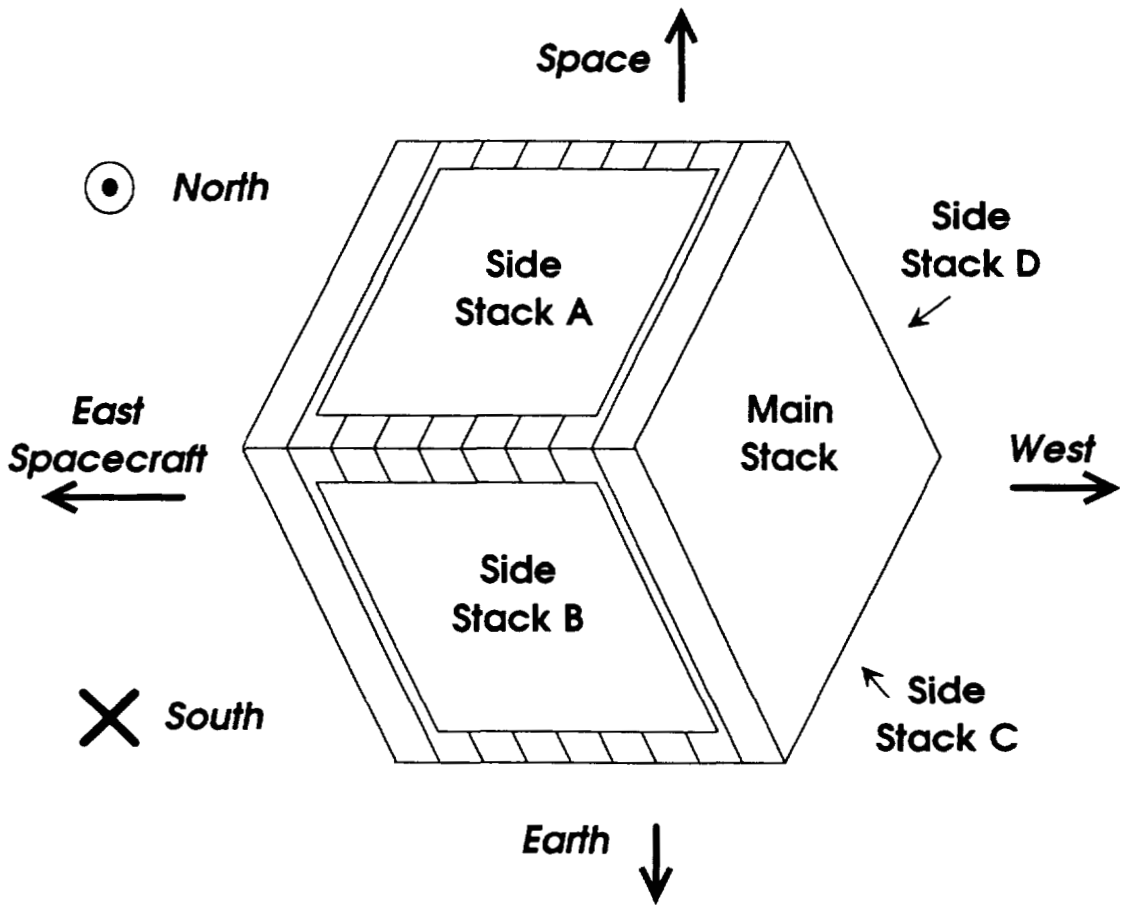

Figure 1: Block scheme of the P0006 experiment on LDEF. Measurements were made in the main stack at 0.6 and 9.5 g/cm^2 shielding depths at the center of the CR-39 (DOP) plastic nuclear detector sheets.

EXPERIMENT

The P0006 experiment was located in the F2 tray of the LDEF satellite. It consisted of one main and four side stacks of plastic nuclear track detectors as shown in Figure 1. In previous experiments we have measured total track density[3] and linear energy transfer (LET) spectra[4] in these stacks. These measurements indirectly confirmed the existence of proton fluence directionality and defined it as being nearly normal to the main stack of the P0006 experiment. The orientation of side stacks (and the main stack) was determined by finding the best agreement between experimental and expected directional dependent effects.

In the present experiment, directional distribution and mission fluence of protons were measured directly with PNTDs (CR-39 with DOP). CR-39 is a threshold detector and for etching conditions of the current experiment, it can detect protons only close to their stopping points. The trapped protons of different energies passing through detector layers will stop at different depths in the stack in accordance

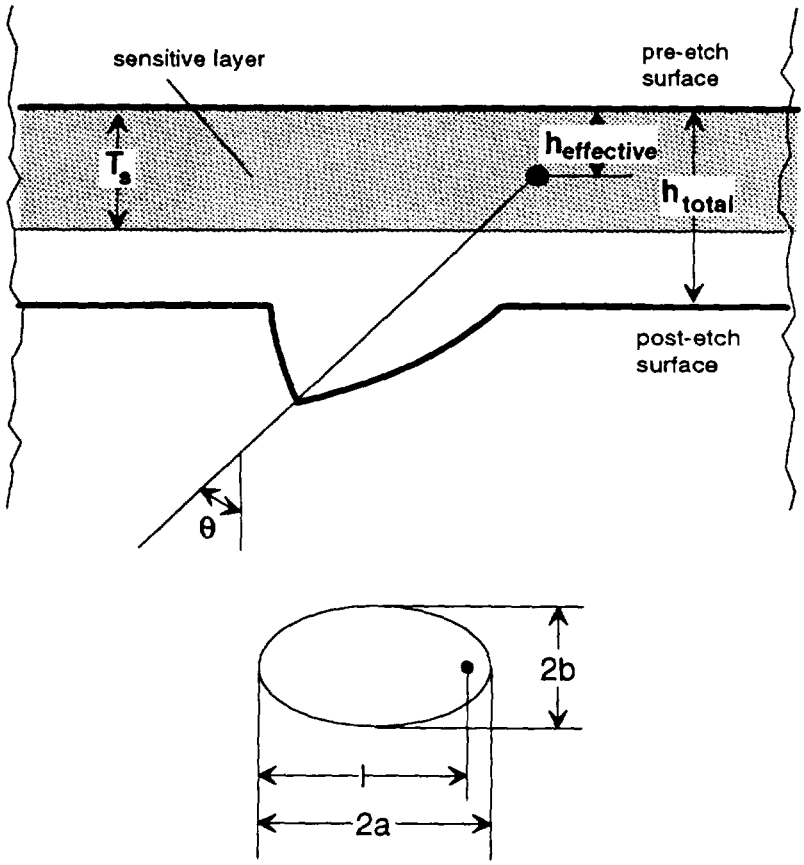

Figure 2: The measurable parameters of an etched track formed by a proton which stopped in the sensitive layer near the bottom surface of the detector.

with the values of their ranges. Measuring the stopping proton density in certain sensitive detector layers makes it possible to obtain the differential energy fluence of protons with energy E in the energy interval ΔE, where E is defined by the matter thickness above the considered detector layer and ΔE is defined by the thickness of the sensitive layer.

CR-39 with DOP under 0.6 and 9.5 g/cm^2 shielding depths were chosen for measurements. The detectors were processed for 36 hours in 6.25 *N* NaOH solution at 50°C. Measurements were made at the center of the detectors using the double layer track anti-coincidence method. After etching, two adjacent layers of CR-39 were reassembled into their flight configuration relative to one another on the microscope stage. A particle event was selected for measurement when a pointed (non-rounded) etched track was produced on the bottom surface of the top layer and no corresponding track was found on the top surface of the bottom layer. The major a and minor b axes of the track opening and the distance between the "back" of the track opening and its tip l were measured (Figure 2) using a videomicrometer.

We supposed all tracks chosen by the above procedure were produced by stopping protons. Tracks of heavy recoil particles are overetched and rounded, and the contribution of heavier primary elements is negligible.

A proton track of the selected type can be described by two parameters: dip angle δ, the angle between the particle trajectory and the detector surface, and the effective removed layer h, the distance between the particle stopping point and the post-etch surface (Figure 2). To obtain these parameters from the etched track size measurements, we used the theory of track development kinetics[5]. First we tried to use the constant etch rate ratio approximation[6] but it provided spurious results. This is not surprising since, near the stopping point of the particles, LET and the directly proportional etch rate ratio along the particle trajectory changes rapidly. Hence we used a variable etch rate ratio model. The form of the detector response curve was chosen to be:

$$V = 1 + A\mathrm{REL}_{200}^{B}, \tag{1}$$

where REL_{200} is the restricted energy loss rate; A and B are parameters. Using equation (1) and the theory of etched track development, the minor and major axes and the l distance were calculated as a function of the dip angle and effective removed layer. From comparison of calculated and measured track sizes, the dip angle and the effective removed layer were determined for each particle.

In order to be detected, the proton has to stop in some sensitive layer thickness T_s of the detector (Figure 2). T_s is a function of the track size selection criteria. In our experiment we can effectively detect only tracks with sizes greater than 2 μm. Through the detector response function (1) and the theory of track development, this value defines the upper boundary surface of the sensitive layer. Particles which stop above this surface have tracks which are too small to be detected.

Since the sensitive layer is very thin in a small scanning area, the volume density of stopping protons should be uniform. This means that the distribution of the experimental effective removed layers should also be uniform. We used this criterion to find the best values of the A and B parameters in the (1) detector response curve. Figure 3 shows three examples of distribution of effective removed layers using different sets of A and B values. Since the maximum effective removed layer was 9 μm in our case, curve No. 2 was chosen in Figure 3, and the thickness of the sensitive layer was determined to be 4 μm.

RESULTS AND DISCUSSION

The polar angle is defined as the angle between the particle trajectory and the normal of the detector surface in the main stack of the P0006 experiment. Tracks with polar angles $\theta \leq 30°$ ($\delta \geq 60°$) were selected for further analysis. This choice was determined in order to minimize the effect of scanning inefficiency at higher polar angles. Altogether 269 and 300 tracks were selected in layers which were located at main stack depths of 0.6 and 9.6 g/cm^2, respectively.

The arriving directions of stopping protons are presented in Figures 4 and 5. It can be seen that the preferred directionality of the arriving protons is not normal to the main stack. Both distributions have a maximum at polar angles of about 20° and at an azimuthal angle which corresponds to the West direction.

To assess the eastward directed trapped proton fluences, we chose the track in the highest density quadrants around the west direction in Figures 4 and 5. 185 and 139 tracks were found in these quadrants

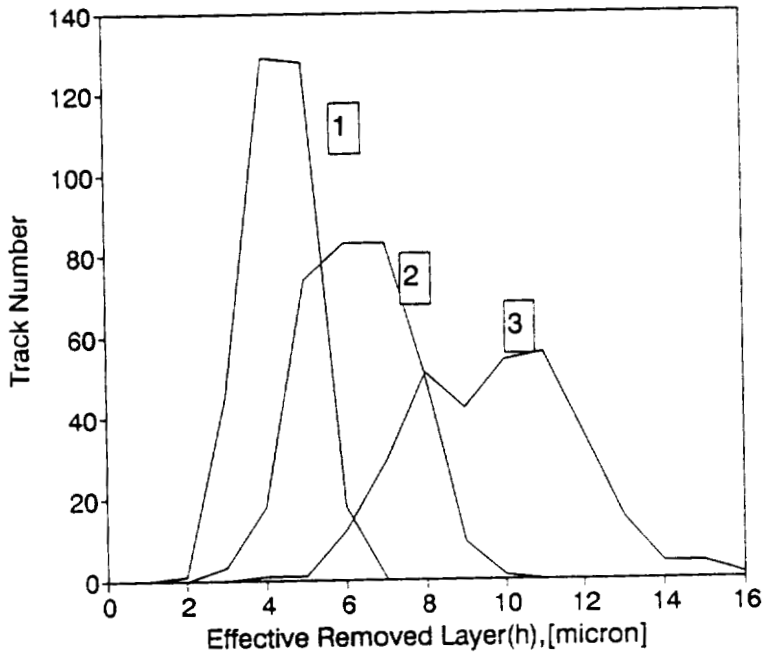

Figure 3: Distributions of calculated effective removed layers using different detector response functions: 1) $V = 1 + \mathrm{REL}^{1.4}/162$, 2) $V = 1 + \mathrm{REL}/100$, and 3) $V = 1 + \mathrm{REL}^{1.1}/432$.

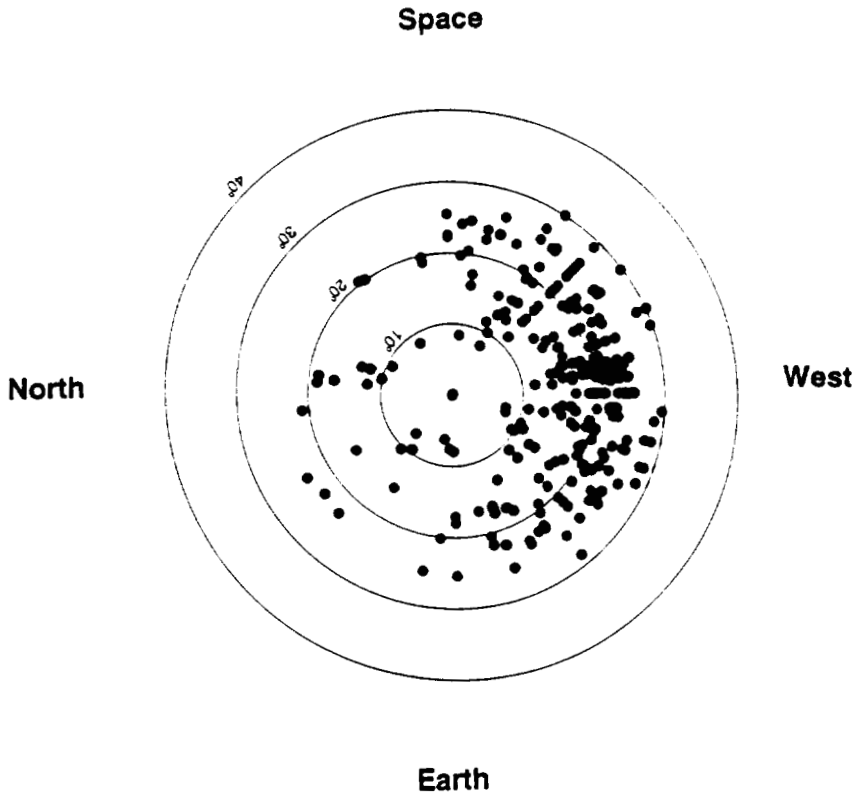

Figure 4: Distribution of arriving directions of stopping protons at 0.6 g/cm^2.

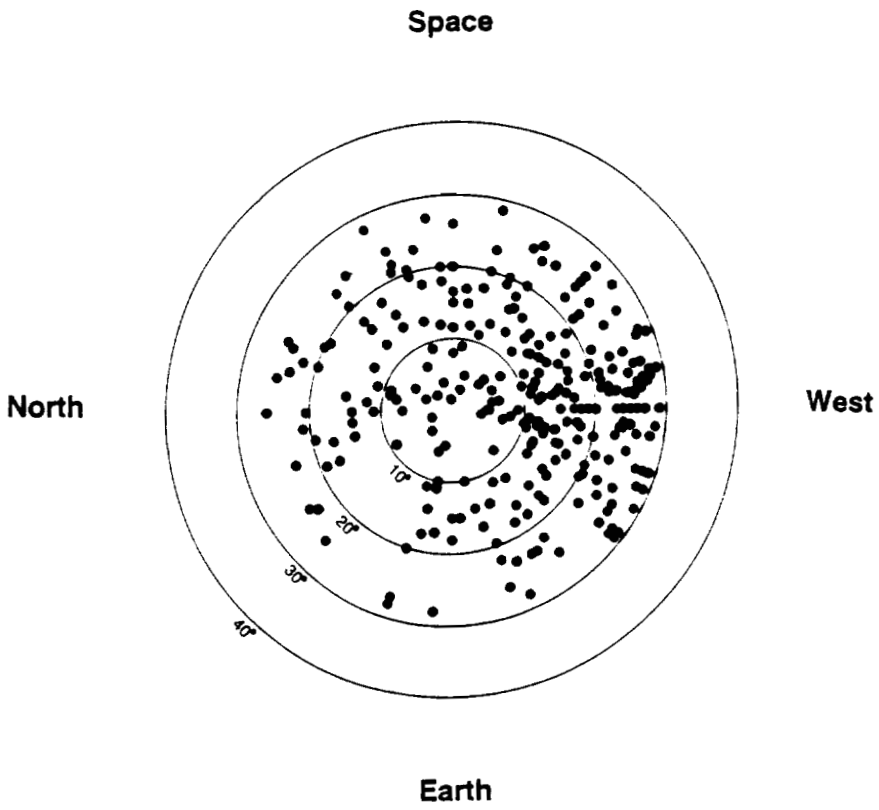

Figure 5: Distribution of arriving directions of stopping protons at 9.5 g/cm^2.

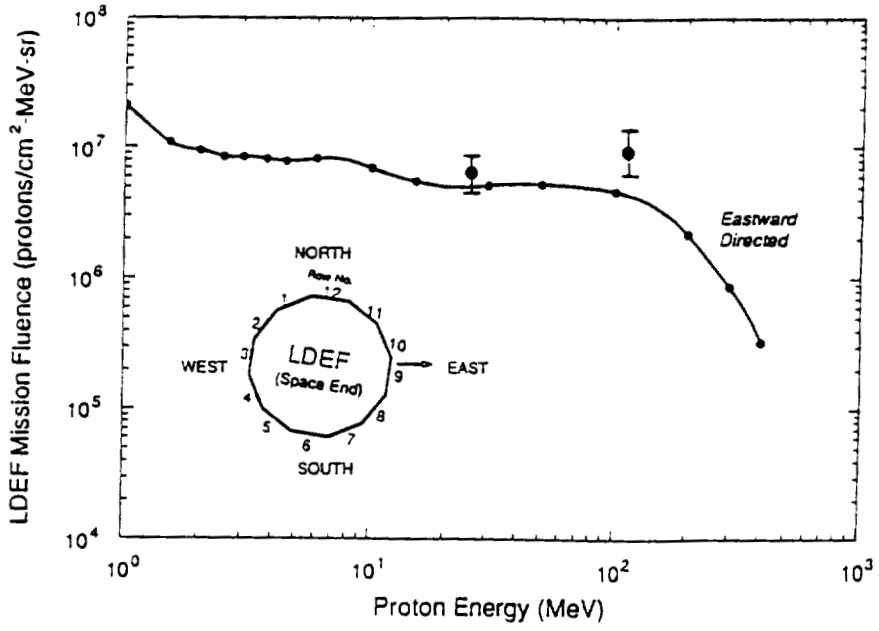

Figure 6: Comparison of calculated LDEF mission fluence of Eastward directed trapped protons (Armstrong and Colborn) with the upper limiting results of measurements.

at 0.6 and 9.5 g/cm^2 depths, respectively. However, not all of these tracks were due to primary protons. The contribution of secondary protons may be significant, especially at the higher shielding depths. On the other hand, not all primary protons reach their stopping points without nuclear interactions. We have estimated the survival probability of a proton to be 97% and 86% for the two shielding depths. Assuming that all tracks are from primary protons and taking into account the survival probability, we estimated an upper limit of the average mission fluence of trapped protons in the selected solid angle intervals. The corresponding energy intervals vary between 24 and 26 MeV for 0.6 g/cm^{2}and between 109 and 118 MeV for 9.5 g/cm^{2}shielding depths as the polar angle varies from 0° to 30°. The estimated average fluences are 6.3×10^6 and 9.2×10^6 tracks/(cm^2·MeV) at the 25 and 114 MeV mean energies. The relative error due to counting statistics of these estimates is about 8%. Significantly larger error (about 25%) may be introduced from the estimation of the thickness of the sensitive layer. We suppose other sources of error are negligible compared to these estimates. The relative error of our experiment is estimated to be about 30%.

Figure 6 shows a comparison of our measurements with model calculations of Armstrong and Colborn[7]. This comparison shows a very good agreement at 25 MeV which may reflect that at the corresponding depth, the contribution of secondary particles is negligible. At 114 MeV. the experimental upper bound is significantly higher than that of the model calculations. This requires further analysis of contribution of secondary protons at this depth. Differences may also come from the fact that (probably) no absolutely identical solid angle intervals were used to measure and calculate fluences. These difficulties in the comparisons would disappear if calculation of directional distribution of stopping proton volume density were available. Concerning the observed high anisotropy of trapped protons, a measurement with better statistical power would also be reasonable for comparison of experimental results with model calculations.

REFERENCES

1. Benton, E. V., Heinrich, W., Parnell, T. A., Armstrong, T. W., Derrickson, J. H., Fishman, G. J., Frank, A. L., Watts, J. W., and Wiegel, B., "Ionizing radiation exposure of LDEF: Pre-recovery estimates." *Nuclear Tracks and Radiation Measurements*, Vol. 20, No. 1 1992, pp. 75-100.

2. Sawyer, D. W., and Vette, J. I., "AP-8 Trapped Proton Environment Model for Solar Maximum and Solar Minimum." National Space Science Data Center, Goddard Space Flight Center, NSSDC/WDC-A-R&S 76-06, December 1976.

3. Csige, I., Benton, E. V., Frigo, L. A., Parnell, T. A., Watts, J. W. Jr., Armstrong, T. W., and Colborn, B. L., "Three-dimensional Shielding Effects on Charged Particle Fluences Measured in the P0006 Experiment on LDEF." *Second LDEF Post-Retrieval Symposium*, NASA CP-3194, Part 1, 1993.

4. Benton, E. V., Csige, I., Oda. K., Henke, R. P., Frank, A. L., Benton, E. R., Frigo, L. A., Parnell, T. A., Watts, J. W. Jr., and Derrickson, J. H., "LET Spectra Measurements of Charged Particles in the P0006 Experiment on LDEF," *Second LDEF Post-Retrieval Symposium*, NASA CP-3194, Part 1, 1993.

5. Somogyi, G., "Development of Etch Nuclear Tracks," *Nucl. Inst. and Meth.* Vol. 173 pp. 21-42, 1980.

6. Henke, R. P., and Benton, E. V., "On Geometry of Tracks in Dielectric Nuclear Track Detectors," *Nucl. Inst. and Meth.* Vol. 97 pp. 483-489, 1971.

7. Armstrong, T. W., and Colborn, B. L. "Radiation Model Predictions and Validation Using LDEF DATA." *Second LDEF Post-Retrieval Symposium*, NASA CP-3194, Part 1, 1993.

CONTRIBUTION OF PROTON-INDUCED SHORT RANGE SECONDARIES TO THE LET SPECTRA ON LDEF*

E. R. Benton, I. Csige, E. V. Benton and L. A. Frigo
Eril Research, Inc.
P. O. Box 150788
San Rafael, CA 94915-0788 U.S.A.

SUMMARY

The contribution to the LET spectrum from proton-induced short range secondaries was investigated by making measurements of total track density and LET spectra in CR-39 Plastic Nuclear Track Detectors (PNTDs) at varying shielding depths in the A0015 West-side stack. Proton-induced short range secondaries were found to make a significant contribution to the LET spectra, especially in the region above 100 keV/μm. At present, calculational models do not include this component.

Total track density was measured at five shielding depths and was seen to increase as a function of shielding. LET spectra were measured under two shielding depths (2.6 and 9.2 g/cm^2) and stayed fairly constant as a function of shielding. Prerecovery estimates of LET spectra dropped off rapidly in the 100-300 keV/μm region, while the measured LET spectra extended to higher LETs. Track density and LET spectra measurements of secondaries were made in a CR-39 PNTD stack exposed to 154 MeV accelerator protons. Similarities in LET spectra measured in the A0015 experiment and in the 154 MeV accelerator proton stack demonstrate that a useful first step in modeling the contribution to the LET spectra of secondaries induced by the spectrum of trapped protons would be to model a mono-energetic proton beam being transported through a one-dimensional geometry.

INTRODUCTION

Space radiation models for low Earth orbit are based in large part on the assumption that most of the total dose absorbed from the trapped proton environment is from primary particles and that the contribution of secondaries to the total absorbed dose is of lesser importance[1,2]. However, as the flux of primary trapped protons penetrates the shielding of a spacecraft, the cross section for the production of secondaries increases as the energy of the primary protons is attenuated. Thus, it is possible that the contribution of secondaries to the total dose is of greater importance than has been previously considered. Little work has been done in the past to either measure or model the contribution of secondaries to the

*Work supported by NASA Contract No. NAS8-38610, Marshall Space Flight Center, Huntsville, AL 35812

LET spectrum. An attempt was made by Benton *et al.*[3] in connection with ionizing radiation measurements made aboard Biosatellite III. One reason why this component is usually neglected in computer-based models is the complexity of the problem. To accurately model the contribution of secondaries, one must propagate the entire proton energy spectrum incident upon the spacecraft in three dimensions through the known thickness and composition of shielding, taking into account the cross-sections of all possible interactions.

To investigate the contribution of secondaries to the LET spectrum, total track density and LET spectra were measured in CR-39 PNTDs as a function of shielding depth in the LDEF A0015 West-side stack. Due to restrictions imposed by detector processing and analysis, LET spectra could only be accurately measured for tracks from particles with ranges >16 μm. Total track density measurements included all recognizable tracks, including those from particles with range <16 μm, as is the case for many proton induced secondaries. LET spectrum and total track density measurements were carried out for a ground-based experiment in which a stack of CR-39 PNTDs similar to that of the A0015 experiment was exposed to a fluence of 154 MeV protons similar to that estimated for the West-side of LDEF. Since the LET of 154 MeV protons is below the threshold of track registration in CR-39, it was known that all tracks visible in the ground based experiment were the result of secondary particles. The ground based measurements compared favorably to those measurements made in the A0015 stack in terms of both LET spectra and total track density as functions of shielding depth.

EXPERIMENT

The A0015 West-side stack consisted of a variety of passive radiation detectors interspersed with layers of aluminum absorber. It was located in tray C2 on the West (trailing) side of LDEF. Figure 1 shows the position of the A0015 West-side stack on LDEF. Figure 2 illustrates the configuration of detectors in the A0015 West-side stack. Due to the fixed orientation of the LDEF relative to the Earth and the location of the A0015 experiment, the PNTD layers in the West-side stack were oriented normal to the beam of incoming trapped protons arriving from the West. The total shielding thickness of the A0015 stack was $\sim$11.9 g/cm^2. The stack was kept at $\sim$1 atm. pressure during the mission. The CR-39 layers were processed in a bath of 6.25 N NaOH at 50°C for 36 hr. A thickness of $\sim$8 μm was removed from each detector surface.

As a preliminary study to the measurement of LET spectra at different shielding depths in the A0015 stack, total track density (total number of particle tracks per unit area) was counted at five shielding depths. Track density was counted in single layers of CR-39 PNTD. Track selection criteria for counting included both conical and round (stopping) tracks. Spherical etch pits, which could have been produced by either particles or defects in the PNTD material, were not counted. All tracks from particles of range down to $\sim$1 μm were counted. The CR-39 detector layers were 7×7 cm^2 in area. Track density was counted in a 13×13 array. Each field of view was separated by 5 mm. The area of each field of view was 0.0018 cm^2.

A ground-based experiment consisting of a thick stack of CR-39 PNTDs interspersed with layers of

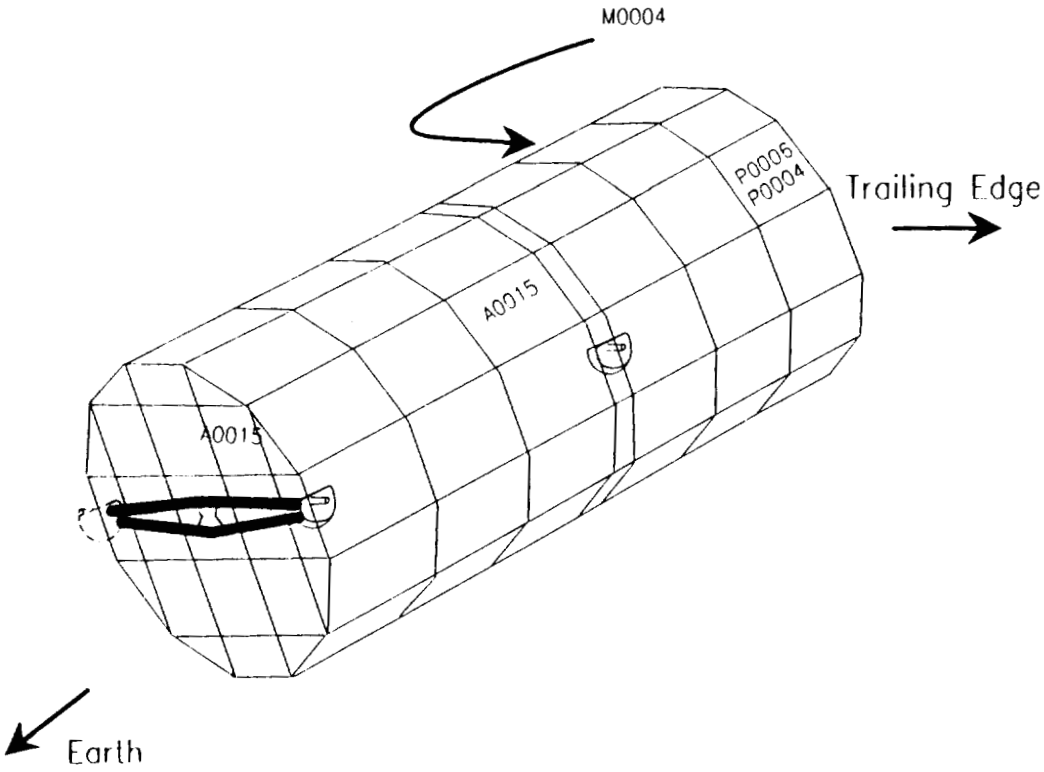

Figure 1: Location of the A0015 West-side stack on LDEF.

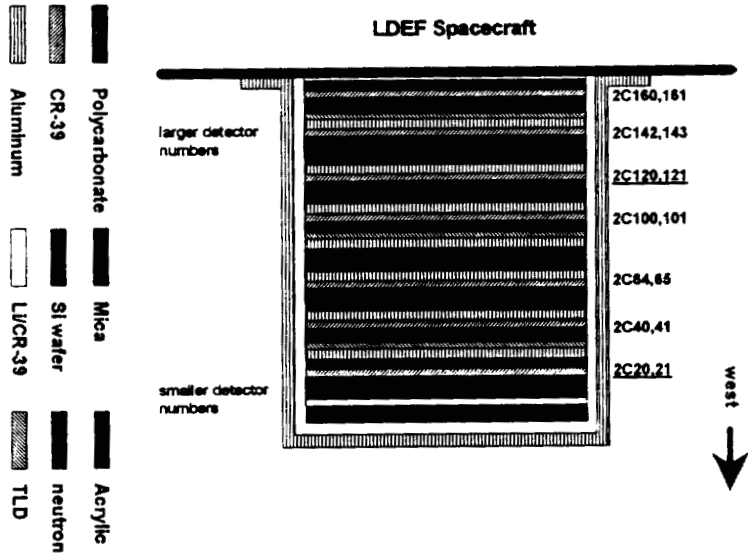

Figure 2: Configuration of detectors inside the A0015 West-side stack.

Al absorber was exposed to 154 MeV protons at the Harvard Cyclotron. Protons of this energy are close to the peak energy of the trapped proton energy spectrum[2]. The stack was exposed to ~10 rads or $\sim 10^8$ protons/cm^2. The stack was oriented normal to the incident proton beam. The range of 154 MeV protons in Al is ~21 g/cm^2. Under the lesser shielding depth in which the track densities were counted in the A0015 stack, 154 MeV protons cannot form visible tracks since their LET is below the threshold for track registration. Hence all tracks seen under this shielding are the result of secondary particles. These tracks are from elastic and inelastic collisions between the primary protons and hydrogen, carbon and oxygen nuclei of the stopping material. After ~18 g/cm^2 of shielding, the proton energy has attenuated sufficiently to allow formation of tracks from the primary protons. However, 18 g/cm^2 is well in excess of the 11.9 g/cm^2 shielding of the A0015 West-side stack. The CR-39 PNTDs from the 154 MeV proton experiment were processed and readout in the same manner as those from the LDEF experiment.

LET spectra were measured under two shielding depths of the A0015 West-side stack, 2.6 and 9.2 g/cm^2, and under three shielding depths in the 154 MeV proton stack, 2.9, 8.5 and 14.4 g/cm^2. Tracks were selected for measurement using the coincident pair method; two adjacent layers of CR-39 were processed and then reassembled into the experiment configuration. Particle events were selected for measurement if a pair of companion tracks were found on the middle adjacent surfaces and only conical tracks were measured. This insured that all the particle events had been formed during the period encompassing the experiment. Since the amount of material removed from each surface (bulk etch) was ~8 μm, all measured events, both primary and secondary, are from particles of range >16 μm.

The standard method used by this laboratory to reduce particle track data into LET spectra involves the assumption that the flux of particles is isotropic. For both the A0015 and the 154 MeV proton experiments, this was not the case. The beam of protons was incident normal to the surface of the CR-39 PNTDs for the ground-based exposure while there was a preferred direction of arrival from the West, nearly normal to the detector surface, for the A0015 West-side stack. While it might be argued that isotropy is still valid in the case of inelastic collisions, there is a directional dependence, based on the directionality of the primary protons, for elastic collisions. Instead of generating integral LET spectrum based on the assumption of isotropy, the track data was reduced in such a way as to yield the average differential LET spectra for a given solid angle. A solid angle of 20° normal to the detector surface was chosen. This angle was a compromise between a small angle, which is better from the point of view of detector efficiency, and an angle large enough to measure enough tracks for good statistics. Measured tracks that did not fall within this acceptance angle were rejected.

LET spectrum data was collected by measuring the major and minor axes of 300 track pairs in each detector. These track parameters, along with the bulk etch, were then transformed into LET values by a calibration function. For the detectors on the A0015 West-side stack, an additional 50 long range events were measured. Long range events are from particles which left tracks on each of the four surfaces of the reassembled detector pair. These events are considered to be from relativistic Fe and were used as part of an internal calibration. They were not included in the LET spectra.

RESULTS

The track density measurements for the A0015 experiment were plotted as a function of x-y coordinates to produce track density profiles. Figure 3 shows the profiles for each of the five layers counted. Shielding depth of each counted layer is to the left of the corresponding profile. While there appears to be little discernible structure in the total track density as a function of x-y position on the detector surface, total track density is seen to increase as a function of shielding. The track density on the frontside of the CR-39 detector under 2.6 g/cm^2 shielding was 1.08 $\times$ 10^5 tracks/cm^2. This increased to 1.62 $\times$ 10^5 tracks/cm^2 under 11.9 g/cm^2. Total track density measurements were also made on the backside surface of each detector. The backside of the 2.6 g/cm^2 detector had a track density of 1.09 $\times$ 10^5 tracks/cm^2. Under 11.9 g/cm^2, the total track density was 1.38 $\times$ 10^5 tracks/cm^2 on the backside. Figure 4 shows track density as a function of shielding for the A0015 West-side stack CR-39 PNTDs.

Figure 4 also shows track density as a function of shielding as measured in the CR-39/Al stack exposed to 154 MeV protons. Track density was normalized to the A0015 2.6 g/cm^2 track density. Track density is also seen to increase as a function of shielding until the stopping point for 154 MeV protons at ~21 g/cm^2. Between ~18 and ~22 g/cm^2 shielding, the CR-39 detectors were saturated with tracks making it impossible to accurately count the total track density in this region. However, in the region below 11.9 g/cm^2, the total shielding thickness of the A0015 West-side stack, the LET of the protons is below that for the registration of latent tracks. All tracks seen in this region are the result of secondaries produced by interactions with the 154 MeV primary protons. Total track density increases from an absolute value of 6.69 $\times$ 10^5 and a normalized value of 1.07 $\times$ 10^5 tracks/cm^2 under 2.9 g/cm^2 to an absolute track density of 8.26 $\times$ 10^5 and a normalized track density of 1.32 $\times$ 10^5 tracks/cm^2 under 11.41 g/cm^2. The curve showing the increase in total track density for the 154 MeV proton exposure is similar to those from the A0015 experiment, especially on the back surfaces of the A0015 detectors, for shielding below 11.9 g/cm^2. Since it is known that the tracks in the 154 MeV proton detectors are from secondaries, the similarity between the 154 MeV proton and LDEF curves confirms that a significant fraction of the tracks being counted in the LDEF detectors are the result of secondaries.

Figure 5 is a comparison of the total track density measurements and measured doses from TLDs as functions of shielding depth in the A0015 West-side stack. The TLD dose is seen to decrease with depth, reflecting the attenuation of lower LET particles as a function of shielding. These lower LET particles do not register as tracks in CR-39 PNTDs. Track density increases as a function of shielding due to the contribution of higher LET secondaries.

Differential LET fluence spectra were measured under two shielding depths, 2.6 and 9.2 g/cm^2, of the A0015 West-side stack, and under three shielding depths, 2.9, 8.5, and 14.4 g/cm^2, in the 154 MeV proton stack. Figure 6 is the differential LET fluence spectra measured in the A0015 West-side stack under 2.6 g/cm^2 and is plotted with error bars. Similar errors were calculated for the other four spectra. Note that the y-axis is a logarithmic scale, so while the error appears to decrease with increasing fluence, it is actually increasing. Figure 7 shows the differential LET spectra measured in the A0015 West-side stack under 2.6 and 9.2 g/cm^2. There is close agreement between the two A0015 LDEF curves within the

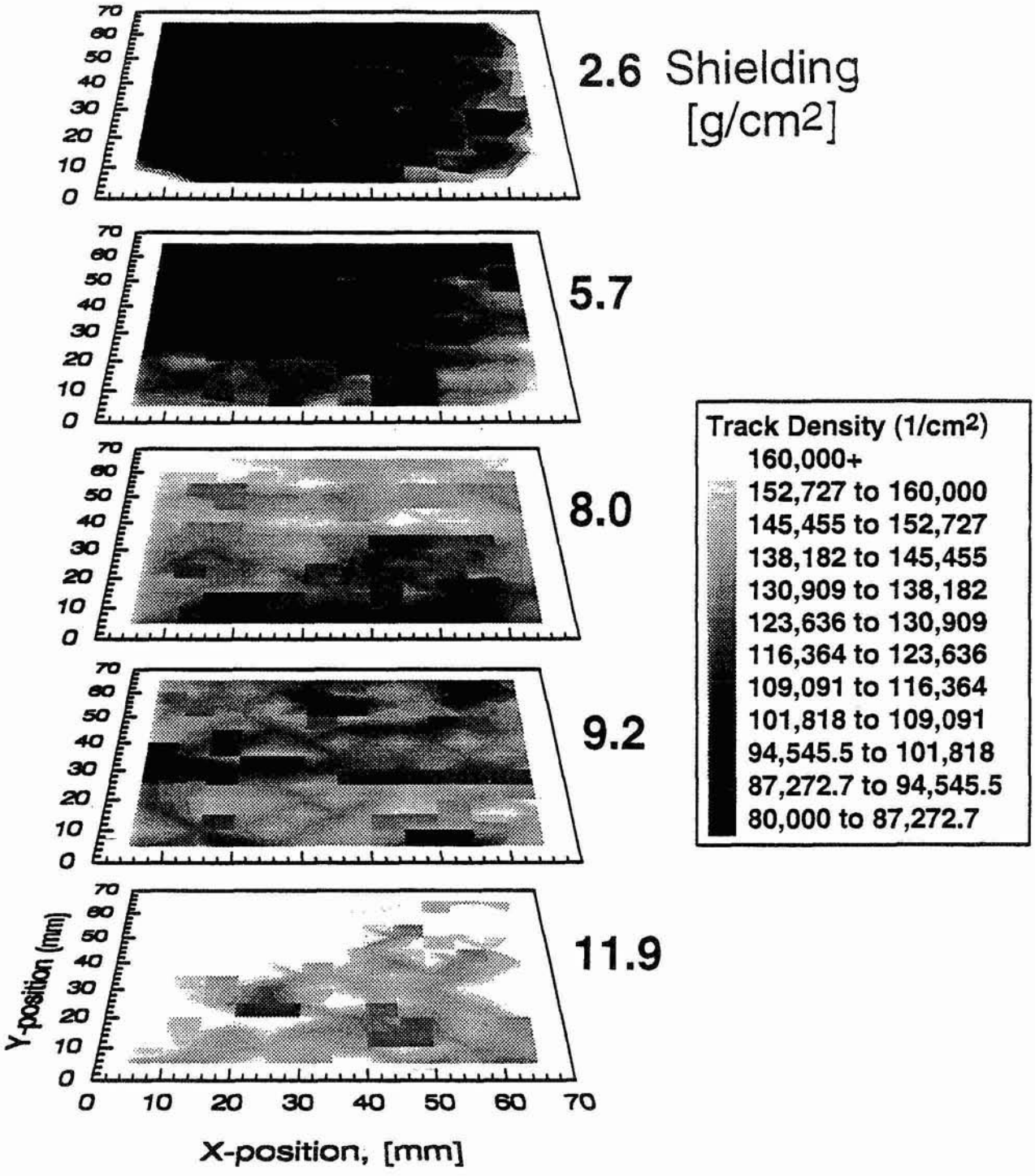

Figure 3: Total track density plots under five shielding depths for the A0015 West-side stack. Track density is seen to increase with greater shielding.

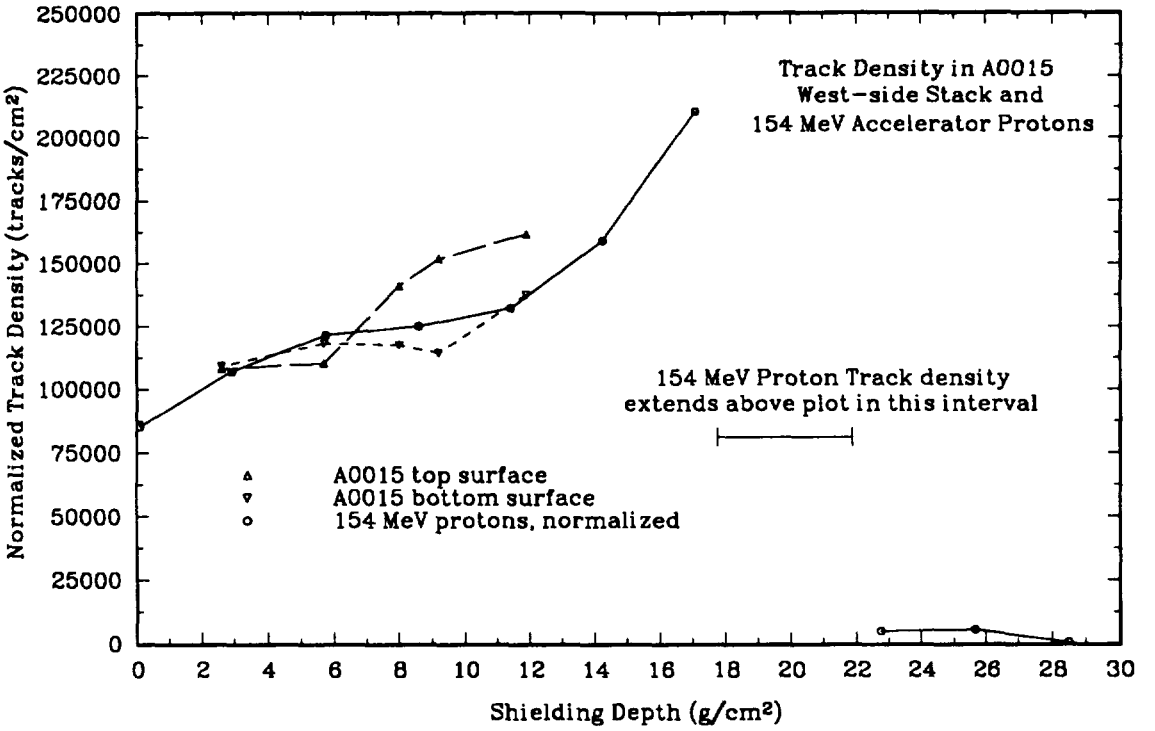

Figure 4: Total track density as a function of shielding depth for the front and back surfaces of the A0015 West-side stack detectors and the front surfaces of the 154 MeV proton detectors. The track density counted in the 154 MeV proton detectors is normalized to the A0015 results under 2.6 g/cm^2.

limits of error. At lower LETs (below 100 keV/μm) much of the spectra is made up of secondaries from elastic proton-proton collisions. Tracks from elastic and inelastic collisions between primary trapped protons and carbon and oxygen nuclei of the stopping material have higher LETs and contribute only to the right-most portion of the spectrum.

Figure 8 shows the differential LET spectra measured under 2.9, 8.5 and 14.4 g/cm^2 in the 154 MeV proton stack. The slopes of the 154 MeV proton curves are similar to those measured in the LDEF detectors, showing that a significant number of the tracks counted in the LDEF detectors are the result of secondaries. Although the three curves lie close together, the fluence increases with shielding depth, presumably because of the increase in cross-section with decreasing primary proton energy. The two sets of curves, A0015 West-side detectors and 154 MeV proton detectors, at similar shielding depths lie close together. The slopes are similar, especially for LET_{∞}·H_2O<100 keV/μm, the region dominated by elastic recoils. At higher LET, there appears to be a larger number of inelastic secondaries in the LDEF detectors. This result might be due to the fact that LDEF was exposed to the full spectrum of trapped proton energies and not to just one mono-energetic proton beam.

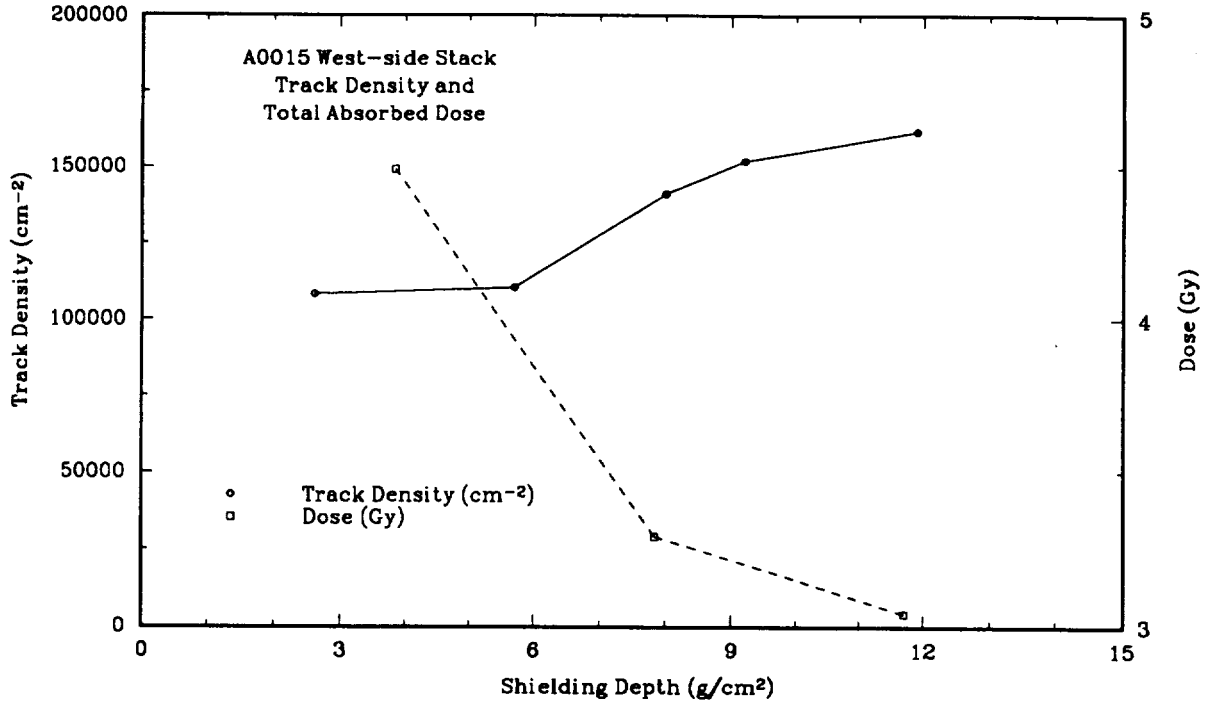

Figure 5: Comparison of total track density measurements with total absorbed dose measurements as a function of shielding for the A0015 West-side stack.

DISCUSSION AND CONCLUSIONS

As had been suggested in earlier work[3], proton-induced, short range secondaries were found to make a significant contribution to the LET spectra. The similarity in slopes between the differential LET spectra measured in the LDEF A0015 West-side detectors and the CR-39 PNTD stack exposed to 154 MeV accelerator protons normally incident to the detector surface supports the conclusion that a substantial fraction of the tracks seen in the LDEF detectors are the result of secondaries. An increase in track density as a function of shielding depth was measured and can be explained by an increase in the cross section for the production of secondaries as the primary proton energy is attenuated. A pronounced increase in fluence as a function of shielding depth was not seen in the differential LET spectra. This is due to the difference in track selection criteria between the two types of measurements. The total track density measurements included all tracks from particles with a range greater than ~ 1 μm while the differential LET spectra measurements consisted of all tracks from particles with range >16 μm. This indicates that the number of short range secondaries increased more rapidly than the number of longer range secondaries as a function of shielding.

Figure 9 is a comparison between the LET flux spectrum measured under 2.6 g/cm^2 in the A0015 West-side stack and model LET spectra under 1.0 and 5.0 g/cm^2 calculated by the CREME code for galactic cosmic rays (GCRs) at the LDEF orbit[1]. In this orbit the particle fluxes are dominated by trapped protons, but a small contribution by GCRs is present. The measured spectrum has been reduced

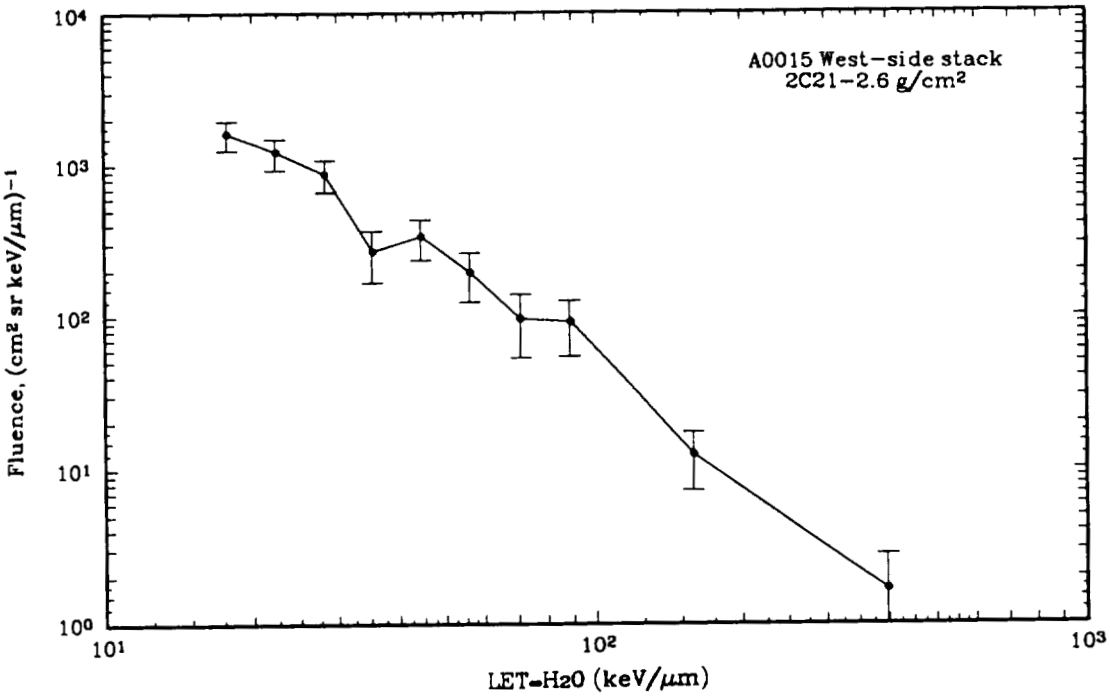

Figure 6: Differential LET fluence spectrum, including error bars, measured in CR-39 under 2.6 g/cm^2 in the A0015 West-side stack.

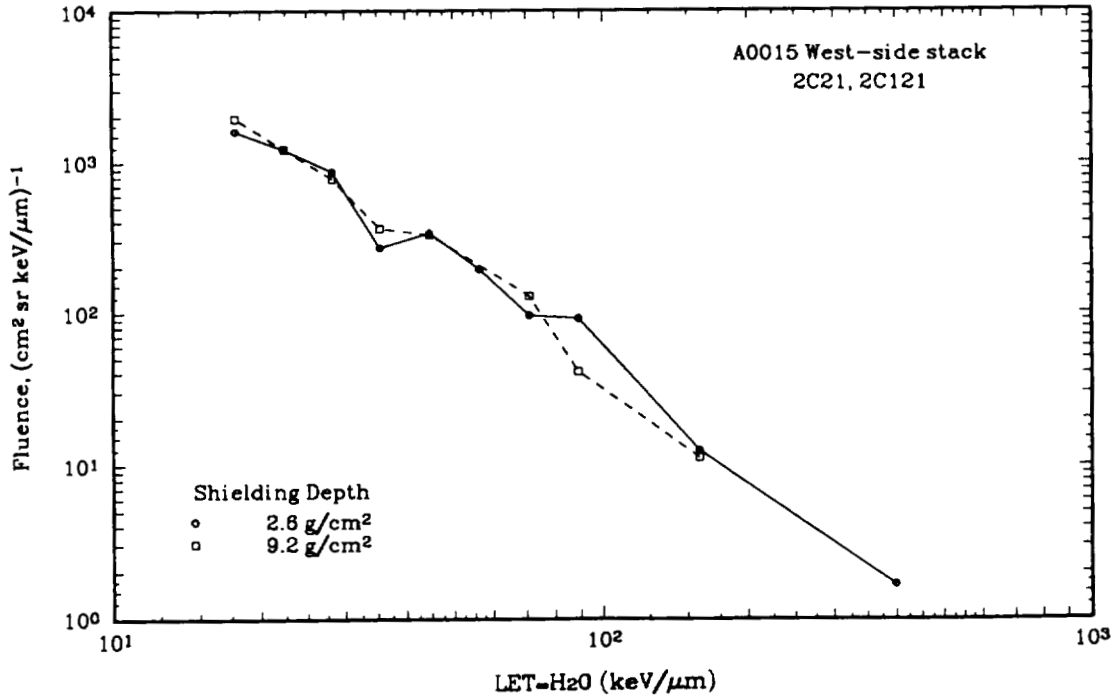

Figure 7: Differential LET fluence spectrum measured in CR-39 under 2.6 and 9.2 g/cm^2 in the A0015 West-side stack.

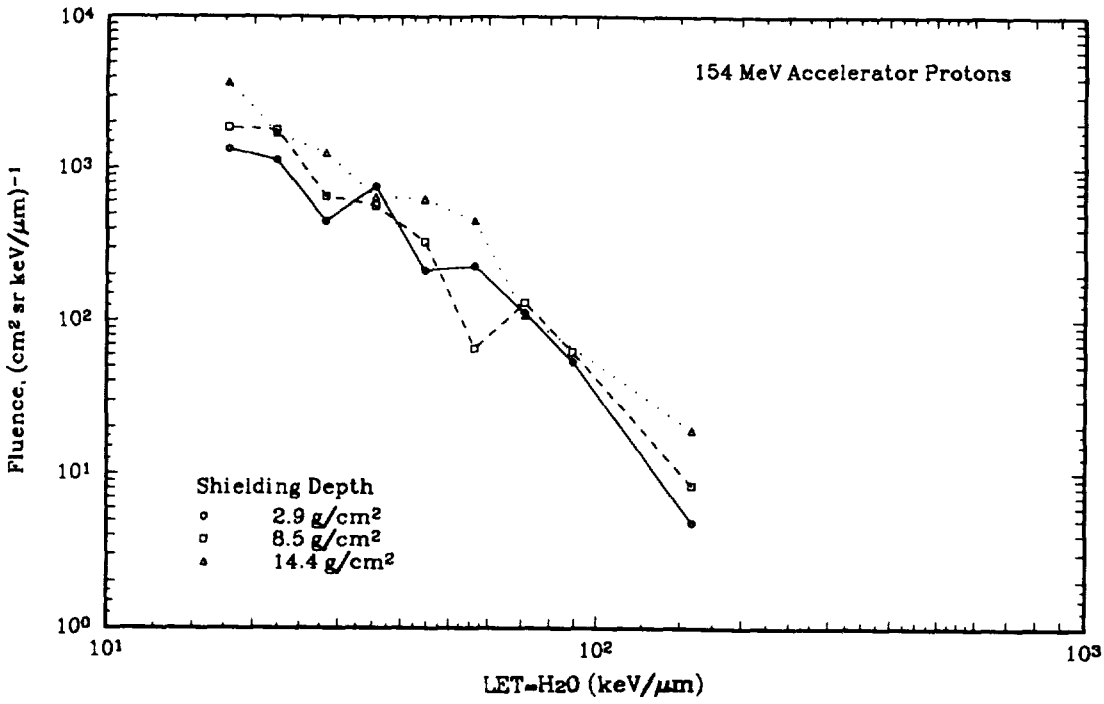

Figure 8: Differential LET fluence spectrum in CR-39 PNTDs under 2.9, 8.5, and 14.4 g/cm^2 for a 154 MeV proton exposure.

by a factor of 4π for a comparison of slopes with the CREME calculations. Both calculated curves drop off between 100 and 300 keV/μm due to the geomagnetic cut-off of Fe. The measured LET spectra extend beyond this drop, illustrating the contribution of high LET short-range secondaries to the LET spectrum.

Previous modeling efforts have not included the contribution of secondaries to the LET spectrum[1]. To accurately model the LET spectra of LDEF, the spectrum of trapped proton energies must be transported through the geometry of the spacecraft shielding while the probability of producing elastic and inelastic secondaries is calculated. The similarities in LET spectra measured in LDEF detectors and those measured for a mono-energetic proton beam and the greater simplicity of modeling such a proton beam through a one-dimensional geometry suggest that measurements and modeling of secondaries from mono-energetic proton beams are potentially useful in incorporating the proton-induced secondary component into LET spectra calculations.

REFERENCES

1. Benton, E. V., Heinrich, W., Parnell, T. A., Armstrong, T. W., Derrickson, J. H., Fishman, G. J., Frank, A. L., Watts, J. W., and Wiegel, B., "Ionizing radiation exposure of LDEF: Pre-recovery estimates." *Nuclear Tracks and Radiation Measurements*, Vol. 20, No. 1 1992, pp. 75-100.

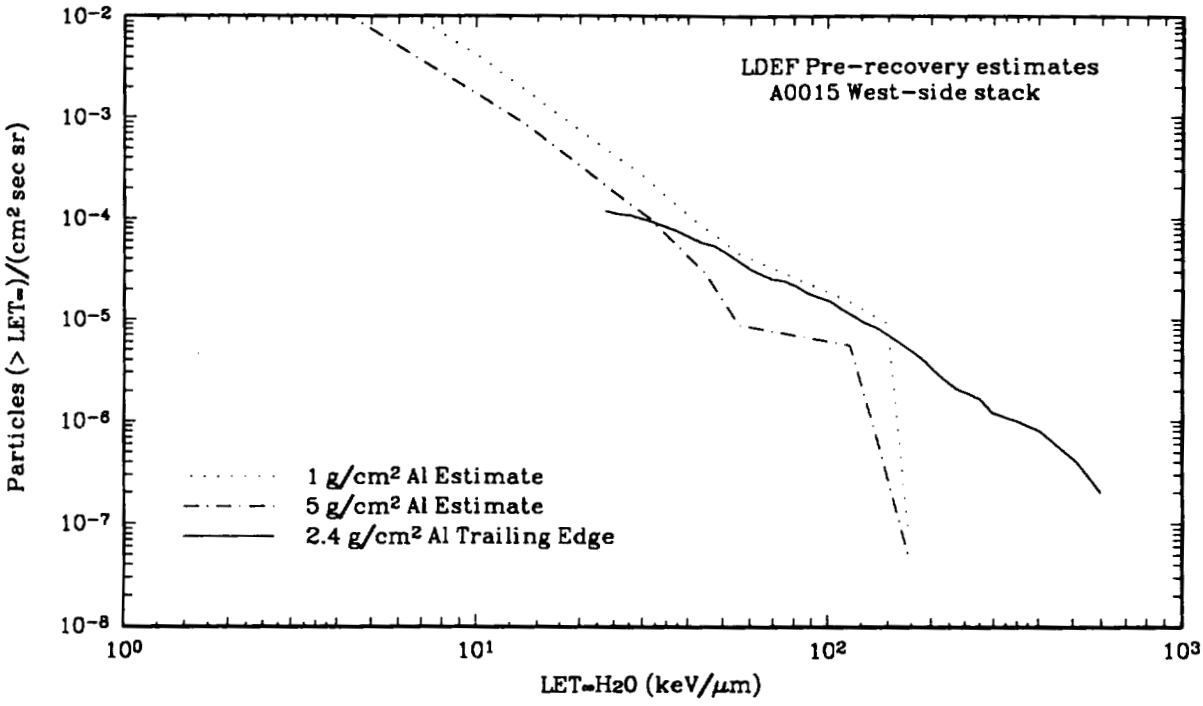

Figure 9: Comparison of measured and calculated LET flux spectra. The measured spectra has been reduced using the assumption of isotropic flux.

2. Armstrong, T. W., and Colborn, B. L. "Radiation Model Predictions and Validation Using LDEF DATA." *Second LDEF Post-Retrieval Symposium*, NASA CP-3194, Part 1, 1993.

3. Benton, E. V., Curtis, S. B., Henke, R. P., and Tobias, C. A. "Comparison of Measured and Calculated High-LET Nuclear Recoil Particle Exposure on Biosatellite III." *Health Physics*, Vol. 23, 1972, pp. 149-157.

CHARGE, ENERGY AND LET SPECTRA OF HIGH LET PRIMARY AND SECONDARY PARTICLES IN CR-39 PLASTIC NUCLEAR TRACK DETECTORS OF THE P0006 EXPERIMENT*

I. Csige, L.A. Frigo, and E.V. Benton
Physics Research Laboratory
University of San Francisco
San Francisco, CA 94117-1080 USA

K. Oda
Department of Nuclear Engineering
Kobe University of Mercantile Marine
Higashinada-ku, Kobe 658, Japan

ABSTRACT

We have measured the charge, energy and linear energy transfer (LET) spectra of about 800 high LET (LET_{∞}·H_2O > 50keV/μm) particles in CR-39 plastic nuclear track detectors in the P0006 experiment of LDEF. Primary particles with residual range at the reference surface greater than about 2 microns and secondary particles produced in the detector material with total range greater than about 4 microns were measured. We have used a multi-etch technique and an internal calibration to identify and measure the energy of the particles at the reference surface. The LET spectrum was obtained from the charge and energy distribution of the particles.

*Work supported by NASA--Marshall Space Flight Center, Huntsville, Alabama

PREDICTIONS OF LET SPECTRA MEASURED ON LDEF

T. W. Armstrong and B. L. Colborn
Science Applications International Corporation[1]
Route 2, Prospect, TN 38477
Phone: 615/468-2603, Fax: 615/468-2676

E. V. Benton
Physics Research Laboratory, University of San Francisco[1]
2130 Fulton St., San Francisco, CA 94117-1080
Phone: 415/666-6281, Fax: 415/666/2469

ABSTRACT

The linear energy transfer (LET) spectra measured by plastic (CR-39) detectors in Exp. P0006 on LDEF are much higher at high LET than expected from methods commonly used to predict LET spectra produced by the space ionizing radiation environment. This discrepancy is being investigated by examining modeling approximations used in the predictions, and some interim results are presented.

INTRODUCTION

The P0006 Experiment on LDEF (ref. 1) contained plastic detectors (CR-39) for measuring linear energy transfer (LET) spectra. Analyses of these data reported to date, Benton, et al. (ref. 2), show observed spectra that are quite different than expected from commonly-used LET prediction methods. Since LET spectra are fundamental in predicting a variety of radiation effects of practical importance (e.g., biological damage, electronics upsets) in spacecraft and mission design, it is important to investigate the reason for this discrepancy, and reported here are some interim results of such work.

The problem addressed is illustrated by Fig. 1. Shown here is the measured LET spectrum (ref. 2) in one of the CR-39 sheets located 6.5 g/cm^2 from the space end of the main detector stack in the P0006 experiment. Also shown is a pre-recovery LET prediction made by Derrickson (ref. 3) using the NRL CREME code of Adams (ref. 4), which is commonly used for predicting LET spectra in performing assessments of space radiation effects on microelectronics. Since this pre-recovery prediction was of a scoping nature to obtain a quick estimate, several approximations were involved -- e.g.: (a) the spacecraft and detector shielding is approximated as an aluminum sphere, (b) the calculated LET spectra are for silicon, whereas the CR-39 data have been converted to LET in water, (c) the calculated spectra are for the space environment at the LDEF insertion altitude and not averaged over the LDEF mission, and (d) the calculation neglects the effects of secondary particles created in the detector and spacecraft, including both "projectile fragments" (secondaries from the breakup of incident ions during nuclear collisions) and "target fragments" (residual nuclei and secondary particles from collisions with detector material nuclei). Discussed below are calculations which remove some (but not all) of the approximations in the pre-recovery LET predictions.

[1]Work supported by NASA Marshall Space Flight Center, Huntsville, Alabama

LET PREDICTIONS

Shielding Effects

Since a detailed 3-D mass model of the LDEF spacecraft, experiment tray F2 contents containing the P0006 experiment, and the P0006 detector stack has been developed (ref. 5) for LDEF radiation analyses, the effects of shielding on the LET spectra predictions can be treated accurately. Therefore, the LET spectrum at a point in the center of the CR-39 layer corresponding to the location of the measured spectrum has been calculated using the LDEF 3-D shielding model. Radiation transport calculations were made for shielding in each of 720 solid angle bins around the detector point. A simplified representation of the shielding distribution is shown in Fig. 2. The transport calculations along each shielding direction were made using the Burrell transport code (ref. 6) for incident trapped protons and the CREME code (ref. 4) for galactic protons and heavy ions. The LDEF exposure to trapped protons predicted by Watts, et al. (ref. 7) was used, which takes into account the trapped proton anisotropy as well as altitude and solar cycle variations during the LDEF mission. Incident galactic cosmic ray spectra for the LDEF orbit were calculated using the CREME code. Average galactic spectra over LDEF altitude and solar cycle variations were computed, but the average results are not significantly different from the solar minimum spectra at the LDEF insertion altitude assumed in the pre-recovery predictions, as illustrated in Fig. 3 for protons. The LET spectrum in water is calculated to correspond to the data, as opposed to LET in silicon for the pre-recovery prediction of Fig. 1.

Results from this calculation are compared with measurements in Fig. 4. There is some improvement compared to Fig. 1 when shielding effects are taken into account, but the large difference for the high-LET "tail" ($\geq$ 1500 MeV $\cdot$ cm^2/g) still exists. The difference at low LET ($\leq$300 MeV $\cdot$ cm^2/g) is understandable because of the inherent insensitivity of CR-39 at low LET and because of the particular etching process used. Thus, the CR-39 has very low detection efficiency for trapped protons. This is illustrated in Fig. 5, which is the same as Fig. 4 but indicates the predicted trapped proton and galactic components.

SEP Iron Contribution

From measurements made by the HIIS experiment of Adams, et al. on LDEF, it was found that the large solar energetic particle (SEP) events during Oct. 1989 made a large contribution to the observed iron spectra in the energy range from $\approx$ 200-800 MeV/nucleon (ref. 8). Since iron $\geq$ 350 MeV/n can penetrate the 6.5 g/cm^2 minimum shielding of the CR-39 layer of interest in Exp. P0006, and since the LET calculations above neglect SEP events, we have checked the contribution of SEP iron to the LET.

These calculations were made by modifying the CREME code to incorporate the Fe spectra measured by HIIS on LDEF. LET spectra are compared in Fig. 6 with and without the SEP iron included. These results show that SEP iron makes some contribution at high LET, but not nearly enough to account for the predicted vs. observed discrepancy in Exp. P0006.

Contribution of Heavy Ion Fragmentation

To check the contribution at high LET from secondary particles generated when incident heavy ions breakup into lower-Z ions due to nuclear collisions, the UPROP code of Letaw (ref. 9) was used. This code accounts for the production and subsequent transport of all secondary particles from ion breakup in nuclear collisions. The results of this calculation (made for a spherical aluminum shield) show that, even for the case of rather thick shielding (50 g/cm^2), the secondaries from ion fragmentation do not significantly increase the LET spectrum (Fig. 7).

SUMMARY

The LET calculations described above remove some of the approximations made in initial, pre-recovery predictions, but they do not explain the large difference at high LET between predictions and measured spectra for Exp. P0006. The calculations to date have not taken into account target nuclei fragments and elastic recoils from nuclear collisions produced by trapped protons, which is suspected as being the most likely cause of the large underprediction at high LET.

To account for the effects of nuclear interaction products from trapped proton collisions with the CR-39 constituents, a more detailed radiation transport calculation is required than possible with the codes used for the above predictions. A calculational approach for accurately simulating the CR-39 measurements is under development, but results are not yet available. The approach consists of two steps in the radiation transport: First, the trapped proton flux in the detector is computed using a standard proton transport code (e.g., ref. 6) and the 3-D LDEF spacecraft/detector model. This procedure, which has been used extensively for dose and activation predictions to compare with LDEF data (e.g., ref. 10), takes into account the trapped proton directionality and accurately treats shielding effects. In the second step, the proton flux in the CR-39 layer is used as the source for a 3-D Monte Carlo transport within the dosimeter. A modified version of the HETC code (ref. 11) can be used for the Monte Carlo calculation to take into account the production and transport of nuclear recoils and secondary particles in the detector region.

REFERENCES

1. Benton, Eugene V. and Parnell, Thomas A.: Linear Energy Transfer Spectrum Measurement Experiment (P0006): in The Long Duration Exposure Facility (LDEF) Mission 1 Experiments, Clark, Lenwood G. et al. (Eds), NASA SP-473, 1984.

2. Benton, E. V.; Csige, I.; Oda, K.; Henke, R. P.; Frank, A. L.; Benton, E. R.; Frigo, L.A.; Parnell, T. A.; Watts, J. W., Jr. and Derrickson, J. H.: LET Spectra Measurements of Charged Particles in the P0006 Experiment on LDEF, Second LDEF Post-Retrieval Symposium, NASA CP-3194, 1993.

3. Derrickson, J. H.: Linear Energy Transfer for the LDEF Mission: in Ionizing Radiation Exposure of LDEF (Pre-Recovery Estimates), E. V. Benton, et al. (Eds), *Nucl. Tracks Radiat. Meas.* 20, No. 1, 75 (1992).

4. Adams, James H., Jr.: Cosmic Ray Effects on Microelectronics, Part IV. NRL Memorandum Report 5901, December 1986.

5. Colborn, B. L. and Armstrong, T. W.: Development and Application of a 3-D Geometry/Mass Model for LDEF Satellite Ionizing Radiation Assessments. Second LDEF Post-Retrieval Symposium, NASA CP-3194, 1993.

6. Burrell, M.O.: The Calculation of Proton Penetration and Dose Rates. George C. Marshall Space Flight Center, Huntsville, AL., NASA TM X-53063, August 1964.

7. Watts, J. W., Jr.; Armstrong, T. W. and Colborn, B. L.: Revised Predictions of LDEF Exposure to Trapped Protons. Second LDEF Post-Retrieval Symposium, NASA CP-3194, 1993.

8. Adams, J. H., Jr.; Beahm, L. P.; Boberg, P. R.; Kleis, T. and Tylka, A. J.: HIIS Observations During the Large Energetic Particle Events of October 1989 (preprint).

9. Letaw, John R.: UPROP: A Heavy-Ion Propagation Code. Severn Communications Corp. Report SCC 89-02, August 1989.

10. Armstrong, T. W.; Colborn, B. L.; Harmon, B. A.; Parnell, T. A.; Watts, J. W., Jr. and Benton, E. V.: Comparison of Model Predictions with LDEF Satellite Radiation Measurements. *Adv. Space Res.* 14, No. 10, 17 (1994).

11. Armstrong, T. W. and Colborn, B. L.: A Thick-Target Radiation Transport Code for Low-Mass Heavy Ion Beams, HETC/LHI. *Nucl. Instr. Meth.* 169, 161 (1980).

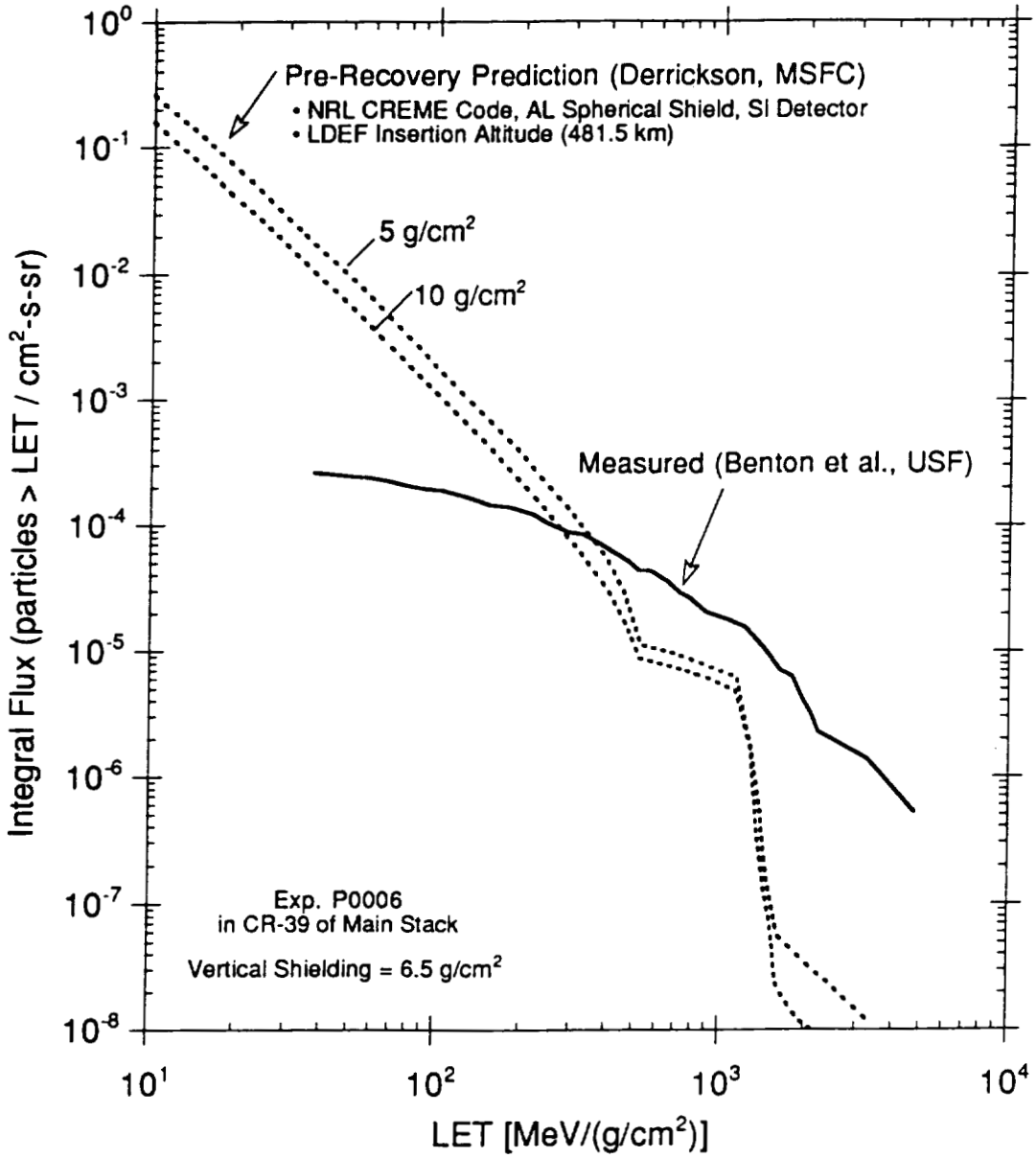

Fig. 1. Comparison of LET spectra measured (ref. 2) by LDEF Exp. P0006 plastic track detector with pre-recovery predictions (ref. 3).

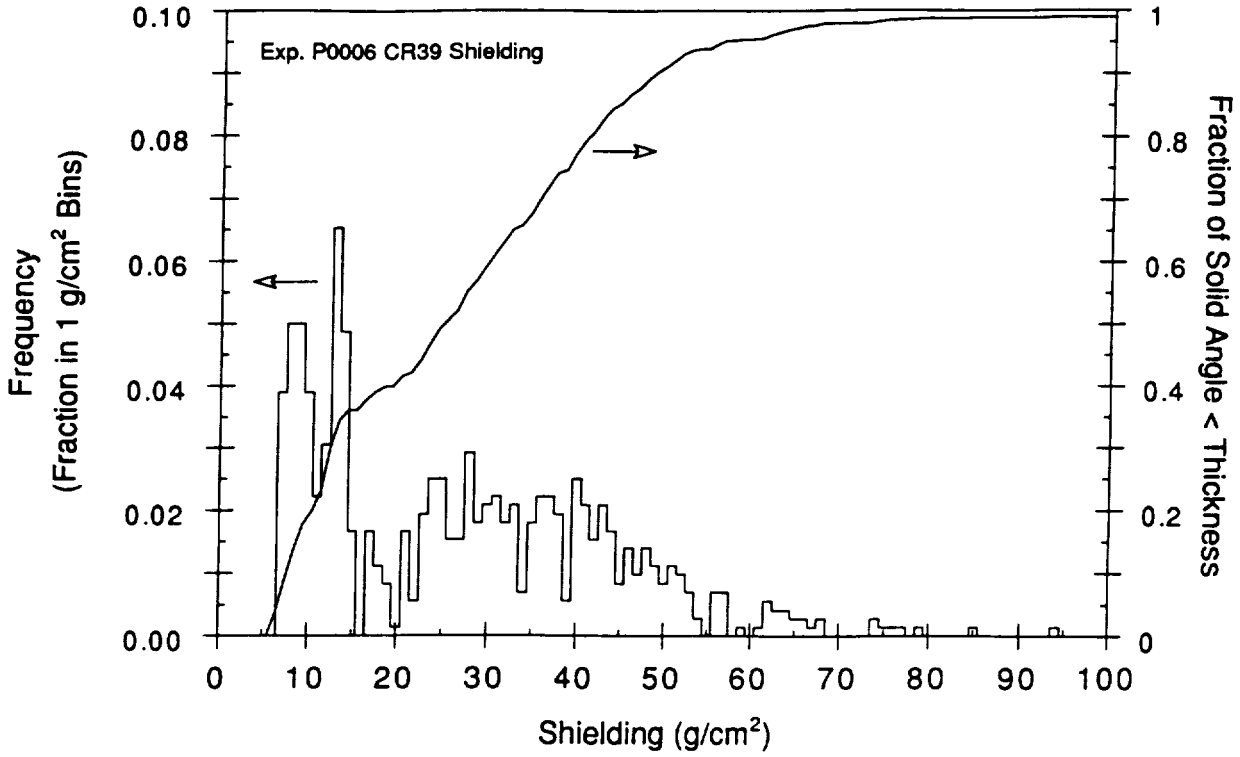

Fig. 2. Shielding distribution for P0006 detector.

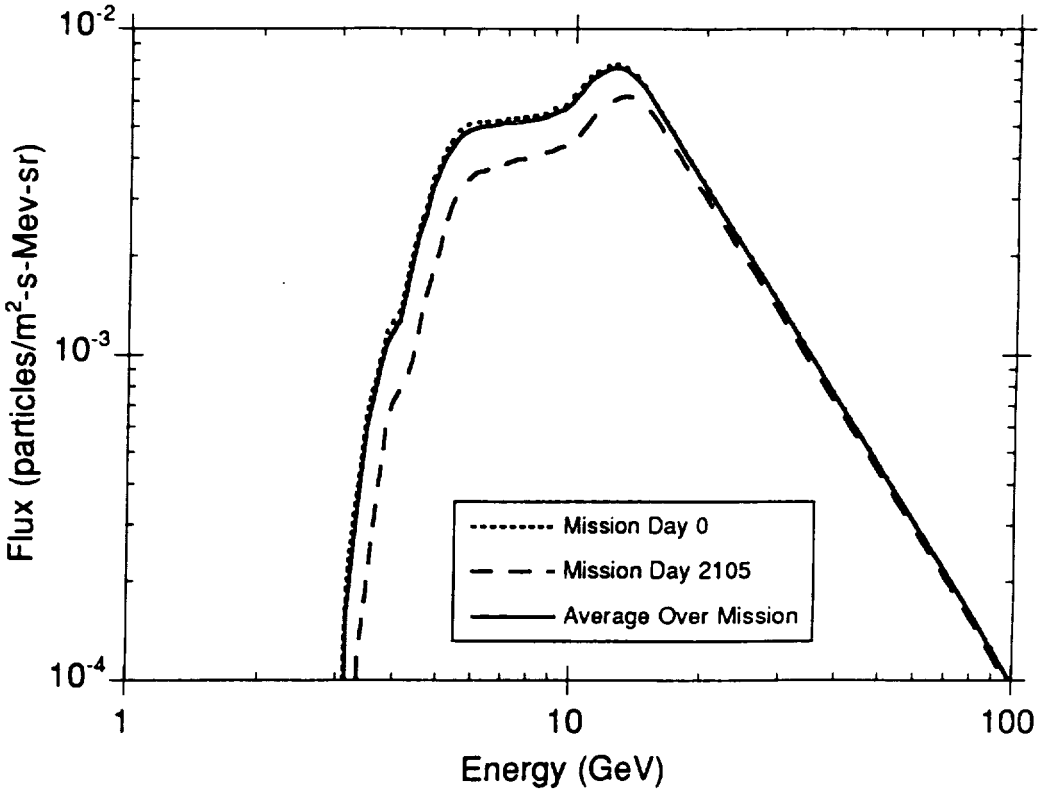

Fig. 3. LDEF exposure to galactic protons.

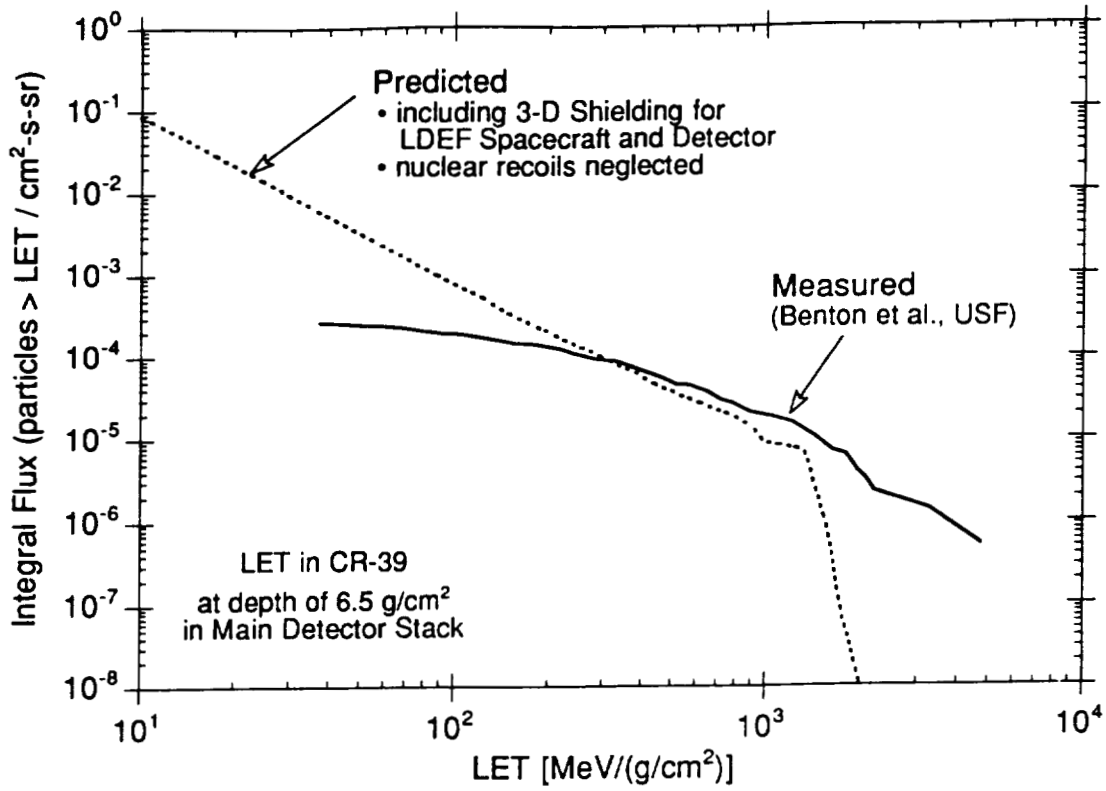

Fig. 4. Predicted LET using 3-D shielding model.

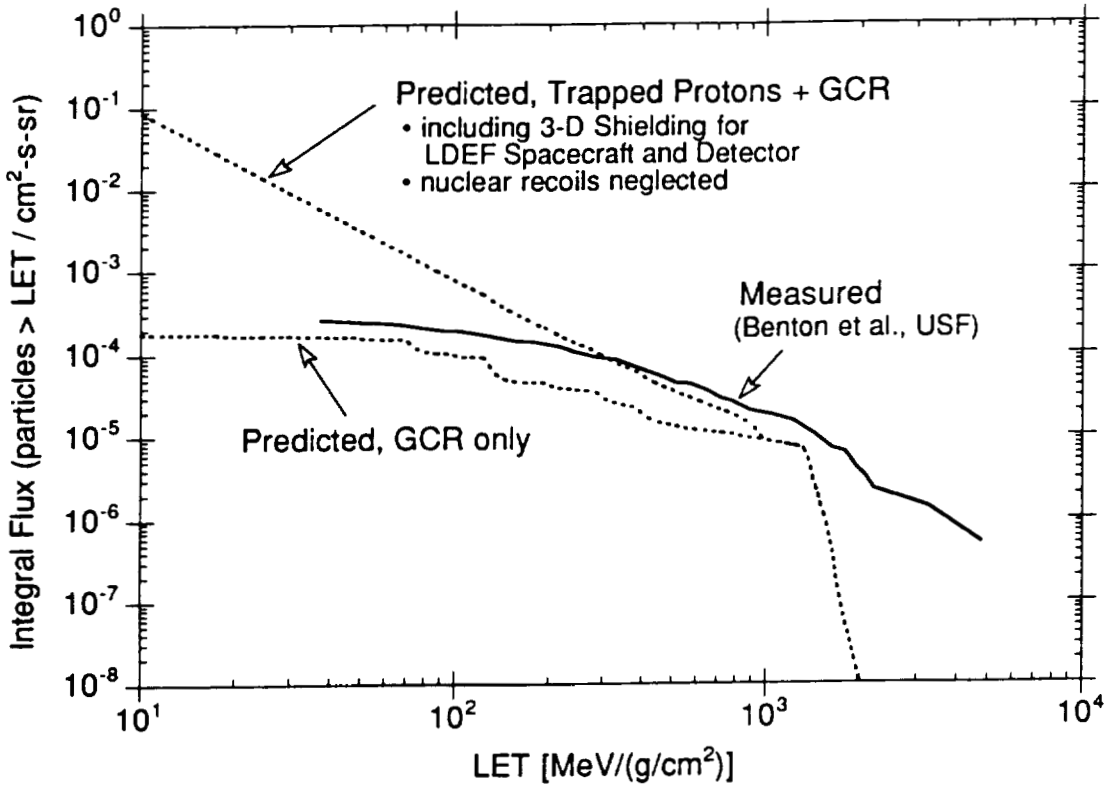

Fig. 5. Contribution of trapped protons to LET.

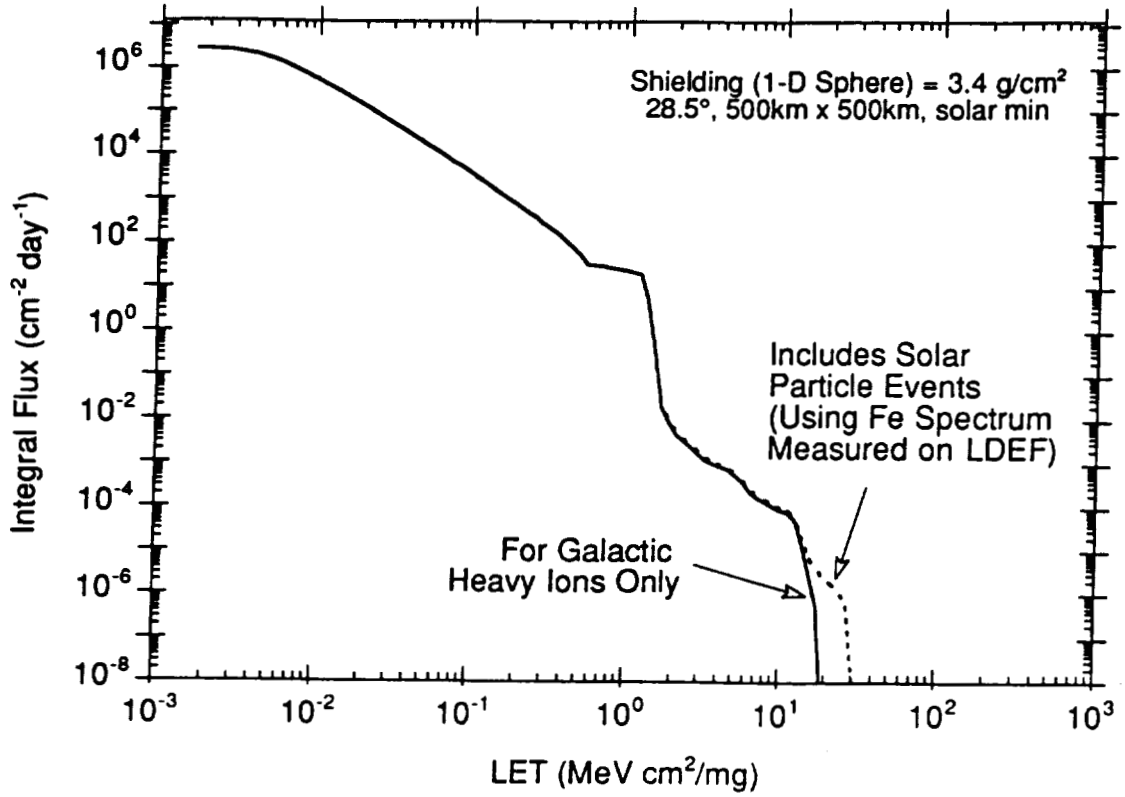

Fig. 6. Influence of SEP iron ions on LET.

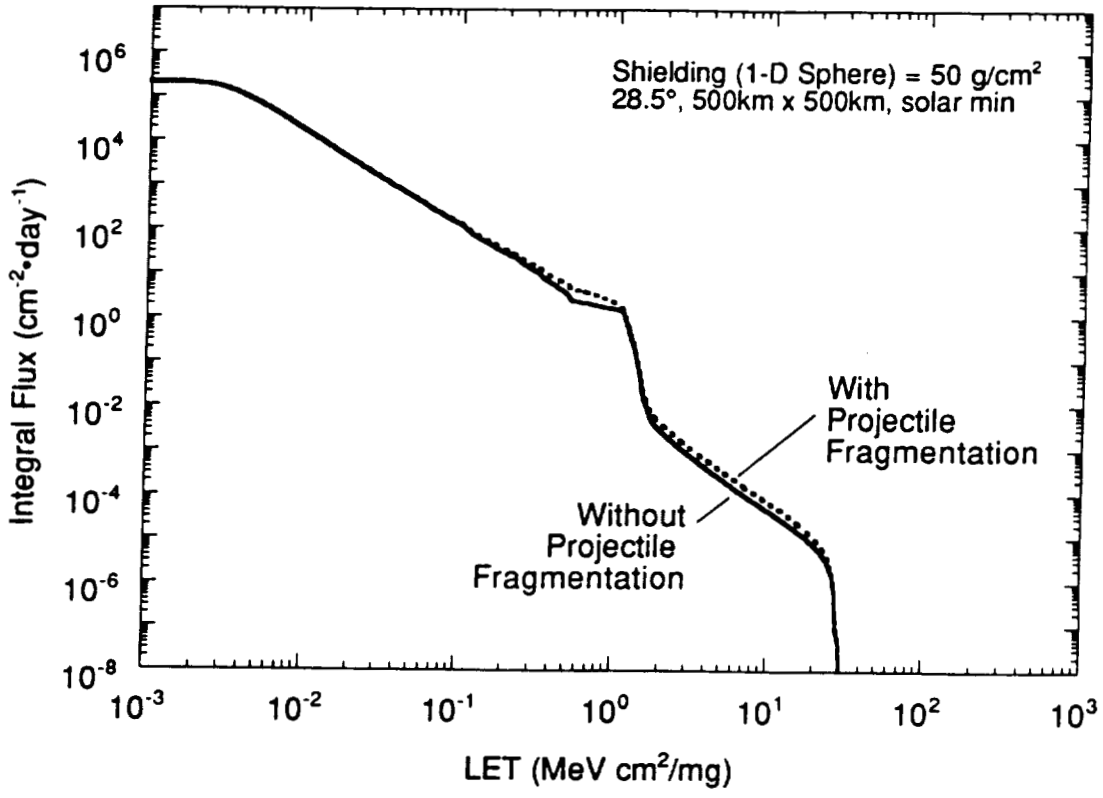

Fig. 7. Influence of ion ("projectile") fragmentation on LET.

DOING PHOTONS WITH MERLIN II AT OROVILLE

Alan R. Smith and Donna L. Hurley
Lawrence Berkeley Laboratory
Berkeley, CA 94720
Phone: 510/486-5679, Fax: 510/486-5888

ABSTRACT

A very large n-type high-purity Ge-semiconductor detector has recently been installed in the Lawrence Berkeley Laboratory's underground low-background facility at Oroville. The detector (named MERLIN II) is mounted in a low-activity cryostat and has a rated "efficiency" of about 115% - - nearly 4 times higher than our original MERLIN detector, which was used extensively to measure the minute amounts of radioactivity in samples from the LDEF satellite. We discuss gamma-spectrometric analyses with MERLIN II on some of the same LDEF samples, providing direct evidence for improvement in performance achieved with the larger detector.

INTRODUCTION

Radiometric analysis of materials retrieved from the LDEF satellite has continued at the LBL Low Background Facility from the time of first receipt (March 1990) until the present. Results of our analyses, along with results from many other members of the radiometric analysis group, are summarized in References 1 and 2. Our lowest background (BKG) detector, the MERLIN I detector at Oroville, was used extensively to measure the smallest activities until its failure in Spring 1991. The MERLIN I detector could not be revived. It was replaced in January 1993 by a similar type detector of much larger size (efficiency), for which a major fraction of counting time has been applied to further analysis of LDEF samples. Some important characteristics of the new detector (MERLIN II) are documented here, along with examples of results obtained with the MERLIN II system on LDEF samples.

The MERLIN II Detector

The Lawrence Berkeley Laboratory's Low-Background Facility operates low-level counting installations at two sites: at the LBL Berkeley Site and in the underground power plant of the Oroville Dam (a facility of the California Department of Water Resources). We have recently installed a new gamma-spectrometer detector system at the Oroville Site, where the overhead rock shielding reduces the surface Cosmic Ray intensity by 1000-fold. The new detector provides nearly a 4-fold increase in detection sensitivity compared to our previous capability, while at the same time maintaining the very low BKG characteristics achieved formerly with a much smaller detector. Since the LBL Low Background Facility is a national User's Facility, it is appropriate to make this new capability known to the community of potential users.

The "MERLIN II" detector, a replacement for our "MERLIN I" detector, is a much larger n-type high purity Ge detector than was our original "MERLIN I" detector. "MERLIN II" has a rated "efficiency" of about 115%, while "MERLIN I" was rated at about 30%. The new detector is 80 mm in diameter and 85 mm in length, weighing about 3 Kg. It is mounted in the manufacturer's (Ortec) "low-BKG" cryostat assembly, for which LBL supplied some special low-activity components, including the boron nitride stand-off insulator and the front-end FET package.

The MERLIN II detector arrived at LBL just after Christmas 1992, and was installed in our underground Oroville Facility in January 1993. Although the detector background (BKG) is still changing slowly (decreasing), it has already been adequately characterized to enable use of the system for measurements with much greater sensitivity than was possible with the original MERLIN system. General characteristics of the new detector BKG, compared to the original MERLIN system, are as follows:

1) All visible peaks in the U-series and Th-series are at about the same intensity (c/min), except for the Pb-210 peak which is about 8-fold higher than before. The K-40 peak, although still very small, is about 4-fold higher than before.
2) The continuum is about 2-fold higher than before in the 100-300 KeV region, crosses over at about 500 KeV and is lower than before at all higher energies.

Almost all the peaks of interest remaining in the LDEF samples are at energies above 500 KeV. These favorable BKG characteristics, combined with the roughly 4-fold increase in efficiency, translates into at least a 4-fold improvement in our capability to measure the very weak activities in these relatively small-size samples.

MERLIN II Detection Sensitivity

The present shield provides a 7-in square by 18-in high internal volume in which the 4-in diameter by 8-in long vertically oriented detector assembly is centered. There is a 7-in square by 8-in high annular space around the detector barrel. A 3-in high by 7-in square free space also exists above the flat face of the endcap. Literally all shapes and sizes of objects/materials that will fit inside the MERLIN shield are candidate samples. Each different configuration may require separate "calibration" runs with known quantities of appropriate radionuclides in matching matrix materials. Such calibration procedures are often quite time-consuming, but are essential for the frequent special cases that cannot be forced into one of the several "standard sample" formats.

Several representative sample formats of the total available range illustrate the detection sensitivity of the new system; these examples can then serve to guide evaluation of potential applications. The comparisons are based on detection of the 1461 KeV gamma-ray from K-40 in KCl or natural materials, and should be interpreted as mainly "geometric" factors: they do not take into account absorption of gamma-rays inside the sample, as will occur with greater sample thickness or higher-Z sample material, or when measuring peaks from lower-energy gamma-rays. The three examples are:

1) Small (2-in diam.) thin sample centered on the flat face of the endcap (maximum sensitivity);
2) Thin layer (about 1/2" thick) around most of cylindrical endcap, including the flat end;
3) Thick layer (1 1/2" to 2" thick) surrounding cylindrical endcap, with 2-3" thick full-diameter layer at end (maximum sample size).

Approximate values for the detector response to K-40 in KCl, NaCl, or common crustal Earth materials, along with the corresponding minimum detectable potassium concentrations, are as follows:

SAMPLE FORMAT	WEIGHT GRAMS	RESPONSE C/MIN/GRAM	MINIMUM DETECTABLE CONCENTRATION
1. (Small/thin)	20	10.	3 ppm
2. (Thin/extensive)	1000	5.	0.1 ppm
3. (Thick/maximum)	6000	2.5	0.04 ppm

Values in the column labeled RESPONSE represent c/min per gram of natural potassium present in the sample material. Values in the column labelled MINIMUM DETECTABLE CONCENTRATION have the following specific definition: they are concentrations equal to one Standard Deviation on the measured BKG in the K-40 peak, and reflect the statistical quality of data accumulated over a one-week period. Another way to interpret these values is to consider them the highest concentrations of the radionuclide that might just escape detection. Reliable measured values should be obtainable from concentrations two to three times these limiting values.

Similarly defined limits for detection of the two natural radionuclide series (at secular equilibrium), using the largest size sample are:

U-series: about 20 ppt (parts per trillion)
Th-series: about 100 ppt.

While longer counting times can provide some improvement (reduction) in the lower detection limit, it would require a one-month count to achieve a 2-fold reduction from the results of a one week counting time. Larger samples (in a larger cavity inside the shield) can also achieve a reduction in this lower limit without extending the counting time - - perhaps a factor of 2 is achievable. However, there does not appear to be a practical route to 10-fold reduction in lower detection limit with our single MERLIN II detector.

The small-sample sensitivity has been determined from a known quantity of KCL chemical in one of our "standard" plastic boxes, which sample was also used with MERLIN I. The container dimensions are a good match to the 2-in square LDEF samples, and it is counted in the same position used for the LDEF samples. The ratio of count-rates in the K-40 (1461 KeV) peak, taken in the sense (MERLIN II)/(MERLIN I), provides a direct measurement of the relative improvement in sensitivity for single-emission (non-cascade) gamma-rays that accompany radionuclide decay. The ratio was measured to be 3.94 for this "maximum sensitivity" position.

Analysis of LDEF NICKEL Samples with MERLIN II

All four NICKEL intentional samples were re-analyzed at LBL in order to measure their Co-60 content with greater accuracy than had been achieved in previous measurements. The samples were counted with the MERLIN II system in June 1993 giving the following results:

SAMPLE	OBSERVED C/MIN	ACTIVITY C/MIN-KG
Nickel #4	0.0551±0.0037	1.05±0.05
Nickel G-12	0.0520±0.0026	1.06±0.03
Nickel I-C3	0.0688±0.0028	1.40±0.06
Nickel Bars(2)	0.0402±0.0022	1.13±0.06

Each sample was counted for the nominal one week period at the highest sensitivity position: centered on the detector endcap. The OBSERVED count rates are derived from the summed contributions of both peaks (1173 Kev plus 1332 Kev). The ACTIVITY values, expressed as c//min-Kg, have been decay-corrected to 1/20/90, the date of LDEF's landing at Edwards Air Force Base.

The above measurements can be linked directly to the previous analyses done in 1990 with MERLIN I: the NICKEL #4 sample was counted in identical "geometries" with both detectors. The Co-60 activity measured with MERLIN I was:

Nickel #4: Co-60 (2-peak sum) = 0.373±0.027 c/min-Kg
Ratio: (MERLIN II/MERLIN I) = 2.82 ±0.26

The sensitivity increase realized with MERLIN II for Co-60 is smaller than the factor measured with the single gamma-ray that accompanies K-40 decay. The major factor contributing to this difference is related to the emission of the Co-60 gamma-rays in coincidence, which means that as detector size increases, the summing effect becomes greater (the peaks are "robbed" in a greater fraction of all detected events).

Although the primary objective has been to obtain more accurate values for the Co-60 content of these samples, we have also been able to make accurate measurements of the Co-57 and Mn-54 activities that remain nearly 3 1/2 years after retrieval of the satellite. In addition, the presence of Na-22 was detected, although at a level with much lower statistical significance. Searches for Ar-42 (33 year halflife) and Ti-44 (47 year halflife) in each sample were unsuccessful (the possibility remains that these isotopes might show up were all four samples counted at the same time). No other gamma-emitting radionuclides were observed.

LONG-LIVED ACTIVITIES IN TRUNNION SLICES

A group of 20 slices from trunnion sections LHG and RHG were counted together with MERLIN II in an effort to achieve more accurate values for the long-lived radionuclides that were just barely detected in our previous work with the MERLIN I detector.
This composite sample consisted of slices 2 through 6 from sets LHG-N, LHG-S, RHG-N, and RHG-S. Sixteen pieces (in two-layer sets) were arranged around the cylindrical surface of the detector endcap, while the four thickest pieces were placed on the flat face of the endcap. Total sample weight was about 1 Kg.

The composite sample was counted for 17735 minutes during the interval 9/9-23/93. Figure 1 shows several peaks in a portion of the spectrum, including very small (but quantitatively useful) peaks from Ti-44 (47-year halflife) and Na-22 (2.6-year halflife). The two dominant peaks in this energy region belong to Co-60 (5.3-year halflife). Listed below are net count rates observed in the signature peaks that are used to measure the induced-activity isotopes found in the composite sample. No absolute efficiency calibrations have been generated for this sample array, because various members of the array contain different activity levels. However, comparisons of relative activity levels can be made through use of decay-corrections to the values given here. For all but Co-57, self-absorption effects can be ignored for these comparisons.

ISOTOPE	ENERGY KEV	OBSERVED NET C/MIN
Mn-54	834	0.442±0.005
Ti-44	1157	0.0052±0.0007
Co-57	122	0.064±0.003
Co-60	1173	0.063±0.002
	1332	0.062±0.002
	BOTH	0.125±0.003
Na-22	1274	0.0125±0.0009
Ar-42	1524	±0.0004

The entry for Ar-42 is derived from this spectral data and represents a single Standard Deviation on a 5-Kev wide interval of the continuum centered at the energy of the 1524 Kev peak. It may be considered an upper limit for the presence of this isotope.

RADIOACTIVITIES IN LDEF PB BALLAST SLICES

Several Pb-ballast slices cut from parts of the satellite's position stabilization assembly have been analyzed recently with our MERLIN II spectrometer, more than 3 years after recovery of the LDEF. The samples analyzed here are 1/4" thick slices which were "shielded" from space by 3/16" of aluminum and 1/8" of Pb.

The only cosmogenically produced radionuclide we can detect from a week-long count on a single 2" x 2" x 1/4" thick Pb square after so long a decay time is the 33-year halflife isotope Bi-207. This nuclide must have been produced mainly through proton reactions on the stable Pb isotopes Pb-207 and Pb-208. The presence of the shielding mentioned above implies a minimum proton energy of about 60 MeV to produce Bi-207 from a reaction on Pb-207.

Each sample was counted for the nominal one week period at the highest sensitivity position: centered on the detector endcap. The OBSERVED count rates and ESTIMATED activities in pCi/Kg are tabulated below, wherein we have used both prominent gamma-ray peaks to calculate the estimated Bi-207 activities:

SAMPLE	PEAK ENERGY	OBSERVED C/MIN	ESTIMATED pCi/Kg
Pb B-8-916-A-3	570 Kev	0.0442±0.0026	4.9±0.3
	1064 Kev	0.0336±0.0021	6.3±0.4
Pb B-8-916-B-3	570 Kev	0.0506±0.0024	5.6±0.3
	1064 Kev	0.0310±0.0017	5.8±0.3
Pb B-8-920-A-3	570 Kev	0.0675±0.0027	7.5±0.3
	1064 Kev	0.0419±0.0020	7.9±0.4
Pb B-8-920-B-3	570 Kev	0.0663±0.0030	7.4±0.3
	1064 Kev	0.0451±0.0023	8.5±0.4

No decay corrections have been made to these results, in view of the long halflife (33 yr.) of Bi-207 compared to the time since recovery of the LDEF. There may be a relatively small systematic difference between activity values obtained from the two different peaks appearing in the spectrum from each sample, possibly arising from errors in determination of either detection efficiencies or self-absorption in these thick high-Z samples. However, the results have the consistency to support some conclusions:

1). Slices 916-A and 916-B have equal Bi-207 activities;
2). Slices 920-A and 920-B have equal bi-207 activities;
3). The 920- slices have about 1.4 times greater Bi-207 activity than do the 916- slices.

Additional information on the very low-intensity activities was obtained from a composite sample consisting of three 2-in square by 1/4" thick Pb slices and a stacked pair of 2-in square by 1/8" thick Pb slices that were also counted for a week-long period. The two Bi-207 peaks (570 and 1064 Kev) showed a 3-fold increase in intensity compared to results from counting each 1/4" thick slice separately. Several additional low-intensity peaks were also observed from the approximately 720-gram total mass of Pb. These peaks are listed below by energy, along with the isotopes believed to be responsible for their presence:

ENERGY KEV	OBSERVED C/MIN	PARENT ISOTOPE	PARENT HALFLIFE	OBSERVED ISOTOPE
328	0.0091±0.0024	Hg-194	520 y	Au-194
355	0.0060±0.0022	Ba-133	10.5 y	Ba-133
834	0.0023±0.0009	Mn-54	312 d	Mn-54
885	0.0021±0.0008	Ag-110m	270 d	Ag-110m
1094	0.0046±0.0008	Hf-172	1.9 y	Lu-172
1173 1332	(both peaks) 0.0104±0.0013	Co-60	5.3 y	Co-60

Although the observed peak intensities are near the limits of detectablilty, the peaks are believed to be real - - and they do not exist in the BKG, except for Co-60 where the summed BKG peaks have intensity 0.0070 c/min. They represent nuclear reactions requiring that the incident particles (mainly protons) have energies in the hundreds of MeV range. The outcome of this measurement again emphasizes the value of having large mass samples for analysis. Pb samples up to 20 times more massive could easily be accommodated in the MERLIN II system, to produce results considerably more precise than are reported here.

Figure 2 shows a portion of the spectral data, including a small (but quantitatively useful) peak at 1093 KeV which verifies the presence of Hf-172 in the sample, an isotope produced in a reaction requiring a few hundred MeV incident particle energy. The nearby (1120 KeV, Bi-214) peak is a BKG peak, while the adjacent elevated structure to the right is the slowly decreasing evidence for Zn-65 in the detector itself (produced by interactions of cosmic-ray particles with the detector during its existence above ground). The dominant (offscale) peak at energy 1063 KeV is the upper of the two most intense peaks from Bi-207 (the other, at 570 KeV).

USE OF THE MERLIN II SYSTEM FOR SHORT-DURATION MISSIONS

The very high sensitivity and low BKG of our MERLIN II system can also be applied to analysis of shorter-lived radionuclides, such as would be appropriate for measurement from flights much shorter than the LDEF Mission: week-long Space Shuttle missions, for example. The enhanced detection capability, when applied to activities produced in a select set of larger samples, would permit acquisition of the same kind of information from the short-duration flights as has been obtained from long-lived radionuclides produced on the LDEF mission.

A special quick-recovery package could be designed for Space Shuttle missions which, when landed at Edwards Air Force Base, could be at the Oroville Facility and ready for counting within 12 hours of touchdown - - without further transport by air. This procedure would establish feasibility for use one of the most convenient threshold reactions, the production of 15-hour halflife Na-24 in various target elements. When target elements such as Mg, Al, Si, Ca, Ti, Mn, Fe, Co, Ni, and Cu are used, we are availed of reaction thresholds ranging from a few MeV to a few hundred Mev. Many other target/reaction combinations exist, leading to radionuclides having favorable decay schemes with halflives ranging from tens of hours to tens of days, and are eminently suitable for shuttle-length missions.

Implementation of this kind of program on frequent Space Shuttle missions would add significantly to our understanding of both the intensity and short-term variability of the radiation field encountered in low Earth-orbit. Results obtained from such a program would be immediately useful in development (or confirmation) of the planning for missions in which both humans and sensitive instruments are expected to perform for long periods of time - - months to years, in low Earth-orbit.

SUMMARY

We have discussed the high detection efficiencies and low BKG characteristics of the new MERLIN II gamma-ray spectrometry system, installed in January 1993 at the LBL Oroville Low Background Facility. The MERLIN II system is in continuous operation, and is available on a part-time basis to qualified users. We have described analysis of samples from the LDEF satellite, to demonstrate the importance of using such a system to measure the tiny amounts (in the pCi/Kg domain) of induced-activity radionuclides in materials recovered from space missions. Measurement of these radionuclides provides important information on the integrated radiation "exposures" encountered during the missions. Although the LDEF experience relates to long-duration missions, suitable sets of elements can be assembled to provide similar integrals for radiation "exposures" encountered on much shorter duration flights, such as Space Shuttle missions.

ACKNOWLEDGMENTS

We again express our deepest appreciation to all NASA personnel associated with the LDEF mission, in particular: the 1984 Challenger crew who launched the satellite and the 1990 Columbia crew who brought it back to Earth; the LDEF mission primary team at Langley, headed by Dr. William Kinard; the Langley team headed by Dr. Arlene Levine, who again organized a very successful symposium; and the Special Investigation Group for radioactivity measurements, headed by Dr. Thomas Parnell and including Drs. Gerald Fishman and B. Alan Harmon. Special thanks are due Alan Harmon for his masterful handling of sample acquisition and timely scheduling of their distribution among participating laboratories.

Our appreciation continues for the superb support in detector and electronics technology afforded by the LBL group formerly headed by Fred Goulding, particularly in regards creation and maintenance of our MERLIN spectrometer systems. We also thank R.J. McDonald, newest member of the Low Background Facility team, for his contribution to data analysis for this presentation. And - -thanks again to Kevin Hurley of the U.C. Space Science Laboratory, whose phone call alerted us to this opportunity of a lifetime: participation in the LDEF analysis program.

We respectfully dedicate all our efforts in the LDEF analysis program to the last crew of the Challenger, lost at launch in early 1986, but long remembered in the annals of mankind's journey into space.

BIBLIOGRAPHY

1. Various authors: Space Environments, Ionizing Radiation, in First LDEF Post-Retrieval Symposium, NASA CP-3134, conference proceedings, pp 199-396, 1991.

2. Various authors: Space Environments, Ionizing Radiation, in Second LDEF Post-Retrieval Symposium, NASA CP-3194, conference proceedings, pp 67-274, 1992.

This work was supported by NASA under Marshall Flight Center Order No. H-06815D through U.S. Department of Energy under contract No.
DE-AC03-76SF00098.

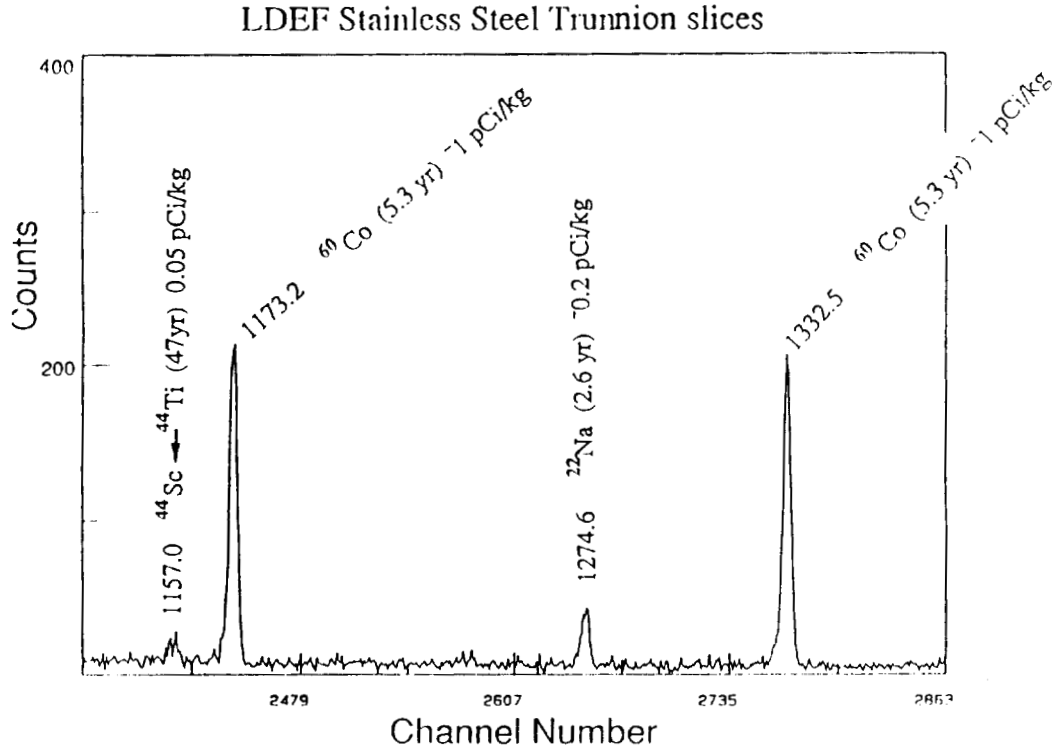

Figure 1. Section of MERLIN II spectrometric data from a 20-pc array of LDEF stainless steel Trunnion Slices, showing peaks in the gamma-ray energy interval 1100-1400 Kev.

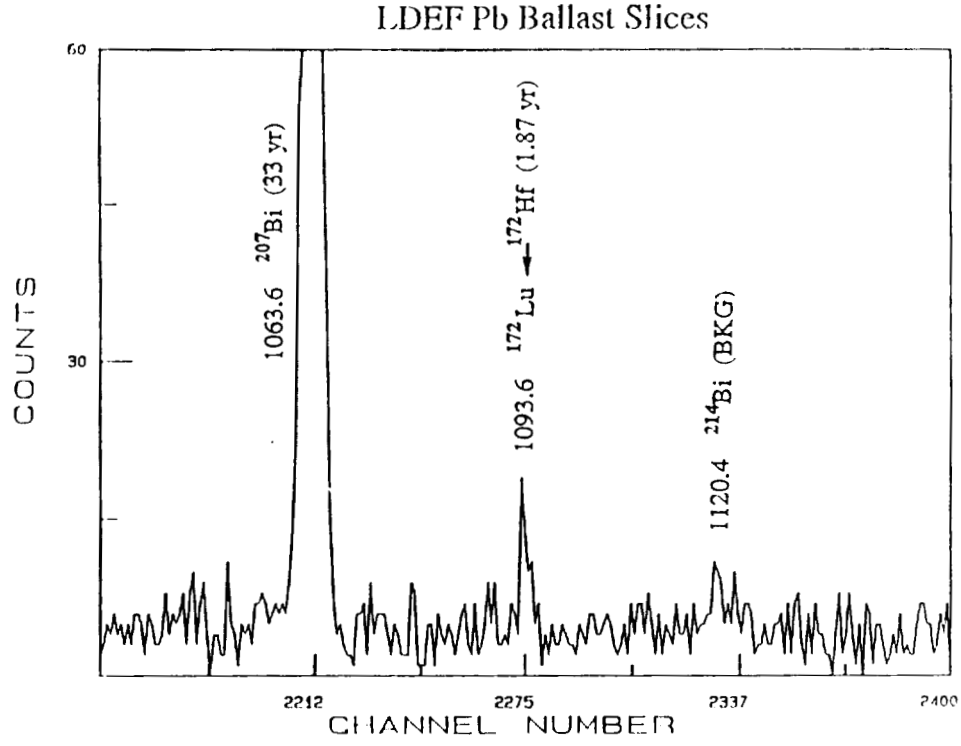

Figure 2. Section of MERLIN II spectrometric data from a 5-pc array of LDEF Pb Ballast Slices, showing peaks in the vicinity of 1100 Kev gamma-ray energy.

STATUS OF LDEF ACTIVATION MEASUREMENTS AND ARCHIVE

B. Alan Harmon and Thomas A. Parnell
ES84, NASA/Marshall Space Flight Center
Huntsville, AL 35812
Phone: 205/544-4924, Fax: 205/544-7754

Christopher E. Laird
Department of Physics, Eastern Kentucky University
Richmond, KY 40475
Phone: 606/622-1526, Fax: 606/622-1020

SUMMARY

We review the status of induced radioactivity measurements for the LDEF spacecraft which includes studies of the nuclide, target, directional and depth dependences of the activation. Analysis of the data has focused on extraction of the specific activities for many materials to develop a global picture of the low Earth orbital environment to which the LDEF was subjected. Preliminary comparisons of data in a previous review showed that it was possible to make meaningful intercomparisons between results obtained at different facilities (Harmon et al., 1993). Generally these comparisons were good and gave results to within 10-20%, although some analysis remains. These results clearly provide constraints for recent calculations being performed of the radiation environment of the LDEF (Armstrong and Colborn, 1993). We are now anticipating a period of production of final activation results. An archive is being prepared jointly between NASA/Marshall and Eastern Kentucky University which will include gamma ray spectra and other intermediate results.

INTRODUCTION

The return of the Long Duration Exposure Facility has provided an extraordinary opportunity to investigate the radiation environment in low Earth orbit. The LDEF Ionizing Radiation Special Investigation Group has conducted, as part of a coordinated effort, an analysis of the induced radioactivity in materials in the spacecraft. This passive technique was particularly useful for LDEF because of the gravity-gradient stabilized configuration, which allowed the directional and depth dependences and the magnitude of the activation to be measured. The trends observed in the activation in a wide range of materials contain signatures of the anisotropic Van Allen trapped fluxes as well as the more energetic cosmic ray protons (Harmon et al. 1991, Armstrong and Colborn, 1991,1993). More subtle components to the activation, fast secondary neutrons in metals such as iron and nickel, and thermal neutrons for samples in proximity to low-Z moderating materials are also observed (Harmon et al. 1993).

MEASUREMENTS

Approximately 400 samples from the LDEF were counted at eight facilities: Westinghouse Savannah River Site, Lawrence Berkeley and Lawrence Livermore Laboratories, Tennessee Valley Authority Western Area Radiological Laboratory, Los Alamos National Laboratory, Battelle Pacific Northwest Laboratory, NASA/Johnson Space Center and NASA/Marshall Space Flight Center. Specific activity data are being collected and evaluated at Eastern Kentucky University and NASA/Marshall Space Flight Center. Preliminary results can be found in several conference presentations (Harmon et al. 1993; Reeves, et al. 1993; Smith and Hurley, 1991, Winn, 1991 and others) on the extracted specific activities for aluminum and steel structural materials, and also vanadium, indium, cobalt, nickel and tantalum foils from different parts of the spacecraft and at various shielding depths. Comparisons of data in a previous review showed that it was possible to make meaningful intercomparisons between results obtained at different facilities (Harmon et al. 1993). Some data analysis remains however. Recent work has concentrated on the metal foils from experiments A0114, M0001, M0002 and P0004. Armstrong et al. 1994 compare High Energy Transport Code calculations to vanadium and nickel activation measurements using the anisotropic trapped radiation doses predicted by Watts et al. 1993. The overall results are consistent with contributions from trapped and cosmic ray proton-induced activation; however, the measured activities are larger than the calculated activities by about a factor of two. Corresponding differences in predicted to measured proton doses in thermoluminscent detectors have also been observed (Bourrieau, 1993; Frank, et al. 1993).

In order to investigate more carefully the dependences on incident proton energy, which reveals something of the mixing of trapped and comsic ray protons, we are endeavoring to reduce the associated systematic errors of the activation measurements at different laboratories to at least the 30% level. For most material samples, we have achieved this level or better (10-20%), and hope to resolve discrepancies that remain. These measurements are among the most sensitive of any space-induced activation measurements, and already strongly constrain the calculations of the radiation environment.

ARCHIVE

An archive of the induced radioactivity results is being constructed jointly by NASA/Marshall Space Flight Center and Eastern Kentucky University (Laird et al. 1993) which will consist of the LDEF induced radioactivity analysis plan and a final report to include specific activities measured for all materials. The final report would also include experimental details, efficiency and calibration measurements, and scoping calculations of the activities. The archive would also contain intermediate reports from counting facilities, sample inventory and run logs, and a set of gamma ray spectra from various counting facilities who participated in this study. Currently the archive contains gamma ray spectra from Savannah River, Lawrence Livermore, Battelle Northwest, and Marshall Space Flight Center. We also intend to archive spectra from the ultralow background facilities at Johnson Space Center and the Lawrence Berkeley Oroville Dam Facility.

REFERENCES

Armstrong, T. W. and B. L. Colborn: Ionizing Radiation Calculations and Comparisons with LDEF Data. First Post-Retrieval LDEF Symposium, NASA CP-3134, 1991, p. 347.

Armstrong, T. W. and B. L. Colborn: Radiation Model Predictions and Validation Using LDEF Satellite Data. Second Post-Retrieval LDEF Symposium, NASA CP-3194, 1993, p. 207.

Armstrong, T. W. et al.; NASA CP-3275, 1995.

Bourrieau, J.: LDEF: Dosimetric Measurement Results (AO138 - 7 Experiment). Second Post-Retrieval LDEF Symposium, NASA CP-3194, 1993, p. 207.

Frank, A. L. et al.: Absorbed Dose Measurements and Predictions on LDEF. Second Post-Retrieval LDEF Symposium, NASA CP-3194, 1993, p. 163.

Harmon, B. A., et al.: Induced Activation Study of LDEF. Second Post-Retrieval LDEF Symposium, NASA CP-3194, 1993, p. 125.

Laird, C. E. et al.: Collection, Analysis and Archival of LDEF Activation Data. Second Post-Retrieval LDEF Symposium, NASA CP-3194, 1993, p. 111.

Reeves, J. H., et al.: Sensitivity of LDEF Foil Analyses Using Ultra-Low Background Germanium Vs. Large Area NaI(Tl) Multidimensional Spectrometers. Second Post-Retrieval LDEF Symposium, NASA CP-3194, 1993, p. 79.

Smith, A. R. and D. L. Hurley: Radioactivities of Long Duration Exposure Facility (LDEF) Materials: Baggage and Bonanzas.. First Post-Retrieval LDEF Symposium, NASA CP-3134, 1991, p. 257.

Watts, J. W. et al.: Revised Prediction of LDEF Exposure to Trapped Protons. Second Post-Retrieval LDEF Symposium, NASA CP-3194, 1993, p. 137.

Winn, W. G.: Gamma-Ray Spectrometry of LDEF samples at SRS. First Post-Retrieval LDEF Symposium, NASA CP-3134, 1991, p. 287.

PREDICTIONS OF LDEF RADIOACTIVITY AND COMPARISON WITH MEASUREMENTS

T. W. Armstrong and B. L. Colborn
Science Applications International Corporation[1]
Route 2, Prospect, TN 38477
Phone: 615/468-2603, Fax: 615/468-2676

B. A. Harmon
NASA Marshall Space Flight Center
Huntsville, AL 35812
Phone: 205/544-4924, Fax: 205/544-7754

C. E. Laird
Department of Physics, Eastern Kentucky University[1]
Richmond, KY 40475
Phone: 606/622-1526, Fax: 606/622-1020

ABSTRACT

As part of the program to utilize LDEF data for evaluation and improvement of current ionizing radiation environment models and related predictive methods for future LEO missions, calculations have been carried out to compare with the induced radioactivity measured in metal samples placed on LDEF. The predicted activation is about a factor of two lower than observed, which is attributed to deficiencies in the AP8 trapped proton model. It is shown that this finding based on activation sample data is consistent with comparisons made with other LDEF activation and dose data. Plans for confirming these results utilizing additional LDEF data sets, and plans for model modifications to improve the agreement with LDEF data, are discussed.

INTRODUCTION

The measured activation of materials on LDEF from radioactivity induced by trapped proton and cosmic ray environments provides an important data set for checking the accuracy of environment models and associated calculational methods for predicting the activation of spacecraft and payload materials in low-Earth orbit. Such modeling accuracy is of particular interest in radiation background assessments and component material selection in the design of space-based sensors.

In the present work, predictions have been made to compare with the observed radioactivity in several metal samples intentionally placed on LDEF as activation experiments. Model comparisons with LDEF activation measurements of spacecraft components and with thermoluminscent dosimetry (TLD) data have been reported previously (refs. 1,2). A result from these previous model/data comparisons is an estimate of the accuracy of the current AP8 trapped proton model for low-Earth orbit applications. The activation experiment sample data considered here provide an important additional data set for model comparisons by allowing a consistency check of the different data sets, previous model/data comparisons, and previous conclusions related to quantifying the trapped proton environment modeling uncertainties.

[1]Work supported by NASA Marshall Space Flight Center, Huntsville, Alabama.

The activation experiment samples consisted of the metals nickel, tantalum, vanadium, indium, and cobalt placed in experiment trays at various locations on LDEF (Table 1), with sample sizes typically 2 in. x 2 in. and either 0.125 or 0.25 in. thick (ref. 3). A total of some 20 radioisotopes have been measured from these samples. We have not made predictions to compare with all of the measured radioisotopes for the following reasons: First, the primary objective of the present calculations is to compare with those radioisotopes which are produced by primary trapped protons so that previous conclusions on the accuracy of the AP8 model derived from model comparisons with other LDEF data can be checked. Some estimates are included here for isotopes produced by secondary neutrons and galactic cosmic rays, but the calculational method used for these estimates is less rigorous than than that used for the trapped proton produced isotopes. Secondly, the activation cross sections needed in predicting certain isotopes are not adequately known to provide the prediction accuracy needed in evaluating trapped proton model uncertainties. For these reasons, the predicted isotopes here are restricted to the nickel and vanadium samples.

The model comparisons made here with activation sample data provide a measure of the trapped proton flux model uncertainties, but information on the trapped proton anisotropy is difficult to interpret from these data because the samples are under different amounts of shielding at different locations (Table 2). The tray clamp activation data, which provide a detailed spatial mapping and are mostly free of shielding effects, provide a better data set for anisotropy model evaluations, as addressed in ref. 2.

The activation modeling approach has been to perform detailed calculations so that differences between the predicted and measured activations can be attributed to uncertainties in the incident radiation environment. Thus, as described below, predictions are based on a detailed treatment of the trapped proton environment (taking into account proton anisotropy, flux altitude dependence with mission time, and solar cycle dependence) and radiation transport using a detailed 3-D mass model of the LDEF spacecraft and experiment trays to account for shielding effects.

PREDICTION METHODS

Radiation Environment -- The LDEF trapped proton exposure predicted by Watts, et al. (ref. 4) is used, which is based on the AP8 omnidirectional flux model (ref. 5), the anisotropy model of Watts, et al. (ref. 6) to obtain directionality of the incident flux spectrum, a detailed altitude dependence during the LDEF mission, and an interpolation of the solar minimum (AP8MIN) and solar maximum (AP8MAX) versions of the AP8 model according to the F10.7 cm. solar flux to account for solar cycle variations of the proton flux during the mission. For incident galactic protons, the LDEF orbit-average exposure from ref. 7 was used, which is based on the interplanetary spectrum of Adams (ref. 8).

Shielding Model -- The 3-D mass model developed for LDEF radiation analyses (ref. 9) was used. This model was extended for the present calculations to incorporate each of the activation samples -- i.e., the actual size and location of all of the individual activation samples were included in the shielding model.

Radiation Transport -- For incident trapped protons, radiation transport calculations were made using the Burrell primary proton transport code (ref. 10) and the 3-D mass model of LDEF with the activation samples included. At each spatial point in the activation samples where flux spectra were calculated, an angular grid of 720 equal solid angle bins around the point was defined, with a different energy spectrum incident in each solid angle to account for the trapped proton directionality. For examining activation produced by incident galactic protons, particle spectra (primary protons, secondary neutrons and protons) from previous (ref. 7) Monte Carlo (HETC code) transport calculations for a simple geometry model (1-D slab of aluminum) were used. Thus, the activation estimates from the galactic environment is approximate due to the geometry simplification, but, as discussed above, the trapped proton activation is the main interest here.

Radioisotope Production -- Flux spectra calculated at the center of each activation sample were folded with measured activation cross sections (shown later) compiled from the literature to compute radioisotope production as a function of time during the mission, with decay rates then applied to obtain the radioactivity at LDEF recovery. (As a check on the approximation of using the flux only at the center of the sample, volume-average fluxes from a fine grid of flux points were computed for several samples and compared with the single point flux; the resulting activations agreed to within about 10% or less).

PREDICTED VS. MEASURED SAMPLE ACTIVATION

A summary of the LDEF activation sample measurement results is given in Table 3. Final data analyses and intercomparisons of measurements at different facilities have not yet been completed for all of the isotopes produced (ref. 11), so the data shown here are preliminary at present.

Vanadium Activation

Activation data for the vanadium sample are well suited for model comparisons because vanadium has a single target isotope (99.75% ^{51}V) and a single measured radioisotope (^{46}Sc), so the production mode is well defined for predictions; the activation cross section is well known (Fig. 1); and the energy threshold for ^{46}Sc production is relatively low ($\approx$ 30 MeV), so the production is almost all ($\approx$ 96%) from incident primary trapped protons rather than from secondaries or galactic cosmic rays.

A comparison of the measured and calculated ^{46}Sc activation for the vanadium samples is shown in Fig. 2. Both the measured and calculated activities indicate only a small dependence on sample locations, suggesting that differences that might be expected due to the trapped proton anisotropy are masked by differences in shielding (Table 2). The average ratio of predicted to measured activity for samples at all locations is 0.49 ± 0.11.

Nickel Activation

Predictions for the nickel sample activation are not as simple as for vanadium because there are various production modes (Table 4), requiring a large number of activation cross sections (e.g., Fig. 3 for proton induced reactions), and secondary neutrons are important in producing some of the isotopes. A comparison of predicted vs. measured activities for the nickel sample in Exp. P0006 (Fig. 4) shows that trapped protons dominate the production of ^{54}Mn and ^{56}Co, but neutrons dominate the ^{58}Co and ^{60}Co production, and cosmic rays dominate the ^{46}Sc production due to its high energy threshold. The calculated and measured activities for nickel samples at all locations are compared in Table 5. The average ratio of predicted-to-measured activities for the two isotopes (^{54}Mn and ^{56}Co) produced by primary trapped protons for all samples is $0.56 \pm \approx 0.08$.

Solar Minimum vs. Solar Maximum Activation

Since LDEF exposure to trapped protons during the early part of the mission was at solar minimum and during the latter part at solar maximum (Fig. 5), activities for long vs. short half-life isotopes can be used to investigate uncertainty differences in the solar minimum (AP8MIN) vs. solar maximum (AP8MAX) trapped proton models. For example, Fig. 6 shows the case of a relatively short half-life product (^{46}Sc from V sample in Exp. P0006, 84 day half-life). Two curves are shown: the production rate vs. mission time, and the contribution of the production at times during the mission to the activity at recovery, which shows that the recovery activity for this isotope is due to proton exposure during solar maximum. The predicted-to-measured activity ratio in this case is 0.49 ± 0.11. For a long half-life

isotope where the activity is at recovery due exposure during solar minimum, we use the ^{54}Mn activity (half-life = 303 days) for the same nickel sample in Exp. P0006, for which the predicted/measured ratio is 0.60 ± 0.12. Therefore, from comparisons with LDEF activation data we find no major difference in the AP8MIN vs. AP8MAX model uncertainties.

MODEL COMPARISONS WITH OTHER LDEF RADIATION DATA

The above comparisons of predicted vs. measured activities for the activation samples placed on LDEF indicate that the AP8 model underpredicts the trapped proton flux for the LDEF mission by about a factor of two. This result is consistent with model comparisons with other LDEF data, as summarized below.

Figure 7 compares predicted and measured ^{22}Na production in the aluminum clamps holding the experiment trays on LDEF, which has been published previously (ref. 2). The average predicted/measured activation around the spacecraft is $0.55 \pm$ about 0.15 (Fig. 7). This ratio is in agreement with dose predictions that have been compared (ref.1) with TLD doses measured on LDEF (ref. 12) at shielding depths where the dose is due to trapped protons.

Figure 8 summarizes predicted vs. measured results for three different sets of data (tray clamp activity, TLD dose, and radioisotopes in activation samples) at the same location on LDEF (Exp. P0006 in Tray F2). These results show that the model/data comparisons are consistent for the different data sets and that the predictions are about a factor of two lower than all of the data sets.

Another data set suitable for including in the comparisons of Fig. 8 is the fission tracks measured from fission foils (^{181}Ta, ^{209}Bi, ^{232}Th, and ^{238}U) included in Exp. P0006 (ref. 13). While these foils respond to protons and neutrons from both trapped and galactic proton sources, an estimate based on particle spectra from 1-D Monte Carlo calculations (ref. 7) shows that the energy dependence of the fission cross section for the Bi foil is such that fission tracks are produced predominately by trapped protons. Detailed calculations taking into account 3-D shielding effects have not yet been made to compare with these data.

Preliminary comparisons of predicted vs. measured activation of the steel trunnions on LDEF, which indicate somewhat better agreement than determined here for the activation samples, have been reported (ref. 14). However, this early work was of a scoping nature and several approximations were made in the predictions (e.g., the current estimate, ref. 4, of the trapped proton environment for LDEF was not available at that time), so these early trunnion activation calculations need to be revised before definitive trunnion data comparisons can be obtained.

SUMMARY

The predictions made here for the activation of metal samples placed on LDEF confirm results from previous comparisons with spacecraft component (tray clamp) activation data and TLD dosimetry data that radiation effects measured on LDEF that are due to the trapped proton environment are underpredicted by about a factor of two. These results indicate that the AP8 trapped proton model underpredicts the actual environment by a factor of two. Additional calculations to compare with other data sets (trunnion activation and fission foil measurements) are planned to further check this conclusion.

An investigation of model improvements that would give better agreement with the LDEF data is also planned. For example, predicted vs. measured differences for the trapped proton anisotropy is likely due to the approximate nature of the effective atmospheric scale heights currently used as input to the

anisotropy model, and work to determine more accurate effective scale height estimates is planned. Also, recent work at the European Space Agency (ESA), ref. 15, shows that improvement to some of the numerical interpolation procedures used in the AP8 model increases the predicted trapped proton flux for low-Earth orbits, and comparisons with LDEF data using the ESA version of the AP8 model are planned.

REFERENCES

1. Armstrong, T. W. and Colborn, B. L.: Radiation Model Predictions and Validation Using LDEF Satellite Data. Second LDEF Post-Retrieval Symposium, NASA CP-3194, 1993.

2. Armstrong, T. W.; Colborn, B. L.; Harmon, B. A.; Parnell, T. A.; Watts, J. W. and Benton, E. V.: Comparison of Model Predictions with LDEF Satellite Radiation Measurements. *Adv. Space Res.* 14, No. 10, 17 (1994).

3. Harmon, B. A.; Fishman, G. F.; Parnell, T. A.; Benton, E. V. and Frank, A. L.: LDEF Radiation Measurements: Preliminary Results. *Nucl. Tracks Radiat. Meas.* 20, 131 (1992).

4. Watts, J. W.; Armstrong, T. W. and Colborn, B. L.: Revised Predictions of LDEF Exposure to Trapped Protons. Second LDEF Post-Retrieval Symposium, NASA CP-3194, 1993.

5. Sawyer, Donald W. and Vette, James I.: AP8 Trapped Proton Environment for Solar Maximum and Solar Minimum. National Science Data Center, Goddard Space Flight Center, NSSDC/WDC-A-R&S 76-06, Dec. 1976.

6. Watts, J. W., Jr.; Parnell, T. A. and Heckman, H. H.: Approximate Angular Distribution and Spectra for Geomagnetically Trapped Protons in Low-Earth Orbit, in: *High Energy Radiation Background in Space,* Proc. AIP Conf.., Vol. 186, pp. 75-85, American Institute of Physics, New York, 1989.

7. Armstrong, T. W. and Colborn, B. L.: Predictions of Induced Radioactivity for Spacecraft in Low-Earth Orbit. *Nucl. Tracks Radiat. Meas.* 20, 101 (1992).

8. Adams, James H., Jr.: Cosmic Ray Effects on Microelectronics. Part IV. NRL Memorandum Report 5901, December 1986.

9. Colborn, B. L. and Armstrong, T. W.: Development and Application of a 3-D Geometry/Mass Model for LDEF Satellite Ionizing Radiation Assessments. Second LDEF Post-Retrieval Symposium, NASA CP-3194, 1993.

10. Burrell, M. O.: The Calculation of Proton Penetration and Dose Rates. George C. Marshall Space Flight Center, Huntsville, AL., NASA TM X-53063, August 1964.

11. Harmon, Alan B.; Parnell, Thomas A. and Laird, Christopher E.: Status of LDEF Activation Measurements and Archive. (These Proceedings).

12. Frank, A. L.; Benton, E. V.; Armstrong, T. W. and Colborn, B. L.: Absorbed Dose Measurements and Predictions on LDEF. Second LDEF Post-Retrieval Symposium, NASA CP-3194, 1993.

13. Benton, E. V.: LDEF Experiment P0006 Linear Energy Transfer Spectra Measurement (LETSME). Evil Research, Inc. Final Report to NASA Marshall Space Flight Center, December 1990.

14. Armstrong, T. W.; Colborn, B. L. and Watts, J. W.: Ionizing Radiation Calculations and Comparisons with LDEF Data. First LDEF Post-Retrieval Symposium, NASA CP-3134, 1991.

15. Daly, E. J. and Evans, H. D. R.: Problems in Radiation Environment Models at Low Altitudes. European Space Agency/ESTEC, preprint.

16. Smith, Alan R. and Hurley, Donna L.: Radioactivities of Long Duration Exposure Facility (LDEF) Materials: Baggage and Bonanzas. First LDEF Post-Retrieval Symposium, NASA CP-3134, 1991.

17. Winn, Willard G.: Gamma-ray Spectrometry of LDEF Samples at SRL. First LDEF Post-Retrieval Symposium, NASA CP-3134, 1991.

18. Laird, Christopher E.: Eastern Kentucky Univ., pri. comm.

19. Harmon, B. A.; Fishman, G. J.; Parnell, T. A. and Laird, C. E.: Induced Activation Study of LDEF. Second LDEF Post-Retrieval Symposium, NASA CP-3194, 1993.

20. Reeves. James H.: Arthur, Richard J. and Brodzinski, Ronald L.: Sensitivity of LDEF Foil Analyses Using Ultra-Low Background Germanium vs. Large NaI (Tl) Multidimensional Spectrometers. Second LDEF Post Retrieval Symposium, NASA CP-3194.

21. Harmon, B. Alan: NASA Marshall Space Flight Center, pri. comm.

Table 1. Location of activation samples on LDEF.

Contained in Exp. No.	Exp. Tray	Tray Position	Activation Samples				
P0006	F2	Trailing Side		Ni	V	Ta	In
A0114	C9	Leading Side	Co			Ta	In
A0114	C3	Trailing Side		Ni	V		
M0001	H12	Space End	Co	Ni	V	Ta	In
M0002	G12	Earth End	Co	Ni	V	Ta	In

Table 2. Vertical shielding for activation samples.

	Vertical shielding (g/cm^2) of activation sample in LDEF experiment tray:				
Sample	H-12	G-12	C-3	C-9	F-2
V	thermal cover	2.8	1.7		13
Ni	thermal cover	2.8	1.7		13
Co	thermal cover			1.7	13
Ta	thermal cover	8.0		1.7	13
In	thermal cover	8.0		1.7	13

Table 3. Summary of LDEF activation sample measurements - preliminary.

		Tray H12 (space end) Exp. M0001		Tray G12 (Earth end) Exp. M0002		Tray C9 (leading side) Exp. A0114		Tray C3 (trailing side) Exp. A0114		Tray F2 (trailing side) Exp. P0006	
Activation Sample	Product Isotope	Activity (pCi/kg)	Ref.	Activity (pCi/kg)	Ref.	Activity (pCi/kg)	Ref.	Activity (pCi/kg)	Ref.	Activity (pCi/kg)	Ref.
Nickel	Sc-46							11 ± 4	(c)	1.6 ± 0.4	(a)
	Mn-54	52 ± 7.8	(c)	25 ± 3.4	(e)			68 ± 6	(c)	27 ± 0.9	(a)
		72 ± 3.6	(d)	39 ± 8	(c)						
	Co-56	66 ± 28	(c)	29 ± 4.8	(e)			61 ± 9	(c)	33 ± 1.3	(a)
		70 ± 2.6	(d)	62 ± 27	(c)					67 ± 16	(c)
	Co-57	400 ± 7.2	(c)	403 ± 35	(e)			466 ± 18	(c)	322 ± 2	(a)
		395 ± 15	(d)	399 ± 23	(c)					360 ± 24	(c)
	Co-58	73 ± 3.4	(d)	62 ± 7.3	(e)			59 ± 11	(c)	42 ± 1.6	(a)
				93 ± 17	(c)					69 ± 11	(c)
	Co-60	7.6 ± 3.4	(d)					11 ± 4	(c)	4.7 ± 0.3	(a)
		9.0 ± 0.87	(g)								
		12 ± 7.8	(c)								
Tantalum	Lu-172	56 ± 2.1	(h)	40 ± 1	(h)			75 ± 2	(h)	47 ± 1	(h)
										36 ± 1.1	(a)
	Lu-173	120 ± 9.8	(h)	171 ± 12	(h)			143 ± 5	(h)	91 ± 4	(h)
										161 ± 8.3	(a)
	Hf-175	38 ± 5.7	(h)	19 ± 2	(h)			39 ± 2	(h)	25 ± 2	(h)
										37 ± 1.9	(a)
	Ta-182	116 ± 8.1	(h)	45 ± 4	(h)			38 ± 2	(h)	135 ± 4	(h)
										90 ± 2.3	(a)
Vanadium	Sc-46	21 ± 6.0	(b)	16 ± 1.3	(b)	20 ± 1.5	(b)			17 ± 1.1	(a)
		13 ± 1.7	(g)	16 ± 1.4	(e)	24 ± 2.0	(h)			21 ± 2.7	(c)
						19.5 ± 11	(c)				
Indium	Rh-102	2.2 ± 0.6	(a)	2.3 ± 0.3	(a)	3.2 ± 0.4	(a)			2.2 ± 0.9	(a)
	Ag-110m	3.2 ± 0.8	(a)	2.3 ± 0.3	(a)	3.9 ± 0.5	(a)			5.1 ± 1.0	(a)
	Sn-113	35 ± 4.2	(a)	21 ± 1.2	(a)	41 ± 2.7	(a)			54 ± 3.6	(a)
				22 ± 3.8	(e)	47 ± 19	(c)				
	In-114m	190 ± 115	(a)	35 ± 15	(a)	55 ± 35	(a)			105 ± 20	(a)
Cobalt	Mn-54			91 ± 3.8	(e)	41 ± 1.1	(a)				
				62 ± 1.4	(f)						
	Co-56			22 ± 3.8	(e)						
	Co-57			303 ± 5.4	(e)	125 ± 1.6	(a)				
				211 ± 1.6	(f)						
	Co-58			116 ± 20	(e)						
	Co-60	204 ± 20	(g)	26 ± 2.2	(e)	19 ± 0.5	(a)				
				23 ± 0.8	(f)	27 ± 2.7	(g)				

(a) LBL measurements (Smith and Hurley, ref. 16)
(b) SRL measurements (Winn, ref. 17)
(c) MSFC/EKU measurements (Laird, ref. 18))
(d) Battelle measurements (from Laird, ref. 18)
(e) LLNL measurements (Camp, from Harmon, ref. 19)
(f) LBL measurements (Smith and Hurley, from Harmon, ref. 19)
(g) Battelle measurements (Reaves, ref. 20)
(h) JSC measurements (D. Lindstrom, ref. 21)

Table 4. Production modes for nickel activation products.

Product	Half-life	Production by Protons	Production by Neutrons	Production by Decay
Sc-46	83.8 days	Ni-58 (p,8p5n) Sc-46 Ni-60 (p,8p7n) Sc-46		
Mn-54	303 days	Ni-58 (p,4p1n) Mn-54 Ni-60 (p,4p3n) Mn-54		
Co-56	77 days	Ni-58 (p,2p1n) Co-56 Ni-60 (p,2p3n) Co-56		Ni-58(p,p2n)Ni-56 $\xrightarrow[6.1\ d]{EC}$ Co-56
Co-57	270 days	Ni-58 (p,2p) Co-57 Ni-60 (p,2p2n) Co-57	Ni-58 (n,np) Co-57	Ni-58(p,pn)Ni-57 $\xrightarrow[36\ hr]{EC,\beta+}$ Co-57
Co-58	71.3 days	Ni-60 (p,2pn) Co-58	Ni-58 (n,p) Co-58	Co-58m $\xrightarrow{9.2\ hr}$ Co-58g
Co-60	5.26 years	Ni-62 (p,2pn) Co-60	Ni-60 (n,p) Co-60	Co-60m $\xrightarrow{10.5m}$ Co-60g

Table 5. Ratio of predicted-to-measured activity at recovery for nickel activation samples.

	Sample Location on LDEF			
Isotope	Exp. P0006	Exp. A0114	Exp. M0002	Exp. M0001
Sc-46	0.29			
Mn-54	0.62	0.34	0.58	0.38
Co-56	0.44	0.69	0.78	0.64
Co-57	0.46	0.48	0.46	0.63
Co-58	0.53	0.70	0.44	0.57
Co-60	0.84	0.50		
AVERAGE:	0.53	0.54	0.57	0.55
Average for all isotopes in all samples: 0.55 ± ≈ 0.1				

Data Sources: Harmon (NASA MSFC) Smith and Hurley (LBL) Reeves (PNWL)
Laird (EKU) Camp (LLNL)

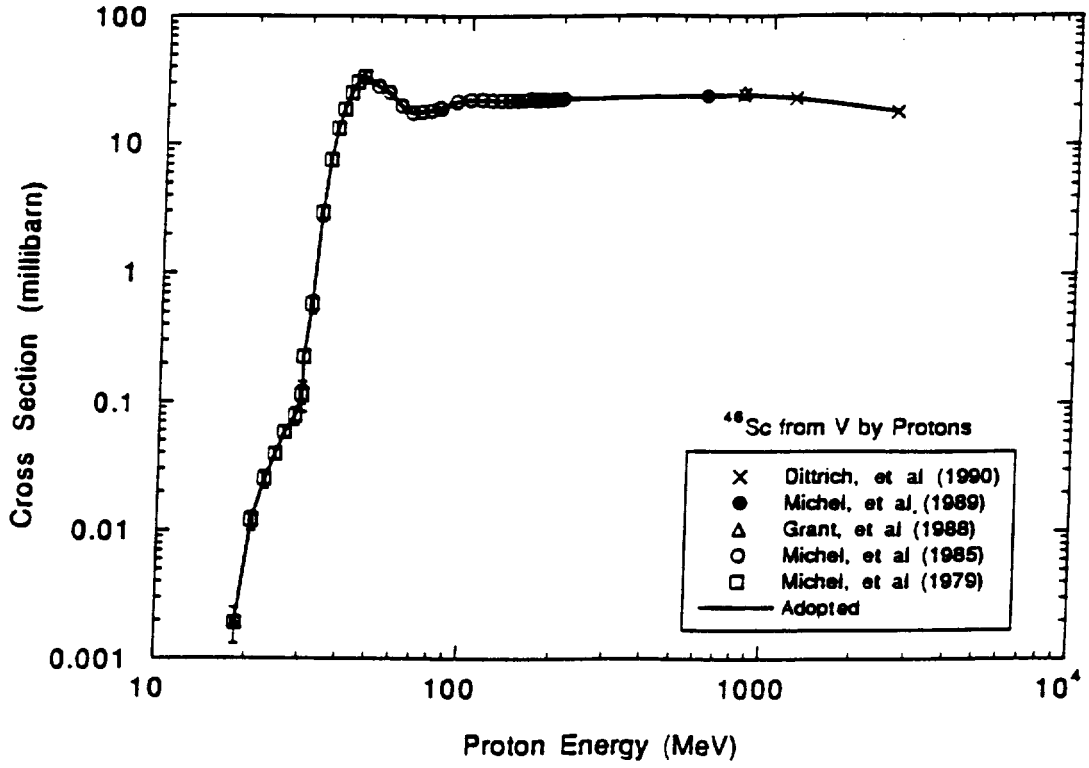

Fig. 1. Cross section for the production of ^{46}Sc from vanadium by protons; points represent measured cross sections.

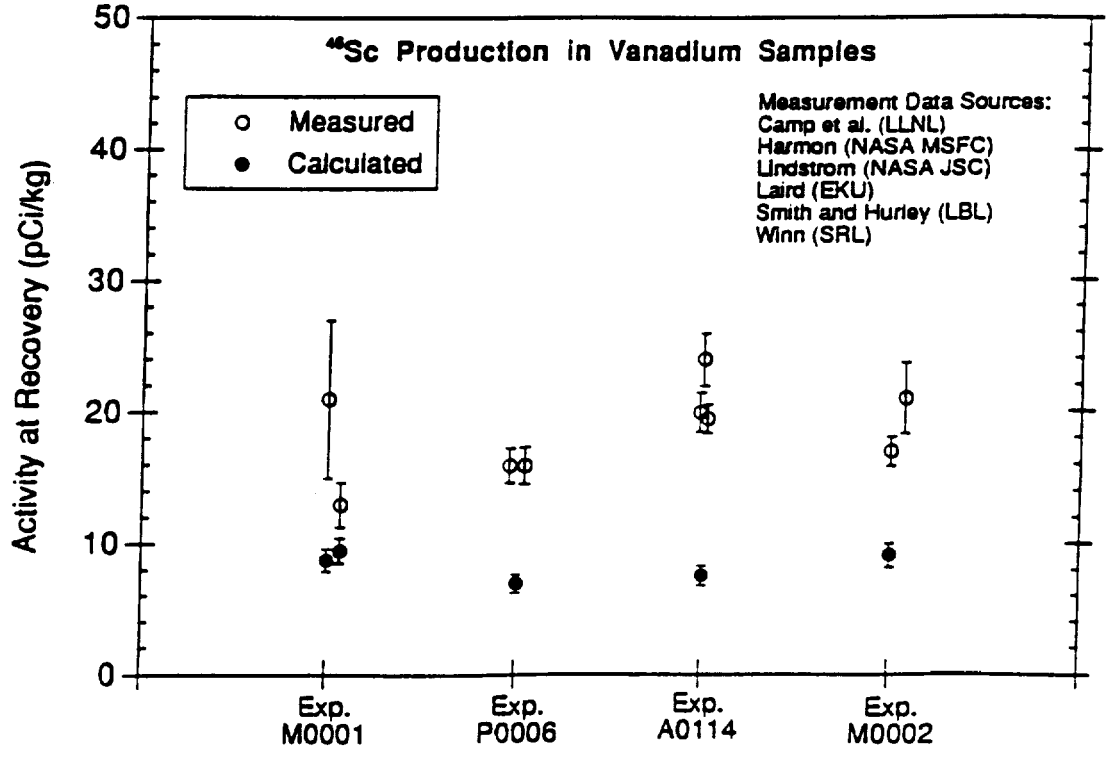

Fig. 2. Comparison of calculated and measured ^{46}Sc activation from vanadium samples.

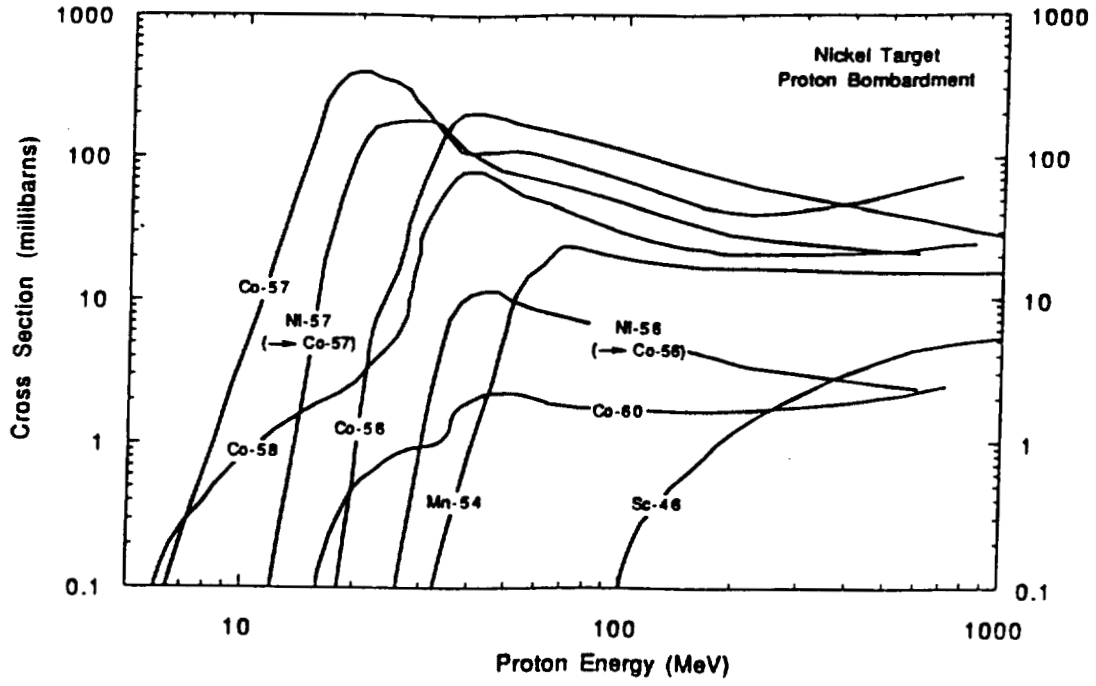

Fig. 3. Cross sections for the production of radioisotopes in nickel by protons, based on measured cross sections compiled from various sources.

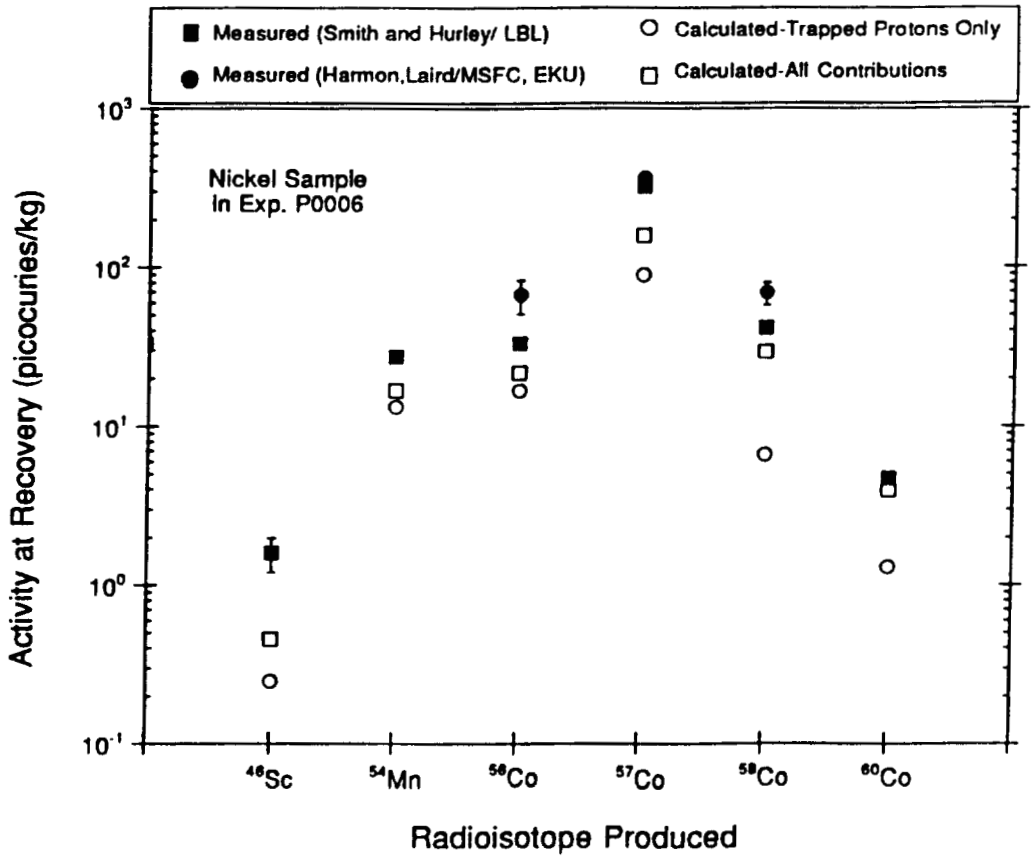

Figure 4. Comparison of predicted vs. measured (preliminary) activation products from nickel sample contained in LDEF Exp. P0006.

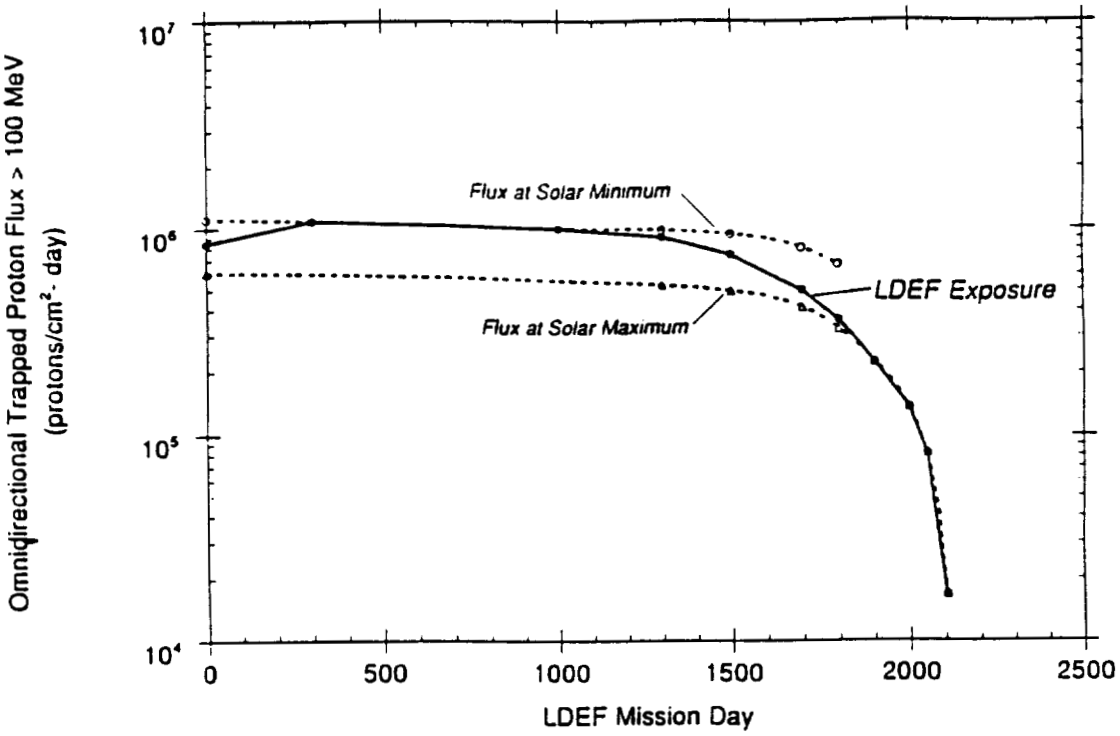

Fig. 5. Predicted trapped proton flux > 100 MeV during LDEF mission, from ref. 4.

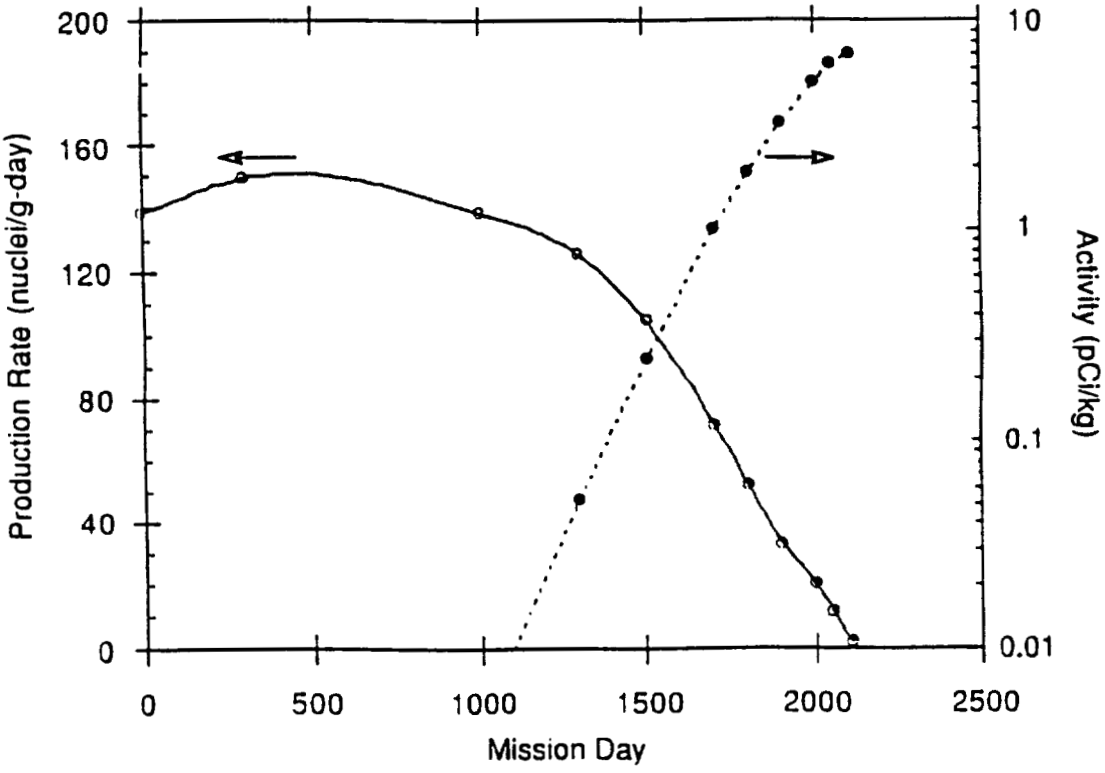

Fig. 6. Time dependence of ^{46}Sc production (solid curve) and the contribution of this production to the activity at recovery (dotted curve) for vanadium sample in Exp. P0006.

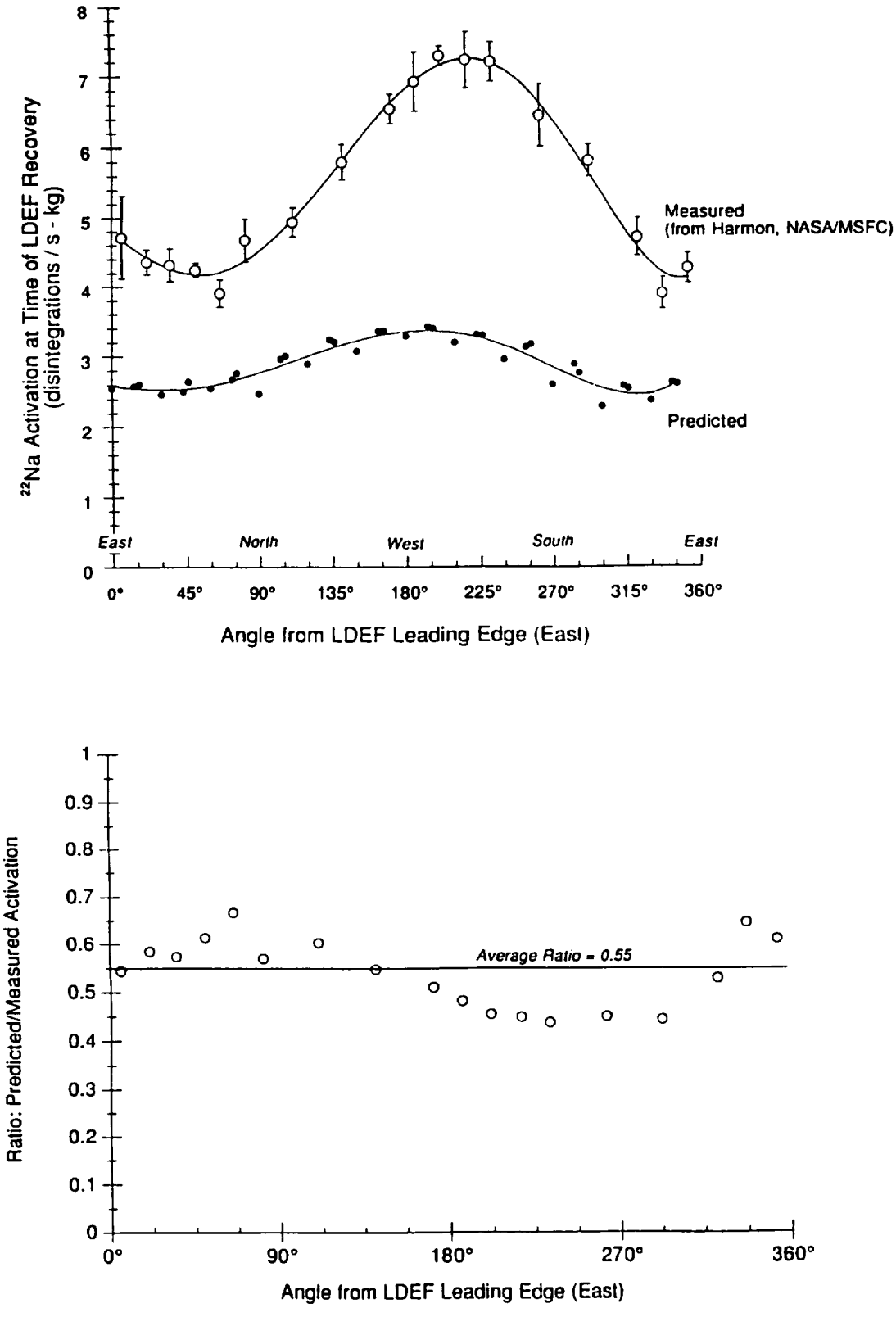

Fig. 7. Measured and predicted ^{22}Na activation of LDEF aluminum tray clamps (top), and predicted/measured ratio (bottom).

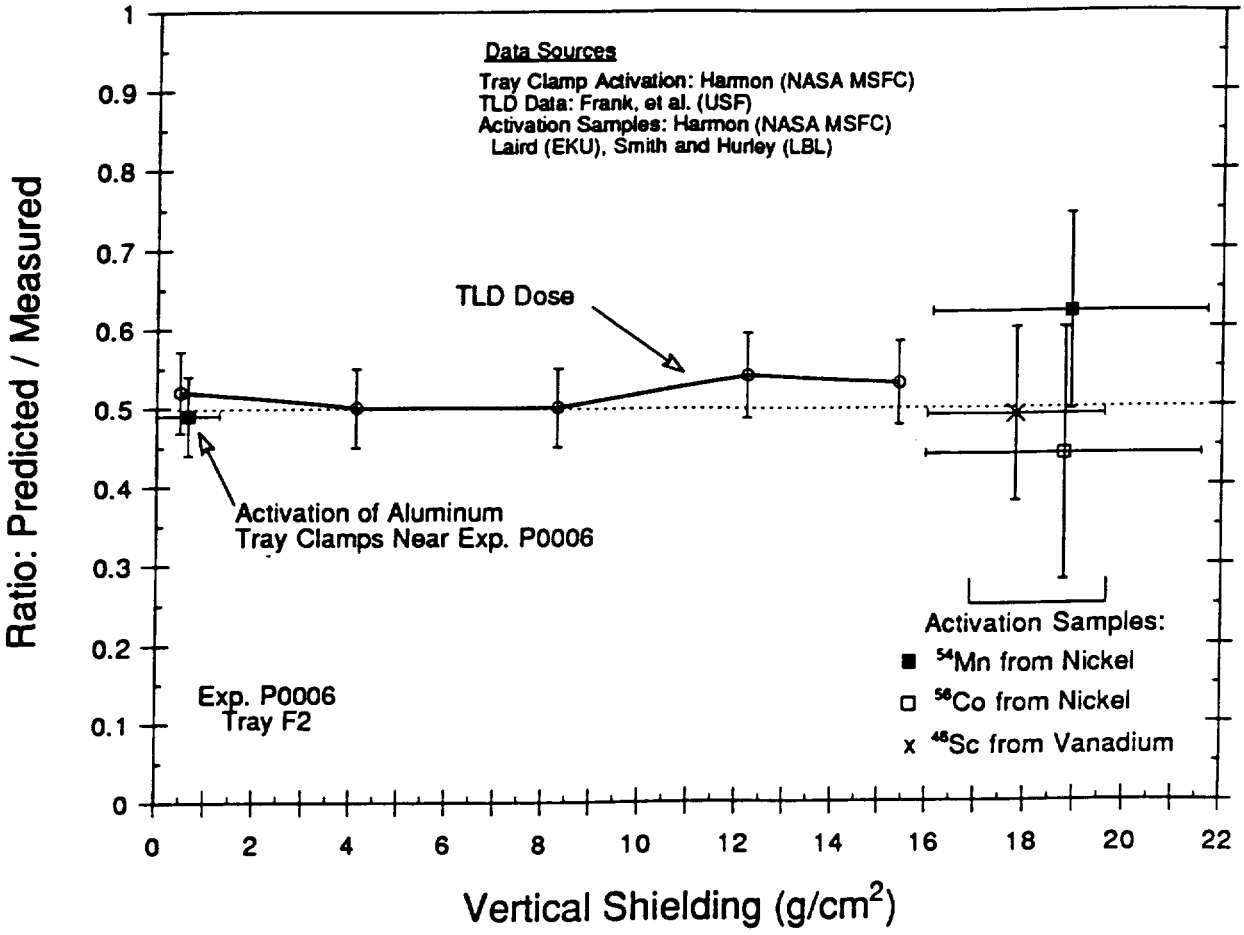

Fig. 8. Comparison of predicted vs. measured effects from trapped protons in LDEF experiment P0006 (Tray F2, trailing side).

STATUS OF LDEF RADIATION MODELING

John W. Watts
ES84, NASA/Marshall Space Flight Center
AL 35812
Phone: 205/544-7696, Fax: 205/544-7754

T. W. Armstrong and B. L. Colborn
Science Applications International Corporation
Route 2, Prospect, TN 38477
Phone: 615/468-2603, Fax: 615/268-2676

ABSTRACT

The current status of model prediction and comparison with LDEF radiation dosimetry measurements is summarized with emphasis on major results obtained in evaluating the uncertainties of present radiation environment model. The consistency of results and conclusions obtained from model comparison with different sets of LDEF radiation data (dose, activation, fluence, LET spectra) is discussed. Examples where LDEF radiation data and modeling results can be utilized to provide improved radiation assessments for planned LEO missions (e.g., Space Station) are given.

INTRODUCTION

The return of LDEF has provided a unique opportunity to test current ionizing radiation models with a great variety of measurements. Figure 1 (ref. 1) describes the characteristics of the LDEF mission and measurements that are important for these comparisons and figure 2 (ref. 1) shows the models and programs whose outputs have been compared to the measurements of various LDEF experiments.

PROTON DOSE

There were a number of experiments (ref. 2, 3) which contained thermoluminescent dosimeters (TLD) with sufficient shielding so that the geomagnetically trapped protons contributed nearly all the accumulated dose observed. These measurements provide a good test of the Vette trapped proton model AP8MIN and AP8MAX(ref.6). Figures 3, 4, and 5 from (ref. 7) show comparisons of measurements with predictions both as ratios (Figures 3 and 5) and mission dose (Figure 4). The Figure 3 ratios suggest that the Vette models predict fluxes that are about 0.6 of the actual fluxes. Energy dependence of the ratio is not evident since the ratio is constant over a large range of effective shield thicknesses. Figure 5 shows a test of the directional model(ref. 8) against measurements. The higher observed ratios suggest that the proton scale heights used in

the model are low. The comparisons are somewhat complicated by the effects of shielding geometry. Both a complex geometry model of the spacecraft and accounting of the proton directionality are required to match the trends observed in the measurements. One is not sufficient without the other.

ELECTRON DOSE

TLD measurements behind thin shields ($< 1.0 g/cm^2$) provide a test of the AE8MIN and AE8MAX geomagnetically trapped electron models(ref. 9). These were a number of measurements on LDEF that meet this requirement(ref. 4, 5). In Figure 6 from (ref. 7) these measurements are compared to predicted values for a plane slab shielding geometry(ref. 10) with generally good agreement considering the difficulty of the measurements for very thin geometries. The high predictions at the thinnest shielding may reflect an excess of low energy electrons in the models or geometry effects where the detector thicknesses are comparable with the shield thickness.

PROTON ACTIVATION

The LDEF measurements of activation samples for so many location and shielding depths on a single satellite with a long-term stable attitude is unique. The ^{22}Na activation measurements of the tray clamps are little confused by geometry and the surface is well mapped by numerous samples. In Figure 7 from (ref. 11) these measurements(ref. 12, 14) are compared with the directional flux model(ref. 8, 11, 12) combined with both detailed and simple geometrical shielding models. The predictions are lower than the measurements by about the same ratios seen in the TLD versus predicted dose comparisons, again suggesting that the Vette proton flux model(ref. 6) predicts low fluxes for low orbital altitudes. The anisotrophy of the proton flux is more evident in these measurements than in any others on LDEF.

Table 1. Ratio of predicted-to-measured activity
at recovery for nickel activation samples from (ref. 11)

	Sample Location on LDEF			
Isotope	Exp. P0006	Exp. A0114	Exp. M0002	Exp. M0001
Sc-46	0.29			
Mn-54	0.62	0.34	0.73	0.33
Co-56	0.66	0.69	1.24	0.59
Co-57	0.49	0.48	0.46	0.63
Co-58	0.71	0.69	0.55	0.56
Co-60	0.84	0.49		
Average	0.60	0.54	0.74	0.53

Average for all samples: 0.60±0.15

Tables 1 and 2 from (ref. 11) show intentional sample measurements for nickel (Table 1) and vanadium (Table 2) at a variety of shielding depths. Again the measurements are higher than

the model predictions with most of the ratios near those observed for dose and ^{22}Na activation. Some of the other ratios may be explained by contributions from galactic cosmic rays or uncertainties in activation cross sections used in the models. The general trend supports the conclusion from the other comparisons that the Vette flux predictions(ref. 3) are low.

Table 2. Comparison of Sc-46 activation in vanadium samples from (ref. 11)

Sample Location			Activity at Recovery (picocuries/kg)		Ratio
Exp.	Tray	Position	Measured	Calculated	Meas./Calc.
P0006	F2	trailing edge	17±1.1 (a)	7.00	0.40
			21±2.7 (b)		0.33
A0114	C9	leading edge	20±1.5 (b)	7.65	0.38
M0001	H12	space end	20±13 (b)	8.76	0.44
			22±6.8 (b)	9.50	0.44
M0002	G12	earth end	16±1.3 (b)	9.16	0.57
			16±1.4 (c)		0.58
				Average	0.46±0.16

LET SPECTRA

The long mission exposure on LDEF allowed the measurement of the Linear Energy Transfer (LET) spectra to be extended to higher LET with better statistical accuracy than has been achieved previously(ref. 15). Measurements at higher LET are significant because particles with higher LET are more likely to produce Single Event Upsets (SEU)s of microelectronic devices (an important problem for spacecraft applications). Figure 8 from (ref. 16) shows comparisons between model(ref. 17) and measured LET spectra. At high LET the measurements are significantly higher than the model. At low LET where protons are the most common particle the model results are higher. This suggest the possibility that not all the protons are being detected due to their very thin tracks. The differences at high LET are more difficult to explain, but the modeling approach ignores nuclear interactions and the produced fission fragments.

Iron nuclei fluxes are of interest because these particles have the largest charges and therefore largest LET of any particles that are fairly abundant. (elemental abundances takes a major step downward just beyond iron.) Figure 9 from (ref. 18) show LDEF measurements of the iron energy spectra. The excess over fluxes expected from galactic cosmic rays in the energy range (100-800 MeV) has been attributed to particles arriving during the large solar particle events in the fall of 1989. For iron nuclei in this energy range to arrive at the LDEF orbit through the Earth's magnetic field they must not have been completely stripped of electrons and the results suggest a charge near +12-13 similar to iron in the corona. In Figure 10 from (ref. 11, 19) the

LDEF measured Fe fluxes are used to replace the Fe fluxes used in CREME(ref. 17) for a 500 km altitude orbit at 28.5°. (The flux is not strongly dependent on altitude.) The result suggest that CREME predicts high fluxes of the low energy component of the heavier particles.

SUMMARY

The LDEF ionizing radiation measurements continue to provide a unique opportunity to test the current models of the particle environment that will not be repeated in the foreseeable future. Careful use of the models considering the details of shielding geometry and particle anisotrophy, and model assumptions are required to explain some of the trends observed in the measurements. Only with this attention to detail can we locate where the models have significant problems describing the environment or the measurements have observation difficulty.

REFERENCE

1. Armstrong, T. W.,; Colborn, B. L. and Watts, J. W.: Radiation Calculations and Comparisons with LDEF Data. First LDEF Post-Retrieval Symposium, NASA CP-3134, 1991, pp. 347-360.

2. Benton, E. V.; Frank, A. L.; Benton, E. R.; Csige, I.; Parnell, T. A. and Watts, J. W.: Radiation Exposure of LDEF: Initial Results. First LDEF Post-Retrieval Symposium, NASA CP-3134, 1991, pp. 325-338.

3. Frank, A. L.; Benton, E. V.; Armstrong, T. W. and Colborn, B. L.: Absorbed Dose and Predictions on LDEF. Second LDEF Post-Retrieval Symposium, NASA CP-3194, 1992, pp. 163-170.

4. Bourieau, J.: LDEF: Dosimetric Measurements Results (A0138-7) Experiment. Second LDEF Post-Retrieval Symposium, NASA CP-3194, 1992, pp. 157-162.

5. Blake, J. B. and Inmamoto, S. S.: A Measurement of the Radiation Dose to LDEF by Passive Dosimetry. Second LDEF Post-Retrieval Symposium, NASA CP-3194, 1992, pp. 147-155.

6. Sawyer, Donald M. and Vette, James I.: AP-8 Trapped Proton Environment for Solar Maximum and Solar Minimum. National Science Data Center, Goddard Space Flight Center, NSSDC/WDC-A-R& S 76-06, 1976.

7. Armstrong, T. W. and Colborn, B. L.: Radiation Model Predictions and Validation Using LDEF Satellite Data. Second LDEF Post-Retrieval Symposium, NASA CP-3194, 1992, pp. 207-220.

8. Watts, J. W.; Parnell, T. A.; and Heckman, H. H.: Approximate Angular Distribution and Spectra for Geomagnetically Trapped Protons in Low-Earth Orbit. High Energy Radiation Background in Space, Proceedings of AIP Conference, Sanibel Island, Florida, Vol. 186, 1989, pp. 75-85.

9. Vette, J. I.: The AE8 Trapped Electron Model Environment. National Space Science Data Center, Goddard Space Flicht Center, NSSDC/WDC-A-R&S 91-24, 1991.

10. Watts, J. W.; Parnell, T. A.; Derrickson, J. H.; Armstrong, T. W.,; and Benton, E. V.: Prediction of LDEF Ionizing Radiation Environment. First LDEF Post-Retrieval Symposium, NASA CP-3134, 1991, pp. 213-224.

11. Armstrong, T. W. and Colborn, B. L.: Prediction of LDEF Induced Radioactivity and Comparison with Measurements. Third LDEF Post-Retrieval Symposium, NASA CP-3275, 1995.

12. Colborn; B. L. and Armstrong; T. W.: Development and Application of a 3-D Geometry/Mass Model for LDEF Satellite Ionizing Radiation Assessments. Second LDEF Post-Retrieval Symposium, NASA CP-3194, 1992, pp. 195-206.

13. Harmon, B. A.; Fishman, G. J.; Parnell, T. A.; and Laird, C. E.: Induced Radioactivity in LDEF Components. First LDEF Post-Retrieval Symposium, NASA CP-3134, 1991, pp. 301-312.

14. Harmon, B. A.; Fishman, G. J.; Parnell; T. A. and Laird; C. E.: Induced Activation Study of LDEF. Second LDEF Post-Retrieval Symposium, NASA CP-3194, 1992, pp. 125-136.

15. Benton, E. V.; Csige, I.; Oda, K.; Henke, R. P.; Frank, A. L.; Benton, E. R.; Frigo, L. A.; Parnell, T. A.; Watts, J. W. Jr.; and Derrickson, J. H.: LET Spectra Measurements of Charged Particles in the P0006 Experiment of LDEF. Second LDEF Post- Retrieval Symposium, NASA CP-3194, 1993.

16. Armstrong, T. W. and Colborn, B. L.: Prediction of LET Spectra Measured on LDEF. Third LDEF Post-Retrieval Symposium, NASA CP-3275, 1995.

17. Adams, J. H. Jr.: Cosmic Ray Effects on Microelectronics, Part IV, Naval Research Laboratory NRL Memorandum Report 5901, December 1986.

18. Tylka, A. J.; Adams, J. H.; Bealm, L. P.; Boberg, P. R. and Kleis, T.: Results from the HIIS Experiment on the Ionic Charge State of Solar Energetic Particles. Third LDEF Post-Retrieval Symposium, NASA CP-3275, 1995.
tion.)

19. Space Station Ionizing Radiation Emission and Susceptibility for Ionizing Radiation Environment Compatibility. SSP 30512, National Aeronautics and Space Administration, 1991.

Unique Features of LDEF Mission	Importance to Ionizing Radiation Data Collection	Importance to Model/Code Validation	Importance to Future LEO Missions
• Well-instrumented for ionizing radiation measurements	• Extensive radiation dosimetry: - *6 different types of dosimetry* - *multiple dosimeters of each type (≈ 200 TLD's, > 500 PNDT's, > 400 activation samples)* - *multiple dosimetry locations (in 16 different experimental trays)*	• Data sufficiently extensive and detailed to allow variety of modeling checks - e.g.: - *absorbed dose* - *proton and heavy ion fluence* - *energy spectra* - *LET spectra* - *secondary neutron fluence and spectra*	• Allows benchmarking and improvements of predictive methods for addressing ionizing radiation issues: - *dose to astronauts electronics upset/burnout* - *materials damage* - *radiations backgrounds to sensitive instrumentation*
• Long mission duration	• High statistical accuracy of dosimetry results	• Unprecedented data accuracy for checking model predictions of high-LET radiation from high-Z cosmic rays and nuclear recoils	• High-LET radiation component is of key importance in assessing "single-hit" phenomena: - *biological effects* - *Single-Event-Upsets of electronics*
• Fixed orientation (< 0.2° wobble during mission)	• Allows measurement of trapped proton anisotropy	• Unprecedented data for testing models of trapped proton anisotropy	• Trapped proton anisotropy important for LEO, fixed-orientation spacecraft (such as Space Station Freedom, EOS)

Figure 1. Significance of LDEF data for validation of ionizing radiation models from (ref. 1).

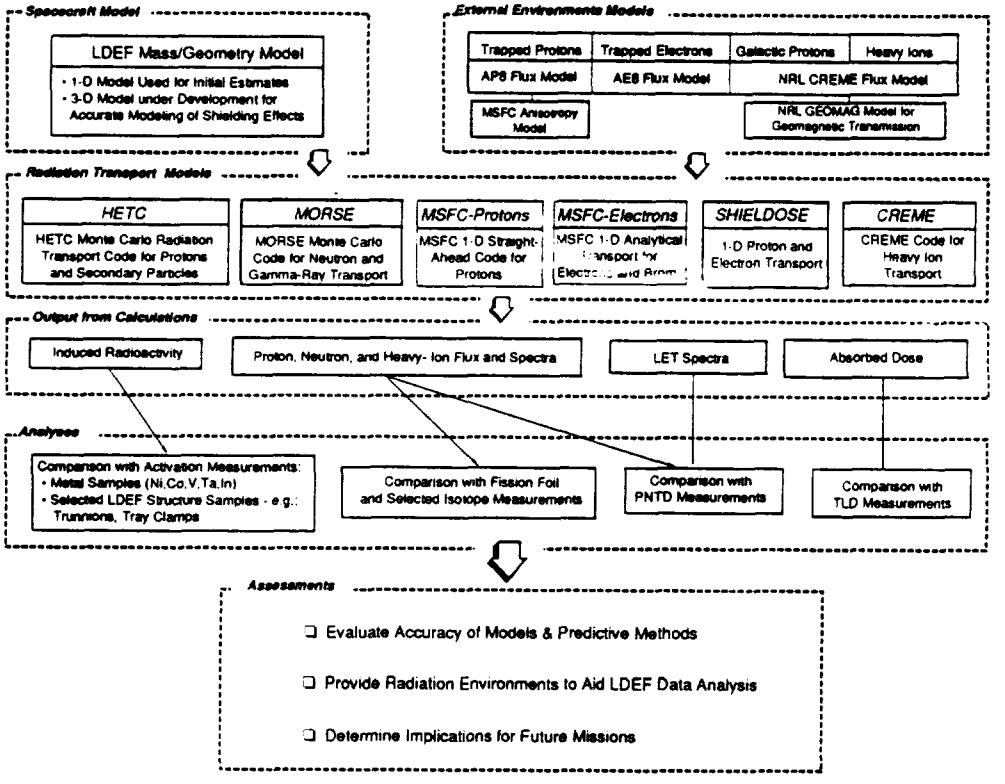

Figure 2. Overview of approach and models for LDEF ionizing radiation calculations from (ref. 1).

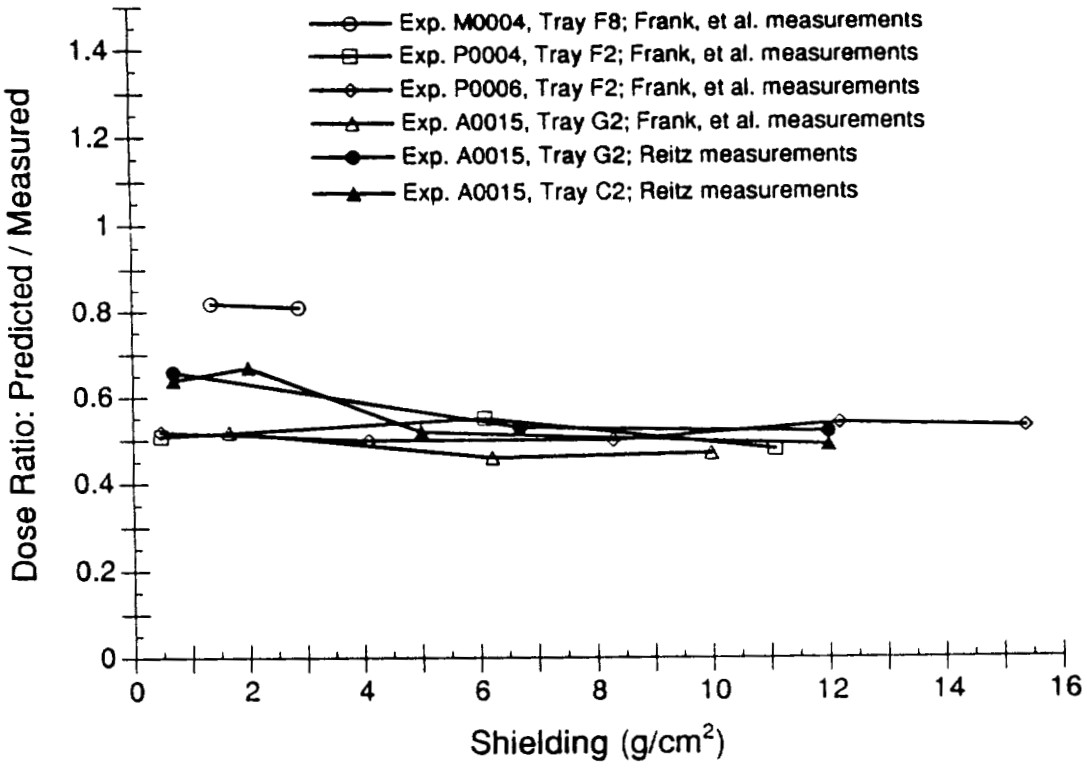

Figure 3. Ration of predicted-to-measured radiation dose (in tissue) due to trapped proton environment based on LDEF data from thermoluminescent dosimeters from (ref. 7).

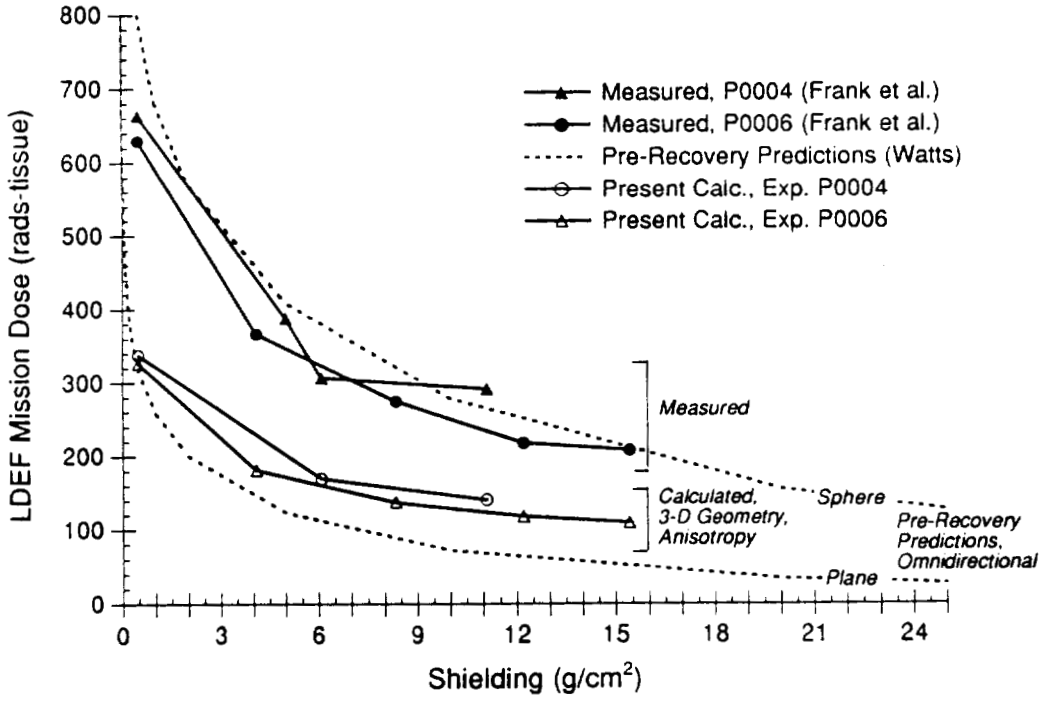

Figure 4. Influence of geometry model and environment anisotrophy on predicting LDEF dose from trapped protons from (ref. 7).

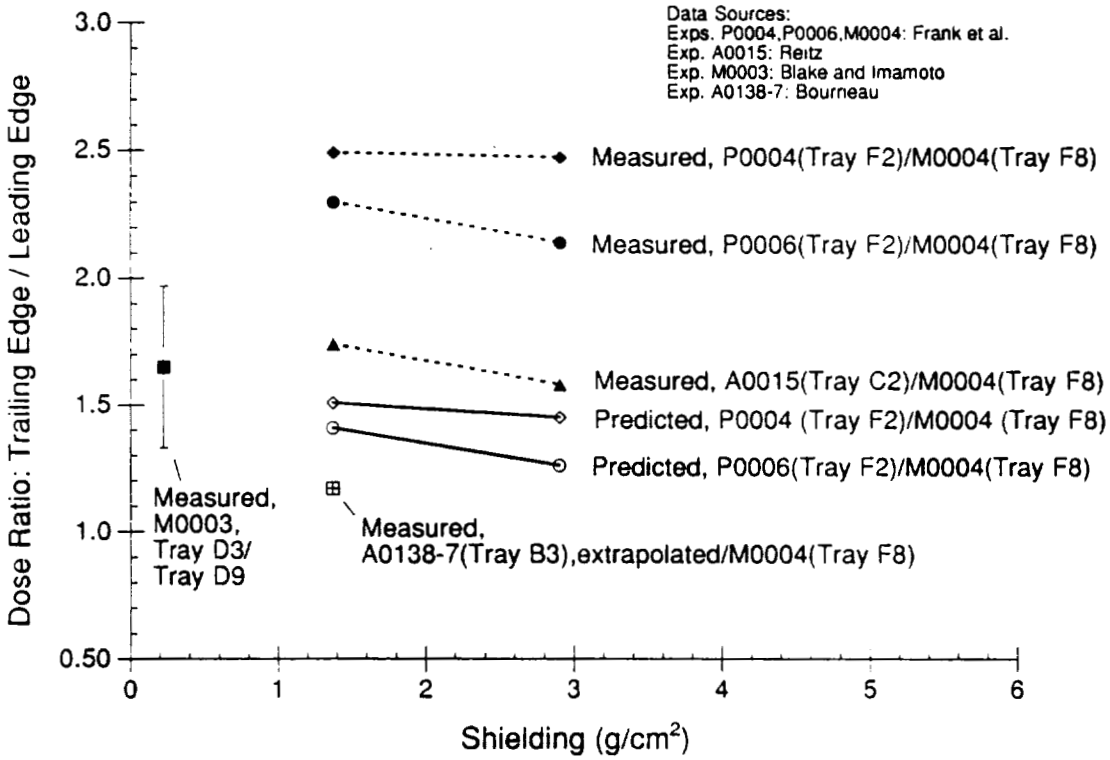

Figure 5. Radiation dose anisotrophy on LDEF due to the directionality of the trapped proton environment. Shown are predicted and measured values of the ratio for the dose on the trailing (west) side LDEF to the dose on leading (east) side from (ref. 7).

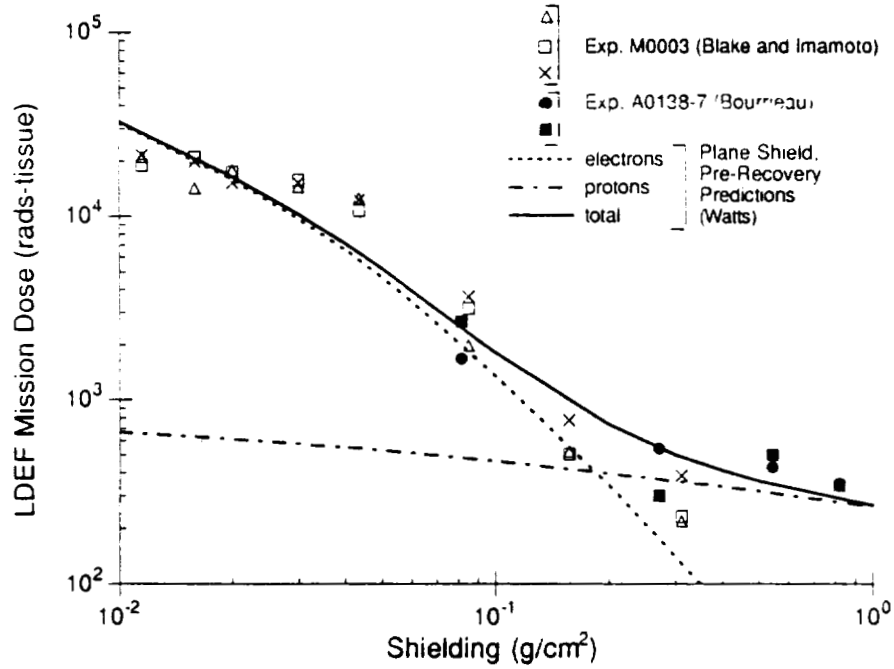

Figure 6. Comparison of measured and predicted absorbed dose for thermoluminescent dosimeters having thin shielding where the dose is due to the trapped electron environment from (ref. 7).

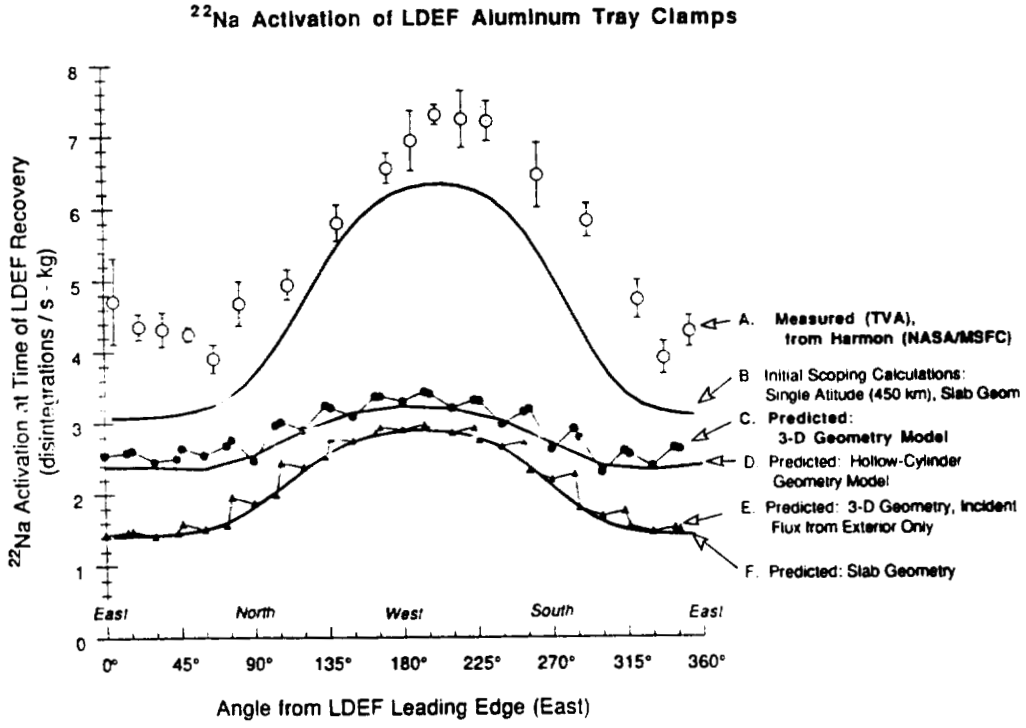

Figure 7. Preliminary comparison of predicted vs. measured effect (ref. 13, 14) of trapped proton anisotrophy in terms of ^{22}Na radioactivity induced in aluminum clamps of LDEF experiment trays from (ref. 11).

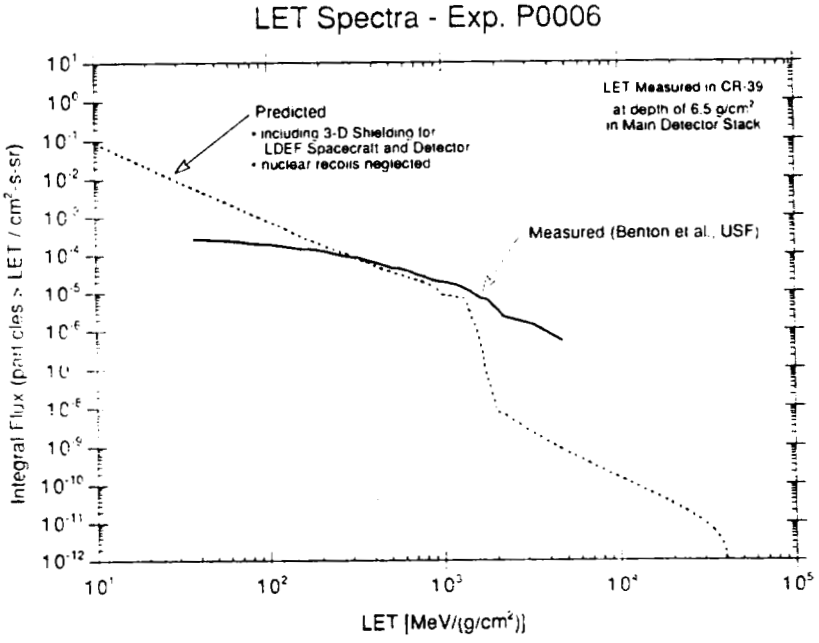

Figure 8. Comparison of LDEF predictions of Linear Energy Transfer (LET) spectra and interim results from measured spectra in experiment P0006(ref. 15). The predictions were made using the CREME code(ref. 17) and a 3-D shielding geometry from (ref.16) .

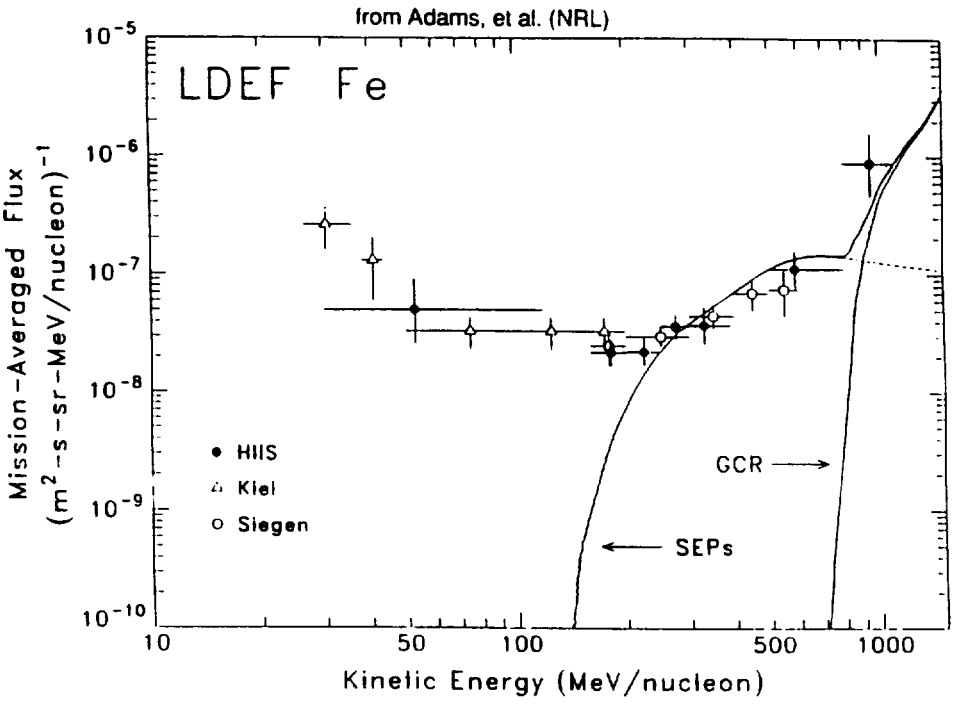

Figure 9. Measured low energy Fe spectra measured by HIIS experiment on LDEF from (ref. 18).

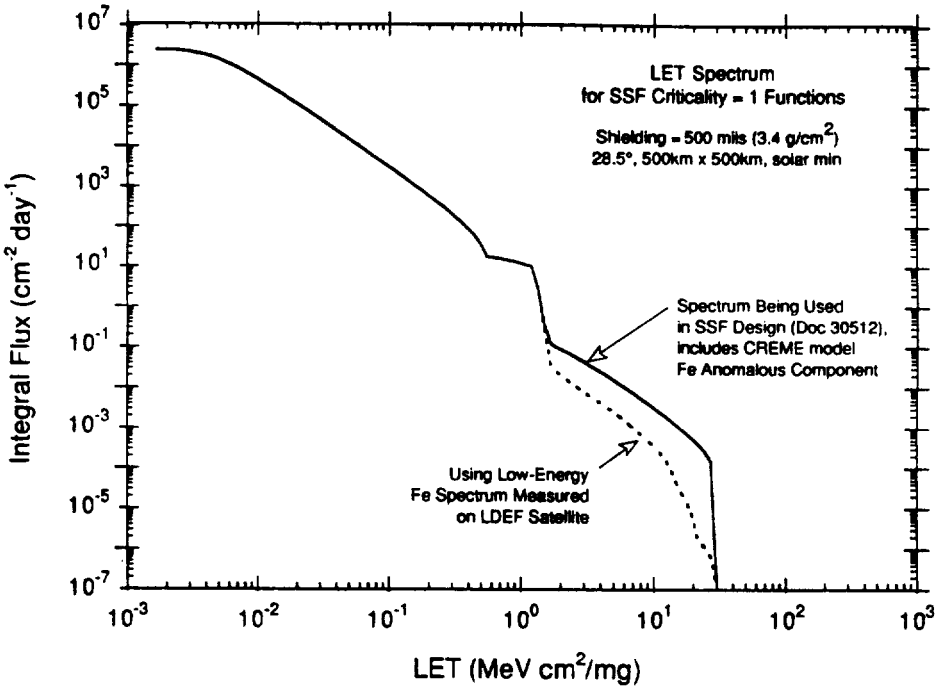

Figure 10. Comparison of Space Station Freedom Requirement document SSP 30512 (ref. 19) spectra vs. LET and measured results from the HIIS experiment on LDEF from (ref. 16).

^{10}Be IN TERRESTRIAL BAUXITE AND INDUSTRIAL ALUMINUM: AN LDEF FALLOUT

J.C. Gregory
The University of Alabama in Huntsville
Department of Chemistry
Huntsville, AL 35899-2900
Phone: 205/895-6028, Fax: 205/895-6061

A. Albrecht and G. Herzog
Rutgers Univerity
Department of Chemistry
New Brunswick, NJ 08901
Phone: 908/932-3955, Fax: 908/932-5312

J. Klein and R. Middleton
University of Pennyslvania
Physics Department
Philadelphia, PA 19104-6396
Phone: 215/898-8832, Fax: 215/898-2010

B.A. Harmon and T.A. Parnell
NASA, Marshall Space Flight Center
Space Science Laboratory, ES62
Huntsville, AL 35812
Phone: 205/544-4924, Fax: 205/544-7754

SUMMARY

Work has continued on the search for ^{10}Be on metals other than aluminum flown on LDEF. Much time-consuming extractive chemistry has been perfomed at Rutgers University on turnings obtained from the ends of two stainless steel trunnions from LDEF and the prepared samples will be run on the University of Pennsylvania accelerator mass spectrometer.

We have continued to investigate our discovery of naturally-occurring ^{10}Be contamination in bauxite and industrial aluminums from different sources. Measurements of ^{10}Be in ores from three different sites, and from four different samples of commercial aluminum have been made. Our investigators indicate that the contamination in commercial aluminum metal originates in its principal ore, bauxite. The levels in some bauxite samples were much greater than the maximum possible for *in situ* production by cosmic ray secondaries. Adsorption of atmospheric ^{10}Be by surface ores exposed to rainfall is a reasonable explanation.

INTRODUCTION

The discovery of ^{7}Be on front surfaces of LDEF (ref. 1) pointed the way towards an investigation of the possibility of finding other radionuclides produced in the atmosphere (ref. 2). At the present time these appear practically limited to ^{10}Be and ^{14}C, though ^{26}Al must certainly be present in very small quantities (from Ar spallation).

^{10}Be quantification is particularly attractive since its surface and atmospheric chemistry will be virtually identical to that of ^{7}Be. The production and sink functions of both nuclides are well known; therefore, if both surface densities were known on the same piece of satellite material, we should obtain a probe of the vertical transport mechanism of the isotopes in the atmosphere. If the process is diffusion-controlled, the different isotope masses should provide clear indication.

The first attempt to obtain this information was foiled by the discovery that much, if not all, commercial aluminum, including that used to make LDEF and A0114 is naturally contaminated with ^{10}Be. This is not surprising since many bauxite ores are found close to, or on the ground surface, and may be wetted by rainfall which has scrubbed the Be isotopes out of the air.

In this work we describe some measurements of a sampling of several metal samples from different sources (e.g., kitchen foil, shop aluminum and LDEF metal) and of some bauxite ores from different locations. This gave some idea of the variance, but was not a systematic survey.

Table 1 shows the raw data obtained by AMS. The metals showed levels of 40 to 110 x 10^{6} (±10%) atoms of ^{10}Be per g Al.

Table 1. ^{10}Be concentrations of aluminous materials.

Sample	Source	Mass [mg]	MassAl[1] [mg]	$^{10}Be/^{9}Be$ [10^{-15}]	^{10}Be [10^{6} atom/g Al]	Normal Be [10^{-9} g/g Al]
Al AA Sol'n		140.0	140.0	63±4	61±3	159
Al foil		327.3	327.3	102±7	41±3	58
Al plate	LDEF[2]	256.7	256.7	122±8	75±3	
	LDEF 9-7[3]	219.7	219.7	101±6	63±5	
	Shop	315.2	315.2	223±22	111±11	140
Bauxite	NBS 69A	1371.8	381.3	74±10	22±2	
Bauxite, Ark.	A 21485[4]	361	141.5	48±4	15±2	
Bauxite, Haiti		497.7	52.2	33000±200	57200±3800	
Blank[5]				6±2		
Blank[6]		2085		5±1		

Notes: 1) Aluminum concentrations in the bauxites from Arkansas and Haiti were determined by DCP analysis to be 39.2% and 10.5%, respectively; NIST bauxite NBS 69A was used as a standard (27.8% Al). 2) Not flown; 3) Flown. 4) Label given by the American Museum of Natural History (New York, NY, USA); 5) Reagent blank; 6) Procedural blank run with stainless steel.

Bauxites, on the other hand, showed values from 20 to 57,000 x 10^6 atoms ^{10}Be per g of Al in the ores. Aluminum and beryllium oxides are chemically quite similar and typical bauxites contain normal ^{9}Be at levels of about 10 ppm. During aluminum refining this is reduced by a factor of about 70 times.

Thus, if we take our measured value for typical metal of 5-10 x 10^7 atoms ^{10}Be /gAl, this would require a level of 5x10^9 atoms ^{10}Be/g Al in the ore. This compares with measured values in ores of 2x10^7 atoms per g Al in the Arkansas ore and 6 x 10^{10} atoms per g Al in the Haitian ore (equivalent to 6 x 10^9 atoms per g of Haitian ore).

Table 2 shows ^{10}Be densities per gram of soil or ore. The theoretical maximum was estimated from an average U.S. rainfall and assumes the only sink function to be radioactive decay. On this scale the concentration of ^{10}Be in the Haitian ore seems remarkable, but not impossible.

Table 2. ^{10}Be atom densities per gram soil or ore

Theoretical max (1m)	1 x 10^{10} atoms g^{-1}
US Typ. soil (surface)	2 x 10^8 - 1 x 10^9
NBS and Ark ore	1 x 10^7
Haitian ore	6 x 10^9

Implications for AMS:

Analysts may wish to determine both ^{26} Al and ^{10}Be in a rock, in which case they may add both Be and Al carriers, but 5 mg of modern Al may contain 5 x 10^5 (^{10}Be atoms), providing a significant unwanted ^{10}Be background (for comparison, 5g quartz from Bandelier Tuff contains 5 x 10^6 atoms of ^{10}Be).

- need to use selected carriers
- Al cathodes should not be used for AMS sputtering

CONCLUSIONS

- Modern commercial Al contains
  ^{10}Be at the level of 5-10 x 10^7 atoms/g
  and ^{9}Be at the 50-100 ppb level.
- Bauxite contains ~ 10 ppm 'normal' ^{9}Be. About 1% of the Be (both isotopes) makes it through the refining process to Al metal.

- ^{10}Be was almost certainly produced from atmospheric sources rather than *in situ*.
- ^{10}Be concentrations in bauxites reveal their exposure histories to rainfall.
- A study of the distribution of ^{10}Be in an ore body would give more information on Be transport and retention.
- AMS analysts will now take more care with Al carriers used in ^{26}Al and ^{10}Be assays.

A more complete description of the accelerator mass spectrometry measurements and of rock dating using ^{26}Al and ^{10}Be is given by the authors in ref. 3 and references therein.

REFERENCES

1. *Observation of Be-7 on the Surface of LDEF Spacecraft*, Fishman, G.J., Harmon, B.A., Gregory, J.C., Parnell, T.A., Peters, P., Phillips, G.W., King, S.E., August, R.A., Ritter, J.C., Cutchin, J.H., Haskins, P.S., McKisson, J.E., Ely, D.W., Weisenberger, A.G., Piercey, R.B., and Dybler, T.: **Nature**, 349, 1991, pp678-680.

2a. *The Interactions of Atmospheric Cosmogenic Radionuclides with Spacecraft Surfaces*, J.C. Gregory, G.J. Fishman, B.A. Harmon, and T.A. Parnell, **The LDEF First Post-Retrieval Symposium**, Orlando, FL; June 1991. NASA Conference Publication 3134, part 1, p. 237-247.

2b. *Cosmogenic Radioisotopes on LDEF Surfaces*, J.C. Gregory, A. Albrecht, G. Herzog, J. Klein, R. Middleton, Abstracts of Second LDEF Post-Retrieval Symposium, San Diego, CA, June 1-5, 1992, NASA Conference Publication 10097, page 25; **Proceedings of Second LDEF Post-Retrieval Symposium**, NASA Conference Publication 3194, pages 231-238.

3. *^{10}Be in Bauxite and Commercial Aluminum*, R. Middleton, J. Klein, B. Dezfouly-Arjomandy, A. Albrecht, S. Xue, G.F. Herzog, J. Gregory, Accepted for publication by **Nuclear Instruments & Methods**, February 1994.

Germination, Growth Rates, and Electron Microscope Analysis of Tomato Seeds Flown On The LDEF

Ernest C. Hammond, Jr.
Department of Physics, Morgan State University
Cold Spring Lane & Hillen Road, Baltimore, MD 21239
Phone: 410/319-3405, FAX 410/319-3272

Kevin Bridgers
Department of Physics, Morgan State University
Cold Spring Lane & Hillen Road, Baltimore, MD 21239
Phone: 410/319-3405, FAX 410/319-3272

Cecelia Wright Brown
Department of Physics, Morgan State University
Cold Spring Lane & Hillen Road, Baltimore, MD 21239
Phone: 410/319-3405, FAX 410/319-3272

ABSTRACT

The tomato seeds were flown in orbit aboard the Long Duration Exposure Facility (LDEF) for nearly six years. During this time, the tomato seeds received an abundant exposure to cosmic radiation and solar wind. Upon the return of the LDEF to earth, the seeds were distributed throughout the United States and 30 foreign countries for analysis. The purpose of the experiment was to determine the long term effect of cosmic rays on living tissue. Our university analysis included germination and growth rates as well as Scanning Electron Microscopy and X-ray analysis of the control as well as Space-exposed tomato seeds.

In analyzing the seeds under the Electron Microscope, usual observations were performed on the nutritional and epidermis layer of the seed. These layers appeared to be more porous in the Space-exposed seeds than on the Earth-based control seeds. This unusual characteristic may explain the increases in the space seeds growth pattern. (Several test results show that the Space-exposed seeds germinate sooner than the Earth-Based seeds. Also, the Space-exposed seeds grew at a faster rate). The porous nutritional region

may allow the seeds to receive necessary nutrients and liquids more readily, thus enabling the plant to grow at a faster rate.

Roots, leaves and stems were cut into small sections and mounted. After sputter coating the specimens with Argon/Gold Palladium Plasma, they were ready to be viewed under the Electron Microscope. Many micrographs were taken. The X-ray analysis displayed possible identifications of calcium, potassium, chlorine, copper, aluminum, silicon, phosphate, carbon, and sometimes sulfur and iron. The highest concentrations were shown in potassium and calcium. The Space-exposed specimens displayed a high concentration of copper and calcium in the two specimens. There was a significantly high concentration of copper in the Earth-based specimens, whereas there was no copper in the Space-exposed specimens.

Introduction

The long-term effect of cosmic environmental condition on the normal growth and development of living plant tissue is a key component in understanding man's capabilities for space colonization. Obtained from NASA were Rutgers California Supreme Tomato seeds (Lycopersicon esculentum, var. commune) that were part of the LDEF (Long Duration Exposure Facility) satellite mission. The seeds were hermetically packaged at Park Seed Co., in Greenwood, South Carolina. A portion of the seeds remained at Park Seed Co., in a controlled climate of 21 C with 20% humidity. On April 6, 1984, the Space Shuttle Challenger placed in orbit an additional portion of seeds on board the LDEF. During the LDEF's orbit, the seeds were kept in a scientifically controlled climate of 14 psi with 15% humidity.

The effective use of Scanning Electron Microscopy, Digital Imaging Processing and X-ray Microanalysis were primary techniques used in the understanding of internal and external structures as well as variations in tissue structure of the Rutgers tomato seeds, while excluding water. Hamly (1932) believed that water exclusion was a property of the outer layers of the coat, that is the suberized walls and caps of the Malpighian cells but, more importantly, he showed that impermeability was lost when the highly stressed cells at the strophiole (lens) separated, thus forming a strophiolar cleft and permitting water entry.

The environmental conditions of space such as cosmic radiation, temperature, constant pressure and humidity are examples of abnormal conditions that cause additional stress on plant and animal tissue. This additional stress is thought to be responsible for creating strophiolar clefts in Space-exposed tomato seeds that are larger in size than those created under Earth-based conditions. The two basic internal layers of the seed which include the embryonic layer (contains the ovary) and the endosperm (stores nutrients for growth) are visibly observed by digitally imaged micrographs, taken with the Scanning Electron Microscope, at very high magnification (micrographs 1 and 2). Moreover, note the relative thickness of the LDEF outer seed coat in comparsion with the control seed outer coat; the outer seed coat is 75% smaller for the same position on the seed.

Potential risks to plant and humans in future Space-based controlled ecological life support systems have not been addressed directly (Norman & Schuerger, 1990). The purpose of this study is to show structural changes, along with qualitative element

identification and germination rate variations between Earth-based and Space-exposed tomato plants.

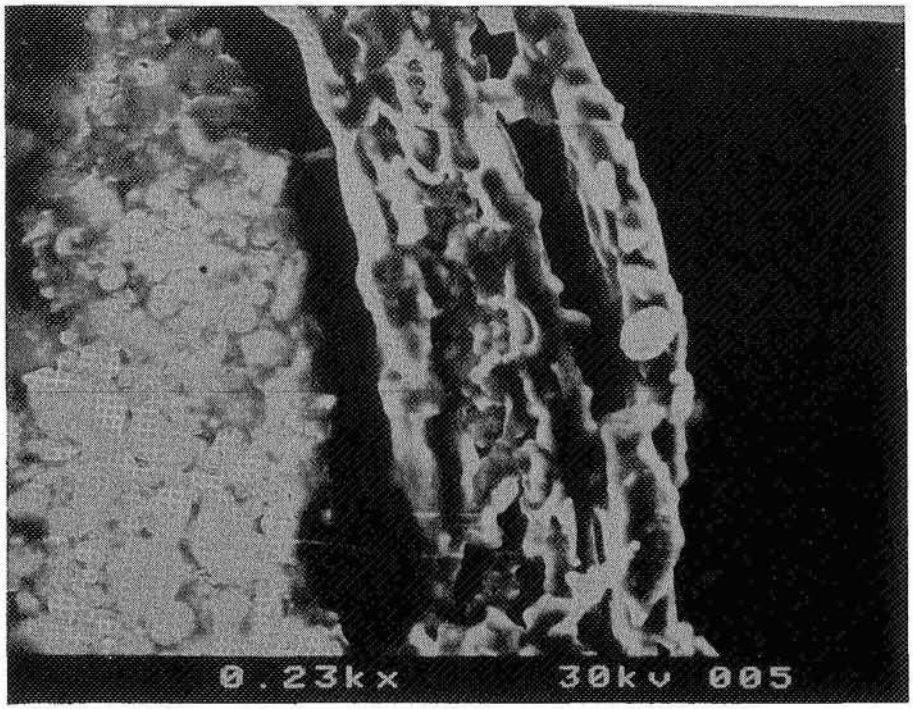

Figure 1. Outer Seed Coat for the Control Seed

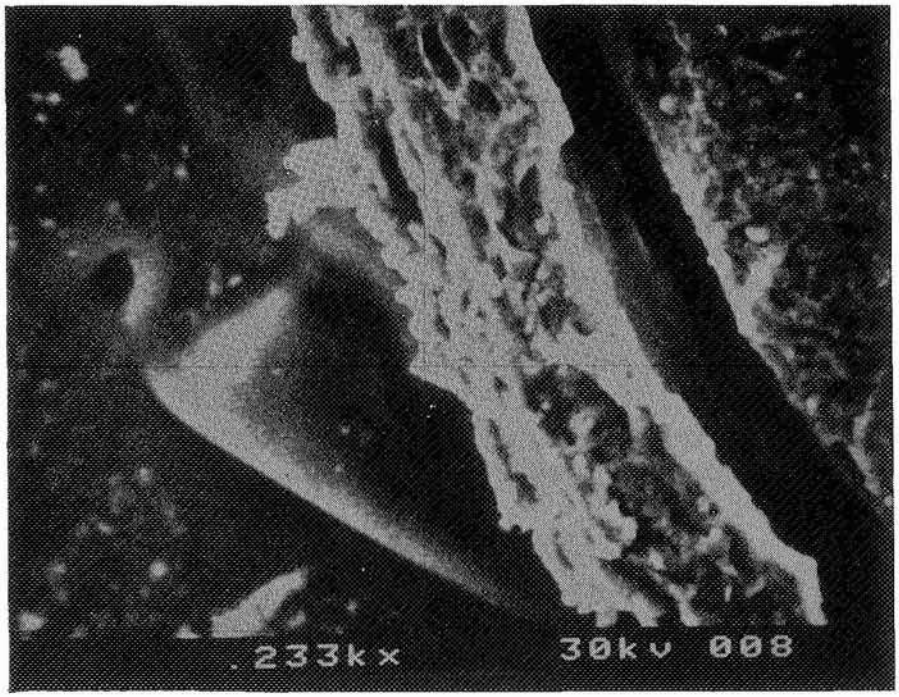

Figure 2. Outer Seed Coat for the LDEF Exposed Seed

Table 1 indicates the relative size of the strophiole clefts of the seed coat measured at a magnification of 11.1 KX. The heights of the controls show dramatic increases, while there is a modest increase for the strophiole widths.

TABLE 1.
STROPHIOLE CLEFTS OF THE SEED COAT
BASED ON MEASUREMENTS TAKEN AT A MAGNIFICATION OF 11.1 kx

	SPACE		EARTH	
	HEIGHT	WIDTH	HEIGHT	WIDTH
1.	12.4	4.4	7.1	3.2
2.	11.8	4.2	6.6	3.4
3.	11.4	5.2	6.2	4.1
4.	12.2	5.6	6.3	4.2
5.	13.1	5.1	5.7	4.2
6.	12.6	5.0	5.2	3.8
7.	12.4	4.7	6.1	3.4
8.	10.8	5.1	6.0	3.7
9.	11.9	4.5	5.3	3.1
10.	12.5	4.7	5.5	3.1
MEAN VALUE	12.1	4.8.5	6.0	3.6.1

Table 2

Table 2 shows a relative growth rate analysis over the 3 month period that the sample tomato plants germinated. Note that the group growth rate for A, B, and C of the LDEF exposed seeds have greater heights then the earth based plants heights during the first month of growth. The initial measurements of the heights for the groups A and D show that group A's position had the highest rate of growth when compared to group D's position. Subsequent heights measurements indicate that the earth based plant seeds in comparison with the LDEF show minimal statistical variation in height after the third month.

TABLE II.

GROWTH MEASUREMENTS OF RUTGERS TOMATO PLANTS

DATE RECORDED	MAY 22	JUNE 24	JULY 18
EARTH BASED PLANTS HEIGHT (cm)	2.2 cm	16.4	32.7
SPACED EXPOSED PLANTS HEIGHT (cm)			
GROUP - A	4.41	21.0	30.5
GROUP - B	4.15	17.8	33.7
GROUP - C	3.71	18.5	32.8
GROUP - D	2.7	13.9	28.8

Surface Coat of the Seed

SEM studies have been conducted that demonstrate a unique difference between the LDEF seeds and the control seeds. The control seeds have a wave like surface with minimal surface pores. Moreover, the seed for both the LDEF and control seed have cylindrical structures of some organic nature, but the LDEF exposed seeds have cylindrical structures which are less symmetrical as shown in micrograph Figures 4 and 9. The most fascinating observation is that the LDEF exposed seed have many porous structures which are visible in the center portion and outer edge of the seed. This may explain why the LDEF exposed seeds have faster germination rate than the control seeds.

The seeds may have undergone some type of early germination, while in the LDEF for the 69 month trip. The 3000X micrograph Figure 6 indicates the internal structure of the numerous pores observed using the LDEF seed. In micrograph Figure 3 one can clearly see the pores on the LDEF exposed-seeds. Micrograph Figures 4, 5, 6 indicate increased magnification of the pores region 209X to 3150X magnification. Figure 6, the highest magnification level, shows the organic matter of an individual pore in the LDEF exposed-seeds.

Figures 7, 8, 9 show increased magnification of the control seed whose surface has minimal porous openings. In Figure 9 at 210X magnification the surface shows minimal indication of pores for the control seed.

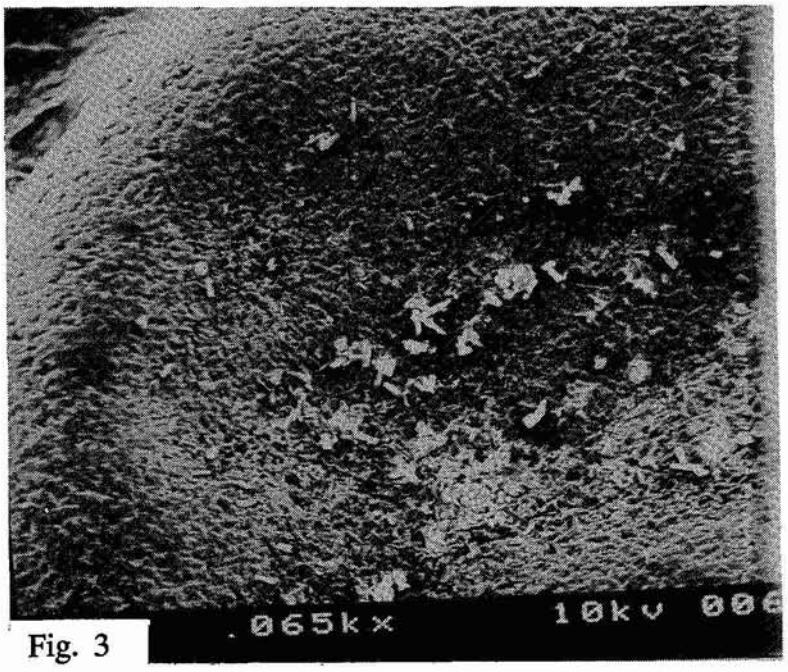

Fig. 3

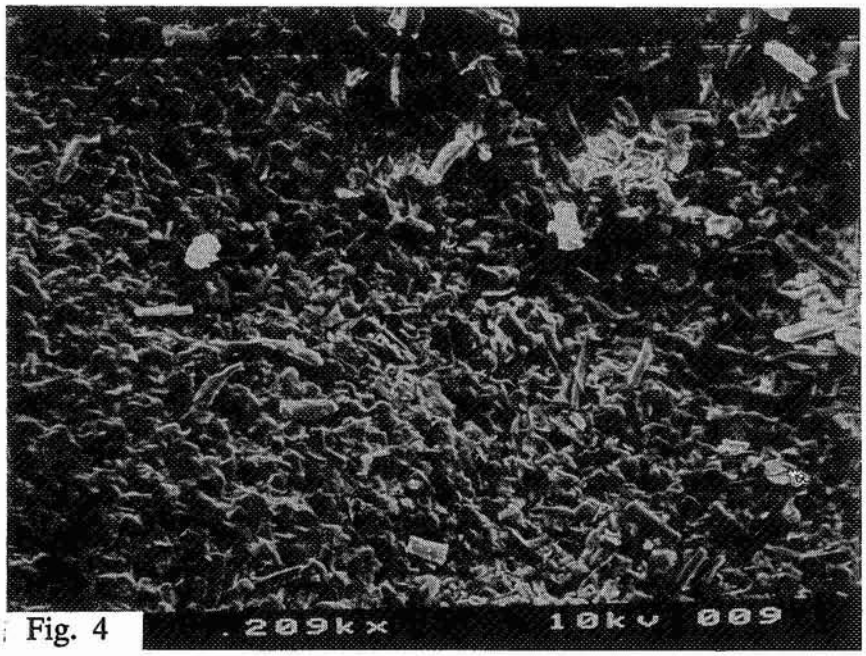

Fig. 4

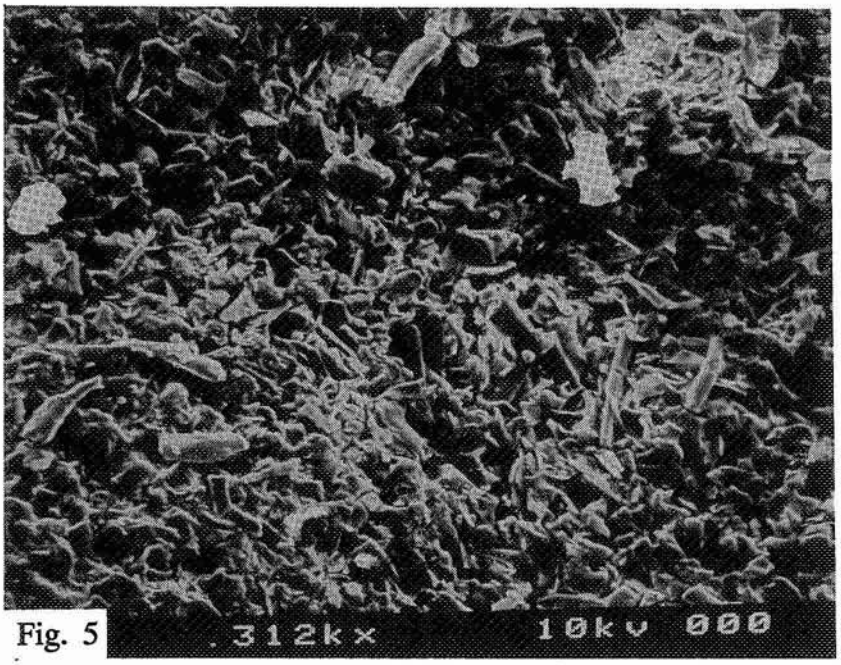

Fig. 5

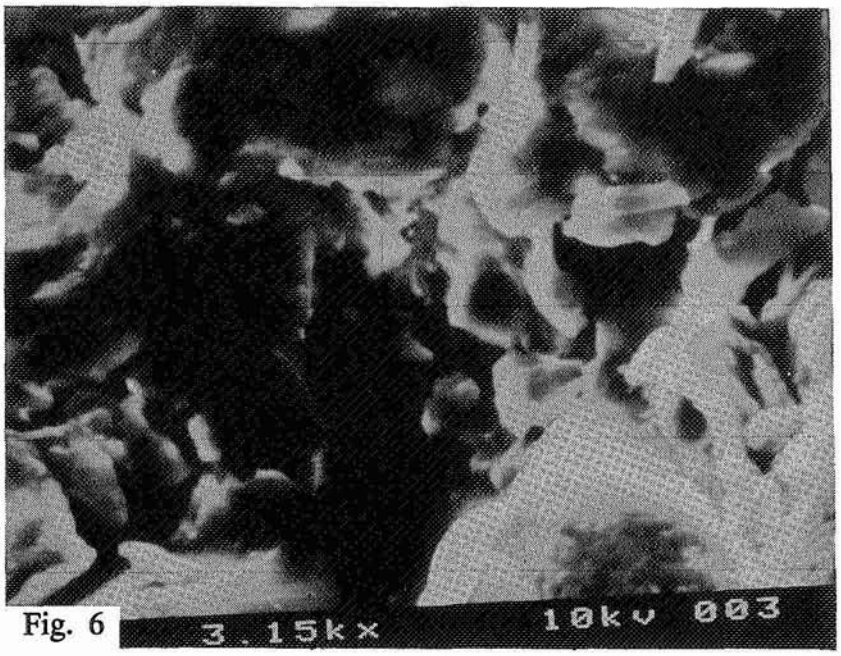

Fig. 6

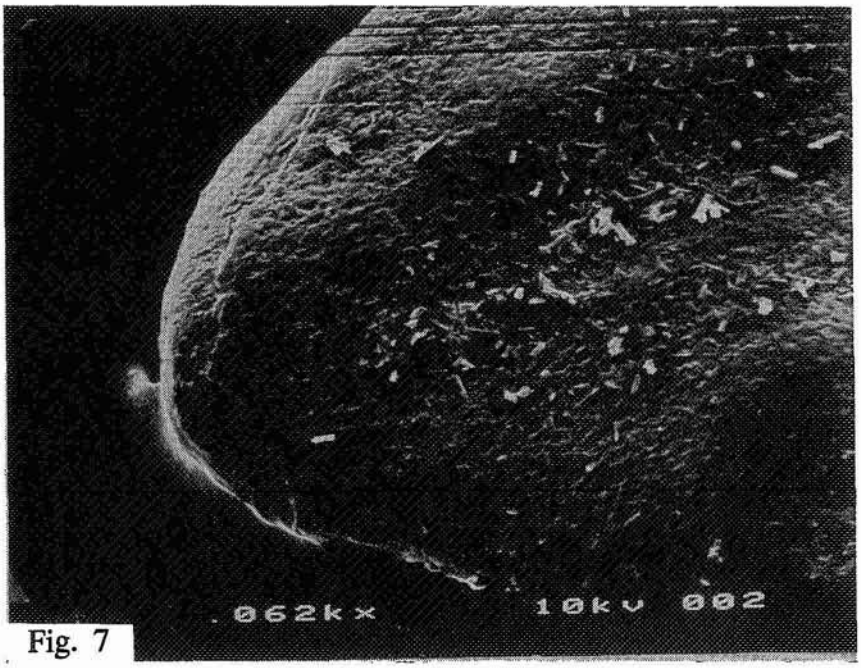

Fig. 7

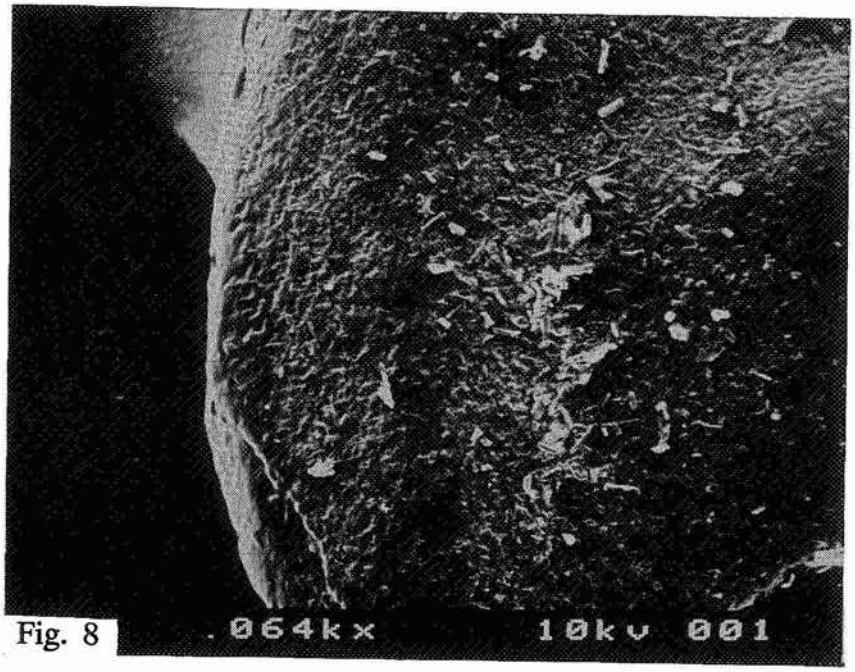

Fig. 8

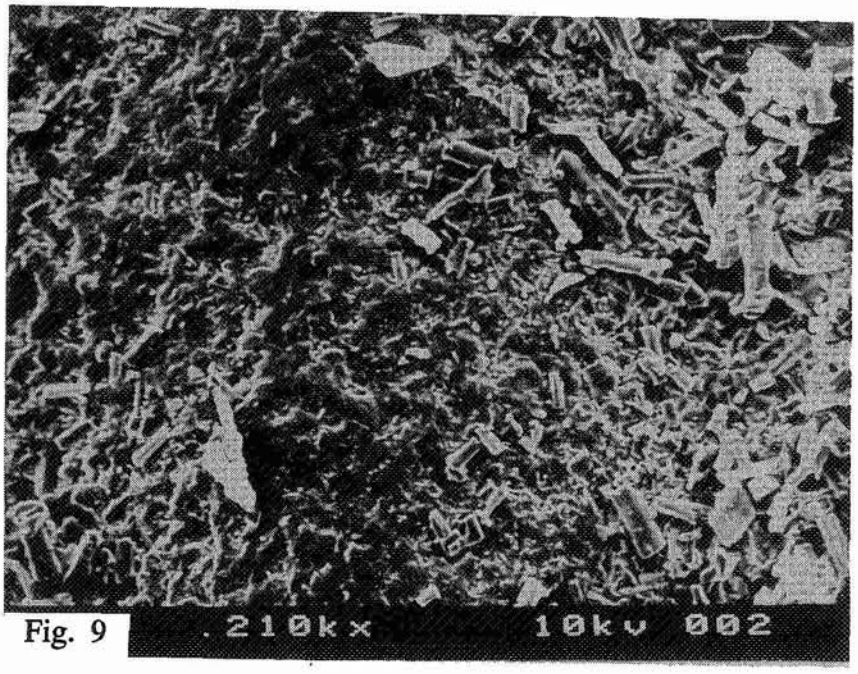

Fig. 9

Comparative Analysis of the Internal Seed Structure

The dramatic difference between the LDEF exposed seed is observed when the seed is opened to expose the tomato plant embryo, the nutritional layer and the outer seed coat. There is a unique and distinct separation between the embryo and the nutritional layer and the nutritional layer and the outer seed coat. The LDEF exposed seeds have a porous material, flaky in nature between the seed embryo, and the nutritional layer. The space between the seed coat and the nutritional layer displays less of the porous filling effect than the inner seed layers. The control or earth bound seeds when opened have distinct absences of an organic material between the embryo and nutritional layer and the nutritional layer and the outer seed coat.

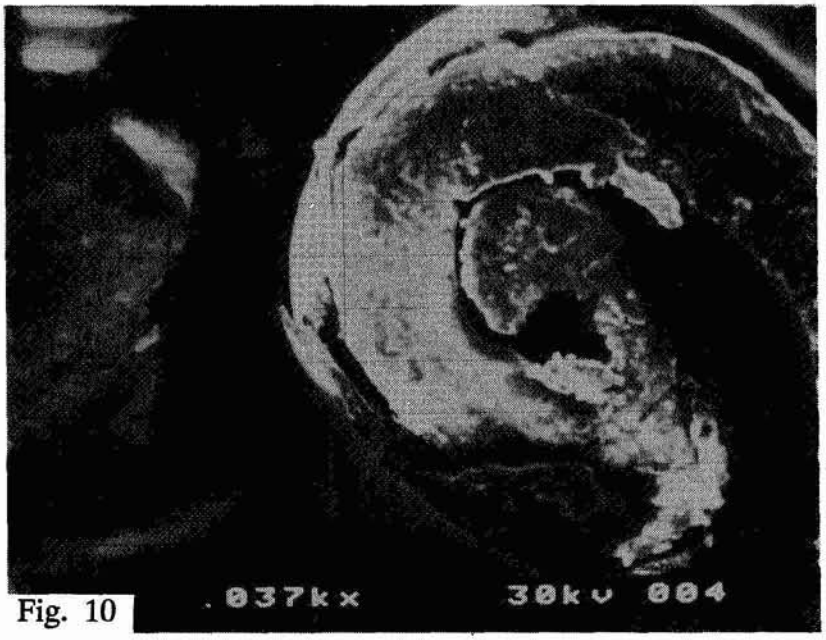

Fig. 10

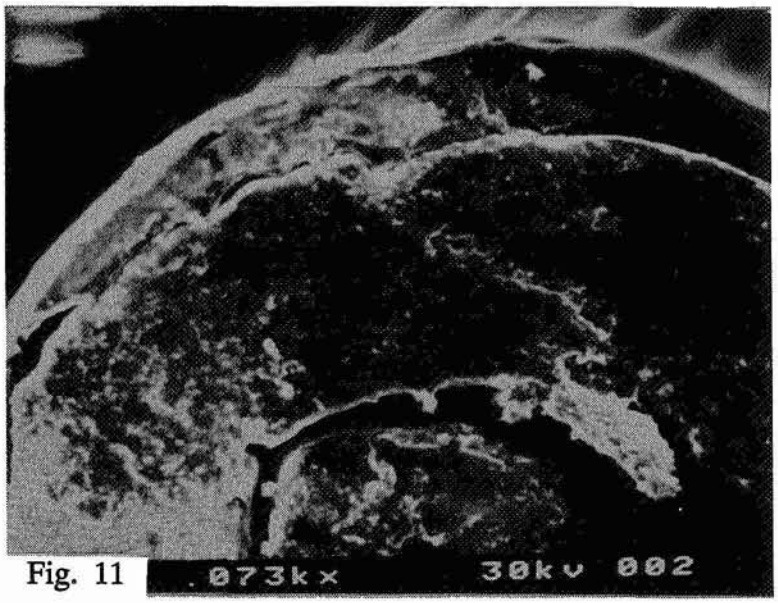

Fig. 11

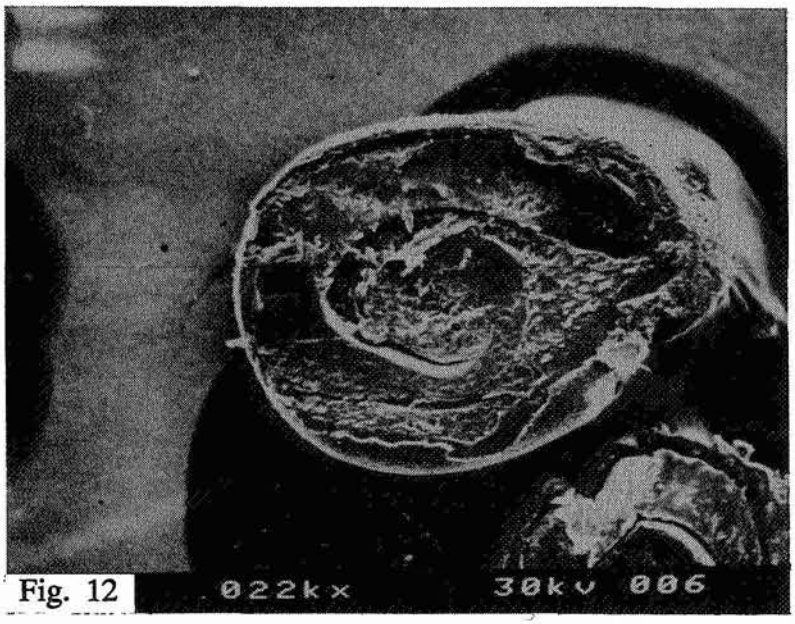

Fig. 12

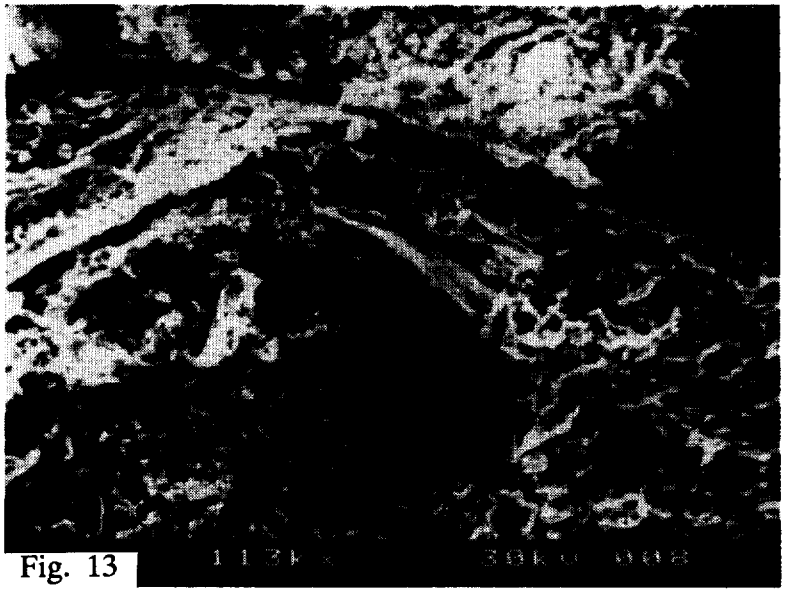

Fig. 13

Root Structure Of Tomato Plant After Germination

The root structure for the LDEF seeds and the control seeds do produce subtle changes in the cluster of materials and other web like structures observed. The earth-control seeds have a higher density of material clusters, stringy web like structures, than the LDEF seeds. An actual quantitative measure requires a study using statistical techniques to demonstrate the validity of the above preposition.

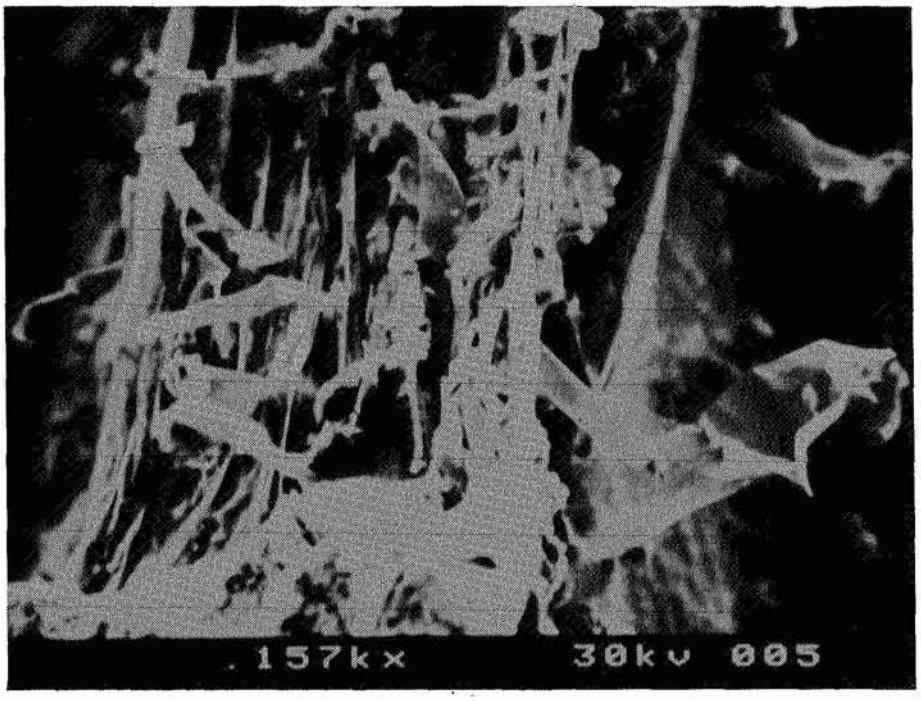

Figure 14. Young Root from LDEF Seed

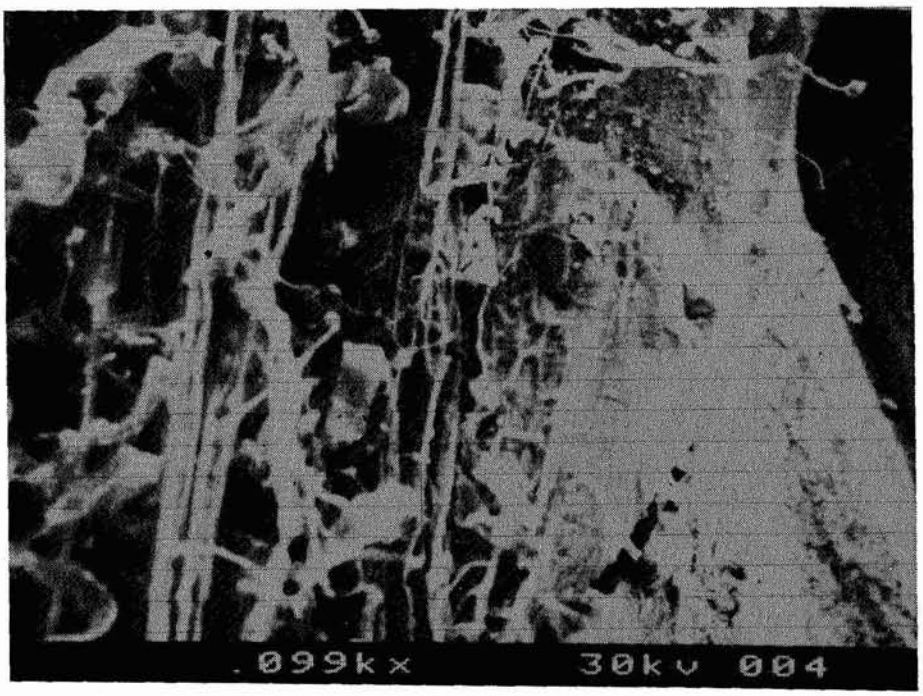

Figure 15. Young Root from Control Seed

Leaf Structure And Calculation Of Comparable Structures

The leaf structure of the LDEF young plant versus the control young plant is remarkable because of the wave like structure that permeates the young leaf surface. The micrograph of the control leaf was taken at 980X, while the Space plant leaf was taken at 300X magnification. The leaves were removed at the same time from the young tomato plant. A calculation of similar structures in the LDEF leaf produces 6 times the length of the control germinated plant leaf structure. This further confirms the increased germination rate of the plant from the LDEF exposed seed.

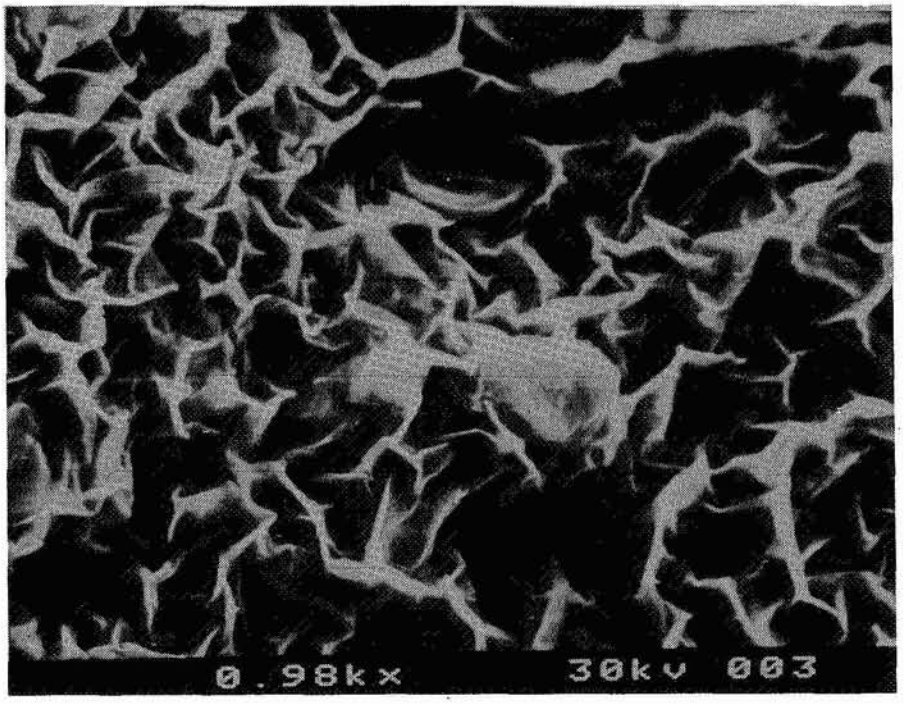

Figure 16. Leaf from Control Seed

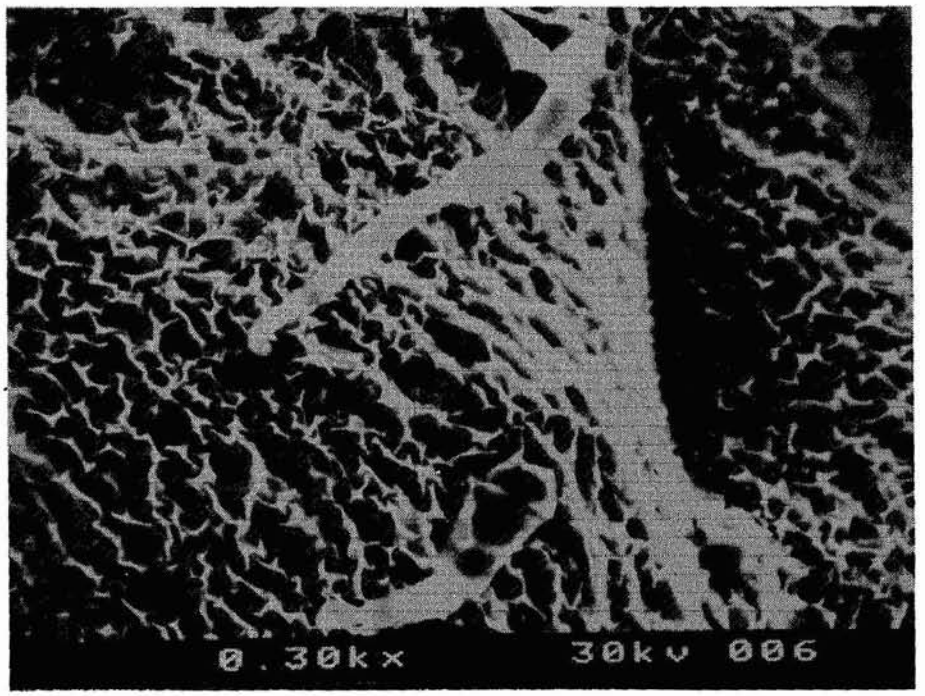

Figure 17. Leaf from LDEF Exposed Seed

The EDS X-ray micro analysis produces a list of eight elements which are common to the space as well as the earth seeds. Aluminum and silver peaks are observed because the SEM mounts were made of aluminum and silver paint used to fasten the seeds to the stub. The peaks associated with carbon, potassium, copper, and calcium have been observed by other researchers including John N. Lott and colleagues. Elements such as chlorine and rhenium cannot be explained except that it may be another elemental peak masking as those elements. The most unique observation is that iron is seen in the controls while the seeds on board LDEF produced substantial peaks of magnesium, phosphorus and sulfur. Other Lott research team reports assert that there are globoid crystals clusters in the embryo region containing P, K and Mg. The question remains why the existence of these elements P, K and Mg in the LDEF exposed seeds, while the element Fe was observed in the controls. This may be an artifact of the particular seed examined.

RESULTS

X-RAY MICROANALYSIS

THE X-RAY MICROANALYSIS RESULTS OF THE ELEMENTAL COMPOSITION OF BOTH EARTH-BASED AND SPACE-EXPOSED RUTGERS TOMATO PLANTS AND SEEDS ARE AS FOLLOWS:

SPACE	EARTH
C	C
Al	Al
Cl	Cl
K	K
Cu	Cu
Si	Si
Ca	Ca
Re	Re
Mg	Fe
P	
S	

Discussion

The Strophiole region of the seed coat is considered to be the region more susceptible to permeability than any other region of the seed coat. The Strophiole clefts (pores of the strophiole region) of the Space-exposed seeds were larger in size than those clefts found in the strophiole region of Earth-based tomato seeds. Thus, allowing the rate of permeability in the Space-exposed seeds, to occur at a high rate than permeability in the Earth-based seed. This is related to the higher germination rates in the Space-exposed seeds. However, during the remainder of plant development, the Earth-based plants sprouted and grew to the approximate size of the Space-exposed plants.

The visual observation of the internal and external structures of the Rutgers tomato seeds showed a greater separation of the seed coat from the endosperm/cotyledon layer of Space-exposed seeds in comparison to the Earth-based seeds.

The elemental composition found in the globoid crystals of the tomato seed contain P, K and Mg, but some may also have traces of Ca, Fe and Mn (Spitzer and Lott, 1980). Throughout the embryo in the endosperm, the occasional cells contain Ca in its globoid crystals (Murray, 1984). In this study we found that the elemental composition of both Earth-based and Space-based seeds contained, the elements that were found in previous studies. However, there were additional elements found in this study that had not been cited previously. The relationship of these elements to the growth and development of the seeds in this study has not yet been concluded.

Future research should refine the technique of analyzing the organic material on the seed coat, the germinating root structure, and the leaf and stem structure. It is hoped that higher magnification will be achieved utilizing the Scanning Electron Microscope and ultimately the Scanning Tunneling Microscope and Atomic Force Microscope to look at biological structures of seeds at atomic resolution levels. Micrograph Figure 18 shows an in-depth picture of one of the pores within the Space-exposed seeds surface at approximately 5000X magnification. As a prime example of the microscopic limits using the tomato seeds. Figure 19 shows globoid clusters at magnifications of 1000X and X-ray analysis can reveal its elemental composition with accuracy. Moreover, Fluorescence studies of the LDEF exposed seeds in comparison to the controlled seeds using excitation frequency of 300 nm and emission maximum frequency of 587 nm indicate that the surface of the LDEF seeds have a 30% increase in Fluorescent intensity compared to the control seed

Fluorescence. There is also a slight shift toward the higher wavelength for the control seed which has the reduced intensity.

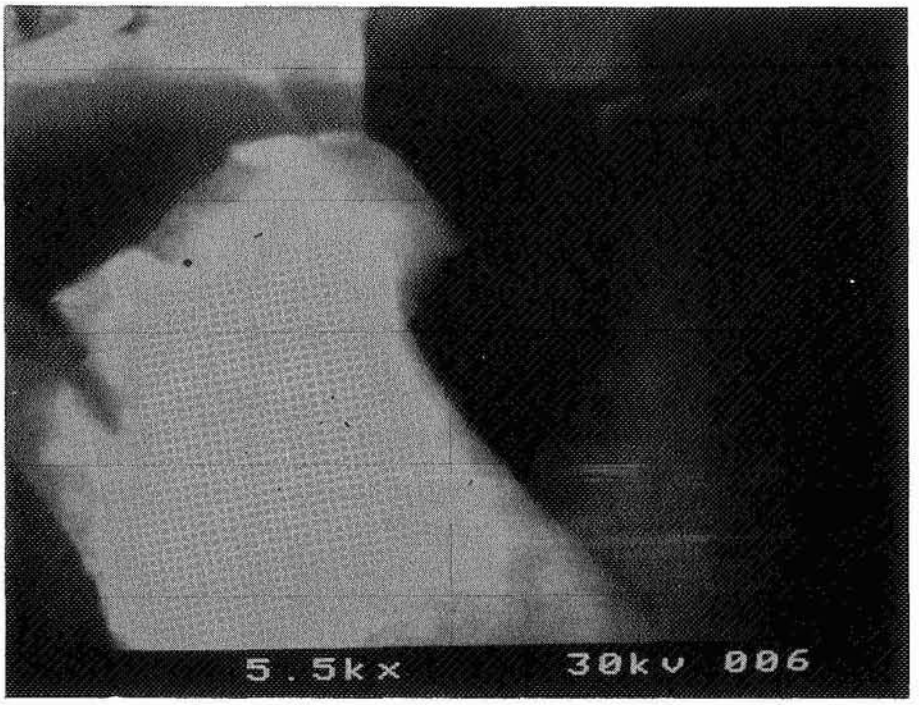

Figure 18. Isolated Pore in LDEF Exposed Seed

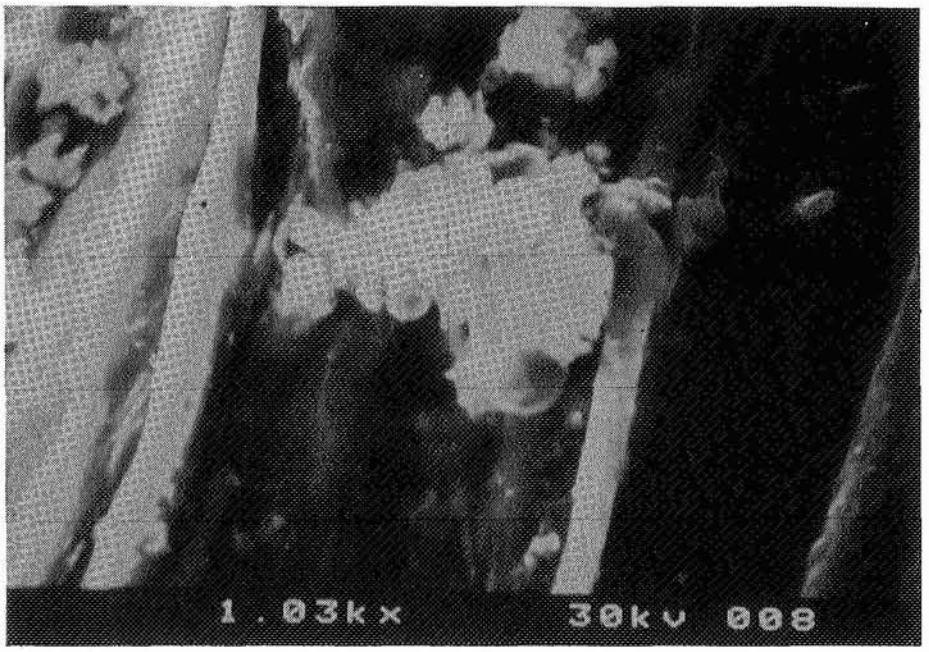

Figure 19. Globoid cluster at 1030X magnification

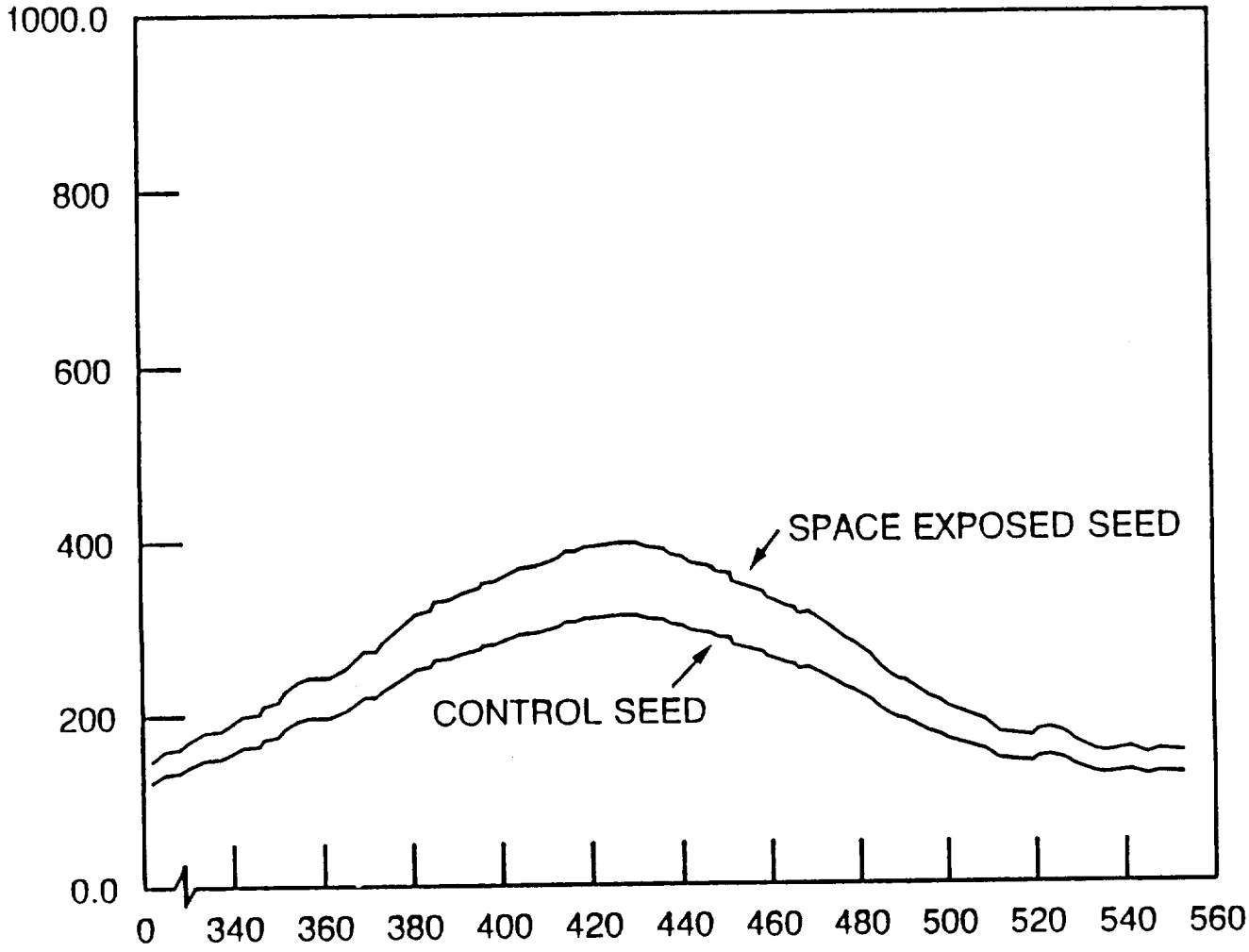
1000.0
800
600
400
200
0.0
SPACE EXPOSED SEED
CONTROL SEED
0
340
360
380
400
420
440
460
480
500
520
540
560

Figure 20

References

1. Barber, T. A. (1976). In Principal and Techniques of SEM: Biological Application, Vol 5, ed. M.A. Hayat, Van Nostrand Reinhold, New York.

2. Chandler, J.A. (1977). "X-Ray Microanalysis in the Electron Microscopy", In Practical Methods in Electron Microscopy, Vol 5, ed. A.M. Glauert, North-Holland, Amsterdam.

3. Goldstein, Newbury, Echlin, Joy, Foiri, Lifshin (1977). Scanning Electron Microscopy and X-Ray Microanalysis. Plenum Press, New York.

4. Hamly, D.H. (1932) Bot. Gaz. 39, 345-375.

5. Murray, D.R., and Roxburgh, C. Mc C. (1984) J. Sci. Food Agric. 35.

6. Spritzer, E., and Lott, J.N.A. (1980) Can J. Bot. 58. 699-711.

7. Taylor, N. (1989). Taylor Encyclopedia of Gardening Horticulture and Landscape Design 4th edition, Houghton, Mifflin Co. Boston, MA.

8. Wyman , D (1977). Wymans Gardening Encyclopedia, Macmillian Publishing Co., Inc. USA.

SPACE ENVIRONMENTS
Meteoroid and Debris

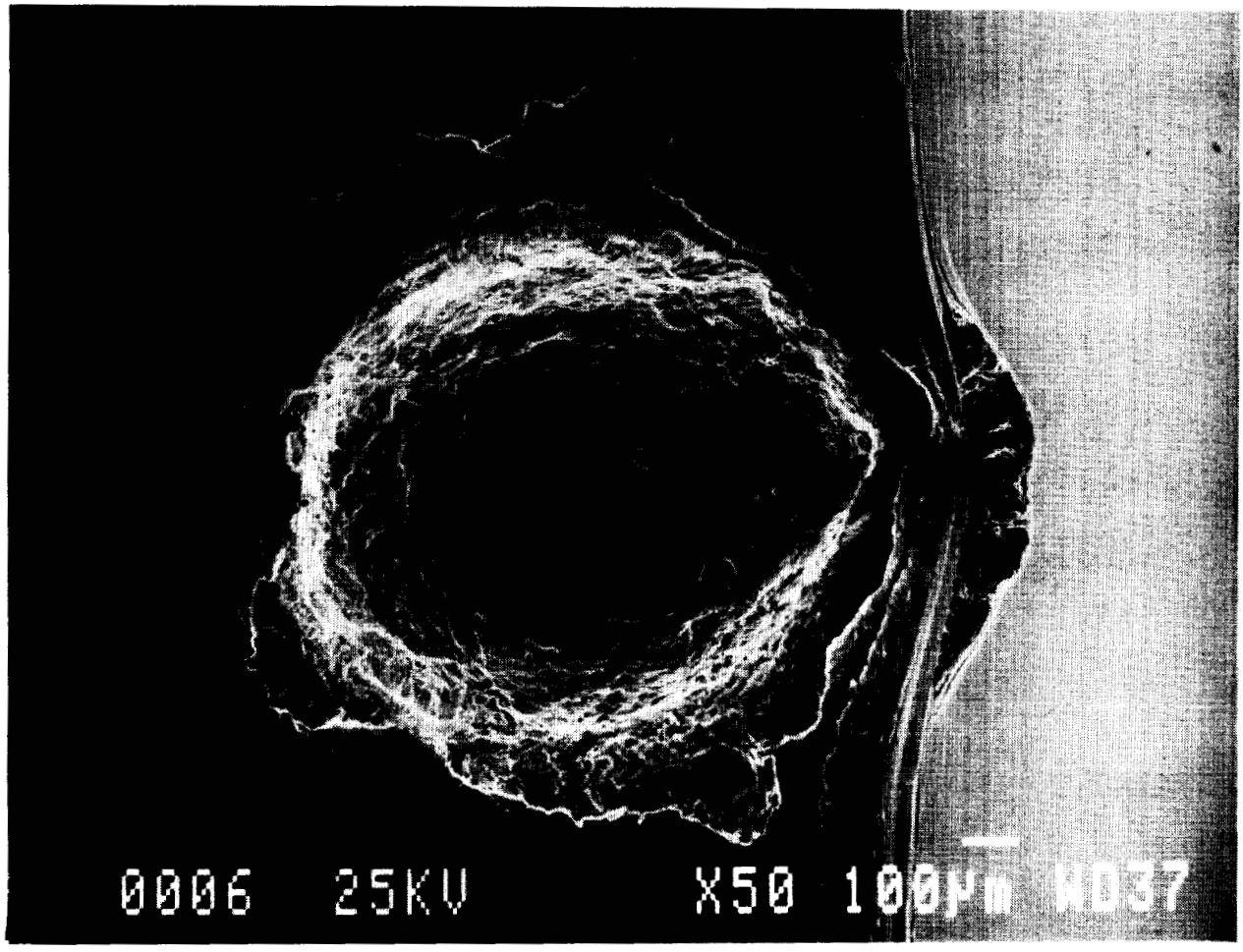

L-94-3925

STATUS OF LDEF CONTRIBUTIONS TO CURRENT KNOWLEDGE OF METEOROID AND MANMADE DEBRIS ENVIRONMENTS AND THEIR EFFECTS ON SPACECRAFT IN LEO

William H. Kinard
NASA Langley Research Center
Hampton, VA 23681-0001
Phone: 804/864-3796; Fax: 804/864-8094

ABSTRACT

The analyses, which are currently being performed by the LDEF Meteoroid and Debris Principal Investigators and the other LDEF Meteoroid and Debris Special Investigation Group Members of the data derived from the seven meteoroid and debris experiments that were flown on the LDEF and the post-retrieval scans of the impact sites found on other experiment and LDEF surfaces will, when they are completed, result in many very significant contributions to our knowledge of the meteoroid and debris environments and the effects these environments can have on spacecraft in LEO. This paper provides a status report on the analyses that have been performed to date and the preliminary contributions indicated by these analyses. This paper also discusses new questions that have been raised by the completed analyses regarding these environments and their effects on spacecraft.

LDEF METEOROID & DEBRIS SPECIAL INVESTIGATION GROUP INVESTIGATIONS AND ACTIVITIES AT THE JOHNSON SPACE CENTER

Thomas H. See
Lockheed Engineering & Science Co.
Houston, Texas 77058
(713) 483-5027 / FAX (713) 483-5347

Michael E. Zolensky
NASA / Johnson Space Center
Houston, Texas 77058
(713) 244-5128 / FAX (713) 483-5347

Ronald P. Bernhard
Lockheed Engineering & Science Co.
Houston, Texas 77058
(713) 483-5018 / FAX (713) 483-5347

Jack L. Warren
Lockheed Engineering & Science Co.
Houston, Texas 77058
(713) 483-5122 / FAX (713) 483-5347

Clyde A. Sapp
Lockheed Engineering & Science Co.
Houston, Texas 77058
(713) 483-5141 / FAX (713) 483-5347

Claire B. Dardano
Lockheed Engineering & Science Co.
Houston, Texas 77058
(713) 483-5329 / FAX (713) 483-5347

INTRODUCTION

Since the return of the Long Duration Exposure Facility (LDEF) in January, 1990, members of the Meteoroid and Debris Special Investigation Group (M&D SIG) at the Johnson Space Center (JSC) in Houston, Texas have been examining LDEF hardware in an effort to expand the knowledge base regarding the low-Earth orbit (LEO) particulate environment. In addition to the various investigative activities, JSC is also the location of the general Meteoroid & Debris database. This publicly accessible database contains information obtained from the various M&D SIG investigations, as well as limited data obtained by individual LDEF Principal Investigators.

LDEF exposed ~130 m^2 of surface area to the LEO particulate environment, ~15.4 m^2 of which was occupied by structural frame components (*i.e.,* longerons and intercostals) of the spacecraft. The data reported here was obtained as a result of detailed scans of LDEF intercostals, 68 of which reside at JSC (Figure 1). The limited amount of data presently available on the A0178 thermal control blankets was reported last year (ref. 1) and will not be reiterated here. As was the case in Ref. 1, the data presented here are limited to measurements of crater diameters and their frequency of occurrence (*i.e.,* flux).

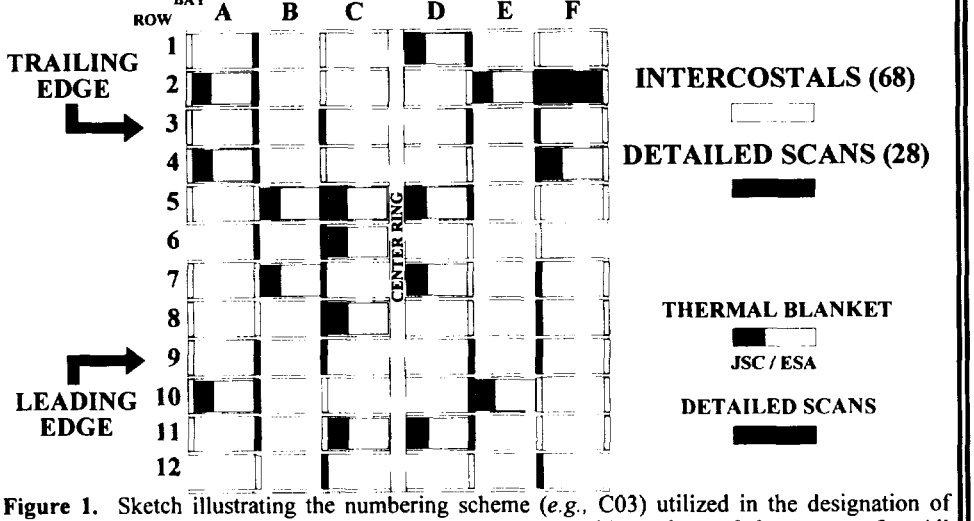

Figure 1. Sketch illustrating the numbering scheme (*e.g.,* C03) utilized in the designation of experiment-tray locations and the nominal leading and trailing edges of the spacecraft. All intercostals, except those from the end rings on Rows 6 and 12, are located at JSC and are being scanned for impact features down to ~10 μm. Solid dark areas indicate frame and LDEF thermal blanket surfaces that have been scanned; only intercostal data is included in this report.

Since our last report

(ref. 1) we have scanned another 14 intercostals and now have detailed information on at least two intercostals from each of LDEF's 12 rows. In addition, we have scanned two more intercostals each from Rows 3 and 9 for a total of 28 intercostals.

RATIONALE FOR EXAMINING LDEF'S STRUCTURAL FRAME

The size of a crater or penetration hole depends on the physical properties of the target and projectile materials, and on the projectile's mass and impact velocity. On LDEF, a given impactor would generate craters of different sizes depending on the location or pointing direction of the target because of the different encounter velocity, assuming a constant target material. The quantitative relationships for these parameters are known for some LDEF materials, but only over a restricted range and set of initial conditions. Because of the M&D SIG's desire to determine particle frequencies as a function of pointing direction it was necessary to characterize impact features on identical target materials so that the physical properties of the target remain constant. Furthermore, because of the highly stochastic nature of the collisional environment, it is also necessary to study materials which exposed sufficient surface areas to have accumulated a representative population of impact features. Finally, it was necessary to select surfaces which could be made available to the M&D SIG for study. Few surfaces on LDEF met such criteria. The A0178 Teflon thermal blankets were not present on Rows 3, 9 and 12, although they did expose ~20 m^2 of surface area to the LEO particulate environment; one third of each blanket is curated at JSC. In addition, the majority of impact features on these surfaces were penetrations and not craters. Lastly, the penetration and/or cratering behavior of this material is not presently well understood, although such studies are now underway (ref. 2). Another set of candidate surfaces was the 25 Meteoroid & Space Debris Impact Experiment trays (S0001; exposing ~26.3 m^2 of aluminum) that were located on every row of LDEF (including the space and Earth ends) except for Row 9. These various factors pointed to LDEF's structural frame as the best candidate surfaces to fit all of these criteria.

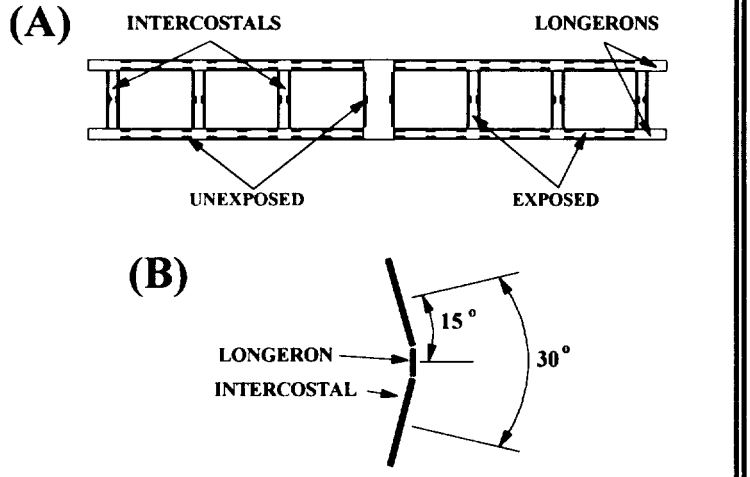

Figure 2. Geometric relationship of LDEF frame components. (A) Distribution of longerons and intercostals in a typical "Row" of LDEF Bays and instrument locations. (B) A view down the axis of the spacecraft illustrating the angular relationship between a longeron and adjacent intercostals (ref. 1.).

LDEF's entire structural frame was fabricated from 6061-T6 aluminum, a commonly used spacecraft material whose response to hypervelocity impact has been studied in great detail (*e.g.*, refs. 3, 4, and 5). The frame components formed an open-grid, 12-sided structure that produced individual instrument bays (Bays A-F; Figure 1) and provided attachment points for the experiment trays. The longitudinal frame members (~4.6 m long) were termed "longerons" (Figure 2a), while cross members between longerons were called "intercostals" (~1 m in length; Figures 2a and 3). Individual rows were assigned

sequential numbers (1-12), with Row 9 facing in the nominal velocity vector (leading-edge direction) and Row 3 in the trailing-edge direction. For more detailed information regarding the numbering scheme utilized by the M&D SIG interested readers are referred to Refs. 1 and 6. Because of their size and mass, and because of their significance to the overall structural integrity of the spacecraft, the longerons and the components from the Earth- and space-facing ends could not be made available for detailed study in the laboratory. On the other hand, the small size and mass, as well as the higher than average surface polish, made the intercostals well suited for removal and detailed scanning within the Facility for the Optical Inspections of Large Surfaces (FOILS) laboratory at JSC.

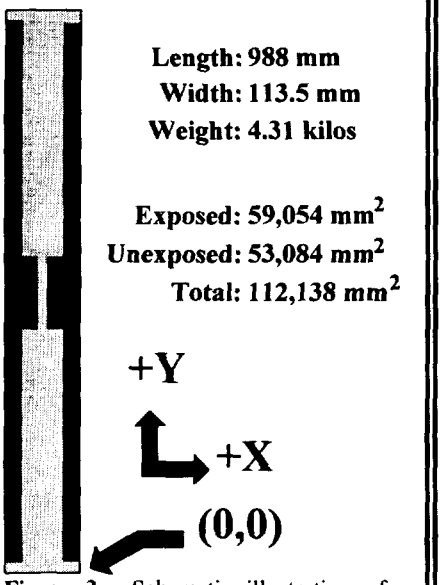

Figure 3. Schematic illustration of typical LDEF intercostals giving average dimensions and mass. The M&D SIG detailed scans are conducted on the exposed (light-colored) areas.

SURFACE AREAS AND PROCEDURES

Each intercostal exposed ~0.06 m^2 of surface area to the LEO particulate environment (Figure 3), while a complete row of intercostals, not including the center ring (*i.e.*, the four mid and two end-ring intercostals; see Figures 1 and 2), totaled ~0.32 m^2; end-ring intercostals exposed only ~0.04 m^2 each. Multiply by 12 and subtracting the two Row 6 and two Row 12 intercostals not included results in a total exposed surface area for the 68 intercostals of ~3.68 m^2, ~1.65 m^2 of which are included in this report.

As has been our practice throughout our LDEF investigations, reported crater diameters refer to rim-crest-to-rim-crest dimensions (Figure 4). For a detailed discussion on the crater morphology and associated measurement techniques for craters in aluminum, as well as impacts into other materials that were on LDEF, interested readers should see Refs. 6 and 7.

Table 1 lists the number of impact craters, sorted by size, documented in our study, as well as the exposed surface areas which have been examined on each row

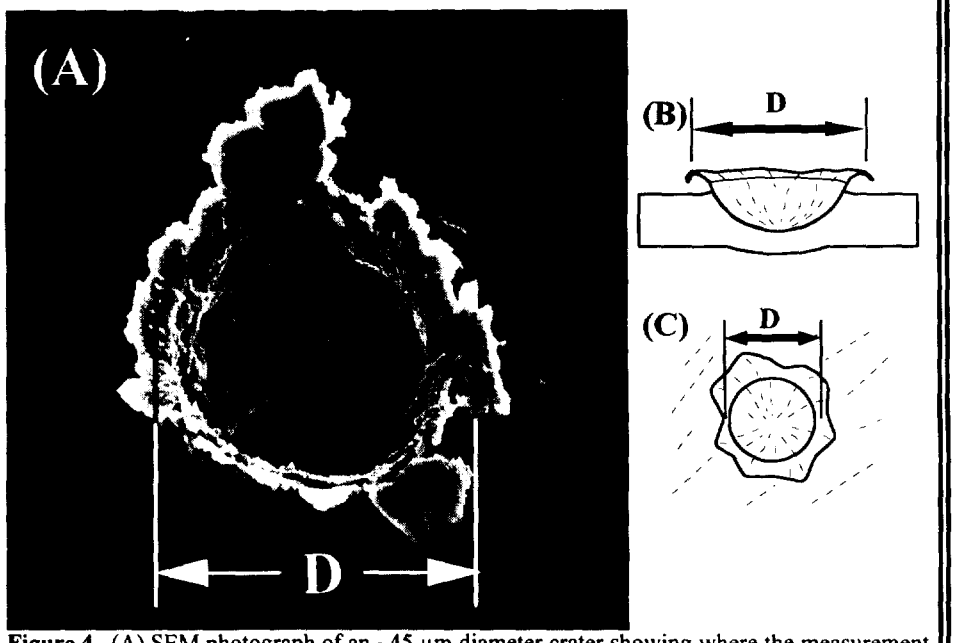

Figure 4. (A) SEM photograph of an ~45 μm diameter crater showing where the measurement of "D" would be made. (B & C) Schematic of a typical round crater illustrating location of diameter measurements.

C-4

thus far. All scanning was carried out within the FOILS laboratory at JSC; the intercostals were scanned at a 40x magnification which easily permits the identification of all craters >30 μm in diameter on the relatively smooth intercostal surfaces. *Thus, for craters below ~40 μm in diameter the coverage is not complete.*

Table 1. Number of individual features documented in each size bin for the 12 LDEF rows as determined from the detailed scans of the intercostals, along with the associated exposed surface area for each row. Size bins are inclusive on the lower end of each bin (*i.e.*, bin 10 contains all particles ≥10 μm and <14 μm in diameter.

LDEF Row Number	<10	10	14	20	28	40	57	80	113	160	226	320	453	640	905	1280	1810	2560	3620	5120	TOTALS	LDEF Row Number	Surface Area (m^2; exposed)
Row 1				3	6	16	15	14	7	6	3		1								**71**	**Row 1**	**0.118650**
Row 2				10	14	12	11	14	3	3	1	1									**69**	**Row 2**	**0.117385**
Row 3			2	6	6	15	13	9	6	7	4	3	1	1							**73**	**Row 3**	**0.232544**
Row 4				1	1	6	8	7	4	4	1	1	1			1					**35**	**Row 4**	**0.120025**
Row 5		1	5	34	16	12	8	6	6	4	1	1	1	1							**96**	**Row 5**	**0.118361**
Row 6	1		2	17	28	42	11	10	9	10	5	1	3	1							**140**	**Row 6**	**0.119976**
Row 7	1	41	61	236	150	106	27	36	21	21	11	6	2	1							**720**	**Row 7**	**0.117871**
Row 8				10	45	83	46	46	33	20	16	16	2	2	1						**320**	**Row 8**	**0.117433**
Row 9		12	15	98	114	195	117	108	73	57	34	15	12	5	1	1					**857**	**Row 9**	**0.234776**
Row 10				22	59	90	57	55	41	29	18	7	13	3	2						**396**	**Row 10**	**0.118871**
Row 11	1	1	8	67	70	106	46	50	25	24	9	7	3	1		1		1			**420**	**Row 11**	**0.119729**
Row 12		2	6	33	36	60	29	32	22	9	9	2		2							**242**	**Row 12**	**0.119334**
TOTALS		**57**	**99**	**537**	**545**	**743**	**388**	**387**	**250**	**194**	**112**	**60**	**39**	**17**	**4**	**3**		**1**			**3439**	**TOTALS**	**1.654955**

ANALYTICAL RESULTS

Impact Frequency

One of the goals of the M&D SIG is to determine the impact frequency of natural meteoritic and man-made particles on LDEF. To date, a limitation in resources has prevented an extensive effort along these lines at JSC; there are several reasons for this. First, the actual samples are far too large to be accommodated by a Scanning Electron Microscope (SEM) and/or Microprobe without putting forth a considerable effort to section the intercostals via an end-mill. Second, the composition of the target material (*i.e.*, aluminum) makes identification of man-made aluminum impactors virtually impossible; aluminum is known to constitute a significant fraction of the man-made particle population. Lastly, other metallic surfaces, such as the A0187-1 99.99% pure gold meteoroid detectors (ref. 8), revealed that nearly half of all craters analyzed do not contain sufficient quantities of projectile residue to permit detection and classification of the impactor, whether meteoritic or man-made, via SEM techniques. As a result, the focus of this intercostal investigation has been to simply determine the frequency with which LDEF was impacted by all particle types and how the frequency varied from row to row (*i.e.*, pointing direction), and not to determine the percentages of craters formed by either natural or man-made particles.

To gain an *estimate* of the original projectile diameter from the measured crater diameter in metallic surfaces, M&D investigators commonly assume that the resulting crater is on the order of four to five times larger than the diameter of the projectile. We could do this also, but choose not to for the following reasons. As mentioned earlier, the size of a crater in a given target material not only depends on the physical properties of the target and projectile, but also on the projectile's velocity. On LDEF, not only

did the average encounter velocity vary as a function of pointing direction, it also varied depending on whether the projectile was man made or natural; in general, natural particles possess higher encounter velocities than do man-made particles (refs. 3 & 4). Thus, with so many unknowns, any attempt to determine particle-type frequency would result in flux curves with extremely large degrees of uncertainty.

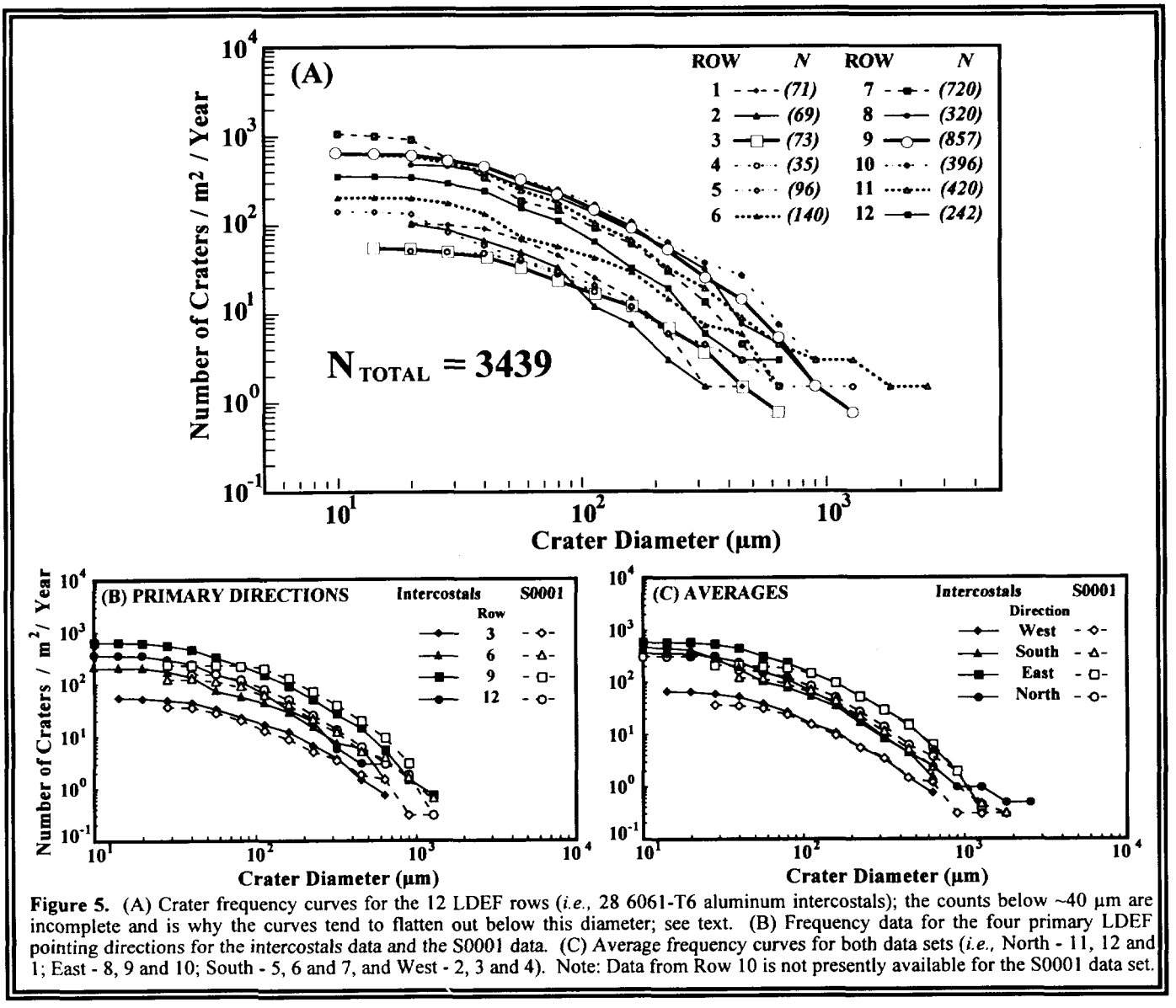

Figure 5. (A) Crater frequency curves for the 12 LDEF rows (*i.e.*, 28 6061-T6 aluminum intercostals); the counts below ~40 µm are incomplete and is why the curves tend to flatten out below this diameter; see text. (B) Frequency data for the four primary LDEF pointing directions for the intercostals data and the S0001 data. (C) Average frequency curves for both data sets (*i.e.*, North - 11, 12 and 1; East - 8, 9 and 10; South - 5, 6 and 7, and West - 2, 3 and 4). Note: Data from Row 10 is not presently available for the S0001 data set.

Figure 5a displays the crater frequencies for the 28 intercostals examined to date. In general, the additional data acquired over the past year have done little to alter our interpretations and have mainly served to improve the overall fidelity of the data. These data continue to be in good agreement with our earlier results (ref. 1), as well as that of others (*e.g.*, ref. 9), with the highest cratering rates being observed in the forward-facing directions (*i.e.*, Rows 8, 9 and 10) and the lowest frequencies being found in association with the rearward-facing surfaces (*i.e.*, Rows 2, 3 and 4).

Over the past year D. Humes (Langley Research Center [LaRC]) has forwarded copies of his S0001 experiment data to the M&D SIG for inclusion in the M&D Database. At least one S0001 experiment tray was present on each of LDEF's 12 rows, except for Row 9; S0001 also occupied at least one bay on the

Earth- and space-ends of LDEF. Because of Row 9's importance, Humes acquired several aluminum surfaces from the S0010 experiment (Bay B09) from W. Slemp (LaRC). These data are also included in the M&D database.

Comparison of the M&D SIG intercostal and the Humes S0001 data sets can be seen in Figure 5b, where only the four major pointing directions are plotted for the sake of clarity. For most surfaces, Humes did not attempt to document craters below ~80 μm in diameter (Humes, personal communications), which accounts for the flattening of his flux curves below this diameter. For the intercostal data, we believe the data to be complete down to ~40 μm diameter craters, which is where the intercostal flux curves begin to flatten out. In addition, Humes includes data for all crater sizes, including those that were previously documented at the Kennedy Space Center by the M&D SIG A-Teams (ref. 6). On average, Humes' diameter measurements for the same craters tend to be on the order of 8% to 12% larger than the KSC reported diameter. This may account for the minor differences seen between the cratering frequencies plotted in Figure 5b, which are in generally good agreement for identical pointing direction. As can be seen, the S0001 data tends to exhibit slightly higher cratering frequency (above his cutoff diameter of ~100 μm) for all directions except Row 3, the trailing-edge direction.

Like Figure 5b, Figure 5c again compares these two extensive data sets. In this figure, however, the frequency curves represent averages (*i.e.*, East represents the average flux for Rows 8, 9 and 10; S0001 Row 10 data not included at this time) for the four cardinal pointing directions (*e.g.*, North [Row 12], East [Row 9], etc.) of LDEF. When this averaging is done to both data sets, the differences between the two become negligible, particularly for the East- and West-facing directions; for the West-facing direction the two curves lie right on top of each other between 100 to 1000 μm diameter craters (Figure 5c).

Leading-Edge To Trailing-Edge Ratios

In general, the slopes for the various flux curves in Figures 5a - 5c are very similar, suggesting that the overall ratios of large to small particles remain relatively constant, regardless of LDEF pointing direction. Of greater interest are the relative production rates between the leading- and trailing-edges of LDEF. Prior to LDEF's recovery, it was believed that the leading-edge surfaces would receive ~20 times more impacts per unit surface area than the trailing-edge surfaces (ref. 4). However, both the intercostal data and that of the S0001 experiment seem to indicate that the pre-LDEF estimates of these ratios were too high.

In Figure 6a, the intercostal data (solid bars) exhibits the maximum leading-edge to trailing-edge ratio of ~10:1 for craters ≥40 μm in diameter. What is also noticeable is that this ratio appears to decrease as crater size increases, reaching a minimum of ~7:1 for craters ≥640 μm in diameter. The S0001 data (open bars), although possessing higher absolute leading-edge to trailing-edge ratios, exhibits a similar trend ranging from a maximum of ~15:1, for craters ≥113 μm in diameter, to ~10:1 for craters ≥905 μm in diameter. (Recall that the S0001 data is only 100% complete for craters above 100 μm in diameter, while the intercostal data is believed to be 100% inclusive for craters down to ~40 μm in diameter). The average leading-edge to trailing-edge ratio for the two data sets is ~9:1 for the intercostals and ~12:1 for the S0001 surfaces.

Figure 6b represents the ratios of the forward-facing surfaces (*i.e.*, Rows 8, 9 and 10) to those of the rearward-facing direction (*i.e.*, Rows 2, 3 and 4). As was the case for the frequency data depicted in Figure 5, the differences between the two data sets all but disappear when the data are averaged in this fashion, both sets yielding an average forward-facing to rearward-facing ratio of ~8:1. In addition,

although it is not nearly as pronounced as in the Row 9 to Row 3 data of Figure 6a, the decrease in the forward-facing to rearward-facing ratio for the larger size craters is still apparent, reaching a minimum of ~5:1 for craters ≥905 in diameter for both sets of data.

Last year when we first noted this trend we pointed out that the number of craters ≥500 μm in diameter was extremely small (~2%), when compared to the ≥10 μm in diameter crater populations for intercostals on Rows 3 and 9. However, since that time we have tripled the scanned surface area for Row 3, and doubled the scanned surface area for Row 9. With these greatly improved counting statistics we find little change in the percentage (*i.e.*, ~3%) of craters ≥500 μm in diameter for Rows 3 and 9; as for the overall LDEF intercostal crater population ≥10 μm in diameter, the percentage of craters ≥500 μm in diameter is ~11.1%. For the S0001 data this percentage is ~6.5% for Rows 3 and 9, and ~11.3% for all S0001 surfaces examined to date. Nevertheless, this change in leading-edge to trailing-edge ratio as a function of crater size appears to be real. Additional evidence for such a change can be found in the thermal-blanket and MAP (ref. 10) experiment data illustrated in Figure 5c of Ref. 1. For the larger penetration features (~500 μm in diameter) the leading- to trailing-edge ratio is ~10:1, while for the smallest features for which data is available on both Rows 3 and 9 (*i.e.*, ~5 μm in diameter) the leading-edge to trailing-edge ratio climbed to ~50:1. Although some of these effects may be related to the projectile sources, and hence the associated velocities of the different particle-population sizes, it does appear as though the larger particle population may be slightly more isotropically distributed.

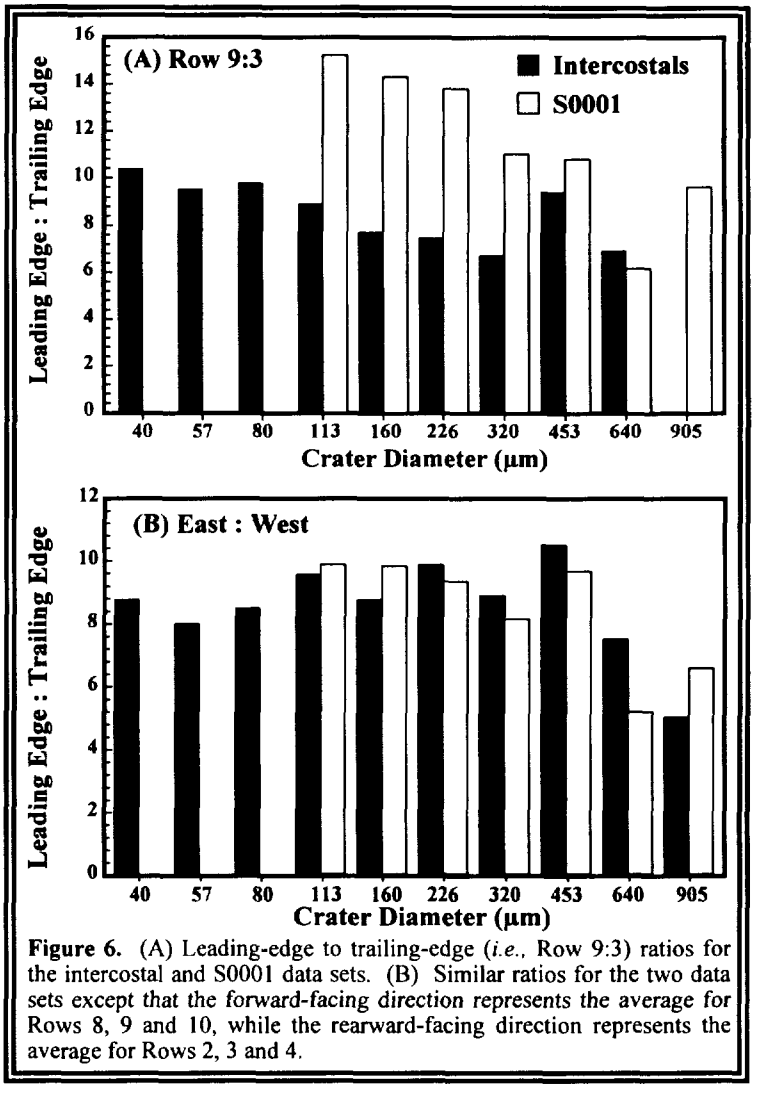

Figure 6. (A) Leading-edge to trailing-edge (*i.e.*, Row 9:3) ratios for the intercostal and S0001 data sets. (B) Similar ratios for the two data sets except that the forward-facing direction represents the average for Rows 8, 9 and 10, while the rearward-facing direction represents the average for Rows 2, 3 and 4.

The measured ratios, Row 9 to Row 3, of the spatial density of impact craters do not agree with current theoretically predicted ratios for either meteoroids (ref. 11) or for Earth-orbital debris (ref. 12). It follows that the present theoretical models are inadequate to explain the data (ref. 13). For meteoroids to produce a front-to-back ratio as low as 7:1, a much larger fraction of high-velocity meteoroids than previously modeled seems to be required. If orbital debris is the primary source for the observed impact craters, the data suggest that there is much more debris in geosynchronous transfer orbits than is currently included in models -- especially those with orbital inclinations near 28.5° (ref. 12). It appears as though a careful reexamination of such models (for incorrect assumptions) is in order.

High-magnification optical examination of intercostal F07F02 has revealed an anomalous number of craters on this intercostal, the majority of which are ≤40 μm in diameter. In an effort to understand this phenomena and to identify the source of these features, the M&D SIG has analyzed (*i.e.*, Scanning Electron Microscopy / Energy Dispersive X-ray Analysis [SEM-EDX]) 251 of the 540 (~46%) impacts on intercostal F07F02. The objective of these examinations was to evaluate the chemical variability and possible clustering of discrete particle types and, hopefully, determine their source(s). Craters containing detectable projectile residues were classified as either micrometeoritic or as man-made debris, while sources of surface contamination were identified when ever possible.

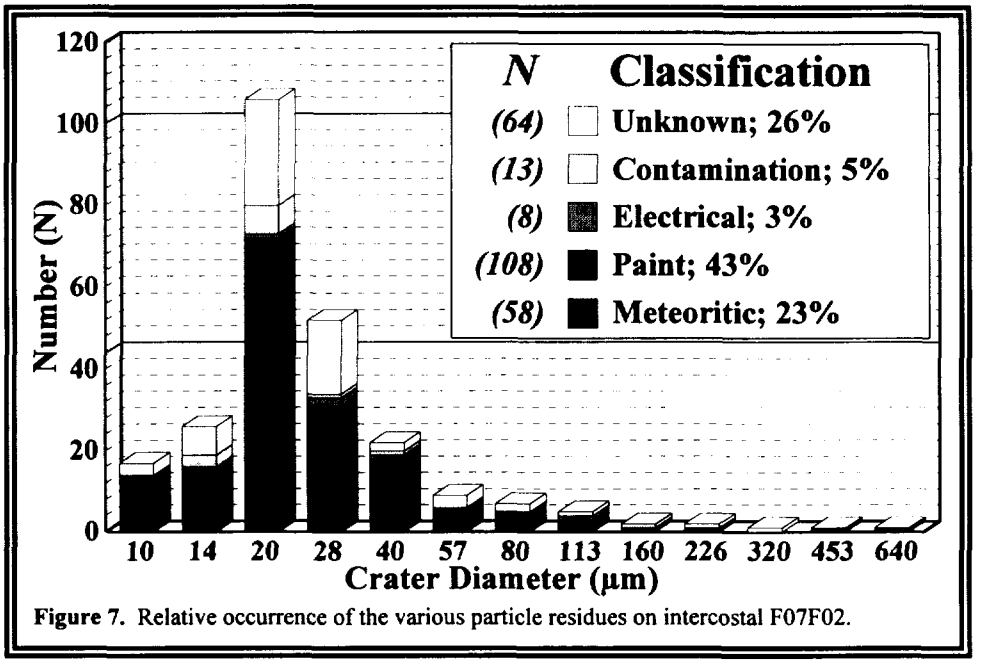

Figure 7. Relative occurrence of the various particle residues on intercostal F07F02.

The occurrence of the various projectile types has been tabulated in histogram form and is illustrated in Figure 7, which displays the relative frequencies of micrometeoritic, man-made debris particles (*i.e.*, paint and electrical components), indeterminate, and contamination samples for the smaller size bins. Examination of Figure 7 illustrates the trend toward a high occurrence of all particle types in the 14 to 40 μm size range, especially in the ≥20 μm to <28 μm size bin which contains ~63% of the analyzed craters. There is a particular increase in the relative amount of paint-type residues as compared to residues found on the gold surfaces from experiment A0187-1 and the experiment tray clamps (refs. 8 & 14, respectively). SEM characterization of the crater morphologies shows that the depth to diameter ratios, the crater rim characteristics, and the residue remnants are similar within this suite of impact features as those found within these other studies. The SEM-EDX spectra of the chemical residues associated with the majority of the impacts formed by paint-flake particles indicate that the paint was a Si, Cl, Ti-rich paint low in Zn (see Figure 8). Such data suggest that the paint type may have been Chemglaze A-276, or a paint of similar composition.

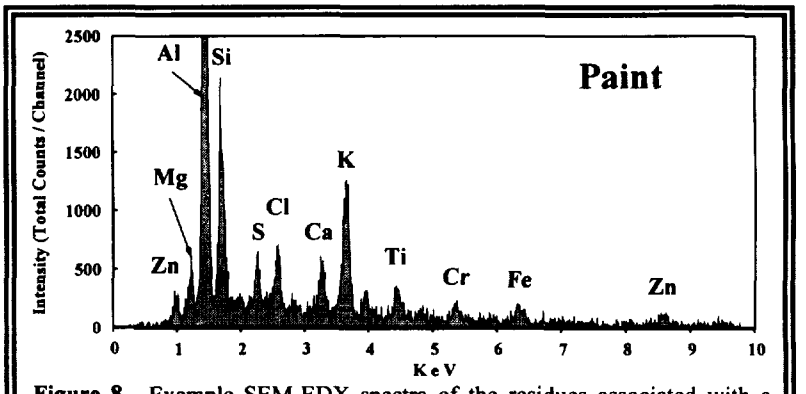

Figure 8. Example SEM-EDX spectra of the residues associated with a typical F07F02 paint impact.

STS-41C, the LDEF deployment mission in 1984, was also the Solar Maximum Satellite repair mission. Analysis of returned Solar Max hardware revealed that Chemglaze A-276, and similar paints which possessed organic binders, do not hold up well under long exposures in LEO (ref. 15). In short, the organic binders in these types of paint were readily broken down or eroded by atomic oxygen. As a result, spacecraft manufacturers today utilize paints with non-organic binders whenever possible.

Returning to intercostal F07F02, the anomalous increase in craters has not, to date, been documented on any other LDEF hardware, with the exception of the S0001 experiment-tray lips which were in direct contact with intercostal F07F02 (Humes, personal communications). Intercostal C07F02, from the other end of Row 7, does not exhibit this phenomenon, nor do intercostals in the same area of LDEF on adjacent rows on either side of Row 7. The similar chemical composition indicates that the projectiles originated from a common source. Photographs of LDEF have been examined in an effort to locate an object which could have served as a location for a primary impact that could have generated a large number of secondary craters on this intercostal. No such source is evident. Secondly, the particles may have been traveling as a dense cloud or group of orbital debris, yet this too seems unlikely considering the tightly packed or dense nature of the apparent debris swarm. Since neither of the previous sources seems likely, it appears as though these particles may have been Shuttle derived, originating during a primary impact into some Shuttle hardware (*e.g.,* Remote Manipulator System [RMS], within the cargo bay, etc.), during either deployment or retrieval of LDEF.

Future Scanning Efforts

Members of the M&D SIG at JSC will continue to gather data from the detailed scans of the LDEF intercostals as long as funding permits. In related matters, the past year saw the return of the EURECA spacecraft, as well as the Hubble Space Telescope (HST) repair mission. The M&D SIG has already acquired sections of EURECA's thermal insulation materials which are presently being scanned at LaRC by D. Humes. Prior to the HST repair mission the M&D SIG had requested pieces of the return solar panels for examination. However, during the repair activities one of the two solar panels would not completely fold to a configuration permitting its return to Earth, and thus, was jettisoned over the side of the Shuttle. Whether or not the M&D SIG will still acquire any of this material for examination has yet to be determined. Nevertheless, LDEF will serve as the baseline or snap shot of the LEO particulate environment for the time period of April, 1984 to January, 1990. Future data will be compared to the data acquired from LDEF to evaluate how the LEO particulate environment is evolving with time.

3-DIMENSIONAL IMAGE ANALYSIS

Image Collection

During the three-month deintegration of LDEF, the M&D SIG generated ~4,500 digital, color stereo-image pairs of impact related features from all space-exposed surfaces, the idea being to reduce these images to yield more accurate feature information (*e.g.,* crater depth and diameter with respect to the original target surface). In an earlier paper (ref. 16) we described the theory and practice of determining

this 3-dimensional feature information from stereo imagery, while a second paper (ref. 17) described some of the problems and solutions encountered during development of the algorithm that would be used to garner such information.

Initial Analysis Plan

Initial economic and portability constraints were the main factors involved in the decision to utilize stereo imagery as a means for extracting 3-D information from LDEF impact craters. The initial analysis plan was to perform automated, full-image windowed cross-correlation to determine a high resolution surface morphology of the crater images. Several problems (*e.g.*, specular reflectivity) encountered during the initial phases of the analysis demonstrated the impracticality of such an approach (ref. 17).

Our next approach was to use a parametric definition of the crater geometries using manually selected tie-points. A tie-point is a pair of points, one from each of the two images, which represent the same point on a surface (*i.e.*, a tie-point "ties" two images together at a single point). This approach made the assumption that crater geometries could be accurately defined by a paraboloid. It was eventually determined via a series of tests performed on a set of cross-sectioned craters (ref. 17) that a 2^{nd} order (paraboloid) 3-D curve was not accurately describing the crater geometries adequately. Further analysis revealed that a 6^{th} order curve resulted in a fairly accurate representation for the cross-sectioned profile of typical, experimentally derived impact craters.

6^{th} Order Fit Decision

In order to perform a least-squares, 3-D 6^{th} order curve fit on the stereo images, a much larger set of data points was required than for the 2^{nd} order curve fits. This was a significant problem because of the man-hour intensive tie-point collection process, and because -- frequently -- the operator was unable to locate sufficient tie-points to perform the analysis. A technique was developed which utilized the initial tie-points (which had previously been collected for the paraboloid estimation) as "seeds" for a local area modified cross-correlation. These seed tie-points were used to center small search regions within the image over which to perform a modified cross-correlation search for more tie-points to be used as inputs to the 6^{th} order curve fit.

AVODE Filter

The majority of the impact craters we were utilizing involved materials with a high degree of specular reflectivity (*i.e.*, aluminum). The effect of this reflectivity is to cause large differences in the photometric intensity of areas on the surfaces as observed from each camera due to the change in viewing angles with a stereo microscope. This meant that it was not feasible to perform traditional correlation techniques which assume that equivalent areas will appear equivalent on both images. In order to compensate for this problem the images were pre-filtered using an AVODE (Absolute Value Omni-Directional Edge) algorithm which was developed specifically for this purpose. The output from this filter is an image in which each pixel has encoded within it eight, 1-bit flags which indicate whether an edge exists in each of the primary eight directions. Note that these flags do not indicate the sign of the edge (bright to dark or dark to bright), nor do they indicate the magnitude of the edge. Neither of those traits is particularly relevant when dealing with specularly reflective materials. The advantages of this filter are that it leaves out irrelevant information and permits cross-correlation of the resultant images using a logical XNOR,

which is fairly CPU inexpensive. An XNOR is a bitwise operation which returns a 1 if the two inputs are the same and a 0 if they are different. The measure of agreement in a correlation is then just the sum of the bits in the output from the XNOR operation.

Iterative Photometric Calibration

One of the problems (and a lesson learned) with the original data collection was that the video-camera pairs, which were assigned to individual stereo-microscope systems (see ref. 6), were not photometrically calibrated prior to data acquisition. Unfortunately, this resulted in a significant difference in the photometric responses of the individual cameras, and forced us to perform an iterative, localized photometric calibration, which was incorporated into the AVODE filtering. It was not possible to perform a straightforward gain correction because of the reflectivity of the material.

Bi-directional Logical XNOR Correlation

After the input regions were processed through the AVODE filter, a windowed, logical XNOR cross-correlation was performed. This involves selecting a small reference area in one image and measuring its correlation with each possible location in the region of interest on the other image. The maximum correlation is then given a confidence value based on the sum of the bits in the XNOR output, the likelihood of the step size as compared to other surrounding tie-points, and the total number of bits turned on in the input regions. This last check is necessary to guard against areas with no edges correlating exactly.

After some experimentation it was determined that a bi-directional correlation drastically added to the trustworthiness of the results. This step consisted of swapping the reference and search images, and repeating the entire correlation process. Agreements between the two correlation passes give a much higher confidence to the resultant tie-points (*i.e.*, if A points to B and B points to A then it's much more likely that A & B form a valid tie-point than if A points to B, and B points to C).

Tie-Point Selection

The output of the bi-directional cross-correlation is an array of "best guess" tie-points with their corresponding confidence values. From this array is selected a subset of tie-points which pass a set of acceptance criteria. These new tie-points are then used as inputs to the 6^{th} order surface solver. Note that the entire correlation process is performed separately for the internal crater surface and for the ambient plane.

Simplex Solution Of Crater Geometry

After several approaches were attempted, the final method used in solving for the coefficients of the 6^{th} order curve was a downhill simplex algorithm (ref. 18). The benefits of this approach are that it is fairly simple to implement and modify, it requires only function evaluations (not derivatives), and it permits the addition of solution constraints (*e.g.*, ensuring that the center of the crater is the lowest point). This technique was also adapted to solve for the equation of the ambient plane.

Depth And Diameter Determination

Once the coefficients for the 6^{th} order curve and ambient plane equations have been determined, the crater depth and diameter are calculated. The crater depth is defined as the distance between the ambient plane and the center (*i.e.*, bottom) of the 6^{th} order curve. The crater diameter is defined as the diameter of the circle formed by the intersection of the ambient plane and the 6^{th} order curve.

Error Estimation

In order to estimate the accuracy of the final results a Monte Carlo analysis was performed. This analysis consists of repeatedly adding random errors to the initial inputs and processing the results through the same algorithm as the original data. The random error is normally distributed about zero with the standard deviation based on the residuals of the initial curve fit. A large number of passes through this process were performed and a statistical analysis of the resultant outputs was used to estimate the accuracy of the initial fit.

Description Of Test Craters And Manual Measurements

To determine the overall accuracy and reliability of the analysis system described above, a set of eight test craters were carefully measured. For this purpose, eight >300 μm in diameter craters were chosen from various aluminum LDEF tray clamps. Binocular images of these craters were then collected in the FOILS Laboratory at JSC, utilizing the same type system and parameters that were employed in gathering the stereo-image pairs during LDEF deintegration. Seed tiepoints were collected for these image pairs in preparation for processing.

Tuneable Parameters

A total of 37 different parameters within the various data-reduction routines were determined to be "tuneable" (*i.e.*, parameters whose settings could affect the overall accuracy and reliability of the analysis algorithm). An example of a tuneable parameter is the size of the reference area to be used. All parameters were initially set at what were felt to be reasonable values and all eight test craters processed. Ideally, a 37-dimensional array of results would have been generated, and the best settings for all parameters would be defined as the point in that array which gave the most accurate results. Due to time, intelligence, and CPU limitations, however, it was decided to make the assumption that the effects of each of the tuneable parameters were independent (at least to first order) and each parameter was individually adjusted while leaving all other parameters at a fixed value. Multiple passes of this process eventually resulted in a set of values for the tuneable parameters which gave the most accurate results. Each run of the analysis software not only outputs an estimate of the crater depth and diameter, but an estimate of the potential error associated with those results. A significant portion of the parameter tuning involved attempting to minimize these errors while maximizing the trustworthiness of the error analysis (*i.e.*, ensuring that the true answer lay between the error bars).

When the tuning had been completed, a 90% trustworthiness was achieved with semi-acceptable error bars. Unfortunately, when the overall analysis routine was applied to a subset of the unknown images, the error estimates were unacceptably large (less than 25% of the unknown craters that were processed possessed error-bar ranges of less than 10%) as to make any studies based on the results futile. After an

extensive effort it was decided to abort any further attempts to improve the analysis results of these stereo-image pairs, mainly because of the poor initial image quality (*e.g.*, lack of photometric calibration, extremely narrow depth of field, synchronization problems during digitization, etc.).

3-Dimensional Image Acquisition; Lesson Learned

As a result of the efforts made in attempting to reduce the stereo-image pairs acquired at KSC by the M&D SIG, there are several key parameters and/or conditions which should be addressed before any such future efforts are undertaken. By addressing these issues up front, much of the work needed to reduce the data could be eliminated. These issues are:

1) A photometric calibration should be performed on the entire image acquisition system prior to data collection to ensure similar photometric response between the two images.

2) A method for increasing the depth-of-field of the optical system needs to devised.

3) The orientation and type of lighting utilized at image acquisition needs to be investigated (*e.g.*, a 360° ring lighting may give better results than spot lighting).

4) The intensity of the light source should be increased over what was utilized by the M&D SIG, or use more sensitive video cameras, or both. This may also enable the aperture to be closed down, and aid with the depth-of-field problems.

5) Image "noise" must be minimized. This can be accomplished by averaging a sequence of images, or by increasing the light and turning down the camera gain.

MISCELLANEOUS M&D SIG ACTIVITIES AT JSC

With FY 94 bringing to a close the initial investigative phases of LDEF, the M&D SIG is active on several fronts in consolidating information and attempting to make it available for future use by M&D workers and spacecraft engineers.

M&D Database

In a continuing effort to make all M&D data available to the general user community, the M&D SIG at JSC is constantly updating the M&D Database with data from all possible sources, including data generated at JSC, as well as data provided by various LDEF investigators. At the time of this writing the database contained detailed information on more than 16,000 individual impact features that have been documented on LDEF. A little more than half of this data has been generated by direct M&D SIG

activities and investigations, while the remainder has been provided by various LDEF investigators. However, the M&D SIG would like to receive more data from any and all potential sources and are requesting that anyone having such data please forward it to T.H. See or M.E. Zolensky. Details regarding the format of such information should be discussed with either T.H. See and/or C.B. Dardano.

Access to, and use of the data contained within the M&D Database is encouraged. In addition, although FY 1994 will bring to a close the initial and intensive LDEF investigation, the M&D Database at JSC will continue to serve as a repository for M&D type data. Therefore, M&D investigators are encouraged to continue to send such data for inclusion with this extensive M&D Database. The M&D Database is accessible via any of the following techniques.

A) DECNET:
1) Log onto host computer.
2) Type SET HOST 9300.
3) Type PMPUBLIC at *Username:* prompt.

INTERNET:
1) Type TELNET 146.154.11.35
or
TELNET CURATE.JSC.NASA.GOV
2) Type PMPUBLIC at *Username:* prompt.

MODEM: The modem may be 300, 1200, or 2400 baud; no parity; 8 data bits; 1 stop bit. The area code is 713 for long distance calls.
1) Dial 483-2500.
2) Type SN_VAX in response to the *Enter Number:* prompt.
3) Hit <CR> 2 or 3 times after the *CALL COMPLETE* message.
4) Type J31X in response to the # prompt.
5) Type C CURATE in response to the *Xyplex>* prompt.
6) Type PMPUBLIC at the *Username:* prompt.

Periodic updates on the state of the JSC holdings of LDEF, as well as other meteoroid-related activities, are issued by the Office of the Curator at JSC in the form of the *Dust Courier*. Parties interested in being added to the distribution list of this publication should contact M.E. Zolensky.

LDEF-Related Images On CD-ROM

Presently, members of the M&D SIG at JSC are actively involved in the curation and distribution of various photographic images related to the deployment, retrieval and post-retrieval documentation of LDEF. Already in progress at JSC is the transfer of the ~4,500 stereo images of various LDEF impact features that were taken during the initial deintegration and examination of LDEF at the Kennedy Space Center, as well as all of the subsequent images acquired at JSC. All of these images have been converted into a TIFF file format and are being transferred on to CD-ROM. The disks are readable on both PC and MAC systems (*i.e.*, the data was written to disk in standard ISO 9660 format). A set of CDs consists of ~12 individual disks, the last of which also contains a complete copy of the M&D database as of the time of

this writing. Copies of these CDs are available on a temporary loan basis from the LDEF Curator (*i.e.*, M.E. Zolensky) at JSC.

The LDEF Science Office located at Langley Research Center, Hampton, Virginia is considering CD-ROM storage of the on-orbit LDEF survey and general-view type pictures, as well as the post-flight deintegration and experiment tray stand pictures, for the purpose of long-term archiving and general access. The exact format in which these later files will be written to CD has not been determined. However, once completed these images will be available via computer link or on a temporary loan basis for interested workers. Finally, along these same lines, the M&D SIG presently plans to archive all LDEF M&D data it can acquire on CDs. However, this will only occur if the various LDEF investigators provide the M&D SIG with their data.

M&D SIG Report

The M&D SIG is in the process of putting together a report summarizing all M&D LDEF results and what they mean to the survivability of both manned and unmanned spacecraft in LEO. This report will include recommendations for further M&D-type activities and investigations on future spacecraft, as well as a long-term outlook as to ways in which the population of LEO particles can be monitored, as well as possible mitigation of its orbital-debris components.

Future Activities

Although FY 94 will conclude the initial LDEF activities, it will not mean an end to M&D-type studies and investigations. At the recently held 3rd LDEF Post-Retrieval Symposium in Williamsburg, Virginia, NASA Headquarters and the LDEF Science Office presented plans for the formation of a Space Environments & Effects (SEE) program. This program would encompass the various LDEF SIGs, as well as private industry and academia, and would be a customer-oriented program, focusing on issues related to designing, placing and safely maintaining both manned and unmanned payloads into Earth orbit.

REFERENCES

1) See, T.H., Mack, K.S., Warren, J.L., Zolensky, M.E., and Zook, H.A. (1993) Continued Investigation of LDEF's Structural Frame and Thermal Blankets by the Meteoroid & Debris Special Investigation Group. *LDEF - 69 Months in Space, Second LDEF Post-Retrieval Symposium, NASA CP-3194*, p. 313-324.

2) Hörz, F., Cintala, M.J., Bernhard, R.P., Cardenas, F., Davidson, W., Haynes, G., See, T.H., Winkler, J. and Knight, J. (1994) Cratering and Penetration Experiments in Teflon Targets at Velocities From 1 to 7 km/s. *NASA Technical Memorandum*, in press.

3) Kessler, D.J. (1991) Orbital Debris Environment for Spacecraft in Low Earth Orbit, *J. Spacecraft, 28, 3*, p. 347-351.

4) Zook, H.A. (1991) Meteoroid Directionality on LDEF and Asteroidal Versus Cometary Sources (abstract). *Lunar Planet. Sci. XXII*, Lunar and Planetary Institute, Houston, Texas., p. 1577-1578.

) Cour-Palais, B.G. (1987) Hypervelocity Impacts in Metals, Glass, and Composites, *Int. J. Impact Eng., 5*, p. 681-692.

5) See, T.H., Allbrooks, M.A., Atkinson, D.R., Simon, C.G. and Zolensky, M. (1990) *Meteoroid and Debris Impact Features Documented on the Long Duration Exposure Facility, A Preliminary Report, Publication #84, JSC #24608*, 583 pp.

7) See, T.H., Hörz, F., Zolensky, M.E., Allbrooks, M.K., Atkinson, D.R. and Simon, C.G., (1992) Meteoroid and Debris Special Investigation Group Preliminary Results: Size-Frequency Distribution and Spatial Density of Large Impact Features on LDEF. *LDEF - 69 Months in Space, First LDEF Post-Retrieval Symposium, NASA CP-3134*, p. 477-486.

8) Bernhard, R.P., See, T.H., Hörz, F. and Brownlee, D.E. (1994) Natural and Orbital Debris Particles on LDEF'S Trailing and Forward-Facing Surfaces, *LDEF - 69 Months in Space, Third LDEF Post-Retrieval Symposium, NASA CP-3275,* 1995.

9) Humes, D. (1994) Small Craters on the Meteoroid and Space Debris Experiment. *LDEF - 69 Months in Space, Third LDEF Post-Retrieval Symposium, NASA CP-3275,* 1995.

10) McDonnell, J.A.M. and Stevenson, T.J. (1992) Hypervelocity Impact Microfoil Perforations in the LEO Space Environment (LDEF, MAP A0023 Experiment). *LDEF - 69 Months in Space, First LDEF Post-Retrieval Symposium, NASA CP-3134*, p. 443-458.

11) Zook, H.A., (1992) Deriving the Velocity Distribution of Meteoroids From the Measured Meteoroid Impact Directionality on the Various LDEF Surfaces. *LDEF - 69 Months in Space, First LDEF Post-Retrieval Symposium, NASA CP-3134*, p. 569-579.

12) Kessler, D.J., (1993) Origin of Orbital Debris Impacts on LDEF's Trailing Surfaces. *LDEF - 69 Months in Space, Second LDEF Post-Retrieval Symposium, NASA CP-3194,* p. 585-594.

13) Coombs, C., Watts, A., Wagner, J. and Atkinson, D. (1992) *LDEF Data: Comparisons with Existing Models.* A final report to the M&D SIG under subcontract NAS9-17900, SC-02N0165768 to Lockheed - ESC.

14) Bernhard, R.P. and Zolensky, M.E (1994) Analytical Electron Microscopy of LDEF Impactor Residues. *LDEF - 69 Months in Space, Third LDEF Post-Retrieval Symposium, NASA CP-3275,* 1995.

15) Warren, J.L., Zook, H.A., Allton, J.H., Clanton, U.S., Dardano, C.B., Holder, J.A., Marlow, R.R., Schultz, R.A., Watts, L.A., and Wentworth, S.J. (1989) The Detection and Observation of Meteoroid and Space Debris Impact Features on the Solar Max Satellite, *Proc. Lunar Planet. Sci. Conf., 19th*, p. 641-657.

16) See, T.H., Allbrooks, M.K., Atkinson, D.R., Sapp, C.A., Simon, C.G., and Zolensky, M.E. (1992) Meteoroid & Debris Special Investigation Group: Data Acquisition Procedures. *LDEF - 69 Months In Space. First Post-Retrieval Symposium, NASA CP-3134*, p. 459-476.

17) Sapp, C.A., See, T.H., and Zolensky, M.E. (1992) 3-D Crater Analysis of LDEF Impact Features From Stereo Imagery, *LDEF - 69 Months In Space. Second Post-Retrieval Symposium, NASA CP-3194*, p. 339-345.

18) Press, W.H., et. al. (1987) *Numerical Recipes*, p. 289-293.

MICROMETEOROIDS AND DEBRIS ON LDEF COMPARISON WITH MIR DATA

Jean-Claude Mandeville
Lucinda Berthoud
CERT-ONERA / DERTS
2, Avenue E.Belin, 31055 Toulouse Cedex (France)
Phone: (33) 61557117, Fax (33) 61557169

ABSTRACT

Part of the LDEF tray allocated to French experiments (FRECOPA) has been devoted to the study of dust particles. The tray was located on the face of LDEF directly opposed to the velocity vector. Crater size distributions have made possible the evaluation of the incident microparticle flux in the near-Earth environment. Comparisons are made with measurements obtained on the other faces of LDEF (tray clamps), on the leading edge (MAP) and with results of a similar experiment flown on the MIR space station.

The geometry of impact craters, depth in particular, provides useful information on the nature of impacting particles and the correlation of geometry with the chemical analysis of projectile remnants inside craters makes possible a discrimination between meteoroids and orbital debris. Emphasis has been laid on the size distribution of small craters in order to assess a cut-off in the distribution of particles in LEO. Special attention has been paid to the phenomenon of secondary impacts.

A comparison of flight data with current models of meteoroids and space debris shows a fair agreement for LDEF, except for the smallest particles : the possible contribution of orbital debris in GTO orbits to the LDEF trailing edge flux is discussed. For MIR, flight results show differences with current modelling: the possible enhancement of orbital debris could be the due to the contaminating presence of a permanently manned space station.

1. INTRODUCTION

The NASA Long Duration Exposure Facility (LDEF) has been retrieved after 2105 days in orbit. During its mission LDEF was stabilized with the long axis continually pointed toward the center of the earth, and surfaces perpendicular to this axis pointed at fixed angles with respect to the direction of orbital motion /1/.
The tray allocated to French experiments (FRECOPA) was located on the face of LDEF (B3) directly opposed to the velocity vector. Two passive experiments have been flown for the detection of microparticles. The first was composed of a set of thick metallic samples (Al, Au, Cu, W, Stainless Steel) and quartz surfaces; the second was composed of aluminium multilayer thin foil detectors. Detailed description of the hardware has been given elsewhere /2,3/.

The MIR Russian Space Station has been in orbit, between 350 and 425 km, since February 1986. The experiment, "Echantillons", was deployed outside the station during the Aragatz Mission in December 1988; it was retrieved 13 months later.
Dust detectors flown on MIR carried basically the same passive sensors as those on LDEF, with two sets of stacked thin foils (DMC) looking in two opposite directions, and an active capacitor type dust detector (DIC) /4/.

2. CRATER DISTRIBUTION AND MORPHOLOGY

Crater size distribution on the various targets enables, using laboratory calibration with solid particle accelerators, the evaluation of the incident microparticle flux. /5,6 7/.
It is important to remember that it is difficult to discriminate between craters of debris origin and those of meteoroid origin from a simple image of the crater. There are no specific characteristic forms for craters of different origins. However, crater morphology is determined by the interaction between particle and target. Particle and target properties will therefore have a major influence on crater parameters. Even when the particle has long since vapourised, craters may provide clues to its characteristics. Whilst pre-LDEF work concentrated on the interpretation of crater diameter (or spall and pit diameter for brittle targets), depth and depth to diameter ratio 'P/D', current crater morphology descriptions now also include crater cross-sectional profile, circularity and type of impact according to target thickness.

2.1. Crater diameter

Crater diameter has been shown in previous work to be dependent on many factors including particle size, density, velocity, impact angle and target properties, especially thickness /6,8/. In the case of semi-infinite space-exposed samples, the target properties are known and all the same. Therefore if the density and velocity of impacting particles are assumed, their sizes can be estimated. This size estimation is most rapidly found using one of the existing empirical equations developed from laboratory simulation tests. The crater diameters on LDEF examined in this work varied in size from 1.5 μm to 1070 μm and those for Mir varied from 0.5 to 300 μm. Calibration tests carried out recently /9/ showed that the Cour-Palais equation appeared the most suitable for converting micron-sized impacts on semi-infinite targets. Modelling values for velocities can be used with the Cour-Palais equation to convert the crater sizes mentioned above to particle sizes. This would give particle sizes of 0.5 μm to 395 μm for LDEF and 0.2 to 72 μm for Mir. Different crater measurement techniques create discrepancies when data is compared.

There can be up to a factor of 5 difference between the impact diameters formed on finite and semi-infinite targets for the same impactor size. This lead to only the 'thicker' foils on the Mir experiment being used to deduce crater size distributions. The observed crater size distributions for LDEF and Mir show two notable differences when compared to our model calculations and to McDonnell's experimental results /10/. The first is the 'bulge' in the distribution from crater diameter 5-50 μm on LDEF and from 1 to 10 μm on Mir. This is thought due either to secondary impacting or to the difference in scanning techniques. The second is the 'dip' in the distribution for craters < 5 μm on LDEF and < 1 μm on Mir. The dip could be explained by inadequate microscope resolution for Mir, but cannot be explained for LDEF leading and trailing edges, where it occurs for larger diameters (see figures 6,7 and 9).

2.2. Crater depth and crater depth to diameter ratio

The crater depth is examined here only as part of the P/D ratio. It is influenced by all the same parameters as the crater diameter. However, the hydrodynamic processes are different for crater depth and diameter formation. This can be seen experimentally for decreasing target thickness: the crater diameter remains constant up to and slightly beyond marginal perforation, whereas the crater depth increases. There is therefore no reason to believe that the depth and diameter will show the same parameter indices in their respective empirical equations. CTH calculations show that final crater depth is attained before final crater diameter /11/.The momentum enhancement effect is expected to slightly deepen craters for very high velocities due to the vapourisation of the target material. The depth is clearly affected by target material properties and thickness, particle shape and material properties.

The exact nature of parameters affecting the crater depth to diameter ratio have not yet been determined. Previous use of the ratio to deduce projectile density was based on the idea that the P/D depends only upon the density of projectile and target. As the density of the target was usually known the density of the projectile density was inferred from comparison with impact experiments. It was suggested that projectile density could provide a clue as to the composition of the particle. From experiments carried out in the laboratory we we have found that P/D is not influenced by impact velocity up to 14 km/s, when that velocity is above the target low stress bulk sound velocity. This is if agreement with Fechtig et al. Some research offers experimental evidence to the contrary /12,13/. Another complicating factor for P/D interpretation is the particle shape. The results from recent experiments show that fragmentary particles produce a wider variation in and a higher average of P/D compared to spherical particles /9/. The P/D is clearly a function of the position of the fragment when it strikes the target surface. The average P/D's found on spacecraft surfaces were above the expected 0.5-0.55.

For Mir, no P/D data could be extracted so far. But for LDEF, the P/D data we collected for a few hundred craters found on exposed surfaces may be useful for indicating particle densities.

For the trailing edge of LDEF (Figure 2), the craters of diameter < 100 μm were more uniformly spread over the P/D range and had a higher average P/D ratio than those of diameter > 100 μm. This implies that they were caused by particles of more widely varying densities/compositions with a higher average density than for larger particles. These large particles were more centered in the 0.5-0.6 range with small high and low density components. If the majority of impacts on the trailing edge are due to meteoroids, then the wide range of densities for smaller particles may reflect the heterogeneity of grain compositions. These different grains may come together to form a compact agglomerate, as seen in cosmic dust collections. The average density of such an agglomerate particle may well be around 2-3 g/cm^3, the value required to produce a P/D equal to 0.5-0.6 in the aluminium surfaces examined, as shown by test data.

On the leading edge of LDEF (Figure 3), an even wider spread of P/D was observed for the craters < 100 μm. The variety of densities implied by this spread could be explained by a wide variety of impactor types. For the smaller size range, debris are expected to dominate. Chemical analysis has already demonstrated the diversity of the debris family and this appears to be confirmed by the depth to diameter ratios. The larger craters were on average shallower and centered in 0.5-0.7 range. They are more likely to be due to meteoroids with lower average densities than debris. No particular 'families' of different impactors were discernible for these surfaces, such as those identified by Le Sergeant d'Hendecourt at 3 g/cm^3 and 8-9 g/cm^3 (corresponding to P/D's of 0.5 and 0.9 approx.) /14/.

One of the problems in the interpretation of these values is the vast range of compositions (and therefore densities) of impactors. It can be seen from the following that distinction between debris and meteoroid by P/D alone is not possible. Meteoroid and debris densities both cover the same range, resulting in similar P/D ratios:

P/D	(the target material is aluminium)
0.3-0.5 :	most likely to be meteoroids of low density. Could be paint flakes, (densities 0.5-1 g/cm^3)
0.5-0.6 :	likely to be aluminium or anything with a density similar to that of aluminium such as silicates including glass, stony meteoroids. (densities 2-3 g/cm^3)
0.6-0.7 :	some of the heavier elements and their alloys including titanium, silver etc. stony iron meteoroids (densities 4-5 g/cm^3).
0.7-1.0 :	most likely to be iron-based ie: either steel (debris) or iron meteoroids, or copper or copper alloy (densities 8-10 g/cm^3).

3. COMPARISON OF DATA WITH ESABASE MODELLING

The aim of the ESAbase meteoroid and debris application software /15/ is to assess particle flux and impact risk for a user-specified spacecraft geometry, mission parameters, spacecraft shielding, range of particles, particle flux models and damage equations. In this work the particle flux section of the code was exploited. The advantages of the code lie in its ability to describe the particle flux relative to an entire moving spacecraft (not just a single tumbling surface in space). Calculations take into account shielding effects, particle arrival direction and varying spacecraft attitude and pointing directions.

The Grün polynomial 1985 model /16/ is used for meteoroids (isotropic distribution) and the Kessler 1990 flux model is used for orbital debris; for more details see Anderson, ref. /17/. The velocity distribution relative to earth is taken from the Cour-Palais model /17/. Earth shielding and gravitational focussing are computed. For conversion from crater diameter (D) to particle diameter (d), or mass (m), the following equation is used (Cour-Palais) :

$$P / d = (5.24\, d^{0.056} / H^{0.25})\ (r_p/r_t)^{0.5}\ (V/c_t)^{0.667}$$

with : P : depth of crater and P/D = 0.56 for meteoroids and P/D = 0.63 for debris (measured)

d : diamater of particle in cm, r_p and r_t density of particle and density of target in g/cm^3

H : 90 (Brinell)

V : impact velocity in km/s, sound velocity in target : c_t= 5.4 km/s

3.1. LDEF flux model

The LDEF satellite is modelled by a 12-sided polygon. The mesh system allows identification of the flux on the different rows. The model includes the 8° offset towards row 10 with respect to the velocity vector which was observed on the return of the satellite.

ESAbase can be used to calculate the meteoroid and debris collision velocities for given spacecraft surfaces. Figure 4 shows the average calculated values for each different row on LDEF. The meteoroid velocities vary between 14.8 km/s and 22.8 km/s, velocity is 15.3 km/s for row 03 and 22.5 km/s for row 09. The debris velocities vary between 0 km/s (no flux) on row 03, and 11.5 km/s (rows 08 and 11), the debris velocity on row 09 is 10.7 km/s. ESAbase predicts a large difference in the debris flux for leading and trailing edges. All the rows towards the leading edge have an approximately similar debris flux; however, at row 05 (and its symmetric equivalent 01) the debris flux starts to fall off. By row 04, there is a factor 1000 difference and for 03 there is no debris flux at all. The modelled meteoroid flux does not show such a wide difference as the debris flux. There is a factor 10 difference between row 09 and row 03 for the meteoroids. The model predicts that the meteoroids will dominate the particle flux for crater diameters greater than 10 μm on rows 02, 03 and 04. See Figure 5.

We can perform a detailed comparison of model and observed data for row 09 by comparing crater size distributions with model data calculated by ESAbase. The model particle diameter and mass values were converted to crater diameters using the Cour-Palais empirical equation. Figure 6 shows that the experimental data lie between model predictions for meteoroids and debris for crater diameters less than 10 μm. For crater diameters larger than 10 μm, the experimental data approximately follow the total flux. From this we propose that the debris model is predicting too high a flux for small particles. This is consistent with findings by McDonnell and suggests that the micron end of the Kessler debris model needs modifying /18/.

On Figure 7, the crater size distributions found on FRECOPA surfaces is compared to the model for the trailing edge of LDEF. The occurrence of orbital debris in elliptical orbits could explain the difference between predicted and measured flux on the trailing edge. A cut-off in the distribution occurs for craters with a diameter smaller than 1 mm.

3.2. Mir flux model

The 1 m^2 Echantillons experiment module, with two sides AV and AR, was mounted on the conical part of the MIR station at 45° to the two symmetrical solar arrays.
According to information from CNES and from photographs, the longitudinal Y axis of the module was pointed at 45° to the sun and the Z axis at the Earth. However, due to certain orbital manoeuvres, the details of the orientation of the station are not known.
ESAbase calculates the impact velocity on the experimental surfaces for a given number of orbital points. Thus the variation of the impact velocity around the orbit can be monitored (Figure 8).
The debris velocity ranges between 0 and 13.5 km/s for the AV side (mean 7.6 km/s), 0 and 12.6 km/s for the AR side (mean 6.35 km/s). The meteoroid velocity ranges between 14.5 and 25.8 km/s (mean 19.2 km/s) for the AV side, and between 17.7 and 29.8 km/s for the AR side (mean 22.6 km/s).

ESAbase computes a meteoroid flux and a debris flux. These have both been converted to crater diameter using the Cour-Palais empirical equation and results are shown in Figure 9. The two crater size distributions can then be added together to give a total flux which might be seen on the experimental surface. It is now possible to compare the observed results for Mir and the ESAbase Mir model predictions. The model prediction underestimates the observed flux by a factor of around 6 for crater diameters between 1 and 50 μm.

Secondary impacts are common on some parts of MIR detectors. This is expected for complex large structures and can lead to an overestimate of actual flux. Hopefully the size distribution of secondaries is usually distinctive, with a large number of ovoid submicron craters. Discrimination is therefore usually possible. If the contribution of secondaries is removed, the flux of small particles on MIR orbit is still higher than expected by the models and similar to the flux on the leading edge of LDEF. The difference in altitude or inclination between Mir and LDEF cannot entirely explain the difference. It is possible that the environment of a permanently manned space station is populated by a large number of small, short-lived orbital debris.

4. ACKNOWLEDGEMENTS

The authors would like to express their thanks to Dr. F. Hörz and members of the Hypervelocity Gun Laboratory at NASA JSC in Houston and to Professor E. Grün at MPI in Heidelberg for carrying out acceleration tests, and to Professor J.A.M. McDonnell at the Univ. of Kent, Canterbury for LDEF MAP samples. This work was partly supported by a European Commission research grant under the 'Science' programme.

5. REFERENCES

1. A.S. Levine ed., *LDEF : 69 Months in Space*, NASA CP-3134 (1991), pp. 397-584.

2. J.C. Mandeville, AO138-1 and AO138-2 Experiments, in: *LDEF Mission 1 Experiments*, eds L.G. Clark, W.H. Kinard, D.J. Carter, J.L. Jones, NASA SP-473, (1984) p.121.

3. J.C. Mandeville and J.A.M. McDonnell, Micrometeoroid multiple foil penetration and particle recovery experiments on LDEF, in: *Solid Particles in the Solar System*, ed. I. Halliday and B.A. McIntosh, D.Reidel (1980) p.395.

4. J.C. Mandeville, Aragatz Mission Dust Collection Experiment, *Adv.Space Res.* 10, 3, 397, (1990).

5. J.C. Mandeville, Orbital debris and micrometeoroids : LDEF and MIR data, in: *Materials in a Space Environment,* Cepadues-Toulouse, (1992).

6. L. Berthoud and J.C. Mandeville, Empirical impact equations and marginal perforation, *Proceedings First European Conference on Space Debris,* ESA SD-01, (1993)

7. D. Humes, Large craters on the meteoroid and space debris impact experiment, in *LDEF - 69 Months in Space,* NASA CP-3134, (1991).

8. F.Hörz, R.P. Bernhard, T.H. See, D. Atkinson, M. Allbrooks, M and D SIG Progress Reeport : Laboratory simulations of LDEF impact features, in *LDEF - 69 Months in Space,* NASA CP-3134, (1991).

9. L.Berthoud, Micrometeoroids and orbital debris observed in low Earth orbit, Thesis, ENSAE, Toulouse, (1993).

10. J.A.M. McDonnell, Factors affecting the choice of foils for penetration experiments in space, in *Space Research X,* North Holland pub. (1970).

11 . A. Watts, D. Atkinson and S. Rieco, Dimensional scaling for impact cratering and perforation, *Report POD/Associates* , (1993).

12. H. Igelseder and E. Igenbergs, Crater morphology at impact velocities between 8 and 17 km/s, *Int. J. Impact Eng.,* vol.10,271-280, (1990).

13. J.Vedder and J.C. Mandeville, Microcraters formed in glass by projectiles of various densities, *JGR,* vol.79, 23, (1974).

14. L.B. Le Sergeant D'Hendecourt and Ph. Lamy, On the size distribution and physical properties of interplanetary dust grains, *Icarus* 43,350-372, (1980)

15. J. de Kruijf, ESABASE, A most versatile and flexible system engineering tool, *ESA BR-54,* (1988).

16. Grün E., Zook H. et al., Collisional balance of the meteoritic complex, Icarus 62, 244-272, (1985).

17. Anderson B.J., Meteoroid and orbital debris, NASA SP-30425, (1990).

18. J.A.M. McDonnell et al., Impact cratering from LDEF's 5.75 yr exposure, *Proc. Lunar Planet. Sci.* 22, 185-193, (1992)

Figure 1 : Crater depth to diameter ratio (P/D) against diameter (D) for clamps on various rows of LDEF.

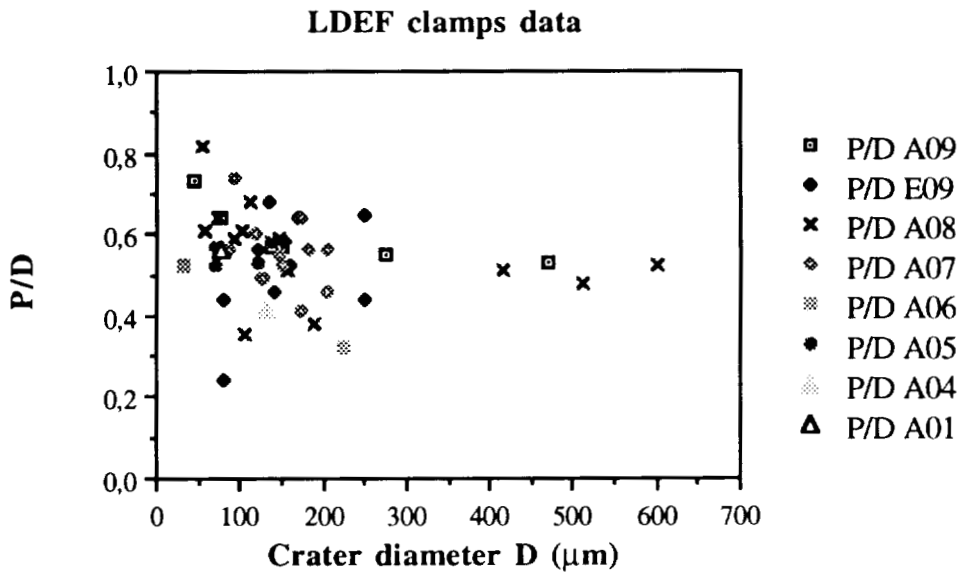

Figure 2 : Depth to diameter ratio (P/D) for craters on trailing edge (row03) of LDEF.

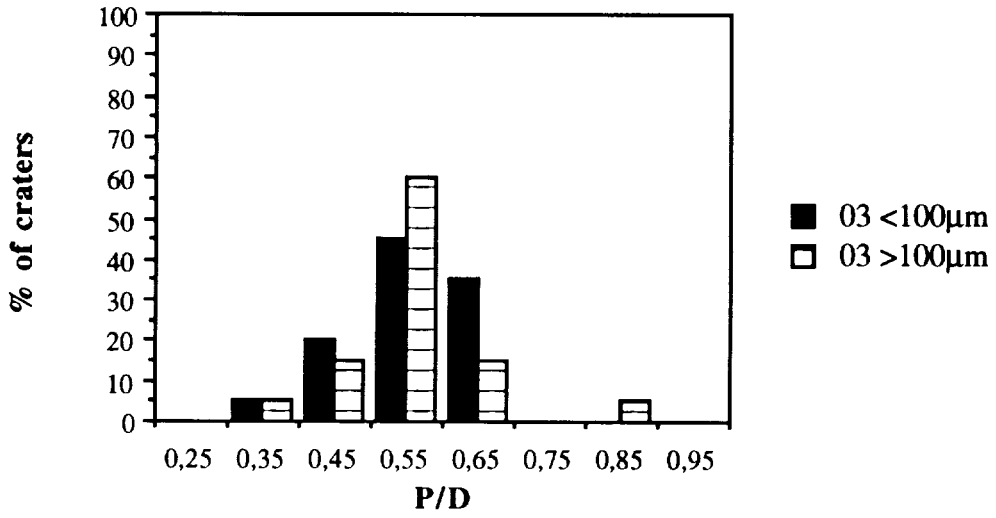

Figure 3: Depth to diameter ratio (P/D) measured for craters on leading edge (row 09) of LDEF.

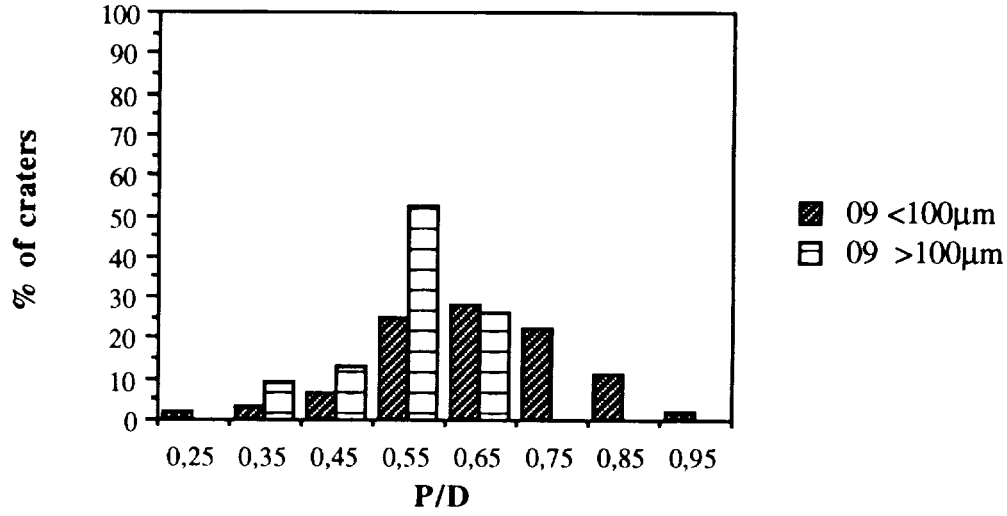

Figure 4. ESAbase calculated meteoroid and debris velocities for LDEF rows.

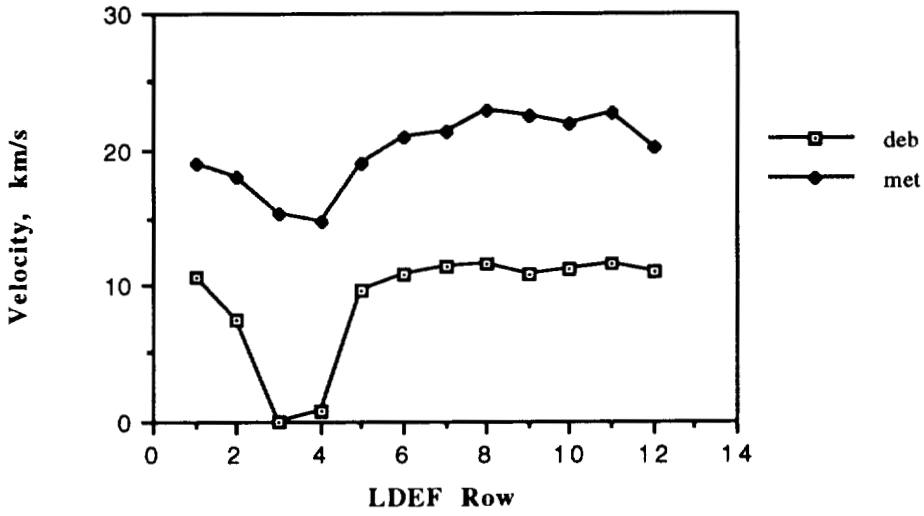

Figure 5 . ESAbase model predictions for meteoroids (modmet), debris (moddeb) and the sum of these (modtot) on all LDEF rows for craters with D > 10 μm (using Cour-Palais equation for the conversion crater diameter to particle diameter).

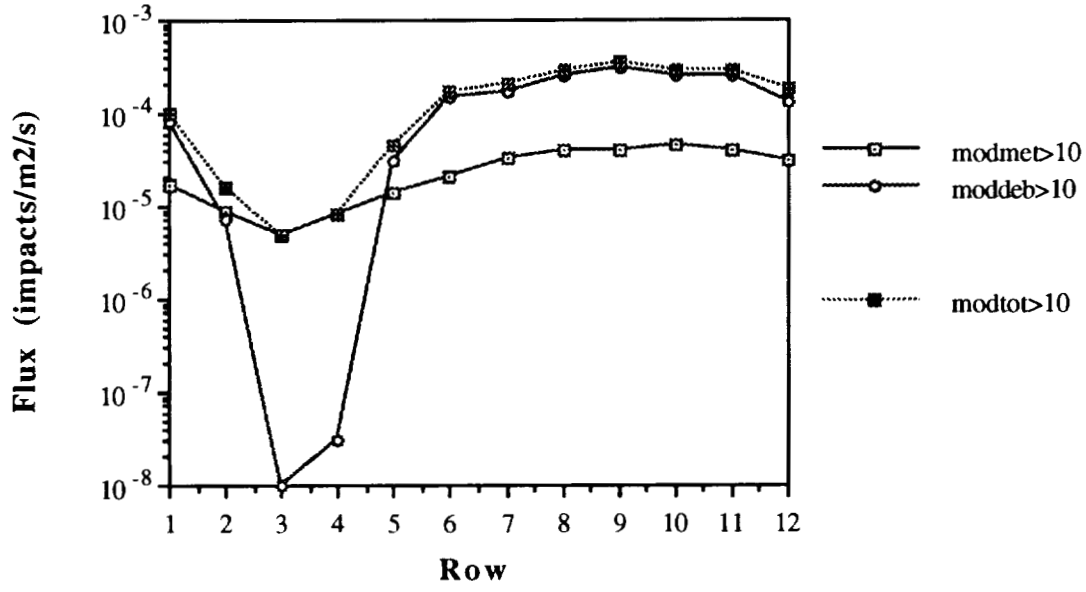

Figure 6 : ESAbase model predictions for debris (moddeb09) and meteoroids (modmet09) for the leading edge of LDEF compared to our experimental data (expt09).

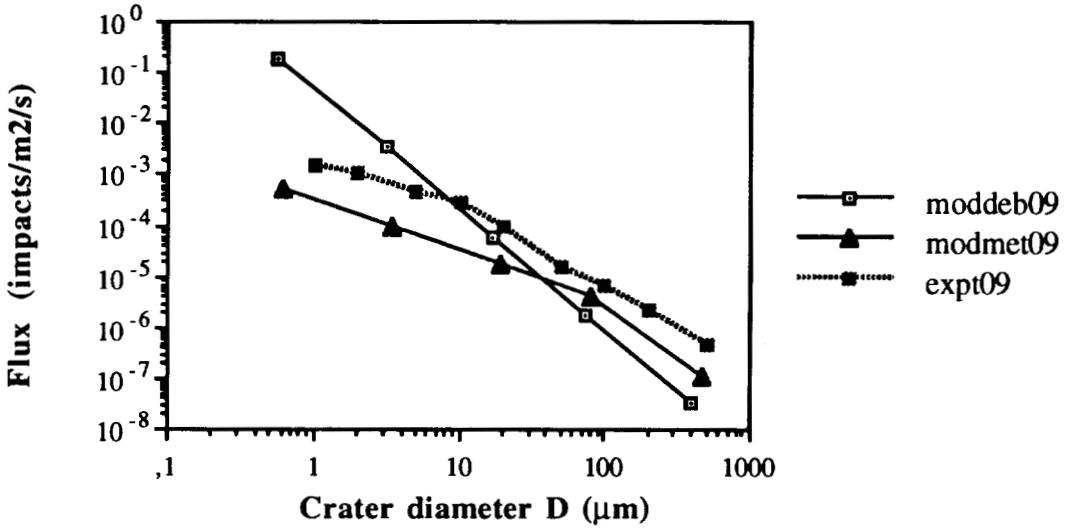

Figure 7 : ESAbase model of total flux for LDEF trailing edge (modmet03) compared to LDEF observed crater data (expt03).

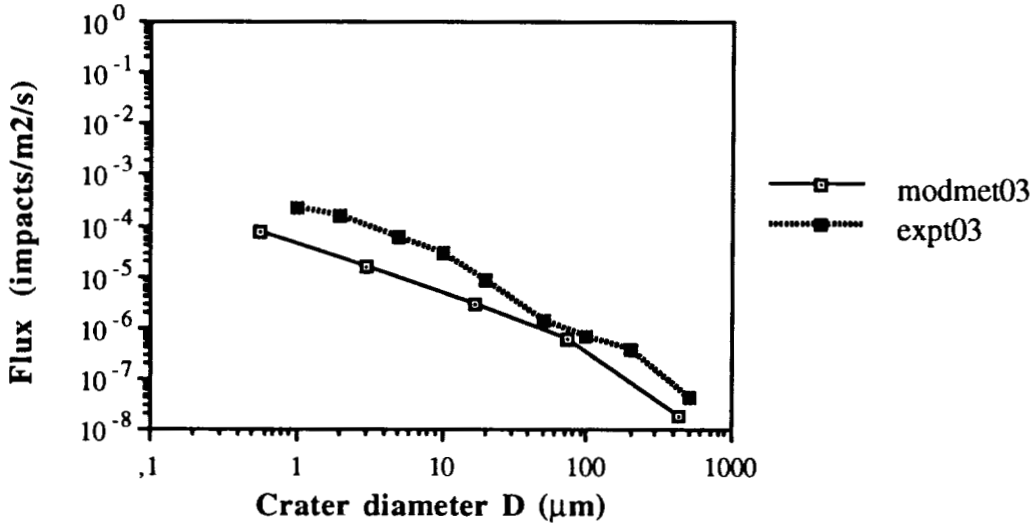

Figure 8 : Variation of meteoroid and debris velocities on Mir experiment around one orbit .

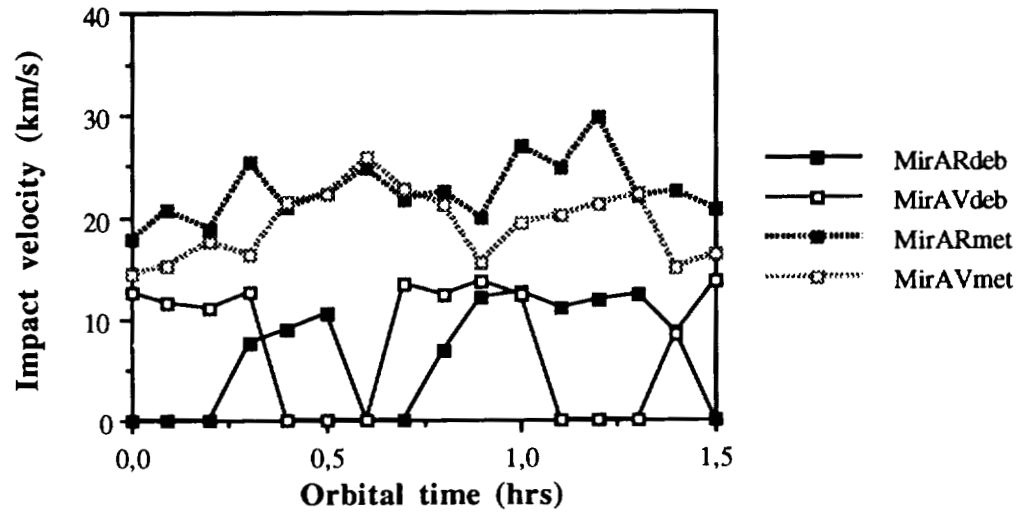

Figure 9 : ESAbase model of meteoroid (MirAVmet) and debris (MirAVdeb) flux compared to observed values (expAVthick) using Cour-Palais equation to convert d to D.

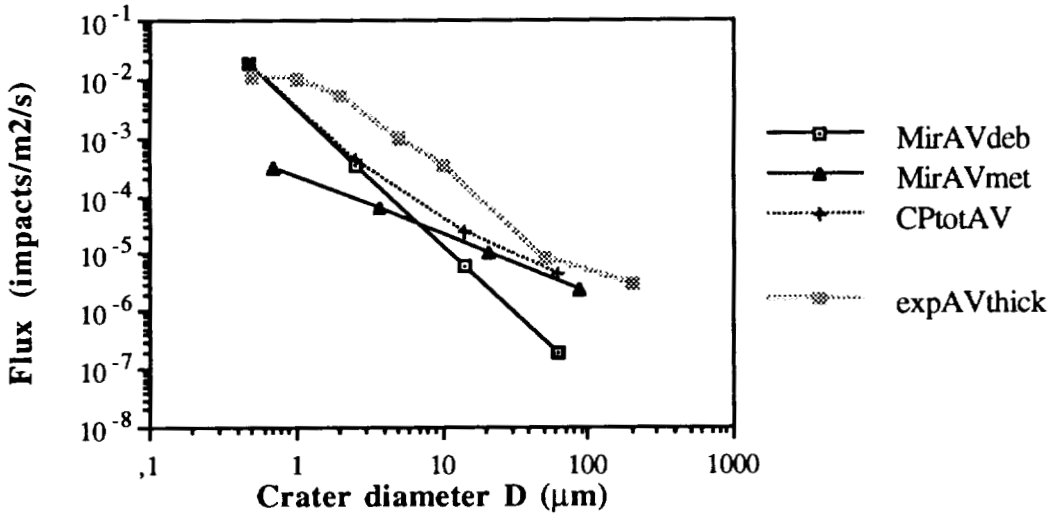

SMALL CRATERS ON THE METEOROID AND SPACE DEBRIS IMPACT EXPERIMENT

Donald H. Humes
NASA Langley Research Center
Hampton, VA 23665-5225
Phone: 804/864-1484, Fax: 804/864-7730

SUMMARY

Examination of 9.34 m^2 of thick aluminum plates from the Long Duration Exposure Facility (LDEF) using a 25X microscope revealed 4341 craters that were 0.1 mm in diameter or larger. The largest was 4 mm in diameter. Most were roughly hemispherical with lips that were raised above the original plate surface. The crater diameter measured was the diameter at the top of the raised lips. There was a large variation in the number density of craters around the three-axis gravity-gradient stabilized spacecraft. A model of the near-Earth meteoroid environment is presented which uses a meteoroid size distribution based on the crater size distribution on the space end of the LDEF. An argument is made that nearly all the craters on the space end must have been caused by meteoroids and that very few could have been caused by man-made orbital debris. However, no chemical analysis of impactor residue that will distinquish between meteoroids and man-made debris is yet available. A small area (0.0447 m^2) of one of the plates on the space end was scanned with a 200X microscope revealing 155 craters between 10 μm and 100 μm in diameter and 3 craters smaller than 10 μm. This data was used to extend the size distribution of meteoroids down to approximately 1 μm. New penetration equations developed by Alan Watts were used to relate crater dimensions to meteoroid size. The equations suggest that meteoroids must have a density near 2.5 g/cm^3 to produce craters of the shape found on the LDEF. The near-Earth meteoroid model suggests that about 80 to 85 percent of the 100 μm to 1 mm diameter craters on the twelve peripheral rows of the LDEF were caused by meteoroids, leaving 15 to 20 percent to be caused by man-made orbital debris.

INTRODUCTION

For nearly six years, the Long Duration Exposure Facility orbited the Earth with 57 scientific experiments on board that were to be evaluated when the spacecraft was returned to the ground. There was no communication with the LDEF while it was in orbit. The Meteoroid and Space Debris Impact Experiment, designated S0001 by the LDEF Project Office, consisted of many thick aluminum plates distributed around the spacecraft to study the population, directionality, and chemical composition of meteoroids and man-made orbital debris. All the data will be obtained from examination of the craters left in the aluminum plates. In some places in the literature this experiment is referred to by a shortened title as the Space Debris Impact Experiment.

Meteoroids are small interplanetary particles that travel through our solar system undetected and whose encounter can only be treated statistically. They are natural particles that are in orbit about the sun. Meteoroids that pass near the Earth are drawn toward the Earth by its gravitational field and some strike spacecraft as they speed toward the atmosphere. Meteoroids have been considered a hazard to spacecraft since the beginning of space exploration. NASA has published models of the meteoroid environment near the Earth (ref.1) and in interplanetary space (ref.2), and a design criteria document for protection against meteoroids (ref.3). However, the interest in meteoroids is broader than the concern about the hazard they present to spacecraft. Meteoroids may include unaltered primal material whose composition and orbital paths are important clues to the origin and evolution of the solar system.

Space debris is the man-made material left in space as a result of our space activity. It ranges in size from microscopic fragments created during explosions in space to large spent rockets. Some man-made debris escapes the Earth's gravity but most is left in orbit about the Earth and is of concern as a potential hazard to spacecraft. Large pieces of debris are tracked and cataloged and possible collisions with the Space Transportation System (STS) orbiter are checked for each mission so that evasive measures can be taken if necessary. Small pieces cannot be tracked and their encounter, like that of meteoroids, must be treated statistically. NASA now has a model of the man-made orbital debris environment (ref.4) to be used in hazard analysis.

The LDEF maintained a three-axis gravity-gradient stable orientation, which provided a new level of sophistication in flight data on meteoroids and man-made debris. In previously obtained flight data in near-Earth space, see ref.1, the number of meteoroid impacts was obtained but the orientation of the impact site at the time of the impact was unknown. The number density of craters for the different fixed surface orientations on the LDEF provides a direct measurement of the degree to which the hazard to spacecraft is directional. The variation in the number density of craters with surface orientation depends on the orbital distribution of the particles. While the orbits of individual particles cannot be determined with this experiment, theoretical orbital distributions can be checked by seeing if they are in agreement with the crater distribution found on the LDEF.

Some aluminum plates donated to the LDEF Meteoroid and Debris Special Investigation Group (M&D SIG) by principal investigators of other LDEF experiments were examined and the results are included in this paper. Wayne Slemp donated the aluminum base plates, sample holders and cover plates from his experiments (S0010 and AO134) on the only side of the LDEF from which the Meteoroid and Space Debris Impact Experiment plates were missing. His contribution is especially significant because that side of the LDEF received the greatest concentration of impact craters. William Berrios donated the aluminum thermal panels from both ends of the LDEF. The dummy plates that covered two unused experiment compartments on the Earth-facing end of the LDEF were also examined.

The research reported in this paper is a continuation of that presented in ref.5. There, craters with a diameter of 0.5 mm or greater, found in thick aluminum plates from all fourteen faces of the LDEF, were counted and measured, and a model of the near-Earth meteoroid environment, based on the magnitude of the crater density and its variation with location around the spacecraft, was presented. Here, the research is extended down to 0.1 mm craters, and for the

space end, down to 10 μm diameter craters. The new data is used to improve the near-Earth meteoroid environment model. Throughout this paper paragraphs can be found that were copied verbatim from ref.5 for completeness.

EXPERIMENTAL HARDWARE

The Meteoroid and Space Debris Impact Experiment exposed 26.29 m^2 of thick aluminum plates (4.8 mm thick) to the space environment. The location of the plates on the LDEF is shown in Fig.1. The plates were mounted on the bottom of 7.6 cm deep trays, except for the plates in Tray D6, which were mounted even with the top of the tray.

The nineteen peripheral trays that were totally dedicated to this experiment had two plates measuring 0.62 m by 0.95 m in each tray. The three peripheral trays that were shared with other experiments had two plates measuring 0.41 m by 0.95 m in each tray. These individual plates are identified by the tray location number and the relative position of the two plates in the tray. For example, the two plates in the tray in location F10 are identified as plates F10G and F10H, with F10G being the plate nearest the G-end or Earth-facing end of the LDEF. The three end trays each contained a single plate that was 0.72 m by 0.72 m.

In ref.5 the area of the Meteoroid and Space Debris Impact Experiment was mistakenly given as 26.32 m^2. The 0.03 m^2 target on plate A6H, that was used as a berthing aid, shielded part of the plate. It was removed during de-integration and was not examined as part of this study.

The Meteoroid and Space Debris Impact Experiment plates were made of aluminum alloy 6061-T6. They had a thin oxide layer on both sides produced by chromic anodization and a coat of black paint on the back for spacecraft thermal control. The space-exposed side of the plates had a green or a pink tint due to the oxide layer produced during anodization. The plates from the Earth end and the space end (at locations G4, G8, and H5) were exceptions. They had the usual gray color of aluminum with only a natural oxide layer. They also were smoother than the plates from the peripheral trays. It would appear that they did not undergo the same sodium hydroxide cleaning and chromic anodization as the plates in the peripheral trays, even though records show that they were treated like the other plates.

The plates donated by Wayne Slemp were from his tray at location B9. They were anodized aluminum, 6061-T6, of various thicknesses from 1.6 mm to 6.4 mm. The plates that were studied and the identification numbers used for them are shown in Fig.2. Plate B9P5 was a large specimen holder under the B9P4 retainer plate, but only a small portion of it was exposed to the space environment. B9P1 and B9P5 were 6.4 mm thick, B9P4 and B9P6 were 2.1 mm thick, and B9P2 and B9P3 were 1.6 mm thick. Twenty-nine of the 32 clamps used to hold specimens on the plates were also examined. All the clamps were 2.2 mm thick aluminum 6061-T6. When the clamps were removed from the tray they were not individually identified and were mixed together with clamps from the back of the tray that had been used to hold control samples to the plates.

Then identification numbers ranging from B9P7 to B9P63 were assigned to the clamps. Later, the space-exposed clamps were identified by impact craters and contamination patterns.

The thermal panels donated by William Berrios covered the area around the edges of the two ends of the LDEF that was not being used for experiments. The twelve thermal panels on the space-facing end were assigned identification numbers H13 to H24, and those on the Earth-facing end, G13 to G24, by the LDEF M&D SIG (see Fig.1). Each thermal panel was bent to wrap around the corner of the spacecraft, exposing a small rectangular area along one of the spacecraft rows. The two surfaces of a thermal panel, with their orthogonal viewing directions, are considered as two separate plates in this paper. A symbol in parenthesis following the thermal panel identification number designates the orientation of the surface, (S) for a space-facing surface, (E) for an Earth-facing surface, and (R6) for a surface along Row 6, for example. The thermal panels were made of 1.6 mm thick aluminum (6061-T6) and had coatings for thermal control. Those on the space end were anodized to reflect sunlight and were painted black on the back. Those on the Earth end were plated with elemental nickel (nominally 15 μm thick) and then coated with black chrome (nominally 0.1 μm thick) to absorb sunlight reflected off the Earth. The back of the Earth end thermal panels were apparently masked during the plating process and were then painted black, except along the edges.

The two dummy plates on the Earth-facing end were anodized aluminum (6061-T6), 2.3 mm thick. Each plate had an area of 0.90 m^2. One was identified as G9 by the LDEF M&D SIG, and the other as G3.

LDEF MISSION

The LDEF was deployed by the STS-41C crew on April 7,1984. It was initially placed in a near-circular orbit with an apogee of 480 km, a perigee of 474 km, and an inclination of 28.5 degrees. By the time it was recovered by the STS-32 crew on January 12,1990, it had fallen to an altitude of 331 km.

It was intended for the longitudinal axis of the spacecraft to be aligned with its Earth-centered position vector and for the normal to the Row 9 trays to be aligned with the velocity vector. Post-flight analysis showed that the actual orientation had a misalignment of about eight degrees in yaw and one degree in pitch; see ref.6. As a result, the leading edge of the LDEF was between Row 9 and Row 10. The one degree pitch angle gave the space-facing end a slight view of the forward direction of flight.

DESCRIPTION OF CRATERS

The craters in aluminum on the LDEF look very much like craters produced with hypervelocity accelerators in the laboratory at impact speeds greater than 6 km/s. The craters are

generally round with lips that rise above the surface of the plate. The photograph in Fig.3 shows the top view of a crater on the F10H plate. This 4 mm diameter crater is the largest on any of the Meteoroid and Space Debris Impact Experiment plates and is the largest crater examined in this study.

Most of the craters are round and symmetric, which is surprising considering that the impacting particles were undoubtedly irregular in shape and must have struck at oblique angles. The cavity below the plate surface is usually nearly hemispherical. The typical shape of the craters is shown in Fig.4. Three dimensions are shown: the diameter at the top of the raised lips, the diameter at the plate surface, and the depth. The diameter at the plate surface is considered to be a more fundamental dimension than the diameter at the top of the raised lips, but it is more time-consuming to measure, so in this study the lip diameter is reported. The diameters shown in the figures and in the tables in this paper are all lip diameters.

The shape of the craters varies with crater size. Craters with a lip diameter of 0.5 mm or greater are usually very nearly hemispherical ($P/d_c = 0.5$) while smaller craters are usually deeper than hemispheres, with 100 μm craters having a depth about 0.56 times the diameter at the plate surface.

The shape of the craters was determined with a high-power microscope, typically 200X or greater. The very short depth of field of a high-power microscope is required to measure the depth of the crater and to measure the diameter at the plate surface. To obtain the crater shape data in Fig.4, the diameter at the top of the raised lips was also measured with the high-power microscope.

However, the scanning of the aluminum plates to obtain crater fluxes, for craters with a lip diameter of 100 μm or greater, was done with a low-power microscope, and a systematic difference of about 6 percent was found in the lip diameter measurements obtained with the low-power microscope and the high-power microscope, probably due to the effect that the difference in lighting had on the judgement of the location of the crest of the lips. The low-power microscope used an external ring light attached to the objective lens. The high-power microscope used light passing out of the objective lens for illumination. The lip diameters measured were about 6 percent greater when the high-power microscope was used.

Equations that relate crater size to projectile size, speed, density, impact angle and other properties use crater depth or crater diameter at the plate surface. The diameter at the top of the raised lips is never used. The equations, however, can be modified to calculate the crater lip diameter using the crater shape information in Fig.4, and that has been done in this paper when theoretical calculations were made to compare the near-Earth meteoroid model to the spacecraft data. The variation in crater shape with crater size for craters with a lip diameter less than 500 μm was estimated from the two cases shown in Fig.4.

There were no craters on any of the plates examined that penetrated through the entire thickness of the plate. The impact that created the largest crater on the Meteoroid and Space Debris Impact Experiment, the 4 mm crater on the F10H plate, produced a very short, raised dome on the

back of the 4.8 mm thick plate. The dome was less than 25 μm high. It is not known if it is just the black paint that delaminated and raised up or whether the aluminum plate is actually bulged.

The two thinnest donated plates from Row 9 had a total of four craters in the 1.6 mm thick aluminum that caused the back of the plates to bulge.

There was one near penetration of the 1.6 mm thick thermal panels. An impact that created a 1.02 mm deep crater on the portion of the G23 thermal panel that was along Row 10 caused spallation of aluminum from the back of the thermal panel.

There were ten impacts that caused a bulge in the back of the thermal panels. Most of the bulges occurred on the unpainted areas near the edges of the thermal panels. There were twelve impacts on the thermal panels that caused the black paint on the back to spall. Most of the paint spallation occurred without any detectable bulge in the aluminum.

NUMBER AND LOCATION OF CRATERS

A low-power (25X) microscope was used to scan 9.34 m^2 of aluminum plates that came from all fourteen faces of the LDEF in order to obtain the number density of craters with a lip diameter of 0.1 mm or greater on each face. While scanning the plates from the space-facing end, special attention was taken, and an attempt was made to find all craters with a lip diameter of 60 μm or greater. The survey was probably complete for 80 μm diameter craters and larger but was probably incomplete for 60 μm craters. A total of 4824 craters were found with the low-power microscope, 4341 of which had a lip diameter of 0.1 mm or greater and 483 of which were craters smaller than 0.1 mm from the space-facing end.

A 0.0447 m^2 area in the center of the space-facing plate from Tray H5 was scanned a second time, using a high-power (200X) microscope to obtain the number density of craters with a lip diameter of 10 μm or greater. A total of 138 craters with lip diameters between 10 μm and 60 μm were found along with the 51 craters with a lip diameter of 60 μm or greater that had been previously found during the low-power (25X) microscope survey. Three craters smaller than 10 μm were also found. The survey was probably complete for craters with a lip diameter of 20 μm or greater but some craters between 10 μm and 20 μm may have been missed.

In addition, the entire 26.29 m^2 of the Meteoroid and Space Debris Impact Experiment and 15.84 m^2 of plates donated to the M&D SIG were reexamined using a 12.5X microscope to obtain the number density of craters with a lip diameter of 0.5 mm and greater on all fourteen faces of the LDEF. The number densities differ slightly from those reported in ref.5. The fluxes presented in this paper are slightly higher for all the faces except for the space end and the trailing edge (Row 3) where they are lower, and for Row 9 and Row 10 where they are the same. A total of 965 craters with a lip diameter of 0.5 mm or greater were found on the 42.13 m^2 examined.

The distribution around the LDEF of the 5678 craters with a lip diameter of 10 μm or greater is given in Table I and Table II. The orientation of the plates on the sides of the LDEF is given by the angle between the spacecraft velocity vector and the normal to the plate surface. The plates on each face are grouped together because the flux should be constant on any face from both meteoroids and man-made orbital debris. The area of the plates given is the actual area. No correction has been made for the shielding that occurs for the plates that were mounted on the bottom of the 7.6 cm deep trays.

The variation in the cumulative crater flux on the twelve peripheral rows of the LDEF is shown in Figs.5, 6 and 7 for various threshold crater sizes as a function of the surface orientation. The cumulative crater flux is the number density of craters of a given threshold size or larger divided by the duration of the mission. The flux is greatest at the front of the spacecraft for all size craters and decreases smoothly toward the back, except for the plates nearest the trailing edge where the flux increases again for all but the smallest craters. The row with the minimum measured crater flux varied with crater size.

The error bars, which are the 90 percent confidence limits calculated using the chi-squared distribution function in the manner suggested in ref.7, are appreciable because of the small number of craters, especially near the back of the LDEF. It may be that the increase in crater flux measured near the trailing edge for large craters is just a statistical variation.

The data points in Figs.5, 6 and 7 are alternately from the southern side and northern side of the spacecraft. The smoothness of the data shows that there is a north/south symmetry in the particulate environment in the size range considered in this paper.

The cumulative crater flux on the two ends of the LDEF is shown in Fig.8 for craters with a threshold lip diameter between 0.1 mm and 1 mm. The flux on the space-facing end is 30 to 60 times the flux on the Earth-facing end in that size range.

The cumulative crater flux on the space-facing end, extended down to a threshold lip diameter of 10 μm, is shown in Fig.9. The slope between adjacent data points gets continuously flatter as smaller size craters are considered. This suggests that there may be a lower limit to the size of the meteoroids, i.e., a cutoff in the size distribution of meteoroids.

The data points in Figs.5,6,7 and 8 are the average flux for each face. In most cases, all of the plates on the same face give the same flux within the 90 percent confidence limits. One of the exceptions is the variation in flux between plates B9P2 and B9P4 which were side-by-side on the leading edge and differed by a factor of 1.3 in the flux of craters with a lip diameter of 0.1 mm or greater. With the number of craters of that size found on these two plates (400 total), we can be 90 percent confident that they were not exposed to the same environment. Of course, there is about a 10 percent chance that they were. The most likely explanation for the discrepency is that there was a slight difference in the properties of the plates, or the oxide layer on the surface, that affected the formation of the crater lips.

PREVIOUS MODELS OF THE PARTICULATE ENVIRONMENTS

In the first paper on the results of this experiment (ref.5), data on large craters was presented on craters with a lip diameter of 0.5 mm or larger. The number of those craters and their distribution around the spacecraft suggested that more than 80 percent had been caused by meteoroids and less than 20 percent by man-made orbital debris. A new model of the near-Earth meteoroid environment was presented in ref.5 based on the assumption that all the large craters were caused by meteoroids. The man-made orbital debris model of Kessler (ref.4), which predicted that man-made debris was only a minor component in this size range, was seen to be plausible and no modifications to it were suggested.

Knowing the distribution of these large craters around the three-axis gravity-gradient stabilized LDEF provided the information needed to bring a new level of sophistication to the modelling of the near-Earth meteoroid environment. Proposed speed distributions and directionality distributions of meteoroids could be checked by comparing the variation in the number density of craters around the spacecraft suggested by these distributions, to the LDEF data thought to be primarily from meteoroids. Of the four speed distributions studied, the distributions of Erickson (ref.8) and Kessler (ref.9), which are essentially identical to each other, were found to provide the best agreement with the LDEF data. The directionality distribution of meteoroids relative to the Earth was biased toward the zenith in that model, rather than being random, in order to agree with the larger than expected flux seen on the space-facing end of the LDEF.

The new model of the near-Earth meteoroid environment presented in ref.5 is discussed in detail. In it meteoroids were assumed to have five properties: (1) a population in the near-Earth space expressed in terms of spatial density or number per unit volume, (2) a size distribution, (3) a speed distribution, (4) a direction of motion distribution with respect to the Earth, and (5) a mass density. It was assumed that the size distribution, speed distribution and directionality are independent of each other. The mass and size of the Earth affect the meteoroid environment and appear in that model in the form of (1) the gravitational focusing factor, which expresses the degree to which the impact flux tends to be enhanced by the Earth's gravitational field as the Earth is approached, and (2) Earth shielding, which tends to decrease the impact flux as the Earth is approached. Also, the equations used to relate meteoroid properties to impact damage were included as an essential part of the model.

However, when the near-Earth meteoroid environment model in ref. 5 is used to predict the flux of small meteoroid craters on the LDEF, it gives values that are higher than the measured crater flux, for every face, being about a factor of 1.4 higher for 100 μm diameter craters. Apparently, the size distribution of meteoroids in that model, which was obtained from the NASA near-Earth meteoroid model in ref.1, is wrong, having too many small meteoroids. Modifications to that near-Earth meteoroid environment model to correct that discrepancy are discussed in the following section of this paper.

The author of this paper has made no attempt to model the man-made orbital debris environment even though a comparison of the LDEF data and the modified near-Earth meteoroid

environment model in the following section of this paper suggests that the man-made orbital debris model of Kessler (ref. 4) is not accurate. There may be more man-made debris than predicted by Kessler (ref. 4) and its orbital distribution may be different.

MODIFIED MODEL OF THE NEAR-EARTH METEOROID ENVIRONMENT

Modifications to the near-Earth meteoroid environment model in ref.5 that bring it into agreement with the new data on small craters found on the LDEF are discussed in this section. It was the size distribution of meteoroids in the previous model that needed changing, but several other components of the model were changed as well. A new set of penetration equations developed by Watts (ref.10) from a more fundamental, physics-based analysis than those in ref.5 are used. The structure of the previous model is retained, i.e., the same properties of the meteoroid environment and the Earth are used and their relationship to each other is the same.

Approach

There are two components to the particulate environment near the Earth: meteoroids and man-made orbital debris. Chemical analysis is not yet available to determine which of the craters examined in this study were caused by meteoroids and which were caused by man-made debris. But in order to model the meteoroid environment, it is desirable to isolate the meteoroid craters from the man-made debris craters. That has been done on the space-facing end of the LDEF simply due to its orientation.

The crater flux on the space-facing end was 30 to 60 times the flux on the Earth-facing end for craters in the 0.1 mm to 1 mm size range (Fig.8). This shows that essentially all the craters on the space-facing end, in this size range, were caused by meteoroids. Very few, 2 to 3 percent, could have been caused by man-made orbital debris because the orbital debris would produce about the same crater flux on both ends of the LDEF. If the longitudinal axis of the LDEF had been aligned with its geocentric position vector, then Earth-orbiting particles would have the same relative speed and same impact angle when approaching the Earth-facing end from below as they would have when approaching the space-facing end from above, and the flux on both ends would be the same. This argument is not valid if the particles are very near the end of their orbital lifetime and their orbits are decaying rapidly. Then the particles would produce a greater flux on the space-facing end. But it is assumed here that the man-made orbital debris particles encountered by the LDEF in the size range needed to make 100 μm to 1 mm diameter craters were more permanent members of the orbital debris environment.

The longitudinal axis of the LDEF, however, was not exactly aligned with its position vector. The spacecraft was pitched forward about 1 degree so that the space-facing end had a slight view of the forward direction. This would tend to increase the flux on the space-facing end and

decrease the flux on the Earth-facing end, which was facing slightly backwards. This, however, did not account for any significant part of the factor of 30 to 60 difference in the flux on the two ends. The crater flux on the space-facing end was about the same for the H5 plate as it was for the thermal panels, even though the H5 plate was at the bottom of a 7.6 cm deep tray and the thermal panels were flush with the end of the LDEF. The recessed location of the H5 plate eliminated about 5 degrees from its field of view with little affect on the flux, so the 1 degree forward pitch of the LDEF could not have made a significant difference in the fluxes on the two ends. Therefore, we can assume that essentially all the craters on the space-facing end in the 0.1 mm to 1 mm size range were caused by meteoroids.

The size distribution of meteoroids can be determined from the size distribution of the craters on the space-facing end of the LDEF. The approach taken here to correct the size distribution of meteoroids in the model was to test various candidate meteoroid size distributions in the near-Earth meteoroid environment model from ref.5 and select the one that agreed best with the size distribution of craters on the space-facing end of the LDEF. The spatial density that gave the proper crater flux was determined at the same time.

Then the crater flux on the other faces of the LDEF, from meteoroids alone, was calculated. The difference between the calculated meteoroid flux and the greater measured flux would be assumed to be caused by man-made orbital debris. But before that was done, several other modifications were made to the model from ref.5. Independent reevaluations of all the other components of the model lead to changes in the directionality and mass density of meteoroids, to the gravitational effect of the Earth on meteoroids, and to the set of equations used to relate meteoroid properties to impact damage. The speed distribution of meteoroids and the height of the Earth's atmosphere (165 km) were not changed.

The following sections describe the components of the modified near-Earth meteoroid environment model.

Directionality

The directional distribution of meteoroids is the distribution of directions from which meteoroids would approach a stationary spacecraft. A distribution that was biased toward the zenith, rather than being random, was suggested in ref.5 to agree with the larger than expected relative flux on the space-facing end of the LDEF. New data from the examination of the thermal panels from the space-facing end, included in this paper, increased the area of the space-facing end examined from the 1.15 m^2 reported in ref.5 to 5.48 m^2, and the average flux of craters with a lip diameter of 0.5 mm or greater dropped from the 2.0×10^{-7} $m^{-2}s^{-1}$ reported in ref.5 to 1.6×10^{-7} $m^{-2}s^{-1}$. The data now available on the relative flux of craters with a lip diameter of 0.5 mm or greater on all the fourteen sides of the LDEF is consistent with a random directionality. As discussed in ref. 5, there is some theoretical basis for the random directionality of meteoroids with respect to stationary spacecraft, and so a random directionality is used in the modified near-Earth meteoroid environment model.

Speed Distribution

Four speed distributions of meteors published by astronomers were examined in ref.5 and the distributions of Erickson (ref.8) and Kessler (ref.9), which are essentially identical, provided the best agreement with the variation around the LDEF in the flux of craters with a lip diameter of 0.5 mm or greater. The reexamination of the plates studied in ref.5, and the inclusion of some additional plates in this paper, has resulted in slight changes in the relative flux of craters with a lip diameter of 0.5 mm or greater on the twelve peripheral rows of the LDEF, but the speed distributions of Erickson and Kessler still provide the best agreement and are used in the modified near-Earth meteoroid environment model.

A mathematical description of the Erickson and Kessler speed distributions is given by Zook (ref.11) as

$$f_\phi(V) = 0.112 \qquad 11.1 \leq V < 16.3 \text{ km/s}$$

$$f_\phi(V) = 3.328 \times 10^5 \, V^{-5.34} \qquad 16.3 \leq V < 55.0 \text{ km/s}$$

$$f_\phi(V) = 1.695 \times 10^{-4} \qquad 55.0 \leq V < 72.2 \text{ km/s}$$

where $f_\phi(V)$ is the probability density for meteoroids entering the atmosphere with speed V, in km/s. This is actually the speed distribution of meteors in the Earth's atmosphere, corrected to a constant mass, while the model requires the speed distribution of meteoroids in space. The method of converting the speed distribution of meteors to the speed distribution of meteoroids in space is discussed in ref.5.

Gravitational Focusing

The flux of meteoroids on a spacecraft is enhanced by gravitational focusing, so that the closer the spacecraft is to the Earth, the greater the meteoroid flux tends to be. In this modified model, as in ref.5 and ref.2, the flux on a spacecraft is calculated first, ignoring gravitational focusing, and then that flux is multiplied by the gravitational enhancement factor, G, which for the Erickson (ref.8) or Kessler (ref.9) speed distribution is, according to Kessler (ref.9)

$$G = 1 + (r_e/r)$$

where r_e is the radius of the Earth and r is the distance of the spacecraft from the center of the

Earth. The expression for the gravitational enhancement factor, G, used in ref.5 actually applies to the speed distribution of meteoroids given in ref.1, and was mistakenly applied to the speed distributions of Erickson and Kessler in ref.5.

Earth's Atmosphere

While meteoroids have been assumed to approach a stationary spacecraft randomly from all directions, the Earth and its atmosphere shield the spacecraft from some of those meteoroids. In this modified model of the near-Earth meteoroid environment, as in ref.5, the Earth's atmosphere is assumed to extend to an altitude of 165 km. It is assumed that all meteoroids entering the atmosphere are destroyed.

Penetration Equations

Recently, Watts (ref.10) developed, from fundamental physics-based analysis, equations for the diameter of a crater and for the depth of a crater that a projectile would produce in a target as a function of the projectile and target properties. These two equations were developed independently, recognizing the differences in the stress history near the surface of a target and deep within the target. Watts also developed an equation for the thickness of material that a projectile can penetrate. These three equations have been adopted as an integral part of the modified near-Earth meteoroid environment model.

The Watts equation for the diameter of a crater at the surface of a target, d_c, is

$$d_c/d_p = 1.0857\, F\, (\rho_p/\rho_t)^{0.2857}(\rho_t/Y_t)^{0.2857}(c_t/c_p)^{0.2857}(u_o\cos\theta)^{0.5714}/(1+(\rho_p/\rho_t)^{1/2})^{0.5714}$$

where d_p is the diameter of the projectile, ρ_p is the density of the projectile material, ρ_t is the density of the target material, c_t is the speed of sound in the target, c_p is the speed of sound in the projectile, Y_t is the yield strength of the target material, u_o is the impact speed, θ is the impact angle measured from the normal to the target surface, and the scaling factor, F, is

$$F = 1/(1+(2\Delta/d_c)^{1/2})^N$$

where N is assumed to be 1/3 by Watts (ref.10) for aluminum 6061-T6 targets and is assumed to be 1/3 for all target materials in this paper, and Δ is a target material "grain size" parameter given by

$$\Delta = \pi\, G_t\, \gamma_s / Y_t^2$$

where G_t is the target material shear modulus, and γ_s is the target material surface energy per unit area for opening cracks. The "grain size" parameter, Δ, is not easy to obtain for all materials because γ_s is not often quoted. Watts suggests that Δ is about 50 μm for aluminum 6061-T6. The speed of sound in the meteoroid material (c_p) is not known and undoubtedly varies from particle to particle, but has been assumed to be 5 km/s in this paper.

The Watts equation for the depth of a crater, P, is

$$P/d_p = F\,(1/4)(4/3)^{1/3}(\rho_p/\rho_t)^{1/3}(\rho_t/Y_t)^{1/3}\{(c_{ot}+s(u_o\cos\theta-u_{t,crit})/(1+(\rho_t/\rho_p)^{1/2}))(u_o\cos\theta-u_{t,crit})\}^{1/3}$$

where c_{ot} is the speed of sound in the target when it is unstressed (c_t), s is $(1+\Gamma)/2$ where Γ is the Gruneisen parameter, and $u_{t,crit}$ is the critical impact speed for the target material above which the equation applies and is given by

$$u_{t,crit} = (2Y_t/\rho_p)^{1/2}\,(1+(\rho_p/\rho_t)^{1/2}).$$

There is a critical impact speed for the projectile material also, $u_{p,crit}$, that must be exceeded for the penetration equation to apply. That is,

$$u_{p,crit} = (2Y_p/\rho_p)^{1/2}(1+(\rho_p/\rho_t)^{1/2})$$

where Y_p is the yield strength of the projectile material. Y_p is not known for meteoroid material and undoubtedly varies from particle to particle, but if meteoroids have less strength than the target material then the target material will determine the critical impact speed. For the targets considered in this paper, that is assumed to be the case, and that probably is the case for most spacecraft materials. The critical impact speed, $u_{t,crit}$, is modest, less than 1 km/s for aluminum targets being struck by meteoroids or man-made orbital debris, so the equation is applicable to nearly all of the impacts on a spacecraft.

The Watts equation for the thickness of material a projectile can completely penetrate, T, is

$$T/d_p = F\,(1/8)(4/3)^{1/3}(\rho_p/\rho_t)^{1/3}(\rho_t/Y_t)^{1/3}\{(c_{ot}+s(u_o\cos\theta-u_{t,crit})/(1+(\rho_t/\rho_p)^{1/2}))(u_o\cos\theta-u_{t,crit})\}^{1/3}$$

$$+ F(1/4)\{\rho_p(u_o\cos\theta)^2/(2\sigma_s(1+(\rho_p/\rho_t)^{1/2})^2)\}^{1/N}$$

where a value of 2 is suggested for N by Watts in ref.10 and where σ_s is the ultimate strength of

the target material. The material properties of the target needed in these equations is given in Table III for three aluminum alloys.

Density

The crater size equations of Watts (ref.10) can be used to calculate the ratio of crater depth to crater diameter (P/d_c). A projectile density near 2.5 g/cm^3 is needed to obtain the depth-to-diameter ratios of 0.50 to 0.56 seen in the aluminum 6061-T6 plates on the LDEF, and that density has been assumed for meteoroids in the modified meteoroid model. The meteoroid density of 0.5 g/cm^3 used in ref.5 and in the NASA near-Earth meteoroid environment model (ref.1) would give depth-to-diameter ratios near 0.24.

Size Distribution and Spatial Density

With the modifications just described fixed, various meteoroid size distributions were tested in the near-Earth meteoroid model to see how well they predicted the crater size distribution on the space-facing end of the LDEF, which is assumed to be almost entirely from meteoroids. The results for three meteoroid size distributions are shown in Fig.10. The spatial density was adjusted to force all three curves to go through the LDEF data point for craters with a lip diameter of 0.5 mm or greater. The calculations were for plates that were flush with the end of the LDEF, like the thermal panels.

The size distribution from NASA SP-8013 (ref.1) predicts a flux of 0.1 mm diameter and larger craters that is about a factor of 1.1 higher than the measured flux on the LDEF. That is much less than the factor of 1.4 that prompted the rejection of that size distribution for use in the near-Earth meteoroid environment model in ref.5. The other modifications made to the model have improved the prediction of the flux of small craters making the selection of a new meteoroid size distribution less important for predictions in that size range. Changing the density of meteoroids from 0.5 g/cm^3 to 2.5 g/cm^3 probably had the greatest effect because in the penetration equations of Watts used in this paper, and in those used in ref.5, high density projectiles are predicted to create larger craters than low-density projectiles of the same mass. The change in meteoroid density caused a shift in the calculated mass of meteoroids responsible for the craters left on the LDEF. This shift, while improving the predictions for small craters, will cause the flux of large craters to be overestimated. That can be seen in Fig.10 for 1 mm and larger craters. The size distribution from SP-8013 is still found to be inaccurate.

The meteoroid size distribution of Grün (ref.12) agrees fairly well with the LDEF data in the flux of 0.1 mm to 0.5 mm diameter craters on the space end of the LDEF. It appears that the Grün size distribution also was based on the assumption that meteoroids had a density of 0.5 g/cm^3. If the Grün curve were shifted, it would fit the data very well. But as it is, when used

with a meteoroid density of 2.5 g/cm^3, it will overestimate the number of large craters created in a spacecraft, as seen in the 1 mm and greater diameter craters.

A new meteoroid size distribution is proposed that provides excellent agreement with the LDEF data, not only in the 0.1 mm to 1 mm diameter crater range, but also for craters between 10 μm and 0.1 mm. It is not known if all the small craters on the space-facing end, 10 μm to 0.1 mm, were caused by meteoroids or whether a significant fraction were caused by man-made orbital debris. The flux of these very small craters has not been measured on the Earth-facing plates so an argument based on the space end to Earth end ratio cannot be made. But it is assumed here that essentially all the small craters on the space end also were caused by meteoroids. If that assumption is incorrect the modified near-Earth meteoroid environment model will overestimate the flux of small craters caused by meteoroids on a spacecraft.

The proposed size distribution of meteoroids and their spatial density, S, in m^{-3} is

$$\log_{10}S = -8.362 \qquad m < 1.31 \times 10^{-12} \text{ g}$$

$$\log_{10}S = -18.251 - 1.664 \log_{10}m - 0.070 (\log_{10}m)^2$$

$$\log_{10}S = -18.188 - 1.213 \log_{10}m \qquad m > 5.00 \times 10^{-7} \text{ g}$$

where m is the meteoroid mass, in g.

TESTING THE MODEL

The model of the near-Earth meteoroid environment was then tested against three other sets of data: (1) the crater flux on the peripheral rows and on the Earth-facing end of the LDEF, (2) the crater flux in the aluminum louvers from the Solar Max spacecraft, and (3) the penetration flux through thin sheets of material on the Explorer 16, Explorer 23, and the three Pegasus spacecraft.

The meteoroid crater flux calculated for the twelve peripheral rows of the LDEF must match the measured fluxes if man-made orbital debris is not a significant component of the particulate environment in this size range, or be less than the measured flux if man-made debris is a significant component. If the calculated flux exceeds the measured flux, then the model is inaccurate and must be rejected. Likewise, for the Solar Max crater data, the calculated meteoroid crater flux must agree with or be less than the measured crater flux. The penetration flux data from the Explorer 16, Explorer 23, and the three Pegasus satellites was obtained in the 1960s when man-made orbital debris was, presumably, not significant, so the meteoroid model should match the fluxes measured.

Comparison With Other LDEF Crater Data

The calculated cumulative meteoroid crater flux on the twelve peripheral rows of the LDEF is compared with the measured flux in Figs.11,12, and 13 for craters with a threshold lip diameter of 0.1 mm, 0.2 mm, 0.3 mm, 0.5 mm and 1 mm. The calculation is for plates at the bottom of 7.6 cm deep trays taking into account the shielding provided by the tray walls. The calculated meteoroid crater flux is, in general, about 80 to 85 percent of the measured crater flux, suggesting that 15 to 20 percent of the craters in these size ranges were caused by man-made orbital debris.

The calculated cumulative meteoroid crater flux for the Earth end is compared to the measured flux in Fig.14 for plates that are flush with the end on the LDEF. The calculated meteoroid crater flux agrees with the measured crater flux within the 90 percent confidence limits, suggesting that most of the craters on the Earth end in the 0.1 mm to 1mm diameter range were caused by meteoroids.

The model passes the first test; it does not predict more craters on the peripheral rows and the Earth end of the LDEF than were actually found. It predicts what would seem to be a reasonable fraction of the crater flux measured.

Comparison With Solar Max Crater Data

The calculated cumulative crater flux for meteoroids striking the aluminum louvers on the Solar Max spacecraft is shown in Fig.15 along with the data obtained from examination of the louvers after they were returned to the Earth (ref.13). The data is also presented in Table IV.

The properties of the 1145-H19 aluminum alloy used to make the louvers are listed in Table III. The value of the "grain size" parameter, Δ, is not known so the results obtained using various values of Δ are presented in Fig.15.

Following the suggestion in ref.13, the Solar Max louvers were assumed to have been randomly oriented with respect to the Earth and to have been significantly shielded by other spacecraft components so that the measured flux was only 71 percent of that which an unshielded plate would experience. It was the lip diameter that was measured in ref.13 and so the theoretical crater diameter equation was converted to predict the lip diameter. For this conversion it was assumed that the craters in the 1145-H19 aluminum alloy were the same shape as those in the 6061-T6 aluminum alloy. In Fig.15, both the calculated fluxes and the Solar Max data are for an unshielded plate.

Watts suggests in ref.10 that Δ for some aluminum is about 50 μm. Unless the uncertainties in the assumptions account for the lack of agreement between the $\Delta = 50$ μm calculation and the data (and that is quite possible), it appears the "grain-size" parameter, Δ, for the

1145-H19 aluminum alloy is greater than that for the 6061-T6 aluminum alloy, being between 200 μm and 500 μm. The calculated meteoroid flux, using Δ = 200 μm, falls about 10 percent below the measured flux, and using Δ = 500 μm, falls about 20 percent below the measured flux. It is estimated in ref.14 from chemical analysis of impactor residue found in many of the large penetration holes in the louvers (180 μm to 820 μm in diameter), that about 85 percent of the holes were caused by meteoroids and 15 percent by man-made orbital debris.

The accuracy of the model cannot be strictly evaluated by comparing it with the Solar Max data because of uncertainties about the louver material properties and the shape of the craters, but the model seems to be fairly accurate.

Comparison With Early Penetration Detector Experiments

In the 1960s, penetration detectors were flown in low-Earth orbit aboard Explorer 16, Explorer 23, and the three Pegasus satellites to measure the frequency with which meteoroids would completely penetrate thin sheets of material. This was not data on craters in a thick plate, but on perforation through a thin sheet. Explorer 16 used pressurized cells with a thin beryllium copper wall, either 25 μm thick or 51 μm thick. On Explorer 23, pressurized cells of 25 μm and 51 μm thick stainless steel were used. The detectors on the Pegasus spacecraft were capacitors with a 38 μm, 200 μm or 400 μm thick aluminum penetration plate backed by a 13 μm thick mylar dielectric and a rear capacitor plate. The detector plate was aluminum alloy 2024-T3 for the two thicker detectors and aluminum alloy 1100 for the thinnest detector. The meteoroid penetration fluxes measured by these spacecraft (refs.7,15) are presented in Table V and are plotted in Fig.16 as a function of detector thickness. No adjustment has been made to account for differences in the detector material. The actual detector thickness is plotted. The solid (filled in) data points are for the detectors that were made of aluminum. The flux plotted is the flux for an unshielded plate calculated using the transmission factors in Table V. The data from the three Pegasus satellites has been combined as suggested by Naumann (ref.15).

Data from the Solar Max spacecraft on the penetration flux through 50 μm kapton, 75 μm kapton, and the 125 μm thick aluminum louvers (ref.13), while not 1960s data, is also shown in Fig.16, and is presented in more detail in Table V.

The curve in Fig.16 is the calculated meteoroid penetration flux for aluminum 2024-T3 detectors that are randomly oriented with respect to the Earth, in a circular orbit at an altitude of 700 km, and that are not shielded by other spacecraft components. A value of 50 μm was assumed for the "grain size" parameter, Δ.

The model prediction is in excellent agreement with the data. The model curve agrees with the thick aluminum detector data, is above the Explorer 16 and Explorer 23 data for materials expected to be more resistant to penetration than aluminum, and is below the Solar Max data for kapton which is expected to be less resistant to penetration than aluminum. The only data point that seems to be out of place is that for the thin aluminum detector on Pegasus.

The way the Solar Max aluminum louver data falls in line with the Pegasus data suggests that the penetrations through the louvers were nearly all caused by meteoroids, just as the chemical analysis confirmed (ref.14). It also suggests that the meteoroid environment did not change significantly from the mid 1960's to the early 1980's.

DISCUSSION

Several improvements to the near-Earth meteoroid environment model from ref.5 have been presented in this paper. The use of the penetration equations developed by Alan Watts and their implication that meteoroid densities must be near 2.5 g/cm^3 instead of the previously assumed value of 0.5 g/cm^3, is a significant improvement. The refinement of the size distribution of meteoroids is another significant improvement. Changes in the size distribution of meteoroids in the model were made only in the size range of the data obtained on the LDEF. The size distribution of large meteoroids was not changed, and this model would predict essentially the same meteoroid hazard to a space station, for example, as the previous model. As far as sub-micron meteoroids go, the model presented in this paper does not apply. It has a cutoff in the size of meteoroids at 1 μm, just as the previous model did. Certainly sub-micron meteoroids exist, as shown by the Interplanetary Dust Experiment on the LDEF for instance, but they may very well be meteoroids of a completely different nature than those that are larger than a micron, and may need to be modelled as a separate component of the meteoroid environment. The sub-micron meteoroids may be influenced by forces that do not affect larger particles and may have a speed distribution and a directionality with respect to the Earth quite different from the larger meteoroids so that it would be inappropiate to include them in the model presented in this paper.

There is some question as to whether the anodized layer caused the craters from small meteoroids to be undersized so that the crater size distribution on the space-facing end of the LDEF does not properly reflect the size distribution of meteoroids. It may be that the small craters would have been slightly larger in a plate that was not anodized and that the size distribution of meteoroids from the NASA model (ref.1) is accurate for small meteoroids. Hypervelocity impact tests should provide insight. However, it has been assumed in this paper that the aluminum oxide layer on the one plate from the space-facing end, used to determine the size distribution of small meteoroids (plate H5), did not affect the crater size noticeably, based on the observation that that plate did not appear to have an aluminum oxide layer other than the natural oxide layer that occurs due to exposure to the atmosphere. For most of the other plates examined in this study, the aluminum oxide layer probably did affect the size of small craters, perhaps even the formation of lips on larger craters, e.g. the B9P2 and B9P4 plates. Future meteoroid studies of this nature should not use anodized plates if possible.

It was assumed that all meteoroids have the same density (2.5 g/cm^3) because no data on the distribution of meteoroid densities were available. However, there is a recent study awaiting publication in which Love (ref.16) will show that interplanetary dust particles in the 5-15 micron size range, that were captured in the stratosphere, have a distribution of densities ranging from 0.3g/cm^3 to 6.2 g/cm^3 with a mean of 2.0 g/cm^3. When a correction is made for the effect that

particle density has on the atmospheric fall speed, and thus on the collection rate, it was found that the mean density of meteoroids in space, just outside the atmosphere, is 2.8 g/cm^3 This is in good agreement with the mean density assumed in this study. Future models of the near-Earth meteoroid environment should include the distribution of meteoroid densities. Of course, the density distribution may vary with particle size and additional data will be valuable.

The uncertainty in the data that results from the statistically small number of craters found on the LDEF (which is seen in the 90 percent confidence limits in the figures) is not the only uncertainty in the data. Measurement of the crater lip diameter requires judgement, and different people using different microscopes with different illumination sources will systematically differ in their measurement of crater lip diameters. A 10 percent systematic difference in the measurement of the lip diameter, which is certainly possible, can produce a difference in the reported flux of craters above a given threshold size, much greater than 10 percent, because the size distribution is such that many craters tend to be near the threshold size.

While the size distribution of meteoroids was determined from a set of craters on an LDEF face that was essentially free of man-made debris impacts, the speed distribution and directionality of meteoroids were determined from data on all the faces of the LDEF, and most were contaminated to an unknown degree by impacts from man-made debris. It can only be said that the Erickson and Kessler speed distributions and the random directionality are reasonable. Other speed distributions and directionalities could be found that are also reasonable, and those distributions could suggest either a greater or a lesser amount of man-made debris. While it would appear that meteoroids dominate the particulate environment in the 20 μm to 200 μm diameter size range, the extent of that domination is still uncertain.

REFERENCES

1. Meteoroid Environment Model - 1969 (Near Earth to Lunar Surface). NASA Space Vehicle Design Criteria (Environment). NASA SP-8013, 1969.

2. Meteoroid Environment Model - 1970 (Interplanetary and Planetary). NASA Space Vehicle Design Criteria (Environment). NASA SP-8038, 1970.

3. Meteoroid Damage Assessment. NASA Space Vehicle Design Criteria (Structures). NASA SP-8042, 1970.

4. Kessler, D.J.; Reynolds, R.C.; and Anz-Meador, P.D.: Orbital Debris Environment for Spacecraft Designed to Operate in Low Earth Orbit. NASA Technical Memorandum 100471, 1989.

5. Humes, D.H.: Large Craters on the Meteoroid and Space Debris Impact Experiment. LDEF - 69 Months in Space, First Post-Retrieval Symposium, NASA CP-3134, pp.399-422, 1991.

6. Peters, P.N.; Whitehouse, P.L.; and Gregory, J.C.: Refinements on the Pinhole Camera Measurements of the LDEF Attitude. LDEF - 69 Months in Space, Second Post-Retrieval Symposium, NASA CP-3194, pp.3-12, 1992.

7. Alvarez, J.M.: Statistical Analysis of Meteoroid Penetration Data Including Effects of Cutoff. NASA TN D-5668, 1970.

8. Erickson, J.E.: Velocity Distribution of Sporadic Photographic Meteors. Journal of Geophysical Research, vol.7, no.12, 3721-3726, 1968.

9. Kessler, D.J.: Average Relative Velocity of Sporadic Meteoroids in Interplanetary Space. AIAA Journal, vol.7, no.12, 2337-2338, 1969.

10. Watts, A.; Atkinson, D.; and Rieco, S.: Dimensional Scaling for Impact Cratering and Perforation. Presented at the Third LDEF Post-Retrieval Symposium, Williamsburg, VA, 1993.

11. Zook, H.A.: The State of Meteoritic Material on the Moon. Proceedings of the Sixth Lunar Science Conference, pp. 1653-1672, 1975.

12. Grün, E.; Zook, H.A.; Fechtig, H.; and Giese, R.H.: Collisional Balance of the Meteoritic Complex, Icarus, vol.62, p.244, 1985.

13. Warren, J.L.; Zook, H.A.; Allton, J.H.; Clanton, U.S.; Dardano, C.B.; Holder, J.A.; Marlow, R.R.; Schultz, R.A.; Watts, L.A.; and Wentworth, S.J.: The Detection and Observation of Meteoroid and Space Debris Impact Features on the Solar Max Satellite. Proceedings of the 19th Lunar and Planetary Science Conference, pp.641-657, 1989.

14. McKay, D.S.: Microparticle Impacts in Space - Results from Solar Max Satellite and Shuttle Witness Plate Inspections. NASA Conference Publication 3035, Part 1, pp.301-327, 1988.

15. Naumann, R.J.: The Near-Earth Meteoroid Environment. NASA TN D-3717, 1966.

16. Love, S.G.; Joswiak, D.J.; and Brownlee, D.E.: Densities of Stratospheric Micrometeorites. Submitted to Icarus 17 December 1993; revised 14 April 1994.

TABLE I. Location of the craters on the LDEF, with a lip diameter of 100μm or greater, considered in this paper.

			Number of craters with lip diameter...				
Orientation	Plate	Area,m²	≥100μm	≥200μm	≥300μm	≥500μm	≥1000μm
8°	B9P1	.139				14	3
8°	B9P2	.183	269	106	60	24	2
8°	B9P3	.044				4	1
8°	B9P4	.117	131	51	21	6	0
8°	B9P5	.0185				0	0
8°	B9P6	.0387				2	1
8°	B9P7	.00180				1	0
8°	B9P9	.00144				0	0
8°	B9P11	.00144				0	0
8°	B9P12	.00144				0	0
8°	B9P14	.00144				0	0
8°	B9P15	.00144				0	0
8°	B9P18	.00144				0	0
8°	B9P22	.00180				0	0
8°	B9P24	.00180				0	0
8°	B9P28	.00180				0	0
8°	B9P32	.00180				0	0
8°	B9P33	.00180				0	0
8°	B9P34	.00346				0	0
8°	B9P36	.00346				0	0
8°	B9P37	.00357				0	0
8°	B9P40	.00396				0	0
8°	B9P43	.00266				0	0
8°	B9P44	.00266				0	0
8°	B9P45	.00266				0	0
8°	B9P46	.00453				0	0
8°	B9P48	.00453				0	0
8°	B9P51	.00335				0	0
8°	B9P54	.00180				0	0
8°	B9P55	.00180				0	0
8°	B9P57	.00180				0	0
8°	B9P58	.00335				0	0
8°	B9P60	.00266				0	0
8°	B9P61	.00357				0	0
8°	B9P62	.00396				0	0
8°	G22(R9)	.15				9	2
8°	H22(R9)	.15				9	5

TABLE I. Continued

Orientation	Plate	Area,m²	Number of craters with lip diameter... ≥100μm	≥200μm	≥300μm	≥500μm	≥1000μm
22°	F10G	.59				46	8
22°	F10H	.59	685	262	120	32	9
22°	G23(R10)	.15				14	2
22°	H23(R10)	.15				17	3
38°	B8G	.39	410	176	84	25	2
38°	B8H	.39	366	143	72	28	2
38°	G21(R8)	.15				7	2
38°	H21(R8)	.15				11	2
52°	B11G	.59				36	7
52°	B11H	.59				30	3
52°	E11G	.59				36	1
52°	E11H	.59				32	2
52°	F11G	.59	505	200	95	31	3
52°	F11H	.59				28	4
52°	G24(R11)	.15				3	0
52°	H24(R11)	.15				5	1
68°	C7G	.59				22	1
68°	C7H	.59				16	3
68°	E7G	.59				26	4
68°	E7H	.59				31	3
68°	F7G	.59	410	165	71	18	1
68°	F7H	.59				20	2
68°	G20(R7)	.15				6	3
82°	A12G	.59	312	107	53	17	4
82°	A12H	.59				15	0
82°	H13(R12)	.15				7	4
98°	A6G	.59				7	2
98°	A6H	.56				9	2
98°	B6G	.59	215	83	35	7	1
98°	B6H	.59				11	2
98°	D6G	.39				10	1
98°	D6H	.39				11	0
98°	H19(R6)	.15				5	1

TABLE I. Continued

Orientation	Plate	Area,m²	Number of craters with lip diameter... ≥100μm	≥200μm	≥300μm	≥500μm	≥1000μm
112°	B1G	.59				12	1
112°	B1H	.59				5	0
112°	E1G	.59				18	1
112°	E1H	.59				8	0
112°	F1G	.59	141	44	18	2	0
112°	F1H	.59				8	0
112°	G14(R1)	.15				3	0
112°	H14(R1)	.15				2	0
128°	A5G	.59				5	0
128°	A5H	.59				2	1
128°	F5G	.59	86	31	16	5	1
128°	F5H	.59				2	1
128°	G18(R5)	.15				0	0
128°	H18(R5)	.15				2	0
142°	B2G	.59	70	30	19	3	1
142°	B2H	.59				2	0
142°	D2G	.39				1	0
142°	D2H	.39				2	0
142°	G15(R2)	.15				0	0
142°	H15(R2)	.15				3	0
158°	C4G	.59	56	17	8	0	0
158°	C4H	.59				4	0
158°	E4G	.59				3	0
158°	E4H	.59				4	1
158°	G17(R4)	.15				2	1
158°	H17(R4)	.15				1	0
172°	F3G	.59	48	20	13	5	1
172°	F3H	.59				3	1
172°	G16(R3)	.15				0	0
172°	H16(R3)	.15				2	1

TABLE I. Concluded

Orientation	Plate	Area, m^2	Number of craters with lip diameter... ≥100μm	≥200μm	≥300μm	≥500μm	≥1000μm
Earth	G3	.90				0	0
Earth	G4	.52	9	3	2	1	0
Earth	G8	.52				0	0
Earth	G9	.90				0	0
Earth	G13(E)	.63				1	0
Earth	G14(E)	.35	3	1	1	1	1
Earth	G15(E)	.35				0	0
Earth	G16(E)	.63				0	0
Earth	G17(E)	.35				0	0
Earth	G18(E)	.35				0	0
Earth	G19(E)	.63				0	0
Earth	G20(E)	.35	2	2	1	1	0
Earth	G21(E)	.35				0	0
Earth	G22(E)	.63				0	0
Earth	G23(E)	.35				0	0
Earth	G24(E)	.35				0	0
Space	H5	.52	275	100	56	20	1
Space	H13(S)	.63				19	2
Space	H14(S)	.35				8	1
Space	H15(S)	.35				6	0
Space	H16(S)	.63				21	1
Space	H17(S)	.35				4	0
Space	H18(S)	.35				12	1
Space	H19(S)	.62	348	113	61	23	2
Space	H21(S)	.35				7	1
Space	H22(S)	.63				24	5
Space	H23(S)	.35				8	0
Space	H24(S)	.35				12	3

TABLE II. Location of the craters on the LDEF, with a lip diameter less than 100μm, considered in this paper.

Orientation	Plate	Area,m^2	≥10μm	≥20μm	≥30μm	≥40μm	≥60μm	≥80μm
Space	H5	.52					468 *	338
Space	H19(S)	.62					638 *	453
Space	H5 c	.0447	189 **	141	107	78	51	36

c Square area at center of H5 plate scanned at high power - 1 mm field of view

* Not expected to be a complete count - 14 mm field of view

** Not expected to be a complete count - 1 mm field of view

TABLE III. Material properties of aluminum alloys.

Alloy	Density ρ_t,(kg m^{-3})	Sound Speed c_t,(m s^{-1})	Typical Yield Strength Y_t,(N m^{-2})	Typical Ultimate Strength σ_s,(N m^{-2})	Stress Factor s	Grain Size Parameter Δ,(m)
1145-H19	≈2700	≈5100	1.31×10^8	1.45×10^8	1.50	?
2024-T3	2770	5100	3.45×10^8	4.83×10^8	1.60	?
6061-T6	2700	5100	2.76×10^8	3.10×10^8	1.42	50×10^{-6}

TABLE IV. Number of craters of various sizes in the aluminum louvers on the Solar Max spacecraft (ref.13).

Lip Diameter, μm	≥40	≥60	≥80	≥100	≥120	≥160
Number*	436	267	196	153	120	86
Flux, raw, $m^{-2}s^{-1}$	5.74E-6	3.51E-6	2.58E-6	2.01E-6	1.58E-6	1.13E-6
Flux, unshielded, $m^{-2}s^{-1}$	8.08E-6	4.94E-6	3.63E-6	2.83E-6	2.23E-6	1.59E-6

* Craters and holes, because holes would be big craters in a thick plate.

Area = 0.5800 m^2 (use this, not reduced area, because number of features on the reduced area is not known and there is no reason to use the reduced area for crater analysis.

Time = 1517 days

Transmission factor, which is the fraction of the viewing sphere around the detectors that is not shielded by other spacecraft components, is 0.71.

TABLE V. Penetration data from spacecraft in low-Earth orbit.

Spacecraft				Detector				Data			
Name	Years of operation	Inclination	Altitude, km	Material	Thickness, μm	Area, m^2	Transmission factor †	Penetrations	Duration, days	Unshielded flux, $m^{-2}s^{-1}$	Source
Explorer 16	1962-1963	52°	750-1180	Beryllium-copper	25	1.41*	.70	44	200	3.9×10^{-6}	Ref. 7
Explorer 16	1962-1963	52°	750-1180	Beryllium-copper	51	0.564*	.70	11	200	2.0×10^{-6}	Ref. 7
Explorer 23	1964-1965	52°	458-1000	Stainless steel	25	0.987*	.70	50	370	4.4×10^{-6}	Ref. 7
Explorer 23	1964-1965	52°	458-1000	Stainless steel	51	1.974*	.70	74	370	2.5×10^{-6}	Ref. 7
Pegasus 1,2,3	1965-1966	28.9°-31.8°	496-748	Aluminum + mylar	38 + 13	≈8	1.00	582	—	2.2×10^{-6}	Ref. 15
Pegasus 1,2,3	1965-1966	28.9°-31.8°	496-748	Aluminum + mylar	200 + 13	≈17	1.00	49	—	2.4×10^{-7}	Ref. 15
Pegasus 1,2,3	1965-1966	28.9°-31.8°	496-748	Aluminum + mylar	400 + 13	≈175	1.00	201	—	5.6×10^{-8}	Ref. 15
Solar Max	1980-1984	28.5°	500-570	Kapton	50	1.64	0.55	370	1517	3.1×10^{-6}	Ref. 13
Solar Max	1980-1984	28.5°	500-570	Kapton	75	0.207	0.98	57	1517	2.1×10^{-6}	Ref. 13
Solar Max	1980-1984	28.5°	500-570	Aluminum	125	0.8904	0.71	65	1517	7.8×10^{-7}	Ref. 13

* Area decreases with each cell penetrated

† Transmission factor is the fraction of the viewing sphere around the detectors that is not shielded by other spacecraft components

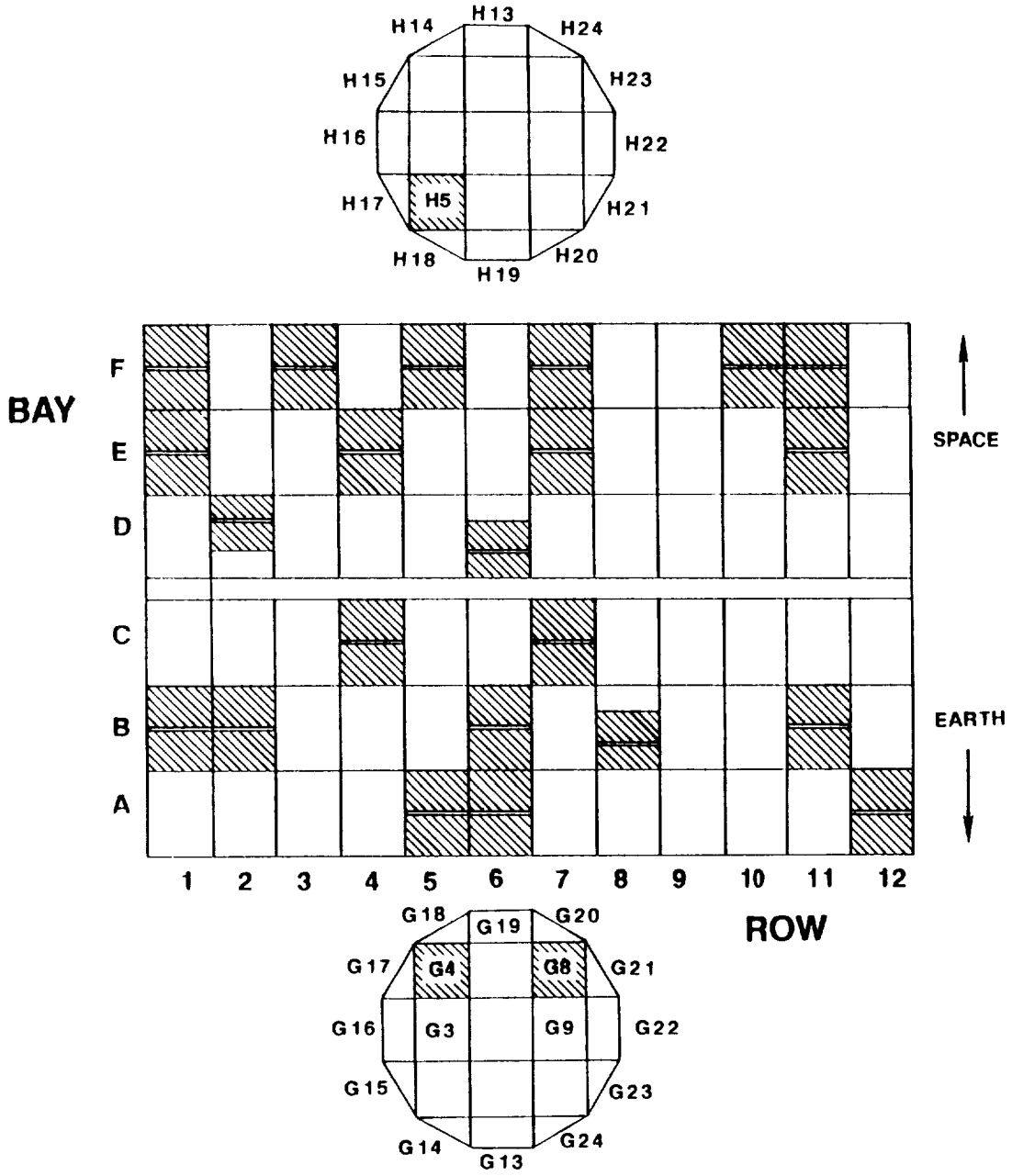

Fig. 1. Identification system used for the tray locations and the thermal panels on the LDEF. The shaded areas show the location of the Meteoroid and Space Debris Impact Experiment plates. The location of the dummy plates used in this study is also shown.

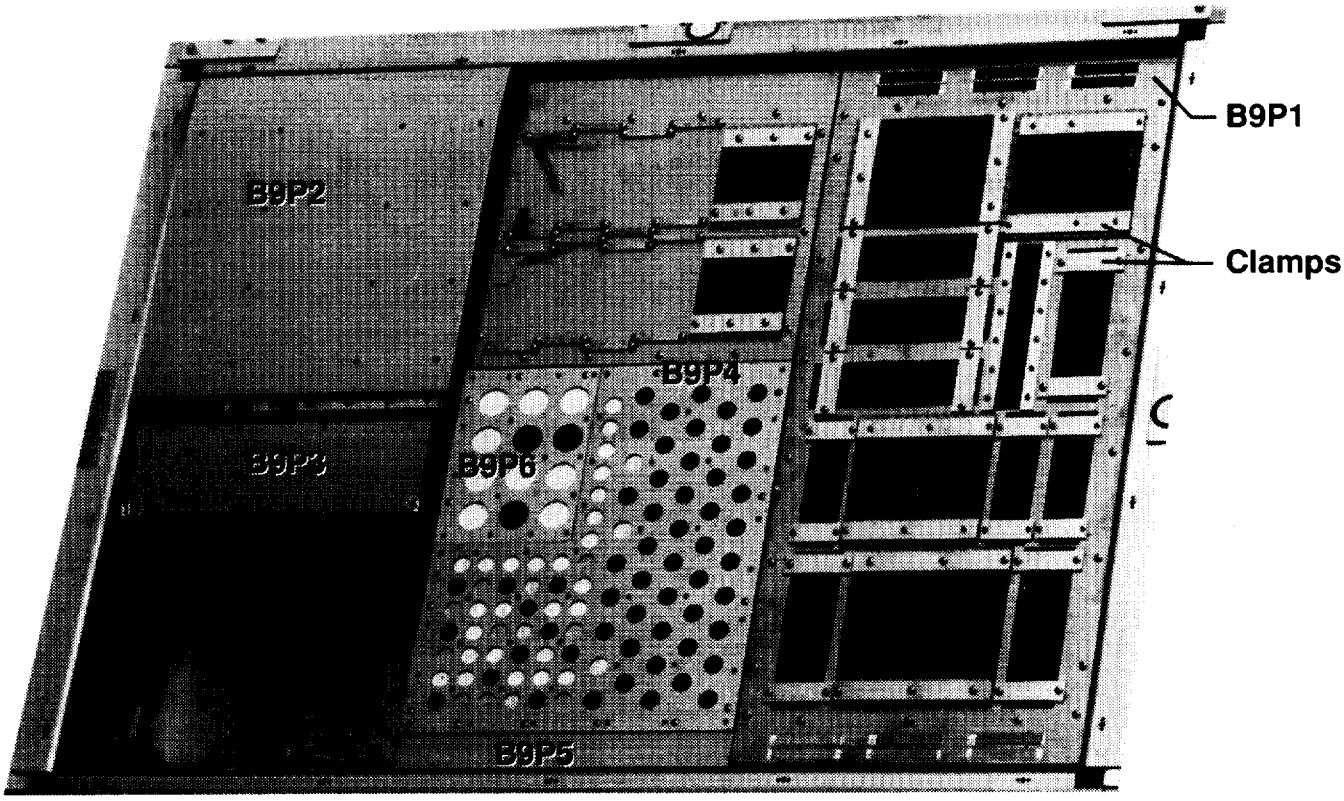

Fig. 2. Tray B9 containing aluminum plates and clamps donated by Wayne Slemp to the LDEF M&D SIG that were examined in this study.

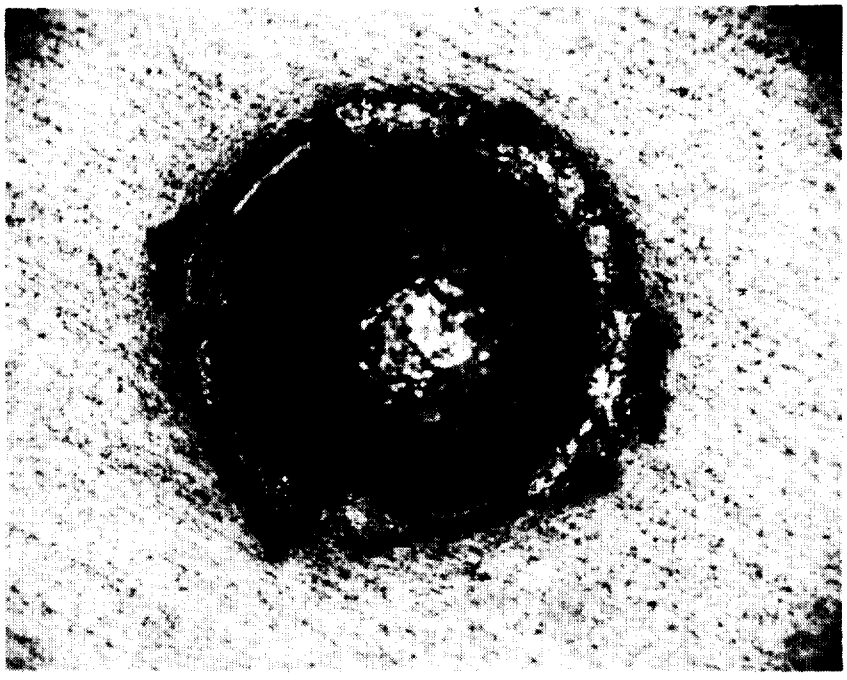

Fig. 3. Largest crater on the Meteoroid and Space Debris Impact Experiment. A 4 mm diameter crater on plate F10H.

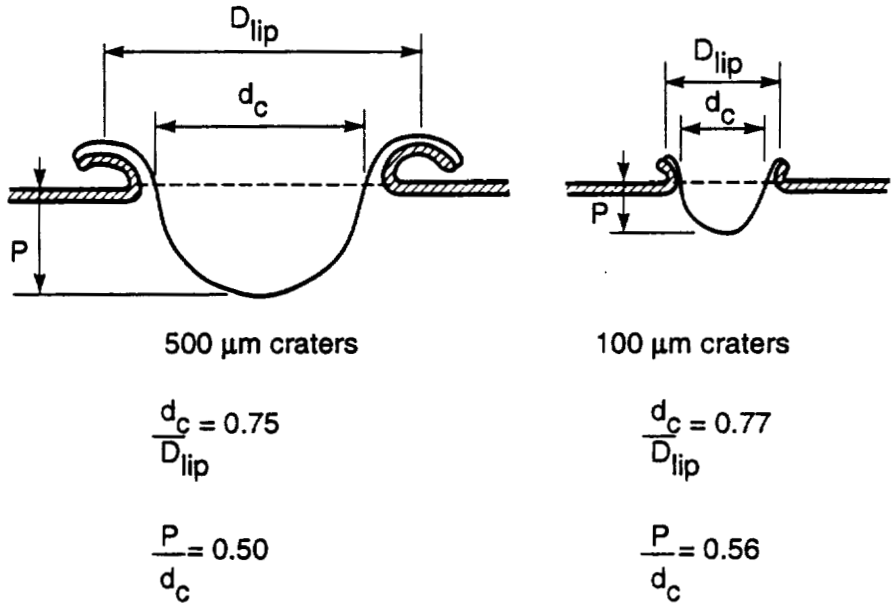

Fig. 4. Typical shapes of craters in aluminum alloy 6061-T6 on the LDEF.

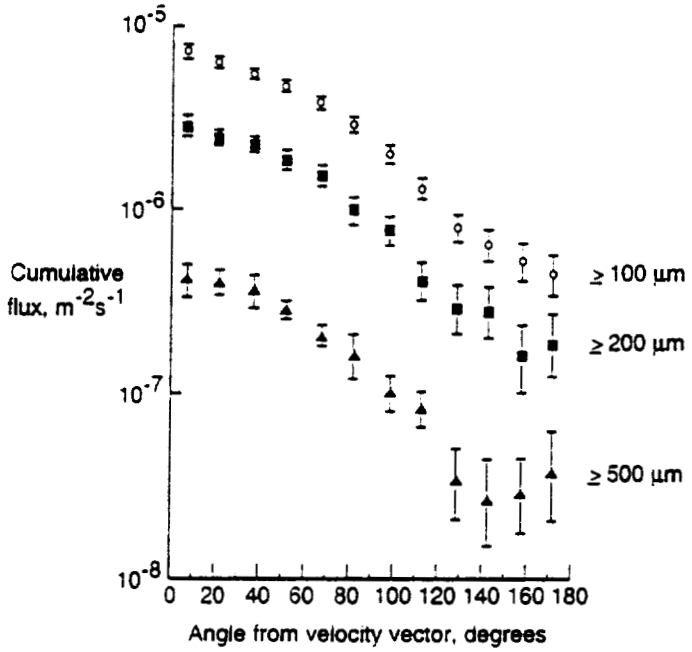

Fig. 5. Measured cumulative crater flux on the twelve peripheral rows around the LDEF, for craters with threshold lip diameters of 0.1 mm, 0.2 mm, and 0.5 mm.

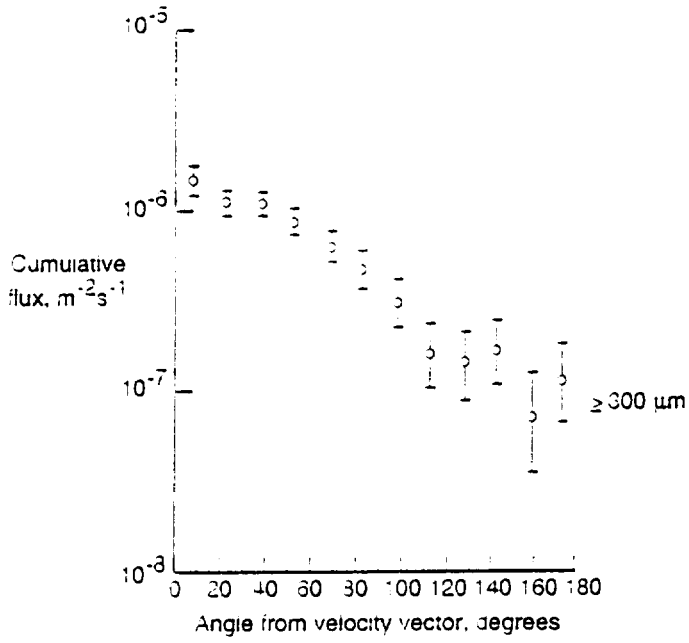

Fig. 6. Measured cumulative crater flux on the twelve peripheral rows around the LDEF, for craters with a threshold lip diameter of 0.3 mm.

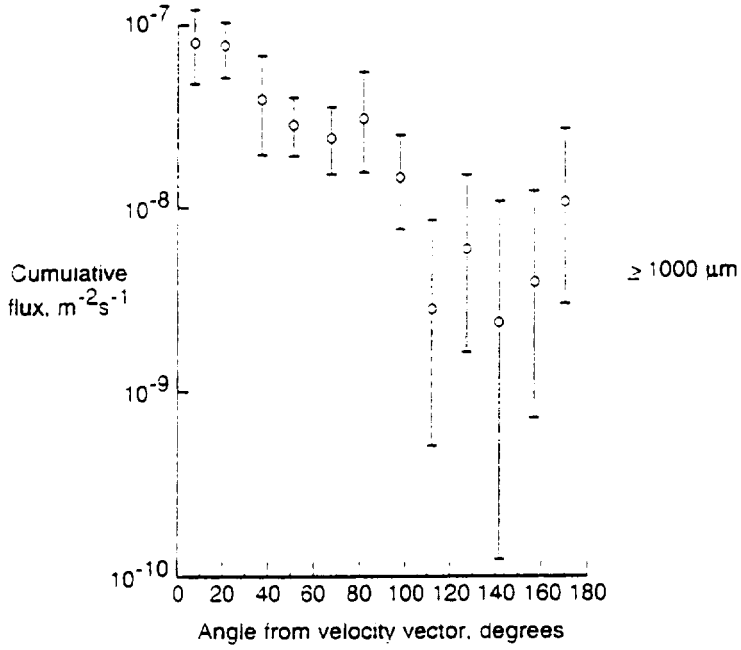

Fig. 7. Measured cumulative crater flux on the twelve peripheral rows around the LDEF, for craters with a threshold lip diameter of 1 mm.

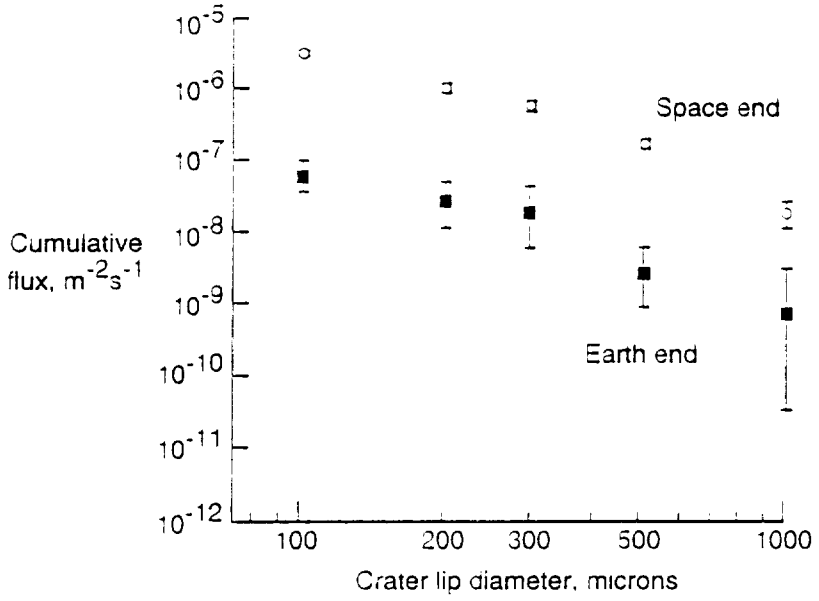

Fig. 8. Measured cumulative crater flux on the two ends of the LDEF, for craters with threshold lip diameters in the 0.1 mm to 1 mm range.

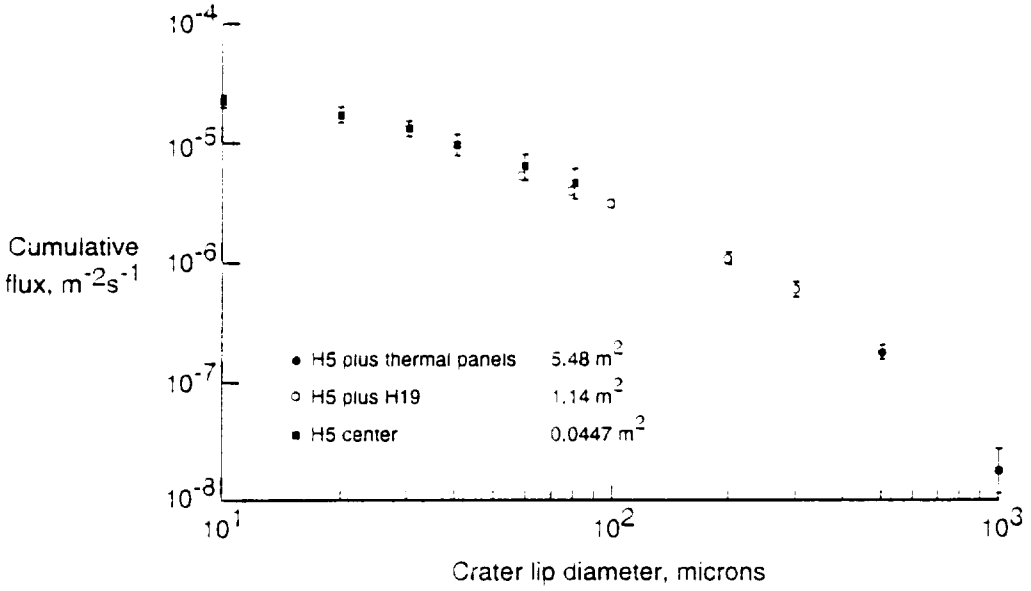

Fig. 9. Measured cumulative crater flux on the space-facing end of the LDEF, for craters with threshold lip diameters in the 10 μm to 1 mm range.

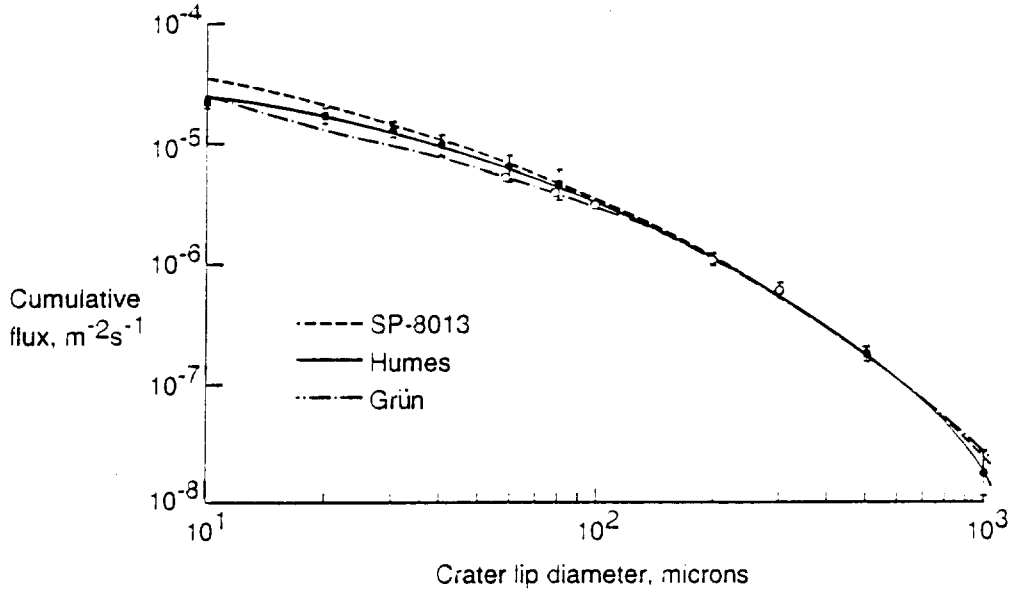

Fig. 10. Calculated cumulative meteoroid crater flux on the space-facing end of the LDEF, for craters with threshold lip diameters in the 10 μm to 1 mm range, compared to the measured crater fluxes.

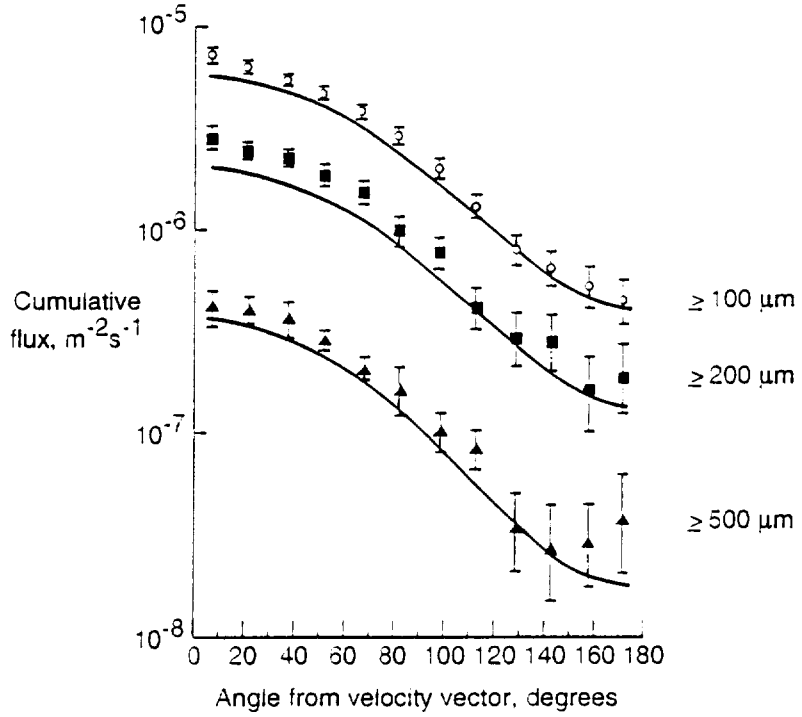

Fig. 11. Calculated cumulative meteoroid crater flux on the twelve peripheral rows around the LDEF, for craters with threshold lip diameters of 0.1 mm, 0.2 mm, and 0.5 mm, compared to the measured crater fluxes.

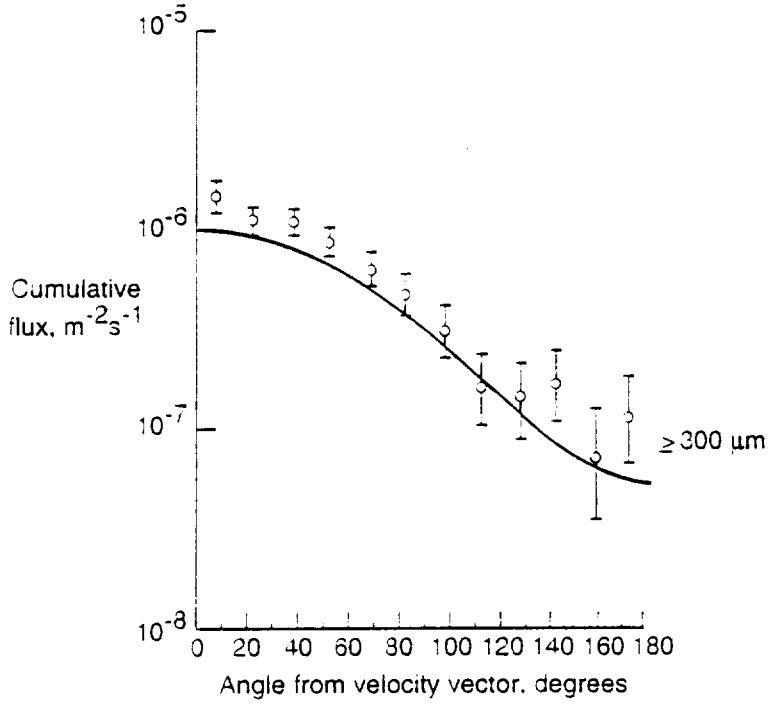

Fig. 12. Calculated cumulative meteoroid crater flux on the twelve peripheral rows around the LDEF, for craters with a threshold lip diameter of 0.3 mm, compared to the measured crater fluxes.

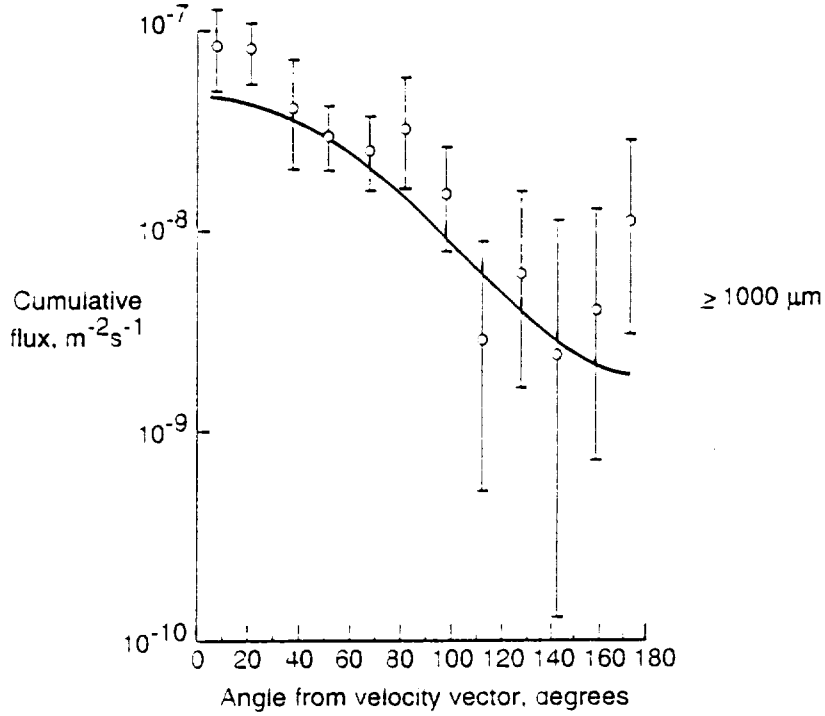

Fig. 13. Calculated cumulative meteoroid crater flux on the twelve peripheral rows around the LDEF, for craters with a threshold lip diameter of 1 mm, compared to the measured crater fluxes.

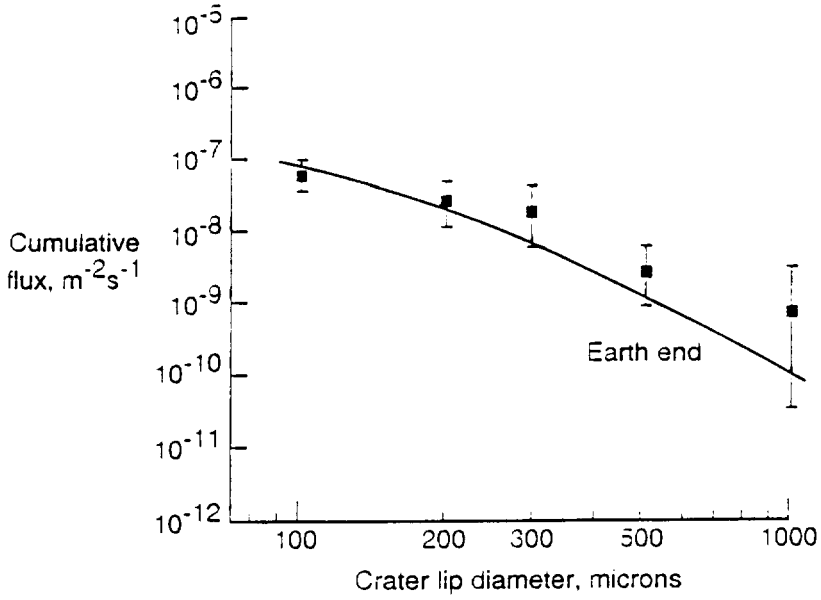

Fig. 14. Calculated cumulative meteoroid crater flux on the Earth-facing end of the LDEF, for craters with threshold lip diameters in the 0.1 mm to 1 mm size range, compared to the measured fluxes.

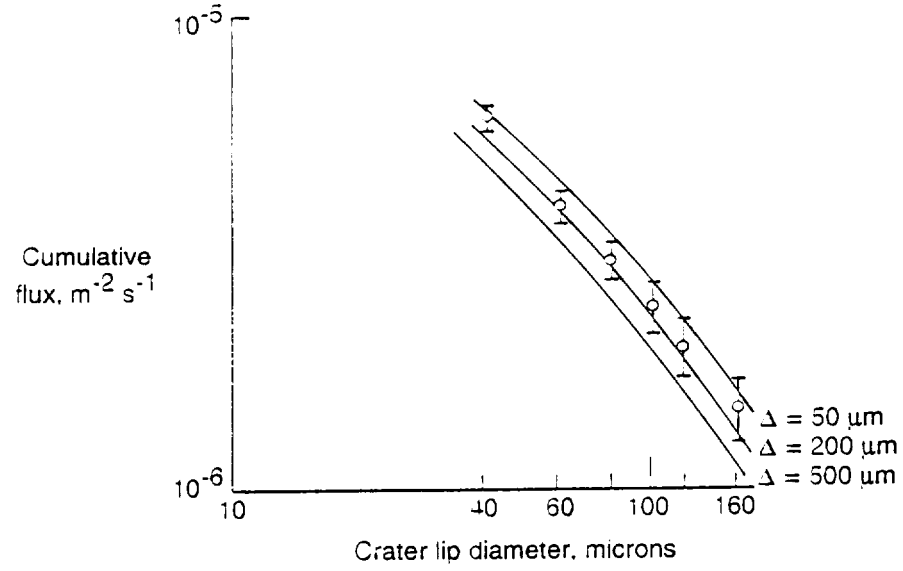

Fig. 15. Calculated cumulative meteoroid crater flux on the aluminum louvers from the Solar Max spacecraft, compared to the measured fluxes.

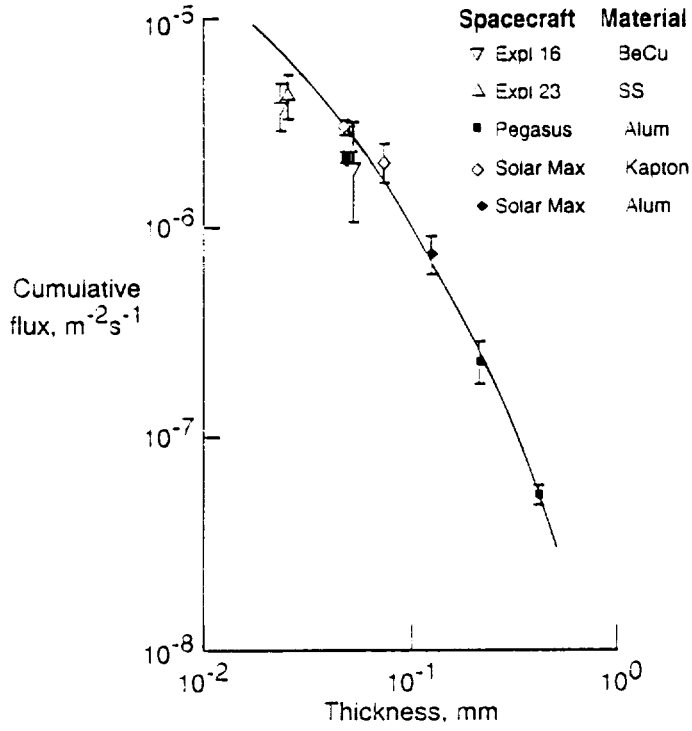

Fig. 16. Calculated meteoroid penetration flux for an unshielded aluminum (2024-T4) plate at an altitude of 700 km, compared to the penetration data for various materials from the Explorer 16, Explorer 23, and the three Pegasus spacecraft. The filled symbols are for aluminum detectors.

LONG TERM *MICROPARTICLE* IMPACT FLUXES ON LDEF DETERMINED FROM OPTICAL SURVEY OF INTERPLANETARY DUST EXPERIMENT (IDE) SENSORS

C. G. Simon[1], J. P. Oliver[2], W. J. Cooke, K. I. Downey[2]
Institute for Space Science & Technology, Gainesville FL 32609

P. C. Kassel
NASA Langley Research Center, Hampton VA 23665
Phone: (804) 864-4621 Fax: (804) 864-7607

[1]Current Address: Air Consulting and Engineering, Inc.
2106 NW 67 Place, S-4, Gainesville FL 32653
Phone: (904) 335-1889 Fax: (904) 335-1891

[2]Also University of Florida, Gainesville FL 32611

SUMMARY

Many of the IDE metal-oxide-silicon (MOS) capacitor-discharge impact sensors remained active during the entire Long Duration Exposure Facility (LDEF) mission. An optical survey of impact sites on the active surfaces of these sensors has been extended to include all sensors from the low-flux sides of LDEF (i.e. the west or trailing side, the earth end, and the space end) and 5-7 active sensors from each of LDEF's high-flux sides (i.e. the east or leading side, the south side, and the north side). This survey was facilitated by the presence of a relatively large (>50 μm diameter) optical signature associated with each impact site on the active sensor surfaces. Of the ~4700 impacts in the optical survey data set, 84% were from particles in the 0.5 to 3 μm size range. An estimate of the total number of hypervelocity impacts on LDEF from particles >0.5 μm diameter yields a value of ~7 x 10^6. Impact feature dimensions for several dozen large craters on MOS sensors and germanium witness plates are also presented.

Impact fluxes calculated from the IDE survey data closely matched surveys of similar size impacts (≥3 μm diameter craters in Al, or marginal penetrations of a 2.4 μm thick Al foil) by other LDEF investigators. Since the first year IDE data were electronically recorded, the flux data could be divided into three long term time periods: the first year, the entire 5.8 year mission, and the intervening 4.8 years (by difference).

The IDE data show that there was an order of magnitude decrease in the long term microparticle impact flux on the trailing side of LDEF, from 1.01 to 0.098 x10^{-4}m^{-2}s^{-1}, from the first year in orbit compared to years 2-6. The long term flux on the leading edge showed an increase from 8.6 to 11.2 x10^{-4}m^{-2}s^{-1} over this same time period. (Short term flux increases up to 10,000 times the background rate were recorded on the leading side during LDEF's first year in orbit.) The overall east/west ratio was 44, but during LDEF's first year in orbit the ratio was 8.5, and during years 2-6 the ratio was 114.

Long term microparticle impact fluxes on the space end decreased from 1.12 to 0.55 x10^{-4}m^{-2}s^{-1} from the first year in orbit compared to years 2-6. The earth end showed the opposite trend with an increase from 0.16 to 0.38 x10^{-4}m^{-2}s^{-1}. Fluxes on rows 6 and 12 decreased from 6.1 to 3. 4 and 6.7 to 3.7 x10^{-4}m^{-2}s^{-1}, respectively, over the same time periods. This resulted in space/earth microparticle impact flux ratios of 7.1 during the first year and 1.5 during years 2-6, while the south/north, space/north and space/south ratios remained constant at 1.1, 0.16 and 0.17, respectively, during the entire mission.

This information indicates the possible identification of long term changes in discrete *microparticle* orbital debris component contributions to the total impact flux experienced by LDEF. A dramatic decrease in the debris population capable of striking the trailing side was detected that could possibly be attributed to the hiatus of western launch activity experienced from 1986-1989. A significant increase in the debris population that preferentially struck the leading side was also observed and could possibly be attributed to a single breakup event that occurred in September of 1986. A substantial increase in the

microparticle debris population that struck the earth end of LDEF, but not the space end, was also detected and could possibly be the result of a single breakup event at low altitude.

These results point to the importance of including discrete orbital debris component contribution changes in flux models in order to achieve accurate predictions of the microparticle environment that a particular spacecraft will experience in earth orbit. The only reliable, verified empirical measurements of these changes are reported in this paper. Further time-resolved *in-situ* measurements of these debris populations are needed to accurately assess model predictions and mitigation practices.

INTRODUCTION

The MOS capacitor discharge impact sensors of the Interplanetary Dust Experiment provided a unique opportunity for measuring the short term and long term time-resolved flux of small microparticles that impacted LDEF during its 5.8 year long mission. We have reported these data in several papers (Refs. 1-7) that address different aspects of the microparticle environment in low Earth orbit (LEO). In this paper we report further results of an optical survey of impacts on IDE sensors that remained active during the entire LDEF mission.

Two different sensitivity MOS sensors made up the IDE experiment. The sensitivity of the detectors is proportional to the thickness of a thermally grown layer of SiO_2 on top of a 250 μm thick, 51 mm diameter Boron-doped Si wafer substrate. The higher sensitivity detectors (0.4 μm thick dielectric, sensitive to ~0.2 μm and larger hypervelocity particle impacts) drained their batteries during the longer-than-planned LDEF mission. However, the low sensitivity IDE detectors (1.0 μm thick dielectric, sensitive to ~0.5 μm and larger hypervelocity particle impacts) remained powered during the entire mission, except for those incapacitated by large hypervelocity impacts.

The first year, time-resolved IDE data are re-presented in this paper in three separate categories: (1) Multiple Orbit Events (MOES), (2) Spikes, and (3) Background. These are described briefly with the tabulated results. More detailed descriptions of these categories, along with examples, can be found in Refs. 6 and 7.

Details of the optical survey procedures were previously published (Ref. 5). Briefly, the IDE sensors have the unique characteristic (among LDEF surfaces) of producing a clearly visible 50 μm diameter "discharge zone" around microparticle impact sites. This zone is formed by the evaporation of the 0.1 μm thick surface layer of aluminum (the top electrode) caused by heat from the electrical discharge of the MOS capacitor when struck by a particle with sufficient energy to breakdown the silicon dioxide insulator and "trigger" the sensor. The electrical discharge spark also creates a central crater with a diameter of ~10 μm. Particles >3-4 μm in size are large enough to form a spall-zone larger than the 10 μm "spark" crater, but impacts from smaller particles that triggered the sensors always resulted in a 10 μm central crater. These characteristics made it possible to quickly scan large areas of even low impact flux surfaces on LDEF (trailing side, space and earth ends) using optical microscopy. Pre- and post-flight photographs of each sensor provided a record of the few discharges produced during manufacturing and pre-flight testing. Careful correlation yielded accurate counts of impact induced discharges.

Another method of determining small particle impact fluxes on large areas of LDEF was counting penetrations through thin foils. The Multiple Abrasion Package (MAP) experiment consisted of large areas of thin aluminum and brass foils dedicated to this purpose (Ref. 8). The MAP foils were mounted adjacent to the IDE sensor arrays on 5 of the 6 orthogonal sides of LDEF (earth end excluded). After retrieval, the foils were back lighted and all penetrations counted. After additional optical and electron microscopic examination and correction for interferences (secondary impacts and non-impact induced pinholes) data from the MAP foils and from witness plates/foils of the FRECOPA experiment (Ref. 9) were plotted in smoothed flux curves (Refs. 10, 11). Although the MAP foils did not provide any level of time resolution, they did provide an excellent independent record of the microparticle impact flux for the entire 5.8 year LDEF mission which closely matched the IDE results for the same time period.

RESULTS AND DISCUSSION

Impact crater morphologies

Crater size data are presented for those interested in the material response of the MOS structure and single crystal germanium (Ge) to hypervelocity impacts. Complete optical survey results for the MOS sensors are appended to the end of this report (Table 1A). Tabulated crater size classification and measurement data are incomplete since these parameters were not part of the initial goals of the survey, but were added after the survey was underway. Results of an optical survey of two 250 μm thick, 25 mm diameter single-crystal Ge witness plates mounted on LDEF tray B-12 (north side) were previously reported (Ref. 12) and are presented here in graphical form. The passive Ge targets were also part of IDE.

Dimensions were recorded for four morphological characteristics of hypervelocity impact craters into the crystalline materials: central crater/shatter zone, inner spall zone, outer spall zone, and fracture zone. Figures 1 and 2 show plots of the measured central crater/shatter-zone maximum dimensions versus the maximum dimensions of the associated outer spalls and fracture zones of craters in the MOS and Ge surfaces, respectively. Note the convergence of the MOS data to a spall zone size equal to the central crater size at 10 μm in Fig. 1 (not predicted by the simple linear fit shown). This is consistent with the domination of the crater formation mechanism by the electrical discharge energy for small impactors (0.5-3 μm) into active MOS sensors. Above this size, the impactor energy dominated the crater formation resulting in "classic" crater/spall morphologies.

Figure 2 shows a linear response for fracture zone maximum dimensions versus central crater size, even for large features in the silicon MOS sensors. (Fracture zones were not measured for the Ge witness plate impacts.) The MOS sensors were bonded to aluminum frames with ~4 mils of silicon RTV. Apparently, shock waves from large impactors were reflected through the silicon adhesive with enough efficiency to cause fractures with the same relative dimensions as seen with smaller impactors. Figure 2 also shows that fractures that extend beyond the outer spall zones are not significant for craters smaller than ~150 μm, but are 6-7 times the maximum central crater dimension in larger impacts.

Figure 3 is a plot of central crater size versus spall zone maximum dimensions for impacts into the Ge witness plates. The largest central crater size observed was 188 μm. The near zero intercept in this plot shows the more "normal" response to small impactors of the passive crystalline Ge substrates compared to the "active" silicon MOS substrates. Observed spall zone maximum dimensions in Ge are ~6x the central crater size, while in Si they are ~3x the central crater size. This is consistent with the relative crystal lattice energies of Ge and Si.

Microparticle Impact Fluxes

Before discussing the IDE optical survey results, it is important to review a summary of the IDE time-resolved data for the first year of LDEF's orbital lifetime. These data are presented in Table 1 by detector sensitivity, location on LDEF, and impactor category (MOES, Spikes or Background). See Refs. 4 and 6 for more discussions of impactor classifications. "Spike" events were identified by visual inspection of the data file. During these events the IDE recorded tens to hundreds of impacts on the space and/or north and/or leading (east) sides of LDEF within a few minutes. These events were dominated by very small particles as evidenced by the large relative proportion of impacts from this category of particle on the high sensitivity IDE sensors compared to their low relative abundance on the low sensitivity IDE sensors.

MOES events were identified both by visual inspection of the data file and by the use of an extraction algorithm. The algorithm searched the IDE data in groups of three arrays at a time (space/north/east, space/south/east, space/south/west, space/north/west, earth/north/east, earth/south/east, earth/south/west, earth/north/west) for multiple impacts within a narrow window (34°, or ± 4.4 minutes). If two out of three adjacent orbits recorded impacts in the window, the impacts were identified as a MOES. While this method necessarily extracted some random data, in practice the MOES were very strong events which dominated the data set and limited the number of identifiable "random" impacts.

Figure 1. Central crater maximum dimensions versus spall zone maximum dimensions for impacts into the 250 µm thick IDE silicon MOS sensors.

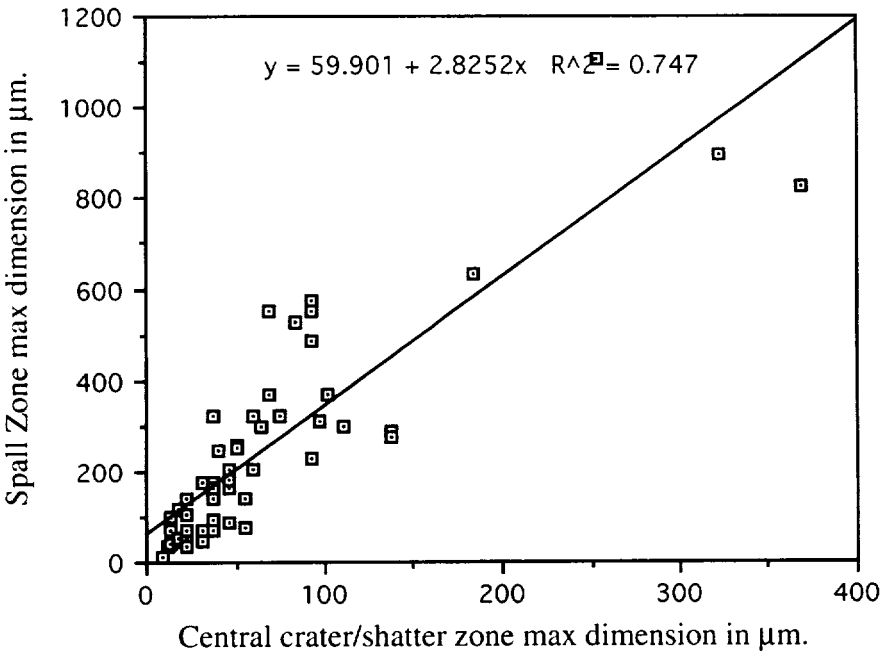

Figure 2. Central crater maximum dimensions versus fracture zone maximum dimensions for impacts into the 250µm thick IDE silicon MOS sensors.

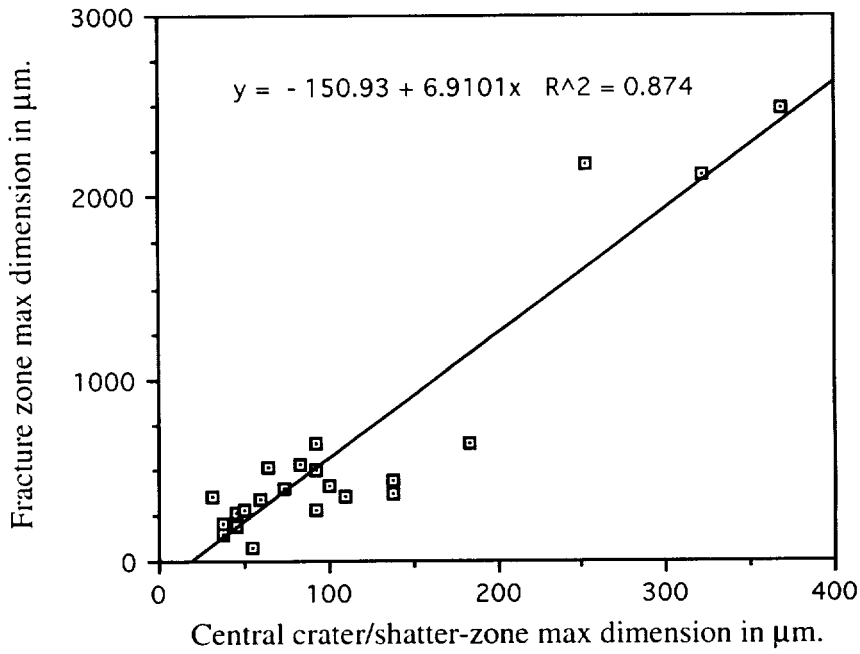

Figure 3. Central crater maximum dimensions versus spall zone maximum dimensions for impacts into 250 μm thick Ge witness plates from LDEF Row 12 (north side).

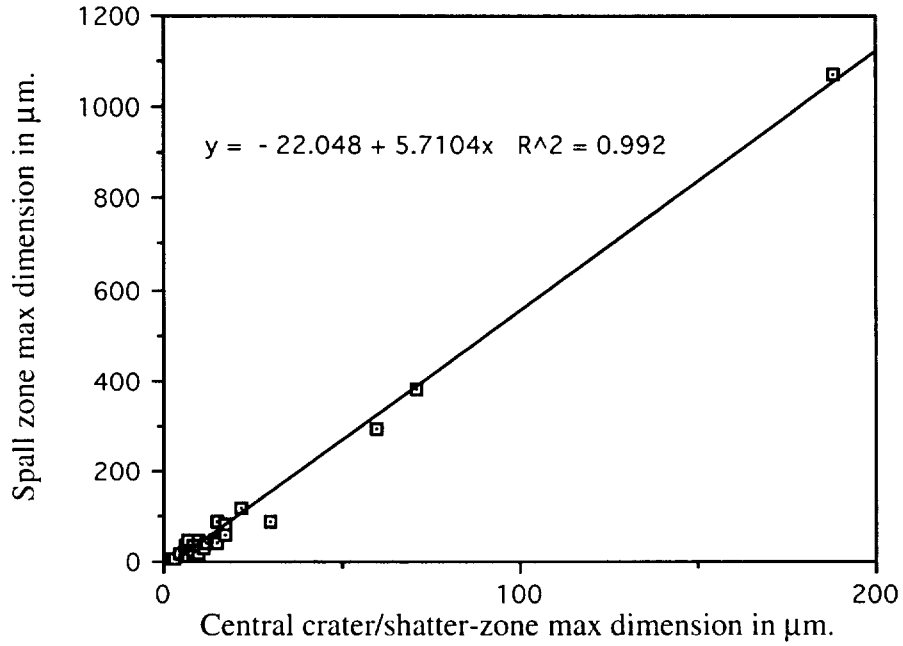

Table 1. Summary of time-resolved IDE microparticle impact data for LDEF's first year in orbit. "High" sensitivity detectors were triggered by hypervelocity particles >0.2 μm in size. "Low" sensitivity detectors were triggered by hypervelocity particles >0.5 μm in size. Results are listed in order of increasing flux.

LDEF Location	Detector Sensitivity	Impact Flux (x $10^{-4}m^{-2}s^{-1}$) Total	MOES	Spikes	Background	% of Total Flux MOES	Spikes	Background
G-10	high	0.162	0.041	0.0	0.121	25	0	75
(earth)	low	0.157	0.037	0.0	0.120	24	0	76
C-3	high	1.59	0.721	0.0	0.869	45	0	55
(west, trailing)	low	1.01	0.368	0.0	0.642	36	0	64
H-11	high	1.85	0.882	0.360	0.608	48	19	33
(space)	low	1.12	0.436	0.043	0.641	39	4	57
B-12	high	9.21	5.00	2.51	1.70	54	27	19
(north)	low	6.14	3.30	0.364	2.48	54	6	40
D-6	high	12.7	10.5	0.017	2.18	83	0.1	17
(south)	low	6.70	5.19	0.0	1.41	77	0	23
C-9	high	17.1	12.1	1.82	3.18	70	11	19
(east, leading)	low	8.61	5.59	0.182	2.84	65	2	33
Totals	high					68	11	21
	low					64	2.5	34

The IDE sensor optical survey results are summarized in Table 2 by LDEF tray location in order of increasing total-mission flux. The size range (0.5 - 3 μm) of impactors labelled "small" in the table is based on the minimum central crater diameter of 10 μm for impact induced discharges on the MOS sensors. As mentioned above, the crater formation is dominated by the electrical discharge energy for small particles. This masks all information about the impactor's size for particles smaller than ~3 μm.

The relative abundance of "small" impactors can be used to define the population of a set of particles that are significantly affected by non-gravitational forces. It is these particles that undergo rapid deviation from their parent body orbits, even when leaving with very small velocity differences (Δv). Thus, the orbits of microparticles shed from large bodies in circular orbits quickly increase in eccentricity and have very limited lifetimes. These particles can remain under the influence of the parent body for some time. For example, if they reside in shaded wake regions they will be shielded from solar pressure and aerodynamic drag effects. As a result, enhanced shedding/breakup events will release three classes of microparticles based on their leaving characteristics: (1) large Δv, (2) small Δv, and (3) "dribblers".

Shedding rate enhancements have a variety of causes, including differential thermal expansion /contraction induced vibrations and frictional wear, reaction wheel motion, solar panel motion, thruster firings, surface charge polarity shifts, plasma discharges, and hypervelocity impacts. Major sources of microparticles released during shedding include fuel residues, residual dust/dirt, and erosion products such as paint particles and thermal blanket flakes. The actual and potential particle release-rates from these sources will change drastically during an orbiting spacecraft's lifetime. These rate changes depend on a spacecraft's materials of construction and its mission operational profile, including the space environment that it experiences during its lifetime. For example, LDEF results showed that impacts into old painted surfaces released more secondary debris (spalled paint) than did impacts into "new" paint (this was due to the loss of organic binder in the paint as a result of exposure to solar ultraviolet [UV] radiation and atomic oxygen [AO]), and metal-coated hydrocarbon based foils such as Al-coated Mylar erode quickly when exposed to AO and UV, releasing bits of residual Al thin film. (See Ref. 13 for discussions of these and other examples.)

Table 2. Results of optical survey of IDE sensors that remained active during the entire LDEF mission (April, 1984-January, 1989). Scanned area = 19.6 cm^2 per sensor. Total exposure time = 2106 days. Sensors responded to iron particles >0.5 μm at velocities >2km/s in ground tests.

LDEF tray	# of sensors scanned	# sensors with craters >1mm	# "active" sensors (n) used for flux calcs.	average # of impacts per "active" sensor	std. dev. (n-1)	% of small (0.5-3 μm) impactors	impact flux $x10^{-4}m^{-2}s^{-1}$
C-3 (west)	32	4 (13%)	23	8.82	7.18 (81%)	92	0.247
G-10 (earth)	32	0 (0%)	31	12.2	6.01 (49%)	99.7	0.342
H-11(space)	22	5 (23%)	14	23.1	6.02 (26%)	77	0.647
B-12 (north)	8	5 (63%)	7	137	13.8 (10%)	85	3.84
D-6 (south)	10	3 (30%)	6	149	16.0 (11%)	78	4.17
C-9 (ram)	9	8 (89%)	5	384	30.2 (8%)	85	10.8

A summary of the long-term flux rates measured by IDE sensors and MAP foils is presented in Table 3. The MAP data are from smoothed curves generated using penetration counts (corrected for secondary impacts) from several different foil thicknesses at each location. Marginal foil penetration occurs at the point where the crater diameter is ~1.1 times the foil thickness for small impacts (Ref. 10). These data indicate that particles that will penetrate a 2.4 μm thick Al foil, or make an ~3 μm diameter crater in Al, will also trigger the low sensitivity IDE sensors. This result is consistent with ground-based calibration tests (Refs. 14, 15). The narrow range (2.34 to 2.72 μm) of equivalent foil penetration thicknesses for MAP fluxes that match IDE fluxes is particularly gratifying. These results were arrived at independently by two different groups of investigators.

The MAP data show a shift to thicker foils for the same flux value on the east side of LDEF compared to the IDE data. This indicates that the velocity enhancement effect on threshold sensitivity of the MOS sensors is not as strong as the enhanced penetration effect of Al foil due to higher velocities.

Table 3. Long-term LDEF impact flux rates measured by IDE sensors and MAP foils. Sensors responded to iron particles >0.5 μm at velocities >2km/s in ground tests. Scanned area =19.6 cm^2 per sensor. Total exposure time =2106 days. MAP data is from smoothed cumulative flux curves for marginal foil penetrations corrected for secondary impacts (Refs. 10, 11).

LDEF tray	days 1-346	days 347-2106	days 1-2106	MAP smoothed fluxes for days 1-2106	equivalent MAP Al foil thickness (μm)
C-3 (west)	1.01	0.098	0.247	0.247	2.36
G-10 (earth)	0.157	0.379	0.342	-	-
H-11(space)	1.12	0.553	0.647	0.647	2.36
B-12 (north	6.14	3.39	3.84	3.84	2.42
D-6 (south)	6.70	3.67	4.17	4.17	2.34
C-9 (east)	8.61	11.2	10.8	10.8	2.72

Flux ratios calculated from IDE and MAP results are presented in Table 4. These data illustrate the limitations of using "typical" microparticle impact flux ratios for environment effects predictions. The data also confirm the higher microparticle impact flux on the south side of LDEF compared to the north side throughout the entire mission, despite the fact that the north side was pointed 8° into the ram.

The changes in flux ratios can be used to identify possible discrete *microparticle* orbital debris component contributions to the total impact flux experienced by LDEF. Our observations show that the fluxes on the north, south and space sides decreased at about the same relative rate (by ~50%), leaving the north/space and south/space flux ratios relatively constant at ~6. These ratios should be 0.78 for meteoroid impacts alone (due to the partial earth shielding of the north and south sides). Thus, it is apparent from the overall flux ratios and from the first year, time-resolved IDE data that the microparticle impact flux on the north and south sides was dominated by orbital debris. Further, the population of debris in orbits capable of striking these surfaces apparently decreased during years 2-6. During the same time period the microparticle impact flux increased by 30% on the ram (east) surface of LDEF.

Kessler has reported on orbital debris component contributions to the observed impact flux on various sides of LDEF (Ref. 16). He showed that particles in highly inclined orbits with apogees near LDEF's would have impacted the leading (east) side of LDEF more frequently than the north or south sides. A specific example in (16) for a near circular orbit inclined 100° with an apogee of ~500 km shows a 3:1 ratio of impactors preferentially striking the leading side versus the north or south sides. An increase in the debris particle population in a highly inclined orbit such as this could produce the observed long term flux increase on the east side of LDEF while allowing for the observed long term flux decrease on the north and south sides. We note that an anti-satellite test took place in September of 1985 (vehicle designation P-78) at an altitude of ~500 km and resulted in a drastic increase in the debris population in orbits inclined ~100° (Ref. 17).

The general hiatus in western launch activities caused by the loss of several vehicles in 1986 had to result in a lower replenishment rate for the population of microparticles in 7° and 28° inclined orbits. This could account for the general lower activity on the north and south sides of LDEF. Since Kessler also showed in (16) that orbital debris particles in elliptical orbits with inclinations of ~5-40°could strike the west side of LDEF (with a peak contribution at LDEF's orbit of 28.5°), this population must also have been drastically reduced during the 1986-1990 time period. The reduction of microparticles released by western launch activities could also account for this observation.

A further observation of the time-resolved IDE data showed that ~40% of the impacts recorded by the low sensitivity detectors occurred over a relatively narrow section of LDEF's orbit (± 30° for the whole mission) centered at ~20° west with respect to the LDEF-Sun angle. (Most of these impacts were identified by the extraction algorithm as belonging to an extended MOES event. See Table 1.) These

events were first thought to be a ß-meteoroid signature, but the space end sensors showed no sign of this signature. In addition, the flux on the west side dropped by an order of magnitude from the first year to years 2-6. We also noted that the west panel average impact rate during the first year was relatively constant. Thus, we are left with the conclusion that this sun-synchronous component contribution must have decreased drastically during years 2-6 and that it could be attributed to a special case of an orbital debris MOES.

A substantial increase in the microparticle debris population that struck the earth end of LDEF (all small particles) but not the space end could possibly be the result of a single breakup event at low altitude. Such an event occurred in September of 1986 when a Delta upper stage in a 23° orbit was struck by a smaller sensor package (the Delta's payload) in a 39° orbit (Ref. 17). The intercept took place at 220 km altitude and should have produced a large outward component of microparticle debris.

Table 4. Long-term LDEF impact flux ratios measured by IDE sensors and MAP foils. These data are for impactors that would create 3 μm diameter or larger craters in an aluminum surface, or penetrate a 2.5 μm thick Al foil.

LDEF tray ratio	days 1-346	days 347-2106	days 1-2106	MAP smoothed data for days 1-2106
H-11/G-10 (space/earth)	7.13	1.46	1.89	-
H-11/C-3 (space/west)	1.11	5.64	2.62	2.87
H-11/D-6 (space/south)	0.167	0.151	0.155	0.146
H-11/B-12 (space/north)	0.182	0.163	0.168	0.166
D-6/B-12 (south/north)	1.09	1.08	1.09	1.13
C-9/C-3 (east/west)	8.52	114	43.6	58.8
C-9/D-6 (east/south)	1.29	3.05	2.58	3.00
C-9/B-12 (east/north)	1.40	3.30	2.80	3.39

CONCLUSIONS

There are several important conclusions that can be drawn from this study. First, the temporal anisotropy of the *microparticle* environment experienced by LDEF extended throughout its orbital lifetime. This has serious implications on environment predictions that rely on isotropic long term flux and flux ratio assumptions, and points to the importance of including discrete orbital debris component contribution changes in these models. Further time-resolved *in-situ* measurements of these debris populations are needed to accurately assess model predictions and mitigation practices.

Second, the IDE experiment proved that most encounters with manmade particles occur with an orbital beat frequency that indicates repeated intersections with streams of orbiting particles shed from larger orbiting objects (Refs. 2-4, 6, 7). These particles are typically very small, submicron to a few microns, and account for ~2/3 of the IDE impacts during the first year. There is no reason to assume that this situation changed during years 2-6. This is also consistent with the 84% of small (0.5 to 3 μm) particle impacts on IDE sensors observed in the optical survey.

At least two other investigators have detected similar multiple-orbit encounters on different missions since the IDE data were first reported (Refs. 18, 19). It is apparent that each spacecraft's local orbital environment will be subject to a different microparticle impact regime based on interactions with the manmade particle environment of the day. Because the particles are small, they are not expected to stay in orbit for long due to perturbation by non-gravitational forces. Thus we are left with the conclusion that for multiple orbit intersections that lasted days to weeks, there must have been a continuous emission source for these particles, such as a satellite shedding paint particles and/or other materials.

All of this leads to the conclusion that changes in the manmade microparticle population that interacted with LDEF were the major reasons for the observed changes in long term *microparticle* impact fluxes. Limited chemical analysis of impact sites on IDE sensors supports this conclusion (Ref. 20). Approximately 1/3 of the sites examined on the space and west side sensors were from manmade microparticles, mostly paint. This is a significantly higher proportion than expected, but is statistically consistent with the flux data.

A third important result is a practical lesson learned in measuring microparticle impact fluxes on surfaces that have been exposed to a very low impact-flux environment, namely that inspections of small areas can lead to radically different flux values due to the statistical uncertainty of the small data set. The IDE sensors on the Earth end and trailing side of LDEF averaged ~10 impacts per sensor, but the range of values for the number of impacts found on individual 20 cm^2 sensors was 1 to 26. We recommend that several hundred cm^2 be carefully examined when determining flux rates based on impact feature densities in the range of one impact per cm^2.

A third conclusion resulting from this study was the utility of careful pre-flight photographic documentation of flight hardware that will eventually be returned for close examination. The pre- and post-flight photographic archive of IDE sensors allowed the long term impact count to be determined with a high degree of accuracy, and identified many pre-flight contaminants that were still in place after retrieval. New contaminants were also easily identified. This situation provides an excellent opportunity for the study of contamination and its effects. All of these photographs are electronically archived with the rest of the IDE data (available on CD), and physically archived along with the IDE hardware at NASA/LaRC.

ACKNOWLEDGEMENTS

This study was supported by NASA grant NAG-1218. The authors gratefully acknowledge the helpful discussions and reviews of this work provided by Don Kessler and Don Humes.

REFERENCES

1. S. F. Singer, J. E. Stanley, *et al.*, "First Spatio-Temporal Results from the LDEF Interplanetary Dust Experiment", Advances in Space Research 11, (12) pp. 115-122, (1991).

2. J. D. Mulholland & J. L. Weinberg, "IDE Data Identifies Orbital Cloud", LDEF Spacecraft Environmental Effects Newsletter 2, #1, 15 March (1991).

3. J. D. Mulholland, S. F. Singer, *et al.*, "IDE Spatio-Temporal Impact Fluxes and High Time-Resolution Studies of Multi-Impact Events and Long-Lived Debris Clouds", LDEF-69 Months in Space: First Post Retrieval Symposium, *NASA CP 3134*, pp. 517-527 (1992).

4. J.P. Oliver, J.L. Weinberg, S.F. Singer, C.G. Simon, W.J. Wortman, W.J. Cooke, J.D. Mulholland and P.C. Kassel, "Estimation of Debris Cloud Temporal Characteristics and Orbital Elements", Proceedings of the IAF/COSPAR World Congress, W. Flury, ed., Pergamon, (1993).

5. C.G. Simon, J.D. Mulholland, J.P. Oliver, W.J. Cooke, and P.C. Kassel, "Long-term Microparticle flux Variability Indicated by Comparison of Interplanetary Dust Experiment (IDE) Timed Impacts for LDEF's First Year in Orbit with Impact Data for the Entire 5.77 Year Orbital Lifetime", LDEF-69 Months in Space: Second Post Retrieval Symposium, *NASA CP 3194*, pp. 393-704 (1993).

6. J.P. Oliver, S.F. Singer, J.L. Weinberg, C.G. Simon, W.J. Cooke, W.H. Kinard, P.C. Kassel, J.D. Mulholland and W.J. Wortman, "LDEF Interplanetary Dust Experiment (IDE) Results", LDEF-69 Months in Space: Third Post Retrieval Symposium, *NASA CP-3275* (1995).

7. William J. Cooke, John P. Oliver and Charles G. Simon, "The Orbital Characteristics of Debris Particle Rings as Derived from IDE Observations of Multiple Orbit Intersections with LDEF", LDEF-69 Months in Space: Third Post Retrieval Symposium, *NASA CP-3275* (1995).

8. J.A.M. McDonnell and T.J. Stevenson, "Hypervelocity Impact Microfoil Perforations in the LEO Space Environment (LDEF, MAP AO 023 Experiment)", LDEF-69 Months in Space: First Post Retrieval Symposium, *NASA CP 3134*, pp. 443-458 (1992).

9. J.C. Mandeville and J. Borg, "Study of Cosmic Dust Particles On Board LDEF, The FRECOPA Experiments AO138-1 and AO138-2", LDEF-69 Months in Space: First Post Retrieval Symposium, *NASA CP 3134*, pp. 419-434 (1992).

10. D.H. Niblett, S. Mullen, M.J. Neish and J.A.M. McDonnell, "Comparison of Flux Data Deduced from Observed Impacts on LDEF with Predictions from Meteoroid and Debris Models", First European Conference on Space Debris, April 5-7, Darmstadt, Germany, *ESA SD-01*, pp. 165-170 (1993).

11. J.A.M1010. McDonnell, et al., "The Near Earth Space Impact Environment - An LDEF Overview", Proceedings of the IAF/COSPAR World Congress, W. Flury, ed., Pergamon, (1993).

12. C.G. Simon, J.L. Hunter, D.P. Griffis and J.J. Wortman, "Ion microprobe elemental analysis of impact features on Interplanetary Dust Experiment sensor surfaces", LDEF-69 Months in Space: First Post Retrieval Symposium, *NASA CP 3134*, pp. 529-548 (1992).

13. A.F. Whitaker and J. Gregory, eds., "LDEF Materials Results for Spacecraft Applications", *NASA CP 3257* (1994).

14. P.C. Kassel, "Characteristics of Capacitor-Type Micrometeoroid Flux Detectors When Impacted With Simulated Micrometeoroids", *NASA TN D-7359* (1973).

15. J.J. Wortman and P.C. Kassel, "Metal-Oxide-Silicon Capacitor Detectors for Measuring Micrometeoroid and Space Debris Flux" (submitted to Journal of Spacecraft and Rockets, 1994).

16. D. Kessler, "Origin of Orbital Debris Impacts on LDEF's Trailing Surfaces", LDEF-69 Months in Space: Second Post Retrieval Symposium, *NASA CP 3194*, pp. 585-593 (1993).

17. D.J. Nauer, "History of On-orbit satellite Fragmentations", 7th ed., Teledyne-Brown Technical Report CS93-LKD-018, July (1993).

18. C.R. Maag, W.G. Tanner, T.J. Stevenson, J. Borg, J.-P. Bibring, W.M. Alexander and A.J. Maag, "Intact capture of hypervelocity impact particles and ejecta", First European Conference on Space Debris, April 5-7, Darmstadt, Germany, *ESA SD-01*, pp. 125-130 (1993).

19. J. Edelman, ed., "Summary: Second International Space Forum in Toronto", Space Flight Environment International Engineering Newsletter, Vol. 5, No. 2, p. 10 (May-June, 1994).

20. C.G. Simon, J.L. Hunter, D.P. Griffis, V. Misra, D.A. Ricks, J.J. Wortman, and D.E. Brownlee, "Elemental analyses of hypervelocity microparticle impact sites on Interplanetary Dust Experiment sensor surfaces." LDEF-69 Months in Space: Second Post Retrieval Symposium, *NASA CP-3194*, pp. 677-692 (1993).

Table 1A. Optical survey results for IDE low sensitivity MOS sensors listed by LDEF location in order of increasing impact flux. Sensor dielectric thickness =1.0 μm; active surface area =19.6 cm^2/sensor; total exposure time =2106 days. In ground tests, these sensors responded to iron particles > 0.5 μm diameter at velocities >2 km/s (Refs. 14, 15). LDEF data showed that the sensors responded to any impactor that would produce craters in aluminum >3 μm diameter, or penetrate a 2.4 μm thick Al foil. Dimensions for craters are listed in microns (±5) as central-crater-dia/outer-spall-max-dimension/fracture-zone-max-dimension. A question mark (?) indicates that a measurement was not made; a dash (-) indicates that the feature was not present or not discernible. Sensors that gave all indications of having been active during the entire LDEF mission were used to calculate impact fluxes and are marked with an asterisk (*).

C = hypervelocity impact crater with no visual evidence of associated discharge.
d = impact induced discharge, nominal central crater (<14 μm diameter).
D = impact induced discharge, central crater/inner spall 14 - 20 μm diameter.
D̲ = impact induced discharge, central crater/inner spall 20-50 μm diameter.
D̿ = impact induced discharge, central crater/inner spall >50 μm diameter. $\mathbf{D_{tot}}$ = all impact discharges.

Sensor Number	C	d	D	D̲	*D̿*	D_{tot}	D_{tot}+C
Tray C-3 ("west", or "trailing" side)							
*1180	0	7	0	0	60/322/?	*7	7
*1182	0	9	0	0	0	*9	9
1183	?/20/? ?/~400/?	9	0	0	0	9	11
1191(short)	?/~5300/45000	12	0	0	0	12	13
*1192	0	6	0	0	0	*6	6
*1208	0	6	0	0	?/~100/? ?/~100/?	*8	8
*1213	0	7	0	0	0	*7	7
1224	1	6	0	0	?/~500/?	6	7
1237	64/299/506	3	0	0	-/69/106 368/828/2484	5	6
*1248	0	7	0	0	322/897/2116	*8	8
*1249	0	4	0	0	0	*4	4
*1268	0	2	0	0	0	*2	2
*1271	0	5	0	14/69/-	46/184/-	*7	7
*1276	0	4	0	0	37/69/207	*5	5
*1294	0	4	0	0	0	*4	4
*1300	0	24	-/17/-	0	37/140/149	*26	26
*1305	0	?	?	?	0	*12	12
*1310	0	26	0	0	0	*26	26
*1312	0	?	?	?	0	*5	5
*1320	0	?	?	?	0	*6	6
1335(short)	37/322/-	0	0		0	0	1
*1336	0	?	?	?	?	*8	8
*1342	0	2	0	41/248/-	0	*3	3
*1356	0	4	0	-/28/-	0	*5	5
1359	7(secondaries)	18	0	-/30/-	0	19	26
1361	1	9	0	0	0	9	10
*1365	0	4	0	0	0	*4	4
*1382	0	7	-/20/-	-/30/-	1	*10	10
*1387	0	5	0	0	0	*5	5
1395(short)	0	11	0	0	0	11	11
*1401	0	25	0	0	74/322/391	*26	26
1403	253/1104/2185	0	0	23/106/-	0	2	3

Table 1A (continued)

Sensor Number	C	d	D	D	*D*	D_{tot}	D_{tot}+C

NOTE: On C-3, 4 sensors out of 32 have craters >1mm. Sensor 1191 was cracked in half by a large impact. *n=23, mean = 8.82±7.18. 92% of impacts were from hypervelocity microparticles ~0.5 to 3 μm diameter.

Tray G-10 (earth facing side)

*1172	0	21	0	0	0	*21	21
*1173	0	1	0	0	0	*1	1
*1174	0	1	0	0	0	*1	1
*1177	0	5	0	0	0	*5	5
*1210	0	10	0	0	0	*10	10
*1218	0	6	0	0	0	*6	6
*1219	0	16	0	0	0	*16	16
*1220	0	12	0	0	0	*12	12
*1232	0	14	0	0	0	*14	14
*1234	0	15	0	0	0	*15	15
*1239	0	12	0	0	0	*12	12
*1241	0	7	0	0	0	*7	7
*1279	0	6	0	0	0	*6	6
*1280	0	14	0	0	0	*14	14
*1282	0	9	0	0	0	*9	
*1284	0	14	0	0	0	*14*	14
*1290	0	9	0	0	0	*9	9
*1291	0	13	-/18/-	0	0	*14	14
*1297	0	8	0	0	0	*9	9
*1304	0	16	0	0	0	*16	16
*1322	0	7	0	0	0	*7	7
1323(short)	0	1	1	0	0	2	2
*1326	0	2	0	0	0	*2	2
*1349	0	19	0	0	0	*19	19
*1350	0	14	0	0	0	*14	14
*1351	0	20	0	0	0	*20	20
*1360	0	19	0	0	0	*19	19
*1378	0	19	0	0	0	*19	19
*1381	0	23	0	0	0	*23	23
*1386	0	10	0	0	0	*10	10
*1390	0	16	0	0	0	*16	16
*1391	0	19	0	0	0	*19	19

NOTE: On G-10 sensors there were no large impacts. Sensors 1234, 1291, 1297 and 1381 have Al debris spray droplets from distant impacts. No impacts into sensor frames were noted. Sensor 1297 had a piece of Fe/Si rich meteorite residue contained in an Al debris spray droplet (apparently from an impact into the LDEF walking beam). Sensors 1172 and 1297 have suspected wastewater droplet residues. *n = 31, mean = 12.2± 6.01. 99.7% of impacts were from particles 0.5 - 3 μm in size.

Table 1A (continued)

Sensor Number	C	d	D	D	D	D_{tot}	D_{tot}+C
Tray H-11 (space facing side)							
*1193	0	14	0	37x55/138/-	138/290/370 138x184/634/644 101/370/414	*18	18
*1194	0	16	0	18x32/69/- 23x55/74/74 32/175/359 37/161/- 46/88/- 46/99/299	92x110/299/350	*23	23
*1195	0	10	-/14/- -/18/- -/18/-	-/23/- 37/175/- 14/101/-	50/253/-	*17	17
1203	83/529/529	14	18/115/-	23/37/- 23/41/- 46/207/- 50/258/276	0	19	20
*1205	0	24	-/18/-	-/23x28/- 32/46/- 41/-/-	92/575/644	*29	29
1226 (short)	11 (see size listings to right)	1	9/14/-.(C) 12/35/- (C) 14/41/- (C)	23/55/- (C) 23/69/- (C) 23/138/- (C) 37/92/207 (C)	60/207/331 (C) 92/230/276 (C) 97/313/- (C) 92x138/276/437 (C)	1	12
*1244	0	15	18/46/- 18/55/-	23/-/- 23/69/- 37/175/-	69/368/- 69/552/- 92/552/-	*23	23
*1254	0	13	-/18/- 14/37/- 18/115/-	-/23/- -/23/- -/32/- 46/166/265	92/483/493	*21	21
*1255	0	18	0	0	1	*19	19
1261	1	15	1	3	2	21	22
1296(short)	0	7	2	0	3	12	12
*1303	0	27	3	2	1	*33	33
*1313	0	21	3	1	1	*26	26
*1340	0	28	0	1	6	*35	35
*1343	0	12	2	0	1	*15	15
*1370	0	16	2	0	0	*18	18
*1371	0	18	2	0	1	*21	21
1372	2	21	3	1	0	25	27
*1379	0	19	2	1	4	*26	26
1385 (short)	2	13	2	3	0	18	20
1399	1	21	1	0	0	21	23
1400	2	15	1	0	2	18	20

Table 1A (continued)

Sensor Number	C	d	D	$\underline{\underline{D}}$	*D*	D_{tot}	D_{tot}+C

NOTE: On H-11, 5 sensors out of 22 have craters >1mm; sensor 1385 has 2 large craters. Sensors 1203, 1226, 1340, 1379, and 1400 have Al debris sprays from impacts into their frames. Sensors 1195 and 1226 have suspected wastewater droplet residues. *n = 14, mean = 23.1±6.0. 77% of impacts were from particles 0.5 - 3 μm in size.

Tray B-12 ("north" side)

*1175	0	110	28	6	0	*144	144
*1202	0	104	11	13	0	*128	128
1217	5	44	6	2	3	55	60
*1278	0	107	6	2	5	*120	120
*1298	(1)	-	-	-	-	*132	133
*1324	0	145	4	3	3	*155	155
*1352	0	114	5	5	2	*126	126
*1384	0	121	26	6	-	*153	153

NOTE: On B-12, 5 sensors out of 8 examined have craters>1mm. Sensor 1298 has 2 large craters. *n = 7, mean = 137±13.8. 85% of impacts were from particles 0.5 - 3 μm in size.

Tray D-6 ("south "side)

*1186	0	100	20	10	8	*138	138
1187(short)	30	?	?	?	22	52	
*1190	0	122	22	18	0	*162	162
*1212	0	116	20	6	2	*144	144
1225(short)	15	?	?	?	82	97	
1252(short)	14	?	?	?	37	51	
1253	4	64	12	11	9	96	100
*1263	1	130	21	7	0	*158	159
*1311	0	137	23	3	2	*165	165
*1314	0	89	29	6	0	*124	124

NOTE: On D-6, 3 sensors out of 10 examined have craters >1mm. Sensor 1225 has a 6 mm hexagon crack/spall around a large crater. *n = 6, mean = 149±16.0. 78% of impacts were from particles 0.5 - 3 μm in size.

Tray C-9 ("east" or "leading" side)

*1176	0	?	?	?	?	*357	357
1293	10	?	?	?	?	200	210
1333	11	121	13	11	6	151	162
1334(short)	53	?	?	?	?	152	205
*1355	0	321	39	21	7	*388	388
*1383	0	339	18	?	10	*367	367
*1396	0	356	46	22	10	*434	434
*1406	0	305	47	12	8	*373	373

NOTE: On C-9, 8 sensors out of 8 examined have craters >1mm. One sensor has 3 large craters. Sensor 1355 has a large debris spray from an impact into its aluminum frame. Sensor 1293 has a suspected wastewater droplet residue. *n=5, mean = 384±30.2. 85% of impacts were from particles 0.5 - 3 μm in size.

PENETRATION RATES OVER 30 YEARS IN THE SPACE AGE

J.A.M. McDonnell and J.M. Baron
Unit for Space Sciences
University of Kent at Canterbury
Canterbury
Kent CT2 7NR, U.K.

ABSTRACT

Experimental data from spacecraft providing impact penetration rates and cratering for metallic targets is reviewed. Data includes NASA Explorers 16 and 23 and the Pegasus series, the second US-UK satellite Ariel 2, Space Shuttle STS-3 (MFE) , recovered surfaces on Solar Max Satellite, The Long Duration Exposure Facility (LDEF) and EuReCa TiCCE.

Factors concerning exposure to the environment are considered and, especially, material properties which affect the penetration resistance. Reference to a common material, Aluminium alloy 2024-T3, is effected and the data then compared to define firstly an average impact flux over the period. The data is examined, in the context of possible satellite and space debris growth rates, to determine the constancy of the flux. This also provides strong constraints on the current space debris component. It is found that the impact data are consistent with domination by natural meteoroid sources. Growth rates are not evident within the period 1980-1990 and Eureca TiCCE fluxes in 1993, for particles penetrating foils of around 10 microns thickness, supports the constancy of the flux. At larger dimensions the 1993 Eureca TiCCE fluxes show an 8-fold increase (McDonnell et al., 1994) but this is considered not inconsistent with the selective exposure to meteoroid streams of a satellite stabilised in heliocentric co-ordinates for an 11 month period.

1. INTRODUCTION

Experiments to assess hazards in space and to detect meteoroids have been one of the first priorities of exploration established in the USA and USSR. Various methods have been used but success was not always achieved. Early measurements on Explorer 8 reported in (McCracken et al.,1961) were proved to have been influenced by the high susceptibility of piezo - electric microphone detectors in Earth orbit to thermal changes or other factors (Nilsson, 1966). Later reviews (McDonnell 1978) swept much of this early unreliable data away, leaving a core of data from Explorers 16 and 23, and Pegasus 2 and 3 whose high reliability was not 'bettered' until the advent of data from recovered surfaces on Solar Max and LDEF. Penetration and cratering data are seen to offer the most comprehensive definition of the flux rate (i.e. from the same technique) over a wide range of masses. Differing techniques and, even within the penetration data, differing impact materials, can lead to flux differences which may be confused with, or even mask, temporal changes in flux. In this review, to which the latest data from the science experiment TiCCE on the EuReCa spacecraft has also been added, we have selected only penetration experiments, either of single metallic foil, or (with calibration factors), data from retrieved metallic semi-infinite targets. Relevant exposure factors to the space environment and Earth shielding have been presented. More especially, a comprehensive collation of the factors affecting the calibration of the different materials has been made, and an improved penetration formula derived from thin and thick target data, used to reassess the sensitivities of the experiments. This has led to the impact penetration rate for a randomly exposed object, corrected for Earth shielding, at the mean altitude of the experiment deployment, being derived.

2. KEY SPACE EXPERIMENTS IDENTIFIED.

Explorers 16 and 23

Both of these meteoroid satellites carried experiments comprising arrays of pressurised 'beer cans'; a pressure-sensing switch capable of measuring a "once only" leak was activated some short time after the first perforation of any can above the ballistic limit. Experimental details and data for Explorer 16 were presented by (Hastings, 1963 a, b & c ; Hastings, 1964) while those for Explorer 23 were presented by (O'Neal, 1965 & 1968). The data were analysed using chi squared tests regarding possible temporal changes and were found to be random over the exposure epoch. However, this did not preclude possible variations of short duration (e.g. within an orbit) or variations in flux beyond the observation period.

Ariel 2

Aluminium foils were used in a series of active in-situ sensors on board the second US-UK Ariel series; the experiments and analysis were reported by (Jennison et al, 1967). The data, which was analysed by one of the current authors (McDonnell, 1964) in support of his PhD thesis, showed that only one penetration was detected after a total of six months of exposure in space! Because this occurred at the edge of the detector corresponding to the region from which fresh foil was advanced during flight, it could not be ascertained if this was a true space impact perforation or an imperfection in the foil. We might note that the detection threshold for this (photometric) system is larger than that of the ballistic limit because of the need for a significant penetration area for the detection of light. The data nevertheless clearly demonstrated, by virtue of in-flight calibration, that the flux was some 3 orders of magnitude below the piezo-electric data acquired earlier by Explorer 8.

The Pegasus series

Three Pegasus satellites were flown (Naumann, 1965; Clifton & Naumann, 1966; Dozier, 1966). The meteoroid penetration detectors consisted of parallel plate capacitors formed by backing aluminium target sheets with a mylar trilaminate dielectric followed by a vapour-deposited layer of copper. In space, the capacitors were charged to 40 volts and penetrations were registered by discharges through the mylar layers.

It was noted that a penetration slightly larger than the ballistic limit for the thickness specified in Table 1 could be required because of the need to induce a discharge of the sensing capacitor behind the target. Two thicknesses of 2024-T3 aluminium detectors at 203 microns and 406 microns presented reliable data. This data furnished the best assessment of the milligram meteoroid flux until the advent of LDEF, and forms a critical overlap, in terms of sensitivity, with faint radar meteor data (10^{-6} g).

Solar Maximum Mission (Retrieved Louvres)

Repairs to the Solar Max spacecraft, recovered coincidentally at the same time as the launch of LDEF, led to the retrieval, for laboratory analysis, of multi-layer thermal insulation and, of more relevance to this particular study, aluminium louvres. This data (presented by Laurance and Brownlee, 1986) covered a range of crater diameters from sub-micron to millimetre dimensions. The pointing direction of the louvres was assumed to be random regarding the Earth orbital vector because of the dedicated solar pointing direction for spacecraft observations; it has been pointed out, however, (McDonnell, 1992) that the flux data derived in terms of particle **mass** by Laurance and Brownlee was in serious error because of the use of two quite different (and mutually inconsistent) penetration formulae on the same plot; this revised, quite drastically, the interpretation of their microparticle fluxes in terms of space debris. Nevertheless, the original source data, in terms of crater dimension, is incontrovertible and can now be related directly to other penetration data; we must take note of the possibility of some secondary cratering in the SMM data at the smallest dimensions. Although the chemical data of Laurance and Brownlee would seem to be especially relevant to the source of particles, it must be noted that, at very small dimensions, that space debris can be generated efficiently from impacts on surfaces local to the detector (e.g. from the extended SMM solar cell array which was within the acceptance angle for the louvre impacts).

STS-3 Microabrasion Foil Experiment (MFE)

As part of NASA's OSS Pathfinder Payload (OSS-1) an array approaching 1 m^2 in area was exposed for 8 days. Four hypervelocity perforations were detected (McDonnell, et al., 1984); chemical analysis showed silicon rich residues and the morphology was consistent with high velocity natural impactors. The low altitude of MFE (241 km) is of significance in the context of the poor access of microparticles which are in Earth orbit, since their lifetime in circular orbit is measured in terms of hours at this altitude. Access to unbound interplanetary particulates is, however, unabated at this altitude.

LDEF

LDEF's large area-time product and the wide range of materials deployed on it have elevated its importance to a very high level. Further, the many investigators involved have contributed a plethora of papers on the interpretation of the data obtained, in both the Proceedings of the three Post-retrieval Symposia held to-date and in many other journals.

We have chosen data from both experiments and the LDEF M-D Special Investigator Groups (M-D SIG). The small particle penetration data was best defined by the MAP experiment (McDonnell, 1992) for foil thickness and penetration in the range 2 to 30 microns, where detectors pointed in N,S,E,W and Space directions. For the larger impacts, data refers to thick target measurements (Humes, 1991) and data from the thermal control surfaces and the longerons and intercostals of the LDEF frame (See et al., 1993)

The directional stability of LDEF relative to the orbit vector was invaluable in understanding the dynamics of dust particles, but in the context of this survey, it has been "degraded" to imitate a randomly tumbling spacecraft to permit comparison with other data. Therefore, in this context, we have taken the 6-point average of the LDEF data, representing the average flux on the 6 faces of a cube at a given ballistic limit.

EuReCa Timeband Capture Cell Experiment (TiCCE)

Impact data is currently being analysed following the recovery in August 1993 of large areas of thermal blanket, the solar cell arrays and the Science experiment TiCCE (Timeband Capture Cell Experiment). The impact time resolution aspect of the experiment did not function correctly due to an overload in the first exposure epoch. Only flux data comprising thin foil surfaces (with capture cell) and other cratering data from the experiment is currently available, but later publications will extend to the publication of the data from impactor craters in the millimetre range and above on the MLI thermal blankets and the solar cell arrays.

3. EXPERIMENT PENETRATION SENSITIVITIES.

Material specifications for the meteoroid detectors employed on the selected satellites, together with their newly determined conversion factors to 2024-T3 aluminium (derived from our chosen penetration equation) are presented in Table 2. The Earth shielding, gravitational and sensitivity enhancement factors applicable to the data from these satellites are presented in Table 3.

Orbital Data

Orbital data (which is presented in Table 1) is used to find the mean altitude of the spacecraft; orbital parameters change during exposure due to orbit decay and there are also cases of differences between apogee and perigee.

Earth Shielding

The Earth shields an orbiting spacecraft from a proportion of the flux of extra-terrestrial particulate material arriving from 4P steradians of space. This proportion, known as the shielding factor, h , is given by:

$$\eta = \frac{1-\cos\theta}{2}$$ (Cour-Palais, 1969)

where q is the angle subtended by the spacecraft between the distance of the spacecraft from the centre of the Earth and the distance from the spacecraft to a point tangential to and 150 km above the Earth's surface which forms a normal to the Earth's radius.

Gravitational enhancement

As interplanetary particles approach the Earth from far away, their paths will be deflected towards the Earth because of its gravitational attraction. This effect is analogous of the focusing of a parallel beam of light by a convex lens and, because of this, has been termed gravitational focusing. The effect results in a gravitational enhancement of the particulate flux at and near the Earth relative to the flux at a great distance from the Earth. The gravitational flux enhancement factor, c, is given by:

$$\chi = 1 + \left(\frac{V_e^2}{V_\infty^2}\right)$$ (Öpik, 1951)

where V_∞ is the approach velocity to the Earth and V_e is the escape velocity at the altitude of detection H and is given by $V_e(H) = +2GMe/(Re+H)$. Values for c are shown in Table 3.

Sensitivity enhancement

In addition to the increase of the flux of particles near the Earth due to the increase of velocity, we also experience enhanced sensitivity due to the increase of velocity. Thus smaller particles will be detected and hence (due to the size distribution of the particles) a larger number. We find from the LDEF data a cumulative flux index of alpha = 1.7 (mass index .57) between values of f_{max} = 10 microns to 100 microns; using the penetration dependence of $f_{max}/dp \mu V^{.806}$ we find a sensitivity enhancement proportional to $(V_i/V_\infty)^{1.37}$ where V_i is the impact velocity increased by gravitational attraction relative to the interplanetary approach velocity to the Earth, V_∞. This enhancement is **additional** to the gravitational flux enhancement. Both factors are shown in Table 3. Accounting for Earth shielding, gravitational enhancement and sensitivity enhancement factors results in a mean total enhancement factor of 1.0279 for the whole data set. Although the differences between experiments are small, nevertheless, they are possibly significant, now that we have an accurate basis for such intercomparisons.

Earth shielding and gravitational enhancement are applicable, of course, only to the interplanetary component. For space debris in Earth orbit, Earth shielding is irrelevant by definition, but is replaced by much more significant factors, such as the altitude or inclination distribution of the space debris itself. Nevertheless, we see in the results of this comparison, that there is very strong evidence for space debris being a very minor component of the data set in the size ranges considered; our arguments regarding sensitivity to such effects as gravitational enhancement for the natural population are justified.

Penetration Formulae

Numerous formulae are available, the majority being derived from experimental hypervelocity penetration work dating from the beginnings of the space era (Fish & Summers, 1965) and with subsequent developments by many others continuing to the present day (e.g. Naumann, 1966, Frost 1970, McDonnell & Sullivan, 1992). References to many are contained for example in publications such as Proceedings of the Hypervelocity Impact Symposium, 1992. For the interpretation of the ballistic limit foil penetration data, we have used a formula which is based on the experimental calibration at hypervelocities of comparable foils:

$$\frac{f_{max}}{d} = 1.272\, d^{0.056} \left(\frac{\rho_p}{\rho_{Fe}}\right)^{0.476} \left(\frac{\rho_{Al}}{\rho_T}\right)^{0.476} \left(\frac{\sigma_{Al}}{\sigma_T}\right)^{0.134} V^{0.806}$$ (McDonnell & Sullivan, 1992)

where s = tensile strength in Mpa; r = density in g cm $^{-3}$; d= particle diameter in cm; and V = velocity in km sec $^{-1}$

This formula incorporates the tensile strength and density of target and in the absence of a true comparison in space, is the best a priori assumption. For aluminium targets the formula (McDonnell & Sullivan, 1992) extends from 4 to 16 km sec^{-1} based on micron impacts using a 2 MV microparticle accelerator (McDonnell, 1970); it incorporates, for larger dimensions, a dimensional scaling which ensures compatibility with light gun data and hence the valid interpretation of millimetre scale impact craters on LDEF and EuReCa. Other formulae have been presented recently (Watts et al., 1993) which offer promise of more comprehensive inclusion of a wider range of parameters. Current assessment of this formula leads to anomalous results and furthermore the formula is not based on actual penetration data of the type demanded for this comparison. One of us (J.M.Baron) is engaged currently in providing new experimental data towards his doctoral thesis which, it is hoped, will provide valuable penetration data for comparison with predictions from these formulae.

4. RESULTS

Shown in Figure 1 is the "raw" flux, representing the measured impact rate per m^2 referred to the detector thickness in microns or, in the case of impact craters on thick targets, the crater diameters converted to the equivalent marginal penetration thickness (f_{max}). Without sensitivity and exposure factors and conversion factors to a common material, we might have been tempted to consider the flux of LDEF, SMM and Eureca to be significantly higher than earlier satellite data . However, when the data is corrected for the appropriate factors (see Table 3 & Figure 2), it results in a considerable shift, both in the Explorer 16 and 23 sensitivities (as anticipated from the higher density and strength of their detector surfaces) and also between LDEF, Pegasus and SMM data. We have identified the following factors for consideration:

a). LDEF and the SMM (Louvre) data are in remarkably good agreement with the exception of:

(i) the flux below f_{max} = 2μm; where SMM flux increases to be one magnitude higher. This may be attributed to the 'contamination' from secondaries (possibly locally generated as has been observed even at LDEF at this dimension) or, alternatively, to a higher microparticle flux on SMM at these dimensions. Until the local secondary cratering hypothesis for SMM is disproved, we would place stronger emphasis on LDEF's 5.76 year 6-point flux measurement as being most representative, but note that the LDEF data at this value (f_{max} < 25μm) shows a high East to West ratio, which is attributed to orbital particulates (McDonnell, 1992).

(ii) The SMM flux above f_{max} = 128μm (as 2024-T3 aluminium) is lower than LDEF by a factor of ~ 1.5. Noting that the 158 μm flux point (as 2024-T3 aluminium) is the greatest thickness measured on SMM and hence statistically uncertain and, further, that the louvres do not represent a truly isotropic exposure, this is not considered significant. On very similar exposure conditions over 11 months on

Eureca, deployed in a similar sun pointing direction, the average flux varied by a factor of 4 in different pointing directions.

b). The Pegasus 400 μm data is lower by a factor of 1.5 than the LDEF point at f_{max} = 400 microns. This discrepancy could well prove significant and has, potentially, the possible interpretation that between Pegasus' 1965 exposure and LDEF's 1984-1990 epoch, the flux had increased by 50%. A space debris component of 50% on LDEF must therefore be considered at least as a possibility, if the natural particulates are assumed, otherwise, to be constant. But, we must first consider the variability of measurements of the natural flux before supporting this approach. We have emphasised the term *measurements* of the flux, rather than true variations in the flux, because, to date, the exposures have not been unbiased. Even within the LDEF data, the flux distribution at f_{max} = 100 μm is found to have minor irregularities; the average ratios of the North to South flux relative to LDEF's orbit over 5.76 years are not symmetrical, despite proper correction for LDEF's offset. The situation has been analysed (McBride et al., 1994) and is understood in terms of the non-random exposure to the crossing of meteoroid streams and cometary planes. It is found that, despite LDEF's fast precession, the yearly cycle is repeated almost on a heliocentric basis, and access to particular faces such as North and South is markedly anisotropic; in fact, access varies to the point of mutual exclusivity for most meteoroid steams. With the well accepted meteoroid steam anisotropies in both flux and direction at masses corresponding to f_{max} = 100 μm,we cannot say that the meteoroid flux will be measured consistently by any one surface on a satellite, **unless** it is truly randomly exposed from both the geocentric and heliocentric point of view, and, **further**, it is exposed for an integral number of years!

c). We see the MFE flux (at lower altitude) returning a flux at f_{max} = 5 mm, which is lower than LDEF by a factor of 4. If LDEF's flux at this dimension is considered to be partly space micro-debris (e.g. McDonnell, 1992), then this albeit short exposure, which returned only four impacts, could provide a useful figure for the orbital (and possibly debris) component, namely, a debris/natural ratio of 3:1. This can be inferred because orbital lifetime calculations for micro-debris at 241 km (Ratcliff et al., 1993) preclude MFE from seeing particles in orbit. The MFE flux is in good agreement with measures of the space pointing flux from LDEF. We cannot quantify the possible space debris components from flux alone, neither at the micron nor the millimetre range; chemical studies on residues are inconclusive, with about 50% being indeterminate and only some 15% of residues having the "debris" signature of typical elements used in spacecraft construction and operations (Bernhard, et al., 1993). Despite this, even from flux rates alone, we can certainly impose useful constraints on growth **rates,** because of the time difference between these different measurements. We have examined this in section 4.

5. FLUX COMPARISONS

Penetration Distributions

Data from all key LEO penetration experiments shown in Figure 2 may be examined in terms of the epoch of the experiment exposure (Table 1). In general,we can see only small flux differences which could be associated with the epoch. Because LDEF represents a very significant flux measurement at all dimensions, other experiments are compared to this penetration distribution. In Figure 3, the flux for different experiments is plotted to show, in more detail, the measured flux relative to the LDEF flux, but on a time axis. For comparison we also show the NASA + 2% and + 5% growth rate which would pertain to large and small space debris respectively.

We see no suggestion that the flux has changed significantly over 30 years, with one possible exception, namely for particulates corresponding to the penetration of aluminium of thickness f_{max} less than 25 microns (McDonnell, 1992). Although both SMM and LDEF are in good agreement (but with SMM showing a higher flux than LDEF at an earlier epoch and hence opposing a growth trend) it is still possible that these data have a significant orbital particulate component and, possibly orbital micro debris. The MFE data point, measured at an altitude below that where orbital particulates can be sustained, could well represent the "pure" interplanetary flux at the time of SMM exposure. It must be emphasised, though, that there are no reliable penetration flux measurements in the early 1960's to demonstrate that this is a true rate **increase** in the 1980's. The Ariel II upper limit is not below LDEF's 6-point average flux.

Space Activity Profiles

Consideration of the data, and changes in flux resulting from an increase in the space debris population may be examined in the light of space activity profiles. Shown in Figure 4 is the launch and in-orbit population over the period. Total launches have increased by only a small factor, but in-orbit objects and debris have increased by a factor of between 1 and 2 decades. In the absence of significant total impact flux rate changes except possibly at small dimensions, these trends in space traffic growth are not repeated in the data, and the dominance of the natural meteoroid population is strongly asserted even at the current epoch of 1993.

Deserving perhaps special attention, the GTO launch rate is worthy of special study (Figure 5). Analysis by Flury et al (1992) and by Kessler (1990, 1993) have drawn attention to a particular debris population which, being in eccentric orbit, impact on the pointing faces of LDEF. This debris could well be a relatively strong component on the trailing face but may be so only by virtue of the reduced flux of natural meteoroids on this face. This is especially relevant for the LDEF west fluxes below f_{max} = 25 microns, where the LDEF MAP data (McDonnell, 1992) has resulted in an East to West ratio of 20 to 50. However, these West low flux data are not confirmed by the Frecopa data of Mandeville and Berthoud. In questioning which data are more reliable, the LDEF MAP data should be accepted because 1) they were exposed all the time, compared to 11 months for Frecopa, and 2) in the (ubiquitous) presence of secondary ejecta as a contaminant, an experiment which measures the **lowest** flux (and very few MAP penetrations were recorded) must be considered the most significant.

It is from these East-to-West data and associated modelling, and from the IDE experiment that a microparticle orbital population is, indeed, inferred; but the delineation of the source of this data between natural and man-made orbiting remains yet unresolved.

We must caution against arguments considering all orbital particulates as debris and state that the 1993 Eureca TICCE penetration data at 8 microns (equivalent 2024-T3) is in near perfect agreement with LDEF 1984-1990 and Solar max 1980 - 1984 fluxes. If this **is** debris then any and all space debris growth must have taken place before 1980 in this size range! But further to this, orbital swarms and groups were seen in the mid 1970's on HEOS II.

6. MEASUREMENTS AHEAD

Considerable further data on Eureca will be available from the studies performed by ESA on the MLI and Solar Cell Arrays, and from the TICCE experiment. Preliminary data from large impacts on TICCE indicates an 8-fold or more increase for values of f_{max} in the millimetre region compared to LDEF's 6-point average, and the debate of "debris versus natural" particulates will be raised but with increased vigour.

Hubble Space Telescope Solar Array data will also be available under ESA studies currently being initiated. Though the Hubble arrays were returned more recently than Eureca, the mean epoch of exposure actually preceeds Eureca's by 11 months due to the 4 year exposure period! The Eureca data will therefore be the latest source in terms of mean epoch.

Although LDEF's 6-point average and 5.76 year exposure is apparently representative of the average natural meteoroid flux, we must acknowledge the modelling of meteoroid streams by McBride et al (1994); particular faces are prone to very selective exposure to particular, and to high activity meteoroid streams. Arguments will again centre on whether Eurecas's 8 fold increase be explained in terms of the quite natural and yet variable meteoroid streams or by space debris.

ACKNOWLEDGEMENTS

We appreciate and acknowledge all members of the Unit for Space Sciences at Canterbury for their valuable contribution to both experiment development, data analysis, discussion and clerical assistance. We acknowledge the Science & Engineering Research Council, UK for financial support, and NASA's M-D Space Investigation Group for access to LDEF data.

8. REFERENCES

BERNHARD, R.P., SEE, T.H., & HÖRZ, F. (1993) "Projectile compositions and modal frequencies on the"Chemistry of Micrometeoroids" LDEF Experiment" in "LDEF - 69 Months in Space : Second Post - Retrieval Symposium", NASA CP 3194, Part 2, pp. 551-573, edited by Levine, A.S.

COUR-PALAIS, B.G. (1969) "Meteoroid Environmental Model - 1969 [Near Earth to Lunar Surface]", NASA SP-8013.

CLIFTON, S., & NAUMANN, R. (1966) "Pegasus Satellite Measurements of Meteoroid Penetration (February 16 - December 31, 1965)", NASA TM X-1316.

DESHPANDE, S.P. (1994) "Space Debris or Natural? Impacts on NASA's Long Duration Exposure Facility", Ph.D. thesis, University of Kent at Canterbury.

DOZIER, J.B. (1966) "Meteoroid data recorded on Pegasus Flights" in "The Micrometeoroid Satellite Project Pegasus", NASA TN D-3505, Chapter V, pp. 65 - 76.

FISH, R.H. & SUMMERS, J.L. (1965) " The effect of material properties on threshold penetration", Proc. 7th. Hypervelocity Impact Symposium, 6, pp. 1 - 26.

FLURY, W., JANIN, G., JEHN, R. & KLINKRAD, H. (1992) "Space Debris in Elliptical Orbits", 18th International Symposium on Space Technology and Science, Kagoshima, Japan.

FROST, V.C. (1970) "Meteoroid Damage Assessment", NASA SP-8042

HASTINGS Jnr., E.C. (1963a) "The Explorer XVI Micrometeoroid satellite - Description & Preliminary Results for the period Dec 16, through Jan 13, 1963.", NASA TM X-810.

HASTINGS Jnr., E.C. (1963b) "The Explorer XVI Micrometeoroid Satellite; Supplement I, Preliminary results for the period 14 Jan 1963 - 2 Mar 1963, NASA TM X-824.

HASTINGS Jnr., E.C. (1963c) " The Explorer XVI Micrometeoroid Satellite; Supplement II, Preliminary results for the period 3 Mar 1963 - 26 May 1963", NASA TM X-899.

HASTINGS Jnr., E.C. (1964) "The Explorer XVI Micrometeoroid Satellite; Supplement III, Preliminary results for the period May 27 through July 22, 1963", NASA TM X-949.

HUMES, D.H. (1991) "Large Craters on the Meteoroid and Space Debris Impact Experiment", in "LDEF - 69 Months in Space : First Post - Retrieval Symposium", NASA CP 3134, Part 1, pp.399-418, edited by Levine, A.S.

JENNISON, R.C., et al. (1967) "The Ariel II micrometeorite penetration measurements", Proc. Roy. Soc. A, 300, pp. 251-269.

KESSLER, D.J., (1990), "Collision Probability at Low Altitudes Resulting from Elliptical Orbits", Advances in Space Research, Vol. 10, No. 3-4, 393.

KESSLER, D.J. (1993) "Origin of orbital debris impacts on LDEF's trailing surfaces", in "LDEF - 69 Months in Space - Second Post - Retrieval Symposium", NASA CP 3194, Part 2, pp. 585-593, edited by Levine, A.S.

KLINKRAD, H. (1993) Private communication showing launch rate statistics for GTO-type orbits from 1964 to present, extracted from ESA/ESOC/MAS DISCOS catalogue.

LAURANCE, M.R. & BROWNLEE, D.E. (1986) "The flux of meteoroids and orbital space debris striking satellites in low earth orbit", Nature, 323, pp. 136-138.

McBRIDE, N., TAYLOR, A.D., & McDONNELL, J.A.M. (1994) "Asymmetries in the natural meteoroid population as sampled by LDEF", Planetary & Space Science (in submission).

McCRACKEN, C.W. et al. (1961) " Direct measurements of interplanetary dust particles in the vicinity of the Earth", Nature, 192, 4801, pp. 441-442.

McDONNELL, J.A.M. (1964) " The Study of Micrometeorites from Rockets and Satellites", Ph.D. Thesis, Victoria University of Manchester, England.

McDONNELL, J.A.M. (1970) "Factors affecting the choice of foils for penetration experiments in space", Space Res., X, pp. 314-325.

McDONNELL J.A.M. (1978) "Microparticle studies by space instrumentation" in McDonnell, J.A.M., edit. "Cosmic Dust", J. Wiley & Sons, Chichester. pp. 337-426.

Mc DONNELL, J.A.M.; CAREY, W.C.; & DIXON, D.G. (1984) "Cosmic dust collection by the capture cell technique on the Space Shuttle", Nature, 309, pp. 237-240.

McDONNELL, J.A.M. and the Canterbury LDEF MAP Team (1992) " Impact cratering from LDEF's 5.75-year exposure: decoding of the interplanetary and Earth-orbital populations", Proc. Lunar & Planetary Science, 22, pp. 185-193, Lunar and Planetary Institute, Houston.

McDONNELL, J.A.M. & SULLIVAN, K. (1992) " Hypervelocity impacts in space: decoding the projectile parameters", Proc. Workshop on Hypervelocity Impacts in Space, U.K.C., 1991, pp. 39-47.

McDONNELL, J.A.M., DESHPANDE, S.P., NIBLETT, D.H., NEISH, M.J. & NEWMAN, P.J. (1993) "The near Earth space impact environment - an LDEF overview", Adv. Space Res., 23, 8, pp. 87-101.

McDONNELL, J.A.M., RATCLIFF, P.R., & COLLIER, I. (1994) "Micro-particle impact flux on the Timeband Capture Cell experiment of the Eureca spacecraft", Paper to be presented at Cospar, Hamburg.

NAUMANN, R.J. (1965) "Pegasus measurements of meteoroid penetrations (February 16 - July 20, 1965)", NASA TM X-1192.

NAUMANN, R.J. (1966) "The Near-Earth Meteoroid Environment", NASA TN D-3717.

NILSSON, C. (1966) "Some doubts about the Earth's dust cloud", Science, 153, pp. 1242-1246.

O'NEAL, R.L. (1965) " The Explorer XXIII Micrometeoroid Satellite- Description and preliminary results for the period November 6, 1964", NASA TM X-1123.

O'NEAL, R.L. (1968) "The Explorer XXIII Micrometeoroid Satellite - Description & results for the period Nov 6, 1964, through Nov 5, 1965", NASA TN D-4284.

ÖPIK, E.J. (1951) "Collision probabilities with the planets and the distribution of interplanetary matter", Proc. Roy. Irish Academy, 54, Section A, No. 12, pp. 165-199.

RATCLIFF, P.R., TAYLOR, A.D., & McDONNELL, J.A.M. (1993) "The LEO micro-particle population: computer studies of space debris drag depletion and of interplanetary capture processes", Adv. Space Res., 13, 8, pp. (8)71-(8)74.

SEE, T.H. et al. (1993) "Continued Investigation of LDEF's Structural Frame and Thermal Blankets by the Meteoroid & Debris Special Investigation Group", in "LDEF - 69 Months in Space : Second Post - Retrieval Symposium", NASA CP 3194, Part 2, pp.313-324, edited by Levine, A.S.

WATTS, A. et al. (1993) "Dimensional Scaling for impact cratering and perforation", POD Associates Inc., Albuquerque, New Mexico.

Space-craft Name	Initial Altitude Perigee (km)	Initial Altitude Apogee (km)	Final Mean Altitude (km)	Orbital Inclin. (deg)	Launch Date	Exposure Time (secs)	Detector material	Detector Thick-ness (mm)	Detected Flux (no/m^2 sec^{-1})
Explorer 16	750	1180	965	52.0	16 Dec. 1962	1.88E+7 (0.60yr)	Annealed Berylco 25 alloy	29.2 54.9	1.99E-06 3.66E-06
Explorer 23	464	979	722	52.0	06 Nov. 1964	3.15E+7 (1.0yr)	302 Stainless steel (1/2hard)	25.4 50.8	2.4E-06 4.1 E-06
Ariel 2	289	1358	824	51.7	27 Mar. 1964	6.22E+6 (0.20yr)	1201-H6/H9 Al alloy	12 15	5.12E-05 for 15mm detector †
Pegasus 1	502	738	620	31.8	16 Feb. 1965	2.75E+7 (0.87yr)	1100-0 & 2024-T3 Al alloy	38 203 406	2.18E-06 (* see footnote)
Pegasus 2	512	742	627	31.8	25 May 1965	1.90E+7 (0.60yr)	1100-0 & 2024-T3 Al alloy	38 203 406	(* see footnote) 2.42E-07 5.64E-08
Pegasus 3	522	540	531	28.9	30 Jul. 1965	1.33E+7 (0.42yr)	1100-0 & 2024-T3 Al alloy	38 203 406	(* see footnote) 2.42E-07 5.64E-08
Solar Max (louvres)	575	575	533	28.5	14 Feb. 1980	1.31E+8 (4.16yrs)	1145-H19 Al alloy	125	7.85E-07
MFE on STS-3	241	241	241	38.0	22 Mar. 1982	1.53E+5 (0.01yr)	1201-H6/H9 Al alloy	5	2.60E-05
LDEF	476	476	463	28.4	06 Apr. 1984	1.82E+8 (5.77yrs)	1201-H6/H9 Al alloy	1.5 to semi - infinite	5.38E-05 for 4.83 micron detector
TICCE on EuReCa	508	508	508	28.4	01 Aug. 1992	2.83E+7 (0.90yr)	1201-H6/H9 Al alloy	9.2	5.41E-05 for 9.2 micron detector

† 50% confidence limit for Ariel 2. * The 38 microns flux quoted above for Pegasus 1 is the combined 38 microns flux for all three Pegasus satellites, while both the the 203 microns & 406 microns fluxes quoted above for Pegasus 2 & 3 are the combined fluxes for Pegasus 2 & 3 (as adopted by Clifton & Naumann, 1966)

Table 1. Key Satellite Experiments offering significant exposure of metallic surfaces in the LEO environment

Spacecraft detector material	Density (g cm-3)	Tensile strength (MPa)	Conversion factors* to 2024-T3 Aluminium
Beryllium-copper (Annealed Berylco 25) on Explorer 16	8.250	414	1.66
Stainless-steel (Half-hard 302) on Explorer 23	8.020	1030	1.85
Aluminium (1201-H6/9) on Ariel 2, LDEF (MAP), MFE , & TICCE	2.720	175	0.87
Aluminium (1145-H19) for SMM louvres	2.705	145	0.85
Aluminium (2024-T3) on Pegasus 1,2, & 3	2.770	459	1.00
Aluminium (6061-T6) on LDEF	2.700	310	0.94

*Derived from the chosen marginal penetration equation (McDonnell & Sullivan,1992)

Table 2: Target material specifications for penetration data used in Table 1.

Spacecraft name	Mean altitude, H (km)	Meteoroid velocity, Vp (km sec-1)* at H (km) altitude	Earth shielding factor (h)	Gravitational enhancement factor (c)	Sensitivity enhancement factor (S)
Explorer 16	965.18	22.555	0.7291	1.2719	1.1790
Explorer 23	721.79	22.638	0.6967	1.2812	1.1850
Ariel 2	823.50	22.603	0.7112	1.2772	1.1825
Pegasus 2 & 3	578.93	22.689	0.6929	1.2869	1.1887
Solar Max	532.75	22.706	0.6642	1.2889	1.1899
MFE on STS-3	241.00	22.818	0.5827	1.3016	1.1979
LDEF	458.00	22.733	0.6485	1.2920	1.1918
TICCE on EuReCa	508.00	22.715	0.6592	1.2899	1.1905

Table 3. Earth shielding, gravitational & sensitivity enhancement factors

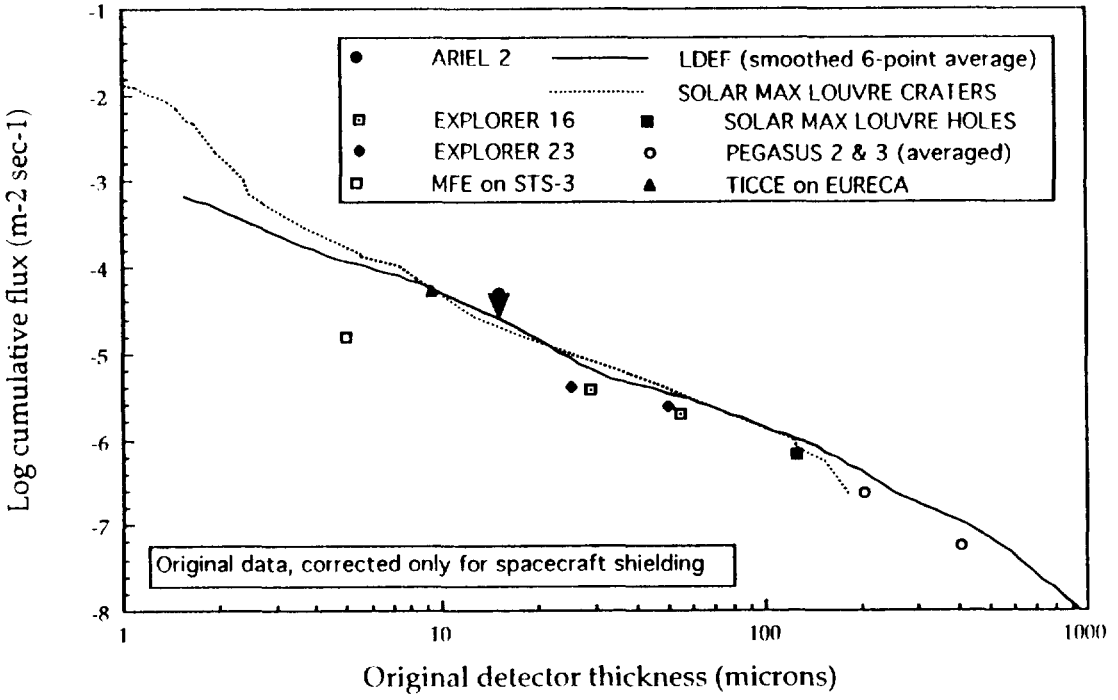

Fig.1: Selected meteoroid satellite data (1962 - 1993) plotted at the detector thickness irrespective at target material. It is corrected for (local) spacecraft shielding but not Earth shielding. (Note: the Ariel 2 datum point is an upper limit).

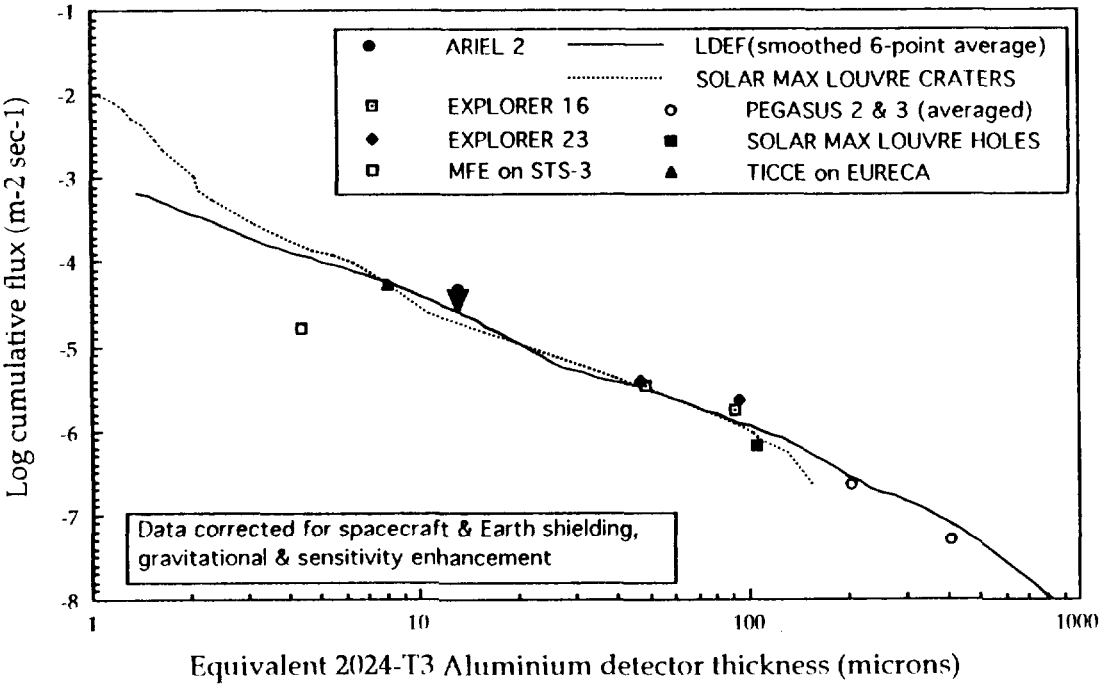

Fig. 2 Meteoroid satellite data (1962 - 1993). The data refer to unshielded exposure at 1 A.U. heliocentric distance at a velocity of 20 km sec $^{-1}$ The corresponding velocity at LDEF's altitude would be 22.3 km sec $^{-1}$ With the exception of data below f max=20 microns, no significant flux changes over the 30 year period are demonstrated. (Note: the Ariel 2 datum point is an upper limit).

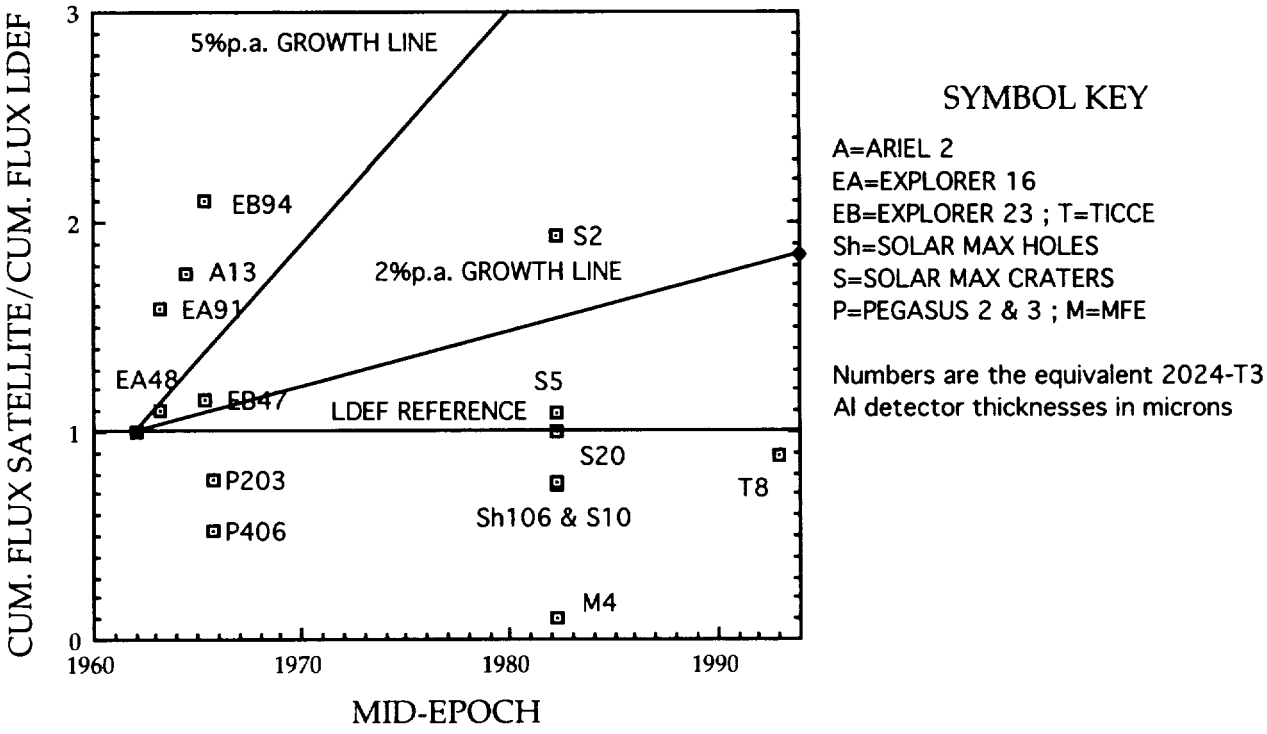

Fig. 3 Selected satellites flux data referenced to the LDEF 1984 - 1990 6-point average flux at the same detector thickness. Also shown for reference are the 2% and 5% per annum growth rates applicable respectively to large and small particles in the NASA Space Station Environmental Models.

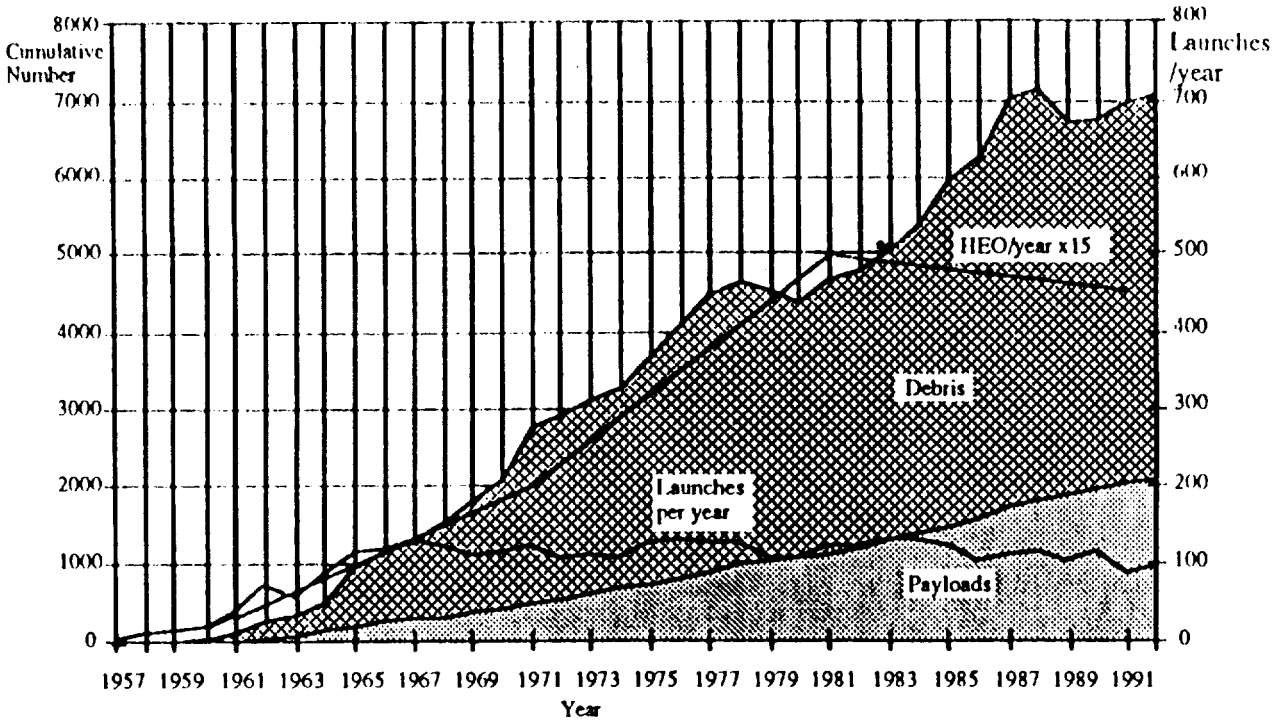

Fig. 4. Satellite launch rates and the in-orbit population of both satellites and space debris. Also shown for comparison is the high eccentric orbit launch rate which is shown in more detail in Fig. 5. Data courtesy S.P. Despande 1993.

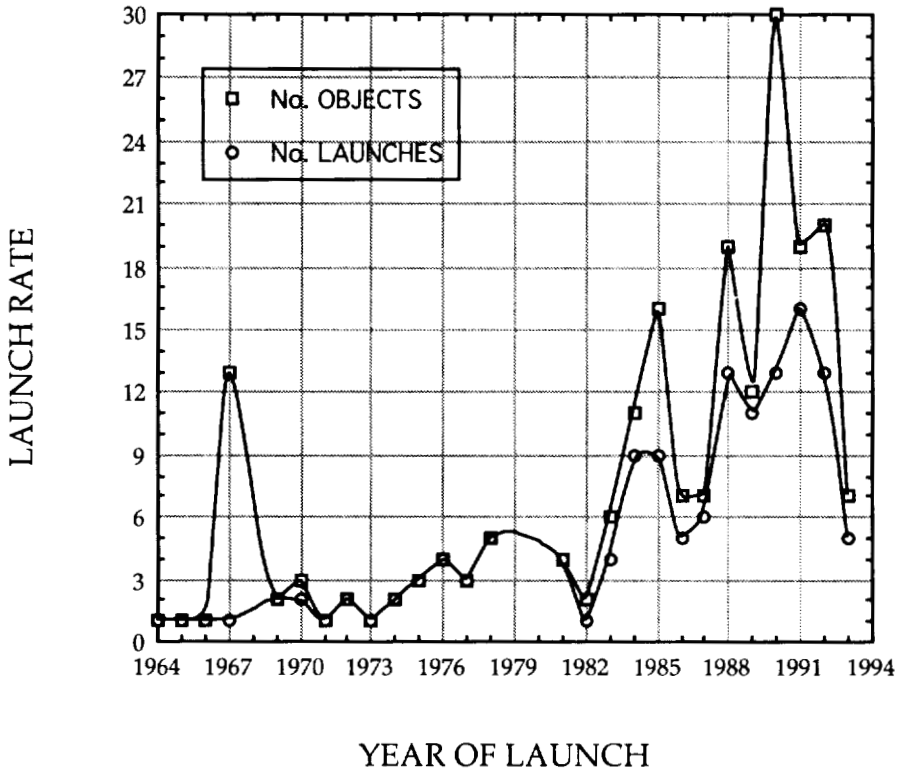

Fig. 5. Launch rate profile for GTO objects with eccentricities between 0.65 and 0.75 and inclinations to 60°. Data from the ESA DISCOS database, courtesy H Klinkrad, 1992.

LDEF INTERPLANETARY DUST EXPERIMENT (IDE) RESULTS

John P. Oliver, S. F. Singer, J. L. Weinberg, C. G. Simon, W. J. Cooke
Institute for Space Science and Technology, 1810 NW 6th Street, Gainesville, Florida 32609
Phone: 904/371-4778, Fax: 904/372-5042

P. C. Kassel, W. H. Kinard
NASA Langley Research Center, Hampton, Virginia 23665-5225
Phone: 804/864-3976, Fax: 804/864-8094

J. D. Mulholland
POD Associates, Inc., Albuquerque, NM 87106
Phone: 505/243-2287, Fax: 505/243-4677

J. J. Wortman
North Carolina State University, Dept. Elec. & Comp. Eng. Box 791, Raleigh, North Carolina 27695
Phone: 919/515-5255, Fax: 919/515-3027

ABSTRACT

The Interplanetary Dust Experiment (IDE) provided high time resolution detection of microparticle impacts on the Long Duration Exposure Facility satellite. Particles, in the diameter range from 0.2 microns to several hundred microns, were detected impacting on six orthogonal surfaces of the gravity-gradient stabilized LDEF spacecraft. The total sensitive surface area was about one square meter, distributed between LDEF rows 3 (Wake or West), 6 (South), 9 (Ram or East), 12 (North), as well as the Space and Earth ends of LDEF. The time of each impact is known to an accuracy that corresponds to better than one degree in orbital longitude. Because LDEF was gravity-gradient stabilized and magnetically damped, the direction of the normal to each detector panel is precisely known for each impact. The 11 1/2 month tape-recorded data set represents the most extensive record gathered of the number, orbital location, and incidence direction for microparticle impacts in low Earth orbit.

Perhaps the most striking result from IDE was the discovery that microparticle impacts, especially on the Ram, South, and North surfaces, were highly episodic. Most such impacts occurred in localized regions of the orbit for dozens or even hundreds of orbits in what we have termed Multiple Orbit Event Sequences (MOES). In addition, more than a dozen intense and short-lived "spikes" were seen in which impact fluxes exceeded the background by several orders of magnitude. These events were distributed in a highly non-uniform fashion in time and terrestrial longitude and latitude.

1. INTERPLANETARY DUST EXPERIMENT

The Interplanetary Dust Experiment (IDE) was conceived to permit a discrimination between cosmic dust and orbital debris, and to characterize the dust in terms of mass, velocity, time, and trajectory[1]. The IDE experiment occupied portions of six trays, one each on the leading and trailing edges, the Earth and space ends, and the "north" and "south" edges. Five of the trays carried 80 active detectors, while the spaceward tray bore only 59. The total detector area was slightly less than one square meter. Each detector was a 50-millimeter diameter metal-oxide-silicon (MOS) semiconductor capacitor («B_Ref287687536 * mergeformat »). Each detector was charged by a bias voltage supply through a current limiting resistor. An impacting microparticle with sufficient energy could vaporize the dielectric layer and cause a transient discharge of the capacitor. The associated electronics counted and time-tagged each discharge. The thickness of the oxide determines the energy required to trigger a discharge of the capacitor. The thinner dielectric requires less impact energy, providing higher sensitivity. The thickness of the oxide dielectric of 60 % of the detectors on each panel was 0.4 microns; it was 1.0 microns for the remaining 40%. Pre-flight calibration indicated that the sensors lower limits of detection, for hypervelocity particles, were roughly 0.2 microns and 0.5 microns diameter, respectively[2]. The upper

hypervelocity particles, were roughly 0.2 microns and 0.5 microns diameter, respectively[2]. The upper detection limit for both types (representing the particle size expected to physically break the detector substrate) was 100 micron in diameter. Identical detectors were flown on Explorer 46 (the Meteoroid Technology Satellite - MTS) in 1972.

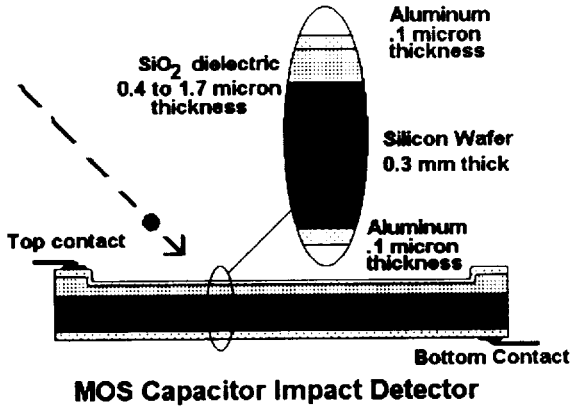

Figure 1. Cross-section of typical MOS impact detector. The IDE sensors used 0.4 and 1.0 micron thick dielectric.

An on-board tape recorder was included to record the time of each impact, identified by panel and by wafer thickness, but not by specific detector. The time resolution of the IDE clock was about 13.1 seconds. About every 2.4 hours, there was also a dump to the tape of the status (illuminated or dark) of six sun sensors, the status (active or shorted) of each detector, and other "housekeeping" information. Sunrise and sunset information from the sun sensors allowed calibration of the IDE clock. IDE activation occurred at 1984 April 07d 17h 23m 43.8s ± 0.3s UTC.

Tape was only supplied for the nominal nine-month mission, and it ran out on day 346. Post-flight verification shows that there was only one recording anomaly during this time and no significant data were lost. About 15,000 impacts were recorded on the 459 detectors during the active phase of the mission. For the remaining 4.7 years of flight, the detectors continued to receive impacts which left physical craters, but no time-resolved information was recorded.

2. TIME-RESOLVED DATA

Much of the information on orbital debris and cosmic dust in the near-Earth space environment has come from the examination of surfaces recovered after exposure in orbit[3,4,5]. While such information has provided valuable information on mean fluxes, it has been deficient in detailing the near-Earth micrometeoroid and space debris environment in two crucial ways. First, most of these spacecraft have not maintained their orientation in an Earth-centered reference frame. Thus the measured fluxes have been averaged over a range of directions relative to the orbital velocity vector and to the celestial sphere. Second, since the time of occurrence of each impact cannot be determined, it is not possible to investigate variations in particle flux with position and time; that is, spatio-temporal information cannot be obtained from such data analysis.

In contrast with these earlier studies, the controlled orientation and high time resolution of the IDE data provide, for the first time, a detailed, extensive data set well adapted to analysis of the spatio-temporal characteristics of orbital debris in near-Earth orbit. An examination of the IDE data

C-5

(«B_Ref287584489 * mergeformat ») shows immediately that the detected particle fluxes were neither uniform in time nor in space. All impacts on the 0.4 micron IDE detectors are displayed in this "seismograph" plot. The entire 346-day active data recording phase of the mission is represented along the horizontal axis. The impact rate on each of the six orthogonal surfaces is indicated by the vertical amplitude of each trace. Note that the impact rates represented in this figure are raw rates, uncorrected for effective area. This does not significantly change the appearance of the plot.

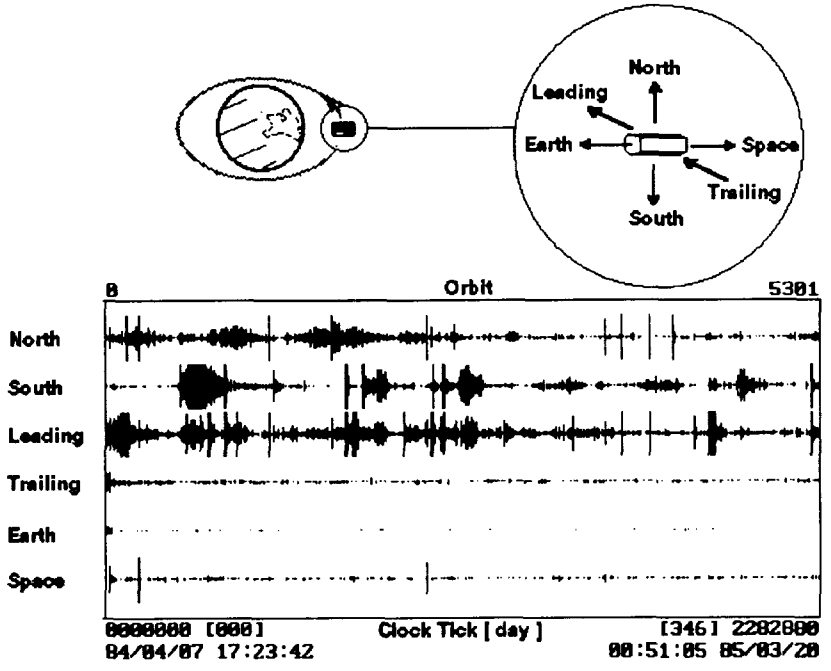

Figure 2. All impacts recorded on the 0.4 micron dielectric thickness (high sensitivity) IDE detectors during the 346-day time-resolved phase of the mission.

Examination of «B_Ref287584489 * mergeformat » suggests a number of interesting points:
•· activity on the northward and southward facing surfaces was very different,
· all surfaces except trailing and Earth exhibited occurrences of short transient "spikes",
· the north, south, and leading edges exhibited extended periods of increased activity which were unseen on the other three surfaces,
the trailing edge, which should be shielded from orbital debris by the body of the spacecraft, showed most of its activity during the early portion of the mission,
· and the Earth facing surface (which should be very well protected by the proximity of the Earth) also showed activity during the first week of the mission.

The activity shown on the trailing edge and the Earth end is almost certainly due the shuttle orbiter. It is well established that the shuttle will be surrounded by a "Spacecraft Induced Atmosphere"[6]. The orbiter moved away from LDEF almost immediately after deployment, partly to avoid contaminating LDEF. The (approximately) one week duration of the impact activity seen on the shielded surfaces of LDEF suggests that a significant amount of material was distributed by the shuttle in orbits which allowed "catching up" with the LDEF from behind and from beneath.

3. MULTIPLE ORBIT EVENT SEQUENCES AND SPIKES

Closer examination of the data shows that in addition to being non-uniformly distributed in time, the IDE impact data are non-randomly distributed in both time and space. In Figure 3, a portion (taken from the leading edge high sensitivity detector data) of the IDE data set is examined at increasing time

resolution. The upper trace in this figure represents the same information as the leading edge trace of Figure 2. The data of 4 June 1984 are selected out and displayed in the middle trace.

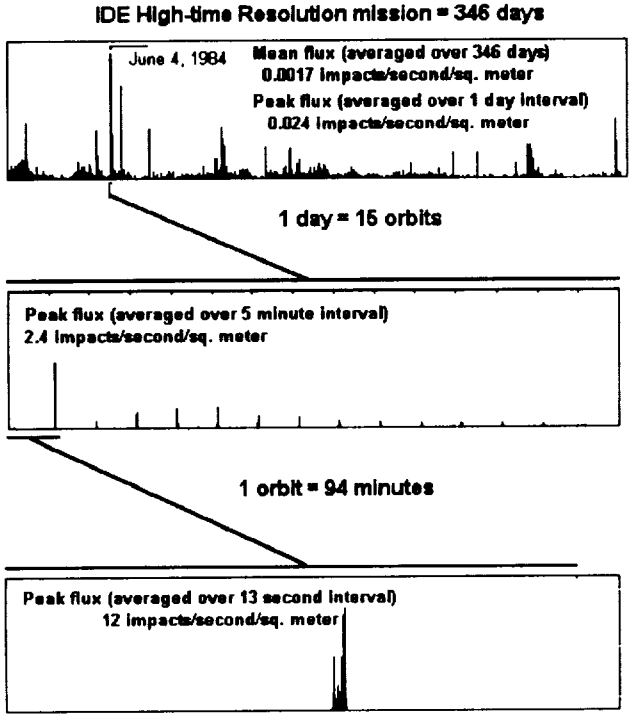

Figure 3. Observed activity on the leading (ram) edge of LDEF as recorded by the high sensitivity (0.4 micron dielectric) detectors of IDE. Note that **every** impact is displayed. The lack of impacts between the obvious events is real.

The regular spacing of the impacts matches the LDEF orbital period of approximately 94 minutes. The final trace of this figure displays a single 94-minute segment of the 4 June data. All the impacts during this segment occurred during a period of less than five minutes. As may be seen in these figures, the IDE data set contains many impacts which occurred in "bursts", during which numerous impacts were recorded in a short time. Such a burst we have designated an event. At the finest resolution, events may show structure. For example, the 4 June event illustrated here appears to be double. A number of these multi-event sequences appear in the IDE data set. As illustrated in Figure 3, events may be seen to reoccur each time the LDEF returned to the same point in its orbit. These we call multi-orbit event sequences (MOES).

A significant conclusion resulting from the high time resolution of LDEF IDE data displayed in Figure 3 is that the instantaneous fluxes observed are much greater than the mean fluxes. As shown in the text imbedded in the figure, the mean flux calculated from the 346-day data set is 0.0017 impacts/second/sq. meter. The peak flux, observed with the IDE time resolution of 13 seconds, was 12 impacts/second/sq. meter, almost 4 orders of magnitude greater! While long-term fluxes may be useful for engineering structures and similar purposes, there are circumstances where peak fluxes may be more useful. The IDE results indicate that an optical surface such as a window (which could be degraded by small particle impacts) could need replacement far sooner than would be predicted by mean fluxes.

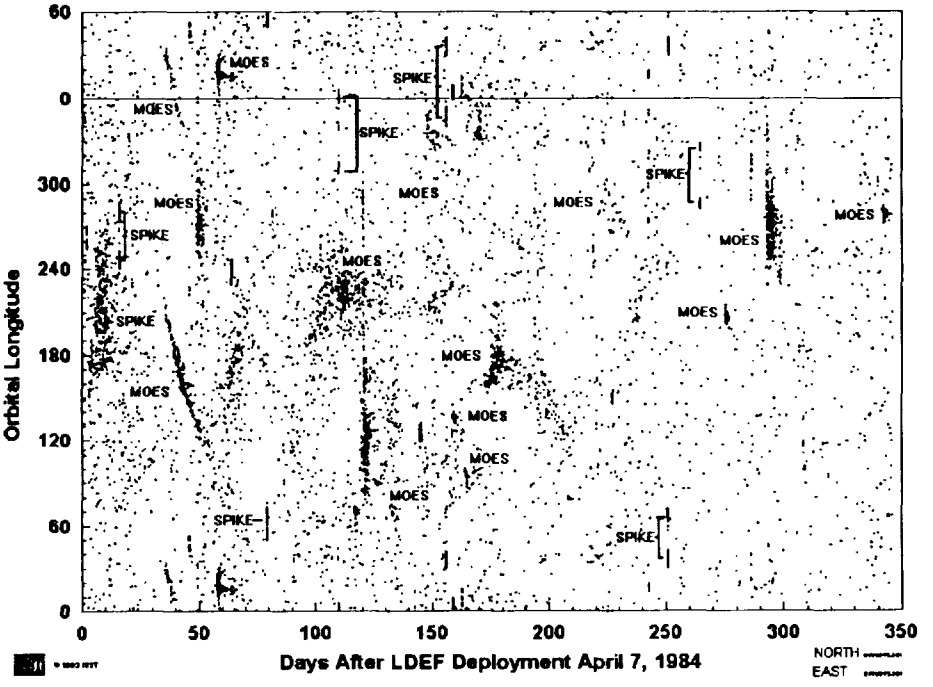

Figure 4. Impacts on the high activity surfaces as a function of LDEF orbital position and time for the 346 day time-resolved data set. Note that the orbital longitude axis partially repeats at the top.

While the structure of an individual MOES is illustrated in Figure 3, the distribution of the observed MOES with orbital location and time is best illustrated in a plot such as Figure 4. In this figure, all impacts on the high sensitivity detectors mounted on the North, Ram, and South LDEF surfaces are plotted as a function of LDEF orbital longitude and time. A number of MOES are indicated. Also indicated are "spikes", defined as sudden bursts of impacts which occurred on only a *single* orbit. These spikes were the most intense individual events observed by IDE. In addition to their lack of multiple-orbit repetition, spikes differ from the events of an MOES by frequently appearing as pairs of events, separated in orbital longitude by 10 to 30 degrees. This "bifurcated" structure of spikes is visible in Figure 4.

Most of the 15,000 impacts recorded by IDE occurred in MOES. It is natural to assume that such events result from the intersection of the orbit of the LDEF with that of a concentration of orbital debris. An examination of a typical MOES (*e.g.* the June 4 event shown in Figure 3.) shows two important characteristics:

1) the orbital debris particle orbits are eccentric; if they were circular, the IDE detectors would register the group twice each orbit since a circular orbit *must* intersect LDEF's orbit (which is essentially circular) at two points, and

2) the particles must be "smeared out" along the orbit in some ring-like or torus structure. If the particles were concentrated in a "clump", the encounters with LDEF would not occur over an extended sequence of consecutive orbits, unless the period of the particle orbit was the same as that of LDEF, an unlikely circumstance in general.

In order to deduce as much as possible about the orbit of the impacting particles in an MOES, we have developed the "method of differential precession".[7] The goal of this method is to obtain the orbital characteristics of the particles which struck the IDE detectors during a MOES by an analysis of the time variation of the LDEF position over the series of encounters. This analysis makes use of the fact that the non-sphericity of the Earth induces the pole of an object's orbit to precess, resulting in a cyclic change in

the position of the line of nodes of the orbit (in the case of LDEF, the period of this precession is approximately 53 days). The oblateness of the Earth also causes the line of apsides of the orbit to precess, the point of perigee advancing if the orbital inclination is low and regressing otherwise. In general, bodies in different orbits will have different rates of these precessions, and should two of these orbits intersect, the differences in the precession rates will cause the point(s) of intersection to vary with time. If the characteristics of one of the intersecting orbits are known, the migration of the point of intersection may be used to determine the precession rates and orientation of the unknown orbit, which then may be used to calculate a family of candidate orbits.

4. DISTRIBUTION OF SPIKES IN TIME AND LOCATION

Spikes are not directly subject to analysis by the method of differential precession since, by definition, they appear to be single events (albeit bifurcated). Never-the-less, the observed spikes show interesting patterns in their times of incidence that may yield useful clues as to their origin. Most spikes occurred on the North and Ram LDEF surfaces. Three spikes occurred primarily on the Space surface. Virtually no spike activity was visible on the South surface.

A plot of all spikes observed on the North LDEF surface as a function of the sub-LDEF terrestrial latitude and longitude is shown in Figure 5. These events were almost all concentrated above the northern hemisphere, and between longitudes 80 and 200 degrees east. An examination of launch activities has shown no correlation between Soviet or other launches and the occurrence of spikes.

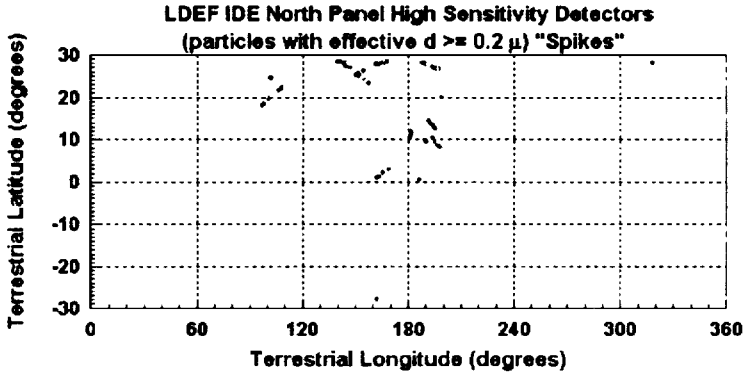

Figure 5. Location of LDEF ground track (sub LDEF terrestrial latitude and longitude) during spikes.

In the process of studying the event times of spikes, it was realized that many, especially those that exhibited bifurcation, appeared to have a 15.5 day periodicity (see Figure 6). This could be explained if the source of the spikes was a highly concentrated clump of material in an orbit whose beat frequency with LDEF was 15.5 days. Unfortunately, the short lifetimes of micron sized orbital debris particles does not allow such a clump to have a lifetime measurable in days, much less months. It appears more likely that the spikes result from material leaving some long-lifetime orbiting object. Again, this hypothetical source object must have an orbit which has a 15.5 day beat frequency with LDEF. One possibility that we have examined is the Solar Maximum Mission satellite (SMM). SMM was in virtually the same orbit as LDEF, differing only in semi-major axis. After deploying LDEF in April, 1984, the shuttle Challenger then increased its altitude by about 20 km. and undertook the repair of the SMM. The beat frequency between the LDEF orbit and that of an object 19.3 km. above (or below) is 15.5 days. The spikes do not, however, coincide with the times of closest approach between LDEF and SMM, as calculated from the appropriate orbital elements. It seems likely, however, that material from SMM is involved in the IDE spikes. The terrestrial latitude and longitude concentration shown in Figure 5 would then presumably be a coincidence.

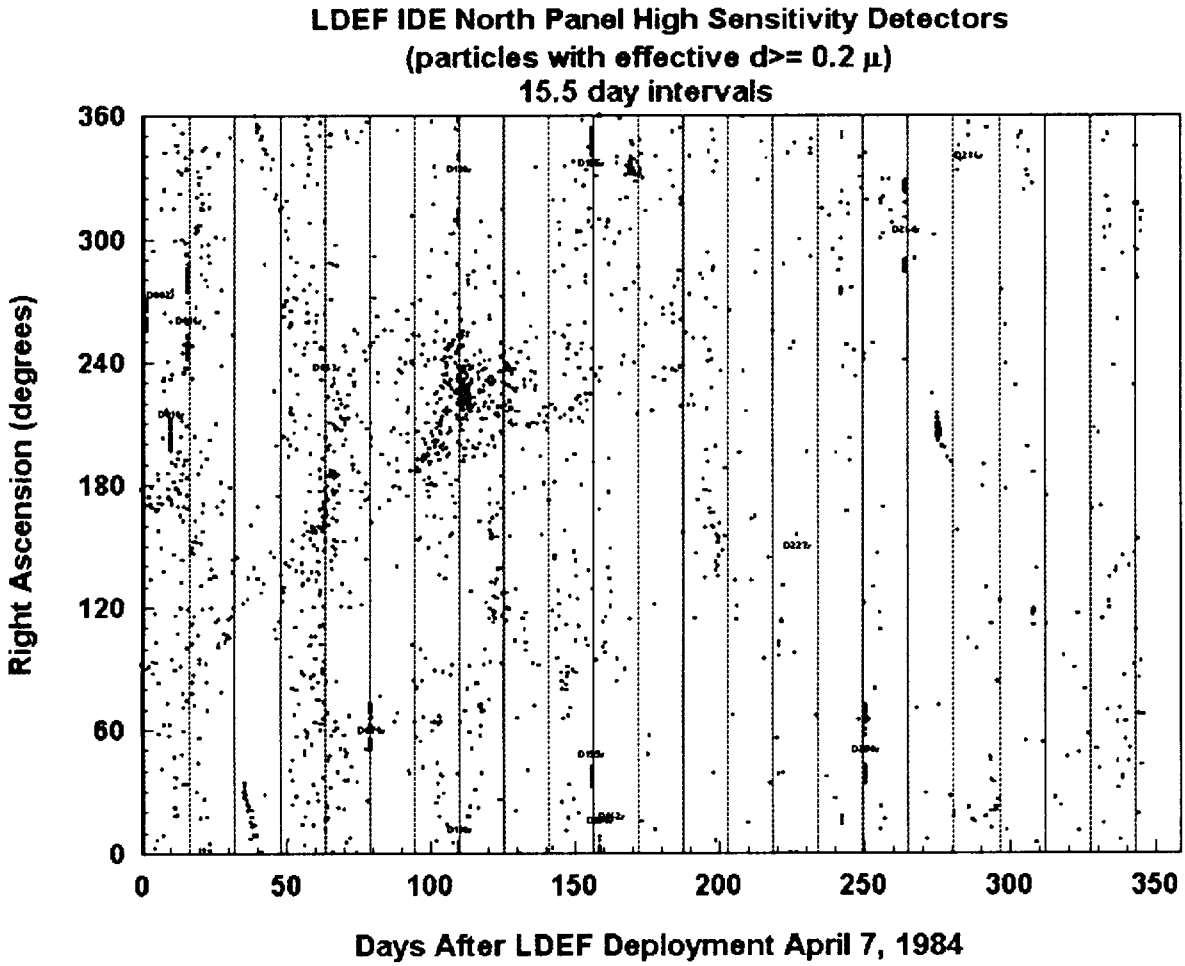

Figure 6. Spikes on LDEF North surface as a function of time. Note that many spikes occurred very near to some multiple of 15.5 days (as indicated by the vertical plot divisions).

5. SUMMARY

The LDEF IDE experiment detected many discrete events which can be associated with orbital debris. Indeed, the majority of micron sized particles detected by IDE were contained in the MOES debris cloud events. Many of these events were long-lived enough that they could be analyzed in terms of the impactor orbital elements. This longevity, in itself, suggests that much of the microparticle orbital debris environment results from material being released from longer-lived larger objects. Discrete events termed spikes were observed that may be the result of material released from the Solar Maximum Mission satellite.

6. ACKNOWLEDGMENTS

We have had a number of useful discussions of these data with many of our colleagues. We wish to particularly acknowledge discussions with Don Kessler. This research was supported, in part, by NASA grant NAG 1-1218.

1. Singer, S. F., Stanley, J. E., and Kassel, P. C., "The LDEF Interplanetary Dust Experiment", in: *Properties and Interactions of Interplanetary Dust*, eds. Giese, R. H. and Lamy, P., Reidel, Dordecht, 117-120 (1985).

2. Kassel, P. C., "Characteristics of capacitor-type micrometeoroid flux detectors when impacted with simulated micrometeoroids", Technical Note D-7359, NASA, Washington D.C. (1973).

3. Zook, H. A., McKay, D. S., and Bernhard, R. P., "Results From Returned Spacecraft Surfaces", in *AIAA/NASA/DOD Orbital Debris Conference: Technical Issues & Future Directions*, AIAA-90-1349 (1990)

4. Laurance, M. R. and Brownlee, D. E., "The flux of meteoroids and orbital space debris striking satellites in low Earth orbit", Nature, Vol. 323, 136-138 (1986)

5. Warren, J. L. et al., "The Detection and Observation of Meteoroid and Space Debris Impact Features on the Solar Max Satellite", in *Proceedings of the 19th Lunar and Planetary Conference*, Lunar and Planetary Institute, Houston, 641-657 (1989)

6. Weinberg, J. L., "Optical Observations From the Space Shuttle", in *Advances in Space Research*, vol. 7, no. 5, 203-205 (1987)

7. Cooke, W. J., Oliver, J. P., and Simon, C. G., "The Orbital Characteristics of Debris Particle Rings as Derived from IDE Observations of Multiple Orbit Intersections with LDEF", presented at the *Third LDEF Post-Retrieval Conference*, Williamsburg, VA, November 1993.

THE ORBITAL CHARACTERISTICS OF DEBRIS PARTICLE RINGS AS DERIVED FROM IDE OBSERVATIONS OF MULTIPLE ORBIT INTERSECTIONS WITH LDEF

William J. Cooke, John P. Oliver and Charles G. Simon
Institute for Space Science and Technology
Gainesville, FL 32609
Phone: 904/371-4778, Fax: 904/372-5042

SUMMARY

During the first 346 days of the LDEF's almost 6 year stay in space, the metal oxide silicon detectors of the Interplanetary Dust Experiment (IDE) recorded over 15,000 impacts, most of which were separated in time by integer multiples of the LDEF orbital period (called *multiple orbit event sequences*, or MOES). Simple celestial mechanics provides ample reason to expect that a good deal of information about the orbits of the impacting debris particles can be extracted from these MOES, and so a procedure, based on the work of Greenberg[1], has been developed and applied to one of these events, the so-called "May swarm". This technique, the "Method of Differential Precession," allows for the determination of the geometrical elements of a particle orbit from the change in the position of the impact point with time. The application of this approach to the May swarm gave the following orbital elements for the orbit of the particles striking LDEF during this MOES: a = 6746.5 km; $0.0165 < e < 0.025$; $i = 66°.55$; $\Omega_0 = 179°.0 \pm 0°.2$; $\omega_0 = 178°.1 \pm 0°.2$.

INTRODUCTION

For 346 days after the deployment of the LDEF satellite on April 7, 1984, the tape recorder belonging to the Interplanetary Dust Experiment (IDE) stored information on over 15,000 impacts made by submicron and larger-size particles on its metal oxide silicon (MOS) detectors[2]. These detectors were mounted on trays facing in six orthogonal directions — LDEF ram and trailing edge, the poles of the LDEF orbit (north and south), and radially inward (towards the Earth) and outward (towards space). The 13.1 second time resolution provided by the IDE electronics, combined with the high sensitivity of the MOS detectors and large collecting area (~ 1 m^2) of the experiment, conclusively showed that the small particle environment at the LDEF altitude of 480 km was highly time-variable, with particle fluxes spanning over four orders of magnitude[3].

---

[1] Greenberg, R., *Orbital Interactions: A New Geometrical Formalism*, Astronomical Journal., **87**, pp. 184-195 (1982)

[2] "IDE Spatio-Temporal Impact Fluxes and High Time-Resolution Studies of Multi-Impact Events and Long-Lived Debris Clouds", J.D. Mulholland, S.F. Singer, J.P. Oliver, J.L. Weinberg, W.J. Cooke, P.C. Kassel, J.J. Wortman, N.L. Montague, W.H. Kinard, LDEF - 69 Months in Space: First LDEF Post-Retrieval Symposium, (NASA CP-3134), January, 1992, pp. 517-528

[3] See "LDEF Interplanetary Dust Experiment (IDE) Results", J.P. Oliver *et al.*, this volume.

It is highly desirable to learn as much as possible about the orbital characteristics of the particles which struck the IDE trays. At a minimum, these characteristics can determine whether the particles were interplanetary in origin or debris from a satellite or spent rocket. If the particles can be identified as debris, then it becomes possible to determine their parent body, which gives a clue as to which objects in Earth orbit are major contributors to the orbital debris population. Unfortunately, the IDE data permit the unique determination of only the position of the impacted particle (which is the same as that of LDEF at the time of impact), whereas an unambiguous determination of the particle's orbit requires a knowledge of both the position and the particle velocity. The IDE sensors were threshold detectors[4], triggered by any particle with sufficient energy to damage the detector dielectric, and so were rough indicators of particle energy, not velocity. It is therefore impossible to use the IDE data to obtain an orbit for a single impacting particle. This situation improves, however, for an impacting group of particles which have the same orbit. In this case, the particles will strike multiple IDE trays, permitting a rough determination of the direction of the group's velocity, which, when combined with the position information, yields a family of possible candidate orbits for the particles. The situation improves even more if the orbit of the group is such that it encounters LDEF multiple times, for then the change in the LDEF position at the encounter times can be used to produce a family of possible orbits, which can be further constrained by the velocity direction information.

Fortunately, most of the 15,000 impacts recorded by IDE occurred in such groups, which we term *events*. These events were of two types — the *spikes*, which were single, isolated events of high intensity and the *multiple orbit event sequences* (MOES), which were series of events with the events separated in time by integer multiples of the LDEF orbital period. The spikes are discussed in another paper in these proceedings; here we shall concentrate on the multiple orbit event sequences, as they were produced by particles with orbital characteristics such that the group had multiple encounters with LDEF. Even though the spikes were generally more intense, the MOES could be quite long-lived, some lasting for many days. As discussed in the previous paragraph, it is these MOES which can yield the most information about the particles' orbit.

Figure 1 is a "seismograph" plot of a typical MOES; time increases to the right along the horizontal axis, and the intensities of the events are roughly indicated by the extent of the vertical lines. A cursory glance reveals two important bits of information about the particle orbits involved in MOES:

1) the particle orbits are eccentric; if they were circular, the IDE detectors would register the group twice each orbit, as a circular orbit would intersect LDEF's orbit (which is essentially circular) at two points, and

2) the particles must be "smeared out" along the orbit in some ring-like or torus structure. If the particles were concentrated in a "clump", the encounters with LDEF would not occur at integer multiples of the LDEF orbital period, unless the period of the particle orbit was the same as that of LDEF, a highly unlikely circumstance.

---

[4] For details on the IDE detectors, see "Long-term Particle Flux Variability Indicated by Comparison of Interplanetary Dust Experiment (IDE) Timed Impacts for LDEF's First Year in Orbit with Impact Data for the Entire 5.77 Year Orbital Lifetime", C.G. Simon, J.D. Mulholland, W.J. Cooke, J.P. Oliver, P.C. Kassel, LDEF - 69 Months in Space: Second Post-Retrieval Symposium, (NASA CP-3194), April, 1993, pp. 693-704

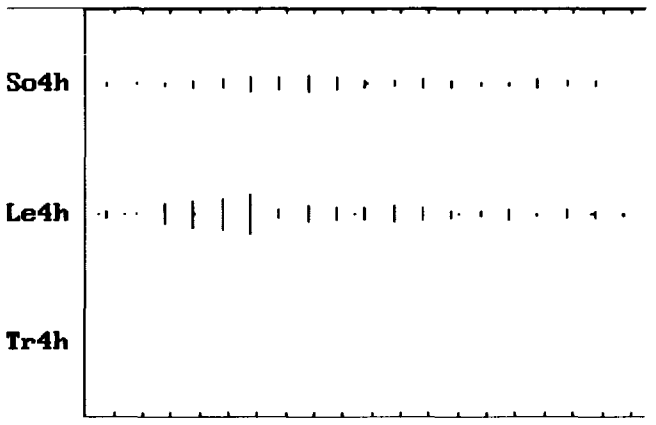

Figure 1: Typical MOES (not the May swarm). Impacts on the south (So4h), ram (Le4h), and trailing (Tr4h) surfaces are shown. The tick marks along the top and bottom are spaced at intervals of a LDEF orbital period.

This information is about all that can be determined from a visual inspection of the MOES in the IDE data set. Clearly, it is necessary to develop a technique that will extract additional information about the particles' orbit. We have arrived at such a technique, the "Method of Differential Precession", which shall be summarized and applied in the following pages.

THE METHOD OF DIFFERENTIAL PRECESSION

Overview

The goal of the Method of Differential Precession is to obtain the orbital characteristics of the particles which struck the IDE detectors during a MOES by an analysis of the time variation of the LDEF position over the series of encounters. This analysis makes use of the fact that the non-sphericity of the Earth induces the pole of an object's orbit to precess, resulting in a cyclic change in the position of the line of nodes of the orbit (in the case of LDEF, the period of this precession is approximately 53 days). The oblateness of the Earth also causes the line of apsides of the orbit to precess, the point of perigee advancing if the orbital inclination is low and regressing otherwise. In general, bodies in different orbits will have different rates of these precessions, and should two of these orbits intersect, the differences in the precession rates will cause the point(s) of intersection to vary with time. If the characteristics of one of the intersecting orbits are known, the migration of the point of intersection may be used to determine the precession rates and orientation of the unknown orbit, which then may be used to calculate a family of candidate orbits.

This concept is illustrated more clearly in figures 2 and 3, which depict the geometry of the situation with regard to LDEF. Following conventional notation, Ω_L represents the position of the ascending node of the LDEF orbit (which is known) and Ω_p represents the ascending node of the unknown orbit of the impacting particles. The position of the perigee of the unknown orbit is represented by ω; LDEF's orbit is essentially circular ($e \sim 10^{-4}$) and so has no perigee. The inclinations of the two orbits are i_L and i_p, and u_L and u_p denote the arguments of latitude of the point of intersection, measured

counterclockwise along the orbits from the respective ascending nodes. We are using the argument of latitude rather than the more conventional true anomaly, ν, due to the fact that one of the orbits is circular. In the case of an elliptical orbit, the two quantities are related by $\nu = u - \omega$. Figure 2 shows that, for any given time, the known quantities Ω_L and i_L determine the location of the unknown orbit's node, Ω_p, provided that the inclination of the unknown orbit is specified. Similarly, figure 3 shows that Ω_L, i_L and u_L determine u_p if i_p is specified. As time progresses, the orbits will precess at different rates, resulting in the movement of the point of impact (intersection), with a corresponding change in u_L and u_p.

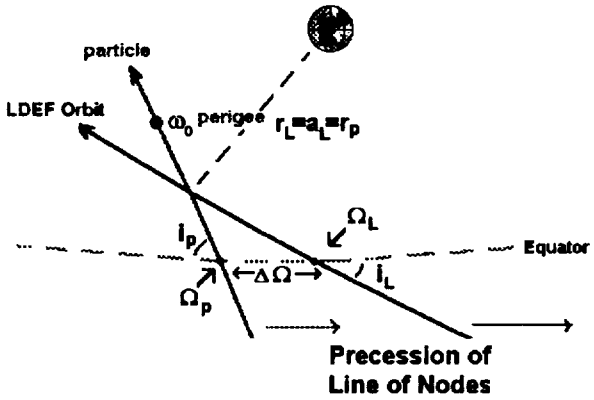

Figure 2: Differential precession of the lines of nodes

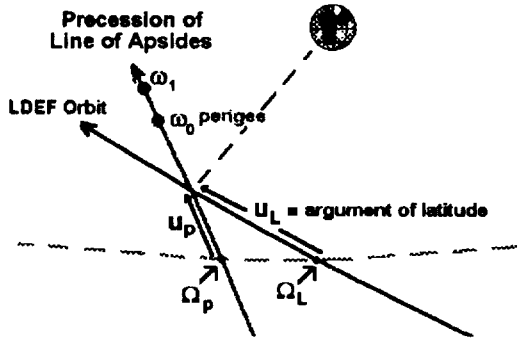

Figure 3: Precession of the line of apsides

Assuming that the inclination of the particle orbit is known, our knowledge of the LDEF orbit enables us to compute Ω_p and u_p for each impact occurring in a given MOES. The variation in Ω_p with time directly yields the precession rate of the line of nodes of the particle orbit, $\dot{\Omega}_p$, which can then be used to construct a family of possible candidate orbits by means of the well-known relation

$$\dot{\Omega} = \frac{-3n}{2} J_2 \left[\frac{R_e}{a(1-e^2)} \right]^2 \cos i_p, \tag{1}$$

where R_e is the radius of the Earth and J_2 is the second gravitational harmonic. The semi-major axis and eccentricity of the particle orbit are denoted by a and e, while n is the mean motion of the particles. The family of candidate orbits will have values of a and e specified by equation (1), and can be constrained by the simple fact that any candidate orbit must intersect that of LDEF at some point. Information about the direction of the particle velocity obtained from the numbers of impacts on the IDE trays during the MOES can also be employed to derive the vector intercept of the particles, which further constrains the range of allowed orbits. It should be noted that even though this technique can completely determine the orientation of the particle orbit (i_p, Ω_p, and ω), the lack of velocity information still prohibits a unique determination of the orbit's size and shape.

Unfortunately, the inclination of the particle orbit is not known, forcing the adoption of an iterative scheme in order to achieve a solution. One starts by assuming a reasonable value for the particle inclination, which will enable the determination of the u_p's and Ω_p's at the times of impact, and, consequently, $\dot{\Omega}_p$. It is also necessary to obtain the rate of the perigee advance of the particle orbit. This

can be done by realizing that, at each impact, the position of LDEF must be the same as that of the particle, thus

$$r_L - \frac{a(1-e^2)}{1+e\cos(u_p-\omega)} = 0 \tag{2}$$

Equation (2) implies that $\dot{u}_p = \dot{\omega}$, and we see that the time variation of the argument of latitude of the impact point, measured along the particle orbit, is equal to the rate of the advance of the perigee. The ratio $\dot{\Omega}_p/\dot{\omega}$ can now be formulated and compared to the theoretical value, which is given by

$$\left(\frac{\dot{\Omega}_p}{\dot{\omega}}\right)_i = \frac{-2\cos i_p}{5\cos^2 i_p - 1} \tag{3}$$

If the ratios are not equal, then a new i_p is calculated according to Newton's method or some similar scheme, and the process repeated until the values agree. In addition to the assumption of no non-gravitational forces, this method also requires that all particles striking LDEF during the MOES share the same orbit, which is perfectly reasonable in light of the short duration of each event belonging to a MOES.

Methodology

Based on the above discussion, one may obtain the family of possible particle orbits by proceeding as follows:

1) Obtain the arguments of latitude (u_L) of LDEF at all impact times in the MOE. This is a simple matter, given the LDEF orbital elements and an orbit propagation code.

2) Assume an inclination (i_p) for the orbit of the particles. Good starting values are 30º, 65º, or 82º, as these are representative of most satellite orbits.

3) The difference between the right ascension of the particle orbit ascending node (Ω_p) and that of LDEF (Ω_L) is determined by the argument of latitude of LDEF at the time of impact (u_L), the inclination of the particle's orbit, and the inclination of LDEF's orbit (i_L). The relevant expressions are[5]

$$\begin{aligned} \Delta\Omega &= \Omega_p - \Omega_L \\ u_L &= \tan^{-1}\frac{-\sin\Delta\Omega}{\cot i_p \sin i_L - \cos\Delta\Omega\cos i_L} \end{aligned} \tag{4}$$

At each impact time, equations (4) may be solved for $\Delta\Omega$ (and hence, Ω_p) via Newton's method or some other scheme.

---

[5] Greenberg, R., *Orbital Interactions: A New Geometrical Formalism*, Astronomical Journal., **87**, p. 186. (1982)

4) The slope of a line fit to the Ω_p's and their associated impact times gives the rate of regression of the nodal line of the particle orbit, $\dot{\Omega}_p$.

5) Once the $\Delta\Omega$'s have been determined for the impacts, the corresponding arguments of latitude for the particle orbit are found from

$$\cos u_p = \cos u_L \cos \Delta\Omega + \sin u_L \sin \Delta\Omega \cos i_L$$
$$\sin u_p = \frac{\sin u_L \sin i_L}{\sin i_p} \qquad (5)$$

6) In the absence of non-gravitational forces, the semi-major axis (a) and the eccentricity (e) of the particle orbit remain constant over time. Therefore, equation (2) requires that u_p - ω must also be constant, or $\dot{u}_p = \dot{\omega}$. The slope of a line obtained by a linear regression performed on the u_p's and their associated times yields the progression or regression of the line of apsides, $\dot{\omega}$.

7) Compute the ratio $\dot{\Omega}_p/\dot{\omega}$ and compare to the theoretical ratio obtained from equation (3), which is a function of only the inclination of the particle orbit. If the two are not equal to within a specified tolerance, compute a new i_p by means of Newton's method and repeat steps 3 through 6 until the values agree.

8) Use the values of i_p and $\dot{\Omega}_p$ to determine a family of possible candidate orbits in (a,e) space by means of equation (1). Constrain the range of potential candidates by imposing the requirements that the particle orbit must intersect that of LDEF and must not enter the atmosphere (i.e., the perigee must be greater than 200 km).

Application to the May Swarm MOES

One of the most prominent multiple orbit event sequences observed by IDE began on May 13, 1984, and so has become known as the "May swarm." This MOES can be characterized as being of low intensity (~3 impacts per orbit) and long duration, lasting for over 20 days (300 LDEF orbits), with several hundred impacts recorded on the IDE trays facing in the LDEF ram direction and towards the south pole of the orbit, the majority occurring on the south-facing tray. The long duration of this MOES made it an especially suitable choice for analysis by the differential precession technique, the only drawback being the low intensity of the events. To avoid contamination by the occasional "random" impact, the times chosen were those in which the high sensitivity (0.4 micron dielectric thickness) IDE detectors on the south tray recorded multiple impacts within the same IDE clock "tick" (13.1 seconds). This resulted in a total of 38 points for use in the analysis, spanning a time interval of some 18 days.

The procedure outlined in the previous section was then applied to these data, with the inclination converging to a value of 66°.55 after only a couple of iterations. Table 1 lists the resulting longitudes of ascending node and arguments of latitude of the impact points for the particle orbit, along with the times of impact (in decimal days from LDEF deploy) and the LDEF arguments of latitude of the impact points.

Impact time	u_L (°)	Ω_p (°)	u_p (°)
40.03233	221.90	226.6	339.7
40.1638	227.25	232.0	337.5
40.2922	215.89	217.9	342.2
40.5546	223.27	224.7	339.1
40.6842	218.59	218.4	341.1
40.7499	221.48	221.3	339.8
40.9452	219.09	217.2	340.8
40.9463	224.94	224.0	338.4
41.0106	219.68	217.4	340.6
41.1417	223.38	220.8	339.1
41.2063	219.80	216.2	340.5
41.4682	224.69	220.1	338.5
41.5339	226.96	222.3	337.6
41.7942	223.49	216.5	339.0
41.8599	225.76	218.7	338.1
41.9906	226.95	219.2	337.7
42.0554	224.20	215.5	338.7
42.1856	222.89	213.1	339.3
43.0342	224.80	209.6	338.5
43.0343	225.64	210.5	338.2
43.1635	218.47	201.3	341.1
43.6219	227.67	208.9	337.4
43.8179	228.63	208.7	337.0
43.9480	226.48	205.3	337.8
44.2092	228.04	205.3	337.2
44.3403	230.91	207.8	336.2
45.1233	231.53	203.2	336.0
45.8412	232.45	199.4	335.6
46.0377	236.77	203.2	334.2
47.2122	236.89	195.4	334.2
47.4733	237.80	194.7	333.9
47.5380	235.06	191.0	334.8
47.7988	234.15	188.1	335.1
50.0854	250.65	192.3	330.6
50.1505	249.59	190.6	330.8
50.4769	250.98	190.0	330.5
52.5007	257.84	184.4	329.4
55.3086	271.25	180.9	328.7

Table 1: May swarm times of impact (days from LDEF deploy) and the corresponding LDEF arguments of latitude, with the values of the longitudes of the ascending node of the particle orbit and the particle arguments of latitude for $i_p = 66°.55$.

The two linear regressions (see figures 4 and 5), involving the impact times, Ω_p, and u_p, yielded

$\Omega_{p0} = 179°.0 \pm 0°.2$ (Initial longitude of ascending node for the particle orbit)

$\dot{\Omega}_p = -3°.26 \pm 0°.05 \text{ day}^{-1}$

$\omega_0 = 178°.1 \pm 0°.2$ (Initial argument of perigee for the particle orbit)

$\dot{\omega} = -0°.85 \pm 0°.05 \text{ day}^{-1}$

These four quantities, along with i_p, uniquely specify the orientation of the particle orbit at any given time. Note that the initial value of the argument of the perigee indicates that these particles are striking LDEF near apogee, a somewhat surprising result.

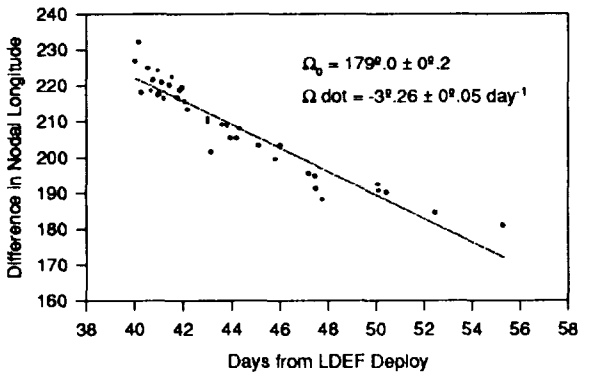

Figure 4: Linear fit to determine nodal line properties

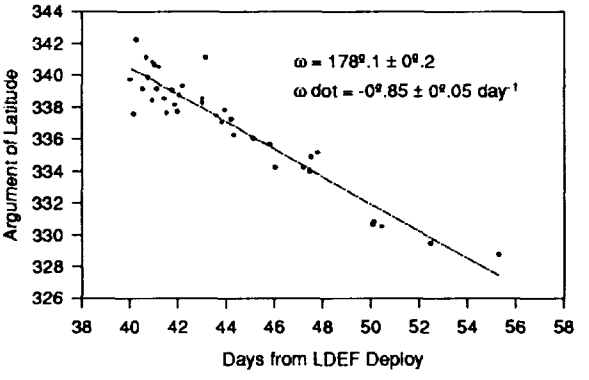

Figure 5: Linear fit to determine apsidal line properties

Next, the precession rate of the particle orbit line of nodes was used in equation (1) to determine the family of possible candidate orbits. These results are displayed in figure 6. Note that the semi-major axis varies little with the eccentricity; in this case, the variation in a is so small that we could confidently set a = 6746.5 km, regardless of the eccentricity. The dual requirement that the candidate orbits have perigees of greater than 200 km in altitude and intersect the LDEF orbit placed strict limits on the allowed values of the eccentricity, which must lie in the range $0.0165 < e < 0.025$.

One of the candidate orbits (e = 0.017) was then chosen for a series of checks on the results of the method. The first check involved the computation of the particle velocity of impact over the duration of the May swarm. These velocities were then resolved into components along the LDEF body axes in order to determine the impact speeds on the IDE trays. For this particular orbit, only the south tray and the ram-facing tray were struck, with the south impact speed being larger than that for the other tray (see figure 7). This is in good agreement with the IDE observations of the May swarm, in which these same two trays recorded large numbers of impacts, with the south tray receiving the most hits. The second check consisted of a comparison of the sky track of the points of closest approach between the two orbits to the sky positions of the individual impacts comprising the May swarm. As can be seen from figure 8, the agreement is excellent, with the sky track of close approach passing neatly through a diffuse band of impact positions.

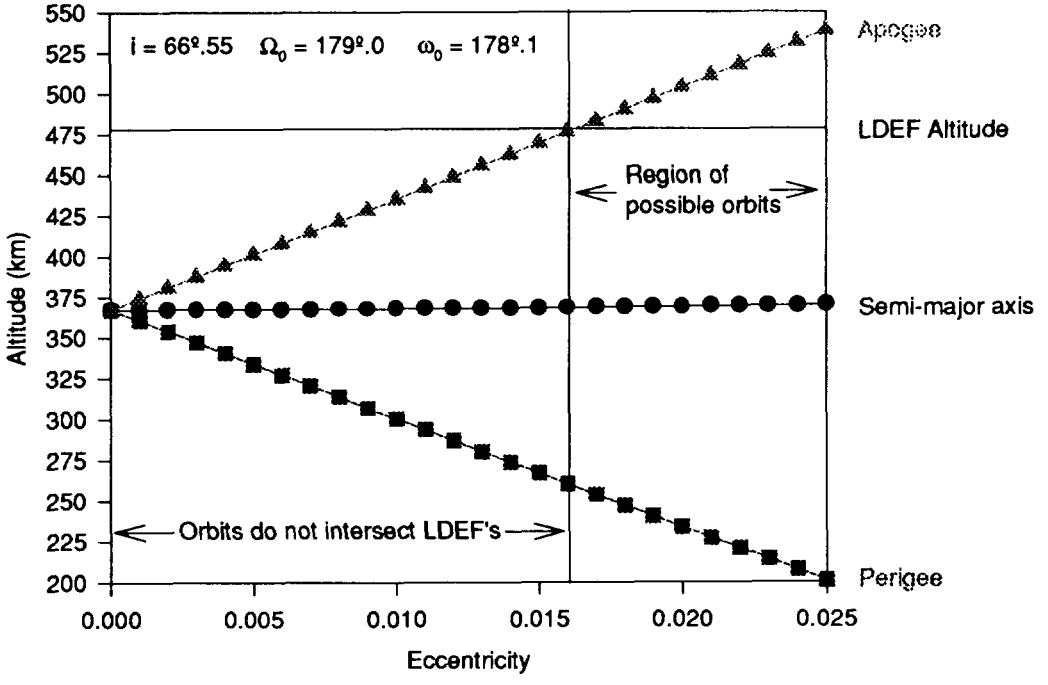

Figure 6: Candidate orbits for the May swarm

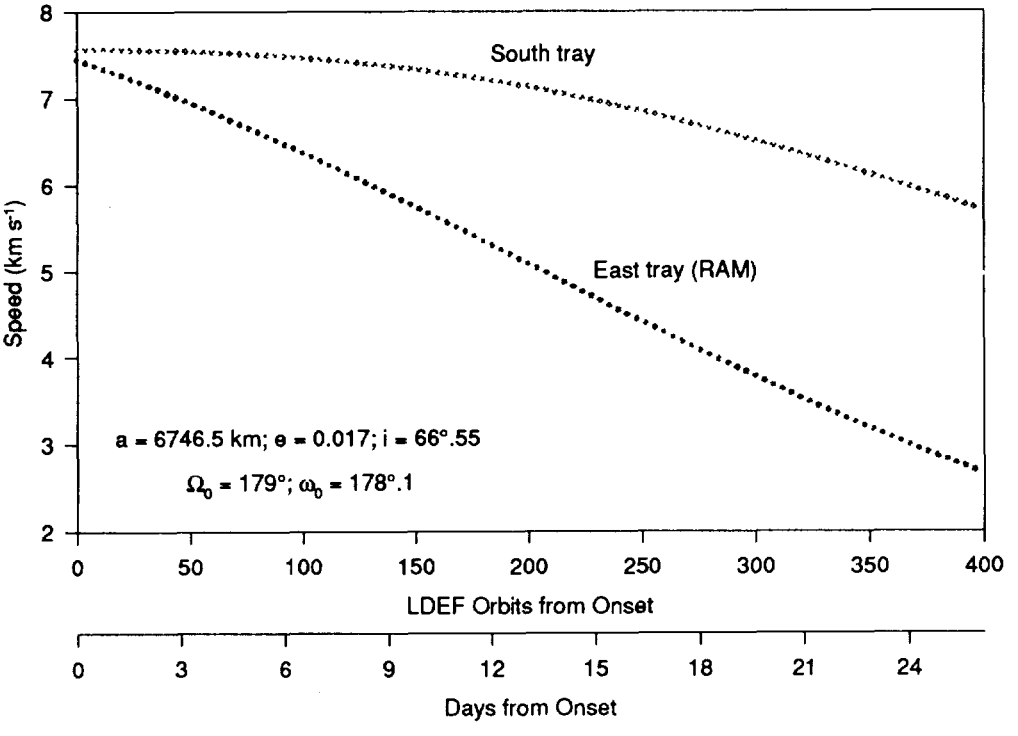

Figure 7: Particle impact speeds along IDE tray normals for test orbit.

In summary, it would seem that the particles impacting LDEF during the May swarm MOES have an orbit that can be characterized by the following parameters:

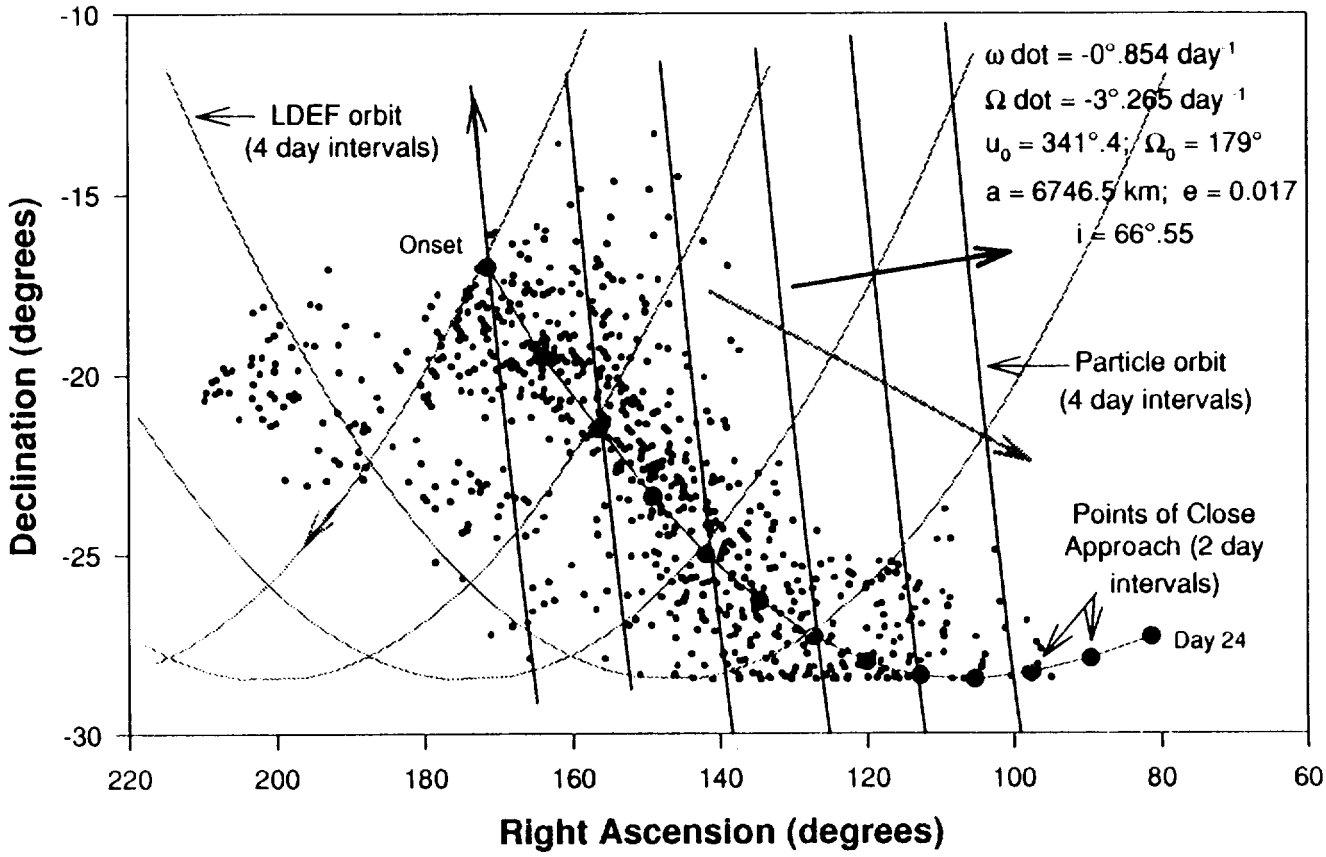

Figure 8: Sky track of close approach between the test orbit and that of LDEF. The particles are moving in a northerly direction, whereas LDEF is moving along its orbit from left to right. At the onset of the May swarm, the impacts are located at the position labeled "Onset", with the impact positions gradually moving towards the lower right as time progresses.

$\Omega_{p0} = 179°.0 \pm 0°.2$ $\quad i_p = 66°.55$

$\dot{\Omega}_p = -3°.26 \pm 0°.05\ day^{-1}$ $\quad a = 6746.5$ km

$\omega_0 = 178°.1 \pm 0°.2$ $\quad 0.0165 < e < 0.025$

$\dot{\omega} = -0°.85 \pm 0°.05\ day^{-1}$

CONCLUSION

It has been pointed out numerous times in the literature that the surface area to mass ratio of a micron-sized particle (the size of many of the LDEF impactors) is large, thus causing the particle to experience significant perturbations from forces such as radiation pressure and atmospheric drag. Indeed, numerical calculations indicate that radiation pressure can cause a one micron diameter particle, initially in an orbit similar to that of LDEF, to enter Earth's atmosphere after only a very few (<10) orbital revolutions. Such calculations leave us hard-pressed to explain how a MOES like the May swarm, which we postulate to be caused by a ring of micron and sub-micron particles, can persist for many days. The only reasonable explanation is that the ring must be replenished by debris from some source during the time spanned by the MOES.

To obtain the geometrical characteristics of this ring, the technique of differential precession looks at the time evolution of the point of intersection with the LDEF orbit. It does not matter that the particles exist in the ring for only a short time; the only requirement is that the orbit shared by the particles at the times of impact with LDEF be similar. In general, this orbit would not be the same as that of the source of the debris particles, for non-gravitational forces would have rapidly acted to alter the particles' orbit from that of the parent body. It should be realized that if the parent body (whose orbit is presumably stable) continually produced particles of similar properties, these particles would have experienced the same perturbations as their predecessors and would therefore have undergone a similar orbital evolution. If any of the future orbits intersected that of LDEF, a MOES would have been observed by IDE, this MOES lasting as long as the source produced particles, or until the geometry of both orbits changed such that there was no longer a point of contact.

The IDE data set is rich, with many MOES of varying characteristics that await analysis by some procedure. The method of differential precession is such a technique, one that appears to be able to extract a good deal of information about the particle orbit involved in a MOES. We fully expect that its application to the other MOES will not only shed some light on possible sources of orbital debris, but will also yield quite a few surprises.

This research was supported by NASA grant NAG-1-1218.

N95-23830

ORBITAL DEBRIS AND METEOROID POPULATION AS ESTIMATED FROM LDEF IMPACT DATA

Jingchang Zhang
Lockheed Engineering & Sciences Company, 2400 NASA Road 1, C102,
Houston, TX 77058
Phone: (713) 333-6266, Fax: (713) 333-7791

Donald J. Kessler
NASA Johnson Space Center, Houston, TX 77058
Phone (713) 483-5313, Fax: (713) 483-5276

SUMMARY

Examination of LDEF's various surfaces shows numerous craters and holes due to hypervelocity impacts of meteoroids and man-made orbital debris. In this paper, the crater numbers as reported by Humes (Refs. 1 and 2) have been analysed in an effort to understand the orbital debris and natural meteoroid environment in LEO. To determine the fraction of man-made to natural impacts, the side to top ratio of impacts (Ref. 1) and results of the Chemistry of Micrometeoroids Experiment (CME, Refs. 3 and 4) are used. For craters in the 100 μm to 500 μm size range, about 25% to 30% of the impacts on the forward-facing surfaces and about 10% of the impacts on the trailing surfaces were estimated due to man-made orbital debris. A technique has been developed to convert crater numbers to particle fluxes, taking the fact into account that the distributions of impact velocity and incidence angle vary over the different surfaces of LDEF, as well as the ratio of the surface area flux to the cross-sectional area flux. Applying this technique, Humes's data concerning craters with limiting lip diameters of 100 μm, 200 μm and 500 μm have been converted into orbital debris and meteoroid fluxes ranging from about 20 μm to 200 μm particle diameter. The results exhibit good agreement with orbital debris model (Kessler, et al., Ref. 5) and meteoroid model (Grun et al., Ref. 6). The converted meteoroid flux is slightly larger than Grun's model (by 40% to 70%). The converted orbital debris flux is slightly lower than Kessler's model for particle diameter smaller than about 30 μm and slightly larger than the model for particle diameter larger than about 40 μm. Taking also into account the IDE data point at about 0.8 μm particle diameter, it suggests to change the slope log(flux) versus log(diameter) of orbital debris flux in the 1 μm to 100 μm particle diameter range from 2.5 (used in the model, Ref. 5) to 1.9.

INTRODUCTION

Since the Long Duration Exposure Facility (LDEF) was recovered in January 1990, many investigators have examined its 14 facing surfaces and analysed craters and holes caused by meteoroid and man-made debris impacts. Very recently, more data concerning craters from 100 μm to 1000 μm lip diameter were published (Ref. 1) , and they can be evaluated to understand the particle environment of orbital debris and natural meteoroids.

The percentage of orbital debris versus meteoroids is of great importance to understanding the LDEF data. Chemical analysis of impact residues provides the possibility of distinguishing between them. However, little data on chemical analysis has been published so far. Pending the publication of more chemical results in the future, we will attempt to estimate the orbital debris fraction from the analysis of orbital dynamics and from other theoretical considerations.

LDEF was unique in that the spacecraft maintained a fixed orientation with respect to the Earth and the orbital velocity vector. This means that directional properties must be considered before comparing LDEF's measured flux with other experiments or models which are usually defined in terms of the flux on a randomly tumbling surface, or "randomly tumbling surface area" flux. It is also common to use the flux through a given cross-sectional area, or "cross-sectional area" flux which is 4 times the "randomly tumbling surface area" flux. Due to its fixed orientation, the flux measured on LDEF is in terms of the flux on an oriented surface, or "oriented surface area" flux. It becomes necessary to find the relation between the "oriented surface area" flux and the "cross-sectional area" flux which is a function of the surface orientation. In addition, one has also to find the relation between the crater diameter and the particle diameter which varies over the different surfaces also. A technique will be presented which can be utilized to conduct such a conversion properly. Using this technique, the data for craters to a limiting lip diameter of 100 μm, 200 μm and 500 μm in Refs. 1 and 2 will be converted to orbital debris and meteoroid fluxes.

This technique was previously used in Ref. 7 to convert the 500 μm data where 46% orbital debris on the forward-facing surface at 52° yaw and 15% orbital debris on the trailing surface at 172° yaw were assumed. However, according to the analysis in this paper, a lower fraction of orbital debris impacts seems to be more appropriate. The 500 μm data will be therefore reanalysed in this paper and a slightly lower orbital debris flux and a slightly larger meteoroid flux than obtained in Ref. 7 is expected.

LDEF IMPACT DATA AND ESTIMATION OF MAN-MADE DEBRIS FRACTION

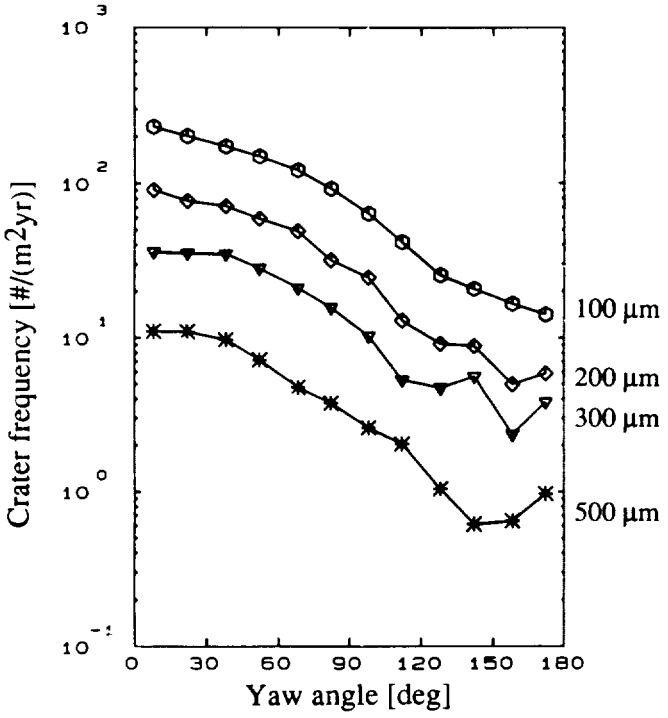

Fig. 1. LDEF impact data of Humes (Refs. 1 and 2).

Fig. 1 illustrates the LDEF impact data of Humes (Refs. 1, 2). Impact frequencies of craters with a limiting lip diameter of 500, 300, 200 and 100 μm are given as a function of the yaw angle which is defined relative to the velocity vector of LDEF. With decreasing crater size, the crater numbers increase. This results in a reduction of statistical fluctuations with decreasing crater size. This is the reason why the curves for smaller craters are more in accordance with theoretical considerations (become smoother and decrease from LDEF's leading surface to trailing surface).

The data in Fig. 1 contain natural meteoroid impacts as well as man-made debris impacts. A major step in evaluating the particle population is to know the fraction of debris impacts versus meteoroid impacts. Chemical analysis of impact residues provides the possibility of distinguishing between them. The results of the Chemistry of Micrometeoroids Experiment (CME) (Refs. 3, 4) will be used for this purpose. However, the CME results do not give the percentage immediately because: i) They are only performed on two LDEF surfaces, namely one on the trailing surface (172° yaw) and another on a forward-facing surface at 52° yaw; ii) about 50% of the craters cannot be identified as man-made or natural since no residue is left or the residue contains the same material as the experiment plate.

Therefore, other considerations are required to estimate the fraction of man-made versus natural particles. In the following, these will be performed by considering only the >100 μm craters, illustrated in Fig. 2.

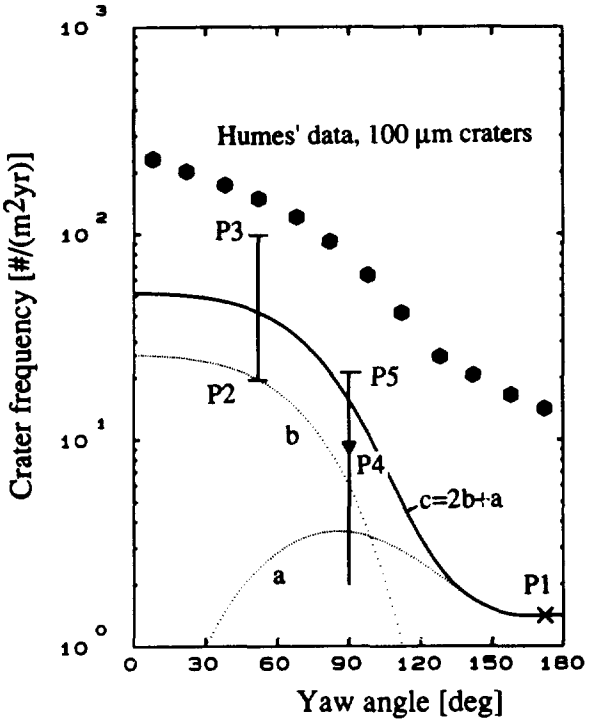

Fig. 2. Estimation of the percentage of orbital debris versus meteoroids. Two particle orbits are used: a=400kmx36000km/28.6°, b=400kmx500km/100°.

One of the CME collectors is the gold plate on LDEF's trailing surface. 15% of the impacts on the gold plate was determined to be man-made, 29% was determined to be natural while 56% had no residue so their source is unknown. Considering only craters > 100 μm, the debris fraction is 10% and meteoroid fraction is 32.5% while 57.5% is unknown. As discussed in Ref. 4, the major loss process of projectile residue on the gold plate is vaporization of the projectile. Since debris particles encounter the trailing surface only with low velocities, they are not likely to be vaporized. Therefore, all impacts with no residue will be assumed to be natural. As a result, 90% of craters > 100 μm is then determined to be natural and only 10% to be man-made. The 10% : 90% ratio of debris versus meteoroids on the trailing surface will be used in this paper. P1 in Fig. 2 indicates the 10% debris impacts point.

CME has also an aluminum plate located in Bay A11, 52° yaw. On the Al-plate, 13% of all craters > 100 μm was determined to be debris impacts (but non-aluminum, because aluminum debris cannot be identified on the Al-plate). 34% was determined to be meteoroid impacts, while 53% could not be identified. The lower density of aluminum (versus gold) means that for a given velocity, vaporization is less likely; however, debris velocities on the forward-facing surface are considerably higher than on the trailing surface, making vaporization of debris more probable than on the trailing surface. On the other hand, one must assume that a considerable fraction of the unknown craters is due to aluminum debris impacts which cannot be detected on aluminum surfaces, since about 80% of man-made impacts found on the gold plate contains only aluminum. However, it is hard to determine the exact percentage. At this point, one knows only that the debris fraction ranges somewhere between 13% (if all unknown craters would be assumed to be natural origin) and 67% (if all unknown craters would be assumed to be man-made origin). P2 and P3 in Fig. 2 indicate this range.

As an additional help, we can use the ratio of impacts on LDEF's side (at 90 ° yaw, which is the average of fluxes on the surfaces at 82° and 98° yaw) to impacts on the top. If there would be only meteoroid impacts, the only difference between the fluxes on the side and top is the Earth shielding effect which reduces the flux on the side. This flux ratio was calculated using meteoroid models and found to be about 0.71 for 100 μm craters according to Ref. 8. Because there are debris impacts on the side, but almost no debris impacts on the top, the measured side to top ratio of all impacts is larger than that of meteoroid impacts alone. The difference between the measured side/top ratio and the modeled meteoroid side/top ratio enables us to determine the debris/meteroid ratio on the side.

As reported in Ref. 1, the measured side/top ratio of 100 μm craters amounts to 0.82 (the nominal ratio). If taking the upper limit of 90% confidence on the side and the lower limit of 90% confidence on the top, this ratio increases to 0.97 (the upper limit of 99% confidence). An additional uncertainty results from the lack of precise calibration between the top and side surfaces. According to Ref. 1, the top surface appeared to have different properties than the other surfaces. It was smoother and had a different color, indicating it was not cleaned and anodized like the other surfaces. As a result, the top surface might make a crater with a lip that would measure larger than an anodized surface. For example, a 10% increase in the crater diameter resulting from a given debris impact would result in about a 25% increase in flux. Therefore, a 10% crater diameter error would easily put the nominal value for the side to top ratio near the upper limit of 99% confidence limit.

The ratio of debris to all craters on the side can be determined as:

$$p_d = \frac{1 - r_m / r_{m+d}}{1 - r_m / r_d} \qquad (1)$$

where

p_d: fraction of debris craters to all craters on the side;

r_d: side/top ratio of debris craters (large, since debris impacts on the top are negligible);

r_m: side/top ratio of meteoroid craters, can be calculated using meteoroid model;

r_{m+d}: side/top ratio of all craters, is measured on LDEF.

If debris impacts on the top are neglected, Eq. (1) becomes:

$$p_d = 1 - \frac{r_m}{r_{m+d}} \qquad (2)$$

According to Ref. 8, r_m is 0.71, if the mean LDEF altitude is assumed to be 460 km, atmospheric height to be 150 km and the slope log(flux) versus log(mass) to be -0.48. The nominal debris fraction on the side is then 13% (P4 in Fig. 2) and the upper limit with 99% confidence is 27% (P5 in Fig. 2).

It should be noted that the calculated side/top ratio of meteoroid craters depends on the assumption of atmospheric height and the slope log(flux) versus log(mass). In Ref. 1, this ratio is calculated in a different way, and $r_m = 0.63$ is obtained. The debris fraction on the side would be thereafter 22% with an upper limit of 34%. Combined with the lack of precise calibration, the debris fraction might exceed 50%. In the following, however, the 13% fraction is still considered as the nominal fraction.

The question now becomes how to find a debris curve which best fits the data points at 52 °, 90° and 172° yaw angles (P1 to P5). The debris point at 90° represents a strict constraint, since all debris orbits which produce a considerable flux either on the trailing surface (172° yaw) or on the forward-facing surface (52° yaw) also contribute a large flux on LDEF's side (Refs. 9, 10). There are not many possibilities which keep the flux at 90° yaw low. The best way to keep the flux on the side low is to use the following two particle orbits:

a) Highly elliptical orbit with about 28.6 deg inclination (curve a in Fig. 2) to account for debris impacts on the trailing surface, and

b) Near-circular orbit with about 100 deg inclination (curve b in Fig. 2) to account for debris impacts on the forward-facing surface. The logic for 100° inclination will be discussed later and is demonstrated in Figure 3.

Curve a in Fig. 2 is normalized to pass through P1 and curve b is normalized to pass through P2. With curve b, only non-aluminum debris impacts on the forward-facing surface are simulated. As reported in Ref. 4, the ratio of aluminum debris to non-aluminum debris on the trailing surface is about 5:1. This suggests one has to assume more aluminum debris impacts than non-aluminum debris impacts on the Al-plate. But one cannot assume too many aluminum debris impacts, because it would lead to a debris flux on the side exceeding the upper limit (P5). The best fit results from assuming as many aluminum debris impacts originating from the 100 deg orbit as the measured 13% of non-aluminum debris impacts. This results in a total of 28% debris impacts on the Al-plate (26% from the 100 deg orbit, 2% from the 28.6 deg orbit). The total debris curve (curve c in Fig. 2) is then obtained by multiplying curve b by 2 and adding to curve a. The debris fraction on the side (90° yaw) is thereafter 20%. These percentages are summarized in Table 1.

Table 1. Estimated Fraction of Debris Craters on the Forward-Facing Surface (52 ° Yaw), the Side (90° Yaw) and the Trailing Surface (172° Yaw)

52 deg	90 deg	172 deg
28%	20%	10%

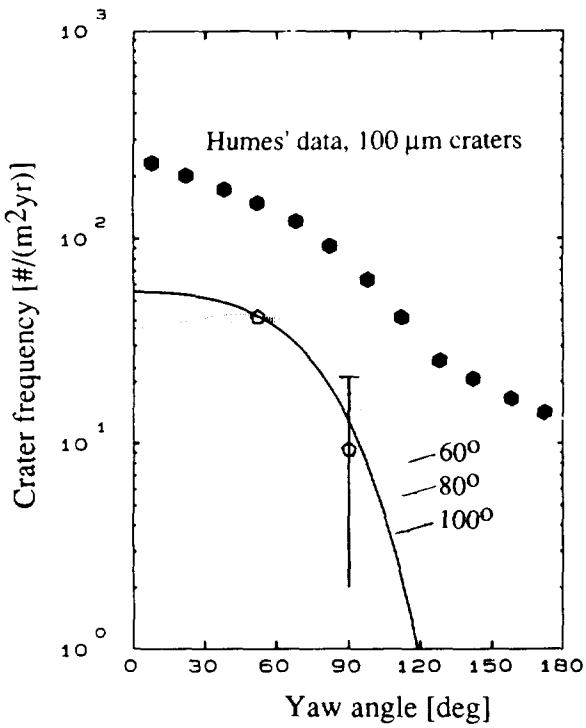

Fig. 3. Crater distribution which would be produced on LDEF from particles in near-circular orbits with various inclinations. Curves are normalized to pass through the measurement point at 52° yaw angle.

The orbital parameter model using the two debris particle orbits mentioned above will be called the "Two-Particle-Orbits-Model" in the following. The reason why 100 deg inclination, not other inclinations like 60 deg or 80 deg, is being considered as the best fit is shown in Fig. 3. All three curves are normalized to pass through the 28% debris point at 52 deg yaw. Only the 100 deg inclination keeps the flux on the side (90 deg yaw) close to the nominal debris point (P4), while other inclinations produce a flux on the side which is too high. The 60 deg curve even exceeds the upper limit with 99% confidence (P5). For the same reason, the 28.6 deg inclination orbit is considered as the best choice to account for debris impacts on the trailing surface.

The use of only two orbits to represent the orbital debris population is not to say that the population consists of only these orbits; rather these two orbits approximate the actual distribution of orbits. The fact that the direction and velocity distribution resulting from these two orbits matches (within the uncertainty of measurements) that using the "modified catalogue" distribution in Ref. 9 is a justification for this use. The Two-Particle-Orbits-Model is

aimed to convert the crater diameter to particle diameter and to convert the oriented surface area flux to cross-sectional area flux, and it appears to perform such a conversion properly.

The man-made debris fraction for 100 μm craters estimated above will also be assumed to apply for craters as large as 500 μm. This seems to be valid as the side to top ratios of Humes's data (Ref. 1) do not show significant variation from 100 μm to 500 μm.

The debris and meteoroid impacts determined for 100 μm, 200 μm and 500 μm craters using above debris/meteoroid percentages are summarized in Table 2. It should be noted that the sum of debris impacts plus meteoroid impacts in Table 2 varies slightly from Humes's data. The modeled values are smoother than the measurement and are considered as the actual fluxes after removing statistical fluctuations.

Table 2. Estimated Debris and Meteoroid Impacts for 100 μm, 200 μm and 500 μm Craters from Humes's Data (Refs. 1 and 2)

yaw angle [deg]	100 μm craters [#/m^{2}yr]		200 μm craters [#/m^{2}yr]		500 μm craters [#/m^{2}yr]	
	debris	met.	debris	met.	debris	met.
8	55.7	159.5	20.5	65.6	2.52	8.97
22	52.9	151.2	20.0	61.7	2.45	8.40
38	47.9	132.9	18.7	54.1	2.30	7.28
52	41.5	112.0	16.4	44.4	2.02	5.88
68	33.7	86.5	12.8	34.2	1.57	4.44
82	23.7	65.7	8.25	24.9	1.02	3.17
98	13.5	46.2	4.27	17.5	0.527	2.17
112	5.81	33.2	1.83	11.9	0.227	1.45
128	2.39	22.7	0.869	8.16	0.108	0.974
142	1.52	17.0	0.577	5.89	0.0721	0.697
158	1.43	13.4	0.488	4.68	0.0610	0.553
172	1.41	12.3	0.480	4.21	0.0600	0.497

CONVERSION OF CRATER FREQUENCIES TO PARTICLE FLUXES

The conversion of the LDEF impact data to particle flux will be accomplished in two steps:

a) Conversion of the crater diameter to particle diameter,
b) Conversion of the crater numbers to cross-sectional area flux.

For the first step, relation between particle size and crater size is needed. It is very common to use the following hypervelocity impact equation (Ref. 2) which is based on laboratory tests:

$$t_\infty = C_1 \rho^{0.519} d^{1.056} (v \cos\theta)^{2/3} \qquad (3)$$

where t_∞=crater depth, ρ=density of the particle, d=particle diameter, v=impact velocity, and θ=incidence angle measured from the normal to the surface; for aluminum plates, C_1=0.334 for ρ in g/cm^3, d in cm and v in km/s.

While Eq. (3) describes the crater depth, a relation to describe the crater diameter is needed, since the data in Refs. 1 and 2 are given to limiting crater lip diameters. As reported in Ref. 2, the lip diameter of most craters observed on LDEF is about 8/3 times the crater depth. Thus, the crater diameter can be expressed as:

$$D_r = C_2 \rho^{0.519} d^{1.056} (v \cos\theta)^{2/3} \tag{4}$$

where D_r=crater lip diameter; for aluminum plates, C_2=0.891 for ρ in g/cm^3, d in cm and v in km/s.

Since the impact velocity and the incidence angle are not measured on LDEF, Eq. (4) cannot directly be used to obtain the particle diameter from the crater diameter. As a common technique, averaged impact velocities and incidence angles are used. We denote the average velocity of the impacts as v_a and the average angle of the impacts as θ_a, both referring to a limiting crater diameter and denoting the average diameter of particles which produce the crater diameter of D_r as d_a.

The quantities of v_a and θ_a can be determined by applying the technique in Ref. 11 for transformation of a flux to a limiting particle size into a flux to a limiting penetration thickness. On the assumption that the cumulative flux of particle diameter ≥ d is proportional to d^{-p}, combined with Eq. (4), the following relation is obtained:

$$v_a \cos\theta_a = \left\{ \frac{\int_{v=0}^{\infty} \int_{\theta=0}^{\pi/2} n_{v,\theta}(v,\theta)(v\cos\theta)^{\frac{2/3p}{1.056}} d\theta dv}{\int_{v=0}^{\infty} \int_{\theta=0}^{\pi/2} n_{v,\theta}(v,\theta) d\theta dv} \right\}^{\frac{1.056}{2/3p}} \tag{5}$$

where $n_{v,\theta}$ is the distribution of the impact velocity and incidence angle, referring to a limiting particle diameter; p is the slope log(flux) versus log(diameter) in the form $F \sim d^{-p}$.

Eq. (5) considers the fact that smaller particles with larger vcos θ can produce the same crater as larger particles with smaller vcosθ, and the number of particles increases with d^{-p} while the particle diameter decreases.

In order to formulate a general relation describing the ratio of average particle diameter to crater diameter, we introduce a q-factor as:

$$q = \frac{d_a^{1.056} \rho^{0.519}}{D_r} = \frac{1}{C_2} (v_a \cos\theta_a)^{-2/3} \tag{6}$$

Combining Eqs. (5) and (6) results in:

$$q = C_3 \left\{ \frac{\int_{v=0}^{\infty} \int_{\theta=0}^{\pi/2} n_{v,\theta}(v,\theta)(v\cos\theta)^{\frac{2/3p}{1.056}} d\theta dv}{\int_{v=0}^{\infty} \int_{\theta=0}^{\pi/2} n_{v,\theta}(v,\theta) d\theta dv} \right\}^{\frac{-1.056}{p}} \qquad (7)$$

where for aluminum plates C_3=1.122 for ρ in g/cm^3, d in cm and v in km/s.

After calculation of the factor q using Eq. (7), the averaged particle diameter d_a which produces the crater diameter D_T can immediately be obtained. For 100 μm, 200 μm, 500 μm and 1000 μm crater diameters, the results are illustrated in Fig. 4.

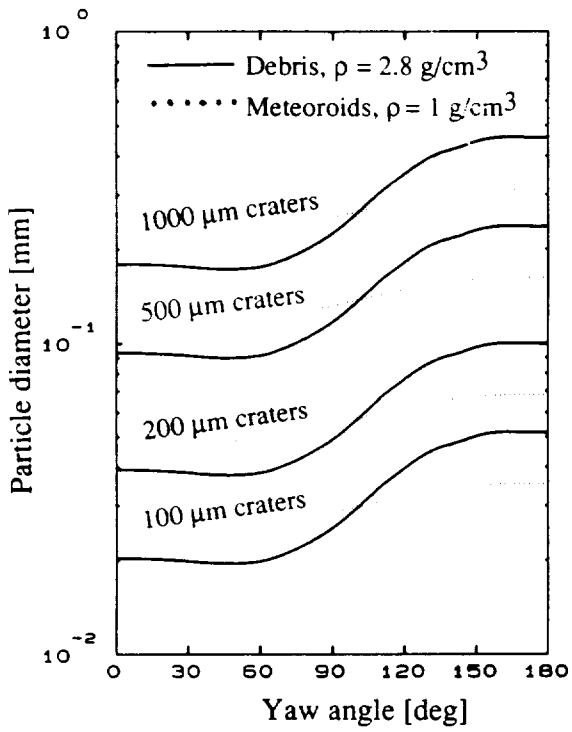

Fig. 4. Average diameter of orbital debris and meteoroid particles producing craters with given crater lip diameters as indicated in the diagram.

To obtain the results in Fig. 4, the distribution of velocity and incidence angle of debris impacts as well as meteoroid impacts for each surface of LDEF is needed.This distribution for debris impacts is obtained by applying the Two-Particle-Orbits-Model mentioned above, while that for meteoroid impacts is obtained by means of the same meteoroid model as used in Refs.7 and 10.

Fig.4 shows that a slightly larger meteoroid particle than debris particle is required to produce the same crater on LDEF's leading surface (about 1.2:1); this is due to the lower density of meteoroid particles. But to produce the same crater on the trailing surface, a larger debris particle than meteoroid particle is required (about 1.5:1), due to very low velocities of debris particles encountering the trailing surface. The particles producing a 1000 μm crater is not exactly 10 times as large as particles producing a 100 μm crater, as the particle diameter goes into the impact equation (4) with the power of 1.056.

The particle diameter that corresponds to a given crater diameter depends on which surface is considered. Fig. 4 shows that a debris particle producing a given crater size on LDEF's trailing surface needs to be about 2.5 times as large as a debris particle producing the same crater size on the leading surface, because of debris particles encountering the trailing surface with much lower velocities than encountering the leading surface. As a result, crater numbers of one crater size give more than one particle flux point. In other words, assuming a given crater diameter, each surface gives one particle size flux point.

The crater numbers measured on LDEF's various surfaces represent a flux on a flat plate with fixed orientation. This flux is to be converted to the cross-sectional area flux (flux on a unit sphere with 1 m^2 cross-sectional area). If the surface area flux is obtained on a tumbling flat plate (like Solar Max), the cross-sectional area flux is 4 times the surface area flux. Considering surfaces with fixed orientation (like LDEF), the ratio of surface area flux to cross-sectional area flux depends on the surface orientation.

Fig.5 illustrates the ratio of the oriented surface area flux to the cross-sectional area flux as a function of the yaw angle by applying the meteoroid and debris models. The two debris curves are obtained by means of the Two-Particle-Orbits-Model applied for 100 μm craters, one by assuming the slope of log(flux) versus log(diameter) to be 1.5 and the other by assuming the slope to be 2.5. It should be noted that the ratio of the oriented surface area flux to the cross-sectional area flux for debris impacts is sensitive to the assumption of the slope. A different slope leads to a different fraction of particles on the two particle orbits to fit the measurement which results in a different ratio of surface area flux to cross-sectional area flux.

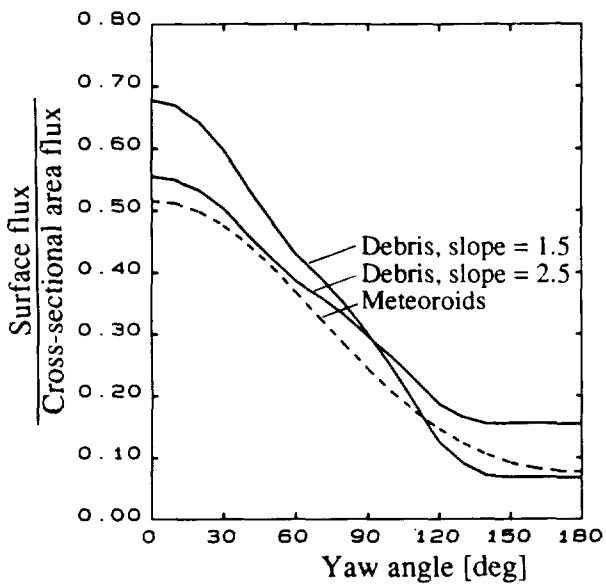

Fig. 5. Ratio of surface flux to cross-sectional area flux. The ratios for orbital debris only apply for using the same assumptions as explained in the text.

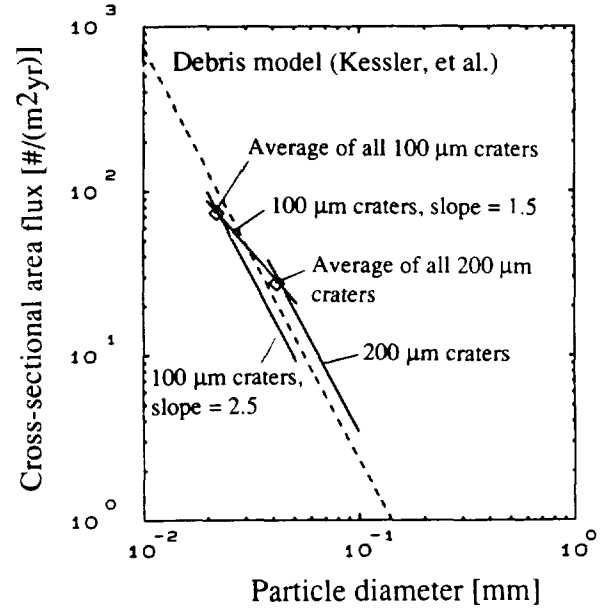

Fig. 6. Conversion of craters > 100 μm to orbital debris fluxes by assuming two different slopes of log(flux) versus log(diameter).

Fig. 6 shows the converted debris particle flux from 100 μm debris craters for two assumptions of the slope log(flux) versus log(diameter). The converted flux curves reflect exactly the slope assumed at the beginning, indicating no conceptual or mathematical errors were introduced.

The diamond symbols indicate an average flux of impacts on all 12 surfaces on LDEF's barrel. The particle diameter is obtained when the converted particle diameters on all 12 surfaces are averaged by weighting the flux on each surface. The flux is obtained when assuming all debris impacts are parallel to the Earth surface (which is valid if considering a spacecraft moving in low earth orbit). Under this assumption, the cross-sectional area flux is π times the flux on LDEF's barrel. Debris flux obtained in this way is not sensitive to various assumptions. With respect to the flux point obtained from 200 μm craters, the 1.5 slope for 100 μm craters can be considered a good choice.

RESULTS

Fig. 7 illustrates the debris and meteoroid fluxes converted from 100 μm, 200 μm and 500 μm craters which cover a particle size range from 20 μm to 240 μm for man-made orbital debris and from 25 μm to 160 μm for meteoroids.

The debris fluxes are obtained by means of two different slopes. While the 100 μm craters are converted using a slope of 1.5, a slope of 2.5 is used for 200 μm and 500 μm craters. The meteoroid fluxes are obtained by means of three different slopes: for 100 μm craters using a slope of 1.5, for 200 μm craters using a slope of 2 and for 500 μm craters using a slope of 2.5.

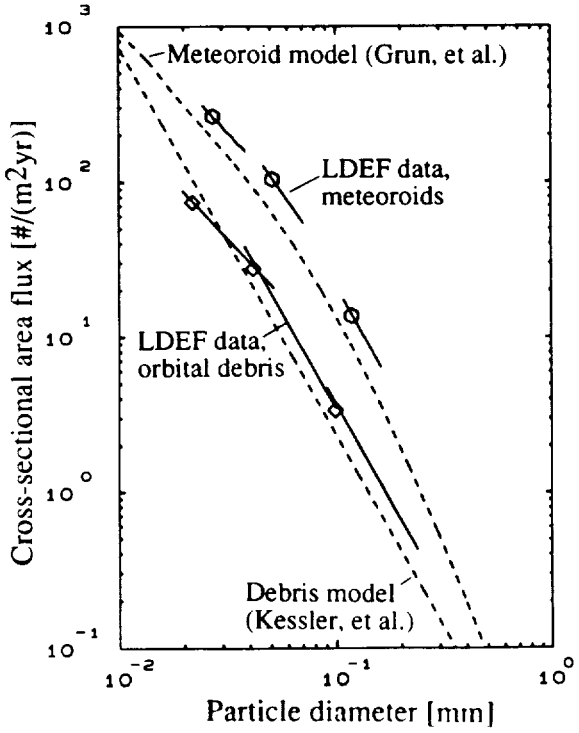

Fig. 7. Orbital debris and meteoroid fluxes converted from Humes's data for craters > 100 μm, 200 μm and 500 μm.

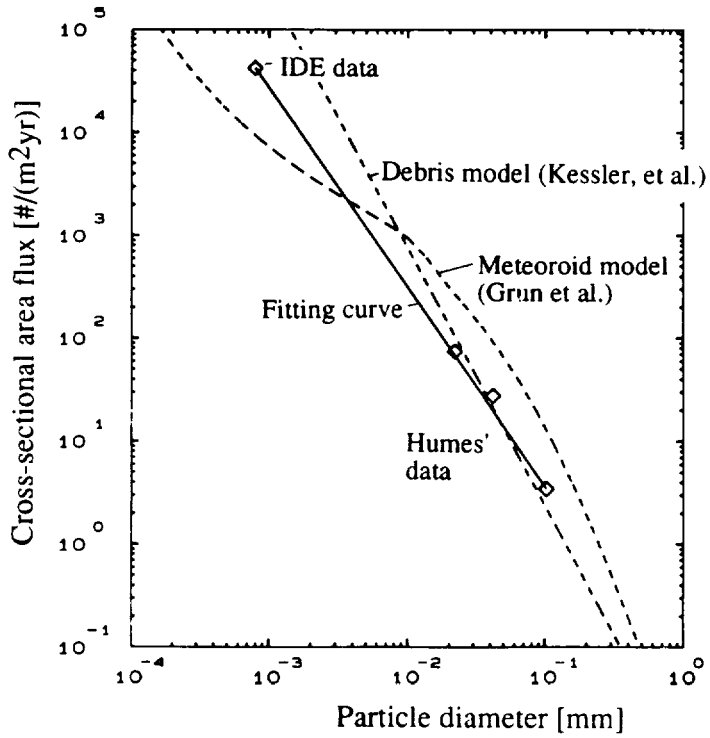

Fig. 8. Orbital debris flux converted from Humes's data and IDE data compared to orbital debris model.

The symbols (hexagon symbols for meteoroids and diamond symbols for orbital debris) represent an average flux of debris or meteoroid fluxes on all 12 surfaces around LDEF. To obtain the average debris flux, the cross-sectional area flux is assumed to be π times the surface area flux around LDEF, as explained in Fig. 6. To obtain the average meteoroid flux, the cross-sectional area flux is assumed to be 3.8 times the surface area flux around LDEF, since according to our meteoroid model, the ratio of the meteoroid flux on LDEF with fixed orientation to that on a tumbling LDEF (hypothetical) is 4:3.8.

A comparison to the debris model in Ref. 5 shows a good agreement. For particle diameter larger than 40 μm, the measurement is slightly larger than the model, while for particle diameter smaller than 30 μm, the measurement is slightly lower than the model.There is also a good agreement between converted meteoroid flux and the meteoroid model in Ref. 6. In general, the measured flux is slightly larger (by 40% to 70%) than the flux from the model.

In Ref. 12, fluxes to a limiting crater diameter of 3 μm measured on six surfaces from the Interplanetary Dust Experiment (IDE) are reported. These fluxes result in an averaged cross-sectional area flux of 4.2 #/(m^2yr) at 0.79 μm particle diameter. Because the IDE measured mainly orbital debris swarms (Ref. 12), the fraction of meteoroid impacts can be neglected, and the flux of 4.2 #/(m^2yr) will be considered

only due to orbital debris impacts. The IDE data point and the three orbital debris flux points from Humes's data are compiled in Fig. 8. It suggests using a log(flux)/log(diameter) slope of 1.9 to fit all of the four data points, as the solid line indicates. It differs from the model in Ref.5 where a slope of 2.5 is used. At 1 μm particle diameter, the measurement is lower than the model by about one order of magnitude.

CONCLUSIONS

The fraction of orbital debris impacts versus meteoroid impacts was analysed for craters in the 100 μm to 500 μm size range. The results indicate a slightly smaller debris population than previous analysis due to better statistics and applying more constraints. The best estimate of the debris population is 28% at 52° yaw and 10% on the trailing surface. However, there is still sufficient uncertainty that the previous results (of 46% & 15%, respectively) are possible. This has to be verified in the future when more chemical data are available.

Humes's data concerning craters from 100 μm to 500 μm in lip diameter were converted to orbital debris and meteoroid fluxes, ranging from 20 μm to 240 μm particle diameter for man-made orbital debris and from 25 μm to 160 μm particle diameter for meteoroids. At larger particle size range, the measured debris flux is slightly larger than the debris model (Kessler et al., Ref. 5), while the measured debris flux is lower than the model at smaller size range. The measured meteoroid flux is 40% to 70% larger than the meteoroid model (Grun et al., Ref. 6). However, if the debris population were about a factor of 2 higher, the meteoroid flux measured by LDEF would be very close to the meteoroid model.

The major uncertainties in the converted fluxes may result from two sources: i) How accurate is Eq. (3) used to convert the crater diameter to particle diameter; ii) How accurate is the estimated percentage of orbital debris versus meteoroids. The impact equation (3) was also used to convert previous impact data (e.g. Solar Max) on which the debris and meteoroid models are based. Therefore, the fluxes converted in this paper should be comparable to existing models. The uncertainty in the percentage of orbital debris versus meteoroids can be reduced when more chemical analyses of impact residues will be performed in the future.

Taking into account the IDE data which gave a debris flux at about 0.8 μm particle diameter, the debris model in Ref. 5 is larger than the measurement at 1 μm particle diameter by about one order of magnitude. The measurement suggests to reduce the log(flux)/log(diameter) slope from 2.5 to 1.9 in the 1 μm to 100 μm particle diameter range.

ACKNOWLEDGMENT

We wish to thank Robert C. Reynolds for helpful discussions and constructive reviews of this manuscript. Significant suggestions were received from the referee Donald H. Humes which were gratefully incorporated into the paper.

REFERENCES

1. Humes, D.H., "Small Craters on the Meteoroid and Space Debris Impact Experiment", Proc. of the 3rd LDEF Post-Retrieval Symposium, NASA CP-3275, 1995

2. Humes, D.H., "Large Craters on the Meteoroid and Space Debris Impact Experiment", Proc. of the 1st LDEF Post-Retrieval Symposium, NASA CP-3134, 1991, pp.399-418

3. Horz, F.; Bernhard, R.P., "Compositional Analysis and Classification of Projectile Residues in LDEF Impact Craters", NASA TM 104750, June 1992

4. Bernhard, R.P.; See, T.H.; Horz, F., "Projectile Compositions and Modal Frequencies on the 'Chemistry of Micrometeoroids' LDEF Experiment", Proc. of the 2nd LDEF Post-Retrieval Symposium, NASA CP-3194, 1993, pp.551-573

5. Kessler, D.J.; Reynolds, R.C.; Anz-Meador, P.D., "Orbital Debris Environment for Spacecraft Designed to Operate in Low Earth Orbit", NASA TM 100471, April 1989

6. Grun, E.; Zook, H.A.; Fechtig, H.; Giese, R.H., "Collisional Ballance of the Meteoritic Complex", Icarus 62, 1985, pp.244-272

7. Zhang, J.; Rex, D., "Decoding of the Particle Population from LDEF Crater Distributions", IAA.6.4-93-749, 44th I.A.F. Congress, Graz, Austria, Oct. 16-22, 1993

8. Zook, H.A., "Deriving the Velocity Distribution of Meteoroids from the Measured Meteoroid Impact Directionality on the Various LDEF Surfaces", Proc. of the 1st LDEF Post-Retrieval Symposium, NASA CP-3134, 1991, pp.569-579

9. Kessler, D.J., "Origin of Orbital Debris Impacts on LDEF's Trailing Surfaces", Proc. of the 2nd LDEF Post-Retrieval Symposium, NASA CP-3194, 1993, pp.585-593

10. Zhang, J.; Kessler, D.J.; Rex, D., "Interpretation of the Distribution of Large Craters on the Long Duration Exposure Facility (LDEF)", Proc. of the First European Conference on Space Debris, ESA SD-01, Darmstadt, Germany, 1993, pp.195-200

11. Kessler, D.J., "A Guide to Using Meteoroid-Environment Models for Experiment and Spacecraft Design Applications", NASA TN D-6596, March 1972

12. Simon, C.G., et al., "Long-Term Microparticle Flux Variability Indicated by Comparison of Interplanetary Dust Experiment (IDE) Timed Impacts for LDEF's First Year in Orbit with Impact Data for the Entire 5.77-Year Orbital Lifetime", Proc. of the 2nd LDEF Post-Retrieval Symposium, NASA CP-3194, 1993, pp.693-703

HYPERVELOCITY IMPACT SURVIVABILITY EXPERIMENTS FOR CARBONACEOUS IMPACTORS: PART II

T. E. Bunch
NASA Ames Research Center
Moffett Field, CA 94035-1000

Julie M. Paque
SETI Institute
2035 Landings Drive
Mountain View, CA 94043

Luann Becker
Scripps Institute of Oceanography
University of California at San Diego, La Jolla, CA 92093

James F. Vedder
NASA Ames Research Center
Moffett Field, CA 94035-1000

Jozef Erlichman
TMA/Norcal
2030 Wright Ave., Richmond, CA 94804

ABSTRACT

Hypervelocity impact experiments were performed to further test the survivability of carbonaceous impactors and to determine potential products that may have been synthesized during impact. Diamonds were launched by the Ames two-stage light gas gun into Al plate at velocities of 2.75 and 3.1 km sec^{-1}. FESEM imagery confirms that diamond fragments survived in both experiments. Earlier experiments found that diamonds were destroyed on impact above 4.3 km sec^{-1}. Thus, the upper stability limit for diamond on impact into Al, as determined from our experimental conditions, is between 3.1 and 4.3 km sec^{-1}.

Particles of the carbonaceous chondrite Nogoya were also launched into Al at a velocity of 6.2 km sec^{-1}. Laser desorption (L^2MS) analyses of the impactor residues indicate that the lowest and highest mass polycyclic aromatic hydrocarbons (PAHs) were largely destroyed on impact; those of intermediate mass (202-220 amu) remained at the same level or increased in abundance. In addition, alkyl-substituted homologs of the most abundant pre-impacted PAHs were synthesized during impact. These results suggest that an unknown fraction of some organic compounds can survive low to moderate impact velocities and that synthesized products can be expected to form up to velocities of, at least, 6.5 km sec^{-1}.

We also present examples of craters formed by a unique microparticle accelerator that could launch micron-sized particles of almost any coherent material at velocities up to ~15 km sec^{-1}. Many of the experiments have a direct bearing on the interpretation of LDEF craters.

INTRODUCTION

The experimental results presented here are part of a continuing program aimed at determining characteristics of carbonaceous matter that has sustained hypervelocity impact. The initial results and objectives were presented at the Second LDEF Post-Retrieval Symposium (ref. 1).

Observations of LDEF impact craters indicate that a small but unknown fraction of the craters contain dark residues, possibly carbon-bearing (e. g., refs. 2 and 3). Information on the behavior of carbonaceous materials on impact is sparse (e. g., ref. 4), although Peterson *et al.*, (1991) (ref. 5) performed shock experiments on amino acid survivability. Two of the three crystalline forms of carbon, diamond and graphite are known to occur in meteorites (ref. 6) and diamond occurs in the interstellar medium (ISM) (ref. 7). Amorphous carbon and poorly crystallized graphite (PCG) in carbonaceous chondrites form the bulk of their carbon inventories together with many organic compounds including polycyclic aromatic hydrocarbons (PAHs) that are also found in the ISM (ref. 8). These and other organic compounds may occur in comets (e. g., ref. 9). The possibility exists that LDEF sampled carbonaceous-bearing particles from all of these environments. The information contained within carbonaceous impactors is vital to understanding their origin and significance.

In attempting to characterize and interpret LDEF carbonaceous residues, several first-order questions are being addressed: 1) Can carbon crystalline phases and organic compounds survive low velocity (≤ 7 km sec^{-1}) impact, and if they do survive, what are their characteristics? 2) If they do not survive impact, what are their breakdown products or shock synthesized products, if any? Light gas gun hypervelocity experiments have been conducted to constrain, within our experimental capabilities, these and other issues. Experiments to further refine techniques and establish additional impactor (projectile) criteria are continuing.

Preliminary results of morphological, compositional, and structural studies made on carbonaceous-bearing experimentally-formed impact residues are given in this report. In addition, some interesting results of experimental impacts via a unique microparticle accelerator (MPA) that were performed between 1970 and 1973 are presented. The data and samples were archived after the MPA was shut down nearly 18 years ago and were just recently reexamined. Only a portion of the MPA experiments were published; and those results, together with new data, are useful in the interpretation of LDEF craters and their residues.

LIGHT GAS GUN EXPERIMENTS: SAMPLE SELECTION, EXPERIMENTAL AND ANALYTICAL TECHNIQUES

Sample Selection and Experimental Conditions

An earlier study (ref. 1), indicated that diamond appears to be totally destroyed on impact into Al at speeds > 4.3 km sec^{-1}. Experiments at lower velocities (2.75 and 3.1) have been performed in order to determine the velocity at which the diamond structure is at least partially retained on impact. An additional higher velocity experiment (5.5 km sec^{-1}) was made to enhance the diamond impactor melt characteristics. The earlier study also indicated that most of the higher mass PAHs (polycyclic aromatic hydrocarbons) in the Murchison meteorite survived impact at 5.9 km sec^{-1} and there was some evidence that some PAHs had been synthesized. In order to confirm these findings and explore them further, we launched particles of the Nogoya meteorite, which has twice the total amount of carbon, into an Al target (6061 alloy) at 6.2 km sec^{-1}. For experiments of this type, the Ames light gas gun (LGG) is limited to acceleration velocities of < 6.5 km sec^{-1}. Peak pressures and temperatures cannot be directly measured.

Experimental Methodology

Two-stage Light Gas Gun Experiments

Projectile grains were loaded into a small (3 mm cavity) Al carrier cup, capped with an Al plate and fitted into a sabot for launching. The two-stage light gas gun (Figure 1) accelerates the sabot down a rifled barrel (1.2 m long; bore dia. = 9 mm) to velocities of ≈ 2-6.5 km sec^{-1} depending on the amount of the powder charge (first stage), which in turn determines the speed of the deformable ram that compresses hydrogen gas (second stage). When the gas reaches a certain critical pressure, a diaphragm ruptures and the gas propels the sabot down the barrel. At the end of the barrel, the sabot, carrier, and particles are separated in a "blast" chamber, particle velocities are electronically recorded, the in-flight particles are photographed, and the particles continue on to impact with the target plate (at 90° to the target) in an evacuated chamber (vacuum pressures nominally <1 mm of Hg). The impacted plate also serves as a witness plate with a 2.5 cm dia. hole through which the carrier travels. This technique allows only particles to impact, the alignment of the launch can be measured, and the range in diameters of the launched particles at the impact point can be measured from the holes in the mylar covering which is attached beneath the hole. This cluster shot approach is necessary for projectiles < 1.0 mm in diameter as smaller grains cannot be individually launched.

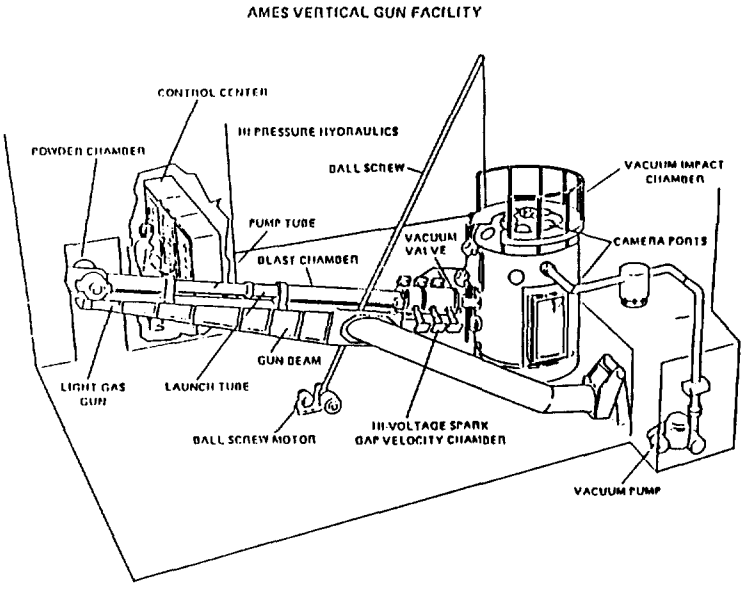

Figure 1

Observational and Analytical Techniques

Samples were dry cut from the target plate. Craters and retained impactor debris were first observed by an optical light microscope, then by field emission scanning electron microscopy (FESEM). Samples were then analyzed for impactor residue by light element equipped energy dispersive spectroscopy (EDS).

Major Analytical Technique

Laser Ionization Mass Spectrometry (L^2MS). The two-step laser methodology has been described elsewhere (ref. 10). In the first step, the pulsed output of a CO_2 laser (10.6 μm; 20 mJ/pulse; 10 μsec pulse width; 5-Hz repetition rate) is focused onto a small stainless steel disk (~1 mm diameter) containing the meteorite sample. The infrared (IR) radiation is readily absorbed by the meteorite minerals and causes the ejection of intact neutral molecules from their surfaces in a rapid, laser-induced thermal desorption process. The fact that desorption dominates over decomposition in rapid laser heating processes is well documented (refs. 10, 11). The sample can be rotated manually in order to expose fresh surface to the desorption laser. After an appropriate time delay (~130 μsec), the fourth harmonic of a Nd:YAG laser (266 nm; 1.5-2.0 mJ/pulse; 10-nsec pulse width; 5-Hz repetition rate) is used to induce 1+1 resonance-enhanced multiphoton ionization (REMPI) of the desorbed

molecules in an interaction region about 5 mm from the surface. REMPI causes soft ionization so that the parent ions of the desorbed aromatic compounds almost exclusively dominate the spectrum. Total ionization efficiency is about a factor of 100 to 1000 greater than that of methods where ions are directly produced on a surface. One of the advantages to the L^2MS system is the spatial and temporal separation of the desorption and ionization which results in more control than in one-step desorption /ionization processes. The laser-generated ions are mass separated in a linear TOF system (mass resolution = 500) and detected with a microchannel plate array. Data for the meteorite samples were averaged over 100 laser shots, although a complete mass spectrum can be obtained from a single shot.

Samples were prepared using MALDI (matrix assisted laser desorption ionization). Previous reports have shown that laser desorption of neutral molecules can be improved by spraying a fine layer of sample on top of a matrix that absorbs at the wavelength of the laser (ref. 12). For our L^2MS system, the organic substrate sinapinic acid was used as the matrix. The matrix is sprayed directly onto the stainless steel disc (100 ng/mm^2) insuring that the substrate is evenly dispersed over the entire surface of the disc. The impacted meteorite sample (sonicated in toluene) is then sprayed on top of the sinapinic acid film. The sample disc is mounted on a 7-mm diameter teflon probe tip and is introduced to the TOF mass spectrometer through a separate antechamber pumped down to zero millitorr before introducing it to the high vacuum (10^{-7} torr) of the system. Sample introduction takes about two minutes and the spectrum can be recorded immediately thereafter.

RESULTS

Diamond Craters. Craters formed by launching diamond into Al at 2.75 and 3.1 km sec^{-1} (Figs. 2-3) show morphological features similar to those formed at higher velocities (4 - 6.1 km sec^{-1}; Fig. 4). The crater morphologies resemble penetration funnels more than they do classical craters formed by other impactors. The depth to diameter ratio is 1-1.6 for craters formed < 4 km sec^{-1} and exceeds 1.5 for craters formed at ≈ 6 km sec^{-1}.

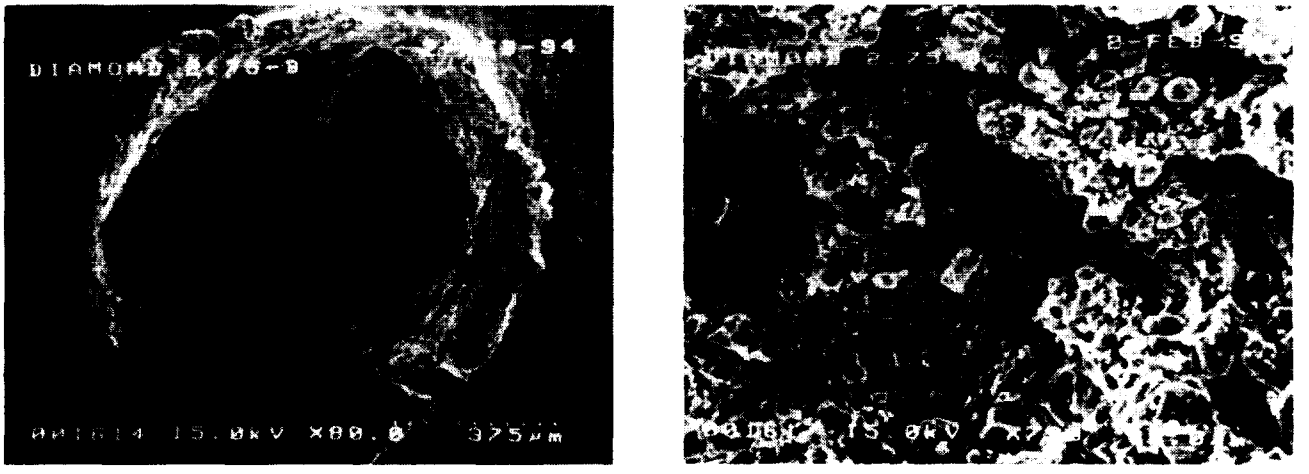

Fig. 2. FESEM images. (a) Diamond impact crater made at 2.75 km sec^{-1}. Note the ridge in the center and twin holes on either side. Apparently, the projectile broke into two main pieces soon after contact with the target. Arrow indicates ridge and area of 2b. (b) Enlargement near arrow showing micron to submicron fragments of intact diamond.

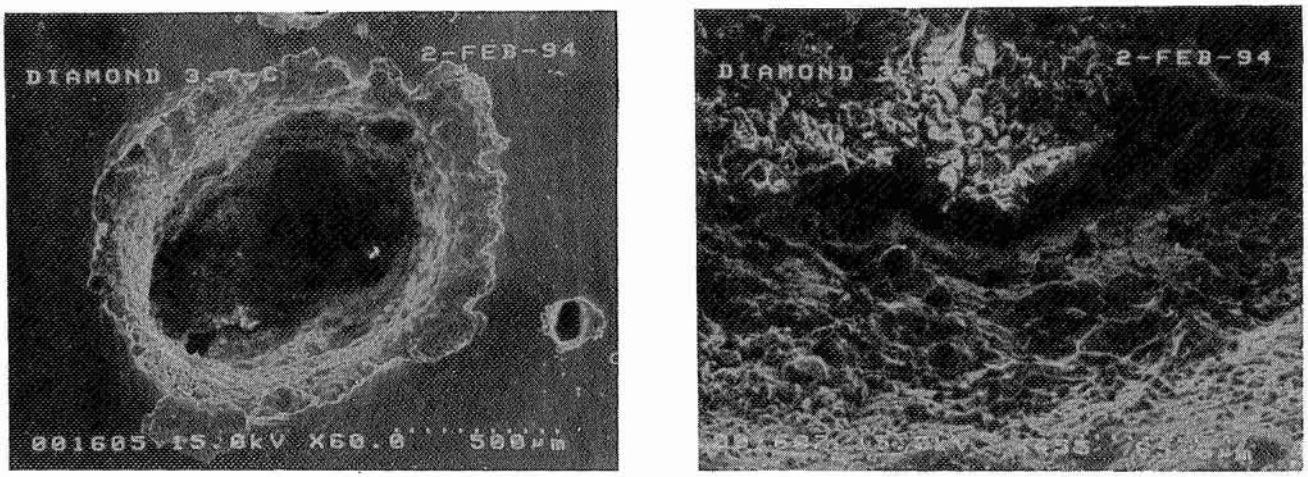

Fig. 3. (a) Diamond impact crater made at 3.1 km sec^{-1}. Arrow points to a ledge half way into the crater and the fragmented diamond in b. (b) Clump of fragmented, intact diamond.

Figure 3 shows a typical diamond crater formed at 3.1 km sec^{-1}. Raman spectroscopy of this crater indicates a strong band at 1330 cm^{-1} (diamond) and less intense bands at 1360 and 1620 cm^{-1} (PCG). In addition, a cluster of fragmented diamond can be seen on a ledge of the crater in Fig. 3a. Another launch at lower velocity (2.75 km sec^{-1}) shows abundant fragments in the center of the crater (Fig. 2). In our earlier report (ref. 1), we found evidence that some of the diamond may have actually melted (at 5 km sec^{-1}), although the carbon spherules observed in those craters may have been only carbon coated Al-melt spherules. To further investigate the problem, we launched diamond (0.3 - 0.5 mm dia.) into Al plate at 5.98 km sec^{-1}. FESEM examination of one crater (Fig. 5) illustrates the extreme P-T conditions that exist in shock impact. The open arrow points to a small, euhedral diamond fragment (0.012 mm in dia.) resting on a melt puddle of mostly carbon with a small amount of Al (solid arrows). The fragment may be ejecta from a nearby crater. Shrinkage cracks are very evident in the melt puddles and strongly infer derivation from a rapidly cooled melt.

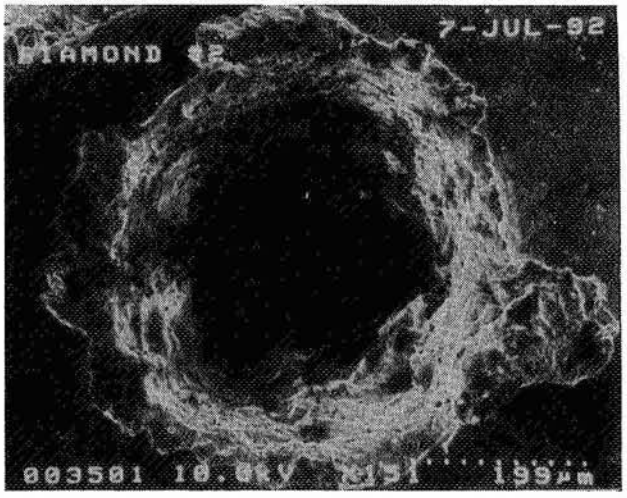

Fig. 4. Diamond crater made at 5.1 km sec^{-1}. Note the great depth and irregular cavity. Essentially no residual diamond; only PGC.

Nogoya Meteorite Impactor Residues. The PAH compositions of Nogoya have never been determined and we report here for the first time the PAH species from mass 128 to 300 (amu). The prelaunch PAH composition from L^{2}MS analyses is shown in Fig. 6a and Table 1 below.

Table 1. PAHs in prelaunched Nogoya.

Mass (amu)	Compound	B.P. (°C) (refs. 13, 14)
178	phenanthrene/anthracene*	340
192	methyl-phenanthrenes/anthracenes*	278,196
202	pyrene/fluoranthene*	393, 375
206	C_{16}-alkylphenanthrenes/anthracenes*	NA
220	C_{17}-alkylphenanthrenes/anthracenes*	NA
252	perylene	350-400
276	benzoperylene	415
300	coronene	525

* These are possible assignments of the observed peaks; different isomers of PAHs cannot be distinguished by L^2MS. NA = not available.

Nogoya differs from Murchison in its PAH content by not having naphthalene (mass 128) or any of the alkyl-substituted species (homologs) of naphthalene (mass 142, 154, 170, 198), *e. g.*, 2-methyl naphthalene (mass 142). *Note*: a single alkyl substitution is a univalent aliphatic radical attached to the PAH structure; CnH_2n+1 = 14 or CH_2. Alkylation comes from the "cracking of the polymer" or the loss of CH_2 from a polymer (ref. 15) that is concentrated in constituent kerogens of the meteorite and attaches itself to the PAH benzene ring structure during a thermal event. Generally speaking, the greater the alkylation of PAHs, the lower the formation temperature (ref. 16). For example, PAHs formed at 2000°C have no alkyl substitutions; 400°C, a few and at 150°C, up to 6 alkyl carbons (ref. 17).

We launched granules of Nogoya matrix (0.1-0.2 mm dia.) into Al plate at 6.2 km sec^{-1}. The post-impact PAH contents are given in Fig. 6b and compared with the prelaunched samples in Table 2.

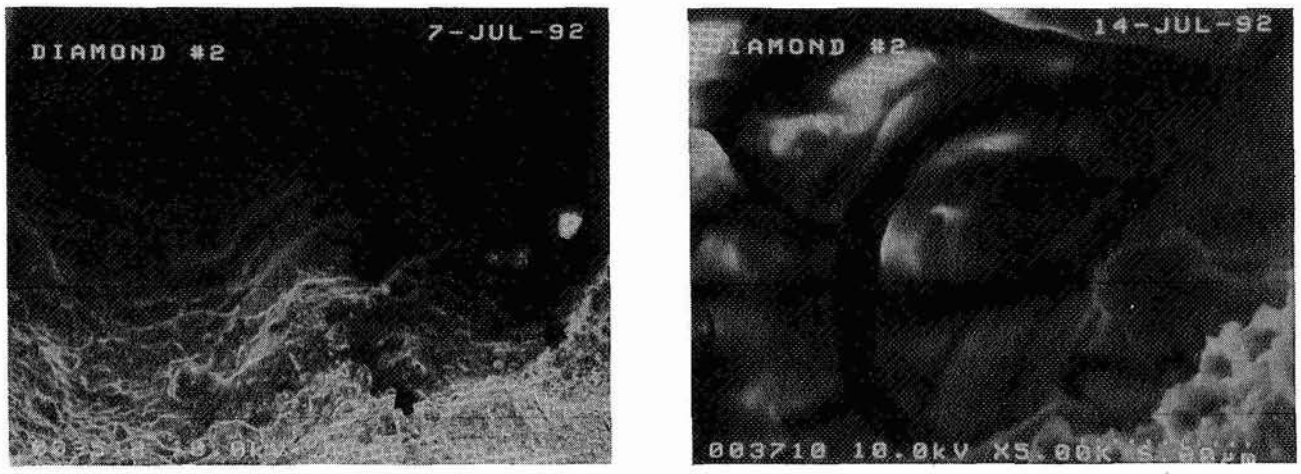

Fig. 5. (a) Diamond crater (enlarged area from Fig. 4) showing a diamond fragment (ejecta?) and two diamond melt "puddles" on the upper wall of the crater. (b) Enlargement of "puddle". Note shrinkage cracks.

MICROPARTICLE ACCELERATOR EXPERIMENTS

Instrument Description and Experimental Conditions

A unique microparticle accelerator (MPA), which produced high velocity, micron-sized projectiles of any cohesive material, was developed in the early years of the space age (ref. 18) and operated for 4 years until it was, unfortunately, shut-down. The samples and data were archived and forgotten for 18 years. We show a few examples of those experiments and discuss aspects of the accelerator because many of the experiments have a direct bearing on the interpretation of craters on LDEF. We plan to inventory the experimental results and samples and make the information available to interested investigators.

Although this accelerator is in the electrostatic class, its method of charging levitated particles surpassed in many ways the commonly used method of contact charging used by other accelerators. Single particles were charged by ion bombardment in an electrodynamic levitator. The vertical accelerator had four drift tubes, each initially at a high negative voltage. After injection of the projectile, each tube was grounded in turn at a time determined by the voltages and charge/mass ratio to give four acceleration stages with a total voltage equivalent to ≈ 1.7 MV. The delay times were set manually or controlled automatically by the particle's charge/mass ratio measured in the source by the operator just before ejection. At the entrance to the accelerator, the particle generated a signal that initiated the timing sequence. In the target chamber, detectors recorded the passage of the particle and provided information on charge, velocity, and position. Velocities between 0.5 and 15 km sec^{-1} were routinely attained and 20 projectiles could be accelerated per day.

Table 2. PAH content in Nogoya after impact at 6.2 km sec^{-1}.

Mass	Compound
Missing:	
252	perylene
276	benzoperylene
300	coronene
Greatly reduced in content:	
178	phenanthrene/anthracene
192	methyl-phenanthrenes/anthracenes
202	pyrene/fluoranthene
About the same:	
206	C_{16}-alkylphenanthrenes/anthracenes
Increased:	
220	C_{17}-alkylphenanthrenes/anthracenes
Synthesized?	
234	C_{18}-alkylphenanthrenes/anthracenes

Table 3 lists some of the projectiles and targets that were used; many thousands of experiments were made over the lifetime of the accelerator. In all cases, the mass, velocity and size of the impactor, the depth to diameter ratio of the crater, and impact energy are known.

Scanning electron microscope images of a few cratering examples are shown in Figs. 7-9. We plan to start an analytical program to investigate impact residues of the impactors where feasible. Examples of residue signatures from ZnS crystals impacted into fused quartz at velocities of 4.6, 6.4 and 10.1 km sec^{-1} are shown in Figs. 10 and 11. Although MPA craters are exceedingly small (<0.001-006 mm), they are similar in size to many of the craters on LDEF and the nominal size of craters examined on the COMET/SALIOUT Mission that mainly sampled particles from the Giacobini-Zinner Comet (J. Borg, pers. comm.). FESEM analyses of the ZnS craters indicate that Zn can still be detected on the rims of the MPA craters up to and including the 10.1 km sec^{-1} crater (Fig. 11).

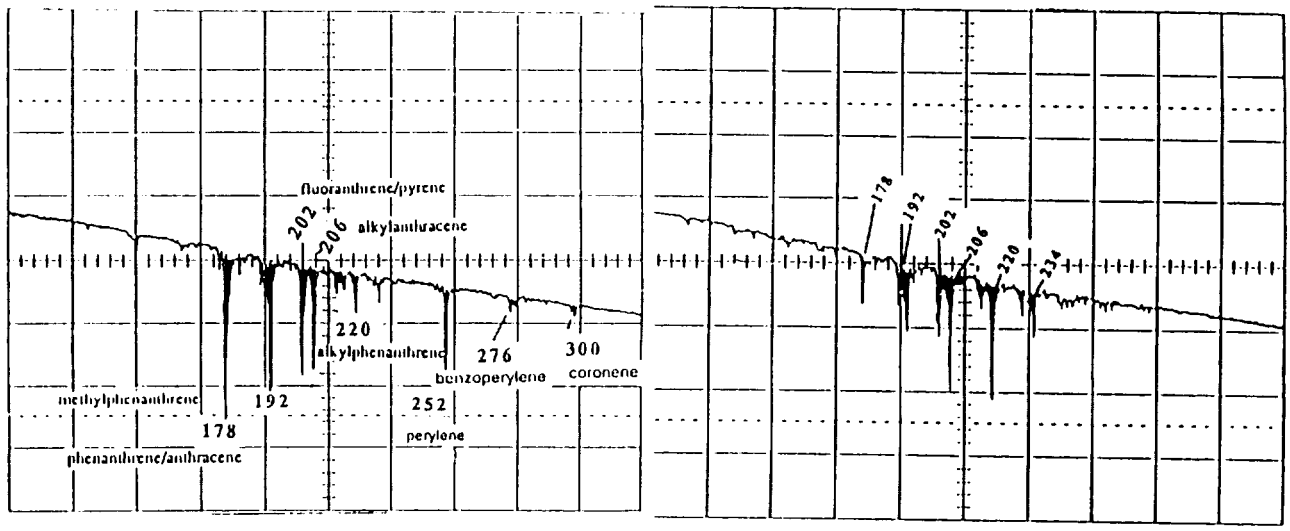

Fig. 6. (a) L^2MS spectrum of non-impacted Nogoya. (b) After impact into Al at 6.2 km sec^{-1}.

Table 3. Examples of MPA projectiles and targets.

Projectile	Velocity range (km sec^{-1})	Targets
Polyethylene	6-14	glass
Polystyrene-DVB	1-14	glass, fused quartz, basalt glass, glass beads, lexan, Al, Cu stainless steel, feldspar silicates, diopside, olivine, chrysotile
Aluminum	1.6-14	Na glass, fused quartz, Al_2O_3, Al, Cu, olivine, feldspars, chrysotile.
Iron	1-15+	glass, basalt glass, fused quartz, olivine, diopside olivine, chrysotile.
SiO_2	1-13	glass, lead glass, olivine, feldspar
Kaolin (clay)	0.4-9.4	glasses, feldspars, olivine, quartz, chrysotile
ZnS	3.5-10.1	fused quartz
Ti-glass	2.4-13.7	stainless steel, quartz, feldspar, Na glass and Pb glass

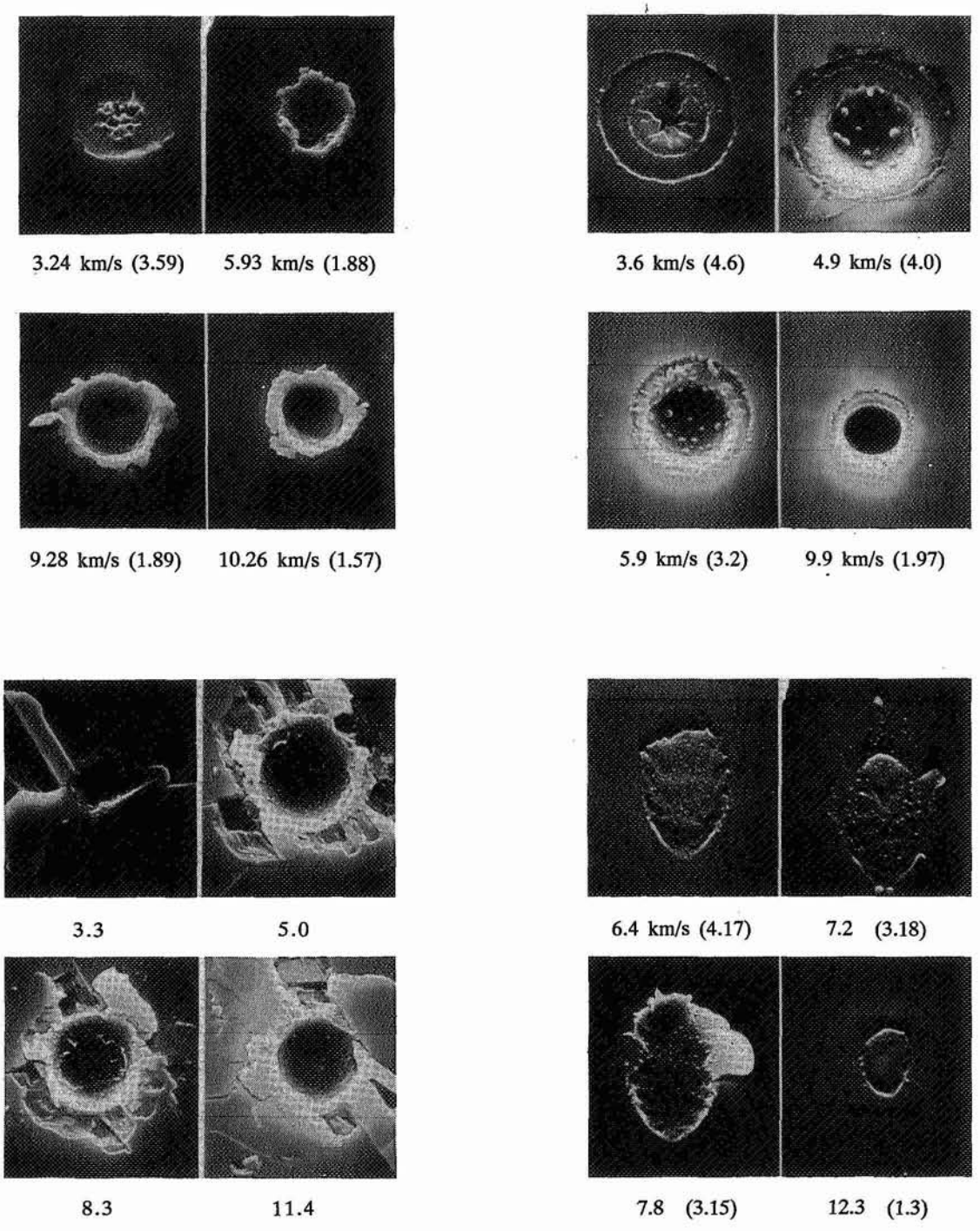

Fig. 7. SEM images of MPA craters: (a) Polystyrene launched into steel. (b) Polystyrene into fused quartz covered by a layer of Al + MgF_2. (c) Polystyrene into plagioclase. (d) Polystyrene into glass (60° from vertical). Impactor diameters in parentheses.

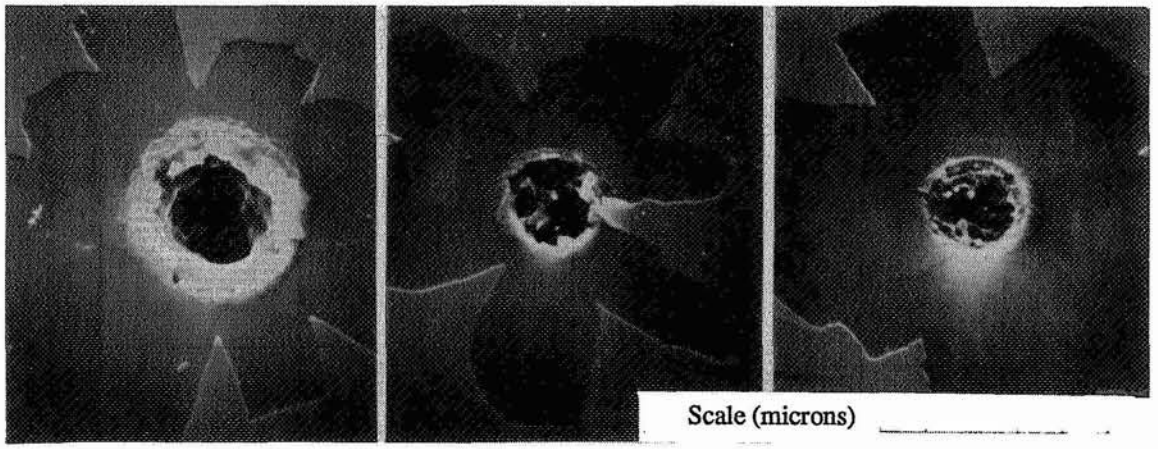

Fig. 8. Polystyrene into chrysotile (clay). Numbers refer to velocities (km sec^{-1}).

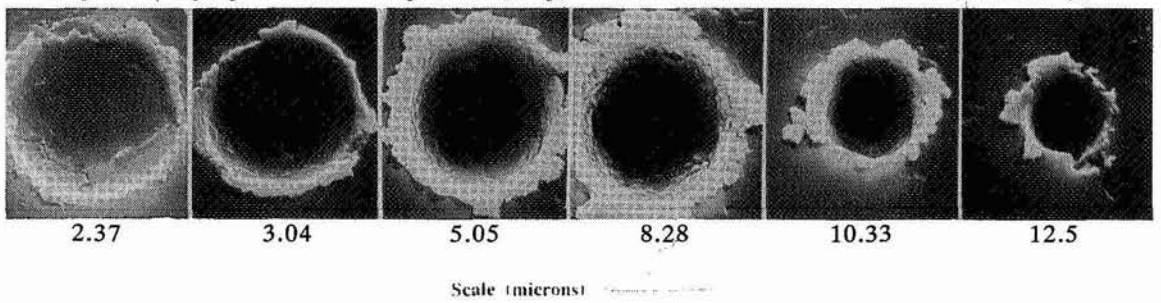

Fig. 9. Polystyrene into steel. Numbers refer to velocities (km sec^{-1}).

DISCUSSION

Diamond From our impact experiments, we find that diamond can, at least, partially survive in impacts > 3.1 to < 4.3 km sec^{-1}. At 4.3 km sec^{-1}, diamond decomposes to PCG with some melting, and clear evidence for melting is developed at impact velocities of 5.5 km sec^{-1}. We can not directly measure peak pressures and temperatures of the experiments, although peak pressures can be extrapolated from equation-of-state information for Al and diamond and from the thermodynamic model that solves for peak stress generated by impactors and their targets (ref. 19). For diamond impacts of 2.75, 3.1, 4.3 and 5.5 km sec^{-1}, peak pressures are calculated as ≈ 35, 39, 60 and 84 GPa, respectively (M. Cintala. pers. comm.). The highest two pressures are sufficient to produce melting of anorthosite on impact into Al (ref. 20); diamond, which is 20% more dense than anorthosite should partially melt at these peak pressures. The time duration of peak pressures and temperatures for these impact events is probably on the order of 10^{-6} to 10^{-9} sec and the total crater formation time is probably less than a few μsec; extrapolated from data of (ref. 21). Although diamonds are not expected to be present as diamond IDPs from the interstellar medium, they are expected to be present as small grains (up to 10s of nanometers in dia.) in chondritic meterorites (ref. 22). The apparent low thermal stability of diamond under shock as shown in these experiments makes the study of any extracted intact meteoritic impact debris from LDEF craters impractical for diamond. On the other hand, our experiments establish a lower limit on diamond stability with respect to impacts into silicates during planetary accretion, *i. e.*, impacts into silicates > 3 km sec^{-1}, would probably destroy pertinent isotopic and noble gas information.

The irregular crater cavities may be attributed to the extreme ease with which diamond cleaves/fragments under impulsive loading. At the inception of impact in our experiments, diamond apparently broke into several large fragments and formed multiple-sized crater cavities at different depths within the crater, dependent on each fragment's mass. Clumps of finely fragmented intact diamonds for the 2.75 and 3.1 km sec^{-1} experiments are observed in the bottom of each cavity of the crater (Figs. 2-3). This phenomenon is also observed to a lesser degree in craters formed by less coherent impactors, e. g., carbonaceous chondrite matrix projectiles which are composed of many weakly bound small grains. At higher impact velocities (ref. 1), the multiplicity of cavities per crater diminish, and the dominant morphology resembles a long, sinuous cavity with small branches from diamond fragmentation during the formation of the main crater cavity.

Nogoya. In our earlier report, we found that lower mass PAHs, naphthalene and alkyl-substituted naphthalenes (homologs), were absent in the impacted Murchison meteorite sample (5.9 km sec^{-1}). This absence was attributed to the higher volatility of these lower molecular weight PAHs which presumably volatilized during impact. In contrast, unshocked Nogoya does not contain PAHs below 178 amu and, in addition, contains PAHs above 252 amu (Fig. 6a). Figure 6b (shocked Nogoya) shows that the unsubstituted PAHs are either absent or greatly reduced by impact at 6.2 km sec^{-1}. This is expected for those below 202 amu, because of their higher volatility, but not for those above 252. For example, coronene has the highest boiling point

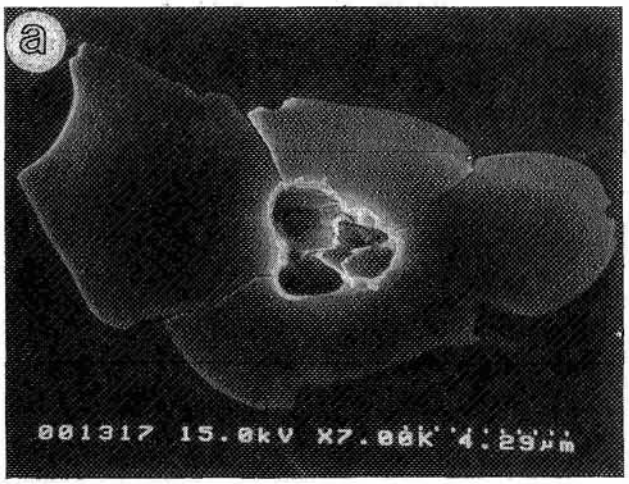

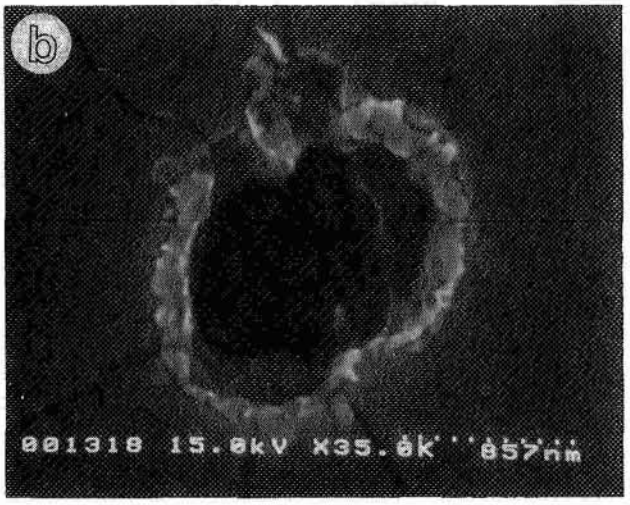

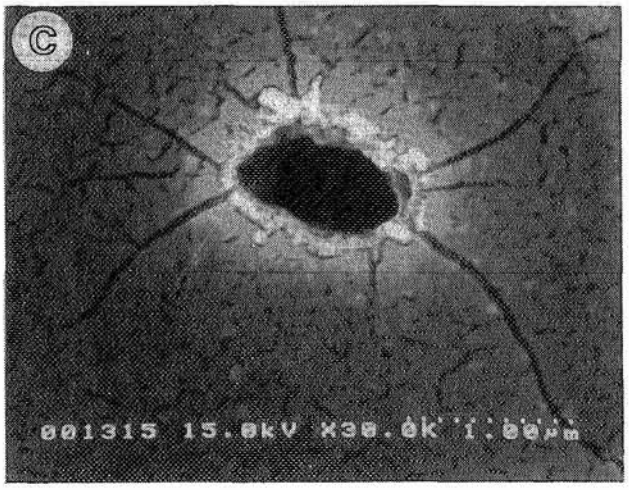

Fig. 10. SEM images of ZnS formed craters in glass: (a) 4.6 km sec^{-1} crater. Impactor apparently separated into 3 fragments at impact. Impactor size was 0.0089 mm. (b) 6.4 km sec^{-1} crater. Cracked surface is due to breakup of Au coating with time. Impactor dia. was 0.001 mm. (c) 10.1 km sec^{-1} crater. Impactor dia. was 0.00066 mm. All crater outlines depart from circularity. All launches were 90° to the target and all rims contain detectable Zn.

of the common PAHs (Table 1) and is the most stable of aromatic compounds (ref. 23). The absence of coronene and benzoperylene in impacted Nogoya may be due to their low abundance in Nogoya, which is estimated from the L^{2}MS spectrum (Fig. 6a) to be 1-5 ppm. The low concentration together with the known highly heterogeneous distributions of meteoritic organics may just be a sampling bias. However, this does not explain the absence of abundant perylene (252 amu) in shocked Nogoya. Moreover, as in the case for shocked Murchison, the alkylated homologs (206 and 220 amu) are the most abundant PAH species. In shocked samples of both meteorites, C_{18}-alkylphenanthrene/anthracene at amu 234 is present, probably as an impact-synthesized PAH. A detailed discussion with regard to the behavior of PAHs under shock loading conditions is beyond the scope of this report. We can conclude that, within our experimental and analytical constraints, some PAHs do survive impact at 6.2 km sec^{-1}, some are destroyed and a few appear to be synthesized (see Table 2).

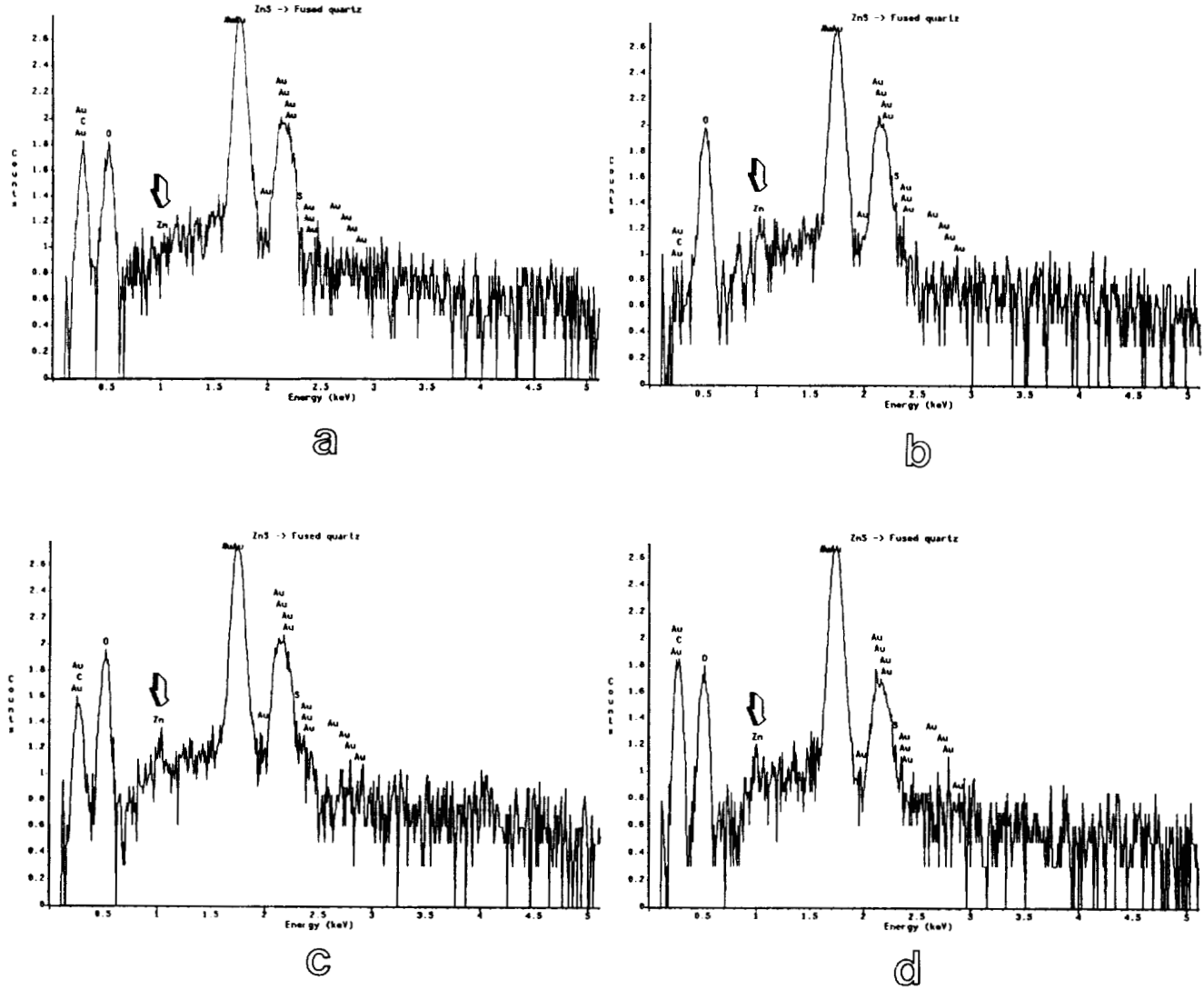

Fig. 11. SEM-EDS spectra of craters in Fig. 11 showing the presence of Zn residues. (a) Background. (b), (c), and (d) are the 4.6, 6.4 and 10.1 km sec^{-1} craters, respectively.

SUMMARY

A summary of the experimental results of the light gas gun experiments to date on carbonaceous impactors are given in Table 4.

Table 4. Summary of hypervelocity impact experiments involving carbonaceous impactors.

Samples	Velocity (km sec^{-1})	Remarks
Graphite	3-5.95	Graphite decomposed to various degrees of poorly characterized graphite (PCG). Correlation of highest disorder with distance away from crater bottom center.
Fullerenes	4-6.2	A small portion of fullerene impactors decomposed to disordered carbon. Fullerenes not formed from carbonaceous impactors.
Diamond	2.75-5.95	Diamond decomposed to PCG and vitreous/amorphous carbon above 4 km sec^{-1} impact velocities.
Murchison	4.35-5.98	PAHs above molecular mass 178 mostly survived impact. Naphthalene and alkyl-substituted naphthalenes were destroyed. Additional alkyl homologs of phenanthrene-/anthracene were synthesized, especially at 220 and 234 amu.
Phthalic	2.1-6.25	Much of the molecule survives at 4 km sec^{-1} and decreases in abundance at higher impact velocities (up to 6.25).
Nogoya	4.3-6.1	Carbonaceous chondrite that contains more water, bulk C, and somewhat different organic chemistry than Murchison. PAHs between mass 178 and 206 amu partially survived impact, although those above 240 amu were also destroyed. Additional alkyl homologs of phenanthrene/anthracene were synthesized, especially at 220 and 234 amu.

ACKNOWLEDGEMENTS

We thank the LDEF Project Office and the NASA Exobiology Program for support of this work.

REFERENCES

1. Bunch, T. E.; Becker, L.; Bada, J.; Macklin, J.; Radicati di Brozolo, F.; Fleming, R. H.; and Erlichman, J.: Hypervelocity impact survivability experiments for carbonaceous impactors. *Second LDEF Sym. NASA* **CP-3194**, 453-477, 1993.

2. See, T.; Allbrooks, M.; Atkinson, D.; Simon, C.; and Zolensky, M.: Meteoroid and debris impact features documented on the Long Duration Exposure Facility a preliminary report. *Planet. Sci Branch Publ.* **# 84** (JSC **# 24608**), 1990.

3. Hörz, F.; Bernhard, R. P.; Warren, J.; See, T.; Brownlee, D. E.; Laurance, M. R.; Messenger, S.; and Peterson, R. B.: Preliminary analysis of LDEF instrument A0187-1 "Chemistry of micrometeoroids experiment". *First LDEF Sym. NASA* **CP-3134,** 487-499, 1992.

4. Bunch, T. E.; Radicati di Brozolo, F.; Fleming, R. H.; Harris, D. W.; Brownlee, D. E.; and Reilly, T.: LDEF impact craters formed by carbon-rich impactors: A preliminary report. *First LDEF Sym. NASA* **CP-3134**, 549-564, 1992.

5. Peterson, E.; Hörz, F.; Haynes, G.; and See, T.: Modification of amino acids at shock pressures of 3 to 30 GPa. *Meteoritics* **26**, 384, 1991.

6. Lewis, R. S.; Tang, M.; Wacker, J. F.; Anders, E.; and Steel, E.: Interstellar diamonds in meteorites. *Nature* **326**, 160-162, 1987.

7. Allamandola, L. J.; Sandford, S. A.; Tielens, A. G. G. M.; and Herbst, T. M.: Diamonds in dense molecular clouds: A challenge to the standard interstellar paradigm. *Science* **260**, 64-66, 1993.

8. Allamandola, L. J.; Sandford, S. A.; and Wopenka, B.: Interstellar polycyclic aromatic hydrocarbons and carbon in interplanetary dust particles and meteorites. *Science* **237**, 56-59, 1987

9. Langevin, Y.; Kissel, J.; Bertaux, J-L.; and Chassefiére E.: First statistical analysis of 5000 mass spectra of cometary grains obtained by PUMA 1 (Vega 1) and PIA (Giotto) impact ionization mass spectrometers in the compressed modes. *Astron. Astrophys.* **187**, 761-766, 1987.

10. Hahn, J.H.; Zennobi, R.; Zare, R.N.: Subfemtomole quantitation of molecular absorbates by two-step laser mass spectrometry. *J. Amer. Chem. Soc.* **109**, 2842-2843, 1987.

11. Engelke, F.; Hahn, J.H.; Henke, W.; Zare, R.N.: Determination of phenythiohydrandion-amino acids by two-step laser desorption/multiphoton ionization. *Anal. Chem.* **59**, 909-912, 1991.

12. Hillenkamp, F.; Karas, M.; Beavis, R.C.; Chait, B.T.: Matrix-assisted laser desorption/ionization mass spectrometry of biopolymolecules. *Anal. Chem.* **63**, 24-37, 1991.

13. Zenobi, R.; et al.: Spatially resolved organic analysis of the Allende meteorite. *Science* **24**, 1026-1028, 1989.

14. *Handbook of Chemistry and Physics*, 67th edition. The Chemical Rubber Co., Cleveland, OH 1987.

15. Ishiwatari, R. and Fukushima, K.: Generation of saturated and aromatic hydrocarbons by thermal alteration of young kerogen. *Geochim. Cosmochim. Acta* **43**, 1343-1349, 1979.

16. Wing, M. R. and Bada, J. L.: Geochromatography on the parent body of the carbonaceous chondrite Ivuna. *Geochim. Cosmochim. Acta* **55**, 2937-2942, 1991.

17. Blumer, M.: Polycyclic aromatic compounds in nature. *Sci. Amer.* **234** no. 3, 34-38, 1976.

18. Vedder, J. F.: Microparticle accelerator of unique design. *Rev. of Sci. Instr.* **49**, 1-7, 1978.

19. Cintala, M. J.: Impact-induced thermal effects in the Lunar and Mercurian regolith. *J. Geophy. Res.* **97**, 947-973, 1993.

20. Bernhard, R. P.; See, T. H. and Hörz, F.: Projectile compositions and modal frequencies on the "Chemistry of micrometeoroids" LDEF experiment. *Second LDEF Sym.* **NASA CP-3194**, 551-573, 1993.

21. Hörz, F.; Fechtig, H. and Janicke, J: Morphology and chemistry of projectile residues in small experimental craters. *Proc. 14th LPSC, J. Geophy. Res.* **88**, B353-363, 1983.

22. Huss, G. R.: Ubiquitous interstellar diamond and SiC in primitive chondrites: Abundances reflect metamorphism. *Nature* **347**, 159-162, 1990.

23. Aihara, Jun-ichi: Why aromatic compounds are stable. *Sci. Amer.* **240**, no. 3, 62-68, 1992.

ANALYTICAL ELECTRON MICROSCOPY OF LDEF IMPACTOR RESIDUES

Ronald P. Bernhard & Ruth A. Barrett
Lockheed ESC, C-23
Johnson Space Center
Houston, Texas 77058

Michael E. Zolensky
Solar System Exploration Division
NASA Johnson Space Center
Houston, Texas 77058

ABSTRACT

The LDEF contained 57 individual experiment trays or tray portions specifically designed to characterize critical aspects of meteoroid and debris environment in low-Earth orbit (LEO). However, it was realized from the beginning that the most efficient use of the satellite would be to characterize impact features from the entire surface of the LDEF. With this in mind particular interest has focused on common materials facing in all 26 LDEF facing directions; among the most important of these materials has been the tray clamps. Therefore, in an effort to better understand the nature and flux of particulates in LEO, and their effects on spacecraft hardware, we are analyzing residues found in impact features on LDEF tray clamp surfaces. This paper summarizes all data from 79 clamps located on Bay A & B of the LDEF.

We also describe current efforts to characterize impactor residues recovered from the impact craters, and we have found that a low, but significant, fraction of these residues have survived in a largely unmelted state. These residues can be characterized sufficiently to permit resolution of the impactor origin. We have concentrated on the residue from chondritic interplanetary dust particles (micrometeoroids), as these represent the harshest test of our analytical capabilities.

INTRODUCTION

LDEF experiment trays were held in place by a series of chromic-anodized aluminum (6061-T6) clamps (Figure 1); eight clamps were used to attach the experiment trays on each of the 12 sides of LDEF, while experiment trays on the Earth and space ends were held in place by 12 clamps. Each clamp was fastened to the spacecraft frame using three stainless steel hex bolts. Clamps exposed an

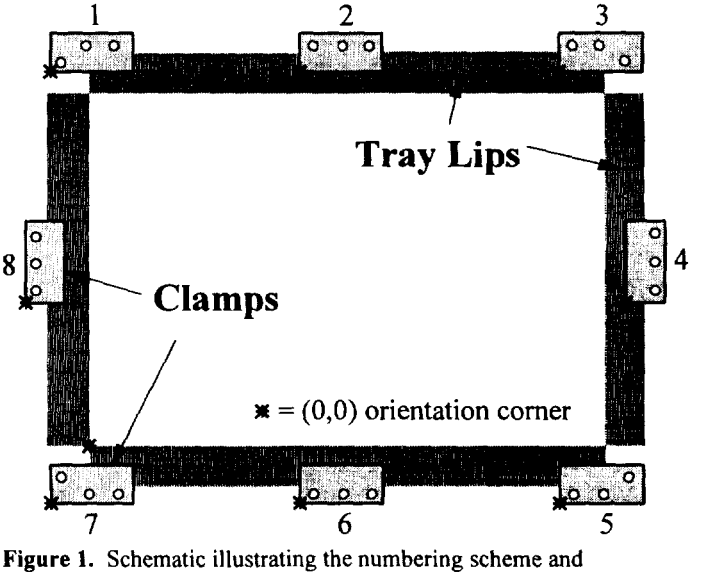

Figure 1. Schematic illustrating the numbering scheme and positioning of the clamps and bolt holes on an LDEF peripheral tray.

approximately 58 cm^2 each (4.8 cm x 12.7 cm x 0.45 cm thick, minus the bolt coverage). All 774 LDEF clamps were surveyed for impact features greater than 0.5 mm in diameter during experiment tray deintegration at the Kennedy Space Center. Some 337 out of 774 LDEF tray clamps have been archived by the M&D SIG in the Curatorial Facility at JSC and are available for scientific examination by qualified individuals.

LDEF affords the opportunity to obtain information about the directionality of the meteoroid and debris fluxes. This data can then be related to the sources of meteoroids and orbital debris only if the progenitor particulate can be identified for each (or a representative population) of impact features. With this goal in mind we are characterizing the bulk chemistry of a large number of impactor residues, and the detailed mineralogy of a fraction of these. This information is needed to deduce the asteroidal versus cometary abundance of impacting meteoroids, and source of spacecraft debris particles.

RESULTS

Clamp Survey

A clamp numbering scheme was devised which would provide hardware location information with respect to its position within a particular bay (Figure 1). From the labeling scheme, it can be seen that a clamp occupying position 1 of Bay B02 would be identified by the label B02-C01, with B02 indicating the experiment location of Bay "B" and Row "02", and C01 interpreted as "C" for clamp and "01" being the clamp number. Each clamp uses a Cartesian coordinate system to reference impact locations on exposed surfaces. The X and Y coordinates were measured in millimeters using a standard origin assigned by the M&D SIG at the lower-left corner of each clamp (Figure 1).

Optical scanning of clamps, starting with Bay A Row 01 and working through the entire satellite, is being conducted in the Facility for Optical Inspection of Large Surfaces (FOILS) at JSC to locate and document impact features as small as 30 microns. These impacts are then examined by Scanning Electron Microscopy/Energy Dispersive X-ray Analysis (SEM/EDXA) to further characterize those features which contain appreciable impactor residue. Based upon the bulk composition of these residues, and using criteria developed at JSC (ref. 1), we have made a preliminary discrimination between micrometeoroid- and space debris-containing impact features. These data are then published in a catalog format which includes: (1) an optical photograph of each clamp, (2) a secondary electron image of the impact, (3) associated parameters such as impact feature size , (4) an EDXA plot of the residue, (5) impactor origin (if applicable), and (6) a curatorial number which will facilitate requests for specific impact features by interested investigators (ref. 2). An example of a page from one of these catalogs is given in Figure 2. All

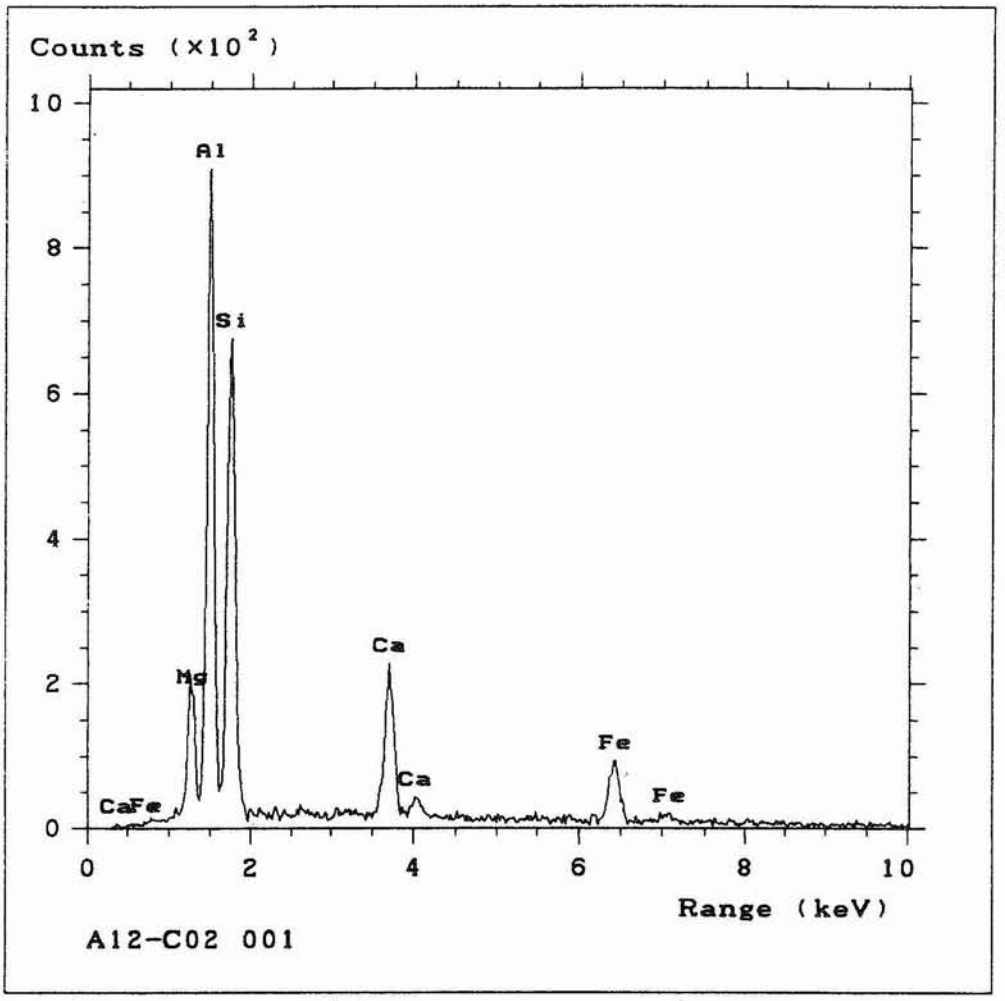

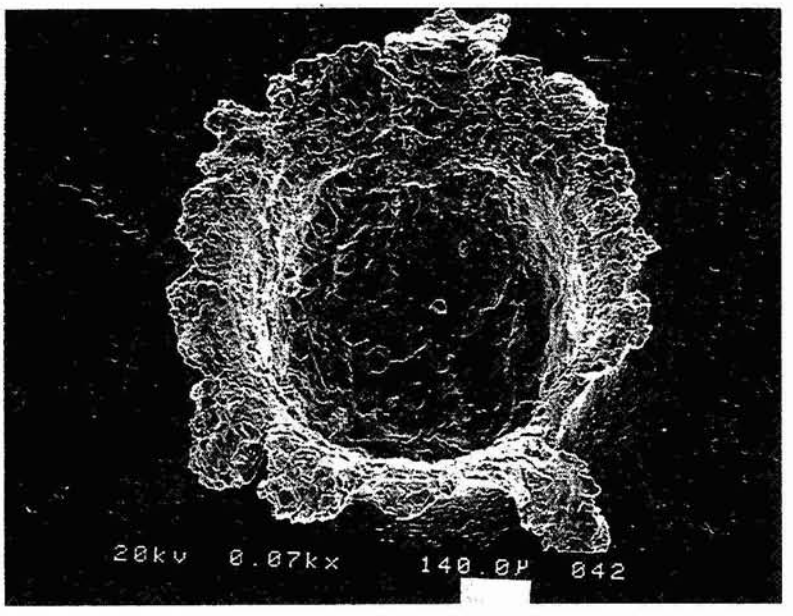

Figure 2. An example page from NASA TM #104759. In these catalogs each crater is documented and a general X-ray spectra of associated impactor residue is illustrated.

results are being input into the M&D SIG computerized database, which documents all LDEF meteoroid and debris results, and is accessible to investigators via Internet or by modem (ref. 1).

Each of the clamps is optically scanned; and all impact features greater than 40 microns (and some as small as 30 microns) are labeled and their position is documented. After scanning, an optical photograph is taken of the clamp illustrating each of the impact features located optically. SEM/EDXA is then conducted on each feature which has been identified optically. Not all features identified are high velocity impacts; in some cases, because of resolution limits during optical inspection, clamp manufacturing flaws, handling flaws, and contamination spots have been mistakenly identified as impact features. During SEM/EDXA analysis these features were properly identified and labeled as such. These features include craters and pits caused during manufacturing and handling of the clamps. Residual abrasive grit, from the polishing step of manufacture, could become trapped between the clamps when they were stacked one upon each other; movement caused these grains to roll and leave tracks and pits (ref. 3).

Because the initial intent of this survey was to identify only those impacts which contained large amounts of micrometeoritic residue, a minimal amount of time has been spent analyzing for small or unobvious projectile remnants. Therefore, many of the impacts are classified as having no definite origin. Detectable residues were classified as either natural or man-made materials (Figure 3), and each of these two main populations may be further broken down into subgroups. Of the 425 craters examined to date, 136 contained residues categorized as natural, being from chondritic interplanetary dust particles. Monomineralic, mafic-silicate (olivines, pyroxenes and phyllosilicates) compositions and Fe-Ni sulfide particles were found to a lesser degree.

In some cases, large amounts of seemingly unmelted projectile fragments have been observed (Figure 4) in LDEF impacts, these projectile residues undergo further analytical processing. A detailed structural and compositional analysis of several impactor residues was performed utilizing transmission electron microscopy (TEM), energy dispersive spectroscopy, and electron diffraction (*e.g.*, ref. 4). Details of the procedures involved for the mineralogical characterization of impactor residues are given below.

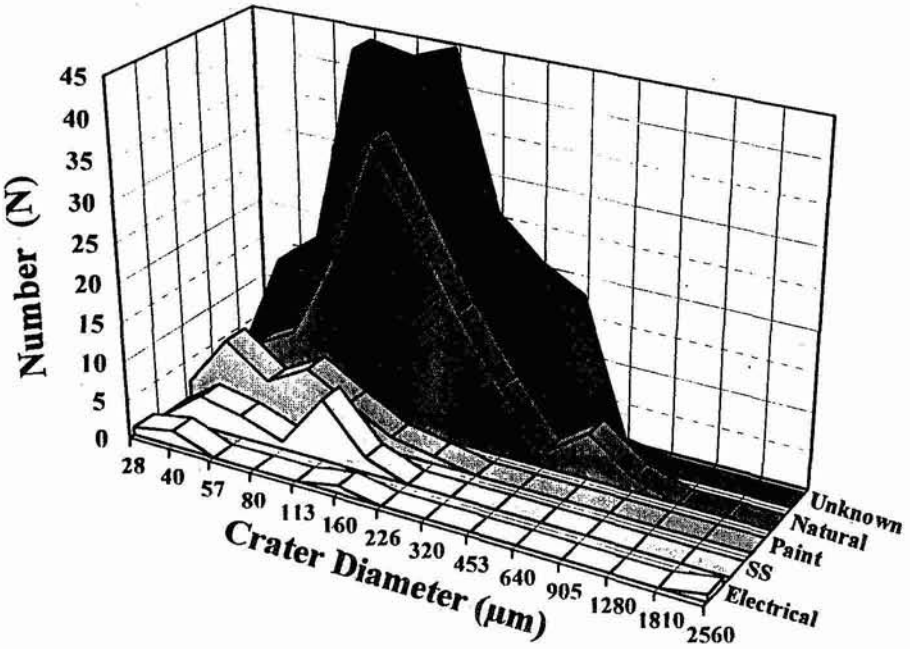

Figure 3. Histogram illustrating the size-frequency distribution of the various particle types.

Man-made debris compositions include spacecraft thermal paint rich in Zn, Ti, Cl, and Si (32 impacts); electrical components

(A)

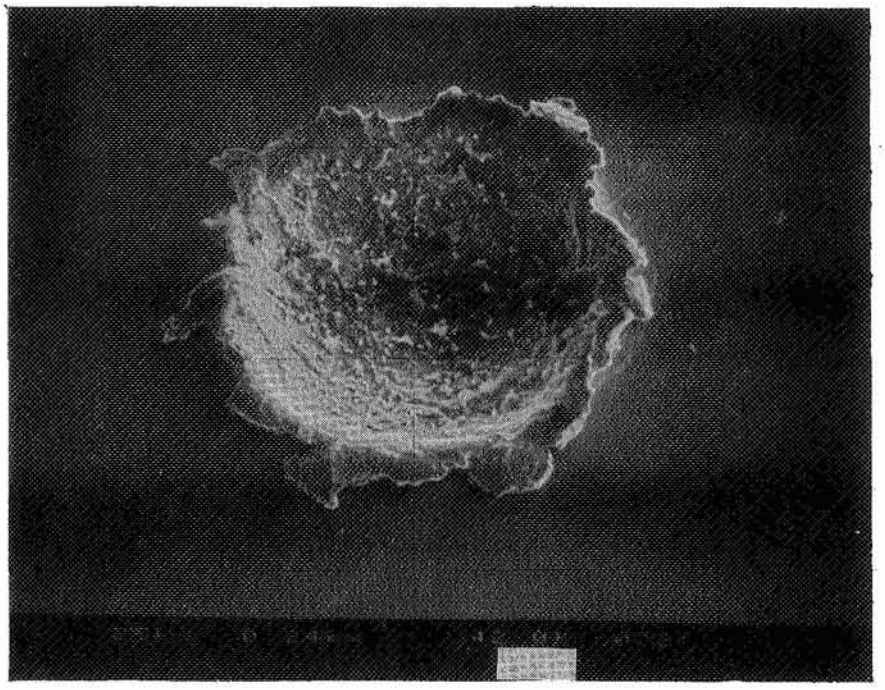

(B)

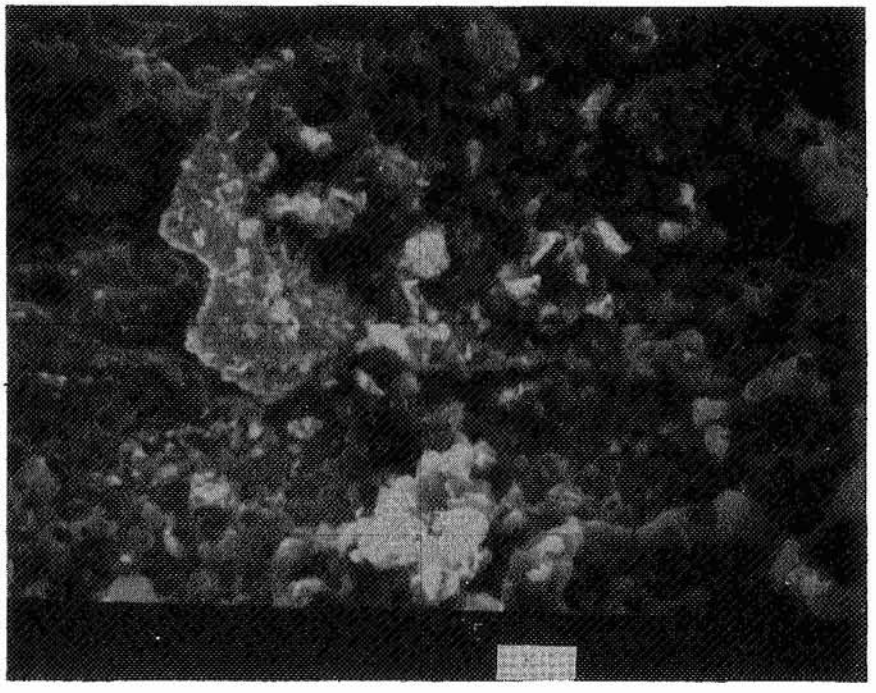

Figure 4. SEM images of chondritic projectile residues detected in crater 102. Portions of these residues were extracted from the crater and analyzed by TEM. (A) 210μm diameter crater, scale bar = 42μm. (B) Closeup of projectile residue, scale bar = 5μm.

seen as Pb, Sn, and Ag (5 impacts); and spacecraft structural hardware consisting predominantly of Stainless Steel and Al/Mg alloys (18 impacts; not easily detected on Al surfaces).

The 234 clamp impact features in which we have found no detectable residues displayed only a composition typical of the clamp aluminum alloy. While we believe that many of these impacts were in fact caused by Al-dominated debris particulates, we also maintain that further, more detailed, analyses will undoubtedly uncover evidence of impactor residues in many of the presently unclassified impact craters, and the support of such subsequent analyses is a primary objective in publishing the catalog. A factor hindering our analyses is the fact that the clamps have all been anodized, a process which deposited a surface layer of Si, Mg, and S, all of which are important elements for the discrimination of natural from man-made materials. For this reason, we would like to discourage the use of anodized coatings in the future where the gain in thermal protection to the spacecraft will be negligible.

As mentioned we have published our data on all 425 impacts found on Bay A and Bay B of the LDEF (ref. 2). Subsequent catalogs will include clamps from succeeding bays of the satellite, and will be published as time and resources permit.

Mineralogy of Impactor Residues

LDEF impactor residues are being characterized to establish the nature and abundance of meteoritic and orbital debris materials in the LEO environment. Although our goal is to characterize residues from *both* orbital debris *and* meteoroids, we have concentrated our initial efforts on the more fragile chondritic meteoroids, since these represent the worst case for hypervelocity impactor residue preservation. If we can be successful with chondritic meteoroids we can surely succeed with the orbital debris residues.

We have developed simple techniques for the study of selected chondritic (containing Si, Mg, Fe, +/- Al, Ca, S, Mn, and Ni in appropriate amounts) impactor residues in shallow craters in gold plates, from the LDEF experiment A0178. A detailed structural and compositional analysis of several of these impactor residues was performed utilizing transmission electron microscopy, energy dispersive spectroscopy, and electron diffraction. The immediate goal of this continuing work has been to determine the shock effects exhibited by chondritic meteoroids (a.k.a. Interplanetary Dust Particles or IDPs), and to compare the impactor residues to chondritic IDPs collected from the stratosphere.

Residues from the interior of several meteoroid impact craters were removed with a tungsten needle, mounted in EMBED-812 epoxy, and ultramicrotomed into 90 nm thick sections. Observation of the sections on carbon-coated copper grids was done by transmission electron microscopic techniques using JEOL 100CX and 2000FX analytical electron microscopes. Chemical analyses were performed with a PGT System 4, and an energy dispersive X-ray spectrometer and reduced with the PGT dedicated software. The structural state of all analyzed materials was assessed by electron diffraction, which proved to be a critical step, considering the non-crystalline nature of many materials observed.

We examined the mineralogy of residues from three impact features: nos. 102, 121, and 295. Impact residue in 102 has abundant, very finely-divided, crystalline augite ($En_{55-59}Wo_{36-40}$) and orthopyroxene (En_{84-96}) showing abundant evidence of intense shock, these being planar deformation features, mosaicism (see Figure 5), and, in some instances, evidence of recrystallization (120° grain intersections). The matrix consists of frothy ferromagnesian glass. Spherical bodies of Fe-Ni metal and pyrrhotite abound locally, particularly at grain boundaries (see Figure 6). Some Fe-Ni grains are metallic glasses (J. Bradley, personal communication, 1993). Impact residue 121 contains fragmental grains of olivine (Fo_{57-67}), orthopyroxene (En_{63-64}), Fe-Ni metal, and abundant frothy glass (see Figure 7). The olivine and pyroxene grains show abundant evidence of shock (see above for criteria). Impact residue 295 contains shocked, fragmental olivine (Fo_{56-71}) and orthopyroxene (En_{71}), pyrrhotite, and glass.

The pyroxenes in residue 102 have Fe-poor, restricted compositions (see Figure 8). For comparison we show the observed compositional ranges of olivines and pyroxenes in chondritic IDPs in Figure 9. As can be seen in the latter figure, the compositional range of ferromagnesian minerals is considerably more restricted in the hydrous IDPs relative to the anhydrous ones. Comparison to the compositions of ferromagnesian minerals in residue 102 (Figure 8) suggests that impactor 102 was a hydrous IDP. The parent bodies for hydrous IDPs are believed to be main belt asteroids.

The compositions of olivines and orthopyroxenes in the other residues characterized in this study are equilibrated compare to anhydrous chondritic IDPs, and also Fe-rich compared to hydrous chondritic IDPs (see Figure 9). They are also Fe-rich as compared to ferromagnesian silicates from partially melted chondritic IDPs (see Figure 8), which are typically on the order of Fo_{90} and En_{90}. The presence of equilibrated and shocked ferromagnesian minerals, recrystallization textures, glass, and melted metal and sulfide bodies decorating grain boundaries, is indicative of varying degrees of shock metamorphism in all impact residues we have characterized. Our failure to locate any magnesian olivines or pyroxenes in these particular residues is illustrative of the pervasive shock metamorphism they experienced. We are continuing to characterize additional IDP impactor residues, including those from suspected orbital debris particulates.

Figure 5. A TEM image of a microtomed residue grain from impact 102. Pyroxene crystals in the field of view have been recrystallized, as indicated by 120° grain intersections.

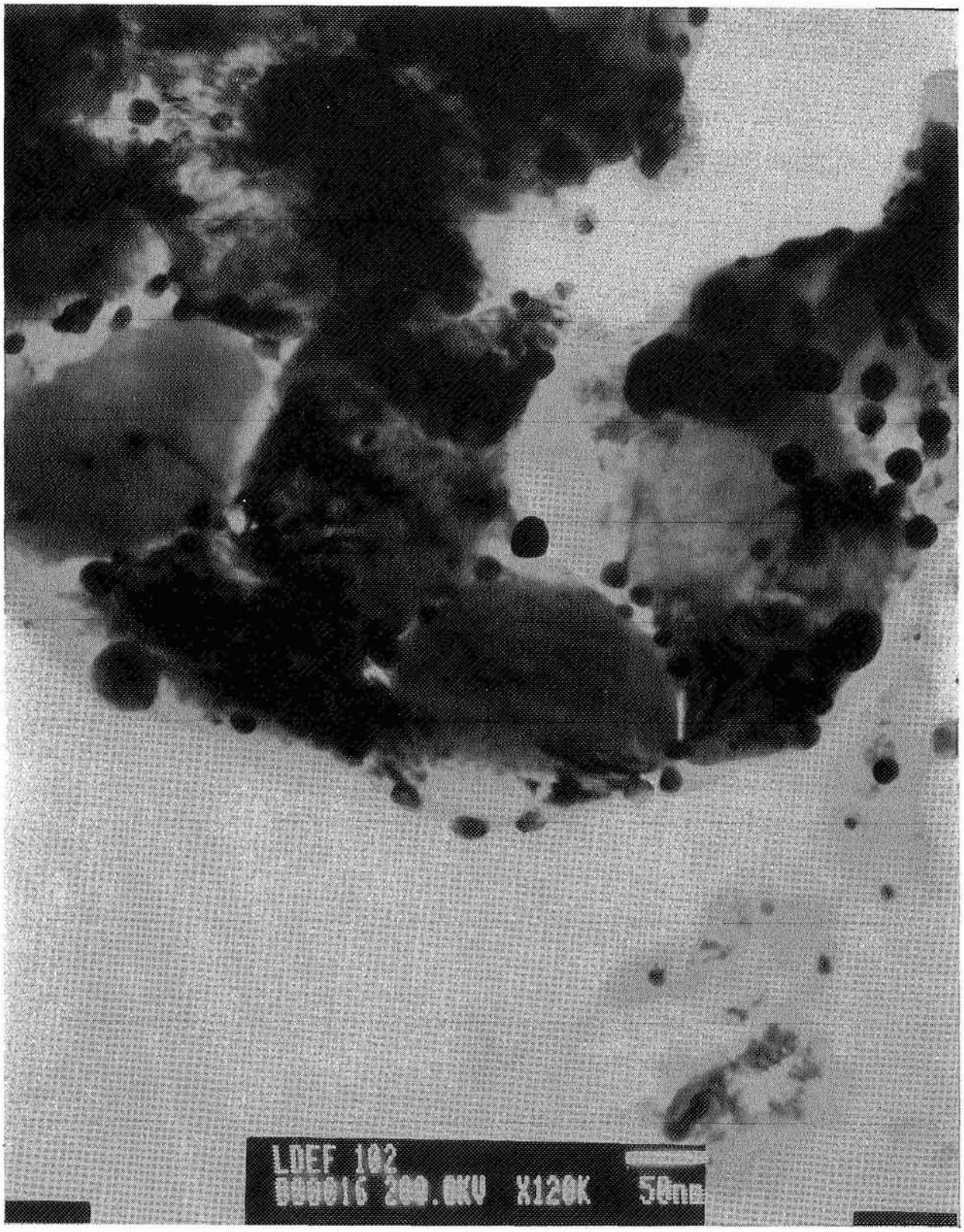

Figure 6. A TEM image of a microtomed residue grain from impact 102. Spherical bodies of Fe-Ni metal and pyrrhotite abound locally, particularly at grain boundaries.

Figure 7. A TEM image of a microtomed residue grain from impact 102. Vesicular glass abounds in the matrix of *impactor residue* 102, probably formed during impact into LDEF.

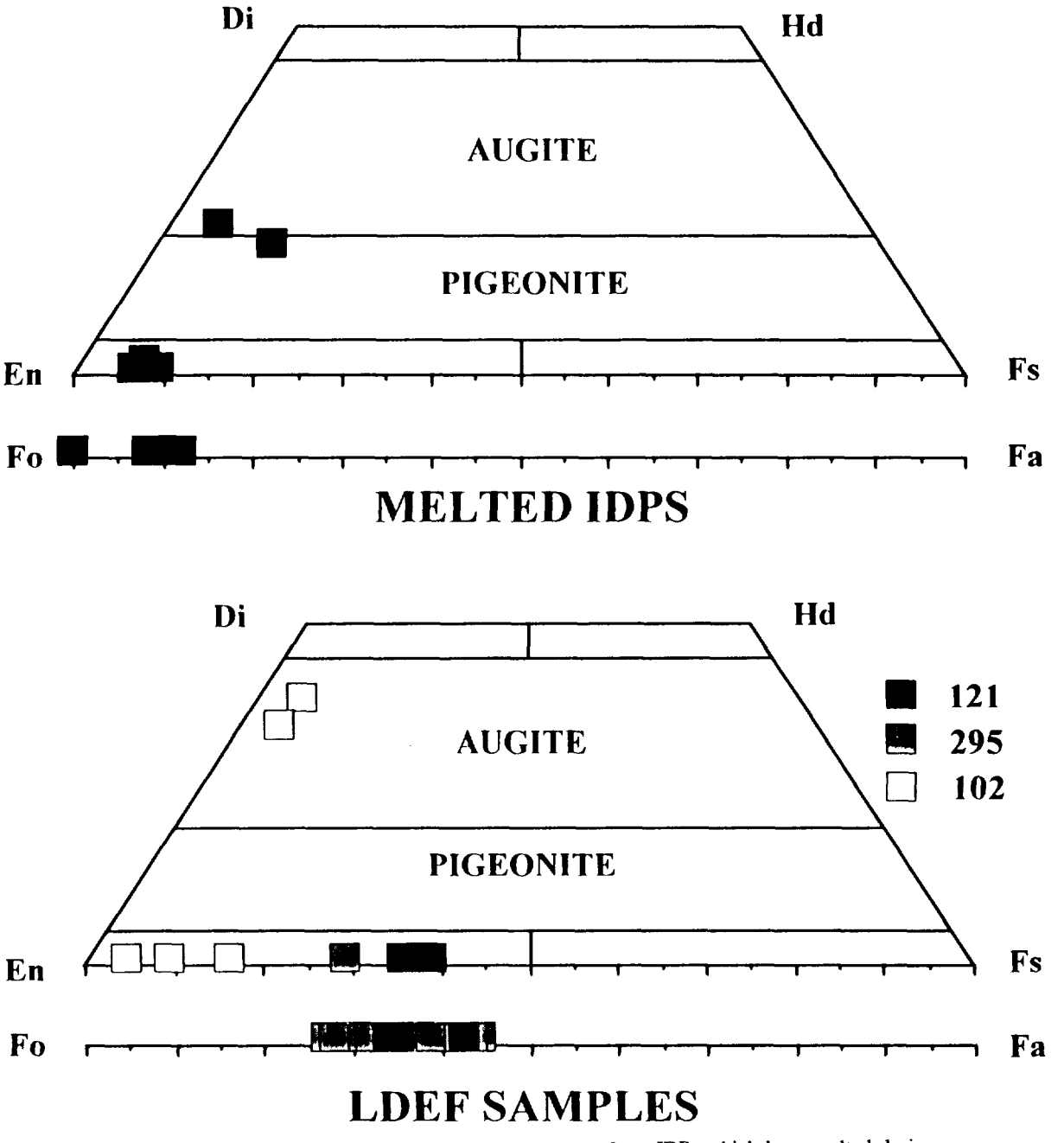

Figure 8. Comparison of the compositional range of olivines and pyroxenes from IDPs which have melted during atmospheric entry (melted IDPs) and IDP residue grains from LDEF impact features.

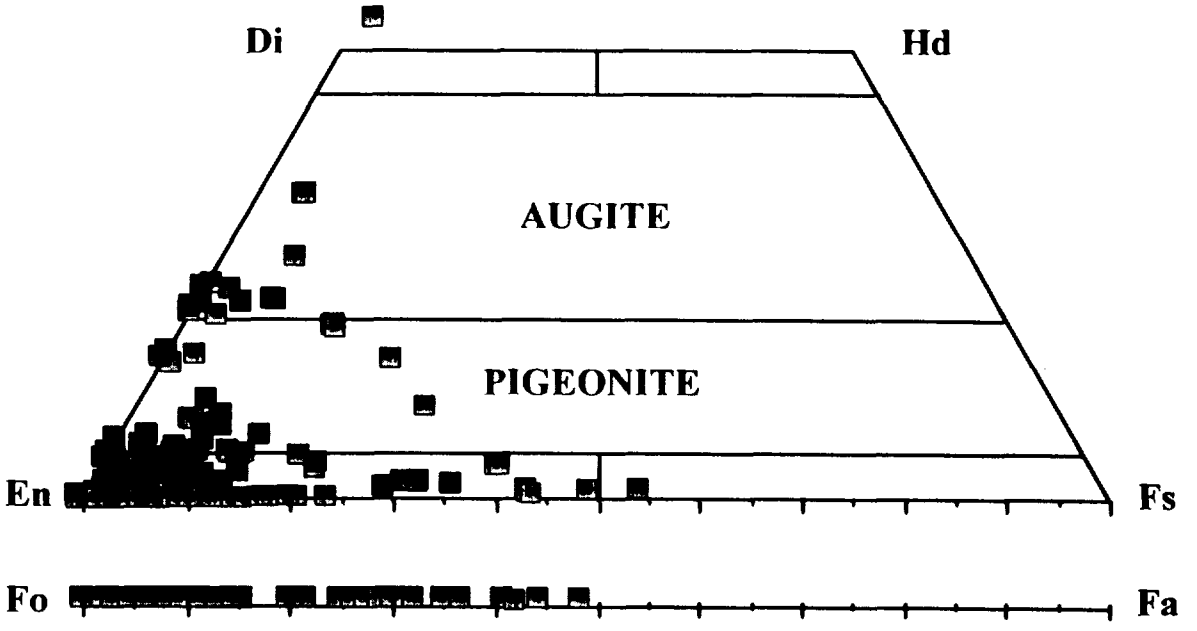

ANHYDROUS IDPS

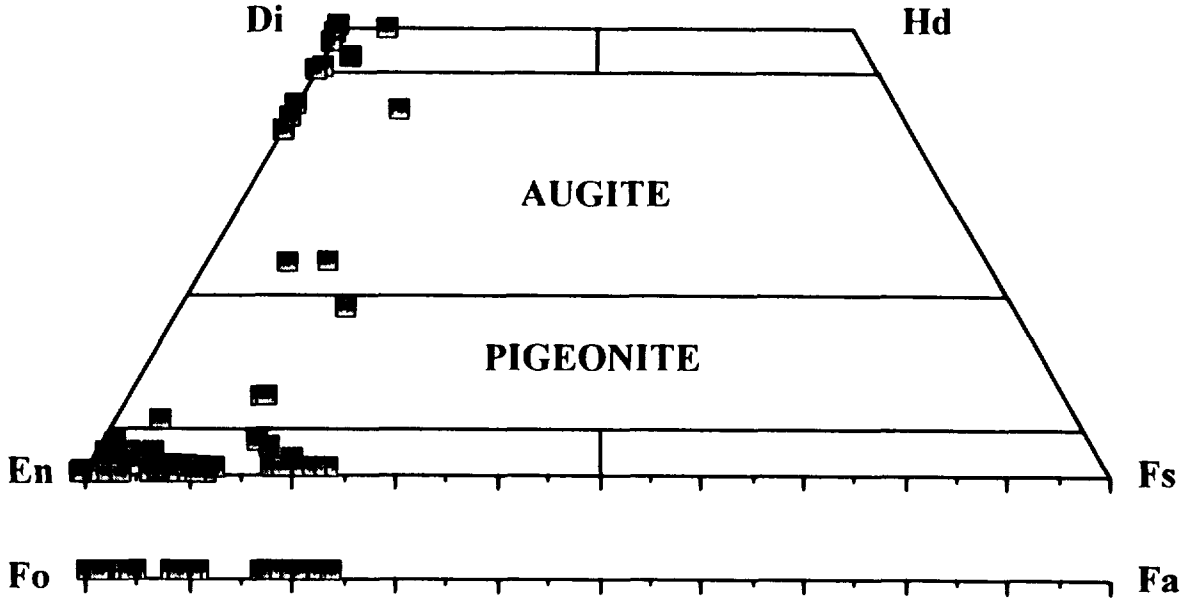

HYDROUS IDPS

Figure 9. The compositional range of olivines (Fo to Fa) and pyroxenes (upper quadrilateral diagrams) in hydrous and anhydrous chondritic micrometeoroids.

ACKNOWLEDGMENTS

We would like to thank Fred Hörz for providing the A0187 experimental surfaces utilized in this study.

REFERENCES

1. Zolensky, M.E., Zook, H., Hörz, F., Atkinson, D., Coombs, C., Dardano, C., See, T.H., Simon, C. and Kinard, W., Watts, A., Interim report of the Meteoroid and Debris Special Investigation Group. *Proceedings of the 2nd LDEF Post-Retrieval Conference*, Eds. A. Levine and W. Kinard, NASA Conference Publication #3194, pp 277-302, 1993. (available from the LDEF Project Office at NASA Langley, Mailstop 404).
2. Bernhard, R.P., Zolensky, M.E., *Analysis of Impactor Residues in Tray Clamps from Long Duration Exposure Facility,* NASA Technical Memoranda # 104759 and #104784.
3. Redd, C. and Zolensky, M.E. (1991) *Too exposed* (Scientific correspondence). *Nature* **352**, 289.
4. Brownlee, D.E., *Cosmic Dust: Collection and Research, Ann. Rev. Earth. Planet. Sci.* **13**, 134-150, 1985.

NATURAL AND ORBITAL DEBRIS PARTICLES ON LDEF'S TRAILING AND FORWARD-FACING SURFACES

Friedrich Hörz
SN4, NASA / Johnson Space Center
Houston, Texas 77058
(713) 483-5042 / FAX (713) 483-5347

Ronald P. Bernhard
Lockheed Engineering & Science Co.
Houston, Texas 77058
(713) 483-5018 / FAX (713) 483-5347

Thomas H. See
Lockheed Engineering & Science Co.
Houston, Texas 77058
(713) 483-5027 / FAX (713) 483-5347

Donald E. Brownlee
Dept. of Astronomy; U. of Washington
Seattle, Washington 98195
(206) 543-8575 / FAX (203) 685-0403

ABSTRACT

Approximately 1000 impact craters on the Chemistry of Meteoroid Experiment (CME) have been analyzed by means of Scanning Electron Microscopy (SEM) and Energy Dispersive X-ray Analysis (EDXA) to determine the compositional make-up of projectile residues. This report completes our systematic survey of gold and aluminum surfaces exposed at the trailing-edge (A03) and forward-facing (A11) LDEF sites, respectively.

The major categories for the projectile residues were (a) natural, with diverse subgroups such as *chondritic*, *monomineralic silicates*, and *sulfides*, and (b) man made, that were classified into *aluminum* (metallic or oxide) and *miscellaneous* materials (such as stainless steel, paint flakes, etc). On CME gold collectors on LDEF's trailing edge ~11% of all craters >100 μm in diameter were due to man-made debris, the majority (8.6%) caused by pure aluminum, ~31.4% were due to cosmic dust, while the remaining 58% were indeterminate via the analytical techniques utilized in this study. The aluminum surfaces located at the A11 forward-facing site did not permit analysis of aluminum impactors, but ~9.4% of all craters were demonstrably caused by miscellaneous debris materials and ~39.2% were the result of natural particles, leaving ~50% which were indeterminate.

Model considerations and calculations are presented that focus on the crater-production rates for features >100 μm in diameter, and on assigning the indeterminate crater population to man-made or natural particles. An enhancement factor of 6 in the crater-production rate of natural impactors for the "forward-facing" versus the "trailing-edge" CME collectors was found to best explain all observations (*i.e.*, total crater number[s], as well as their compositional characteristics). Enhancement factors of 10 and 4 are either too high or too low. It is also suggested that ~45% of all craters >100 μm in diameter are caused by man-made impactors on the A11 surfaces. This makes the production rate for craters >100 μm in diameter, resulting from orbital debris, a factor of 40 higher on the forward-facing sides as opposed to the trailing-edge direction.

INTRODUCTION

The "Chemistry of Micrometeoroids Experiment" (CME; ref. 1) exposed two substantially different collector materials to the hypervelocity particle environment on the Long Duration Exposure Facility (LDEF). The active experiment consisted of clamshell-type devices that could be opened and closed such that the collectors were protected against contamination during all ground handling and LDEF deployment. This instrument exposed ~0.82 m^2 of high-purity gold (>99.99% Au) on LDEF's trailing

edge (*i.e.*, Bay A03). The actual collectors consisted of seven individual panels (~20 x 57 cm each; ~0.5 mm thick). The Au collectors exhibited relatively low crater densities (refs. 1 and 2) because the trailing edge inherently yields the smallest particle flux (ref. 3) on a non-spinning platform, and because the collectors were only exposed for a total of 3.4 years (ref. 1). In contrast, the passive experiment continuously exposed, for 5.7 years, commercial grade aluminum surfaces (Al 1100 series, annealed, >99% pure Al) in the forward-facing, A11 location. Six individual panels (~41 x 46 cm, each; 3.2 mm thick) provided ~1.1 m^2 of cumulative surface area.

The purpose of CME was to obtain compositional information on the residues associated with hypervelocity craters. The present report complements earlier progress reports (refs. 1 and 2) primarily via analyzing additional craters on the A11 aluminum collectors. We now have systematically analyzed ~200 craters on the gold substrates and ~800 craters on the aluminum surfaces. The results refer to all craters above some arbitrary crater size on the respective host materials. Therefore, the findings will be representative for particles larger than some threshold size that impinge on the trailing-edge and forward-facing surfaces of a non-spinning spacecraft, such as LDEF, Mir or Space Station. Unquestionably, the current investigations are of a survey-type nature and remain incomplete in many detailed aspects. The current work primarily attempts to classify the particles into natural and man-made materials, and associated subclasses. Our analyses are qualitative, consistent with and sufficient for the above objectives. However, the presence of unmelted fragments within some of these craters permits -- in principle -- the determination of the detailed chemical and mineralogical make-up of some particles (refs. 2 and 4), as well as their isotopic characteristics (ref. 5) and potential organic-molecule content (ref. 6). However, such detailed analyses are so time consuming that they are not readily adapted to the characterization of entire populations of craters and projectiles (*e.g.*,. refs. 4, 5, 6, 7 and 8).

We have analyzed 199 craters on the Au-collectors and 828 craters on four of the six A11 aluminum panels. In general, we followed the analytical procedures and compositional particle classifications developed during the analysis of interplanetary dust recovered from the stratosphere (refs. 9 and 10), or of space-retrieved surfaces such as Solar Maximum Mission replacement parts (refs. 11 and 12), or the Palapa satellite (ref. 13). The present effort specifically adds to these earlier analyses by characterizing a much larger number of events and by being able to place them into a dynamic dust environment, since LDEF was gravity-gradient stabilized, while all previously analyzed surfaces originated from spin-stabilized spacecraft. Unlike spin-stabilized satellites, LDEF offers the potential to yield substantial directional information (*e.g.*, refs. 3, 14, 15).

ANALYTICAL METHODS AND FINDINGS

Compositional analysis of projectile residues was conducted using an ISI-SR50 Scanning Electron Microscope (SEM), and a LINK eXL Energy Dispersive X-Ray (EDX) analyzer using a Si(Li) detector, arranged at 90° to the beam path. Although we characterize our analyses as qualitative and of a survey-type nature, we spent considerable efforts in optimizing the signal to noise ratio of the X-Ray spectra. Initially it was found that an uncomfortably large fraction of craters yielded spectra that contained no

detectable signal above that of the background. Therefore, we used a number of craters to investigate a range of electron-beam geometries (diameter and take-off angle), low- and high-beam voltage, and widely variable count times (minutes to hours). From these efforts it was determined that a relatively high-beam voltage (25-20 KeV) and long count times (500-1000 seconds) with the specimen tilted at 30° yielded the best results. It is our belief that high-beam voltages are best because the surface relief of the crater interiors tends to be uneven permitting excitation of more near-surface specimen volume compared to less penetrative, low-energy electrons. Count times in excess of 1000 seconds do not appreciably improve signal to noise ratios and do not warrant the additional expenditure of resources.

Contamination of our surfaces was not a significant problem because the composition of common contaminants differ dramatically from many projectile residues. Nevertheless, we have observed Si-Ca rich deposits in some crater interiors that, presumably, were derived from outgassed RTV (ref. 16). Interestingly, such deposits can have distinctly asymmetric distributions in some craters, substantiating the macroscopic LDEF observations of highly directional flow of gaseous contaminants and their condensates. We also observe some intrinsic, heterogeneously distributed contaminants, the result of manufacturing procedures in our collector materials, most notably as in the gold and Si in the aluminum. The anodized layer on the aluminum surfaces varied from plate to plate, but background from this source was taken into consideration. On the A11 aluminum plate E00H every crater analyzed contained significant amounts of Si, Mg, and Fe, as well as other contaminants to the degree that none of these craters was used in the particle population studies below (*i.e.*, these craters were excluded from this report).

The sources for colliding projectiles in low-Earth orbit (LEO) are either "natural" or "man-made". The natural particles encountered are described as micrometeoritic, cosmic dust, or interplanetary dust, and originate from either comets or asteroids (ref. 10). The man-made particles result from explosions and collisions, and the associated fragmentation products of satellites, solid rocket burns, ablation of thermal coatings from small particle collisions, atomic oxygen erosion, and human waste dumped in LEO (ref. 14).

"Natural" particles can be subdivided into (1) chondritic, that are largely made up of relatively well-mixed and homogenized, fine-grained matrices. (2) Monomineralic silicates, characterized by high concentrations of Si, Mg, and Fe; these particles are mostly found in molten form, but on occasion unmelted fragments of olivine and pyroxene are preserved. (3) Fe-Ni-sulfide rich particles are found, yet only as melts; these particles are frequently associated with minor chondritic melts/glasses, suggesting that large Fe-Ni sulfides grains, common in meteorites, had some fine-grained chondritic matrix attached to them.

The "orbital-debris" impacts contained (1) Fe-Ni-Cr rich particles representing stainless steel, (2) Zn-Ti-Cl rich residues characteristic of thermal protective spacecraft paints, (3) Ag, Cu, or Pb-Sn rich residues originating from solar cells or other electrical components of spacecraft hardware, and (4) particles that contain aluminum only, without specifying whether they were metallic or oxidized. Obviously such aluminum impactors could only be detected on the gold collectors and their occurrence on the forward-facing aluminum substrates is not amenable to direct compositional analysis. Throughout this report, the above category 1-3 particles will be referred to as "miscellaneous" debris, as opposed to the pure "aluminum" particles of category 4.

For many individual craters one may obtain x-ray spectra that reflect specific component minerals of natural dust grains (*e.g.*, olivines or pyroxenes) and their mixtures. However, variability within the pure crater melts was observed as well, with the largest variations occurring in those craters that contained unmelted residues, suggesting the presence of incompletely mixed mineral melts (refs. 17 and 18). Generally, this melt variability relates to subtly different elemental ratios among different spectra obtained from the same specimen. Nevertheless, this specimen heterogeneity is slight and does not affect our classification into natural and man-made particle sources.

RESULTS

Most summarizing figures in this report are updates of our earlier progress report (ref. 2), with minor modifications in substance, yet with increased statistical significance. Figure 1 summarizes all analyses to date and plots the number-frequency of recognized projectile types versus crater size. The intent is to illustrate the relative frequencies of the major particle types. We conclude from Figure 1 that the majority of craters that contain identifiable residues were caused by natural, cosmic-dust particles accounting for ~68% on the gold and 77% on the aluminum collectors. It is equally important to note that ~50% of all craters did not contain sufficient residue mass to be analyzed by our SEM methods (also see refs. 2, 5, 7 and 8). Most likely these structures are a velocity-biased set of craters with encounter velocities sufficiently high to eject most or all of the projectile melts from the growing crater cavity (ref. 19), if not as vapors

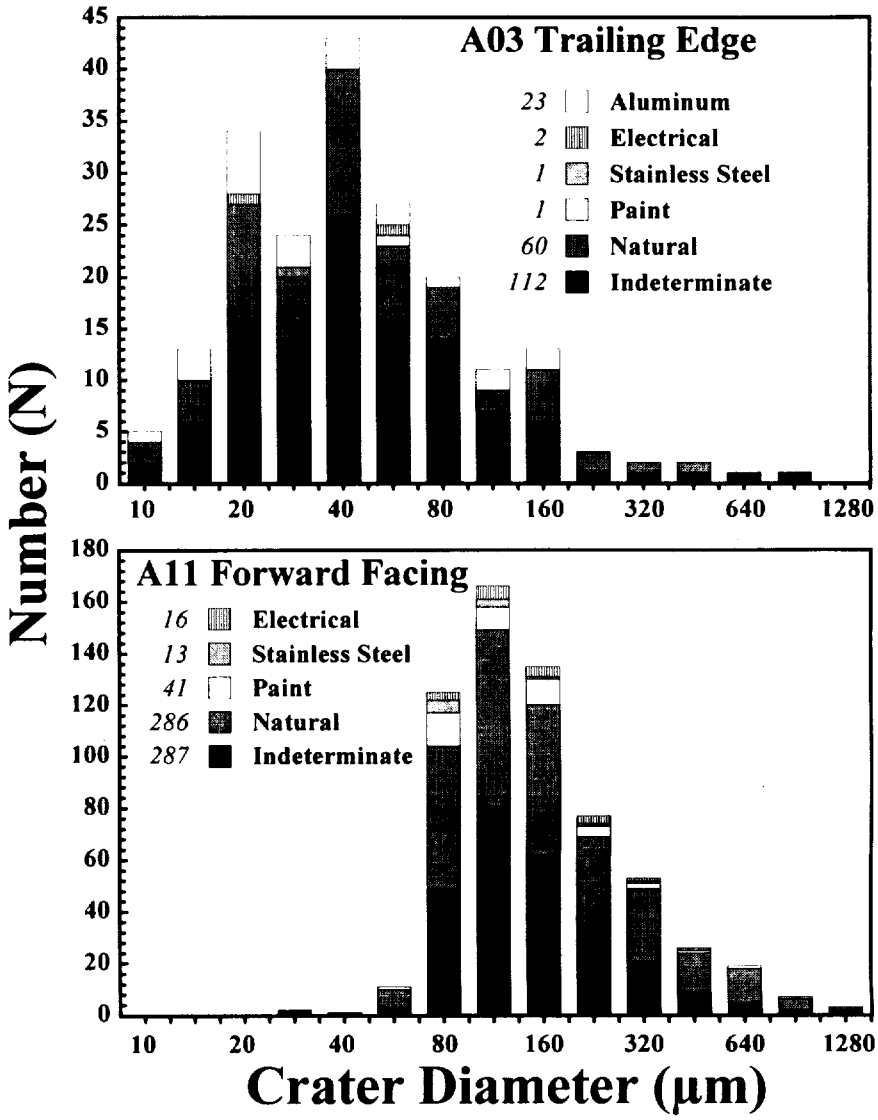

Figure 1. The analysis frequency of man-made and natural impactor residues detected on the trailing-edge (A03) and forward-facing (A11) CME surfaces. Note that aluminum impactors cannot be detected on the A11 aluminum collectors. The indeterminate population of craters either contained insufficient projectile mass to be detected by SEM - EDX methods (predominantly) and/or material that was categorized as contamination (only a few cases). The smallest craters on both surfaces are a representative sample only, and not a complete sampling (see ref. 2).

(*e.g.*, refs. 2 and 5), or they are the result of unusual projectile properties (*e.g.*, highly porous, low-density particles ?) that are easily vaporized.

The man-made sources are totally dominated by aluminum particles on the trailing-edge gold surfaces, (*i.e.*, 23 aluminum particles versus 4 miscellaneous impactors). Note, however, that the forward-facing A11 aluminum collectors do not permit recognition of aluminum and all man-made particles on these detectors are of the "miscellaneous" category, essentially by definition. These include 41 paint flakes, 13 stainless-steel particles and 16 fragments of electrical components on components E00E, E00F and E00G. In particular, note the dominance of paint flakes on the forward-facing surface (41 craters), whereas only 1 paint flake was identified on the trailing edge.

Other investigators (refs. 4, 5, 6, 7 and 8) have analyzed projectile residues associated with LDEF craters from various surfaces and their results are consistent with those observed on the CME collectors. Specifically, the somewhat surprising presence of man-made impactors on the trailing edge (ref. 1, 2 and 15) was confirmed by others (ref. 8).

The size distribution of the crater populations that were analyzed on the two collector surfaces differed in that all craters >30 μm and >75 μm in diameter on the gold and aluminum surfaces, respectively, were investigated. Smaller craters which appear in the data are merely representative of the small crater population. In addition, the absolute number of craters larger than some given size depends on total exposure time of the two collector surfaces (*i.e.*, 3.5 years for the gold and 5.7 years for the aluminum surfaces [ref. 1]). Therefore, it is not possible to directly compare the analysis frequencies of the forward-facing and trailing-edge surfaces as illustrated in Figure 1. It is much more instructive to consider crater-production rates as illustrated in

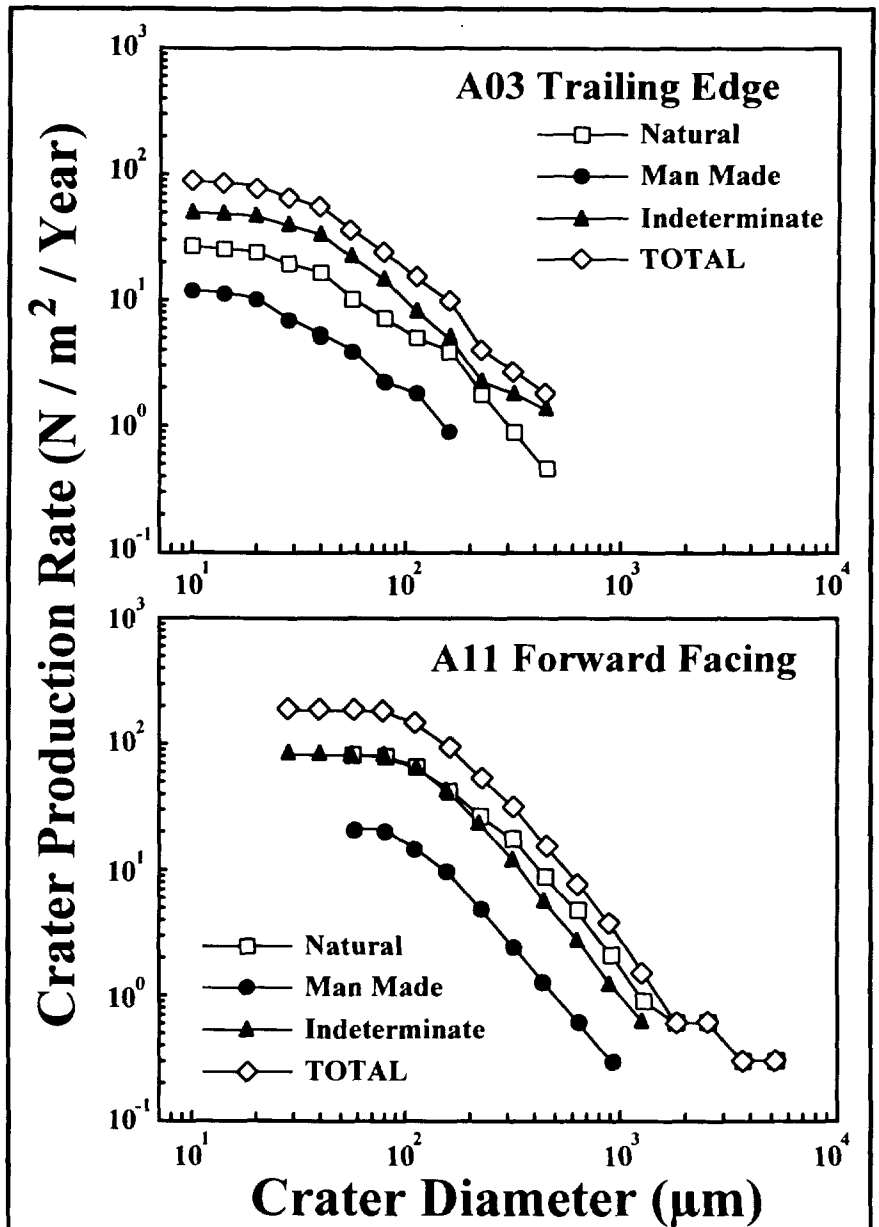

Figure 2. The crater-production rates on LDEF's trailing edge and the A11 location by both natural and man-made impactors. Again, note the substantial population of indeterminate craters. Also note that total production rates on these CME surfaces are akin to those of refs. 20 and 21, as summarized in Table 1.

Figure 2, which corrects for different exposure histories and permits for direct comparison of identical crater sizes (*e.g.*, ref. 3). Note again the unfortunately large fraction of indeterminate craters/projectiles and the inability to analyze for aluminum particles on the aluminum collectors. Also, subtle changes in slope (*i.e.*, relative size frequency) are observed for the different crater classes, yet such differences are not statistically significant; for clarity, we avoided statistical error bars on these cumulative plots.

Table 1 lists specific crater-production rates that were extracted from Figure 2 and compares them with the crater-production rates of Humes (ref. 20 and 21)and See *et al.* (ref. 22). For the A03 orientation our total crater-production rates are in excellent agreement with those of others, yet this is somewhat fortuitous considering the vastly different collector substrates (*i.e.*, gold versus aluminum). The forward-facing surfaces were all composed of anodized aluminum, 6061-T6 in the case of Humes and See *et al.* and 1100 series aluminum for the CME surfaces. Agreement among Humes and See *et al.* is good at all sizes, as is the CME production rate for craters >1000 μm in diameter; the CME data from 100 μm to 500 μm in diameter are modestly higher than those of Humes or See *et al.* by as much as ~20%. While this difference is substantial, it is still within statistical uncertainty. Our lower CME numbers at the 50 μm size range are clearly the consequence of incomplete sampling for craters <75 μm in diameter on our aluminum plates.

Table 1. Crater-production rates ($N/m^2/y$) for select crater sizes on CME's trailing-edge (A03) gold surfaces and the forward-facing (A11; 52° off of LDEF's leading edge) aluminum collectors.

	CRATER DIAMETER (μm)				
	>10	**>50**	**>100**	**>500**	**>1000**
		TRAILING EDGE (A03)			
Total Population					
Humes (1994)	?	39	20	1.6	0.28
See *et al.* (1994)	60	31	17	1.5	?
This Work	90	41	17.5	1.8	?
Natural		26	11.2	5.5	0.41
Man Made		11.5	4.6	1.9	<0.1
Miscellaneous	1.2	0.7	0.4	?	
Aluminum	10.3	3.9	1.5	<0.1	
		FORWARD FACING (A11)			
Total Population					
Humes (1994)		290	145	9.2	2.9
See et al.(1994)		280	137	7.9	1.6
This Work		185	168	12.4	2.75
Natural		81	66	5.3	0.97
Man Made		?	?	?	?
Miscellaneous		20.5	15.8	0.92	0.25
Aluminum		?	?	?	?

The detectors of refs. 20, 21 and 23 were fabricated from aluminum 6061-T6 which differs in strength properties (*e.g.*, refs. 19 and 23) from our 1100 aluminum. However, the difference between aluminum 6061 and 1100 is relatively subtle, in the context of Table 1, based on cratering theory (refs. 19, 23) and empirical crater-shape measurements on LDEF surfaces (ref. 24). Also note the differences between Humes and See et al.for identical materials. In addition, all aluminum surfaces of Table 1 were anodized; the oxide layer which results from anodizing has demonstrably affected many of the small craters in our 1100 Al-alloy collector. Despite its high density, gold is so ductile that the crater size resulting from a

given projectile (ref. 1) is (fortuitously) similar to that of aluminum (ref. 19, 23). Very generally speaking, our total crater-production rates for the A11 and A03 locations are consistent with the observations of others. Furthermore, the total crater-production rate on the CME surfaces is a factor of ~5-7 higher (depending on specific size; see Table 1) on the forward-facing surfaces compared to the trailing-edge direction.

What is new and unique to the present work is that we can assign specific impactor compositions and origins to ~50% of these craters. Those produced by natural impactors are more frequent than orbital-debris craters at all crater diameters analyzed. Typically, cosmic-dust craters outweigh those produced by orbital-debris particles by 2:1 (see Table 1). The production rate of natural cratering events is a factor of 6-10 higher for the A11 direction compared to the A03 location, consistent with (ref. 3).

INTERPRETATIONS

Particle Frequency And Fluxes

As previously discussed in our earlier report (ref. 2), the most general and useful way to characterize the hypervelocity environment in space is on a particle-size or mass basis. This conversion from crater diameter to particle size will be the subject of this section. Particle size and mass not only relate directly to a particle's origin and formative processes, but it is the only way of assigning some kinetic energy, at a given model velocity, to a single particle or to some population of particles when estimating collisional damage and risks under generalized conditions. The conversion of a measured crater diameter to some projectile size and mass is a crucial part of LDEF cratering studies, and the most critical one for collisional risk assessment and management. However, we remind the general reader, as well as some of our peers, that the conversion of a crater diameter to particle mass is not possible at present without substantial model assumptions.

Our major assumptions are as follows (see ref. 2 for details). Principally, we used the cratering equations for aluminum of ref. 23, and our own, dedicated experiments in gold (ref. 1) as the basic empirical insights. Use of Ref. 19 would yield essentially identical results. Projectile velocities, normal to the collector surface, were adopted from Zook (ref. 3) and Kessler (ref. 15) for natural and man-made debris, respectively. We used 12 km/s and 1.75 km/ s for natural and man-made particles respectively on the trailing-edge collectors and 17.9 km/s (natural) and 7.8 km/s (man-made) for the A11 aluminum surfaces. Projectile density for all impactors was assumed to be 2.7 g/cm^3. Most of these assumptions are well constrained except density, which will have substantial effects (refs. 19 and 23; *i.e.,* factors of 3-5 in resulting projectile masses for a reasonable range of densities).

The resulting projectile sizes and their fluxes are presented in Figure 3, along with the crater production rates from Figure 2. Obviously, only those craters which have identified projectile residue can be considered for such a plot, because their man-made versus natural origin provides the impact velocity in the cratering equations; by definition, indeterminate craters possess unknown encounter velocities and

require additional assumptions (see below) to be converted into associated impactors. Projectile calibration simply solves for some *velocity dependent* constant with which the crater diameter relates to the impactor ($D_{crater}=K*D_{impactor}$). At unit crater size fast natural impactors are substantially smaller than the comparatively slow man-made particles. The conversion from crater diameter to projectile size can lead to seemingly confusing results. Note that the man-made craters are less abundant than natural ones on the trailing edge, yet on a projectile-size basis, the reverse applies, and man-made particles (of very slow velocity) become more abundant than (high velocity) cosmic dust.

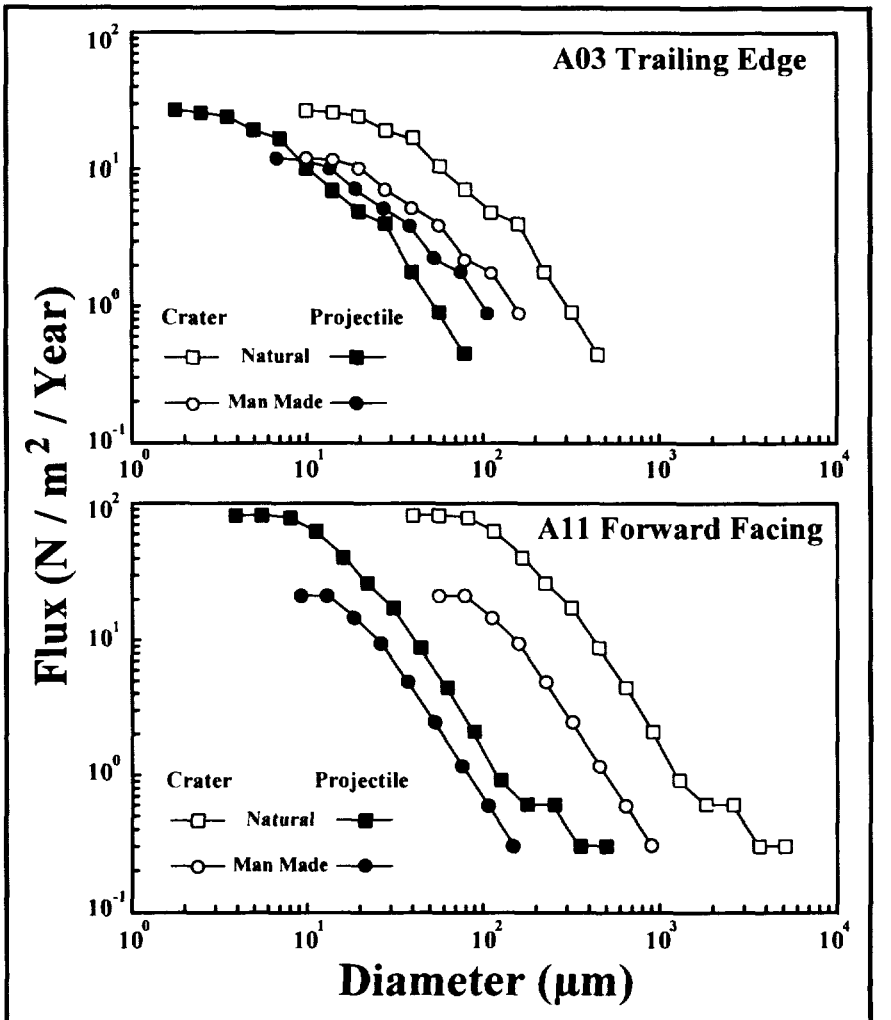

Figure 3. The flux of natural and man-made particles on CME's trailing-edge and forward-facing surfaces. Crater-size frequencies are replotted from Figure 2 to better visualize the constant offset of crater diameter and projectile size for any given velocity (see text for details)

Thus, we re-emphasize (see ref. 2) that great care is necessary when discussing the absolute and relative frequency of man-made versus natural particles on LDEF. Substantially different absolute and relative frequencies may result, depending on whether one argues from an analysis frequency basis (Figure 1), from a crater-productions rate (Figure 2), or from a particle-flux basis (Figure 3). Crater and projectile sizes relate to each other via a velocity dependent constant. Consequently, the absolute and relative frequencies of crater diameters and projectile sizes will shift different amounts (Figure 3) if they are the result of impactors with systematically different velocities.

Table 2 summarizes the observed fluxes for some typical projectile sizes of natural and man-made particles. Debris dominates (by some factor of 3) the population for particles >100 μm in diameter on the trailing edge, whereas natural particles seem to become increasingly more populous with decreasing particle size; man-made debris and natural dust occur in similar proportions at particle sizes <50 μm in diameter and cosmic dust becomes dominant at particle diameters of <10 μm on the trailing edge. Not very much can be demonstrated for the forward-facing A11 surfaces, other than that natural particles dominate the miscellaneous debris category at all sizes, typically by factors of 2-3. Furthermore, the ratio between forward-facing A11 surface and the A03 trailing-edge surface is ~5-6 for natural particles of all

sizes. We did not observe size-dependent effects among the natural impactors between our forward-facing and trailing-edge viewing directions.

We again reemphasize the fact that we could not detect man-made aluminum particles on the A11 surface; this restricts our comparisons of forward-facing and trailing-edge surfaces to the miscellaneous debris category. The latter has an enhancement factor of ~20 on the forward-facing side for small particles (~10 μm in diameter) and a factor of ~7 for particles > 50 μm in diameter. At face value this argues for variable size-frequency distributions of the miscellaneous debris category, with small particles being relatively more abundant in the forward-facing directions.

Table 2. Flux (N/m^2/Year) of known particles of select sizes on CME's trailing-edge (A03) and forward-facing (A11) collector surfaces.

	PARTICLE DIAMETER (μm)				
	>5	>10	>50	>100	>500
		TRAILING EDGE (A03)			
Natural	20.5	10.1	1.2	0.29	<0.1
Man Made	14	11.2	2.5	0.98	<0.1
Miscellaneous	1.6	1.2	0.4	?	
Aluminum	12.4	10	2.1	0.98	
		FORWARD FACING (A11)			
Total Population					
Natural	82	66	7	1.65	0.27
Man Made		?	?	?	?
Miscellaneous	?	22	2.8	0.68	<0.1
Aluminum		?	?	?	?

The Indeterminate Crater Population

The presence of orbital-debris particles on the trailing edge of LDEF was unexpected (ref. 1). These findings were subsequently modeled by Kessler (ref. 15) who demonstrated that (1) only sources in highly elliptical orbits can account for debris on LDEF's trailing edge and (2) these sources were vastly underestimated previously as contributors to the man-made particle environment. Having now a complete and much more comprehensive database, we will re-examine those assumptions used by Kessler that specifically revolve around the possible assignment of the substantial indeterminate crater population to either natural or man-made impactors.

In evaluating the relative roles of natural and man-made impactors we heavily rely on the trailing-edge gold surfaces, where analytical conditions were more favorable, having a >99.99% pure Au substrate. We also use our total crater-production rates (that agree with others [refs. 20, 21 and 22]) to form rigorous constraints on the total crater population; the CME rates (Table 1) are modestly higher than those of Humes and See *et al.*, and neither of our scenarios (presented below) will tolerate the formation of additional craters. Two scenarios are presented, labeled S_1 and S_2 in Figure 4. The first scenario (S_1) assumes that *all* indeterminate craters on the trailing-edge gold surfaces are caused by natural dust particles, due to their high encounter velocities and associated loss of impactor. All debris impacts occurred at very low speeds on the gold and should be quantitatively accounted for, as well as categorized

as either aluminum or miscellaneous debris. In addition, we postulate that the crater-production rate by cosmic-dust particles (ref. 3) on the forward-facing surface (~52° off the actual leading edge) is a factor of 6 higher than on the trailing edge. Scenario 2 (S_2) follows Ref. 15 and transfers the relative frequency of aluminum and miscellaneous debris materials of the trailing-edge gold collector to the forward-pointing aluminum surfaces.

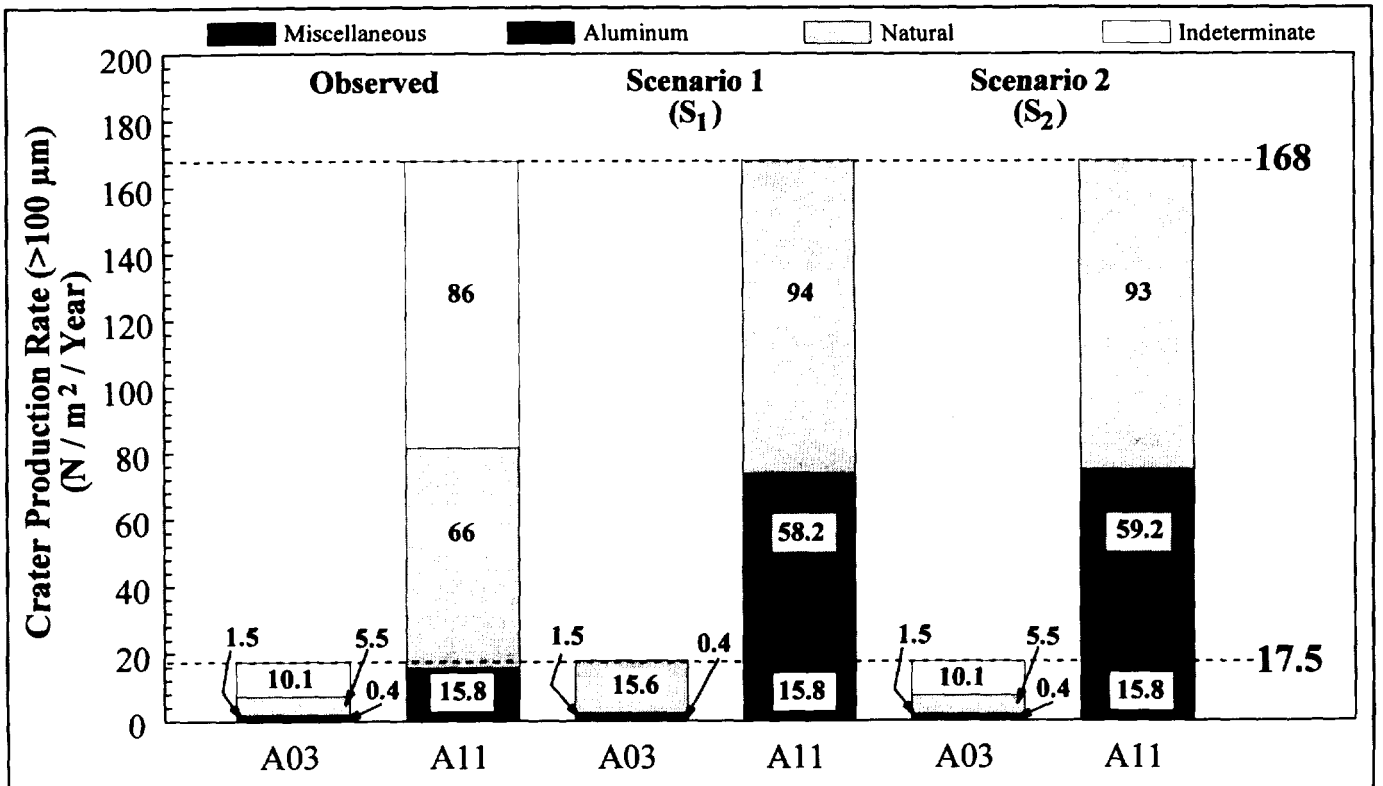

Figure 4. Visualization of the model calculations (S1 and S2) presented in the text. The numbers associated with the various projectile categories refer to the number of craters produced by such impactors. We found illustration of the absolute production rates more instructive and more easily related to Table 1 than normalized fractions and percentages.

Results of these model calculations are visualized in Figure 4, using the observed production rates for craters >100 µm in diameter. This diameter was chosen as being well (best) represented on both CME surfaces. We note that Scenario 1 yields a total of 94 natural craters (15.6 x 6), which compares to the 66 identified craters. This relegates the remaining ~74 craters (168-94) as being man-made, 16 of which are known to have resulted from miscellaneous debris materials. This leaves 58 craters (74-16) in the pure aluminum category for the A11 surface, and an ~3.6:1 ratio (58:16) of aluminum to miscellaneous debris. The overall ratio of man-made to natural dust impacts in Scenario 1 is (74:94) ~0.79 for the forward-facing orientation. Thus, for the A11 location ~55% of all craters seem to be due to natural impactors, ~35% are due to pure aluminum particles and ~10% are caused by miscellaneous debris.

The main feature of Scenario 2 is to first associate a complement of indeterminate craters on the A11 site with a debris origin. We have done this by transferring the observed crater-production ratio of ~3.75 for aluminum and miscellaneous particles (1.5:0.4; see Table 2) from the trailing edge to the forward-facing location. Using the above ratio, one associates with the 15.8 miscellaneous craters (15.8 x 3.75) a total of 59 aluminum craters for A11. This result is virtually identical with Scenario 1, albeit by totally

fortuitous coincidence. It nevertheless shows that the two dramatically different scenarios yield results that seem compatible with the observed crater populations. However, two caveats apply to the detailed numbers:

1) Note that our production rate of 168 craters on the A11 surface is somewhat higher than the values (~140) of Refs. 20, 21 and 22. The latter values could only be accommodated by substantially decreasing the aluminum projectiles (from 58 to ~30) in Scenario 1, and by decreasing the natural impactors from 93 to 65 in Scenario 2. The point here is that relatively modest changes in the total crater-production rate can precipitate substantial changes in the relative frequency of man-made versus natural impactor population(s) observed by CME.

2) Scenario 1 totally depends on the enhancement factor of 6 in the crater-production rate between trailing-edge and forward-facing LDEF orientations. Note that our own (Table 1) enhancement factor for craters >100 μm in diameter is 9.6 (168:17.5). This factor results in a total of 150 natural impacts (15.6 x 9.6) for Scenario 1, and leaves virtually no room for aluminum impactors. As a result, we suggest that an enhancement factor of 10 is too high. On the other hand, an enhancement factor of 4 between trailing edge and the A11 forward-facing surface seems too low for natural particles, because not enough natural craters would result (*i.e.,* 15.6 x 9.6 = 62, yet 66 craters were observed). Note that Scenario 2 is unaffected by this consideration.

Based on the foregoing we conclude that the indeterminate crater population on the trailing edge could be entirely caused by cosmic-dust impacts, whereas that of the forward-facing surface represents a mixture of man-made and natural impactors. Total average fraction of man-made versus natural craters is 0.109 (1.9:17.5) for the trailing edge and 0.44 (74:168) for the forward-facing A11 location. The trailing edge crater-production rate by natural particles seems enhanced by some factor of 6 on the A11 versus the A03 surface; enhancement factors of 10 seem too high, while 4 seem too low to accommodate the compositional observations. Any enhancement factor between 5 and 8 is viable, yet any specific value will precipitate very specific particle populations that differ from those advocated and preferred here.

It must be emphasized again that the above conclusions are valid only for craters >100 μm in diameter. Note in Table 2 the steady increase of aluminum impactors in the population of small craters. The aluminum to miscellaneous debris ratio is 3.75 (1.5:0.4) for >100 μm in diameter particles, 5.6 (3.9:0.7) for >50 μm in diameter particles and 8.6 (10.3:1.2) for the >10 μm in diameter particles. Therefore, it seems difficult to infer the relative frequencies of natural versus man-made impactors at millimeter scales.

While we have argued above that particle diameter or mass are the only proper way to ultimately compare and quantify the different impactor populations, this can be done at present only with craters containing identifiable residues, such as in Figure 3 and Table 2. Deconvolution of the indeterminate crater population into man-made and natural particles differs from the above considerations of crater-production rates. The latter benefits from having the total observed crater population as a firm upper limit and constraint. Because crater diameter depends on both particle size and velocity, repetitive iterations will be needed to approximate the actual fractions of man-made and natural impactors responsible for the indeterminate crater category. Such calculations exceed the scope of this report.

For the time being we use the above crater-production rates and suggest that the particle flux for man-made objects in Figure 3 is essentially correct for the trailing-edge surfaces, and that the natural flux should be increased by some factor of 2.8 ($15.6_{\text{natural modeled}}$:$5.5_{\text{natural observed}}$). By the same token, the flux on A11, following the S1 scenario, should be increased by factors of 1.4 ($94_{\text{natural, modeled}}$:$66_{\text{natural, observed}}$) for natural impactors, relative to Figure 3. Scenarios 1 and 2 leave the miscellaneous debris category essentially untouched and largely deal with the missing aluminum category on A11. The aluminum particle flux on A11 is a factor of 3.75 ($59_{\text{aluminum, modeled}}$:$15.8_{\text{miscellaneous, observed}}$) higher than the miscellaneous flux in Figure 3. Our modeled fluxes are summarized in Figure 5. These fluxes represent the best estimates about the relative roles of natural and man-made impactors that could be extracted from the analysis of ~1000 craters on the Chemistry of Micrometeoroids Experiment.

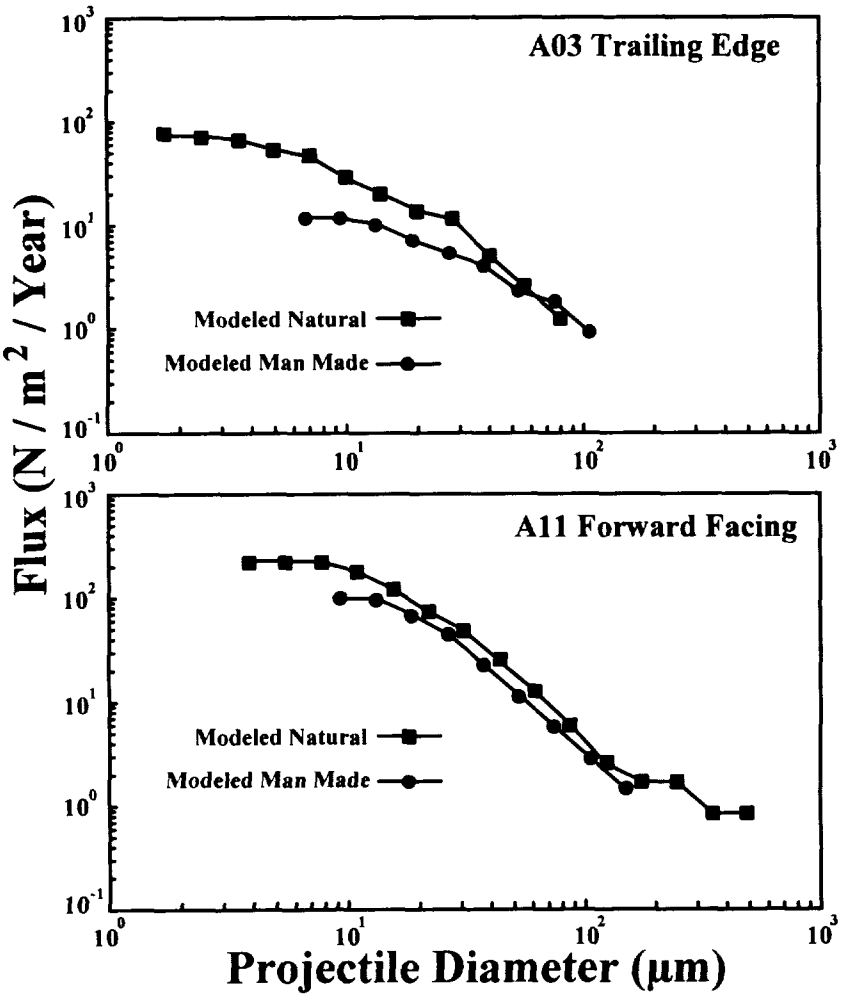

Figure 5. Particle-flux curves that would result from our models (see text), which represent the best estimates about the relative roles of natural and man-made impactors based on the analyses of ~1000 craters on the Chemistry of Micrometeoroids Experiment.

CONCLUSIONS

We have characterized chemically and qualitatively the projectile residue remaining in ~1000 individual craters on the Chemistry of Micrometeoroid Experiment, representing the trailing edge and a forward-facing direction (A11; ~52° off the plane of orbital motion) of the LDEF satellite. The production rate of impact craters >100 μm in diameter and ~50 μm deep (see ref. 24) due to natural particles is a factor of 6 higher in the forward-facing direction compared to the trailing edge. The population consists, in decreasing abundance, of particles with chondritic bulk compositions, followed by mafic silicates (olivine; pyroxene) and Fe-Ni-rich sulfides. Man-made impactors are dominated by pure aluminum particles; a substantial population of paint flakes impinges preferentially on the front surfaces, while steel particles and fragments of electronic devices are significant as well. The production rate of craters >100 μm in diameter by man-made impactors is approximately half that of natural particles in the forward-facing (A11)

direction, and ~10% for the trailing edge. The absolute difference in the crater-production rate by man-made impactors is a factor of ~40 between trailing and forward-facing pointing directions of LDEF.

Although the activity of man-made impactors on the trailing edge is modest, it was nevertheless unexpected and has already lead to some revision of the particulate environment in LEO (ref. 15). The present report provides the statistically most significant compilation of particle compositions to date. It will hopefully assist in the further refinement of environmental models and the associated collisional hazard.

REFERENCES

1) Hörz, F., Bernhard, R.P., Warren, J., See, T.H., Brownlee, D.E., Laurance, M.R., Messenger, R., and Peterson, R.P. (1991) Preliminary Analysis of LDEF Instrument A0187-1 Chemistry of Micrometeoroids Experiment", *LDEF - 69 Months in Space, First Post-Retrieval Symposium, NASA CP-3134*, p. 487-501.

2) Bernhard, R.P., See, T.H. and Hörz, F. (1993) Projectile Compositions and Modal Frequencies on the "Chemistry of Micrometeoroids" LDEF Experiment., *LDEF - 69 Months in Space, Second Post Retrieval Symposium, NASA CP 3194*, p.551-573.

3) Zook, H. A. (1991) Deriving the Velocity Distribution of Meteoroids from The Measured Meteoroid Impact Directionality on the Various LDEF Surfaces, *LDEF - 69 Months in Space, First Post-Retrieval Symposium, NASA CP-3134*, p. 569-579.

4) Brownlee, D.E., Joswiak, D., Bradley, J., and Hörz, F. (1993) Interplanetary Meteoroid Debris in LDEF Metal Craters, *LDEF - 69 Months in Space, Second Post-Retrieval Symposium, NASA CP-3194*, p.577-584.

5) Amari, S., Foote, J., Swan, P., Walker, R.M., Zinner, E., and Lange, G. (1993) SIMS Chemical Analysis of Extended Impacts in the Leading and Trailing Edges of LDEF Experiment A0231-2, *LDEF - 69 Months in Space, Second Post-Retrieval Symposium, NASA CP 3194*, p. 513-528.

6) Bunch, T.E., Radicati di Brozolo, F., Fleming, R.H., Harris, D.W., Brownlee, D.E. (1992) LDEF Impact Craters formed by Carbon-Rich Impactors: a Preliminary Report, *LDEF - 69 Months in Space, First Post-Retrieval Symposium, NASA CP 3134*, p. 549-564.

7) Simon, C.G., Hunter, J.L., Griffis, D.P., Misra, V., Ricks, D.A., Wortmann, J.J., and Brownlee, D.E. (1993) Elemental Analyses of Hypervelocity Microparticle Impact Sites on Interplanetary Dust Experiment Sensor Surfaces, *LDEF - 69 Months in Space, Second Post-Retrieval Symposium, NASA CP 3194*, p. 677-692.

8) Mandeville, J.C. and Borg, J. (1991) Study of Dust Particles On-Board LDEF: The FRECOPA Experiments A0138-1 and A0138-2, *LDEF - 69 Months in Space, First Post-Retrieval Symposium, NASA CP-3134,* p. 423-434.

9) Zolensky, M.E. ed. (1990), Particles from Collection Flag L2405, *Cosmic Dust Catalog, 11, 1, JSC #24461-SN-83,* 170 pp.

10) Brownlee, D.E. (1985) Cosmic Dust: Collection and Research, *Ann. Rev. Earth. Planet. Sci., 13,* p. 134-150.

11) Warren, J.L., Zook, H.A., Allton, J.H., Clanton, U.S., Dardano, C.B., Holder, J.A., Marlow, R.R., Schultz, R.A., Watts, L.A., and Wentworth, S.J. (1989) The Detection and Observation of Meteoroid and Space Debris Impact Features on the Solar Max Satellite, *Proc. Lunar Planet. Sci. Conf., 19th*, p. 641-657.

12) Rietmeijer, F.J.M., Schramm, L., Barrett, R.A., McKay, D.S., and Zook, H.A. (1986) An Inadvertent Capture Cell for the Orbital Debris and Micrometeoroids; the Main Electronic Box Thermal Blanket of the Solar Maximum Satellite, *Adv. Space Res., 6,* p. 145-149.

13) Bernhard, R.P. (1990) *Impact Features on Returned Palapa Hardware*, Internal NASA Report.

14) Kessler, D.J., Reynolds, R.C. and Anz-Meador, P.D. (1988) *Orbital Debris Environment for Spacecraft Designed to Operate in Low Earth Orbit, NASA TM-100 471.*

15) Kessler, D. J. (1992) Origin of Orbital Debris Impacts on LDEF'S Trailing Surfaces, in *LDEF - 69 Months in Space, Second Post-Retrieval Symposium, NASA 3194,* p.585-594.

16) Crutcher, E.R., Nishimura, L.S., Warber, K.J., and Wascher, W.W. (1991) Migration and Generation of Contaminants From Launch through Recovery: LDEF Case History, in *LDEF - 69 Months in Space, First Post-Retrieval Symposium, NASA CP-3134,* p. 125-140.

17) Schaal, R.B., Hörz, F., Thompson, T.D. and Bauer, J.F. (1979) Shock Metamorphism of Granulated Lunar Basalt, *Proc. Lunar Planet. Sci. Conf., 10th*, p. 2547-2571.

18) Stöffler, D. (1972) Deformation and Transformation of Rock-Forming Minerals by Natural and Experimental Shock Processes; Behavior of Minerals under Shock Compression, *Fortschr. Mineral., 49*, p. 50-113.

19) Watts, A., Atkinson, D. and Rieco, S. (1993) Dimensional Scaling for Impact Cratering and Perforation, *NASA Contractor Report NCR 188259,* 160 pp.

20) Humes, D.H. (1992) Large Craters on the Meteoroid and Space Debris Impact Experiment, in *LDEF - 69 Months in Space, First Post-Retrieval Symposium, NASA CP-3134,* p. 399-422.

21) Humes, D. (1994) Small Craters on the Meteoroid and Space Debris Experiment. *LDEF - 69 Months in Space, Third LDEF Post-Retrieval Symposium, NASA CP-3275*, this volume.

22) See, T.H., Zolensky, M.E., Bernhard, R.P., Warren, J.L., Sapp, C.A., and Dardano, C.B. (1994) LDEF Meteoroid & Debris Special Investigation Group Investigations and Activities at the Johnson Space Center. *LDEF - 69 Months in Space, Third LDEF Post-Retrieval Symposium, NASA CP-3275*, this volume.

23) Cour-Palais, B.G. (1987) Hypervelocity Impacts into Metals, Glass, and Composites, *Int. J. Impact Engng., 5,* p. 225-237.

24) Love, S., Brownlee, D.E., King, N.L. and Hörz, F. (1994) Morphology of Meteoroid and Debris Impact Craters Formed in Soft Metal Targets on the LDEF Satellite, Submitted to *Int. J. Impact Engng.*

DEBRIS AND METEOROID PROPORTIONS DEDUCED FROM IMPACT CRATER RESIDUE ANALYSIS

Lucinda Berthoud
Jean-Claude Mandeville
CERT-ONERA / DERTS
2, Avenue E.Belin, 31055 Toulouse Cedex (France)
Phone: (33) 61557117, Fax (33) 61557169

Christian Durin
CNES RA-DP EQ/QM
18, Avenue E.Belin, 31055 Toulouse Cedex (France)
Phone: (33) 61281439, Fax (33) 61274732

Janet Borg
Institut d'Astrophysique Spatiale
Bat 121, 91405 Orsay Cedex, (France)
Phone: (33) 1 6985 8632, Fax: (33) 1 6985 8675

ABSTRACT

This study is a further investigation of space-exposed samples recovered from the LDEF satellite and the Franco-Russian 'Aragatz' dust collection experiment on the Mir Space Station. Impact craters with diameters ranging from 1 to 900 μm were found on the retrieved samples. Elemental analysis of residues found in the impact craters was carried out using Energy Dispersive X-ray spectrometry (EDX). The analyses show evidence of micrometeoroid and orbital debris origins for the impacts. The proportions of these two components vary according to particle size and experiment position with respect to the leading edge of the spacecraft. On the LDEF leading edge 17% of the impacts were apparently caused by micrometeoroids and 11% by debris; on the LDEF trailing edge 23% of the impacts are apparently caused by micrometeoroids and 4% consist of debris particles - mostly larger than 3 μm in diameter - in elliptical orbits around the Earth. For Mir, the analyses indicate that micrometeoroids form 23% of impacts and debris 9%. However, we note that 60-70% of the craters are unidentifiable, so the definitive proportions of natural v. man-made particles are yet to be determined.

Experiments carried out using a light gas gun to accelerate glass spheres and fragments demonstrate the influence of particle shape on crater morphology. The experiments also show that it is more difficult to analyse the residues produced by an irregular fragment than those produced by a spherical projectile. If the particle is travelling above a certain velocity, it vapourises upon impact and no residues are left. Simulation experiments carried out with an electrostatic accelerator indicate that this limit is about 14 km/s for Fe particles impacting Al targets. This chemical analysis cut-off may bias interpretations of the relative populations of meteoroid and orbital debris. Oblique impacts and multiple foil detectors provide a higher likelihood of detection of residues as the velocities involved are lower.

1. INTRODUCTION

One of the objectives of retrievable experiments flown in LEO is the identification of the particles responsible for the formation of craters. This identification is achieved by chemical analysis of particle remnants or residues in and around the crater. In this work, the analysis of a number of craters on various experimental surfaces allows a statistical evaluation of the relative proportions of

meteoroids and orbital debris. The results from the LDEF and Mir experiments will contribute to an assessment of the evolution of these two populations and their origins.

However, the interpretation of impact craters is complicated by the large variety of particles in terms of their composition, shapes, orbits and velocities. This study examines the effect of particle shape and velocity on crater morphology and the possibility of EDX detection of particle residues.

2. EXPERIMENTS TO INVESTIGATE THE INFLUENCE OF VELOCITY

The aim of these experiments was to investigate the effect of velocity on the quantity and form of the remnants in the craters after impact. The idea was to compare the morphology and form of the residues in the simulated impacts with those found in the space-exposed samples. Similar experiments have previously been performed by Mandeville for polystyrene impacting glass targets (1). Our surfaces flown on LDEF and Mir consisted principally of 99% pure Al foils (chosen as the behaviour of Al under impact is well known) and the majority of craters analysed were μm in diameter. In order to simulate these conditions, μm-sized Fe projectiles were accelerated by a 2MV electrostatic accelerator onto the same Al foils. The accelerator facilities were provided by the Max Planck Institut für Kernphysik in Heidelberg. The tests were conducted at 1, 3, 5.5, 8, 10, 12 and 14 km/s.

Figure 1 shows scanning electron microscope (SEM) images for typical craters produced at each velocity. A corresponding elemental analysis spectrum of the remnants was produced for each crater, using an Energy Dispersive X-ray spectrometer (EDX). The images show the evolution of the form of the remnants with increasing velocity. The particle changes from intact (for 1 and 3 km/s) through fragmented (5.5 km/s), both giving strong Fe signals on the EDX spectra, to a thin molten layer where Fe is still detectable (at 8 to 10 km/s) and finally to an invisible vapourised layer where detection becomes more difficult (14 km/s). From these experiments it appears that the velocity limit for Fe particles impacting on aluminium for our EDX detection lies just above 14 km/s.

3. EXPERIMENTS TO INVESTIGATE THE INFLUENCE OF PARTICLE SHAPE

These experiments were carried out using the 5 mm calibre light gas gun at the hypervelocity gun laboratory run by Dr Friedrich Hörz at NASA Johnson Space Center. Six impacts using spheres (diameter 150 μm) and seven impacts using fragments (nominally the same diameter) of soda lime glass were fired at approximately 6 km/s onto thick targets of 6061-T6 aluminium (figure 2). The soda lime glass contains SiO_2, MgO, K_2O, Na_2O and CaO whose presence or absence in the residues give clues to the vapour-fractionation processes during impact.

The sphere craters show considerable symmetry and uniformity in the crater bottom and lip thickness. The glass is in a melt form, pancaking over the bottom of the crater, then breaking up from the centre (figure 3) and 'walking' up the walls. Below the SEM image is a typical EDX spectrum of a sphere crater melt. EDX analysis of the glass melt revealed a strong presence of Al, Si, O, Na, Ca and some Mg. No K was detected, although this was not surprising as K is the most volatile component of the glass.

For the fragment craters, the general morphology was highly irregular (figure 4). The crater bottoms showed shelves and pockets of different depths. This type of irregular geometry was also seen in the larger impact craters on LDEF samples. EDX analyses (see spectrum under SEM image) indicated a strong presence of Al, Si, O and Na, but significantly less Ca and Mg than for the sphere craters, and again no Kwas found. These results are consistent with the relative volatility of the various elements. It is apparently more difficult to detect residues in craters formed by irregularly shaped projectiles. This may be because the layer of residue is thinner, being spread over a larger crater surface area, or that more of the projectile has been ejected.

Even though particles may be travelling at velocities < 10 km/s, where one would expect to find residues, their irregular shape may prejudice EDX detection of residues. The high proportion of craters with no identifiable residues found on space-exposed surfaces may therefore be partly due to impacts by particles of irregular shape.

4. OBSERVATIONS OF CRATERS ON EXPOSED SAMPLES

Crater Forms

Three different forms of micron-sized craters were observed on an aluminium target on the trailing edge of LDEF (reference no.: A54). FESEM images of the three different types are shown in figure 5. Craters of type 'a' are very shallow with small, sometimes nonexistent rims. Craters of type 'b' are also shallow and show a crystalline structure. Craters of type 'c' are typical of the result of a hypervelocity impact with products of fusion on crater bottom, lips and even outside. In 15 out of 17 impacts with diameters 1-7 μm, residues compatible with a micrometeoroid origin were found. The rest of our analyses were performed exclusively on craters of type 'c', as these were most easily distinguishable from material defects, and very few types 'a' and 'b' were seen for the larger craters. However, the FESEM possesses a higher resolution than a normal SEM and therefore allows distinction for craters down to almost submicron levels. It is possible that craters of types 'a' and 'b' have been created by low density or low velocity particles. This requires further investigation.

Residue Forms

Craters on LDEF and Mir surfaces show various states of impact melt. Craters full of solid projectile residue or with unmelted fragments were rare. More frequently impact melt was found in the form of smooth flows of material culminating in droplets. The flows of material have been seen to take serpentine forms in crater bottoms, to stop halfway up the crater walls and to leave signs of fusion out as far as the crater lips. Experiments show that the progression between these states is a function of impactor velocity: the melt appears to 'walk' up the crater walls with increasing velocity.The smallest craters observed were more likely to show signs of fusion on their lips, whereas the larger craters showed most droplets remaining at the crater bottom. The movement of the melt up the wall does not also seem to be a function of impactor size.and could perhaps therefore serve as an indicator of impact velocity.

5. ANALYSIS OF CRATER RESIDUES

A Link EDX analyser and a Jeol 840A SEM were used to carry out elemental analysis of impact features on various LDEF and Mir experimental surfaces. Backscattering electron images and spot analyses in and around the crater were made in the search for particle remnants. It was found necessary to tilt the sample toward the detector (20°- 40°) for large craters in order to avoid a shadowing phenomenon. Long detection times (up to 3000s) were used when a very thin vapourisation layer was suspected. Contaminants deposited at low velocities on the target surface were sometimes easy to identify because of their shape. However, to be absolutely sure, any particle just resting inside a crater, not an integral part of the crater interior, was considered a contaminant. A brief survey of contaminants deposited on the surface of the LDEF clamps revealed glass and carbon fibres released by the atomic oxygen reduction of their matrices, paint flakes (similarly released), salt crystals, silica, spheres of FeO (probably manufacturing debris), gas phase elements which have recrystallised onto the surface and human residues (fingerprints and hairs). Non-aluminium phases inherent within alloy targets were taken into account by systematically performing an analysis of the

experimental surface outside the crater area. In this way, if clumps of the same elements were found both inside and outside the crater they were considered to be inclusions.

The following guidelines were used in the identification of meteoroids (based on analyses of interplanetary dust particles) and debris (based on analyses of craters found on Skylab, Shuttle windows and Solar Max) (2):

Meteoroids:

Fe-S-Ni : High Fe content with smaller proportions of S and Ni
Mafic silicates : Varying proportions of Mg, Fe, Si, Ca with possible Al, S, Ni
Chondrites : High Si content with smaller proportions of Mg, Ca and Fe.

Debris:

Al : Al with smaller proportions of O and trace elements
Steels : Fe with smaller proportions of Mg, Si, Cd, Ti, V, Cr, Ni, Mn, Co, Cu, Zn
Al_2O_3 from solid rocket fuel : Al and O
Paint flakes : Ti, Si and Zn
Alloys : Different proportions of Ca, Si, Ti, K, Zn, Co, Sn, Pb, Cu, S, Cl, Au or Ag.

5.1. LDEF Trailing Edge Results from FRECOPA (row O3)

The French experiment FRECOPA was located on the trailing edge (row 03) of the Long Duration Exposure Facility (LDEF). It was thought that this position would ensure that 100% of the impacts were caused by micrometeoroids, assuming that orbital debris are in circular orbits. Residues were found in craters as small as 1 µm and as large as 250 µm. 49 craters were analysed and the results can be broken down into size categories as follows:

Table 1 : Results of chemical analysis of FRECOPA

Crater size in µm	1<D<200	1 < D < 15	15 < D <100	D > 100
Debris	4%	8%	9%	0%
Meteoroid	23%	29%	18%	25%
Unknown	73%	63%	73%	75%

In comparison, Hörz and Bernhard (3) have analysed 187 craters 10-900 µm in diameter on gold samples on the CME experiment (tray A03). Their findings are resumed along with all the meteoroid/debris proportions that we have found for the different experimental surfaces in table 2.

An example of an impact caused by a natural particle found on FRECOPA ER 3-8 is seen in figure 6 . The ellipticity and shallowness of the crater (P/D=0.3) indicate an oblique impact. The low normal component of the velocity was apparently not sufficient to cause complete melting or vapourisation of the impactor. The residues are seen to be partly unmelted fragments and partly melted droplets. EDX analysis (see spectrum) of the melt residues reveal a micrometeoroid signature, with the presence of Al, Mg, Si, Fe, O, S, Ca and Cr.

The discovery of orbital debris impacts on the trailing edge is particularly significant as it confirms the presence of debris in elliptical orbits around the Earth (2). The impacts showed evidence of stainless steel and paint flake impactors. An example of an impact on sample A5 is shown in figure 7. The impactor is still intact, although slightly fractured, and from the shape of the

crater we deduce that the impact was oblique and of low velocity. EDX analysis of the residues shows the presence of Al (the substrate), Fe, V and Cr, indicating a steel origin.

5.2. LDEF Leading Edge (row 09) from MAP and clamps

The University of Kent at Canterbury supplied us with samples of 25 μm thick aluminium bonded to a gold-plated brass mesh from the **M**icro **A**brasion **P**ackage (MAP) mounted on the leading edge of LDEF (4). However, for the MAP surfaces, no evidence of impact particule residues was found. A high level of impurities/inclusions within the aluminium alloy made analysis extremely difficult.

The LDEF clamps, consisting of plates of 6061-T6 Al, were used to fix experiment trays to the LDEF frame. This alloy also contains the elements Mg, Si, Fe and Cr, which sometimes appear as inclusions of Mg_2Si, AlCrMg and FeAlSi. These inclusions are easily recognizable in a scanning electron microscope from their characteristic forms, so that confusion with extra-terrestrial matter is unlikely. 35 craters with diameters ranging from 60 μm to 900 μm were analysed for the clamps on rows 08 and row 09. For these craters > 50 μm, 11% showed evidence of debris origin, 17% showed evidence of meteoroid origin and 72% were of unknown origin. Figure 8 shows an impact apparently of low velocity onto clamp A06 C06. Unmelted fragments are clearly visible inside the crater. EDX spectra of different areas of the fragments show a wide range of proportions of the elements Al, Mg, Si, Ca, Fe and Cr frequently found in micrometeoroids (see W7027F11 in the Cosmic Dust Catalog for a comparison (5)) revealing the particle's agglomerate nature and similarity to certain chondritic interplanetary dust particles.

5.3. MIR Results from ARAGATZ experiment

The MIR Space Station has been in orbit at an altitude of 350-450 km, inclination 51.6° since February 1986. The French experiment module 'Echantillons' was mounted on the side of the Mir core module on the 9th December 1988 and recovered on the 11th of January 1990. The experiment module consisted of a 1 x 1 x 0.2 m frame supporting five experiments. Two of the experiments consisting of aluminium target surfaces were designed to study the composition and distribution of dust particles in Low Earth Orbit (6).

From the analysis of 65 craters ranging in diameter from 1-200 μm (but mainly 1-10 μm), 68% show no residues, 23% are consistent with natural particle elements and 9% show evidence of orbital debris impact. The debris appear to be principally of glass and flakes of paint.

A summary of the results of analyses carried out during this work is given in table 2.

Table 2.

Surface	Material	Crater D	% met	%debris	%unknown
LDEF09	Al	50-600 μm	17	11	72
LDEF03	Al	1-200 μm	23	4	73
LDEF03	Au*	10-900 μm	30	15 (Al incl.)	55
Mir	Al	1-200 μm	23	9	68

* Analyses carried out by Bernhard, Hörz on gold samples from CME expt. (3)

5.4. Multiple Foil Detectors

Multiple foil detectors were used on Mir and on LDEF. Several chemically interesting impact features on the multiple foil detectors were observed. The thin upper foil apparently slows and fragments the impacting particle, causing secondary craters on the capture surface beneath. The fragments are then easily analysed.

6. DISCUSSION

EDX analysis can only identify elements if significant amounts are present (> 0.2-0.5% of weight analysed). Quantitative analysis inside craters is fraught with problems and EDX is not suited to identifying thin melt or vapour layers, as it analyses a pear-shaped volume. But, being quick and reliable, it does provide an excellent tool in the initial search for residues. Unlike for SIMS, crater shadowing problems with EDX can be solved simply by tilting and rotating the sample. Once the residues have been identified as natural or man-made and extracted from the crater, a more precise analysis technique can be applied (such as ion microprobe or TEM).

The high proportions of craters of unidentified origins are due partly to our aluminium detecting surfaces which preclude the identification of aluminium particles. Hörz and Bernhard found that of the debris they detected, 83% were aluminium-based. They consequently found lower levels of unidentified craters (55% compared to our 70%). Another factor contributing to the proportion of unidentified craters is the velocity of impact. Our acceleration experiments show that if the impact velocity is higher than a certain limit, a large percentage of the particle will be vapourised, leaving a thin layer of melt undetectable using EDX methods. This will happen at lower velocities for the more volatile elements and for heterogeneous particles which may blow apart under impact pressures. Our experiments indicate that the shape of the projectile also plays a part in identification of residues. It was found more difficult to detect the residues of an irregularly shaped particle than those of a spherical particle.

Meteoroid impact velocities on LDEF vary between 16.7 km/s (trailing edge) and 23.2 km/s (leading edge). For Mir the velocities are between 14.5 and 29.8 km/s, depending on the position in orbit (7). Considering these velocities, it is surprising that we have been able to detect residues of meteoroids at all. However, this may be linked to the oblique impacts of a proportion of the particles. In this work we have found that oblique impacts increase the likelihood of finding residues in craters, because they effectively mean a lower normal component of velocity. On LDEF the proportions of oblique impacts found were 3% for the leading edge and 10% for the trailing edge. For Mir the proportions were higher at 10-20% (for a further discussion of this see (8)).

The presence of debris on the trailing edge of LDEF requires an explanation. Previously debris were thought to move uniquely in circular orbits around the Earth. However, these results in conjunction with the higher flux measured on the trailing edge as compared with Grün's meteoroid model implies otherwise. It is possible that debris are also to be found in non-bound orbits or alternatively in elliptical orbits around the Earth (2). Orbital calculations show that it is possible for debris in Geostationary Transfer Orbit to strike the trailing edge of LDEF with a velocity of 2-3 km/s.

7. CONCLUSIONS

The aim of this investigation was to determine the proportions of debris and meteoroids in Low Earth Orbit. This was achieved by analysing particle residues left in hypervelocity impact craters on LDEF and Mir surfaces using EDX. However, no residues could be detected in a large

proportion of the craters. Acceleration experiments on a micron scale were carried out to investigate the influence of impact velocity and particle shape on the eventual form of the residues.

Laboratory acceleration experiments have shown that impact velocity and particle shape determines the possiblity of residue detection in craters. It was found more difficult to detect residues in craters produced by irregularly-shaped particles, than those in craters produced by spherical particles. The limit for detection for Fe particles impacting Al is around 14 km/s. Above this velocity, the particle is significantly melted and vapourised. Chemical identification of residues is therefore easier for low velocity impacts. This means that oblique impacts and multiple foil detectors, which both slow down the impacting particle, are more likely to show residues than normal impacts onto semi-infinite targets. It also means that the analysis results are biased towards orbital debris, as these travel at lower velocities than micrometeoroids.

We propose that the high percentage of unidentified craters is due to aluminium impactors (undetectable on our aluminium collecting surfaces), the vapourisation of the particles due to high impact velocities, and to their irregular shape.

8. ACKNOWLEDGEMENTS

The authors would like to express their thanks to Dr Friedrich Hörz and members of the Hypervelocity Gun Laboratory at NASA JSC in Houston for carrying out acceleration tests; equally to Professor Eberhard Grün and dept. of the MPI für Kernphysik, Heidelberg for providing accelerator facilities, to Dr Michael Zolensky at NASA JSC, Ronald Bernhard and Jack Warren of Lockheed ESC/JSC for providing the LDEF clamps, and to Professor Tony McDonnell at the Univ. of Kent, Canterbury for LDEF MAP samples. This work was partly supported by a European Commission research grant under the 'Science' programme.

9. REFERENCES

(1) Mandeville J.C., Vedder J.F. (1971) "Microcraters formed in glass by low density projectiles", *Earth and Planet. Sci. Letters*, Vol.11, No.4.

(2) Zolensky M.E. et al. (1992): "Interim report of the Meteoroid and Debris Special Investigation Group", Part 2 of *'LDEF-Second Post-Retrieval Symposium'* , NASA Conf. Publ. 3194, pp 277.

(3) Hörz F., Bernhard R.P. (1992) "Compositional analysis and classification of projectile residues in LDEF impact craters"*NASA TM-104750.*

(4) McDonnell, J.A.M. (1984) "Multiple Foil Microabrasion Package" in *'LDEF Mission 1 Experiments'*, eds. L.G. Clark, W.H. Kinard et al. NASA SP-473, pp 117-120.

(5) NASA Cosmic Dust catalog (1983) Vol.4, No. 2, *NASA Pub. 65*, JSC 18928.

(6) Mandeville J.C. (1990) "Aragatz mission dust collection experiment", *Adv. Space Research* Vol. 10, No. 3-4, pp. 397-401.

(7) Mandeville J.C. and Berthoud L. (1993) "Micrometeoroids and debris on LDEF", *' LDEF-Third Post-Retrieval Symposium'* (this volume).

(8) Berthoud L. (1993) "Micrometeoroids and orbital debris observed in low earth orbit (LEO)," PhD thesis, Ecole Nationale Supérieure de l'Aéronautique et de l'Espace, Toulouse, France.

Figure 1: SEM images and EDX analyses of Fe residues in craters for increasing impact velocities (µm Fe particles accelerated onto 99% pure Al targets)

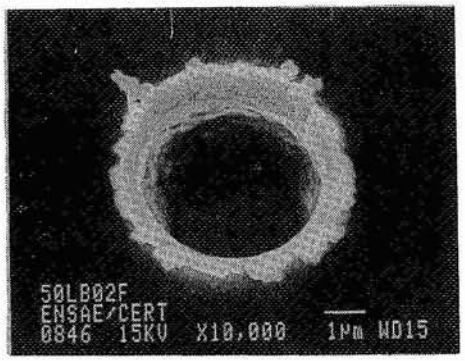

3 km/s

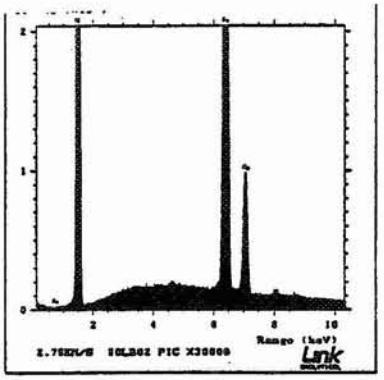

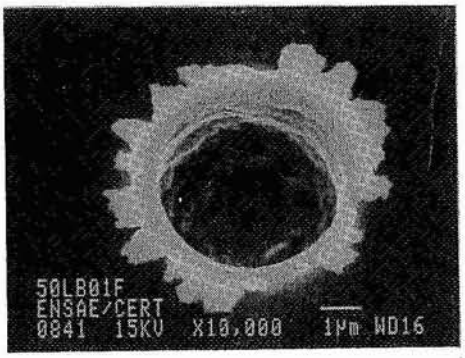

5.5 km/s

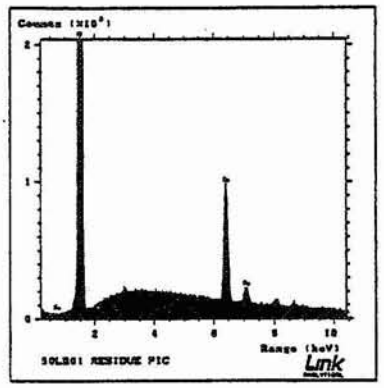

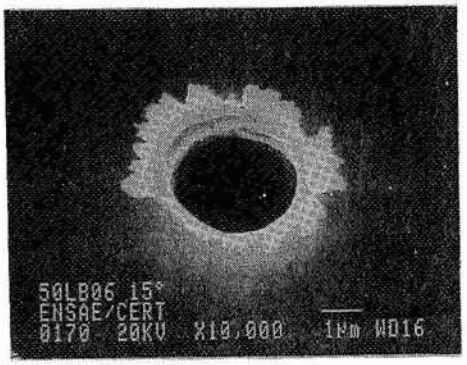

10 km/s

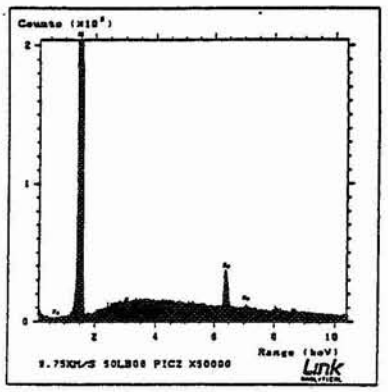

14 km/s

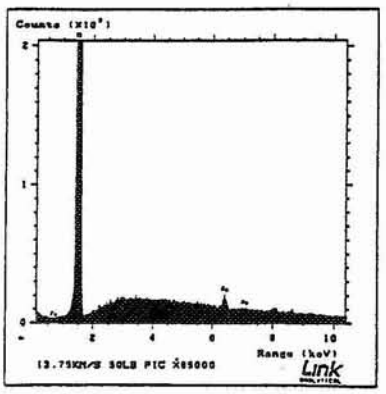

Figure 2: Soda lime glass spheres (diameter 150 μm) and fragments used as projectiles in particle shape simulation experiments (samples provided by NASA JSC)

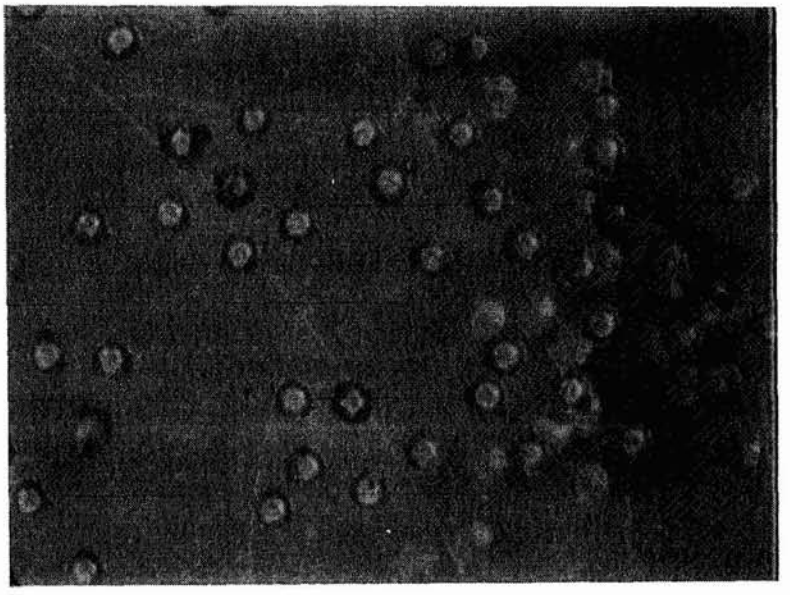

Figure 3: Glass melt from spherical projectile in crater in aluminium target 1217B (D = 450 μm). Experiments carried out at Hypervelocity Gun Lab. NASA, JSC.

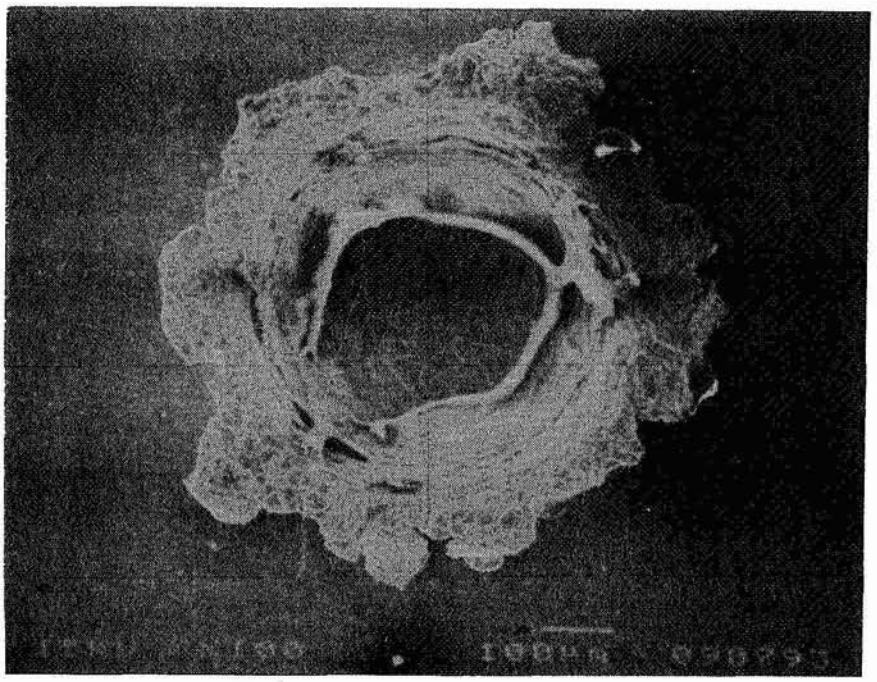

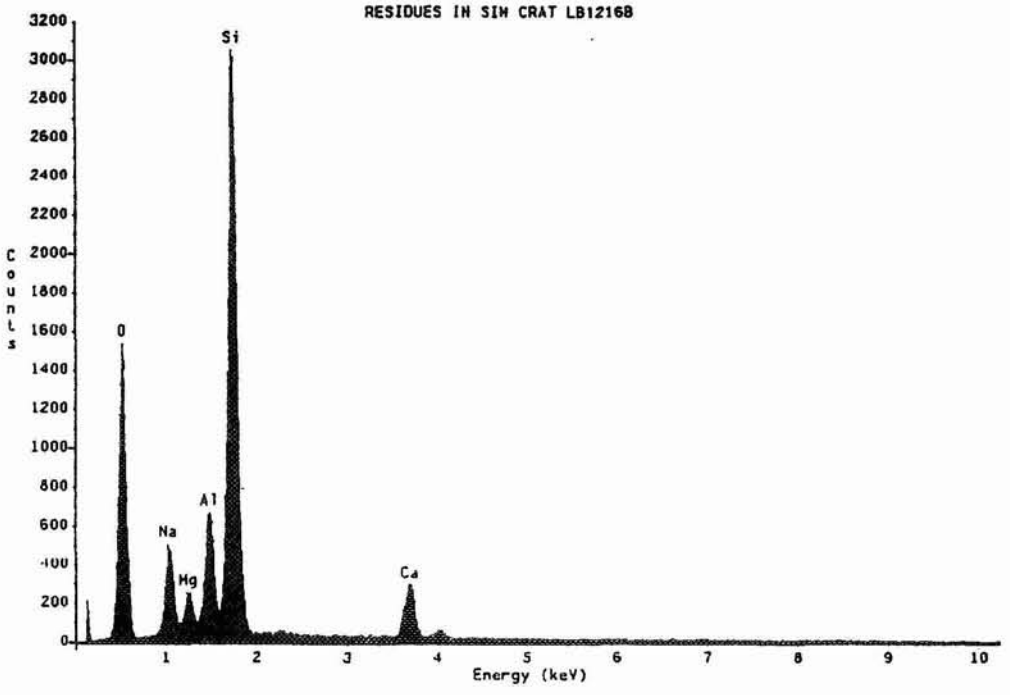

Figure 4: Crater from fragment of glass impact in aluminium target 1225B (D = 235 μm). Experiments carried out at Hypervelocity Gun Lab. NASA, JSC.

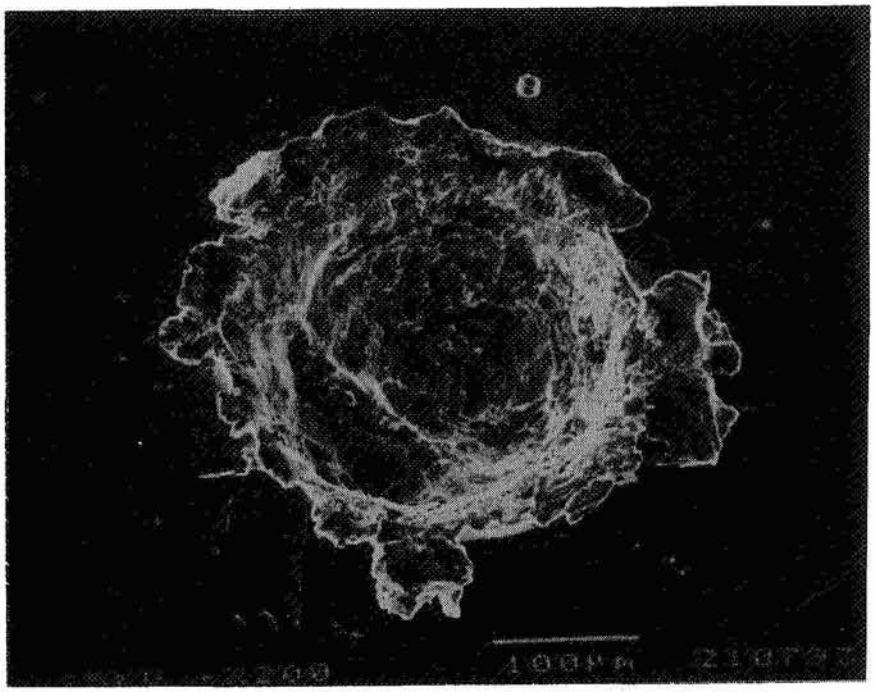

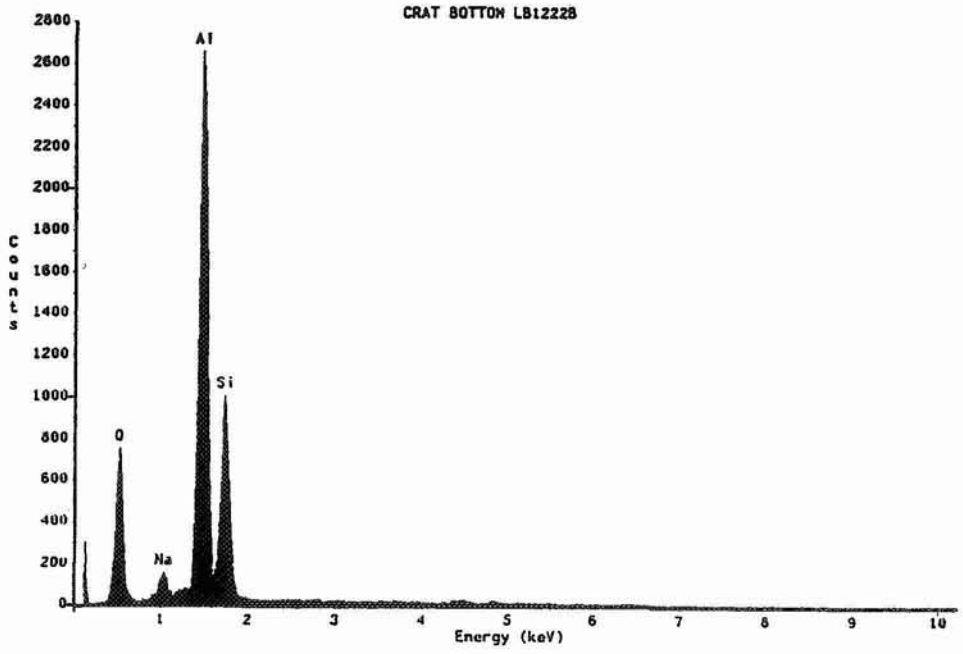

Figure 5: (Janet Borg)

FRECOPA TRAY : A0138-1 experiment

typical micron-sized craters in A54 Al target

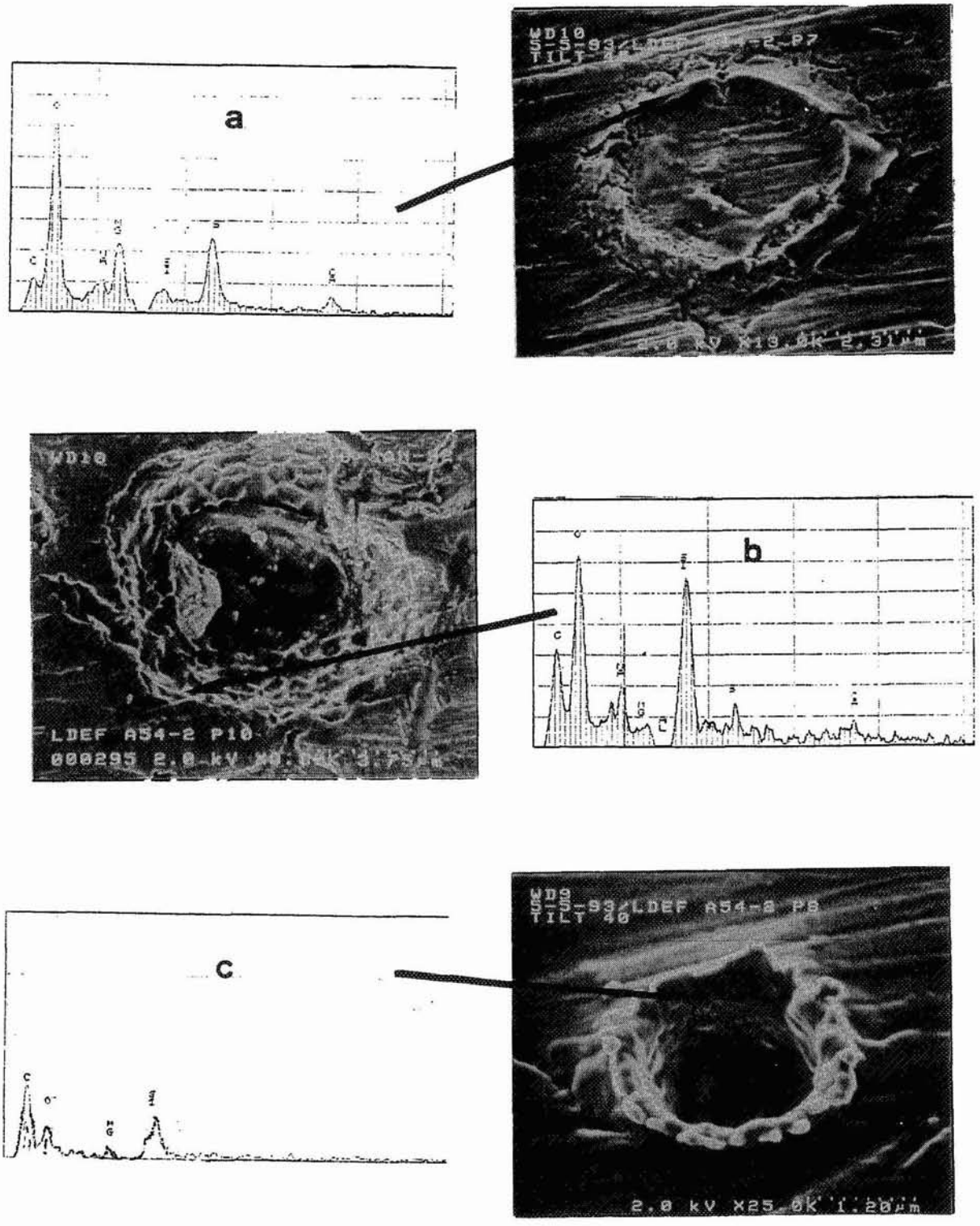

Figure 6: Meteoroid impact on LDEF FRECOPA (03) 'Ecran Rigide'.

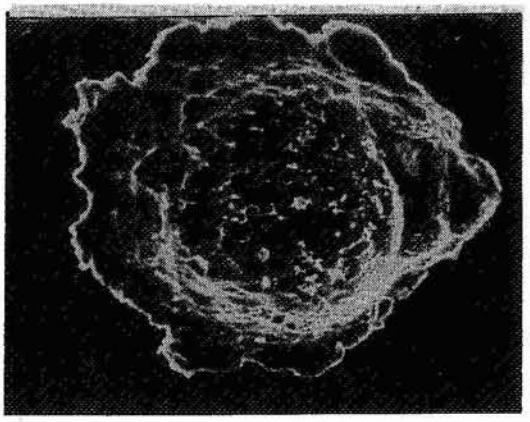

Figure a: Oblique impact (235 x 176 µm) on Al alloy experiment support surface.

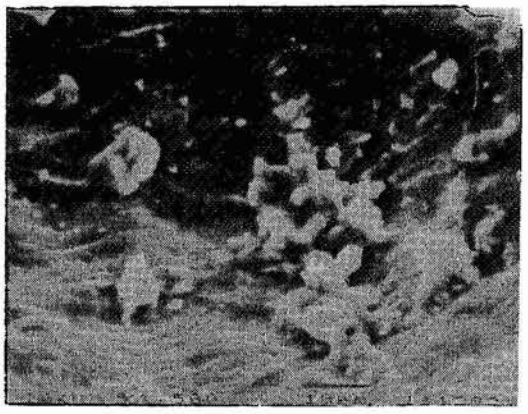

Figure b: Detail showing molten residues.

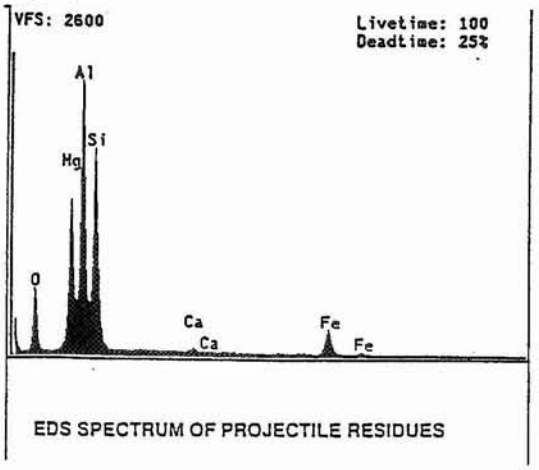

Figure c: EDS spectrum of residues (15 keV).

Figure 7: Debris impact on LDEF FRECOPA.

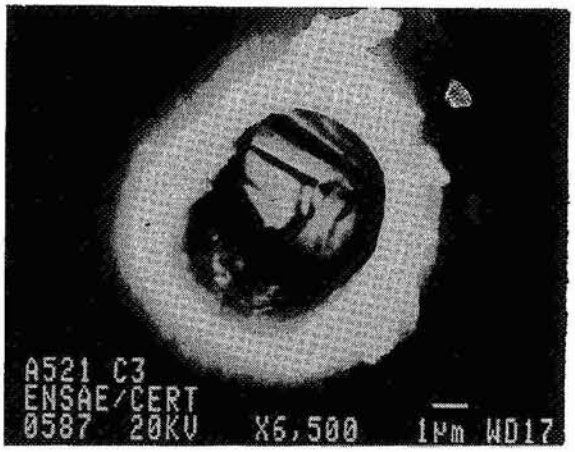

Figure a: Oblique impact (6.6 x 5.4 µm) on 99% pure Al experiment surface.

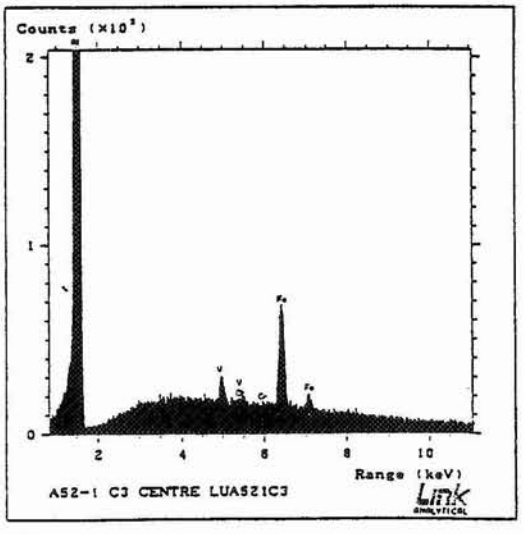

Figure c: EDS spectrum of figure 5a residues (20 keV).

Figure 8: Low velocity impact (33 μm) in LDEF clamp A06C06 with spectra from different areas of the residues to show different grain compositions.

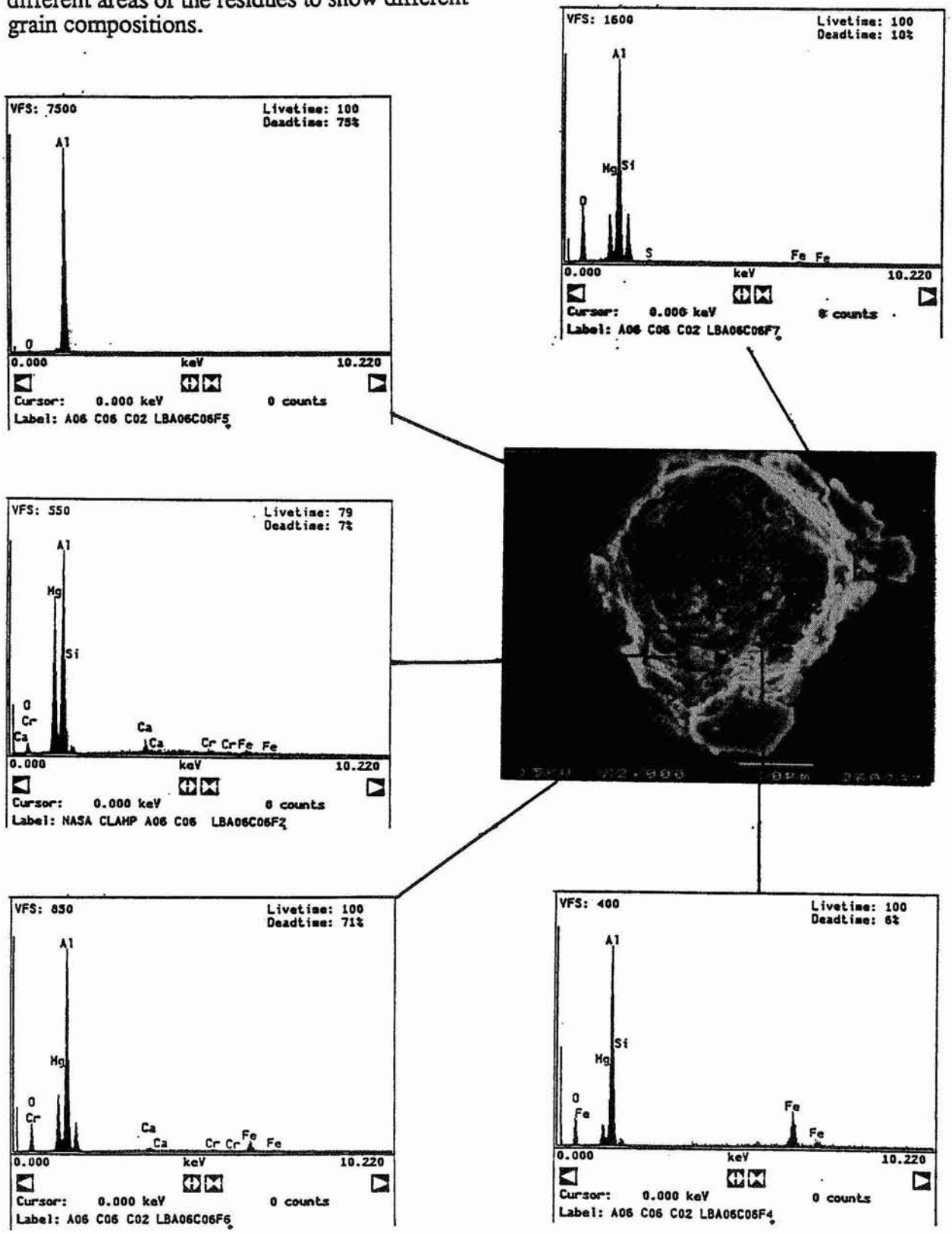

MICRO-ABRASION PACKAGE CAPTURE CELL EXPERIMENT ON THE TRAILING EDGE OF LDEF : IMPACTOR CHEMISTRY AND WHIPPLE BUMPER SHIELD EFFICIENCIES

Howard J. Fitzgerald and Hajime Yano
Unit for Space Sciences,
Physics Laboratory, University of Kent
Canterbury, Kent CT2 7NR
United Kingdom
Phone: +44-227-764000 ext. 7769, Fax: +44-227-762616

SUMMARY

Four of the eight available double layer microparticle capture cells, flown as the experiment AO023 on the trailing (West) face of LDEF (Fig. 1), have been extensively studied. An investigation of the chemistry of impactors has been made using SEM/EDX techniques and the effectiveness of the capture cells as bumper shields has also been examined. Studies of these capture cells gave positive EDX results, with 53% of impact sites indicating the presence of some chemical residues, the predominant residue identified as being silicon in varying quantities.

INTRODUCTION

An exposed area of 0.062 m^2 of both aluminium (Al) and brass foils, ranging in thickness from 1.5 μm to 24.13 μm were examined for hypervelocity perforations (Fig. 2). This initial examination concentrated on perforations in the top and bottom layers only. A total of 47 hypervelocity impact penetrations on the top layers have been found so far and their chemistry has been examined using a Philips 525M Scanning Electron Microscope (SEM) and Energy Dispersive X-ray (EDX) Spectroscopy techniques. Of these, 25 were found to have residues present but in 21 cases, this residue was silicon (Si) in varying abundance. Using a signal to background noise criteria, these were classified as Si-rich or Si-poor.

A natural impactor was identified on one of the top Al foils and one each of natural, man-made and Al-Si impactors were identified on the top brass layer. In addition, 10 perforations occurred in the second layer of a brass capture cell, each having Al residues and all due to a single large impact on the top brass layer. Around the surrounding areas of the secondary perforations, large numbers of craters were also seen. Also found were plasma perforations in 1.5 μm foil due to vaporised glue (ref. 1) which indicated Si residues but were not in fact hypervelocity in nature.

CAPTURE CELL ARRANGEMENT

The principle behind the double layer capture cell is the use of a top foil as a "bumper shield" in order to dissociate hypervelocity impacting particles, and a second foil used as a "catcher" of impactor

residues (Fig 3). Chemical analysis via EDX techniques can then be employed to identify the source of these impactors from these residues.

The capture cells used consisted of triangular sections, with combinations of Al (T6 rolled Al of 99.9 % purity) and brass foils of varying thickness. The top and bottom layers were separated by 2.7 mm except in the case of the W8 section which had a separation of 14 mm. The cells occupied one third of an LDEF experimental tray and were arranged in two groups of 4 with a polished stop plate beneath the bottom layer. This initial investigation concentrated on the chemistry of perforations in both top and bottom layers. Further work remains to be done on matching up top perforations with their residues on the second layer as shown in Figure 4 (a)-(b).

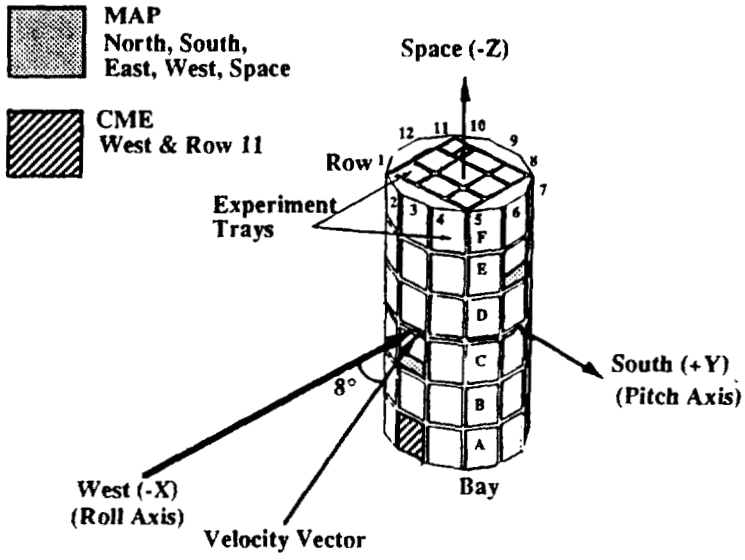

Figure 1. LDEF showing the positions of both the MAP and the CME experiments on the trailing edge.

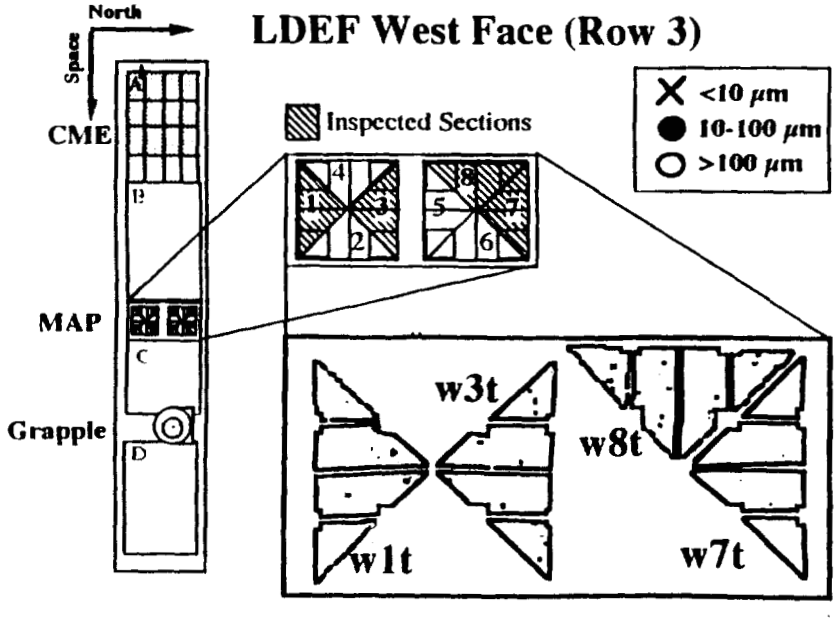

Figure 2. Arrangement of the west MAP foils on the experiment tray highlighting the sections inspected and the number and distribution of perforating impacts grouped into three size ranges.

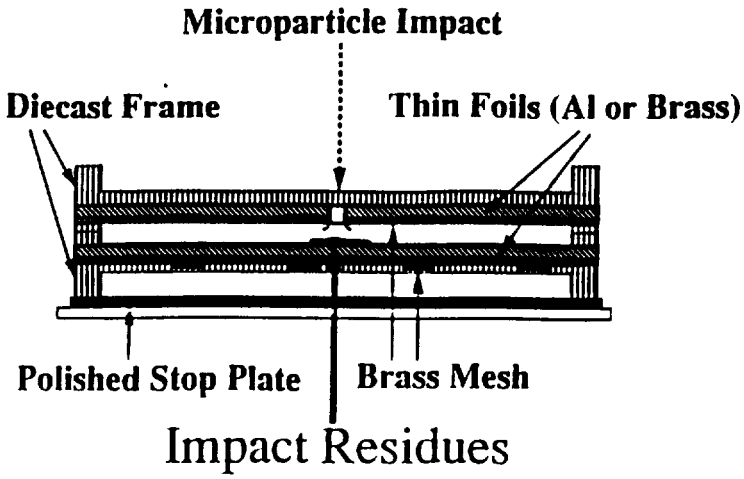

Figure 3. Cross-sectional view of the Micro-Abrasion Package double layer capture cell

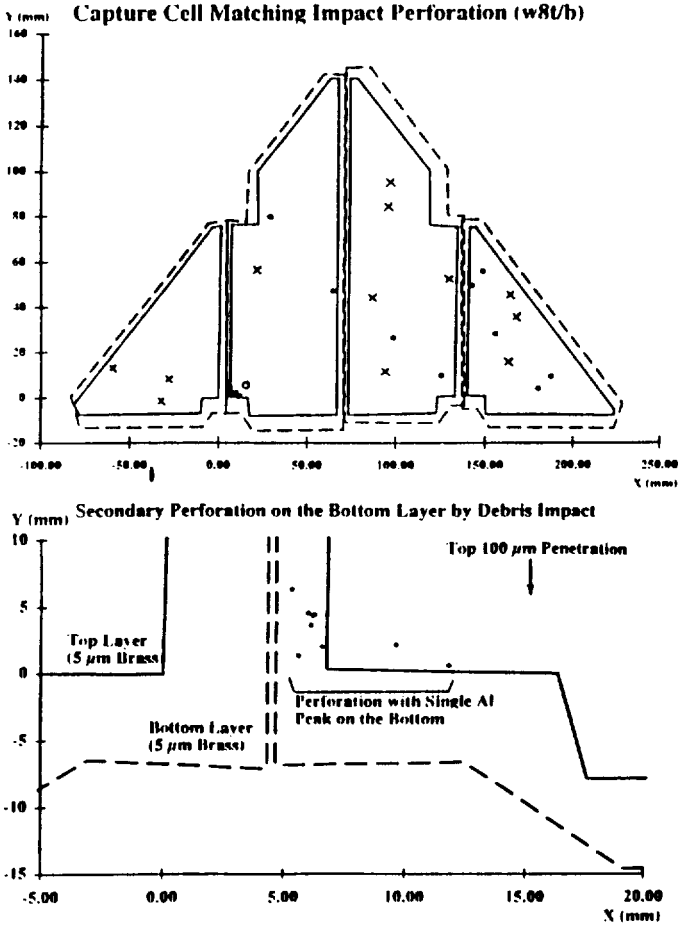

Figure 4 (a)-(b). The two layers (a) of the W8 capture cell are overlaid with the bottom layer shown as dashed lines. Fig. 4b shows a close-up view of the region where 10 secondary perforations occurred in the second layer due to a 100μm impact in the top layer (shown here as a circle). Some of these perforations are very close and so appear to overlap in the diagram but all indicated single Al peaks suggesting the space debris origin.

ANALYTICAL TECHNIQUE

All complete foil sections were first scanned using an automated stereo image CCD camera system called the Large Optical Scanning System (LOSS), for perforations by back illuminating the foils in a class 100 clean room (ref. 2). The penetration diameter size is derived from the CCD pixel count by fitting a photometric calibration curve, using holes which have been measured in the SEM. Initial scanning is at x10 magnification and potential impact sites are revisited at a variety of magnifications up to x40 with a resolution of > 4 μm. This enables most of obvious tears or rips to be distinguished from perforations which are due to actual space impacts.

Next, the foil sections were cut into their a, b, c, and d segments and placed in aluminium sample holders. The perforations were re-located using the co-ordinates derived from the optical scan and each feature was examined for morphology (ref. 3) and size using the SEM at a voltage of 25 kV and 0° tilt from normal. Actual hypervelocity impact sites were then imaged over a voltage range of 8-10 kV and an image taken at both 0° and 30° tilt.

Once a site had been identified as a hypervelocity event, a sequence of 6 X-ray spectra were taken with the EDX using a voltage of 20 kV and a count time of 100 seconds, with the stage tilted at 30°. This consisted of taking one spectrum of the entire site at a low magnification (which would indicate if large amounts of residue were present) followed by splitting the site into quadrants and examining a portion of the lip at high magnification. Finally, an X-ray spectrum of the nearby undamaged foil is taken, some 100-1000's of μm away from the impact site. The purpose of this was to provide a background spectrum for later use. The value for the count time of 100 seconds was chosen as a compromise value between the sensitivity of the instrument and the time available for investigation.

CHEMICAL RESULTS

Of the 47 hypervelocity impacts examined, 53 % (Fig. 5-6) had identifiable residues. A total of 2 naturals, 1 man-made and 1 Al-Si impactors were positively identified. Figures 7 (a)-(c) show three hypervelocity perforations onto 24.13 μm Al foil and an example of a typical X-ray spectrum (d) indicated only silicon in varying quantities. In Figures 8 (a) and (b), the spectrum for the Al-Si impactor and an image of one of the 10 secondary perforations found in the second layer of a 5.0 μm capture cell are shown. An Al and Ni spectra was also indicated from residues on the bottom layer. The spectrum of Figure 9 (a) was obtained from an impact onto a 1.5 μm Al foil and shows peaks for Si and Mg as well as S and was classified as due to a natural particle. The Cl may be due to contamination. The Figure 9 (b) was obtained on a 5.0 μm brass foil and displays strong peaks for Ca, Si, Al and Mg and it was also due to a natural particle. A solid line in the figures indicates a background spectrum.

Only the top layer of the capture cells (except for w8bb) were examined and despite the fact that EDX was performed only on the lips, the results compare well with the Chemistry of Micrometeoroid Experiment (CME, AO187-1) equipped with thick gold (Au) plate target on the same west face of the LDEF (ref. 4-5), where less than 50 % of impact sites had identifiable residues. The bottom layers may have substantial quantities of intact or semi-intact materials which could lead to further identification of unknowns as well as explaining the prevalence of Si residues. It is also noted that there can be different

elemental measurements at different locations (e.g. lip, bottom, side wall) within one hemispherical impact crater due to non-homogeneity of composition of an impactor (ref. 6).

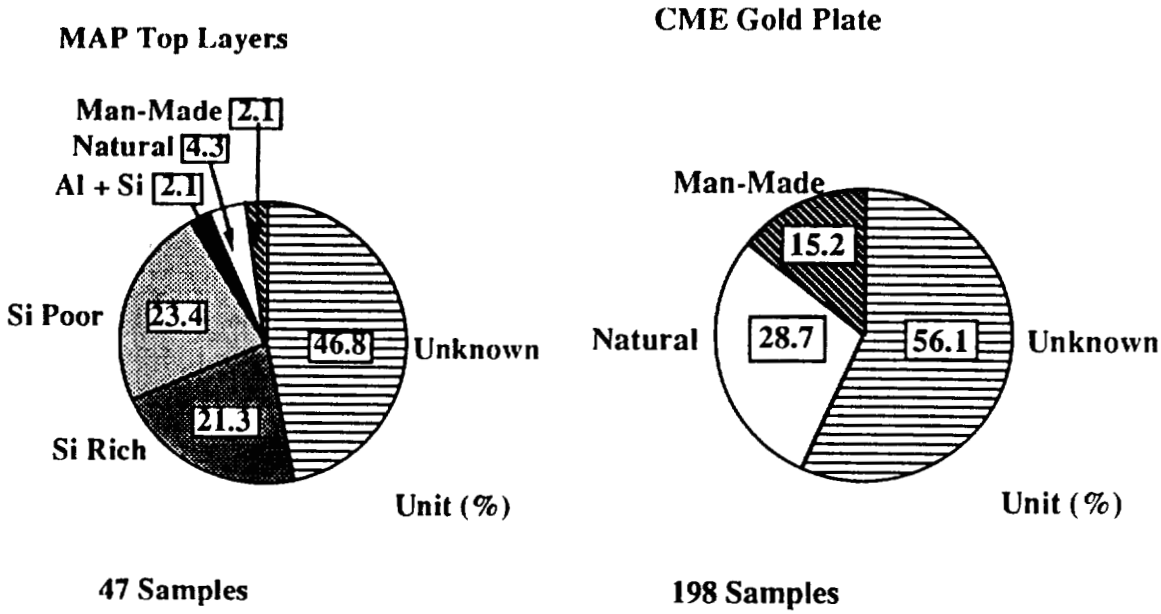

Figure 5. Chemical results of the MAP data comparing to the CME data

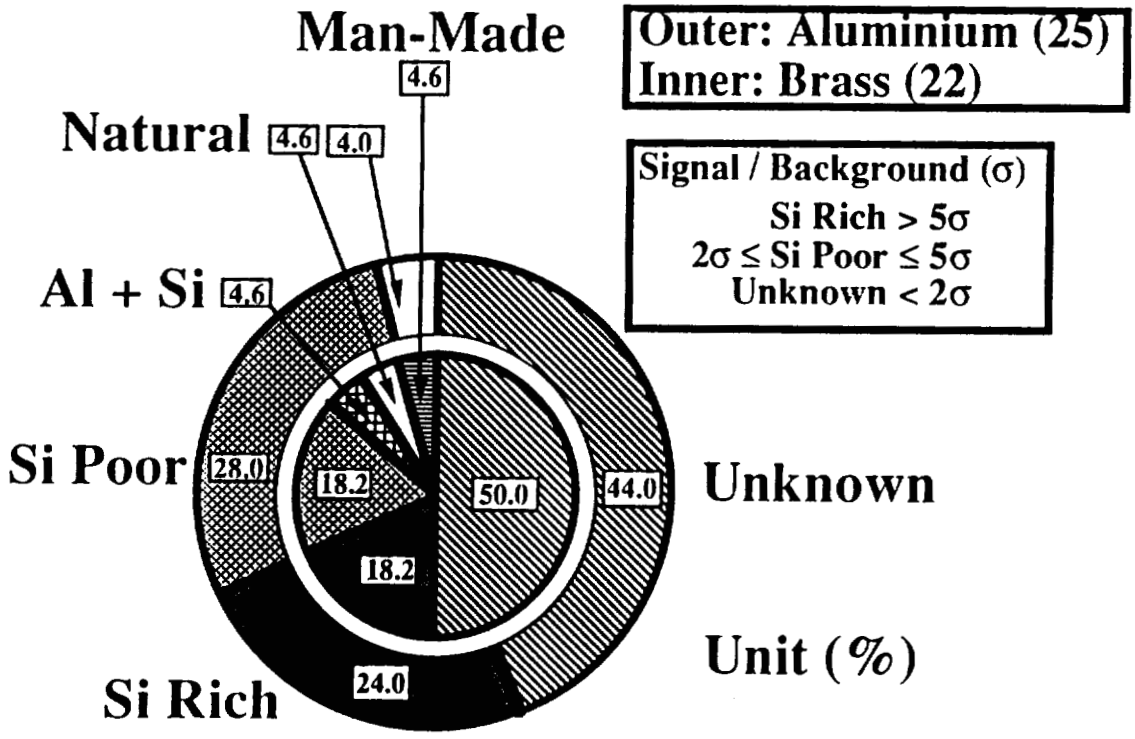

Figure 6. Breakdown distribution of impactors onto respective Al and Brass foils of the west MAP

INTERPRETATION OF THE CHEMISTRY

The majority of hypervelocity impacts with detectable residues were classed as either Si-rich or Si-poor, since the only residue detected was that of silicon. The interpretation of the two sub-groups was made by the following criteria. The Si peak of the best lip spectra was compared to the silicon peak of the background, initially comparing the count rates of these peaks. The Signal/Noise (S/N) was interpreted as the ratio of the two counts. (1) if $S/N < 2$, chemistry classed as unknown; (2) if $2 \leq S/N \leq 5$, chemistry classed as Si-poor; and (3) if $S/N > 5$, chemistry classed as Si-rich.

Then a background subtraction routine was applied to both lip and background spectra. The peak count rates were again compared to verify the first results. A better way of finding the S/N ratio would be to compare the areas under each of the respective peaks. However, the method used was found to be a good approximation to this. The spectra identified as man-made, natural or Al-Si had clear peaks and presented no problem in identification.

FLUX MEASUREMENTS

The experimental data for the flux on the trailing edge of LDEF was in good agreement to previously obtained results, using a variety of sources such as the LDEF intercostals and clamps, which has been combined into a plot known as the west face smooth data (ref. 7). The data shows particularly good agreement at the smaller marginal perforation limit (Fmarg) but diverges from the smoothed curve in the other cases. This can probably be explained as being due to the small sample sizes available for each different thickness (Fig. 10).

The 5.0 μm brass data was initially converted into an equivalent thickness of aluminium by inputting appropriate values of density and tensile strength into the CMD equation for both Al and brass, which resulted that Brass : Al = 1.88 : 1(ref. 7-9). However, this is a rather crude way of equating the two materials and the data was plotted as brass instead. It shows good agreement with the West smoothed plot but diverges at higher marginal perforation values. In order to derive the marginal penetration value (Fmarg) from the experimental values of perforation size (Dh), it was first necessary to normalise the diameter of each hole to some average value, since the majority of perforations were elliptical in nature.

A computer generated program (ref. 11) was then employed to output values of Fmarg and diameter of impacting particle using the CMD equation. The assumption was made that all impactors were natural, with a normal impact velocity of 11.01 km/s and density of 1.00 g/cm^3, since the program did not allow for a combination of natural and man-made debris to be calculated.

COMPARISON OF MAP DATA WITH CDC AND CME RESULTS

The perforation sizes for the MAP data has been converted into particle size using the equation derived by Cour-Palais (ref. 12) in order to make a direct comparison to data from both the Cosmic Dust Catalogue (CDC) (ref. 13) and the CME (ref. 14). CDC data represents micrometeoroid particles that

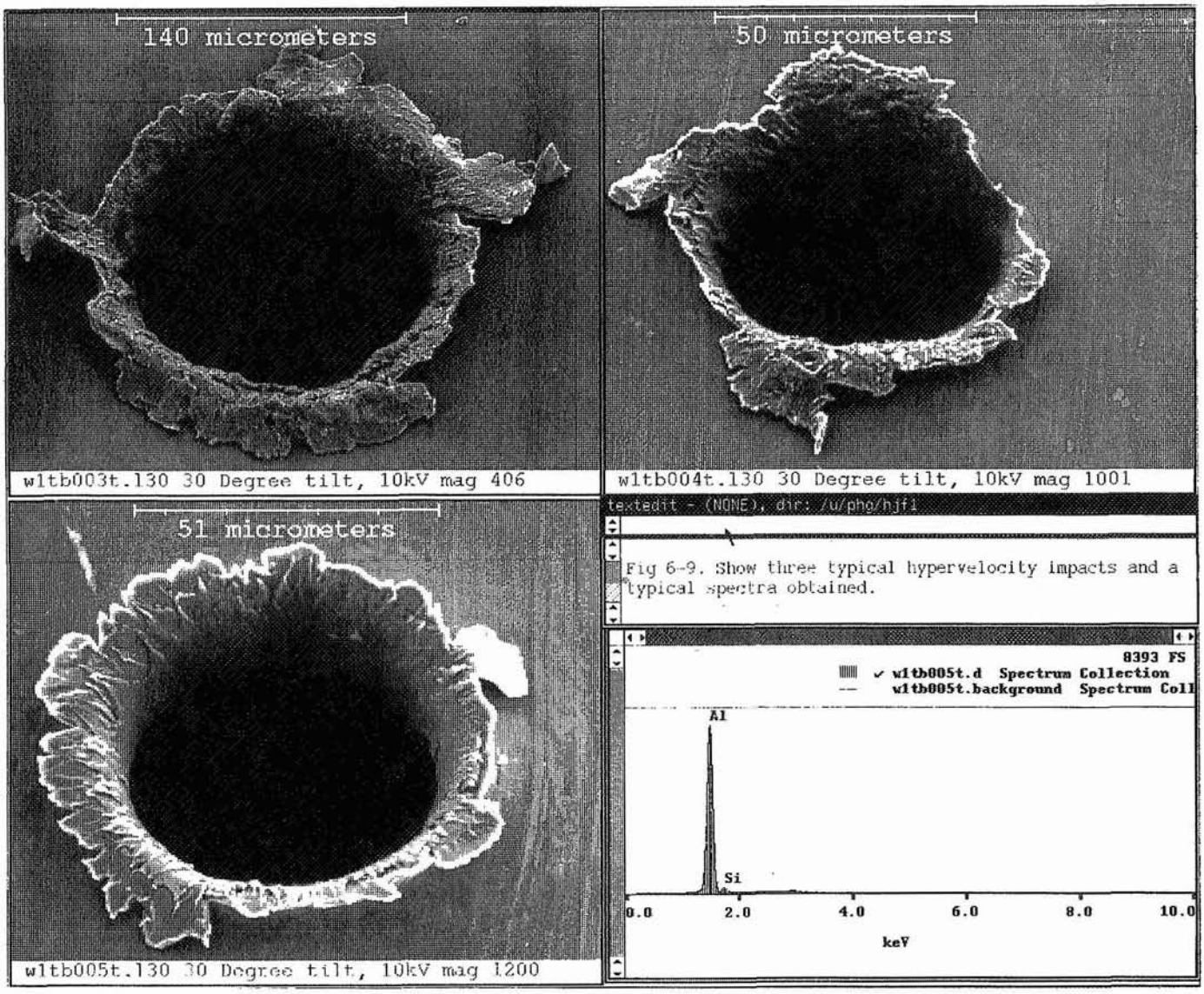

Figure 7 (a)-(d). Three hypervelocity perforations onto 24.13 μm Al foils (a)-(c) and a typical X-ray spectrum (d = bottom right)

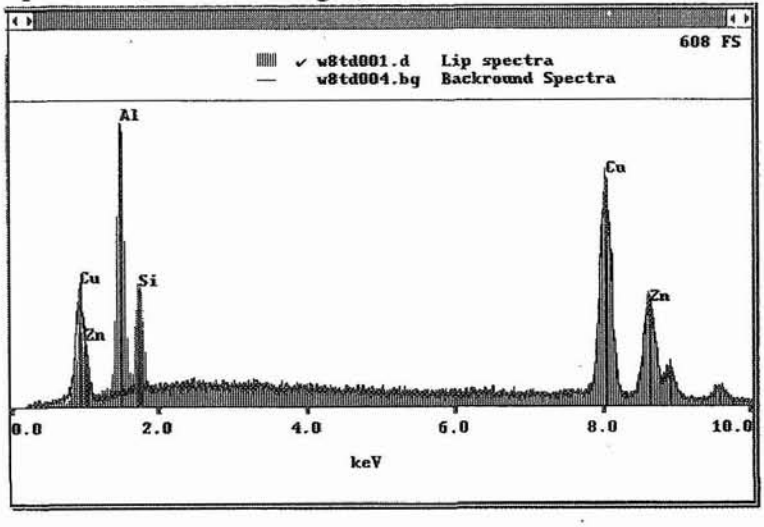

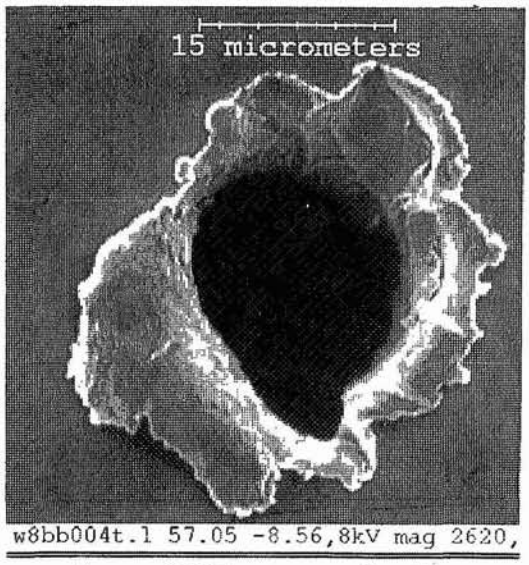

Figure 8 (a)-(b). Spectrum for Al-Si impactor (a = left) and an image of one of 10 bottom perforations on 5 μm capture cell (b = right).

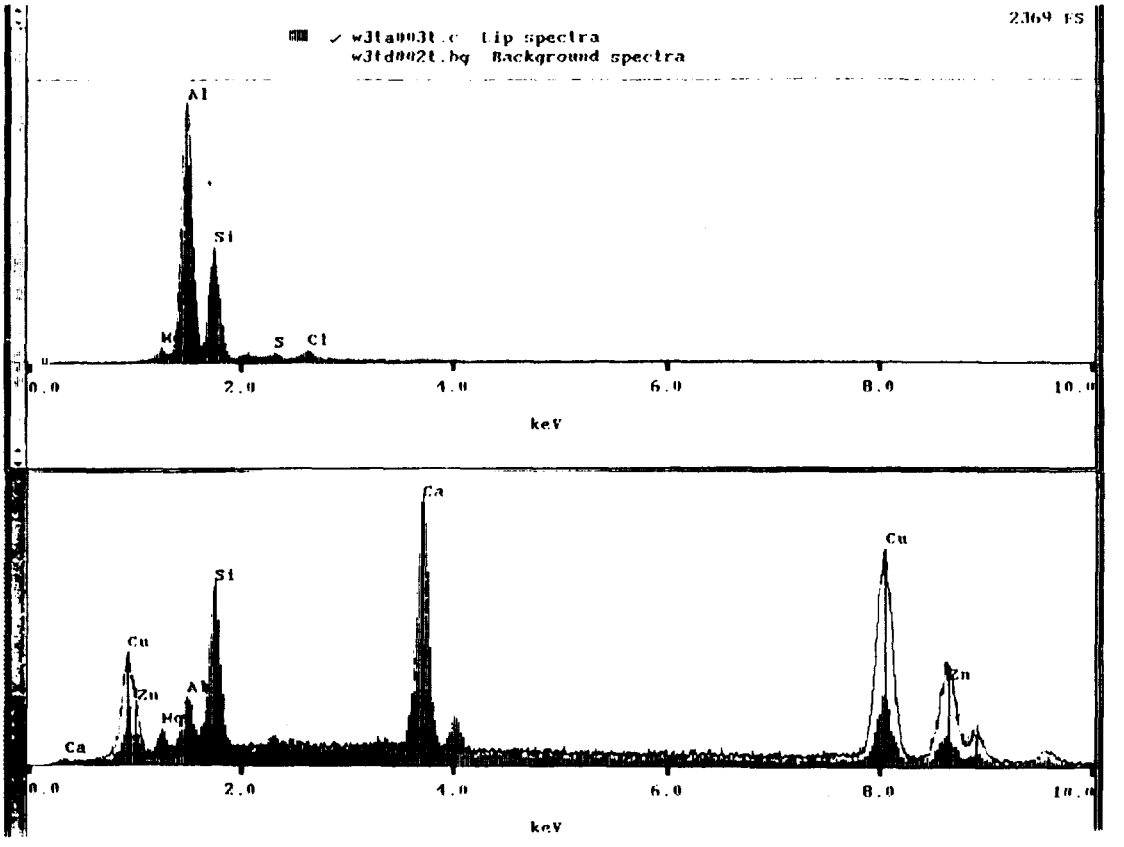

Figure 9 (a)-(b). The spectrum (a = top) was obtained from an impact onto a 1.5 μm Al foil with Si, Mg, and S peaks due to a natural particle. The Cl peak may be due to contamination. The spectrum (b = bottom) was obtained on a 5.0 μm brass foil displaying strong Ca, Si, Al, and Mg peaks also due to a natural particle.

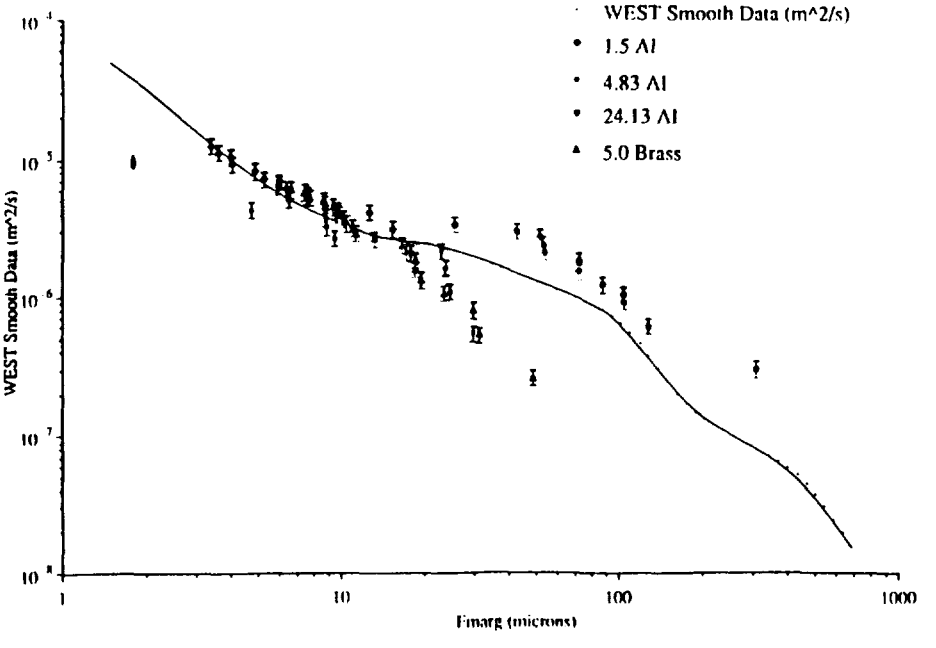

Figure 10. Experimental flux for MAP west foils against a smoothed curve of the same face of LDEF

The trend of MAP unknown particles follows that of CME unknowns and CDC natural particles (Fig. 11). All the CME unknowns are assumed to be caused by natural particle impacts with much higher impact velocities than catching-up debris from the trailing direction of the LDEF. However, higher peaks of Si particles occur in the size range 3-6 μm. These could be due to the larger than previously anticipated Si debris in the LEO. Limitation of CDC data is that detection range is only 3-50 μm and for CME, the use of a semi-infinite target means that it is insensitive to small impactors.

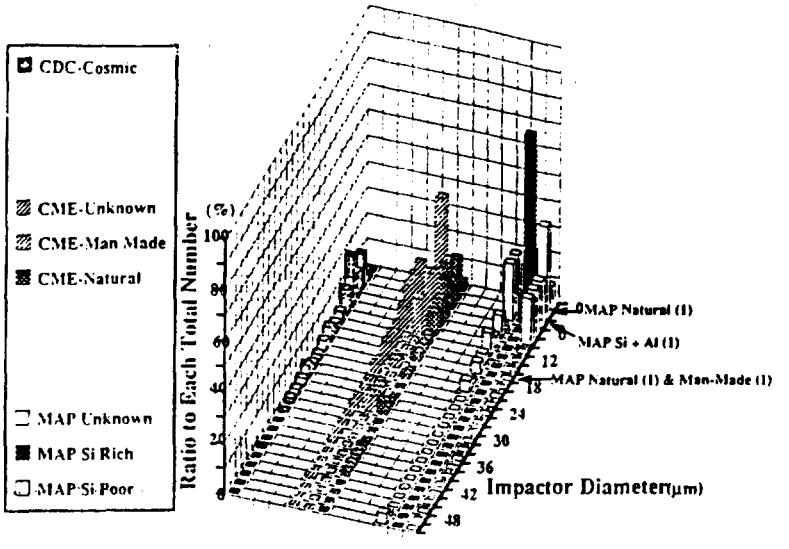

Figure 11. The impactor size distribution for CDC, CME and MAP West data

BUMPER SHIELD EFFICIENCIES

The effectiveness of the capture cells in terms of bumper shields (ref. 15) was investigated by converting the two layer foil thickness into an equivalent single thickness and plotting the thickness of foil that would be just perforated (the marginal perforation limit: Fmarg) against the cumulative flux, using the smoothed data curve.

Segment	Material	Thickness (microns) Top/bottom	Area (cm^2)
w1ta/d	Br	5.0 Br / 12.0 Br	52.54
w1tb/c	Al	24.13 Al / 12.0 Br	101.75
w3ta/d	Al	1.5 Al / 12.0 Br	53.25
w3tb/c	Al	4.83 Al / 12.0 Br	101.75
w7ta	Al	12.13 Al / 4.90 Al	26.73
w7tb/d	Al	24.13 Al / 4.90 Al	78.86
w7tc	Al	14.11 Al/ 4.90 Al	52.13
w8ta-d	Br	5.0 Br / 5.0 Br	155

Table 1 : Lists material, exposed area and possible combinations of thickness of foils evaluated as bumper shields. Only combinations that had not had the 2nd layer penetrated were considered.

The value of flux that can be protected against for the single (equivalent) thickness can be read directly from the diagram (Fig. 12). If the actual flux to which the west capture cells were exposed is higher than this value, and the capture cells have prevented penetration of their second layer, then the efficiency of the bumper shield concept has been proven. Table 1 gives details of thickness and exposed area for the different segments of the capture cells. The analysis indicated however that only one out of four combinations of combined foil thickness of the west MAP capture cells was found to be more efficient than a single shield. This can be explained as being due to too short an exposure time.

However, it was found that a single 100μm impact onto the top 5.0 μm brass foil of the w8 capture cells caused 10 secondary perforations of the 2nd 5.0 μm brass foil, despite a separation of 14.7 mm between the two layers. This suggests that greater attention needs to be paid to the protection of vital components situated on the trailing edge of a spacecraft in LEO.

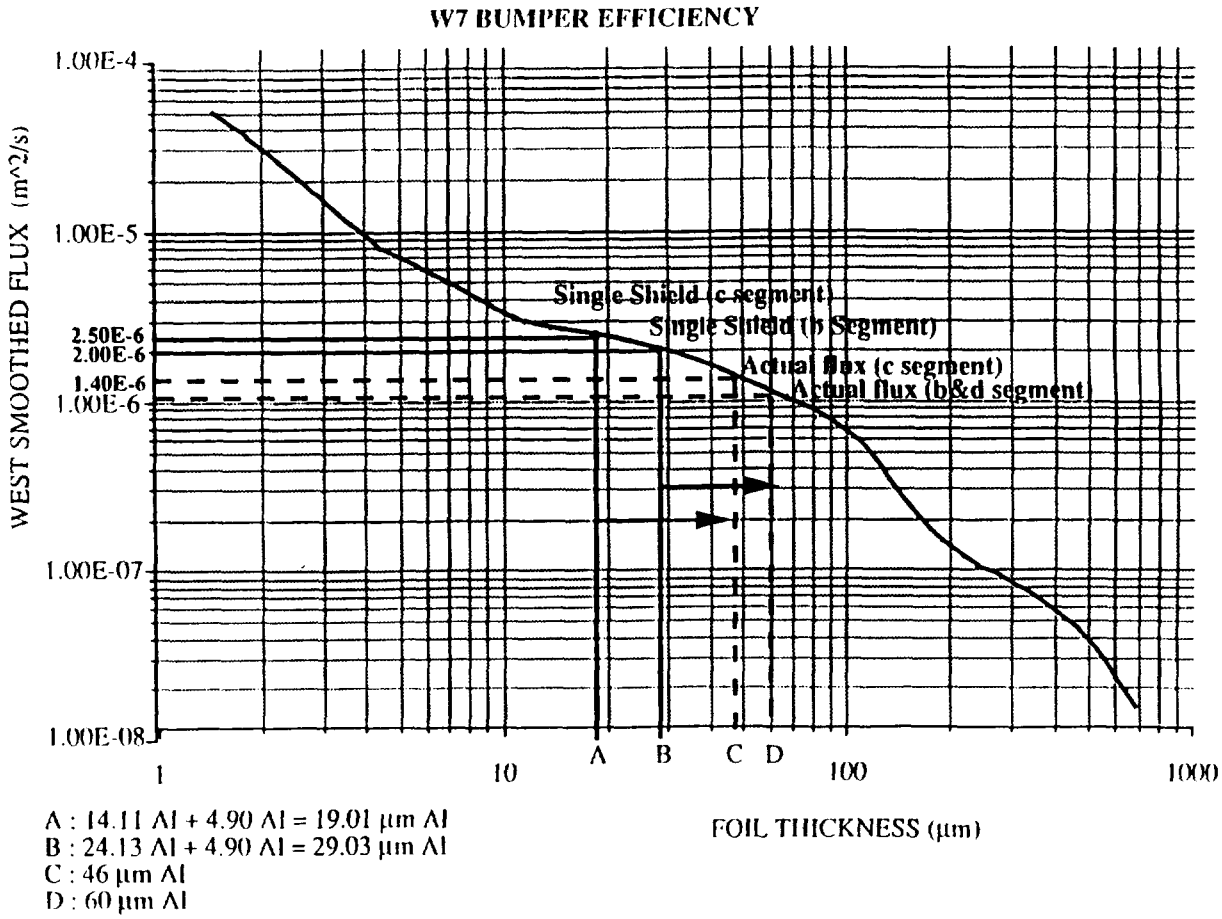

Figure 12. The bumper shield efficiency for the W7 brass foil. A = Sum of bumper shield thickness (14.11 μm Al + 4.90 μm Al), B = Sum of bumper shield thickness (24.13 μm Al + 4.90 μm Al), C = Single shield with equivalent shielding effect of bumper A (46 μm Al), and D = Single shield with equivalent shielding effect of bumper B (60 μm Al).

FOIL SENSITIVITY AND VAPORISATION EFFECTS

The speed at which a particle impacts the capture cell will largely determine the degree of vaporisation that the particle will undergo. Despite the fact that the capture cells were situated on the trailing edge, it is still possible that natural particles can strike the spacecraft at up to ~70 km/s. In the case of space debris, the maximum normal, relative impact velocity is 3.16 km/s, which implies that there would be a greater chance of detecting man-made debris compared to natural particulate. Major sources of man-made debris are aluminium parts of spacecraft and solidified Al_2O_3 rocket propellant spheres. However, 2/3 of the top detector surface was in fact aluminium foil, thus rendering this area insensitive to the detection of those debris with conventional EDX technique. Impact events at speeds > 3 km/s subject both target material and impactor to extremes of temperature and pressure leading to fragmentation, melting or vaporisation (ref. 16) and the most important material parameters for both target and particle are density and the boiling point of the material.

It has been shown that the impact of a high density impactor onto a low density target will experience the least damage while conversely, a low density impactor onto a high density target will result in the most damage. The MAP experiment is an example of the former, where low density (Al) and medium density (brass) foils are used as the target material. The advantage of Al are the lower shock conditions and temperatures generated during the event. The drawback is that the foils are insensitive to the majority of the man-made particle population. Brass foils offer an intermediate detector surface between Al and Au as well as offering a characteristic spectrum which does not interfere with identification of extra-terrestrial materials. However, the 5.0 μm thickness used did prove to be insensitive to the smallest sized micrometeoroid. The CME experiment is an example of the latter, where a high density semi-infinite target material (Au) was used as the detector surface. The result of this is that hypervelocity impact events generate higher shock-stresses and temperatures resulting in a greater degree of vaporisation and subsequent non-detection of residues due to being below the sensitivity of EDX method employed.

In general, EDX analysis requires more than 1 % of the material being examined to be residue. Since in the case of the MAP foils, the major portion of the particle has passed through the top layer, the amount of residue present is close to this 1 % value. It is also possible that at times during the EDX examination, the X-ray beam was actually passing through the surface of lips, since these X-rays may typically penetrate up to 1 μm of material. An X-ray voltage of 3-5 kV has been suggested to overcome this problem and will be used in future analysis of residues on the second layer.

CONCLUSIONS

The effectiveness of the capture cell principle has been demonstrated over the use of higher density semi-infinite detectors. Preliminary results have shown that EDX techniques can be employed successfully in the analysis and identification of residues and compare well with previous studies on the CME.

Note has been taken of comments raised during the conference, namely that lower X-ray voltages, of the order of 5 kV may increase the success rate of EDX analysis. Use of a voltage of 20 kV has probably resulted in the electron beam passing through the residue in some cases. This suggestion will be incorporated in future studies of the second layer. Also noted is the fact that there may be more silicon

debris than earlier anticipated. If this is the case, then the detection of the large number of Si impactors can be explained. In terms of contamination of the foils, Mg-Si pockets of impurities have been reported (ref. 17) but we do not believe this to be detrimental to our results, since only small portion (some 10 μm x 10 μm at most) of hypervelocity lips were examined and the fact that Mg has only been detected at a couple of sites reinforces this view.

Comparison of MAP data with CME and CDC has revealed the MAP foils detected a higher number of particles in the 2-5 μm size range. These particles were identified as Si-rich or Si-poor. This suggests that the population of small size particles is larger than previously estimated and may be due, in part at least, to man-made silicon debris. Overall, the data shows agreement with the trend of decreasing population with increasing particle diameter.

Flux measurements have shown good agreement with previous experimental data. Anomalies and divergence from the smoothed data curve can be explained by the small statistics involved. Additional data has been measured for the lower marginal perforation limit (1.5 μm) and the data shows excellent agreement with the smoothed data. The effectiveness of the capture cells as bumper shields has also been examined with the real space data. However, in the exposure time of the LDEF (5.78 years), their have been insufficient impacts on the trailing edge to prove the efficiency of the MAP structure as a bumper shield.

ACKNOWLEDGEMENTS

Authors are thankful to J.A.M. McDonnell for his supervision, Lucy Berthoud and Sunil Deshpande for providing useful information and discussion, and members of the Unit for Space Sciences for their assistance. This work was supported by the European Social Fund (ESF), the Overseas Research Studentship (ORS), the Daiwa Anglo-Japanese Foundation, and the Anglo-American Educational Exchange Scholarship Fund.

REFERENCES

1. Yano, H. and Fitzgerald, H.J., Determination of directionality and sources of impactors on the double layer foil capture cells of LDEF, *Proc. First European Conf. on Space Debris*, ESA SD-01, 207-210, (1993).

2. Paley, M.T., An automated system for obtaining impact penetration, location, size and circularity on a foil with special reference to the LDEF, Hypervelocity Impacts in Space, J.A.M. McDonnell (Edit), University of Kent at Canterbury, Kent, UK, 48-53, (1992).

3. Mackay, N.G., Green, S.F., Deshpande, S.P. and Newman, P.J., Interpretation of impact crater morphology and residues on LDEF using 3-D space debris and micrometeoroid models, *Proc. First European Conf. on Space Debris*, ESA SD-01, 159-164, (1993).

4. Hörz, F., Bernhard, R.P., Warren, J.L., See, T.H., Brownlee, D.E., Laurance, M.R., Messenger, S., and Peterson, R.B., Preliminary analysis of LDEF instrument AO187-1 "Chemistry of Micrometeoroids Experiment", *Proc. First LDEF Post-Retrieval Symp.*, NASA CP-3134, 487-501 (1992).

5. Hörz, F. and Bernhard, R.P., Compositional Analysis and Classification of Projectile Residues in LDEF Impact Craters, NASA Tech. Memo. 104750, NASA/JSC, Houston, USA (1992).

6. Berthoud, L. and Mandeville, J.C., Further analysis of remnants found in LDEF and MIR impact craters, Presented at the Workshop on Interplanetary Dust Particles, Houston, TX, USA, May, 1993.

7. Neish, M.J., In-house communication, (1993).

8. Deshpande, S.P. and Paley, M.T., Supra-marginal impacts detected on the Micro-Abrasion Package (MAP) experiment situated on LDEF's space face, Hypervelocity Impacts in Space, J.A.M. McDonnell (Edit), University of Kent at Canterbury, Kent, UK, 166-172, (1992).

9. McDonnell, J.A.M., Deshpande, S.P., Niblett, D.H., Neish, M.J., and Newman, P.J., The near Earth space environment - an LDEF overview -, *Adv. Space Res.*, 13, 8, (1993).

10. Berthoud, L. and Mandeville, J.C., Empirical impact equations and marginal perforation, Proc. First European Conf. on Space Debris, ESA SD-01, 459-464, (1993).

11. Deshpande, S.P., In-house communication, (1993).

12. Cour-Palais, B.G., Hypervelocity impacts in metals, glass, and composites, *Int. J. Impact Eng.*, 5, 681-692, (1987).

13. NASA Cosmic Dust Preliminary Examination Team (M. Zolensky et.al.), Vol. 1-13, NASA Johnson Space Center, Houston, Texas, USA, (1982-1992).

14. Yano, H., Comparative studies of chemical components of impact residues on the LDEF, stratospheric particles and Antarctic ice core particles, *Annal. Geophys.*, Part 3, 11, C481, (1993).

15. Whipple, F.L., Meteorites and space travel, *Astron. J.*, 52, p.5, (1947).

16. Yano, H., Fitzgerald, H.J., and McDonnell, J.A.M., Chemical analysis of natural particulate impacts on the Long Duration Exposure Facility, Presented at the IAU Symposium 160 : Asteroids, Comets, Meteors 1993, Belgirate, Italy, June 1993.

17. Berthoud, L., In-house communication, (1993).

SECONDARY ION MASS SPECTROMETRY (SIMS) ANALYSIS OF HYPERVELOCITY MICROPARTICLE IMPACT SITES ON LDEF SURFACES

*C.G.Simon
Institute for Space Science and Technology
*current address: Air Consulting and Engineering, Gainesville, FL
Phone (904) 335-1889 Fax (904) 335-1891

A.J. Buonaquisti, D.A. Batchelor, J.L. Hunter, D.P. Griffis, V. Misra, D.R. Ricks, J.J. Wortman
North Carolina State University, Raleigh, NC 27695
Phone (919) 515-7659 Fax (919) 515-6965

D.E. Brownlee
Astronomy Department, University of Washington, Seattle, WA 98195
Phone (206) 534-8575 Fax (206) 545-0403

S.R. Best and M.S. Crumpler
Space Power Institute, Auburn University, AL 36849
Phone (205) 844-5894 Fax (205) 844-5984

B. Arad, S. Eliezer, S.E. Moshe, S. Maman and I. Gilath
Soreq/NRC, Yavne 70600, Israel
Phone (972) 8 434779 Fax (972) 8 434315

ABSTRACT

Two dimensional elemental ion maps have been recorded for hundreds of microparticle impact sites and contamination features on LDEF surfaces. Since the majority of the analyzed surfaces were metal-oxide-silicon (MOS) impact detectors from the Interplanetary Dust Experiment, a series of "standard" and " blank" analyses of these surfaces are included. Hypervelocity impacts of forsterite olivine microparticles on activated flight sensors served as standards while stylus and pulsed laser simulated "impacts" served as analytical blanks.

Results showed that despite serious contamination issues, impactor residues can be identified in >1/3 of the impact sites. While aluminum oxide particles could not be detected on aluminum surfaces, they were detected on germanium surfaces from row 12. Remnants of manmade debris impactors consisting of paint chips and bits of metal were identified on surfaces from LDEF Rows 3 (west or trailing side), 6 (south), 9 (ram or leading side), 12 (north) and the space end. Higher than expected ratios of manmade microparticle impacts to total microparticle impacts were found on the space end and the trailing side. These results were consistent with time-tagged and time-segregated microparticle impact data from the IDE and other LDEF experiments (Ref. 1).

A myriad of contamination interferences were identified and their effects on impactor debris identification mitigated during the course of this study. These interferences include pre-, post and in-flight deposited surface contaminants as well as indigenous heterogeneous material contaminants. Non-flight contaminations traced to human origins, including spittle and skin oils, contributed significant levels of alkali-rich carbonaceous interferences. A ubiquitous layer of in-flight deposited silicaceous

contamination varied in thickness with location on LDEF, even on a micro scale. In-flight deposited (low velocity) contaminants include urine droplets and bits of metal film from eroded thermal blankets.

The results of this study and all analytical data are archived on CD-ROM available from the LDEF office. Several papers detailing results of this study have been published (Refs. 2-4), and a final summary paper is under preparation for submittal to the Journal of Spacecraft and Rockets.

ACKNOWLEDGEMENTS

This project was partially supported by NASA grant NAG-1218. We gratefully acknowledge the uncompensated contribution by the SOREQ/NRC in providing laser-stimulated blank discharges on retrieved MOS sensors.

REFERENCES

1. "Long-term microparticle impact fluxes on LDEF determined from optical survey of Interplanetary Dust Experiment (IDE) sensors." C. G. Simon, J.P. Oliver, W.J. Cooke, K.I. Downey and P.C. Kassel, presented at LDEF-69 Months in Space: Third Post Retrieval Symposium, *NASA CP- 3275* (1995).

2. C.G. Simon, J.L. Hunter, D.P. Griffis and J.J. Wortman, "Ion microprobe elemental analysis of impact features on Interplanetary Dust Experiment sensor surfaces", LDEF-69 Months in Space: First Post Retrieval Symposium, *NASA CP 3134*, pp.529-548 (1991).

3. C.G. Simon, J.L. Hunter, D.P. Griffis, V. Misra, D.A. Ricks and J.J. Wortman, "Contaminant interferences with SIMS analyses of microparticle impactor residues on LDEF surfaces." *Adv. Space Res.*, Vol. 13, No. 8, pp. (8)115-(8)118, (1993).

4. C.G. Simon, J.L. Hunter, D.P. Griffis, V. Misra, D.A. Ricks, J.J. Wortman, and D.E. Brownlee, "Elemental analyses of hypervelocity microparticle impact sites on Interplanetary Dust Experiment sensor surfaces." LDEF-69 Months in Space: Second Post Retrieval Symposium, *NASA CP-3194*, pp. 677-692 (1993).

SIMS CHEMICAL AND ISOTOPIC ANALYSIS OF IMPACT FEATURES FROM LDEF EXPERIMENTS AO187-1 AND AO187-2

Frank J. Stadermann
Technical University Darmstadt, Material Science Department
Hilpertstr. 31, Geb. H, D-64295 Darmstadt, Germany
Phone: (+49) 6151-813223, Fax: (+49) 6151-813222

Sachiko Amari, John Foote, Pat Swan, Robert M. Walker, Ernst Zinner
McDonnell Center for the Space Sciences and Physics Department
Washington University, St. Louis, MO 63130, USA
Phone: 314-935 6257, Fax: 314-935 4083

SUMMARY

Previous secondary ion mass spectrometry (SIMS) studies of extended impact features from LDEF capture cell experiment AO187-2 showed that it is possible to distinguish natural and man-made particle impacts based on the chemical composition of projectile residues. The same measurement technique has now been applied to specially prepared gold target impacts from experiment AO187-1 in order to identify the origins of projectiles that left deposits too thin to be analyzed by conventional energy-dispersive x-ray (EDX) spectroscopy. The results indicate that SIMS may be the method of choice for the analysis of impact deposits on a variety of sample surfaces. SIMS was also used to determine the isotopic compositions of impact residues from several natural projectiles. Within the precision of the measurements all analyzed residues show isotopically normal compositions.

INTRODUCTION

Among the most noticeable effects of the space environment on spacecraft are impacts produced by the bombardment with small particles from various sources. Several experiments on board the Long Duration Exposure Facility (LDEF) satellite dealt with the analysis of impact craters and projectile debris. There are two basic objectives for such experiments. One is the study of

micrometeoroids in order to determine the flux of interplanetary particles in space and to learn about their nature and origin. The other is the assessment of possible hazards to space flight posed by such impacts. For this purpose it is important to determine (a) the absolute number of impacts and (b) the ratio of natural (micrometeoroids) to man-made (orbital debris) impact particles. Various attempts have been made to estimate this ratio, *e.g.*, by comparing particle fluxes on differently oriented LDEF surfaces. However, a more direct approach to this problem is based on the chemical characterization of particle residues. Since micrometeoroids and orbital debris particles have distinct chemical properties, it is possible to determine the relative contribution of either type to the total particle flux by analyzing the composition of impact debris on LDEF surfaces.

Although all outer surfaces of the LDEF satellite are covered by impact features of various types and sizes, only a few are suited for micro-chemical analysis. What can usually be seen on space exposed materials are only the *effects of hypervelocity impacts* such as craters, dents, and cracks, but not remnants of the impacting particle. Due to the high velocities of impacts (typically several km/sec), practically no projectile material survives the collisions unaltered and only rarely chunks of projectile material can be found within or in the vicinity of impact craters that are large enough for energy dispersive x-ray analysis (EDX) . However, frequently there is a thin layer of debris around impact features where some fraction of the particle material re-condensed after being vaporized during impact. This layer of debris is generally too thin to be seen in either optical or scanning electron microscopes (SEM), but secondary ion mass spectrometry (SIMS) can often be used to analyze this material even when its thickness is only a few atomic monolayers.

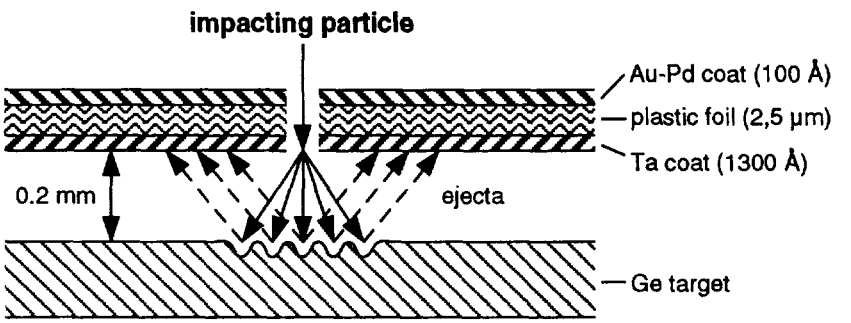

Figure 1. Schematic of capture cell experiment AO187-2.

In principle, impacts on all kinds of surfaces can be analyzed to determine the nature of the projectile material. In practice, however, most accurate analytical results can be achieved from impacts on clean substrates and with relatively large amounts of deposited debris. These conditions are satisfied in the capture cell experiment AO187-2, which was specifically designed for this kind of investigation. The principle of that experiment is shown in Figure 1. A target plate of high-purity germanium is covered with a thin foil separated by a small distance. A high velocity particle of sufficient size penetrates the foil and may be disrupted in the process, spreading out into a debris

shower. This shower impacts the target plate and is further disrupted, melted and vaporized. Some of the projectile material is retained in the impact region on the germanium plate. The projectile material ejected from the impact zone is collected on the backside of the foil and on the surrounding area of the germanium plate. Since only a small amount of material can escape through the impact hole in the cover foil, most impact debris stays in the capture cell and can be analyzed after the cell has been disassembled.

In our previous studies analyses were focused on samples from capture cell experiment AO187-2 (refs. 1, 2). Because most foils did not survive the $5^1/_2$ years of exposure in space, we analyzed extended impact features on the germanium plates, produced by projectiles which had arrived while the plastic foils were still in place. First, several different types of extended impact features were identified during optical and SEM analyses. The chemical compositions of the deposits were then determined by SIMS step scans across the impact features. At each step the composition of the surface layer was measured with an O^- primary beam of 1-2 nA that was rastered over an area of 40 μm x 40 μm. The width of individual steps was chosen between 35 and 60 μm each. Since each measurement consisted of up to 50 steps, these traverses had a typical length of several hundred μm and a width of about 40 μm. The secondary ion signals of the elements O, Mg, Al, Si, Ca, Ti, Fe, Ni, Ge, and Ta were monitored during the scans. These elements were chosen because they are the most abundant elements in cosmic dust particles and/or in the capture cells themselves. Typical results from one of these scans are shown in Fig. 2. The increase in secondary ion signals near the center of the impact can clearly be correlated with impact deposits.

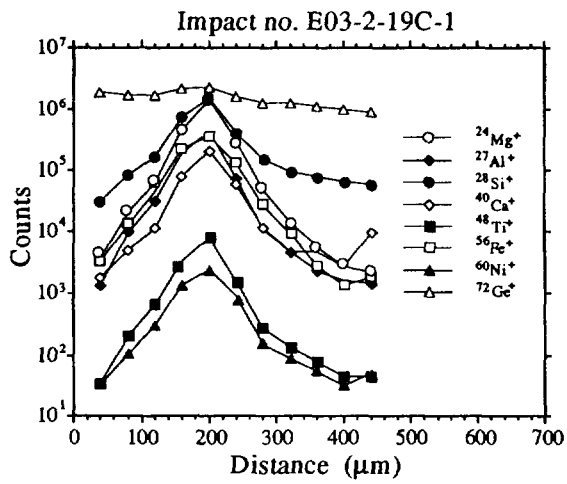

Figure 2. Secondary ion signals of different elements in a traverse across an impact feature on a Ge plate. The center of the impact is located near the 200 μm distance mark.

To date more than 60 extended impacts on germanium plates from experiment AO187-2 have been analyzed by SIMS for the chemical composition of the projectiles. Ion signals associated with material from the impacts could be detected in almost all analyzed impact areas despite serious problems with contamination. It was possible to discern the most likely origins of the projectiles by comparing the compositions of the deposits to those of cosmic dust particles and well known types of man-made debris. Thus we could show that at least 75% of the impacts on the trailing edge of LDEF were caused by micrometeoroids while virtually all analyzed impacts on the leading edge were caused by man-made debris particles (ref. 2).

After having established that SIMS is a useful analytical technique for the determination of the chemical composition of thin layers of impact deposits on the germanium capture cells, we undertook an investigation of its applicability to the analysis of impacts on other LDEF surfaces. We also used SIMS for the measurement of the isotopic compositions of certain impact debris fragments. Such measurements have not yet been possible on thin deposition layers on the germanium plates of the capture cells due to the thinness of the layers, which causes the signal at a given isotopic mass to change rapidly with time.

CHEMICAL ANALYSIS OF GOLD TARGETS FROM EXPERIMENT AO187-1

Next to samples from the capture cell experiment, impacts on witness plates of high-purity Au from experiment AO187-1 appeared particularly interesting because debris analyses on these surfaces had already been performed by conventional SEM-EDX techniques (ref. 3). Unfortunately, in more than 50% of all Au impacts studied no detectable EDX signals could be found, obviously complicating the statistical interpretation of the data. We tried to improve this situation by analyzing these Au samples with the same SIMS analysis technique that we had used earlier on the Ge impacts. For a preliminary investigation Fred Hörz generously provided us with 15 Au samples that had previously been studied by SEM-EDX (ref. 3). Eleven of those impact projectiles had been classified as "natural", one as "man-made" and the origins of the other three were still unknown.

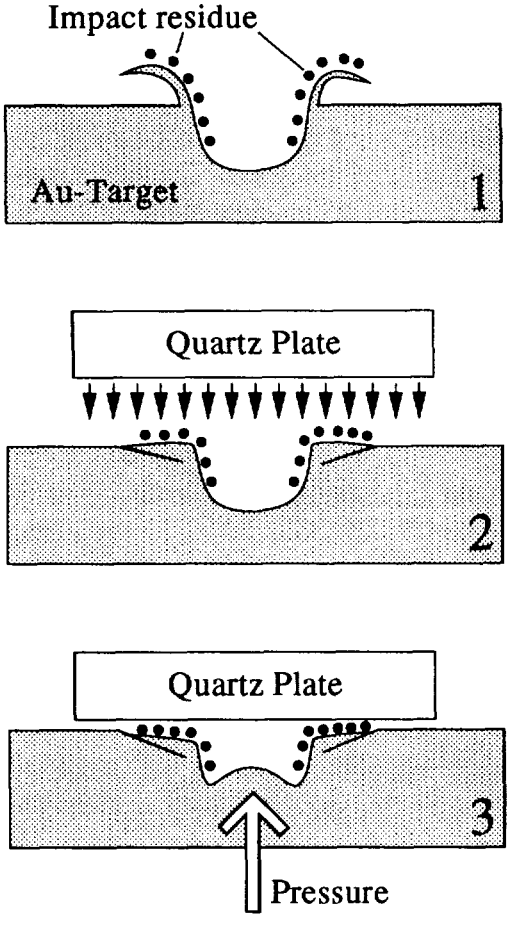

Figure 3: Steps in the sample preparation of Au targets from LDEF.

SIMS measurements of the Au impacts posed some analytical problems. The impact craters in the Au foil are generally relatively deep and are surrounded by a "lip" of Au that rises above the original sample surface. Since SIMS requires a flat sample surface it was necessary to develop a new sample preparation technique for the analysis of these kinds of impact craters (Fig. 3). Preliminary studies had shown that the most interesting areas to analyze in the Au samples are impact residues located inside the crater and on the lip. In order to flatten the lip a quartz plate was pressed onto the sample surface. After the surface was even, a needle was carefully pressed against the underside of the thin Au sheet to push the bottom of the crater up. The entire procedure was monitored under a

stereomicroscope through the quartz disk. That way the surfaces from inside the crater walls became accessible to SIMS measurements on a flat surface. After these preparations, the SIMS scanning technique was applied to the Au witness plates.

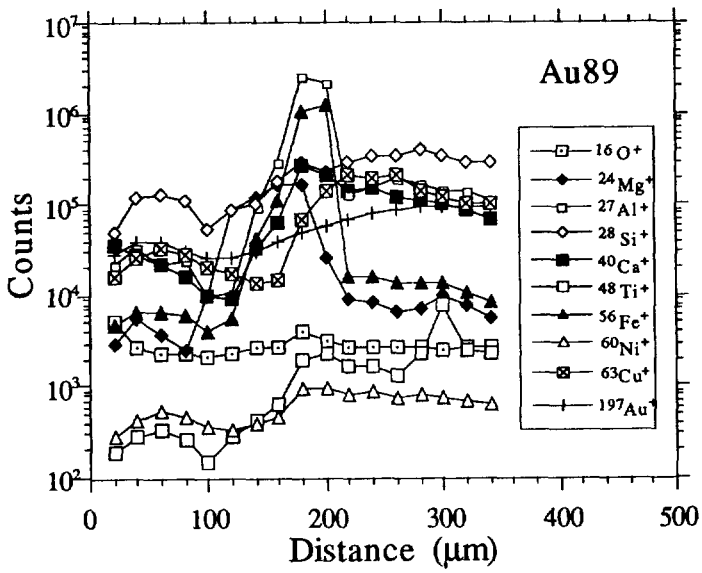

Figure 4: Secondary ion count rates from a SIMS scan across AO187-1 impact "Au89".

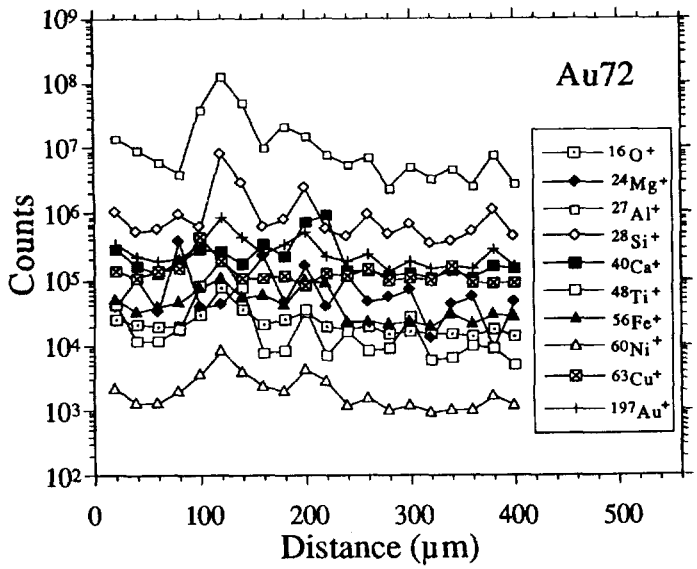

Figure 5: Secondary ion count rates from a SIMS scan across AO187-1 impact "Au72".

The SIMS scans of these "high-purity" Au substrates revealed high levels of contamination that cannot be attributed either to the impacts themselves or to contamination originating from the LDEF spacecraft (see Figs. 4–6). Instead, it appears that the Au target itself contains significant amounts of trace contaminants. In spite of this problem, which led to generally higher background level in most of the measurements, it was indeed possible to determine the origin of the projectiles in several of the Au target impacts. To date SIMS scans have been made across seven flattened craters from experiment AO187-1. Examples of the results are shown in Figures 4–6.

Impact "Au89" (Fig. 4) had originally been classified as "natural" based on the EDX analysis of small chunks of debris that had been found in the crater. The SIMS scan shows a complex pattern with several elements –such as Al, Fe, Ca, and Mg– clearly enriched in the vicinity of the crater whose center is located near the 200 μm distance mark. An elemental signature like this is typical for a natural particle (micrometeoroid). The EDX classification of this impact can therefore be confirmed.

Figure 5 shows data from a scan across impact "Au72" that was classified as "man-made" before. Here too, that classification could be confirmed by the SIMS measurements.

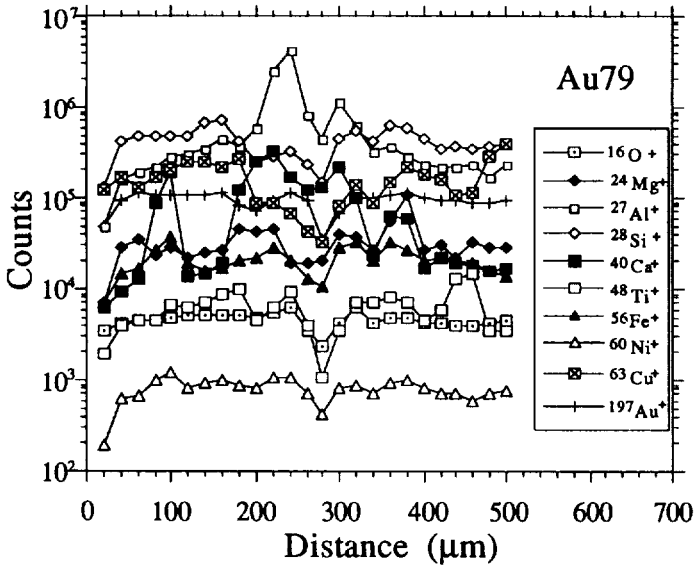

Figure 6: Secondary ion count rates from a SIMS scan across AO187-1 impact "Au79".

The most enriched element at the center of the crater (near the 120 μm mark) is Al, accompanied only by a smaller enrichment of Si. Such a prominent Al-rich composition is highly indicative of an aluminum-oxide particle from rocket exhausts.

The origin of the projectile that caused impact "Au79" was unknown because no debris could be found in the SEM-EDX study that was large enough for a determination of the chemical composition. Here the strength of SIMS as a highly sensitive micro-analytical technique becomes obvious (Fig. 6). Only aluminum is significantly enriched near the position of the crater at the 240 μm distance mark. This impact can unambiguously be classified as "man-made".

The SIMS measurements did not always allow the identification of hitherto unknown projectiles, but the total number of "unknowns" was reduced. It appears that SIMS is the method of choice for the analysis of impact debris on various surfaces, provided the samples can be suitably prepared for SIMS analysis.

In an effort to characterize the chemical composition of some of the "natural" impact projectiles on the Au target plates in more detail, we measured the relative abundances of 24 elements in two chunks of debris from the impacts "Au104" and Au280". The results of these measurements are shown in Figures 7 and 8, together with values of the meteoritic abundances of C1 chondrites. These C1-abundances are well known from the study of meteorites (ref.4) and there is reason to expect that natural projectiles, *i.e.*, micrometeoroids, have compositions that are similar to those of C1 chondrites (ref. 5). Since only relative abundances can be measured with SIMS, all elements are normalized to Si, whose concentration was arbitrarily set to its C1-abundance.

Since two fragments were analyzed from each impact an upper limit of the precision of the measurement can be estimated from the variation between both measurement runs (inherent heterogeneities in the sample would lead to even bigger variations between the two measurements). The precision appears to be quite good for the majority of the elements. However, the accuracy of the determinations is not as good, possibly due to the inherent problems of quantification in the SIMS technique. Still, the similarity between the compositions of the projectiles and the C1-abundances is striking. Since all elemental abundances are normalized to Si, an overabundance of

this element would lead to seemingly lower abundances of the other elements. Interestingly, in impact "Au280" Ca is depleted while in impact "Au104" Fe, Co, and Ni concentrations are lower than the C1-abundances. Both observations agree with earlier measurements of certain cosmic dust particles that were collected in the stratosphere (ref. 5). Clearly, this determination of the abundances of 24 elements leaves no doubt about the natural origin of the particles that caused these impacts.

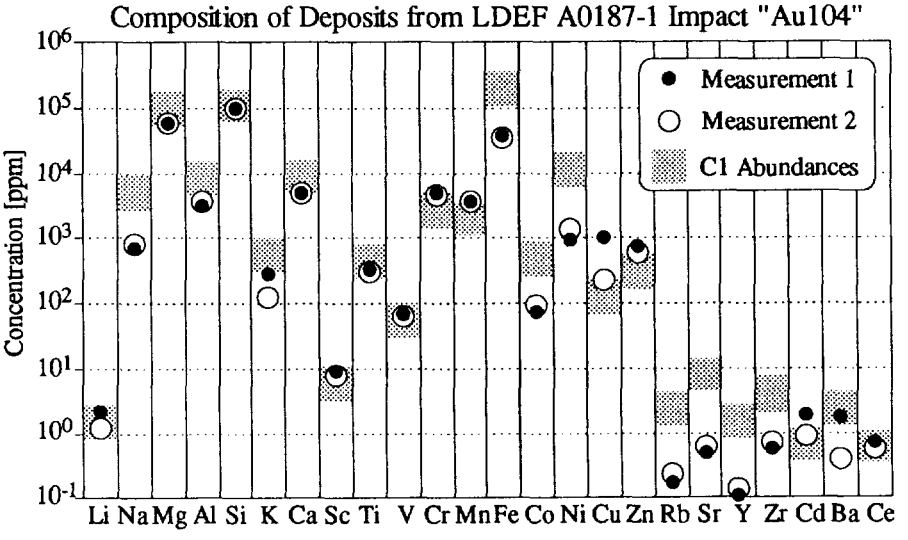

Figure 7: Elemental abundances of two fragments normalized to a condritic Si value and compared to C1-abundances.

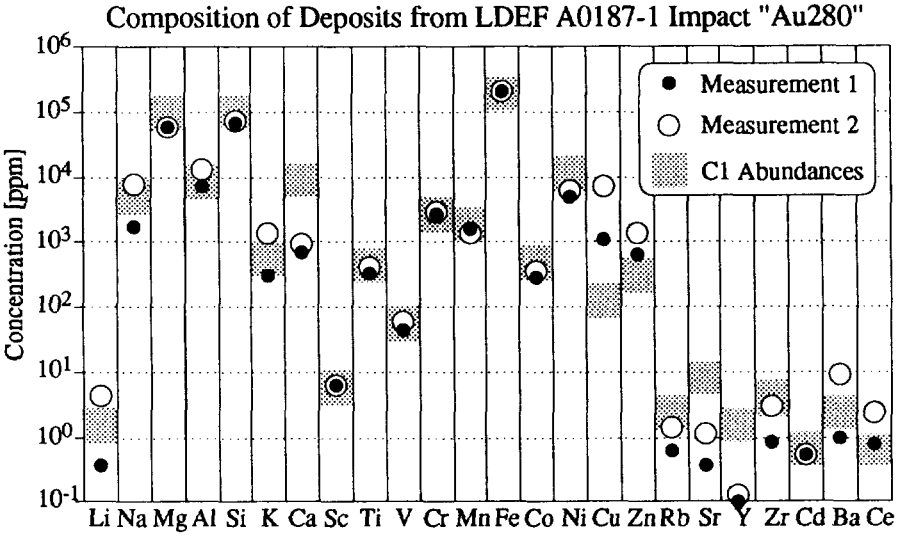

Figure 8: Elemental abundances of two fragments normalized to a chondritic Si value and compared to C1-abundances.

ISOTOPIC MEASUREMENTS IN IMPACTS FROM AO187-1 AND AO187-2

We were also able to perform the first isotopic measurements of impact debris on LDEF. Isotopic analysis of LDEF impacts was one of the original objectives of experiment AO187-2. The isotopic composition of projectile material is of special interest since natural particles (micrometeoroids) are found to have isotopic compositions that sometimes are very different from normal, terrestrial values (refs. 6, 7). If similar anomalies could be found in impact debris that would be one more piece of evidence for an extraterrestrial origin of the projectile material. Moreover, the LDEF impacts represent a different, and possibly isotopically distinct, sampling of the total infall of extraterrestrial material than do micrometeorites recovered in the stratosphere. The results of the isotopic measurements are given here in the δ-notation, which denotes the deviation of the measured isotopic ratio from the normal ratio (*i.e.*, the ratio of a terrestrial standard) in permil (‰). Example: If a measured $^{15}N/^{14}N$ ratio were 5% higher than normal, the corresponding δ-value would be $\delta^{15}N = 50‰$. *Small* variations of the isotopic compositions can also be observed in terrestrial material. Therefore all results have to be compared to the maximum observed range of isotopic compositions in terrestrial material and only an object with isotopic compositions clearly outside of that range can unequivocally be classified as extraterrestrial. On the other hand, a normal isotopic composition does not necessarily imply a terrestrial origin.

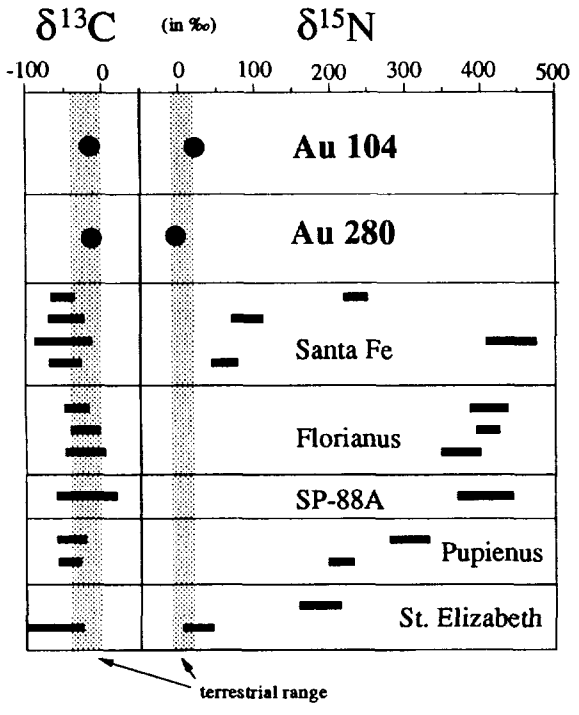

Figure 9: Average C and N isotopic compositions of impact residue from "Au104" and "Au280" and values of IDPs for comparison.

From the Au-foils from LDEF experiment AO187-1 we selected impacts Au104 and Au280 because both have large amounts of apparent projectile residues and both had been classified as "natural" according to the EDX analyses. As shown above, this classification was confirmed by the SIMS measurements of major and trace elements.

In Figure 9 the C and N isotopic compositions of impact residues are compared to the values measured in interplanetary dust particles (IDPs) collected in the stratosphere (ref. 7) and to the range of ratios found in terrestrial samples. Although both projectiles are clearly of natural origin their C and N isotopic compositions are close to normal. This is not very surprising since only one third of all analyzed IDPs show isotopic anomalies in N and none show anomalies in C. The particle "Santa Fe" which is shown for reference has the largest N anomaly among all measured particles of that kind.

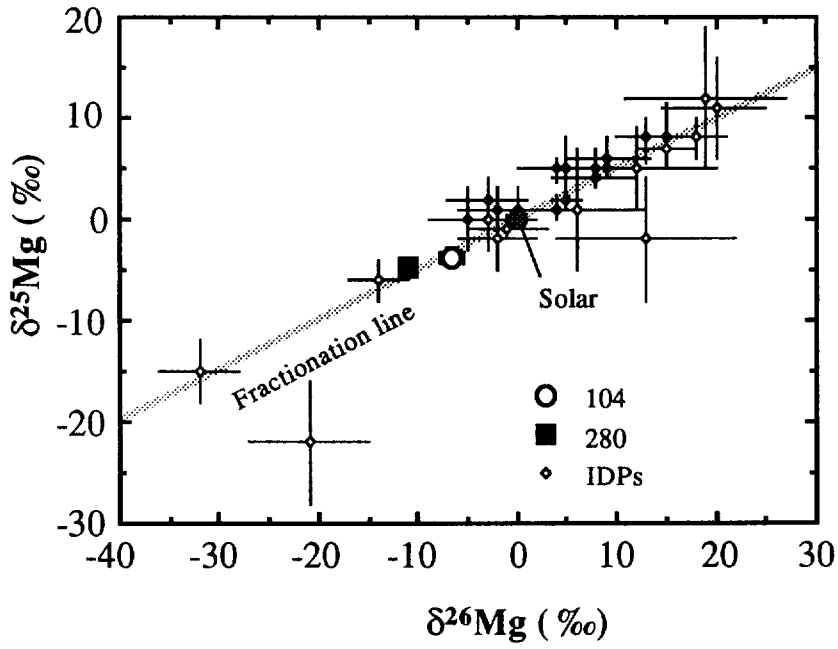

Figure 10: Three-isotope-plot of the Mg isotopic compositions of impact deposits from two AO187-1 impacts and those of Interplanetary Dust Particles (IDPs). The errors shown are 1σ.

Figures 10 and 11 show the Mg and Si isotopic compositions of impact debris from AO187-1 impacts "Au104" and "Au280" in three-isotope-plots. The isotopic compositions of elements with 3 stable isotopes are usually displayed in this way. The $\delta^{25}Mg$ and the $\delta^{26}Mg$ values refer to the $^{25}Mg/^{24}Mg$ ratio and the $^{26}Mg/^{24}Mg$ ratio, respectively ($^{29}Si/^{28}Si$ and $^{30}Si/^{28}Si$ for silicon). The normal isotopic compositions are denoted "Solar" in the diagrams. Small linear mass-dependent isotopic fractionations –which occur frequently, even in the terrestrial environment– would lead to isotopic compositions that are shifted from the "Solar" composition along a slope-$^1/_2$-line in a three-isotope-plot. This line is denoted "Fractionation line" in the diagrams. Any isotopic composition that differs only little from the "Solar" composition and that plots on that line is considered terrestrial while composition that are clearly off that line are indicative of an extraterrestrial origin. As can be seen, the measured impact debris has isotopic compositions of Si and Mg that are essentially terrestrial. The degree of Mg fractionation is also much smaller than the range observed in IDPs collected in the stratosphere, whose compositions are shown for comparison.

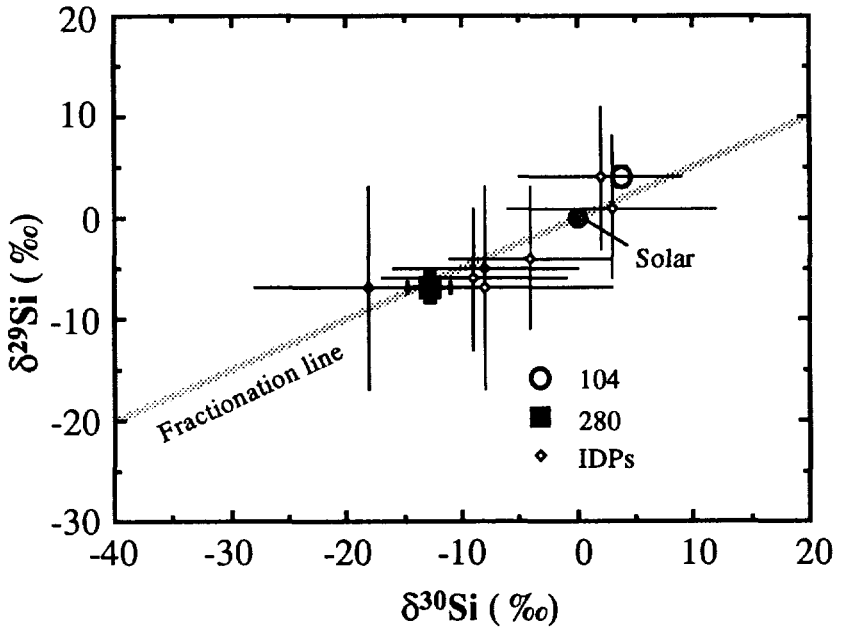

Figure 11: Three-isotope-plot of the Si isotopic compositions of impact deposit and those of Interplanetary Dust Particles (IDPs). The errors shown are 1σ.

Unfortunately, the isotopic analysis of projectile material in extended impacts on germanium plates from experiment AO187-2 is extremely difficult. The reason is the thinness of the impact deposits. An exception is impact C02-2-17C-1, where several solid fragments were found on the rim of the impact feature. The results of the Mg and Si isotopic analysis of these fragments are shown in Figures 12, 13, and Table 1. The isotopic compositions of the fragments plot close to the terrestrial values. Here too, the measured isotopic compositions do not have an identifiably extraterrestrial signature.

	δ^{25}Mg (‰)	δ^{26}Mg (‰)	δ^{29}Si (‰)	δ^{30}Si (‰)
Fragment a	30 ± 13	17 ± 9	-2 ± 14	6 ± 21
Fragment b	13 ± 12	13 ± 9	-6 ± 13	14 ± 17
Fragment c	-2 ± 10	-10 ± 10	-14 ± 13	-16 ± 16
Fragment d	-1 ± 7	28 ± 10	9 ± 12	-11 ± 12
Fragment e	10 ± 11	-7 ± 12	-8 ± 14	27 ± 17
Fragment f	-24 ± 8	-6 ± 8	3 ± 10	7 ± 9

Table 1. Results of the Mg and Si isotopic measurements of individual fragments on the rim of impact C02-2-17C-1. The errors are 1σ.

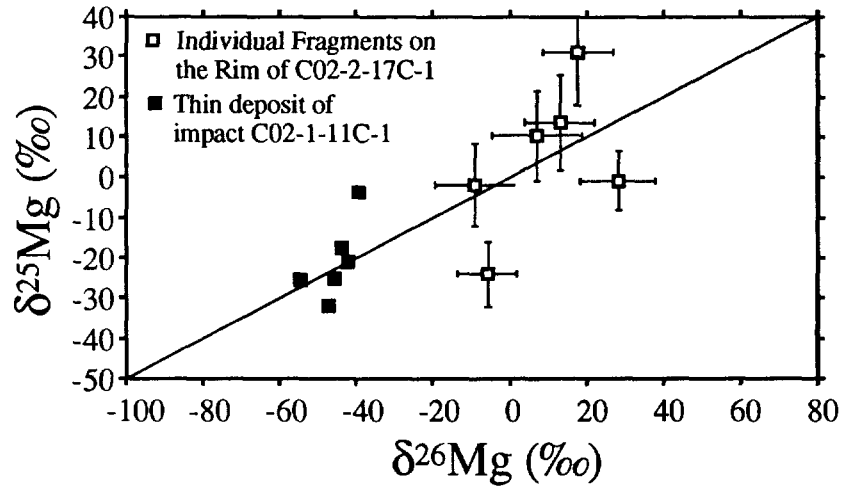

Figure 12. Three-isotope-plot of the results of the Mg isotopic measurements of fragments on the rim of impact C02-2-17C-1 and of deposits in the extended impact C02-1-14C-2. The errors shown are 1σ and the diagonal line is the Terrestrial Fractionation Line.

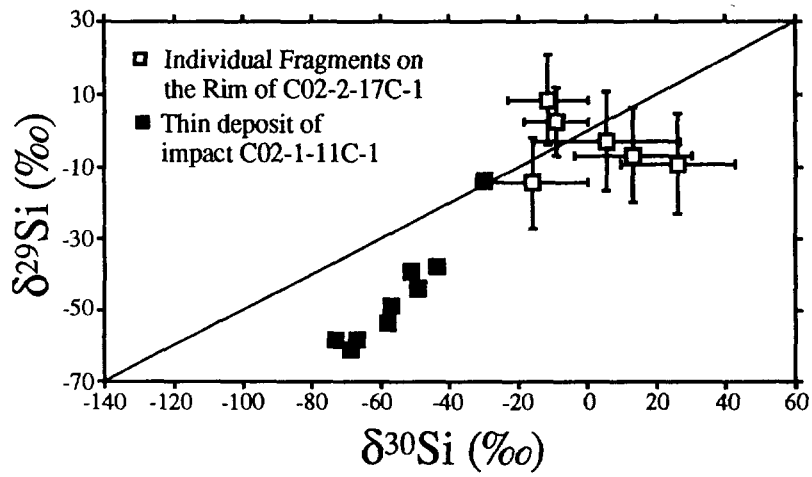

Figure 13. Three-isotope-plot of the results of the Si isotopic measurements of fragments on the rim of impact C02-2-17C-1 and of deposits in the extended impact C02-1-14C-2. The errors shown are 1σ and the diagonal line is the Terrestrial Fractionation Line.

Impact C02-2-17C-1 was the only case of an extended impact from experiment AO187-2 in which we found projectile fragments that had apparently survived the impact. In contrast to the isotopic analyses of these fragments are the analyses of a thin debris layer from impact C02-1-14C-2 (Figures 12 and 13). Here both the Mg and Si isotopic data show large negative (shifts to the lower left, *i.e.* toward more negative δ-values) mass fractionation effects; in addition, the Si data show substantial deviations from the terrestrial mass fractionation line.

A more detailed analysis of these data revealed that these large fractionations and the deviations from the fractionation line are not genuine isotopic effects in the measured material but are artifacts resulting from the small thickness of the impact deposits. Because the layer of deposited projectile is sputtered away during SIMS analysis, the secondary ion signal from a thin layer is not constant but decreases rapidly as a function of time. Since the isotopes of Mg and Si are measured in sequence, the non-linear nature of this decrease can produce the effects shown by the C02-1-14C-2 data. High throughput (large magnet), multiple collector SIMS instruments capable of accurate isotopic measurements are currently being developed for the study of extraterrestrial materials (K. McKeegan, UCLA, private communication). Such instruments may have the required sensitivity and measurement capabilities to permit isotopic measurements of very thin impact deposits.

The extended impacts of LDEF experiment A0187-2 that have already been partially studied by existing SIMS techniques *represent an extremely important scientific resource for future work.* In particular, some of these impacts may make it possible to measure the isotopic composition of cometary material. Dust particles from long-period comets encounter the earth with very high velocities and are thus preferentially destroyed relative to slower, asteroidal particles during atmospheric entry (ref. 8). Cometary particles may thus be grossly under-represented in the stratospheric micrometeoroid collections. In contrast, high velocity particles produce extended impacts with high efficiency and should thus be well represented in the existing collection of capture cell impacts.

Because of their potential scientific importance, continued care should be taken to store the relevant surfaces of experiment AO187-2 under clean conditions so they may be properly analyzed by future, improved analytical instruments.

REFERENCES

1. Amari S., Foote J., Simon C., Swan P., Walker R.M., Zinner E., Jessberger E.K., Lange G., and Stadermann F.J.: SIMS chemical analysis of extended impact features from the trailing edge portion of experiment A0187-2. Proceedings of First LDEF Post-Retrieval Symposium, NASA CP 3134, 503-516, 1991.

2. Amari S., Foote J., Swan P., Walker R.M., Zinner E., and Lange G.: SIMS chemical analysis of extended impacts on the leading and trailing edges of LDEF experiment A0187-2. Proceedings of Second LDEF Post-Retrieval Symposium, NASA CP 3194, 513-528, 1993.

3. Bernhard R.P., See T.H., and Hörz F.: Projectile composition and modal frequencies on the "Chemistry of Micrometeoroids" LDEF experiment. Proceedings of Second LDEF Post-Retrieval Symposium, NASA CP 3194, 551-573, 1993.

4. Anders E. and Grevesse N.: Abundances of the elements: Meteoritic and solar. Geochimica et Cosmochimica Acta, 53, 197-214, 1989.

5. Stadermann F. J.: Rare earth and trace element abundances in individual IDPs. Lunar and Planetary Science, XXII, 1311-1312, 1991.

6. McKeegan K. D.: Ion microprobe measurements of H, C, O, Mg, and Si isotopic abundances in individual interplanetary dust particles. Ph. D. Thesis, Washington University, St. Louis, 187 pp, 1987.

7. Stadermann F. J., Walker R. M., and Zinner E.: Ion microprobe measurements of nitrogen and carbon isotopic variations in individual IDPs. Meteoritics, 24, 327, 1989.

8. Flynn G. J.: Atmospheric entry heating: a criterion to distinguish between asteroidal and cometary sources of interplanetary dust. Icarus 77, 287-310, 1989.

IMAGE AND COMPOSITIONAL CHARACTERISTICS OF THE LDEF "BIG GUY" IMPACT CRATER

T. E. Bunch
NASA Ames Research Center
Moffett Field, CA 94035-1000
Phone: 415/604-5909, Fax: 415/604-6779

Julie M. Paque
SETI Institute
2035 Landings Drive
Mountain View, CA 94043

Michael Zolensky
NASA Johnson Space Center
Houston, TX 77058

ABSTRACT

A 5.2 mm crater in Al-metal represents the largest found on LDEF. We have examined this crater by field emission scanning electron microscopy (FESEM), energy dispersive spectroscopy (EDS) and time-of-flight/secondary ion mass spectroscopy (TOF-SIMS) in order to determine if there is any evidence of impactor residue. Droplet and dome-shaped columns, along with flow features, are evidence of melting. EDS from the crater cavity and rim show Mg, C, O and variable amounts of Si, in addition to Al. No evidence for a chondritic impactor was found, and it is hypothesized that the crater may be the result of impact with space debris.

INTRODUCTION

The largest crater on LDEF measures 5.2 mm in diameter and has a depth to diameter ratio of 0.5. The "Big Guy" crater was located on tray H03; experiment M0001, J. Adams, Principal Investigator. Although the experiment faced out into space, this particular impact occurred on an Al metal Z-frame, which projected in the ram direction (see photographs in ref. 1, p. 410-411). In addition, the impactor penetrated eight layers of lexan before encountering the Al surface. Our objective in examining this crater was to determine the nature and origin of the impactor. The crater was examined carefully for impactor residue or other evidence of the impactor's origin.

METHODOLOGY

The crater was first observed by a stereo microscope, then by field emission scanning electron microscopy (FESEM). Samples were then analyzed for impactor residue by energy dispersive spectroscopy (EDS) equipped with a light element detector, followed by cursory examination by time-of-flight/secondary ion mass spectroscopy (TOF-SIMS; see ref. 2 for instrumental technique).

The Hitachi FESEM is equipped with a light element detector, allowing for the analysis of boron, carbon, nitrogen, and oxygen by energy dispersive spectroscopy (EDS). However, this analysis can be complicated by contamination, which can be very significant if steps are not taken to minimize the effects. The contamination can arise from several sources including sample handling, preparation and contaminants in the electron column. Organic contaminants on the surface will result in polymerization around the electron beam if it is focussed, due to the heat generated in a small area and the electrostatic attraction of the beam. This effect is minimized both by careful handling and by rastering the beam over a several square micron area during analyses.

RESULTS

An FESEM image of the crater is shown in Fig. 1. A small amount of melt is visible in the crater bottom with more melt on the upper wall near the rim. In general, the melt liner appears to be quite thin. No intact projectile or dark patches on the rim were found. The only prominent melt-forms are droplet to dome-shaped columns (see Fig. 2). These objects on the rim appear to be darkened on their top surfaces when viewed through the stereo microscope, although this could also be an artifact due to illumination

under the microscope. Figure 3a shows an example of the unusual domed objects, with the horizontal layering effect. Figure 3b is an example of a melt form that appears to have collapsed before it completely froze.

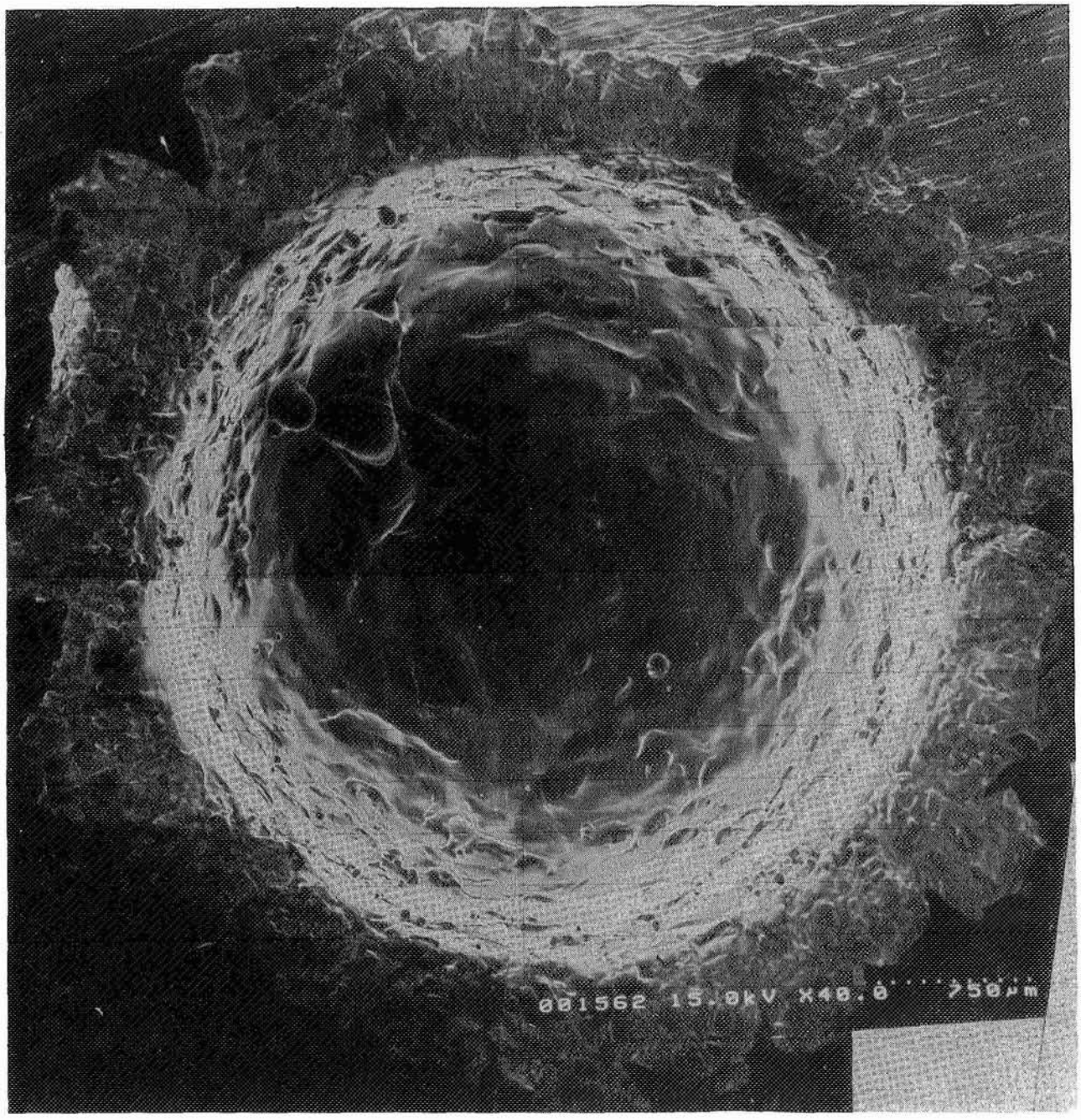

Figure 1. FESEM imagery mosaic of the Big Guy crater.

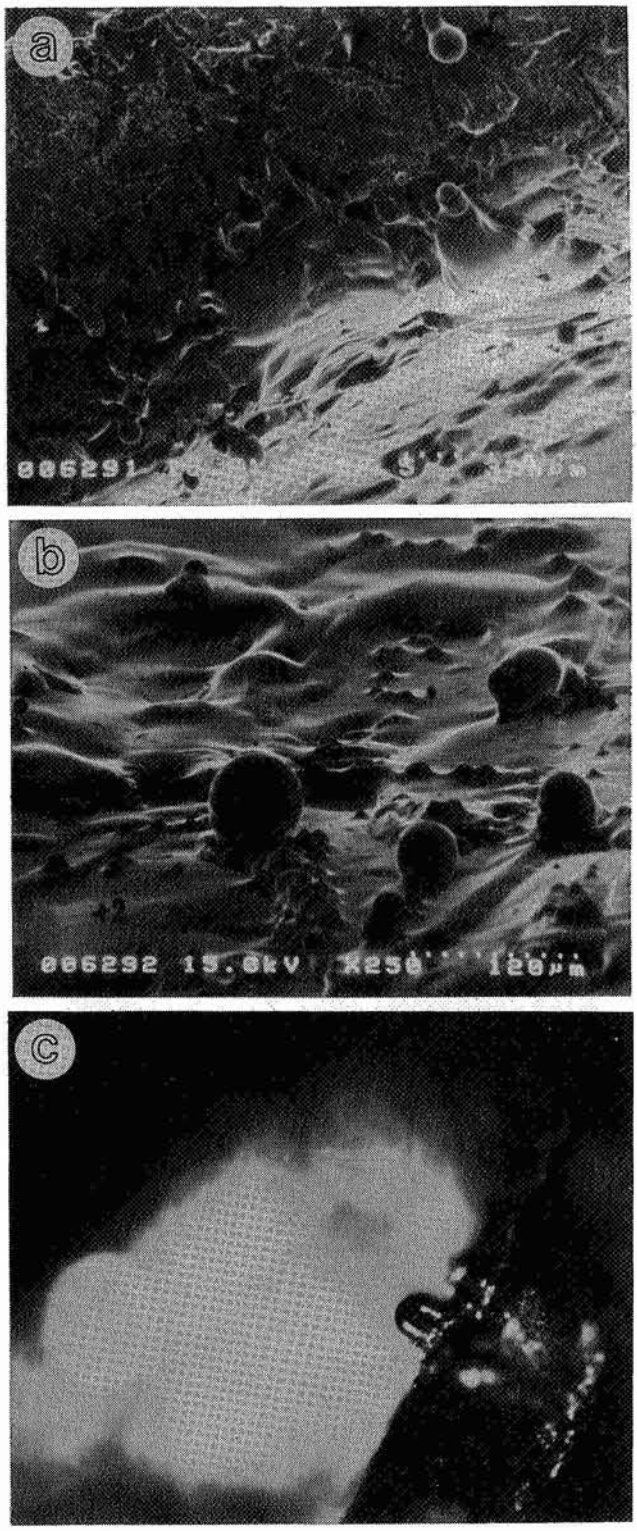

FESEM-EDS analyses of the crater cavity and rim show the presence of Si, Mg, C, and O. The amounts of Si, in particular, vary considerably, depending on the location of the analysis. The top of droplets and dome-shaped columns have the highest amounts of Si, melt liners intermediate amounts and unmelted areas on the rim, the lowest (Fig. 4). The rim analysis also corresponds to an analysis of a point away from the crater that was covered with lexan before it was removed for the crater study. A piece of the frame underside was polished and analyzed by a Cameca electron microprobe. This analysis, and an additional analysis away from the crater in the vicinity of the EDS analysis, show the average Si content to be 0.34 wt % (range, 0.23 to 0.39) and Mg content is 0.94 (range, 0.83 to 1.02). Thus, the EDS spectrum of the point away from the crater is taken to be the background reference composition of uncratered Al. By comparing analyses of melt forms, Si shows an increased content of at least 3-fold or ≈ 1.0 wt %; Mg shows no significant change. The presence of C, intrinsic to the crater, is confirmed by EDS analyses, although some unknown amount is attributed to contamination during analysis. TOF-SIMS analyses indicate, in addition to Si, Mg, C, O, the presence of S, Cl and Na, which are known contaminants of LDEF surfaces.

Figure 2. FESEM images. (a) Top side of rim with a bulb-shaped melt form (arrow) with a broken stem. Lower portion of image looks down into the crater cavity. Note melt liner on the wall surface, but not the rim. (b) Droplet forms on the lower part of wall. Numbers refer to analyzed spots. (c) Domed column atop crater rim (sample tilted 45° for lighting purposes). Stereo photograph; column diameter = 0.08 mm.

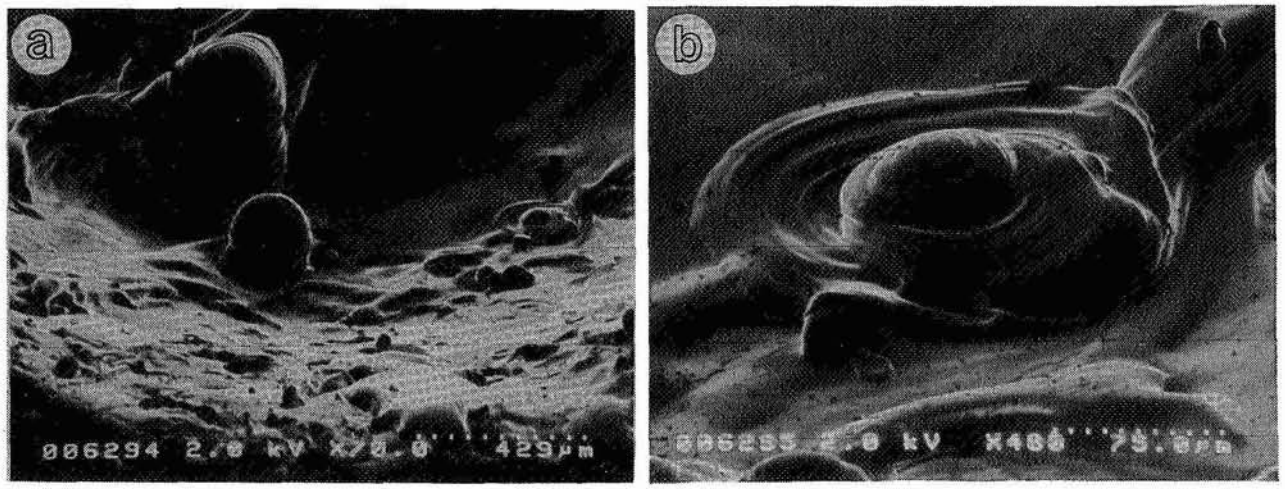

Figure 3. FESEM images. (a) Open arrow points to domed object with prominent rings/layers. Solid arrow indicates a melt droplet that collapsed into a "puddle" before solidifying. (b) Enlarged view of collapsed droplet.

DISCUSSION

Analyses of the crater show no chondritic compositional evidence (Si, Mg, Al, Ca, Fe, S,± Ni) for an extraterrestrial impactor. Silicon and Mg contents are attributed to the intrinsic minor element composition of the 6061 T6 Al plate. Silicon is enriched in the melt liner and melt forms relative to Al away from the crater. The mechanism for increasing Si content in the Al is unknown. Either an enrichment of intrinsic Si occurred during impact melting by some fractionation process or Si was added by an unknown orbital debris impactor. Carbon content is most likely a contaminant that resulted from vaporization of the overlying lexan during impact.

Silicon is added to Al to form a harder, somewhat less ductile alloy; enhanced Si content also increases the viscosity of molten Al (ref. 3). The peculiar layered textures of the melt forms may have resulted from differential cooling rates between the higher viscosity melt surface, which we find to be enriched in Si, and the underlying portions that may be less viscous. These textures may also have arisen, in part, from spiral dislocation arrays promoted by non-equilibrium and rapid cooling conditions. We conclude that compositional heterogeneities together with extremely rapid cooling (the crater forming event was very fast, on the order of 10 μsec; ref. 4) probably gave rise to the unusual forms and textures observed in the Big Guy crater.

It is disappointing to note that the largest crater on LDEF was probably formed by collision with a piece of space junk. Dale Atkinson (pers. comm., 1993) analyzed the orientation of the crater on LDEF and concluded from orbital considerations that the impactor debris could have come from a Vandenburg Air Force Base launch.

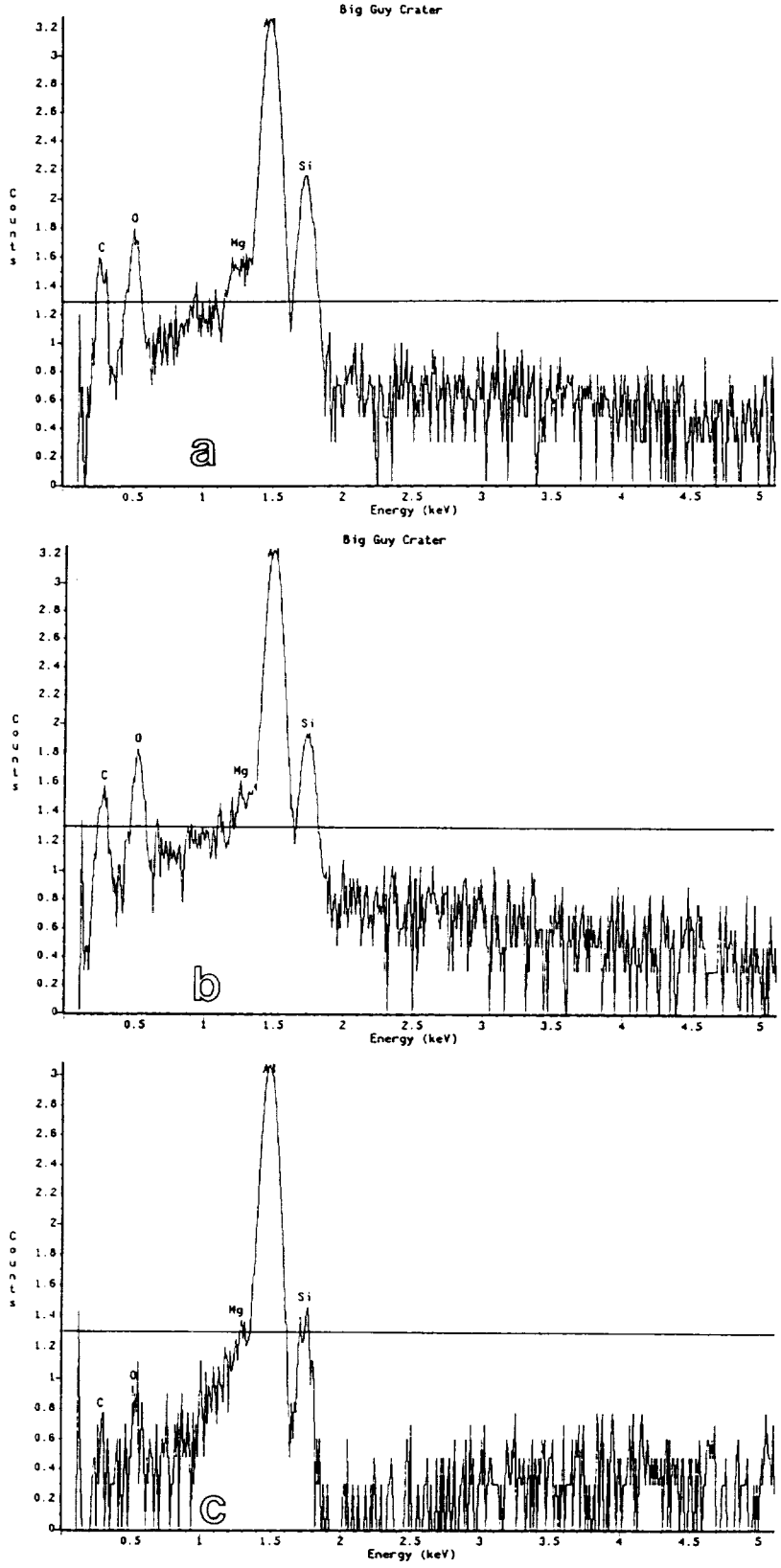

Figure 4. EDS analyses of droplet top (a), domed columns (b), and melt liner (c). Horizontal line in each indicates intrinsic Si content of Al alloy. The y-axis (counts) uses a logarithmic scale to allow examination of minor elements in the presence of Al.

ACKNOWLEDGEMENTS

We thank Jim Adams for the loan of the Big Guy crater and J. Erlichman for technical assistance.

REFERENCES

1. Adams, J.: *Meteoroid and Debris Impact Features Documented on the Long Duration Exposure Facility: A Preliminary Report.* NASA - Johnson Space Center Publ. # **24608**, pp 583, 1990.

2. Bunch, T. E.; Becker, L.; Bada, J.; Macklin, J.; Radicati di Brozolo, F.; Fleming, R. H and Erlichman, J.: Hypervelocity impact survivability experiments for carbonaceous impactors. *Second LDEF Sym. NASA* **CP-3194**, 453-477, 1993.

3. Cottrell, A. H.: *The Mechanical Properties of Matter.* John Wiley and Sons, New York, pp 430, 1964.

4. Hörz, F.; Fechtig, H. and Janicke, J: Morphology and chemistry of projectile residues in small experimental craters. *Proc. 14th LPSC, J. Geophy. Res.* **88**, B353-363, 1983.

THE EFFECT OF IMPACT ANGLE ON CRATERS FORMED BY HYPERVELOCITY PARTICLES

David C. Hill, M. Frank Rose, Steve R. Best, Michael S. Crumpler
Space Power Institute, 231 Leach Center
Auburn University, AL 36849
Phone (205) 844 5894; Fax (205) 844 5910

Gary D. Crawford & Ralph H-C. Zee
Department of Mechanical Engineering, 201 Ross Hall
Auburn University, AL 36849
Phone (205) 844 3320; Fax (205) 844 2672

Michael J. Bozack
Department of Physics, Allison Laboratory
Auburn University, AL 36849
Phone (205) 844 4264; Fax (205) 844 4613

SUMMARY

The Space Power Institute (SPI) at Auburn University has conducted experiments on the effects of impact angle on crater morphology and impactor residue retention for hypervelocity impacts. Copper target plates were set at angles of 30°, 45°, 60°, and 75° from the particle flight path. For the 30° and 45° impacts, in the velocity regime greater than 8 $km.s^{-1}$ the resultant craters are almost identical to normal incidence impacts. The only difference found was in the apparent distribution of particle residue within the crater, and further research is needed to verify this. The 60° and 75° impacts showed marked differences in crater symmetry, crater lip shape, and particle residue distribution in the same velocity regime. Impactor residue shock fractionation effects have been quantified to first-order. It is concluded that a combination of analysis techniques can yield further information on impact velocity, direction, and angle of incidence.

1 INTRODUCTION

Retrieval of LDEF, EURECA, and parts of Solar Max, from low Earth orbit (LEO) has allowed researchers to learn much about the space environment and its effects on spacecraft materials and structures. Within two years of the retrieval of LDEF, personnel of the Meteoroid & Debris Special Investigation Group (M&DSIG) had identified more than 34,000 features attributable to meteoroid and debris impacts. While it is unlikely, due to the low flux rates at higher masses, that the meteoroids or debris typically encountered by LDEF during its 5.75 year exposure could have caused catastrophic structural damage to a spacecraft, nevertheless, they may cause extensive damage to opti-

cal surfaces, solar cells, protective, anti-reflection and thermal control coatings, and other more delicate components or surfaces. Of extreme importance, currently, is the refinement of meteoroid and space debris environmental models in terms of particle masses, compositions, impact velocities, and directionality. This will allow better predictive capability and reliability in design optimization for spacecraft systems engineers.

A significant number of the impact sites identified to date by various researchers are on non-experimental and/or quasi-infinite flat surfaces. The implication of this is that impact angle of incidence (measured with respect to the surface normal) and azimuth (measured in the plane of the target surface) can only be deduced from the morphology of the resultant impact site. Several researchers (Paul, 1993; Mackay *et al.*, 1993; Newman *et al.*, 1992) have emphasized the need to determine incidence and azimuth angles (where possible) for transformation into impact vectors in the LDEF body reference frame so that limits on the impactor orbital parameters can be placed. Additionally, the application of impactor residue chemical analysis, utilizing energy dispersive X-ray spectrometry (EDXS) and/or secondary ion mass spectrometry (SIMS), has been demonstrated to be useful in deducing the relative flux rates of debris and meteoroid particles by numerous authors (Berthoud *et al.*, 1993; Hörz *et al.*, 1993; Simon *et al.*, 1992).

The qualitative effects of impact angle on the cratering process have been elaborated by many researchers (Summers & Charters, 1958; Summers, 1959; Kineke, 1960; Bruce, 1961; Gehring & Lieblein, 1963; Nysmith & Summers, 1962). More recent investigations in the LDEF context were conducted by Newman *et al.* (1992), who provided a basis for the derivation of directional information from analysis of "elliptical" impact craters. In general, the crater which is formed by a normal or near-normal incidence hypervelocity impactor is roughly hemispherical (figure 1). Deviations from this originate in the relationship between impact velocity, impactor/target materials combination, and angle of incidence. For example, if the normal component of velocity for an oblique impact is sufficiently high the resultant crater remains hemispherical. As the normal component of velocity decreases with increasing obliquity, the crater geometry formed departs from that characteristic of normal incidence, exhibiting a hybrid circular-elliptic "footprint" at the target surface and an asymmetric circular-elliptic profile along the impact axis (figure 2).

This paper describes a series of experiments to begin the quantification of oblique impact phenomena. Since there is little previous work on impact obliquity at impact velocities greater than 8 $km.s^{-1}$, it was decided to investigate the 7-13.5 $km.s^{-1}$ impact velocity regime using 20-100μm diameter impactors. In the context of LDEF impact sites, where impact angle and azimuth are unknown, the question arises; *"is it possible to place bounds on impact angle and velocity from a combination of crater shape and residue location?"* The resulting objectives of this program are threefold: (i) to reproduce impact sites in the laboratory typical of LDEF impact sites on quasi-infinite metallic surfaces, (ii) to correlate distinctive morphological aspects of crater structure with impact velocity and angle of incidence, and (iii) to locate and analyze the amount and structure of particle residues as functions of impact velocity and angle.

Observations of crater morphology as a function of angle of incidence and impact velocity were made. EDXS techniques were employed to determine the location and abundance of residues, leading to the suggestion that crater interior residue location is

also useful in extracting information about impact angle of incidence and azimuth, particularly in the case of craters showing near-circular footprints or no cross-sectional asymmetry along the direction of impact.

2 EXPERIMENTS

The Hypervelocity Impact Facility (HIF), a plasma-drag accelerator, at SPI was used for these experiments. Rose *et al.* (1992) provide a description of the HIF system and its performance capabilities. Two pre-cursor test shots were executed, the first shot with the target plate surface normal set at an angle of 30° to the particle flight path, and the second set at 60°. Under this protocol a "0° impact" is at normal incidence whilst a "90° impact" is at grazing incidence.

Olivine particles (75 μm nominal diameter), having the chemical composition $(Mg:Fe)_2SiO_4$ and a Mg:Fe:Si ratio of ~19:1:10, were launched at copper targets. Olivine, although higher in density than that usually accepted for meteoroids (ρ = 0.5-1.5 $g.cm^{-3}$), was chosen as the best meteoroid simulant material that can be accelerated in the HIF system. Note that the mass density of olivine is 3.21 $g.cm^{-3}$ and that of copper is 8.92 $g.cm^{-3}$, resulting in a mass density ratio of ~0.36. This figure corresponds to that for low density (ρ ~ 1 $g.cm^{-3}$) meteoroids impacting aluminum (ρ ~2.7 $g.cm^{-3}$) targets. It should be remembered that the density ratio scaling between different materials combinations is a first order approximation only. Peak impact pressure, post-shock mass velocity, and shock velocity all play rôles that will lead to deviations from density ratio scaling at second order level.

A thin Mylar® film (thickness 0.5 μm) was placed in front of the target plates, such that it was always normal to the particle flight path. The hypervelocity particles pass through the film before striking the plate, allowing the particle size to be found (Carey *et al.*, 1984; Rose *et al.*, 1992). The film also minimizes gun debris contamination of the target surface.

Impact velocity is determined by observing the impact-induced plasma flash with an image converter camera (Hadland Photonics IMACON 790), operating in streak mode. The camera is aligned such that its optical axis is parallel to, and displaced approximately 0.1 mm from, the target surface. Its field-of-view is constrained to a width of ~0.5 mm by an entrance slit, whose image is "streaked" across the film plane at a known rate.

By means of a mirror inclined at 45° with respect to the optical axis both the X- and Y-location of the impact flash may be determined since the optical system produces two images of the flash, vertically displaced positively (X) and negatively (Y). The horizontal position of the twin flash events on the film uniquely determines the impact velocity. Modulated LEDs are placed at the corners of target area to allow easy determination of the X-Y co-ordinates and to facilitate the measurement of the time of impact. Rose *et al.* (1992) describe the diagnostics in detail with schematic diagrams.

Four experimental hypervelocity impact shots were executed, from which resulted in excess of 200 impact sites, identified using an optical scanning system. The minimum

identifiable site diameter was ~5 μm. The X-Y locations of all the sites were logged for subsequent correlation with streak record data. Shot D76 (normal incidence) was conducted to confirm gun performance and to determine the typical morphological structures that could be expected for olivine-copper impacts.

For the purposes of this paper, we selected thirteen impact sites from the four shots for detailed analysis. These, listed below in table 1, are representative of the numerous impact sites observed. Olivine residue was present in all of the selected craters, implying that residue retention can be expected at normal components of impact velocity up to 12 $km.s^{-1}$ for the materials combination used in this set of experiments, and also for meteoroids striking aluminum targets if density ratio scaling is assumed to hold. Preliminary modeling of the flux dynamics of flat plates exposed to an *isotropic* meteoroid flux distribution (with the Erickson velocity distribution) indicates that at least 12% of meteoroid craters on the RAM (East) surface should retain residue at levels detectable using EDXS, while at least 65% of WAKE (West) surface craters should retain similar residue. These numbers should be regarded as order of magnitude computations at present.

Site #	**Angle** [deg]	**Velocity** [$km.s^{-1}$]	**Residue Appearance**
D76-01-17	0	2.9	white, granular, crystalline
D76-01-16	0	4.8	white, granular, crystalline
D76-03-10	0	3.0	white, granular, crystalline
D76-03-13	0	9.9	transparent, glassy
D76-05-04	0	8.0	white, granular, crystalline
D76-05-05	0	9.6	transparent, glassy
D76-05-26	0	12.0	transparent, glassy
D76-05-32	0	12.0	transparent, glassy
D80-05-123	45	10.5	transparent, glassy
D78-05-23	60	8.5	white, granular, crystalline
D78-03-17	60	10.5	transparent, glassy
D79-01-02	75	5.7	white, granular, crystalline
D79-03-04	75	12.5	white, granular, crystalline

Table 1. *Sites selected for detailed SEM and EDXS analysis.*

The normal incidence shot (D76) also provided a baseline for analyzing the residue structure within the craters. Two residue types manifested themselves in this set of craters: white, granular, crystalline; and transparent, smooth, glassy (amorphous). These morphologies are impact velocity dependent, the granular structures being evidence of lower shock intensity while the glassy residue results from shock-induced melting and re-solidification processes. Further discussion of the residue structures and relative elemental compositions follows in sections 3 and 4 below.

3 CRATER MORPHOLOGIES

3.1 Pre-cursor Test Shots

For the analysis of both the 30° and 60° pre-cursor test shot impact sites, a JEOL 840 scanning electron microscope (SEM) with an EDXS sub-system was used. Figure 3 shows a typical crater caused by an olivine particle. The particle velocity was 7.0±0.05 $km.s^{-1}$ and the crater shape is fairly typical of all the craters analyzed. The crater is practically indistinguishable from normal incidence impacts, exhibiting a circular "footprint" and a roughly hemispherical profile with a depth-to-diameter ratio (p/D) of 0.43. The circumferential lip has no characteristics which hint at the direction of tilt of the target plate. The arrow at the bottom left-hand corner of the photomicrograph shows the direction of the component of the impact velocity vector in the plane of the target.

The entire interior of the crater is covered with olivine residue, and the granules inside the crater are "chunks" of olivine. Upon closer qualitative inspection, more olivine residue was located on the trailing interior surface of the crater than on the leading interior surface. This phenomenon was found in all of the olivine craters analyzed.

There is a marked difference between the 60° impacts and the 30° impacts. The main characteristics, shown in figure 2, were as follows: firstly, there is a minimal lip on the crater leading edge whereas an extensive lip was found on the trailing edge; secondly, significantly more particle residue was found on the trailing interior surface; and thirdly, the crater rims were "elliptical" rather than circular in shape.

Figure 4 shows a typical 60° angle of incidence impact crater, formed by an olivine particle traveling at 5.6 $km.s^{-1}$. Note how the crater lip becomes progressively smaller as the leading edge is approached, until it is practically non-existent at the apex of the leading edge. This crater has a coating of olivine throughout the crater interior surface, and a few grains of olivine are also evident. The p/D ratio along the minor axis is 0.30, and is 0.18 along the major axis, with a crater depth of 14 μm. There are more olivine grains located on the trailing interior surface than on the leading surface.

Another very interesting phenomenon seen on some of the 60° impact sites is the presence of small "indentations," some containing small amounts of olivine residue, downrange of the trailing edge crater lip. Clearly, the angle of incidence is such that some material from the top of the impactor has decoupled from the main body of the impactor during the impact and followed a trajectory that passes over the top of the trailing edge crater lip (in process of forming) before striking the target surface downrange of that lip.

Figure 5 shows a 60° impact crater formed by a particle traveling at 4.7 $km.s^{-1}$. It has the same lip asymmetry and residue distribution as the crater shown in figure 4, although its rim is more circular than elliptical. The crater is 43 μm deep at its deepest penetration point, with a minor axis p/D ratio of 0.28. Note that the p/D ratio for olivine particles striking a copper plate for normal incidence impact is between 0.50 and 0.38 in the velocity regime studied, *i.e.* ~3 - 12.5 $km.s^{-1}$.

3.2 Main Experimental Shots

For the purposes of this paper, we selected two representative normal incidence impact sites for more extensive morphological analysis. Site D76-01-17 (figure 6) is a 184±3μm diameter crater, with a circular footprint and raised circumferential lips, exhibiting a p/D ratio of 0.42±0.02, computed from a measured depth of 77±3μm. The impact velocity was 2.9±0.05 km.s^{-1}. Coating the interior of this crater was a whitish-green (when viewed optically) granular residue. Conversely, the lips of this crater were coated with a smooth, glassy residue, typical of that found in the interiors of the impact craters produced by faster impactors.

At the other end of the velocity spectrum is site D76-05-26 (figure 7), produced by an olivine fragment traveling at 12.0±0.05 km.s^{-1}. Again, the circular footprint and raised circumferential lips of a hypervelocity impact are evident. The p/D ratio was computed to be 0.47±0.08 from a crater diameter (D) of 38±2μm and a depth of 18±2μm. The interior of this crater was coated with a smooth, glassy residue, transparent when viewed optically.

The normal incidence crater set was characterized by a division into predominantly granular residues and predominantly glassy residues occurring at an impact velocity of between 8.0 km.s^{-1} and 9.6 km.s^{-1}, which corresponds to a shock pressure of between 185 GPa and 240 GPa, using a computational scheme similar to that used by Ang (1990). The implications of this, for site D76-01-17, is that the impactor residue in the crater interior, in granular form, has undergone a significantly less intense shock metamorphosis than that deposited on the crater lips. It is not clear from the data available from this analysis at what shock pressure threshold the transition from crystalline to amorphous residues occurs.

To obtain a preliminary quantitative idea of the effects of impact obliquity on various crater parameters, we selected five oblique impact sites for further detailed analysis. Data pertaining to these craters are tabulated in table 2, below.

Site #	Diameter [μm]	Depth [μm]	p/D	Velocity [km.s^{-1}]	Angle [deg]
D78-03-17	42±2	17±2	0.40±0.07	10.5±0.5	60
D78-05-23	60±2	19±2	0.32±0.04	8.5±0.5	60
D79-03-04	56±2	25±2	0.45±0.05	12.5±0.1	75
D79-01-02	n/d	n/d	n/d	5.7±0.1	75
D80-05-123	63±2	30±2	0.48±0.05	10.5±0.5	45

Table 2. *Crater parameters of sites selected for further EDXS analysis. The depth is measured at the deepest point and the diameter is measured perpendicular to the impact trajectory axis at that point. Note that for site D79-03-04 the depth is at the deepest point of the major crater.*

Figure 8 shows a deep (p/D = 0.40) crater impact site (D78-03-17) with a circular-elliptical surface footprint. The leading edge lips are less pronounced and more irregular than the trailing edge lips. The crater interior is coated with a smooth, glassy (amorphous) olivine residue over most of the interior surface, but with additional granular deposits in the deepest part of the crater and across the leading edge wall. The normal component of impact velocity is 5.3±0.3 km.s^{-1}, the angle of incidence being 60°.

Figure 9 shows a slightly larger, but more shallow (p/D = 0.32) and more elliptical, crater (D78-05-23), produced during the same experimental shot. The normal component of velocity was computed to be 4.3±0.3 km.s^{-1}, which correlates well with that of D78-03-17 where the higher normal component of velocity produced a deeper crater. The impactor residue appears to be smooth and glassy with few granular elements, suggesting that in this impact velocity regime, 8-11 km.s^{-1}, for oblique incidence, the degree of shock processing of impactor material is a probabilistic process, with both types of residue being present in varying (and unpredictable) relative amounts. This regime can be considered as a transition regime for the olivine-copper system in terms of shock processing. At higher normal component velocities the residue should manifest itself as smooth and glassy (amorphous), whereas at lower velocities the residue is whitish-green and granular (crystalline).

Figure 10 shows impact site D80-05-123, a 45° incidence impact with a velocity of 10.5±0.5 km.s^{-1}. The normal component is computed to be 7.4±0.4 km.s^{-1}. In this case, the crater exhibits a p/D ratio of 0.48 and has a near-circular surface footprint, almost indistinguishable from a normal incidence crater. Residue is almost entirely of the smooth and glassy type, although a few granular structures manifest themselves at higher magnifications. The leading edge lip is of similar extent to the trailing edge lip, except for the large petal in the lower left corner. It is possible that there is some correlation between impact direction and this pronounced structure on the trailing edge, but more evidence is necessary for conclusive proof. It should be borne in mind, though, that it is extremely rare for such asymmetry of lip-petal size to occur for normal incidence impacts.

Taking the oblique impact scenario to an extreme case, we executed one shot for 75° angle of incidence. Two impact sites, D79-01-02 and D79-03-04, were selected, the former representative of the lower (5.7 km.s^{-1}) velocity limit and the latter representative of the upper (12.5 km.s^{-1}) limit for this experiment. These are shown in figures 11 and 12, respectively. For the low velocity impact (normal component = 1.5±0.01 km.s^{-1}) the impactor embedded itself progressively as evidenced by the gouge uprange of the major crater, and then fragmented, leaving downrange impactor residue. The interior of the major crater (center of figure 11) contained granular residues similar to that found in the impact sites analyzed above. Both uprange and downrange impact damage areas also contained olivine residue. Although granular residue features were absent from these locations, we are reluctant to classify the residue as smooth and glassy, as for the higher velocity impact sites, since these surfaces are dominated by substrate (copper target) roughness, most likely artifacts from the impact gouging process.

The final site under analysis for this paper is D79-03-04. The normal component of velocity in this case was 3.2±0.01 km.s^{-1}. The photomicrograph reveals a major crater, having the circular-elliptic footprint typical of 30-45° incidence impacts, and significant

downrange impact damage. Similar to the 60° impacts at lower velocities reported above, the major crater has minimal leading edge lips, more pronounced trailing edge lips, and a p/D ratio of 0.45 at the deepest penetration point. Clearly, the top of the impactor has sheared off during the later stages of the impact, due to the shock front interaction with the impactor rear surface, and the respective trajectories of the fragments have taken them over the trailing edge lips to impact the target surface downrange of the main crater. The transverse component of impact velocity (parallel with the impact direction) is 12.1 $km.s^{-1}$, which is obviously sufficient to cause extreme shear stresses in the impactor. Granular residues were observed in the major crater, embedded in a glassy residue. No grains were observed in the downrange damage sites, although the EDXS analysis (see following section) does reveal significant olivine residue.

4 IMPACTOR RESIDUE ANALYSIS

To further understand the effects of impact obliquity and to provide support for the analysis of impact craters recovered from space-exposed quasi-infinite target surfaces, it is necessary to consider the abundance and distribution of impactor residues in the resultant craters. We, therefore, have begun a program of impactor residue analysis using EDXS techniques. Samples on which hypervelocity craters were produced were placed in an SEM (Cambridge StereoScan 200) and the X-ray spectrum, derived from the excited states of the atoms present in the target/residue materials, was measured using an EG&G Ortec System 5000 X-ray spectrum analyzer. Compositional calculations were done using the SEM community-standard AutoZAP II program.

For all analysis runs the accelerating voltage was set at 20 kV, which allowed the substrate (copper) signal to become significant. Elapsed live time was 100.00 seconds and the beam current varied from 0.3 nA to 4.6 nA. In all cases the specimen tilt angle was 45.0 degrees with respect to the X-axis and 0.0 degrees with respect to the Y-axis. Insertion depth was 60.0 mm with a typical working depth of between 15-19 mm.

We present quantitative data (see table 3), corrected for substrate contamination, from which relative abundances of elements can be computed for each of the craters. Careful orientation of the crater with respect to the electron gun axis and the X-ray detector minimizes the geometric effects of deep craters. For normal incidence impacts location (1) is on the crater inner side wall and location (2) is on the crater lip. For oblique impacts (D78 and D80 sites) location (1) is situated on the leading edge inner side wall and location (2) is on the trailing edge inner side wall. For D79 sites, locations (2) and (3) are in the downrange damage areas beyond the main crater trailing edge.

The first trend to consider is that between the location (1) analyses, excluding D80-05-123 which results in significantly anomalous data. Normal component of impact velocity (V_n) correlates directly with residue Mg:Si ratio (figure 13), implying shock-induced fractionation, i.e. the higher the velocity the more silicon is removed from the material matrix. This effect is confirmed by the appearance of the residue, as noted in section 3.2 above, *i.e.* the whitish-green granular residues are the least shock-fractionated (low Mg:Si ratio), whereas the smooth, glassy residues are the most shock-fractionated (high Mg:Si ratio).

Also, residue percentage (RES%), determined by computing the ratio of residue (Mg, Si & Fe) counts to total counts (Mg, Si, Fe & Cu) for location (1) data shows correlation with normal component of velocity (V_n), with the highest velocities producing the lowest residue percentage, *i.e.* the residue layer thickness is apparently reduced for higher velocities (see figure 14). A further consideration of the ratio of location (1) residue percentage to location (2) residue percentage for impact sites D78-03-17 and D80-05-123 indicates that for oblique angles of incidence more residue tends to be found on the trailing interior surface than the leading interior surface for craters with glassy, amorphous residues. The degree of downrange displacement appears to correlate with V_n with higher normal components of impact velocity producing more displacement. Consideration of the residue ratio (0.9±0.2) for site D78-05-23 shows that for sites with the white, granular, crystalline residue there is no apparent displacement of residue in the downrange direction.

SITE #	Mg	Si	Fe	Cu	Mg:Si	RES%	V_n	(2):(1)
D76-05-26(1)	17.6	5.4	1.1	75.9	8.7	21	12.0	n/a
D76-01-17(1)	28.8	11.0	2.0	58.2	3.4	39	2.9	n/a
D76-01-17(2)	18.7	5.4	0.4	75.5	9.2	22	-	-
D78-03-17(1)	23.7	6.9	2.4	67.0	6.1	30	5.3	1.4±0.2
D78-03-17(2)	33.7	10.9	0.9	54.5	4.0	43	-	-
D78-05-23(1)	25.0	7.3	0.9	66.8	5.8	30	4.3	0.9±0.2
D78-05-23(2)	20.1	8.2	1.4	70.3	4.0	27	-	-
D79-03-04(1)	30.1	10.0	1.7	58.2	4.1	39	3.2	n/a
D79-03-04(2)	23.8	8.1	0.9	67.2	4.7	30	-	n/a
D79-03-04(3)	18.5	5.6	0.5	75.4	8.3	21	-	n/a
D79-01-02(1)	39.5	17.1	2.1	41.3	2.6	57	1.5	n/a
D79-01-02(2)	23.2	7.4	0.9	68.5	5.3	28	-	n/a
D79-01-02(3)	20.4	2.9	0.5	76.2	n/a	23	-	n/a
D80-05-123(1)	15.9	3.9	1.3	78.9	41.8	20	7.4	2.1±0.4
D80-05-123(2)	29.1	10.4	0.7	59.8	3.8	41	-	-

Table 3. *Significant elemental composition by atomic percentage, Mg:Si ratio, and the residue percentage of the total sample. Substrate Si contamination counts were corrected for to obtain the Mg:Si ratio using the measured substrate atomic percentages , i.e. Si=4.27%, Cu=95.73%.*

We were careful to conduct several EDXS analyses for the specified general locations in order to eliminate any localized variations in relative elemental abundances that may be present. It is clear from these preliminary experiments that impact angle definitely affects the degree of shock-fractionation experienced by the impactor material and also the relative amounts of residue as a function of location. Effectively, two processes are at work: firstly, shock-fractionation; and, secondly, the displacement of the residue in the downrange direction as a function of the normal component of impact velocity. With this limited data set we are unable to provide a more detailed insight at present, but we are confident that further experiments will result in a better quantification of the residue location as a function of impact velocity and impact angle.

5 CONCLUSIONS

The results obtained to date suggest that a combination of crater morphology and residue analysis can give evidence of impact azimuth even when the crater profile is near hemispherical as in the case of 30° - 45° impacts. Also, lip structure correlation with impact azimuth, even for impacts in the 0° to 45° range, may be possible. The complex mechanics in oblique impacts where the residue is displaced downrange and undergoes variations in shock fractionation as a function of position have begun to be unraveled. In particular, relative amounts and locations of residue do correlate with impact velocity and can provide limits on that velocity. It is concluded that a combination of analysis techniques can yield further information on impact velocity, direction, and angle of incidence. It remains to be seen whether these findings can be used for LDEF crater analysis where the impact velocities are higher (15-25 $km.s^{-1}$) and residues can only be detected by other techniques such as SIMS.

6 FUTURE WORK

Recognizing the limitations of this work to date, we shall continue to execute hypervelocity impact shots to move from a semi-qualitative analysis with some quantitative indicators to a more quantitative basis. We expect to execute shots using olivine, glass, and polystyrene impactors striking Al1100 and Al6061 targets. These experiments will access lower density impactor phenomena.

7 ACKNOWLEDGMENTS

This work was supported by NASA Langley Research Center under grant number NAG-1-1329, which we gratefully acknowledge. We also thank Don Humes for reviewing this paper and suggesting improvements.

8 REFERENCES

Ang, J.A. (1990). *Int. J. Impact Eng.*, **10**, 1-4, pp23-34.
Berthoud, L. *et al.* (1993). *3rd LDEF Post-Ret. Symp. Abstr.*, pp58, NASA CP-10120.
Bruce, E.P. (1961). *Proc. 5th Symp. Hypervel. Impact,* Denver, CO.
Carey, W.C. *et al.* (1984). *Proc. 85th Coll. Int. Astron. Union Meeting,* Paper B.5.
Gehring, J.W. & Leiblein, S. (1963). *Prog. Astronaut. & Aeronaut.*, vol. 11.
Hörz, F. *et al.* (1993). *3rd LDEF Post-Ret. Symp. Abstr.*, pp57, NASA CP-10120.
Kineke, J.H. (1960). *Proc. 4th Symp. Hypervel. Impact,* Eglin AFB, FL.
Mackay, N.G. *et al.* (1993). *3rd LDEF Post-Ret. Symp. Abstr.*, pp67, NASA CP-10120.
Newman, P.J. *et al.* (1992). *Proc. 2nd LDEF Post-Ret.Symp.*, pp417-30, NASA CP-3194.
Nysmith, C.R. & Summers, J.L. (1962). NASA TN-D-1431.
Paul, K. (1993). *3rd LDEF Post-Ret. Symp. Abstr.*, pp67, NASA CP-10120.
Rose, M.F. *et al.* (1992). *Proc. 2nd LDEF Post-Ret. Symp.*, pp479-92, NASA CP-3194.
Simon, C.G. *et al.* (1992). *Proc. 2nd LDEF Post-Ret. Symp.*, pp677-92, NASA CP-3194.
Summers, J.L. (1959). NASA TN-D-94.
Summers, J.L. & Charters, A.C. (1958). *Proc. 3rd Symp. Hypervel. Impact,* Chicago, IL.

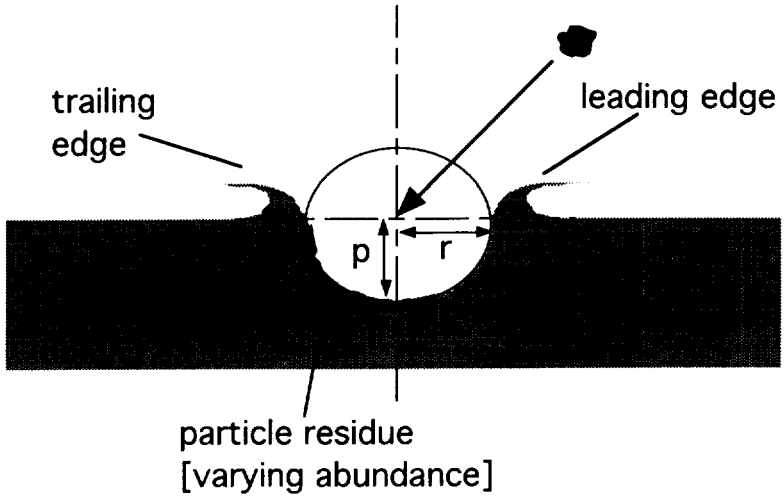

Figure 1. *Schematic of idealized profile of normal-to-45° oblique incidence hypervelocity impact crater. The penetration depth (p) and crater radius (r) are related to the particle diameter (d) and normal component of velocity (v_n) similar to the relationship between penetration depth, particle diameter and impact velocity for normal incidence impacts.*

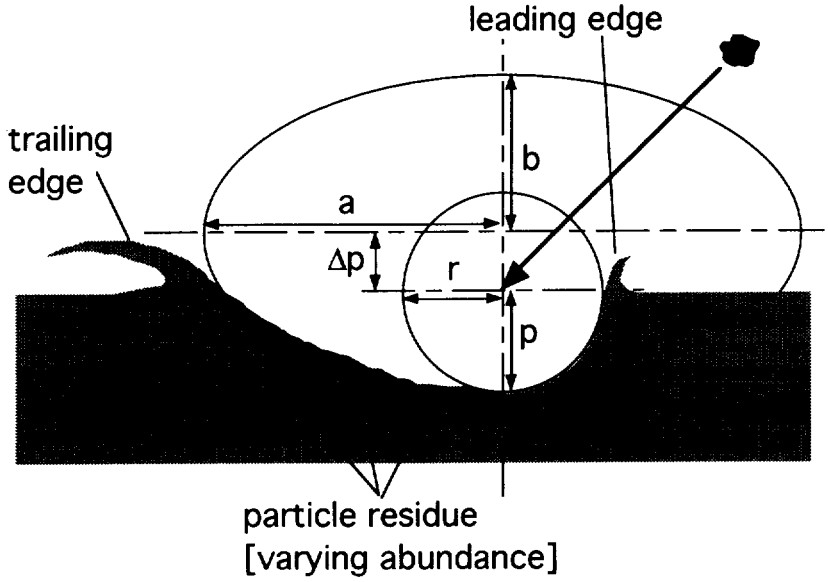

Figure 2. *Schematic of idealized profile of 45°-to-60°oblique hypervelocity impact crater. The minor ellipse (circle, in this case) parameters, penetration depth (p) and crater radius (r) are related to the particle diameter (d) and normal component of velocity (v_n) similar to the relationship between penetration depth, particle diameter and impact velocity for normal incidence impacts. The major ellipse parameters (a), (b) , and (Δp) should be related to the angle of incidence and the shock propagation velocity in the target material.*

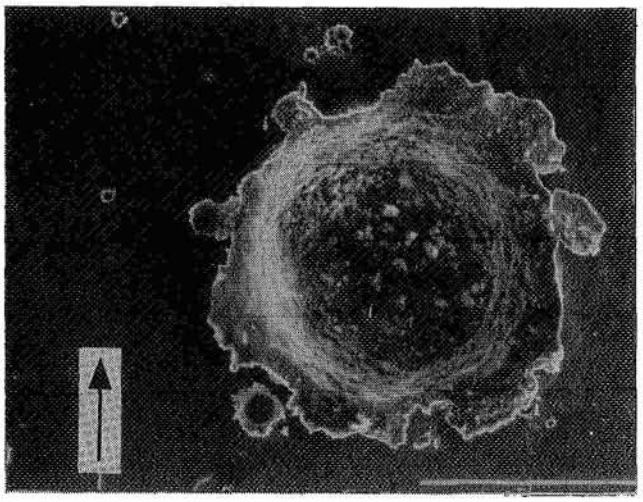

Figure 3. *Photomicrograph of an impact site formed by an olivine particle impacting with a velocity of 7.0 km.s^{-1} at an angle of 30° w.r.t. surface normal. Impact direction is indicated by the arrow. Olivine coating throughout the interior, with visible particle grains. Note the circular footprint and symmetrical lips. [scale bar = 100 μm]*

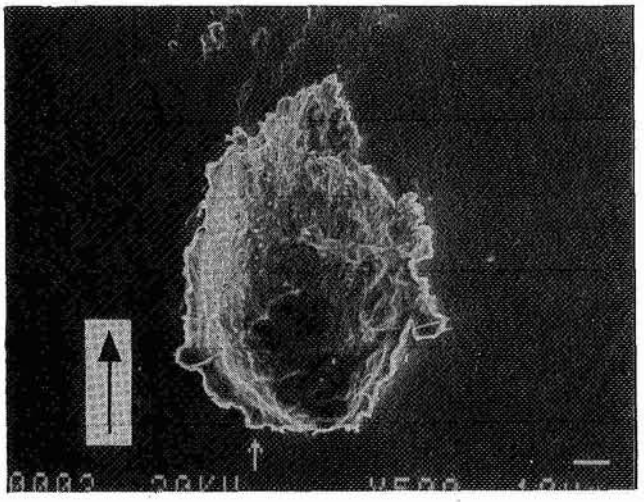

Figure 4. *Photomicrograph of an impact site formed by an olivine particle impacting with a velocity of 5.6 km.s^{-1} at an angle of 60° w.r.t. surface normal. Impact direction is indicated by the arrow. Note the "elliptical" footprint and lip asymmetry between the leading (lower) edge and the trailing (upper) edge. [scale bar = 10 μm]*

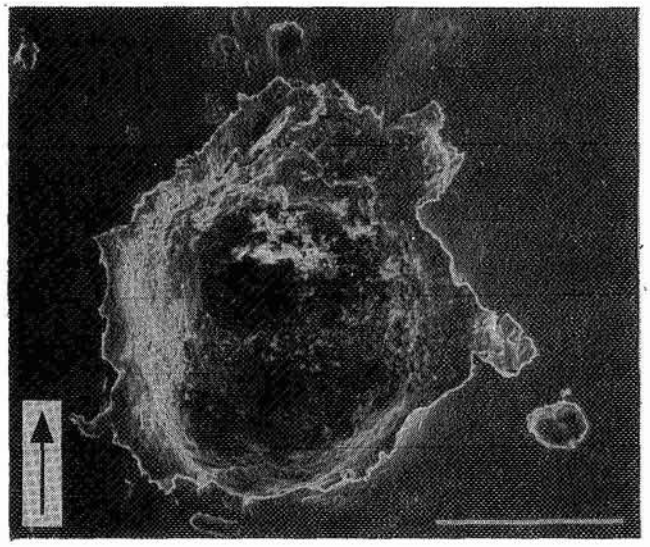

Figure 5. *Photomicrograph of an impact site formed by an olivine particle impacting with a velocity of 4.6 km.s^{-1} at an angle of 60°. Impact direction is indicated by the arrow. Note the "elliptical" footprint and lip asymmetry between the leading (lower) edge and the trailing (upper) edge. Also, note the non-uniformity of the impactor residue, with more residue being located toward the trailing edge of the crater. Some fragmentation damage downrange of the trailing lip is also visible. [scale bar = 100 μm]*

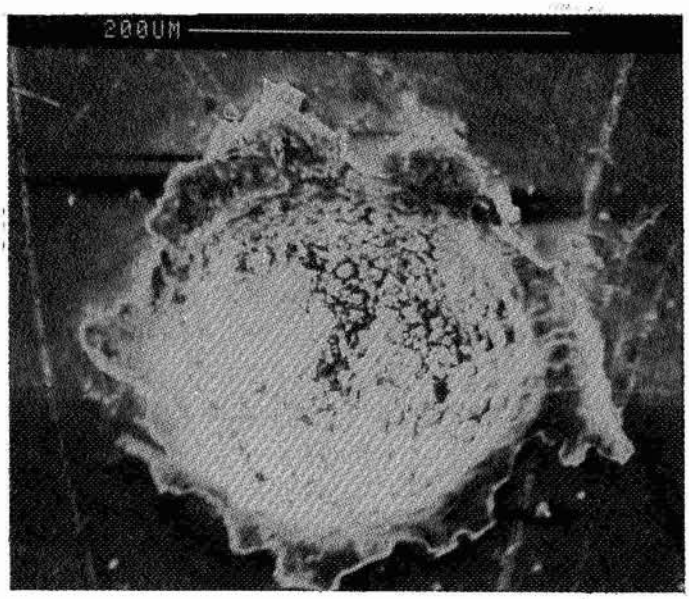

Figure 6. *Photomicrograph of impact site D76-01-17. Impact velocity is 2.9 km.s^{-1} and angle of incidence is normal to the target surface Note the circular "footprint" and symmetrical raised circumferential lips. Since this site was imaged in the SEM without a conductive coating the granular residue typical of lower velocities has saturated the film due to surface charging. It is interesting to note that such residues in craters could provide charging sites in the LEO plasma environment on surfaces regarded as pristine (and not subject to charging) prior to flight.*

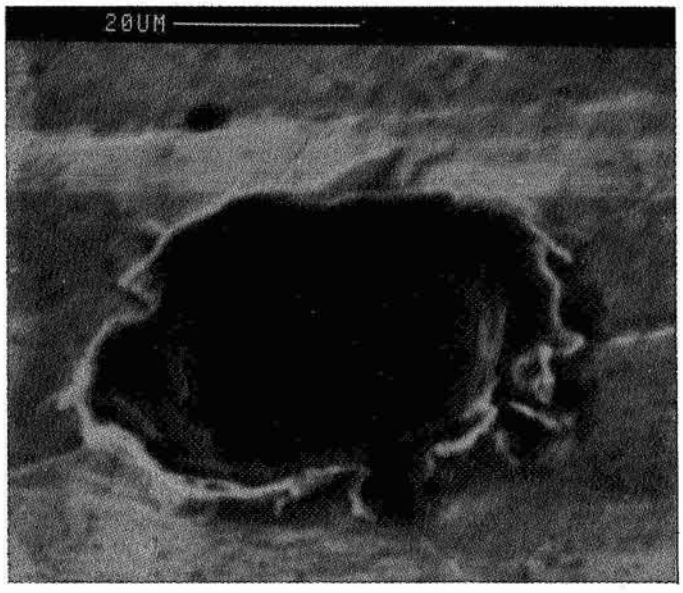

Figure 7. *Photomicrograph of impact site D76-05-26. Impact velocity is 12.0 km.s^{-1} and angle of incidence is normal to the target surface. Again, note the circular "footprint" and symmetrical raised circumferential lips. By comparison to figure 6 there is no evidence of residue charging in the SEM electron beam, even though a glassy, transparent residue was detected using EDXS. This residue was more highly shock–processed with a Mg:Si ratio of 8.7, compared to 3.4 for the interior of site D76-01-17.*

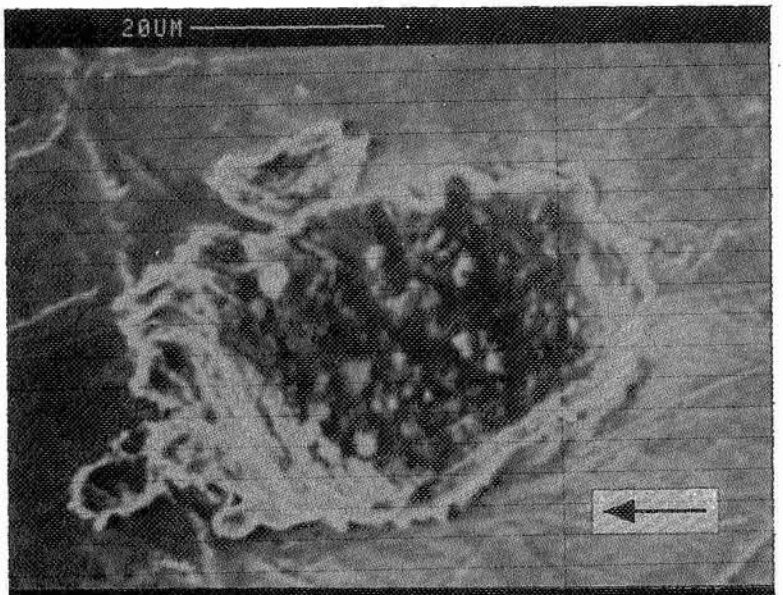

Figure 8. Photomicrograph of impact site D78-03-17. Impact velocity was 10.5 km.s^{-1} and angle of incidence is 60° (w.r.t. surface normal). Impact direction is indicated by the arrow. Note the granular residue and pronounced trailing edge lips. p/D ratio is 0.40.

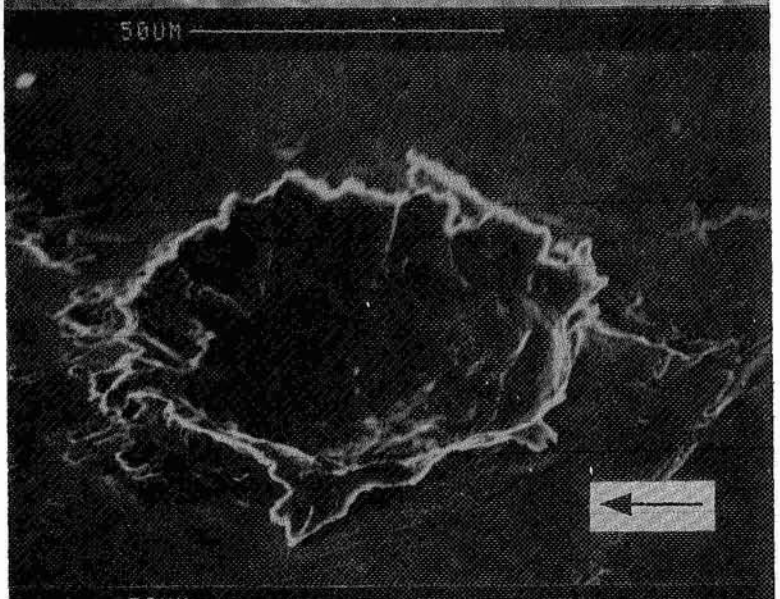

Figure 9. Photomicrograph of impact site D78-05-23. Impact velocity was 8.5 km.s^{-1} and angle of incidence is 60° (w.r.t. surface normal). Impact direction is indicated by the arrow. Note the absence of granular residue, the pronounced trailing edge lips, and downrange impactor fragmentation damage. p/D ratio is 0.32.

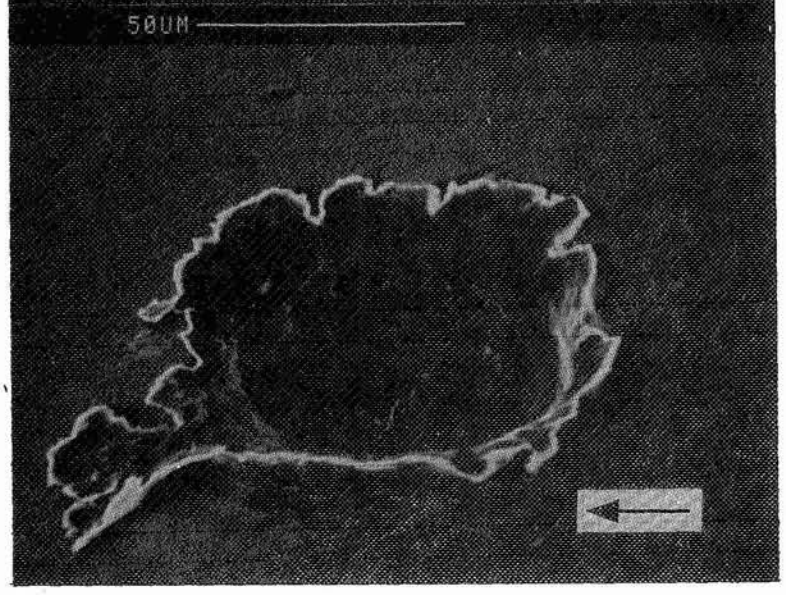

Figure 10. *Photomicrograph of impact site D80-05-123. Impact velocity was 10.5 km.s^{-1} and angle of incidence is 45°. Impact direction is indicated by the arrow. Note the almost circular footprint and lack of asymmetry between leading and trailing edge lips. p/D ratio is 0.48, indicating an almost hemispherical crater which would be indistinguishable from lower incidence impact craters.*

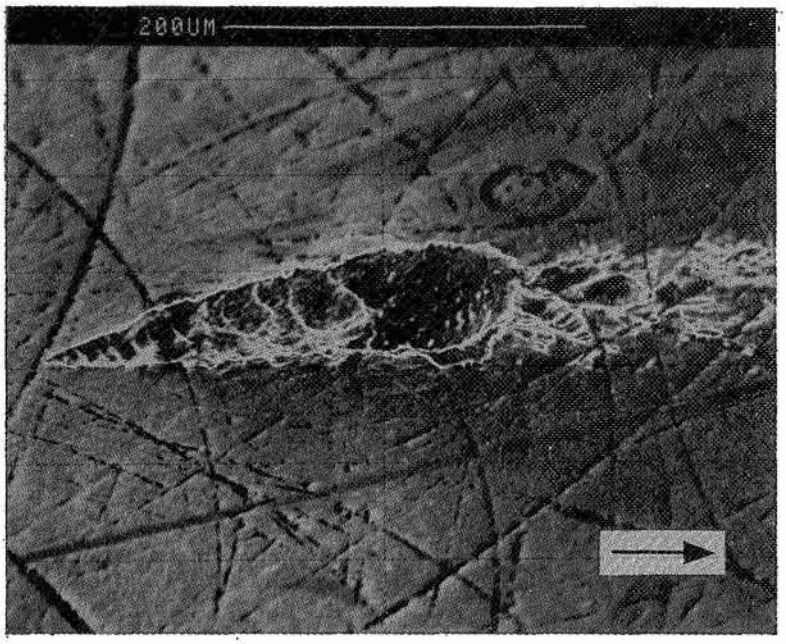

Figure 11. *Photomicrograph of impact site D79-01-02. Impact velocity is 5.7 km.s^{-1} and angle of incidence is 75° (w.r.t. surface normal). Impact direction is indicated by the arrow. Note the uprange gouge, central major "crater" and downrange impactor fragmentation damage.*

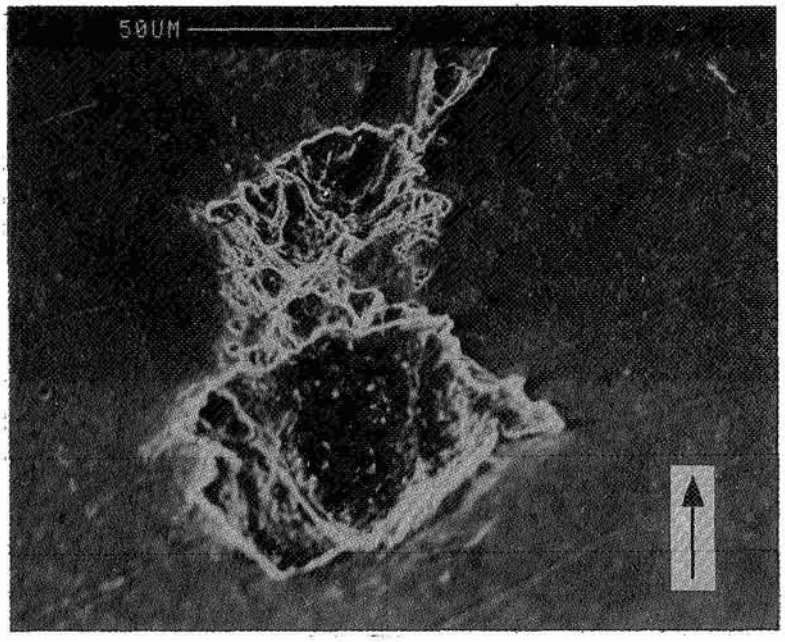

Figure 12. *Photomicrograph of impact site D79-03-04. Impact velocity is 12.5 km.s^{-1} and angle of incidence is 75° (w.r.t. surface normal). Impact direction is indicated by the arrow. Note that there is no uprange gouge, the central major "crater" is deep with significant lips. Downrange impactor fragmentation damage as still present.*

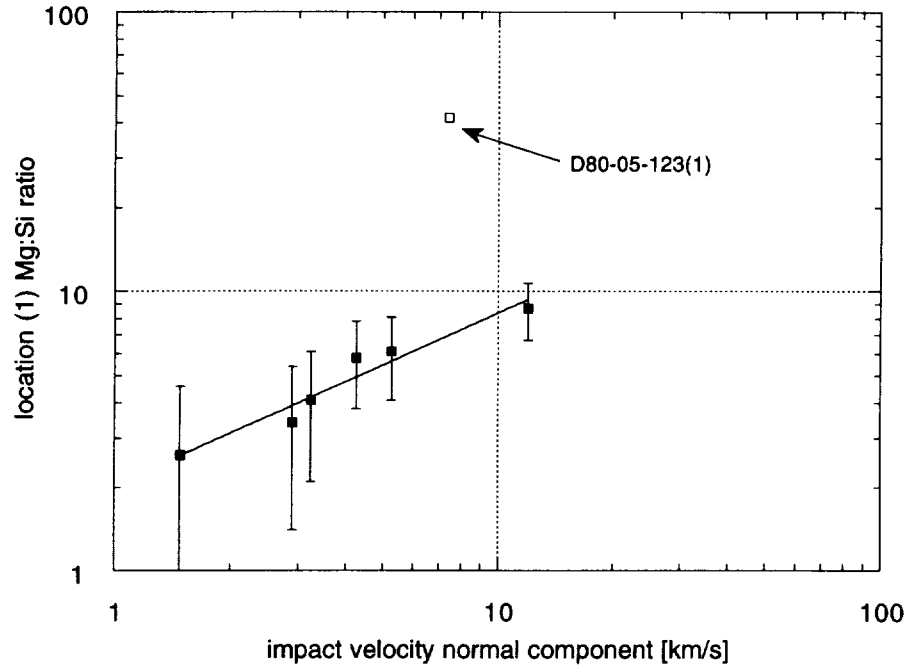

Figure 13. *Graph of location (1) residues Mg:Si ratio showing the increase of shock fractionation with increasing normal component of impact velocity (V_n).*

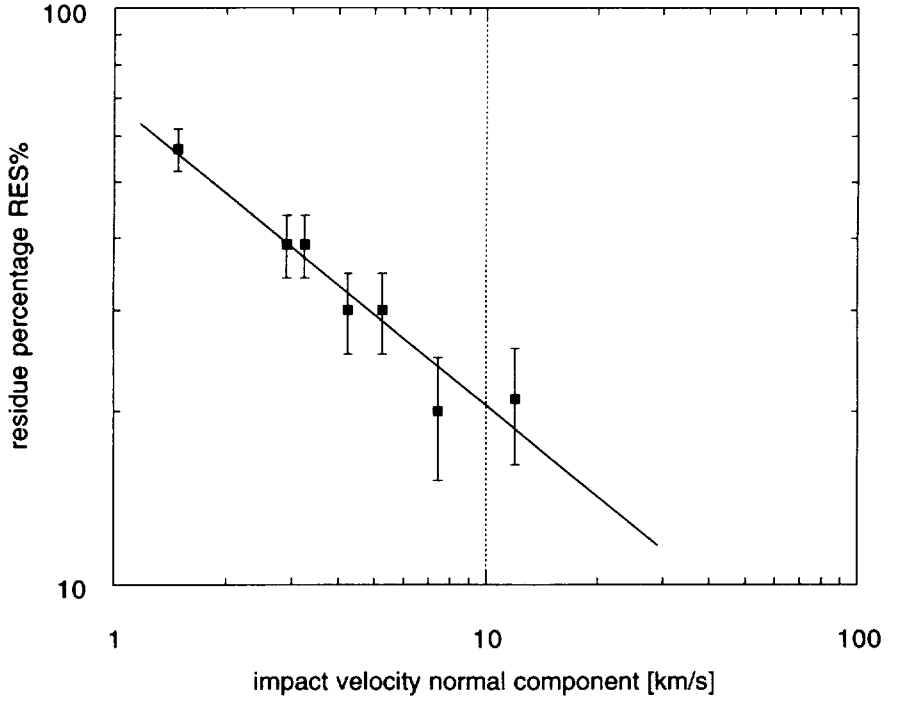

Figure 14. *Graph of location (1) residue percentage versus impact velocity normal component (V_n).*

EXPERIMENTAL INVESTIGATION OF THE RELATIONSHIP BETWEEN IMPACT CRATER MORPHOLOGY AND IMPACTING PARTICLE VELOCITY AND DIRECTION

N.G. Mackay, S.F. Green, D.J. Gardner and J.A.M. McDonnell
Unit for Space Sciences
Physics Laboratory
University of Kent
Canterbury, Kent CT2 7NR
U.K.
Phone: 227 764000 ext. 3266, Fax: 227 762616

SUMMARY

Interpretation of the wealth of impact data available from the Long Duration Exposure Facility, in terms of the absolute and relative populations of space debris and natural micrometeoroids, requires three dimensional models of the distribution of impact directions, velocities and masses of such particles, as well as an understanding of the impact processes. Although the stabilised orbit of LDEF provides limited directional information, it is possible to determine more accurate impact directions from detailed crater morphology. The applicability of this technique has already been demonstrated (Mackay et al, 1993, ref 1; Newman et al , 1993, ref 2), but the relationship between crater shape and impactor direction and velocity has not been derived in detail.

We present the results of impact experiments and simulations:

1) impacts at micron dimensions using the Unit's 2MV Van de Graaff accelerator
2) impacts at mm dimensions using a Light Gas Gun
3) computer simulations using AUTODYN-3D

from which an empirical relationship between crater shape and impactor velocity, direction and particle properties we aim to derive. Such a relationship can be applied to any surface exposed to space debris or micrometeoroid particles for which a detailed pointing history is available.

INTRODUCTION

During analysis of LDEF surfaces, a large number of elliptical craters were observed. These have been interpreted as due to impacts from interplanetary dust or space debris at highly oblique angles (refs 1 and 2) although it has been suggested that they were caused by irregularly shaped impactors. If the former interpretation is valid then these impact sites provide an invaluable diagnostic tool for determination of impact directions and hence orbital distribution of space debris particles impacting LDEF

surfaces.

A series of experiments and hydrocode simulations have been performed in order to investigate the relationship between impact parameters and crater morphology. If a relationship of this nature can be established, it will be possible to use this to help deconvolve the dust/debris environment.
Previous experiments which have been performed by other researchers have included

1) Oblique impacts into rock and rock dust
2) Oblique impacts into glass
3) Oblique impacts into lead
4) Oblique impacts into bumper shields

Most of the experiments into semi-infinite targets were investigating factors such as depth to diameter ratios or volume of the crater excavated, although the bumper shield studies did include hole shapes and angles. The majority of space exposed surfaces suitable for dust particle impact studies are effectively smooth metal semi-infinite or foil targets. We are therefore investigating the effects of impactors of known speed direction and composition onto such targets.

EXPERIMENTAL DETAILS

Accelerator

The first experiments were performed using a 2MV Van de Graaff accelerator (Green et al., ref 3). The accelerator contains a dust source of spherical iron (I1068) particles which are typically less than 10 μm in diameter. The dust is charged with an electric field and accelerated along an evacuated flight tube to velocities from 0.5 km s^{-1} to upwards of 25 km s^{-1} before impacting the target.

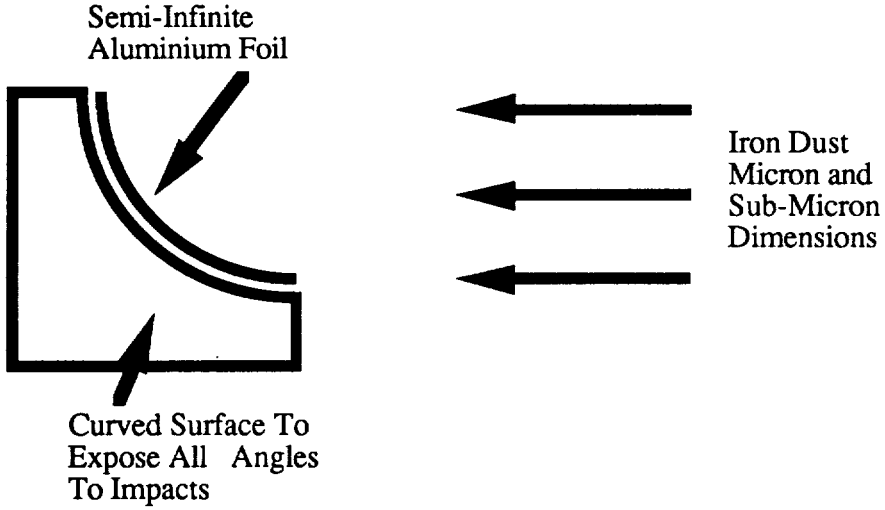

Figure1 Target frame and target used for the Van de Graaff accelerator experiment.

In this case the target was an aluminium foil curved round a target frame in order to expose the full range of angles of 0-90° to the impacting projectiles (as shown in figure 1).

After exposure in the accelerator the foil was removed from the mounting, flattened, and placed on a microscope stub. A preliminary analysis of it was performed using a Philips 525 SEM.

A strip down the length of the foil was examined, covering a range of angles from 90° to about 40°. Each crater located was classified according to its source (ie. hypervelocity or non-hypervelocity) and the quality of image achieved. Those craters from a non-hypervelocity source or with too poor an image to be useful were discarded and the remainder were then measured along both axes.

Light Gas Gun

The second phase of experimentation was performed using a two-stage Light Gas Gun.The Light Gas Gun can launch a solid nylon sabot (4mm in diameter) or smaller projectiles which are initially contained in a split nylon sabot that is stripped off in the flight chamber.

In this case steel ball bearings of 400 μm (AISI420C) and 1mm diameter were used as projectiles. These were fired at a series of discrete angled (55°, 65°, 70°, 75°, 85°) aluminium (HE30) targets (see figure 2). The accuracy of the target frame in defining the impact direction was measured and was found to be within 0.5° .

The targets were then removed from the target frame and the analysis was performed using an optical microscope.

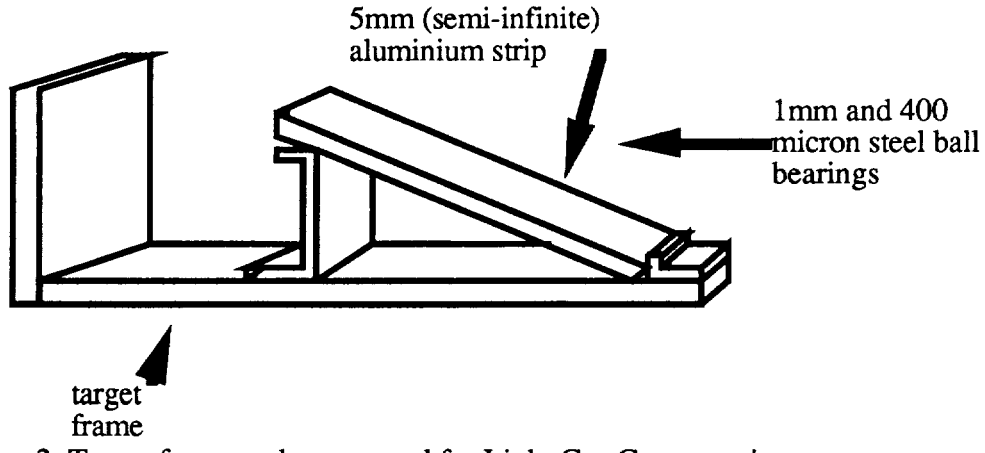

Figure 2: Target frame and target used for Light Gas Gun experiment.

AUTODYN-3D Simulations

AUTODYN-3D is an interactive, integrated hydrocode available on a very wide range of computers (ref 4). Currently a Lagrange processor exists in AUTODYN-3D, with other processors under development (the 2D version already incorporates Euler, ALE, and Shell processors as well).

Most hydrocodes (AUTODYN included) model materials as grids or arrays of cells, which either distort with the material (Lagrange method) or provide the calculation unit for material moving through the grid (Euler method). The Lagrange processor has the advantage of being computationally fast and gives good definition of material interfaces, but normally cannot simulate problems involving large deformations of the cells. This limitation can be overcome by the selective removal of cells, usually on the basis of a user-specified strain. The momentum and mass of these cells may be retained or discarded. Previous experience has shown that the best results (closest to experiment) are obtained by discarding the cells.

For the analyses reported here the Shock (Mie-Gruniesen) equation of state was used together with the Johnson-Cook strength model, thus continuing the data set of previous work (ref 5). All material data values used were exactly as published in references 6 and 7.

All the AUTODYN-3D simulations were Iron projectiles onto semi-infinite aluminium targets. The impacts so far simulated are 60°, 70° and 80° at 4 km s^{-1} and 80° at 16 km s^{-1}.

RESULTS

The preliminary results from the Van de Graaff accelerator experiment are shown in figure 3. Although the accelerator is capable of producing a large range of velocities these consist of small fast projectiles or larger slower ones. As a result of this it is difficult to analyse impacts from the very fast projectiles since they are very small and therefore produce craters which are too small to resolve with sufficient accuracy to determine ellipticity. In the case of the craters analysed so far the velocities were in the range 1-3 km s^{-1}. The craters are still noticeably elliptical at angles as small as 45° for these low velocities. The trend is very distinctly towards increased ellipticity with increased impact obliquity and in the range of 75-80° the craters become extremely long and thin.

Figure 4 shows examples of impact craters formed in the Light Gas Gun experiments with axis ratios plotted in figure 5. As in figure 3 the error bars are due to uncertainties in measurements. The scatter represents a real dispersion in crater properties. The velocities of the projectiles in the case of the Light Gas Gun were approximately (4.6±0.4) km s^{-1} which was slightly faster than the impacts so far measured from the accelerator experiments.

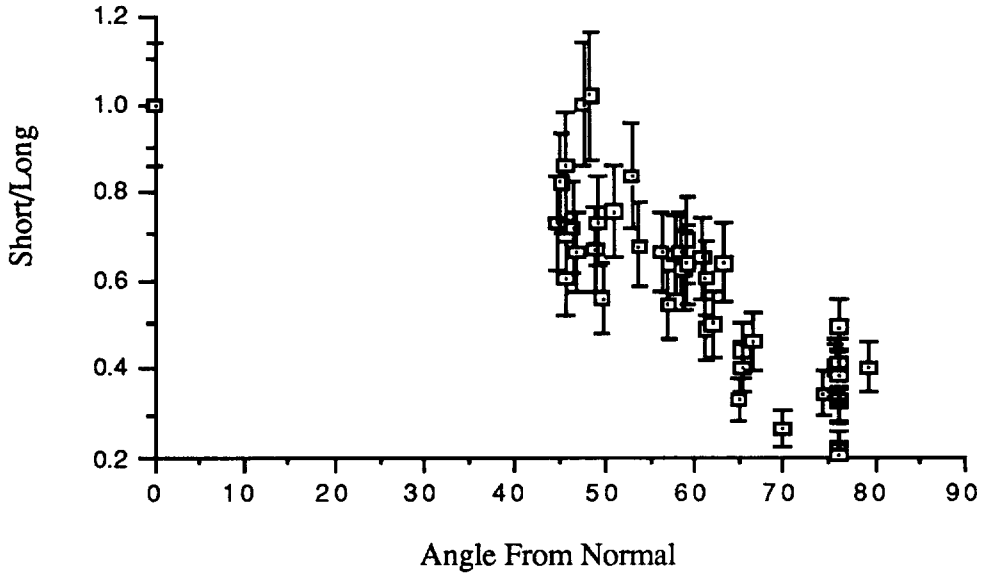

Figure 3: The variance of the ratio of short axis to long axis with angle of impact for craters produced by impacts from the Van de Graaff accelerator.

All impacts are from the left

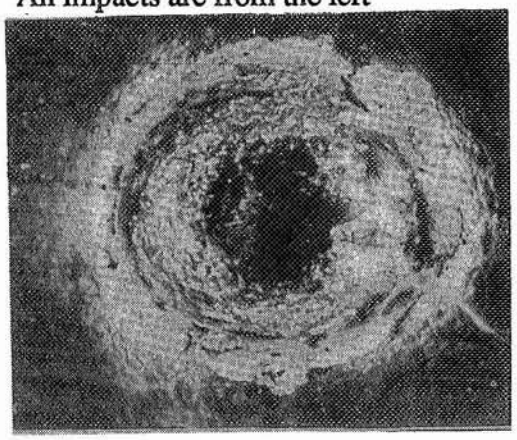

65° 1mm ball bearing
Dimensions (mm) = (6.4±0.1) x (4.0±0.1)

55° 1mm ball bearing
Dimensions (mm) = (6.0±0.1) x (5.1±0.1)

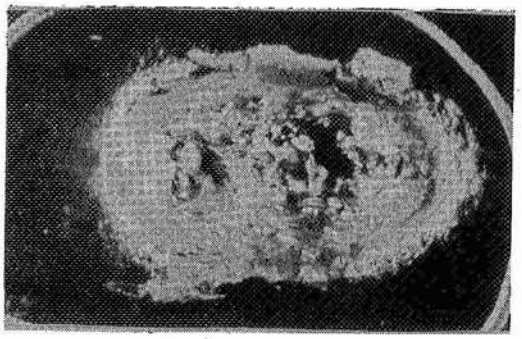

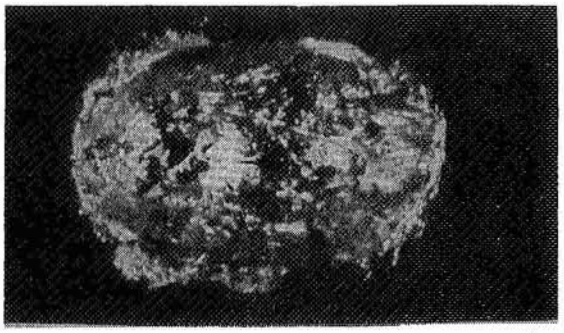

70° 1mm ball bearing
Dimensions (mm) = (5.9±0.1) x (4.6±0.1)

75° 1mm ball bearing
Dimensions (mm) = (5.2±0.1) x (3.1±0.1)
Notice the downstream ejecta

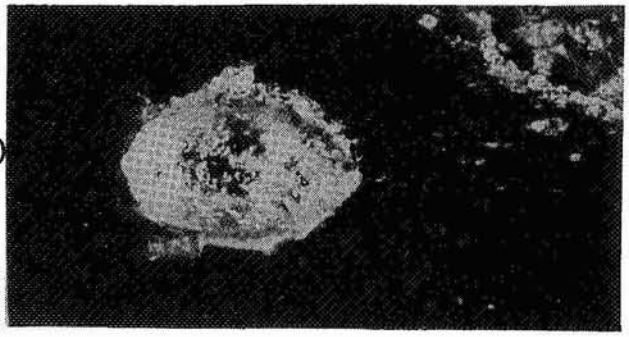

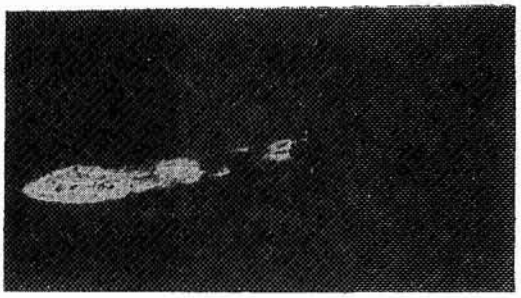

85° 1mm ball bearing
Dimensions (mm) = (5.9±0.1) x (1.0±0.1)
Note the multi-cratering

85° 400μm ball bearing
Dimensions (mm) = (1.7±0.1) x (0.9±0.1)
This example is unusual in that the craters increase in size along the line of flight instead of decreasing as normal.

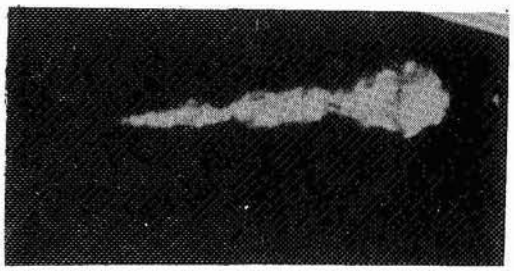

Figure 4: Impact sites from light gas gun

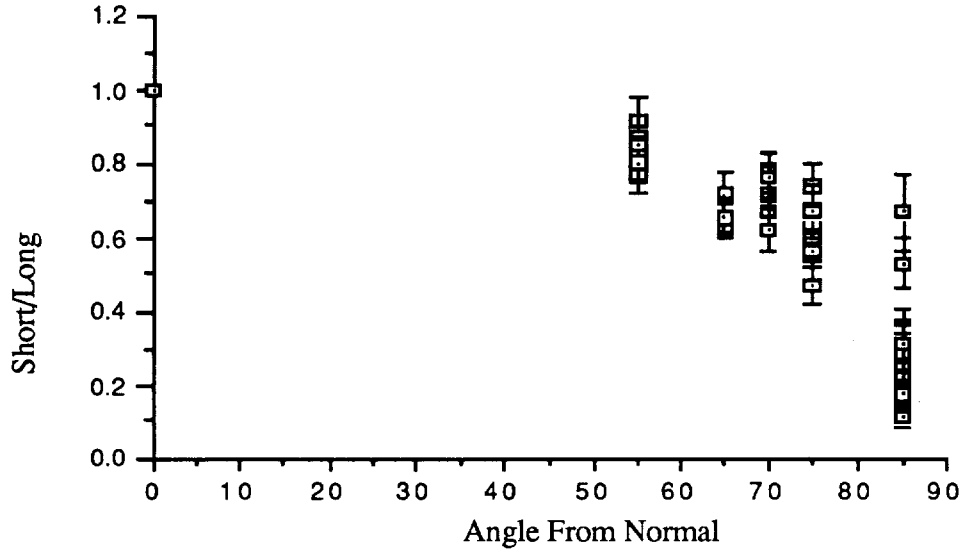

Figure 5: The variance of the ratio of short axis to long axis with angle of impact for craters produced by impacts from the Light Gas Gun.

The craters are noticeably less elliptical at lower angles than comparable impact sites from the accelerator, and as we reach very high angles (85°) multi-cratering begins to occur. (For the instances of multi-cratering the crater length is defined as the length of the longest single crater from the impact.)

Figure 6 shows data taken from Christiansen et al.(ref 8) and converted for comparison with the accelerator and Light Gas Gun experimental results. These data are also the results of Light Gas Gun experiments but this time at the higher velocity regime of 6.5-7 km s^{-1} with aluminium targets and projectiles.

No elliptical craters were observed until 72°, but from there the craters become rapidly more elliptical until multi-cratering is observed at 82°. (In this case the length for multi-cratering sites is defined as the total damage length from an impact.) This data still, in general, follows the observed trend of less elliptical craters for higher velocities.

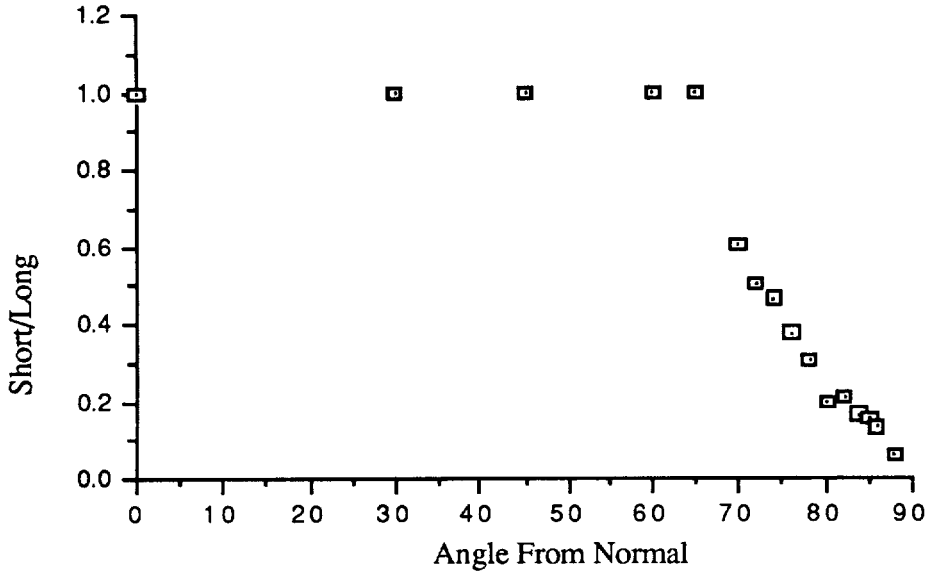

Figure 6: The variance of the ratio of short axis to long axis with angle of impact for craters produced by impacts from Christiansen et al (ref 8)

A comparison of all the data sets is shown in figure 7. The fits drawn to the data are by eye.

In general the data are consistent with the more oblique angles producing more elliptical craters, while increasing the velocity decreases the ellipticity for any given angle. Although Christiansen's data do cross the UKC Light Gas Gun data at about 75°, it is worth bearing in mind that his experiments were for aluminium impacts onto aluminium targets (as opposed to the iron onto aluminium of the UKC experiments) and his different definition of length used for multi-cratering sites.

The 4 km s^{-1} AUTODYN-3D simulations are consistent with the data but the 16 km s^{-1} AUTODYN-3D simulation shows a somewhat higher ellipticity than expected.

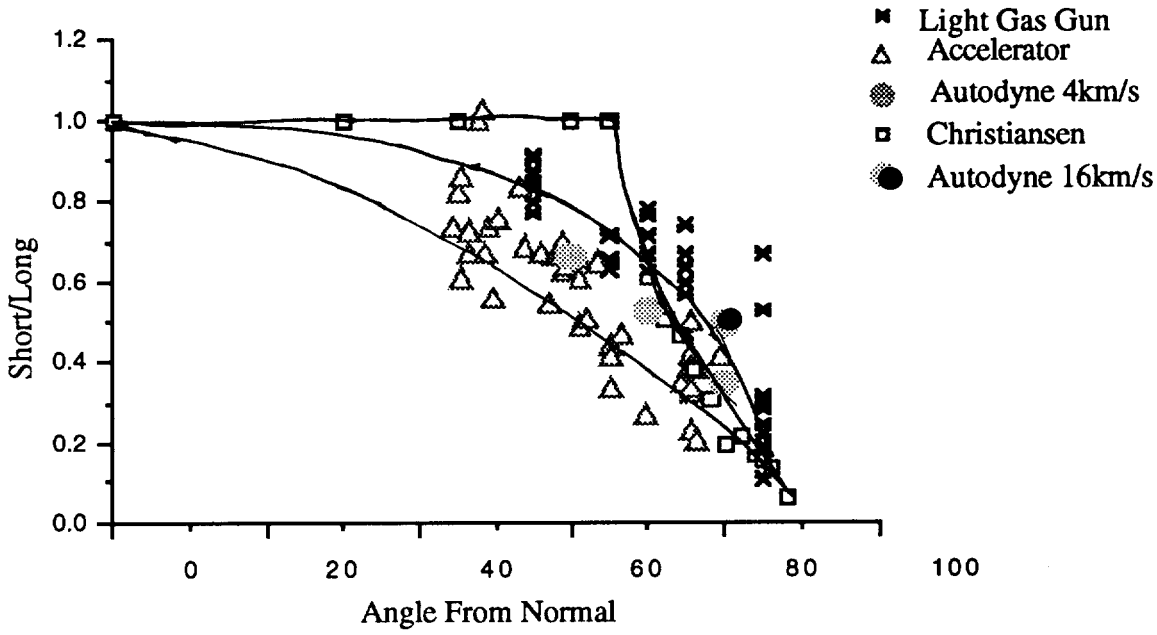

Figure 7: Comparison of results from figures 3, 5, 6

CONCLUSIONS

An experimental programme of hypervelocity impacts has demonstrated that it is potentially possible to use crater ellipticities to decode impact directions on space exposed materials. However we must take into account the differing impact velocities on each face of LDEF, and how this affects crater ellipticity, when attempting to decode impacts. Also we need an independent means of determining impact velocities, in order to deconvolve the effects of velocity and angle of impact. (It may be possible to use depth/diameter ratios of the crater for this.)

The relationship between the angle and velocity of the impact and the ellipticity of the crater requires further investigation and evaluation but we should also investigate the effect of parameters such as material properties, impactor size and shape, on the crater morphology.

The experimental program at UKC will continue with,

1) More curved surfaces being exposed in the Van de Graaff accelerator (future surfaces will be convex to avoid the danger of secondary impacts) using defined velocity windows and a variety of target materials (however only a restricted range of velocities can be investigated because of problems in analysing very small craters).

2)More angled targets in the Light Gas Gun with a variety of projectile sizes,

target materials and projectile materials.

3) Establish that Hydrocodes agree with the experimental results at low (but still hyper) velocities and then use them to extrapolate to higher velocities where controlled experiments cannot be performed.

REFERENCES

1. Mackay, N.G., Green, S.F., Deshpande, S.P., and Newman, P.J., 1993. Interpretation of Impact Crater Morphology and Residues on LDEF using 3-D Space Debris and Micrometeoroid models. Proc. 1st European Conference on Space Debris , Darmstadt, 5-7 Apr. 1993.

2. Newman P.J., Mackay N., Deshpande S.P., Green S.F. and McDonnell J.A.M., 1993. Derivation of Particulate Directional Information from Analysis of Elliptical Impact Craters. Proc. Second LDEF Post-retrieval Conference, NASA CP-3194, 1993.

3.Green, S.F., Clarke, C. D. , and Stevenson, T. J., 1988. A 2MV Van de Graaff Accelerator for Cosmic Dust Simulation. JBIS Vol. 41 No. 9, Sept 1988.

4. Cowler, M., et al. AUTODYN - An Interactive Non-Linear Dynamic Analysis Program for Microcomputers through Supercomputers, 9th International Conference on Structural Mechanics in Reactor Technology, Lausanne, Aug.1987.

5. J.A.M.McDonnell, D.J.Gardner, P.J.Newman, N.J.Robertson, C.J.Hayhurst. Hydrocode Modelling In The Study Of Space Debris Impact Crater Morphology. Proc. 1st European Conference on Space Debris, Darmstadt, April 1993.

6. Group GMX-6, Selected Hugoniots, Los Alamos Scientific Lab. LA-4167-MS, May 1969.

7. Johnson and Cook, A Constitutive Model and Data for Metals Subjected to Large Strains, High Strain Rates and High Temperatures, Proc. 7th International Symposium on Ballistics, The Hague, 1983.

8. Christiansen, E.L., Cykowski, E., and Ortega, J., 1992. Highly Oblique Impacts Into Thick And Thin Targets. Journal of Impact Engineering, Nov. 1992.

DETERMINING ORBITAL PARTICLE PARAMETERS OF IMPACTS INTO GERMANIUM USING MORPHOLOGY ANALYSIS AND CALIBRATION DATA FROM HYPERVELOCITY IMPACT EXPERIMENTS IN THE LABORATORY

Klaus G. Paul*
Lehrstuhl für Raumfahrttechnik, TU München
Richard-Wagner-Straße 18/III
D-80333 München, Germany
Phone: (+) 49 89 2105 2578, Fax: (+) 49 89 2105 2468
E-Mail: kpaul@asterix.lrt.mw.tu-muenchen.de

SUMMARY

This paper describes the work that is done at the Lehrstuhl für Raumfahrttechnik (lrt) at the Technische Universität München to examine particle impacts into germanium surfaces which were flown on board the LDEF satellite. Besides the description of the processing of the samples, a brief overview of the particle launchers at our institute is given together with descriptions of impact morphology of high- and hypervelocity particles into germanium. Since germanium is a brittle, almost glass-like material, the impact morphology may also be interesting for anyone dealing with materials such as optics and solar cells.

The main focus of our investigations is to learn about the impacting particle's properties, for example mass, velocity and direction. This is done by examining the morphology, various geometry parameters, crater obliqueness and crater volume.

LDEF EXPERIMENT A0187-2

Experiment Description

The Experiment "Chemical and Isotopical Measurements of Micrometeoroids using SIMS" has been described elsewhere in greater detail ([2] and [11]). It occupied three locations: one 1/1 tray on bay E08, one 2/3 tray on bay E03, and one 1/3 tray on bay C02. A thin foil covered germanium targets and should cause impacting particles to break up and produce a large amount of residue spray, which we call "extended impacts". See figure 1 for a cross-sectional sketch of the experiment setup.

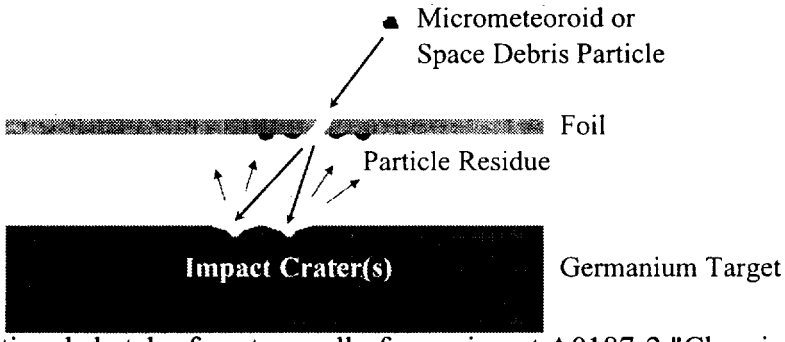

Figure 1. Cross-sectional sketch of capture cell of experiment A0187-2 "Chemical and Isotopical Measurements of Micrometeoroids using Secondary Ion Mass Spectrometry"

After LDEF recovery it turned out that most of the foils were destroyed, thus allowing many impacting particles to produce regular hypervelocity impacts. Only some foils from the trailing edge trays remained intact.

The lrt received nine capture cells from tray E08, each containing four 39x42x0.5 mm germanium wafers, plus two circular impact cells from EEEC experiment S1002. This paper focuses on the capture cells from tray E08.

LDEF Sample Processing

The LDEF samples were first scanned in order to locate impact features using a Cambridge Stereoscan S120 scanning electron microscope at a magnification of 100x. Once an impact feature was found, it was classified as impact, extended impact or unusual pattern. However, the patterns labeled as unusual seemed to be contamination patterns similar to those found on other surfaces as well as reported by several other investigators. Only the impact features with an obvious spray pattern formed during the impact were regarded as extended impacts.

A total number of 907 impact features (895 conventional impacts and 12 extended impacts) have so far been found on two capture cells, resulting in a total scanned area of $13.1 \cdot 10^{-3} m^2$.

Once an impact has been identified its image is stored on a standard, frame-grabber equipped PC. This image is then used to sketch the exact shape of the crater, resulting in grater detail than previous investigations [5], for size and geometry information. The outline image is then converted into an ASCII readable format that can be used for calculating the various crater areas (see figure 2). We distinguish between (a) central crater, (b) secondary spallation zone (i.e. all the visible damaged area) and (c) chips that remained in the impact feature. Radial cracks, visible near some of the impact features, were ignored in the sketches. Up to now, 615 impact features have been sketched.

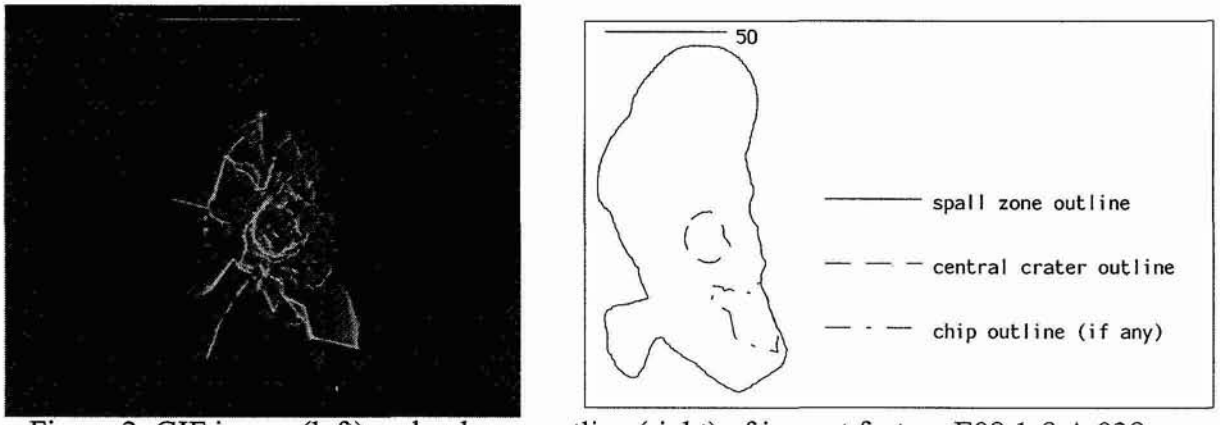

Figure 2. GIF image (left) and redrawn outline (right) of impact feature E08 1-8 A 038

We also take an even closer look at the impact feature geometry. Using a Rodenstock RM600/3-D laser topographer a three-dimensional map of the impact features is created. This instrument typically returns z-coordinates within a range of ± 300 µm and an accuracy of better than 0.5% with some 400 points per mm along its measurement axis and 2µm offsets between each measurement.

This three-dimensional data allows not only the determination of otherwise almost not measurable properties, such as crater or impact feature volume, but also a close look at crater cross-sections and, therefore, crater depths. See figures 19 and 21 for examples of such a scan, figures 24 through 28 for cross-sectional scans, references [6] and [13] for pictures of actual cross-sections showing hidden caverns under the surface that cannot be measured with our topographer.

Impact Morphology

Basically, we discriminate between two different types of impact features: Extended impacts that show signs of foil interaction, and standard high- and hypervelocity impact features resembling the typical patterns already described for example in [1], [10] and [14]. See figures 3 and 4 for examples of such impact features.

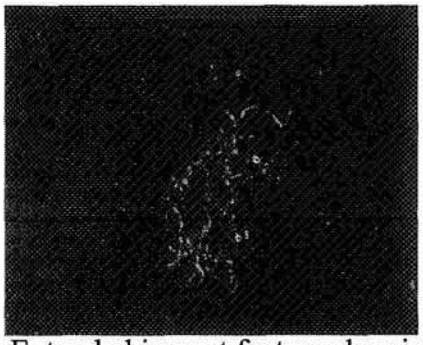

Figure 3. Extended impact feature showing the typical spray pattern of a particle that was broken up

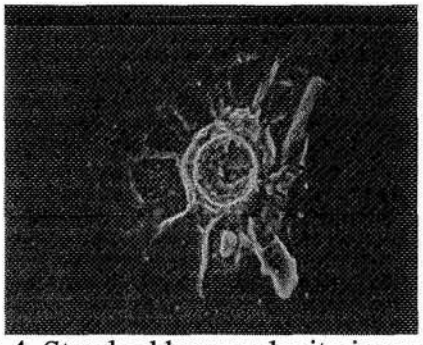

Figure 4. Standard hypervelocity impact with molten central crater and impact residue (molten spheres) around the impact feature

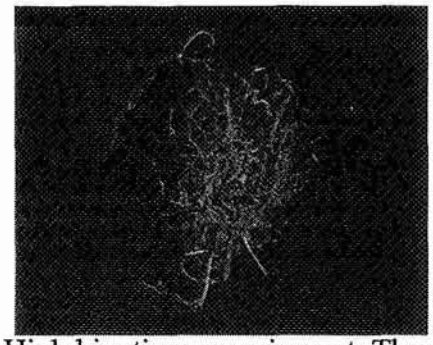

Figure 5. High kinetic energy impact. The central crater was apparently blown away by the force of the shock wave

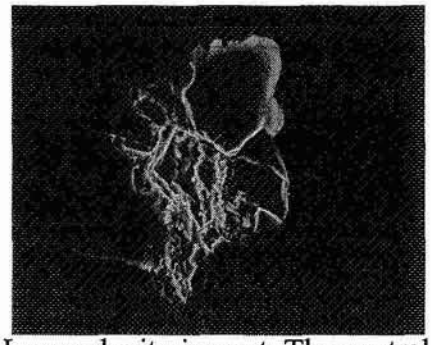

Figure 6. Low velocity impact. The central crater shows no signs of melting; it appears only to be damaged

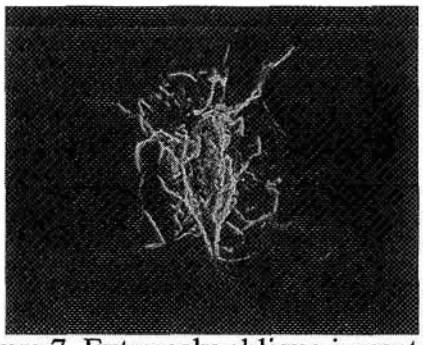

Figure 7. Extremely oblique impact

Whereas the extended impact features were usually clearly classifiable as such (with some exceptions of contamination looking very similar to them), a variety of "standard" impacts can be found on the germanium surfaces.

Therefore, a further subclassification into four standard impact types was made: (1) Hypervelocity impacts (see figure 4), (2) high kinetic energy impacts (see figure 5), (3) low velocity impacts (see figure 6)

and (4) oblique and highly oblique impacts (see figure 7). This classification is mainly possible with experience gathered from impact features found on surfaces with laboratory produced impacts (see also description of the laboratory experiments below) and by comparison with features documented in the literature (as, for example, [3] and [4]).

Especially the oblique and highly oblique impact features are interesting because the orientation and eccentricity of the central crater can give hints to where the particle may have come from.

HYPERVELOCITY IMPACT EXPERIMENTS IN THE LABORATORY

In order to retrieve information on the impacting particle's properties, it is necessary to perform comparative impact experiments in the laboratory where mass, velocity and chemical composition of the impacting particle can be measured or are known, respectively.

Facility Description

The Lehrstuhl für Raumfahrttechnik operates several high- and hypervelocity impact facilities. The laboratory equipment contains (see also [8]):

- an eddy current accelerator covering low velocities from several cm/s up to 400 m/s for particles up to 100 µm diameter,
- an electrothermal accelerator facility with a velocity range up to 5 km/s for particles with up to 1 mm diameter, and
- a plasmadynamic accelerator for particles in the size range of 5 to 150 µm and velocities up to 20 km/s.

For the laboratory impact experiments we used the plasmadynamic accelerator shown in figure 8.

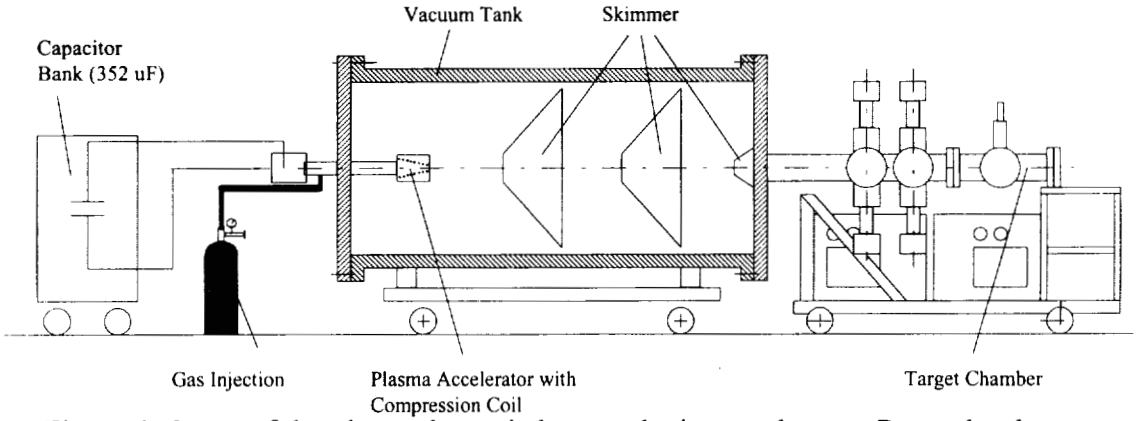

Figure 8. Setup of the plasmadynamic hypervelocity accelerator. Recently, the target chamber has been modified.

The vacuum chambers are evacuated (100 Pa in main chamber, 0.1 Pa in target chamber). To launch particles, the capacitor bank is charged to approximately 16 kV, then Helium is injected into the breech of the coaxial barrel. After triggering, ignitrons switch the discharge, which ionizes the Helium and forms a plasma arc. This plasma is accelerated to about 100 km/s (measured at the barrel muzzle), enters the compressor coil and causes a current to flow from the center electrode to the coil turns. The coil current generates a magnetic field, whose interaction with the currents flowing in the plasma results in Lorentz forces, which in turn compress the plasma. The plasma flow provides a dynamic pressure of up to 1 Billion Pa in the coil muzzle.

The time when the coil is completely filled with plasma is determined via a Rogowsky coil signal. Glass beads placed in the muzzle area are accelerated by the aerodynamic drag. Typical size ranges of these beads are 20-150 μm.

Experiment Evaluation

The particle parameters are measured by detecting the plasma signal from the impact. For this, charge collectors and charge sensitive amplifiers are used as impact detectors mounted close to the surface to be investigated (see figure 9). The impact signal is recorded and can be used for the determination of the time of impact.

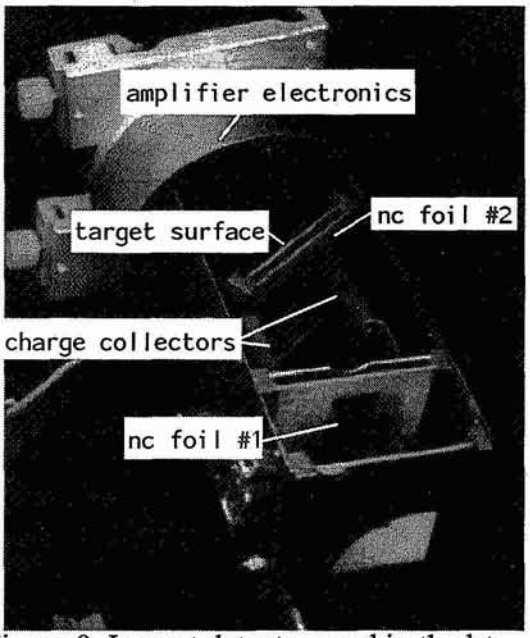

Figure 9. Impact detector used in the lrt plasma accelerator.

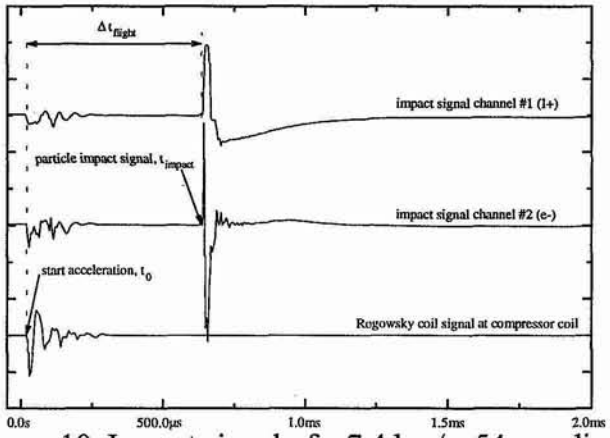

Figure 10. Impact signal of a 7.4 km/s, 54 μm diameter particle

One or two sub micron films in front of the target surface, at a distance of some 100 mm will reveal the particle size since the trace of the particle can be seen after it perforated the foil. Figure 11 shows a penetration hole of one of these particles. In addition, information on ejecta can be gathered, as well, by putting the second foil close to the target, as shown in figure 9.

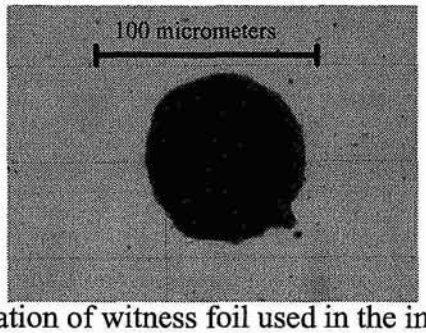

Figure 11. Perforation of witness foil used in the impact detector (revealing a particle diameter 74 μm)

Next, basic crater dimensions are measured using an optical microscope. Both crater diameter and crater depth are measured, the latter by using a differential focusing method. After that, the sample is proc-

essed in the SEM much the same as the LDEF samples to have the geometry of the impact features analyzed. In addition, the laser scanner is used for examination of the impact feature topography.

RESULTS

The following gives an overview on the variety of information that can be retrieved from the LDEF and laboratory experiments.

Feature Analyses of LDEF Surfaces

Crater Size Flux

Figure 12 gives the cumulative average central crater pit diameter flux for the germanium surfaces from E08 for the total exposure time. Note the decrease of the flux numbers for central craters smaller than 4 μm. This might either be due to a decrease in the number of smaller particles at this size regime, or due to our scanning procedure, which was conducted usually at a 100x magnification. Since many of the smaller impacts were located while zooming in on another impact feature, we could have missed some of the smaller craters, as well.

To compensate for this uncertainty, we believe that our data covers *only* those impact features with central crater pits larger than 4 μm. The flux for smaller particles may or may not be higher than these numbers may indicate.

Geometry

Since the aim of our investigations is to deduct particle properties, such as velocity, angle and mass, solely from impact morphology, a look at figure 13 shows an interesting, not yet completely understood relationship. This plot shows the relation between the impact feature's central crater pit area and the total spalled off area for the 615 impact features where the outline has already been redrawn. Since the central crater size is mainly influenced by particle kinetic energy and the spallation mainly by particle velocity, the relationship and the relatively small scatter should be worth having a closer look at.

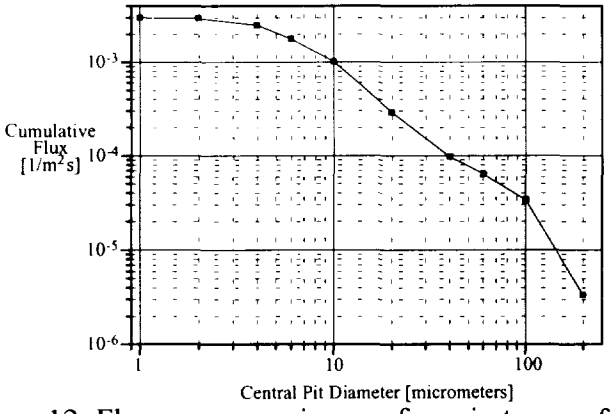

Figure 12. Flux on germanium surfaces in terms of central pit diameter

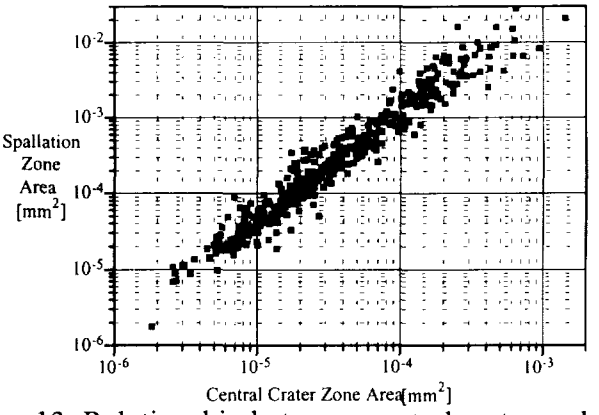

Figure 13. Relationship between central crater and damaged (spalled) area

This relationship has not yet been fully studied. Further experiments in our accelerator facility are currently done to investigate this effect further.

Central Crater Eccentricities

Some of the impact features which were classified as high velocity impacts, i.e. those features that have a molten central crater (see figure 4), show signs of obliquity. Since other LDEF investigators research this field, too, although for different target material, for example [12], we decided to include this phenomenon in our feature evaluation, as well.

We applied a least error squares fit of an ellipse to the central crater outline of those features showing a molten central pit. This resulted in an elliptic curve and revealed directionality information of the impact crater. Figure 13 shows the distribution of the ratio of minor and major axes of the ellipse together with a Gaussian fit on that data. The majority of central craters are almost circular. The small shift toward the 0.9 ratio is consistent with observations made for lunar rocks [7]. There is a reasonable number of impacts with fairly oblique central craters. These might be used for the determination of impact direction.

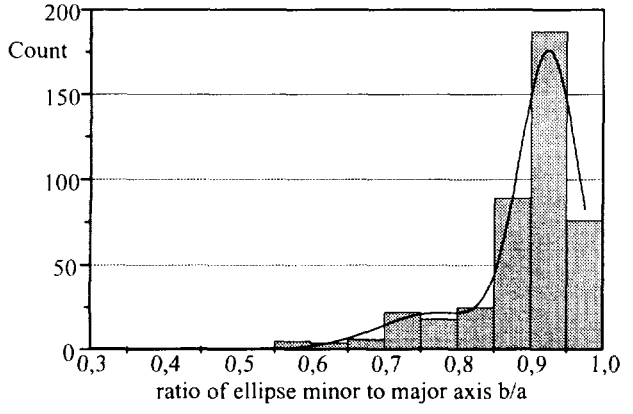

Figure 14. Eccentricity of LDEF central crater fits.

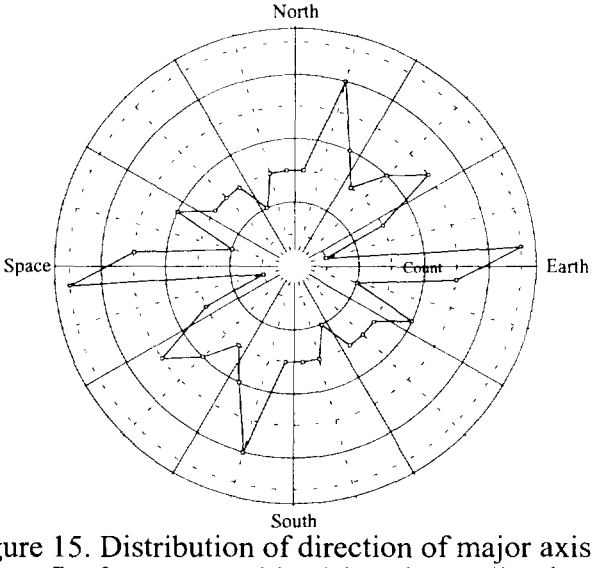

Figure 15. Distribution of direction of major axis ellipse fits for craters with a b/a ratio smaller than 0.7. Coordinate system as if looking from ram direction on bay E08.

Directionality

The direction of the major axis of the impact features with a b/a ratio smaller than 0.7 are plotted in figure 15. Since the direction of the major axis does not tell whether the particle came from one side or the other, this histogram plot is symmetric. There seem to be some preferred impact directions from Space (or Earth), almost North (or South) and Northeast (or Southwest).

Feature Analyses of Laboratory Experiments

The following figures show some of the relationships between particle and impact feature parameters from impact experiments performed in our laboratory.

Particle Size vs. Spallation Zone Size

Figure 16 gives the relationship between particle diameter and damage size (that is, average spallation zone diameter). Note that this data covers the velocity regime from 2 to 17 km/s of laboratory-produced impact features. Since some of the crater forming processes (for example melting of central crater) are

highly velocity-dependent, figure 16 shows an "engineering" relationship for these two parameters, allowing a rough estimate of damage size to germanium surfaces from the common space debris and micrometeoroid flux models by Kessler and Grün or Cour-Palais.

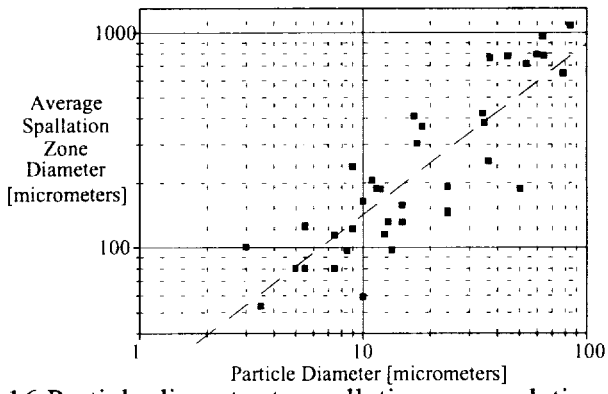

Figure 16.Particle diameter to spallation zone relationship

The parameters for the dotted "engineering" fitting curve are:

$$\log_{10} D_{Spall} \approx 1.348 + 0.800 \cdot \log_{10} D_{Particle}$$

(standard deviation 0,19071, n = 39, valid for velocities between 2 and 17 km/s and spherical glass particles)

Eccentricity for Different Impact Angles

Since one of the major issues of our investigations is to get an idea on where the particles came from, it is important to learn more on the influence of the impact angle on crater obliquity. The following impact data was obtained without any velocity or particle size measurement. It resulted in some data points for 0° and 45° impact angle. Unfortunately, for the 70° impact angle experiments, we got only a single impact which is shown in figures 19 through 21.

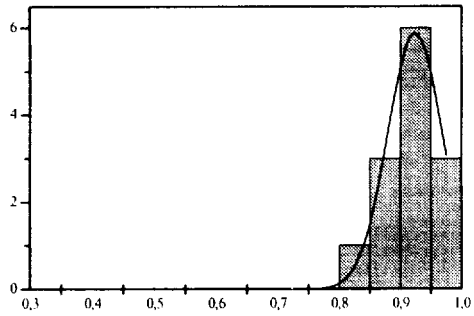

Figure 17. Ratio of major to minor axis of impacts with an impact angle of 0°. (13 impacts)

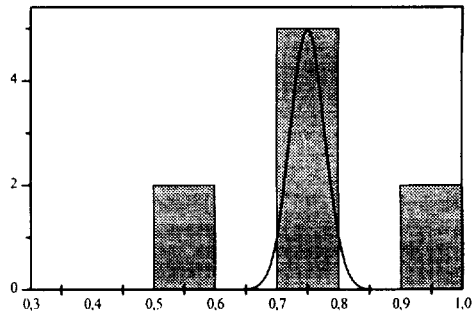

Figure 18. Ratio of major to minor axis of impacts with an impact angle of 45°. (11 impacts)

Figures 17 and 18 give b/a ratio histograms for impacts produced at different angles. Apparently, this ratio shifts to smaller values for increasing impact angles. The effect is not too obvious since the number of data points is not yet significantly high enough for establishing an impact angle-to-crater eccentricity function, but it seems as if central craters in germanium become more oblique at lower impact angles, than for example in aluminum, where usually impact angles larger than roughly 60° are needed for elliptical craters.

Morphology Changes with Impact Angle Variation

As mentioned before, highly oblique impacts show a distinct morphology. Figures 19 through 21 show an impact produced by a particle of unknown speed and size in our plasma accelerator. Impact direction was from the left; particle ejecta is visible at the right side on the SEM image; under the optical microscope the ejecta can be seen to spread over an area almost the same size as the impact feature itself. The feature maps were taken using our 3D laser topographer.

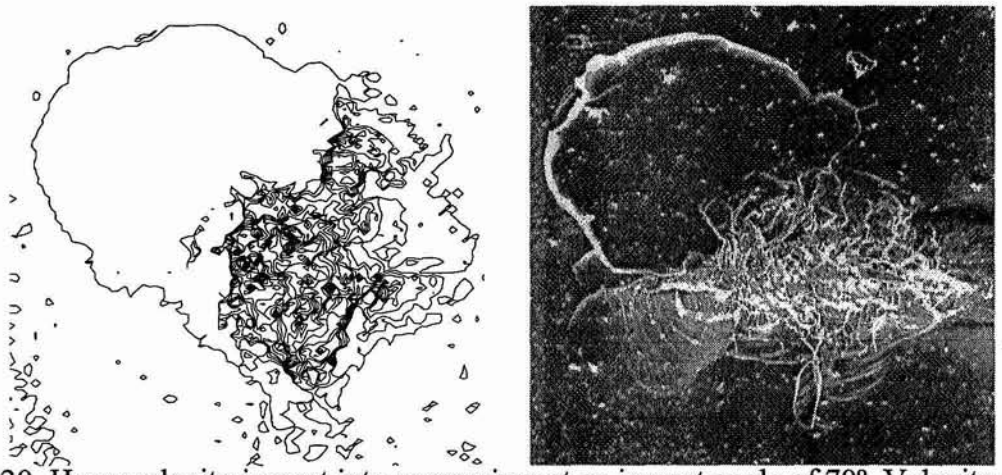

Figures 19 and 20. Hypervelocity impact into germanium at an impact angle of 70°. Velocity and particle size for this particular impact were not measured. Note the ejecta spray on the right side

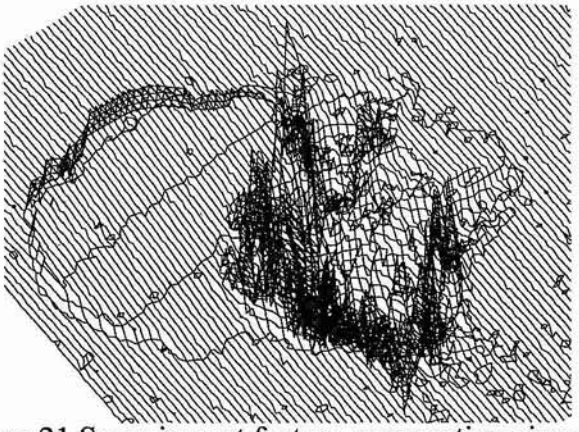

Figure 21.Same impact feature, perspective view.

The angle at which oblique central pits change to this type of feature showing almost ricochet effects has not yet been determined. It seems to be somewhere at 60° or 65°, although mass and velocity effects will have an effect, too.

Combining LDEF and Laboratory Findings

Crater Depth vs. Crater Volume

Since the impact feature morphology for brittle materials is somewhat more complicated than for example aluminum, more parameters can be measured and more effects should have an influence on the shape of the impact feature. Figure 22 shows one of these effects, a plot of the central crater ("penetration") depth vs. the total crater volume (i.e. central crater plus spalled off volume). When plotting the

LDEF data, it appears that there are two distinct clouds of scattered data points visible. Adding the laboratory data this data neighbors the upper cloud of the LDEF data points. The reason for this clustering is not yet understood. It could still be statistical errors, or it could be a density or velocity driven effect, since the glass beads used in our lab resemble space debris as far as density is concerned and the majority of our impact experiments consist of impacts with speeds around 12 km/s.

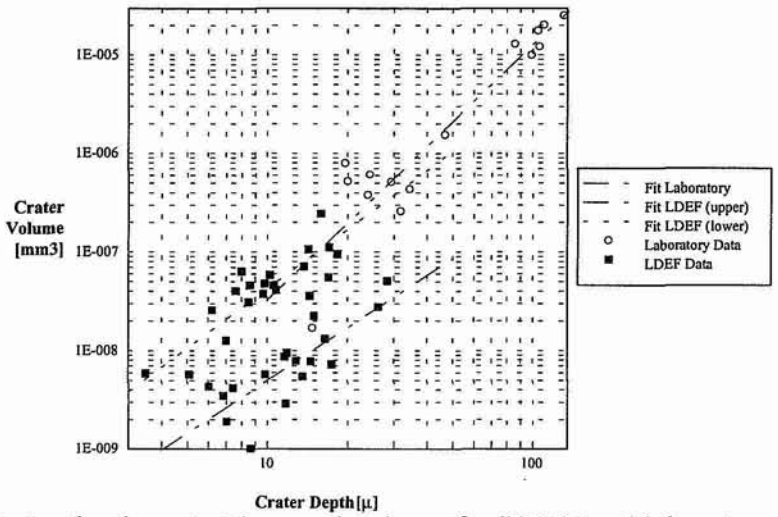

Figure 22. Crater depth vs. total moved volume for LDEF and laboratory impacts.

Cross-Section Changes

As described before, the morphology changes with the impact speeds. Melting occurs at velocities beyond 5-6 km/s. The rims of the central crater become visible in the cross-sections of our laser topographer. Figures 23 through 28 show three craters produced by particles of different velocities. The central crater rim is visible in figure 28 only, which was produced by a hypervelocity particle, as opposed to figure 24 where the central crater region is relatively flat. Also, note the change in the central craters' appearance with an almost circular central crater.

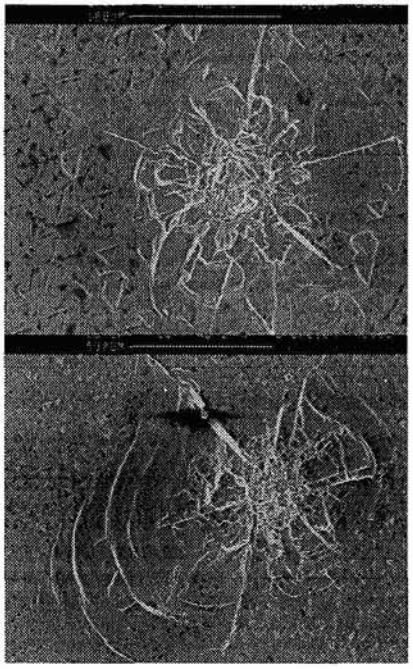

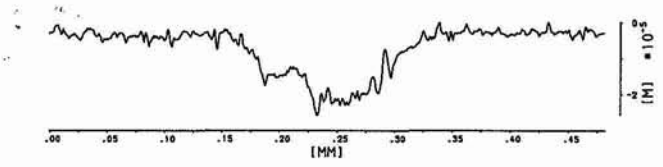

Figures 23 and 24. Image and cross-section of an impact with particle velocity of 2.1 km/s

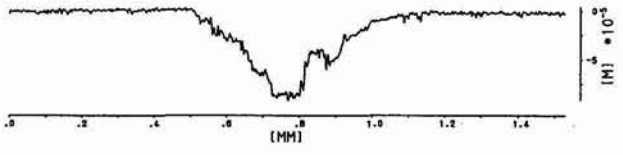

Figures 25 and 26. Image and cross-section of an impact with particle velocity of 5.6 km/s (High kinetic energy impact due to the size of the particle)

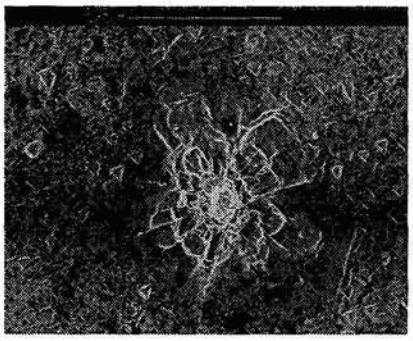

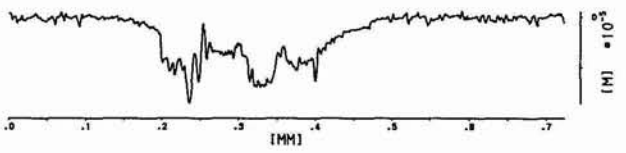

Figure 27 and 28. Image and cross-section of an impact with particle velocity of 7.8 $^{km}/_{s}$

CONCLUSIONS

Summary of the efforts that have been done so far:

- Crater morphology analysis should be able to provide information on certain particle parameters, such as velocity and kinetic energy, and, at least for some impacts, direction.

- This may not be possible for individual craters but rather for a large number of impact features.

We will have to continue our work; it is especially necessary to:

- collect more cross-sectional data of LDEF impact features.

- Together with impact data for other materials, such as aluminum, which was collected at our facility before, more calibration data for different surface materials should become available in near future.

- Analysis of ejecta, in that case, large chips, produced during the impact could give more information on brittle surface materials as sources of orbital debris particles.

- Also, we will continue our efforts to put a Mosaic server on-line. Currently, an experimental database is available via INTERNET connection to

asterix.lrt.mw.tu-muenchen.de [129.187.218.2]

NOTE

This work was supported by DARA (Deutsche Agentur für Raumfahrtangelegenheiten) GmbH contract 50 QV 9194 0. The author is responsible for the content of this paper.

LITERATURE

1. Allbrooks, M. Atkinson, D., *The Magnitude of Impact Damage on LDEF Materials, NASA Contractor Report NCR 188258, NASA JSC and Lockheed ESC,* 1993

2. Amari, S., Foote, J., Simon, C., Swan, P., Walker, R.M., Zinner, E., Jessberger, E.K., Lange, G., Stadermann, F., *SIMS Chemical Analysis of Extended Impact Features from the Trailing Edge Portion of Experiment A0187-2, in: Proceedings 1st LDEF Post-Retrieval Conference, NASA CP-3134,* 1992

3. Brownlee, D., Bucher, W., *Primary and Secondary Micrometeoroid Impact Rate on the Lunar Surface: A Direct Measurement, in: Analysis of Surveyor 3 material and photographs returned by Apollo 12, NASA SP-28,* 1972

4. Cour-Palais, B.G., *Hypervelocity Impacts in Metals, Glass and Composites, Int. J. Impact Engineering, Vol. 5, pp. 221-237,* 1987

5. Fechtig, H., Gentner, W., Hartung, J.B., Nagel, K., Neukum, G., Schneider, E. Storzer, D., *Microcraters on Lunar Samples, The Soviet-American Conference On Cosmochemistry Of The Moon And Planets, NASA SP-370,* 1977

6. Flaherty, R. E., *Impact Characteristics in Fused Silica for Various Projectile Velocities, Journal of Spacecraft, Vol. 7, No. 3, pp. 319-324,* 1970

7. Hörz, F., Morrison, D.A., Gault, D.E., Oberbck, V.R., Quaide, W.L., Vedder, J.F., Brownlee, D.E., Hartung, J.B., *The Micrometeoroid Complex and Evolution of the Lunar Regolith, The Soviet-American Conference On Cosmochemistry Of The Moon And Planets, NASA SP-370,* 1977

8. Igenbergs, E. et al, *Launcher Technology, In-Flight Velocity Measurement and Impact Diagnostics at the TUM/LRT,* International Journal of Impact Engineering, Vol. 5, pp. 371-380, 1987

9. Iglseder, H., Igenbergs, E., *Measured Charge Generation By Small Mass Impact At Velocities Between 1 and 45 km/s, International Journal of Impact Engineering, Vol. 5, pp 381-388,* 1987

10. Kemp, W.T. et. al, *Long Duration Exposure Facility Space Optics Handbook, Final Report, Phillips Laboratory, Kirtland AFB, PL-TN--93-1067,* 1993

11. Kreitmayr, U., *Konstruktion und Bau eines Teilchendetektors für das Raumfahrtexperiment LDEF, Diplomarbeit (Master's Thesis), Lehrstuhl für Raumfahrttechnik, RT-DA 82/3,* 1982

12. Mackay N.G. et al, *Interpretation Of Impact Crater Morphology And Residues On LDEF Using 3D Space Debris And Micrometeoroid Models, Proc. First European Conference On Space Debris, ESA SD-01, 1993*

13. Mandeville, J.-C., *Profile and Depth of Microcraters formed in Glass, Earth and Planetary Science Letters 15 (1972) 110-112,* 1972

14. Vedder, J. F., *Microcraters Formed in Glass by Projectiles of Various Densities, Journal of Geophysical Research, Vol. 79, No. 23,* 1974

Currently at North Carolina State University, College of Engineering, Analytical Instrumentation Facility, Box 7916, Raleigh, NC 27695-7916

CRATERING AND PENETRATION EXPERIMENTS IN TEFLON TARGETS AT VELOCITIES FROM 1 TO 7 KM/S

Friedrich Hörz
NASA / Johnson Space Center
Houston, Texas 77058
(713)483-5042/FAX(713)483-5347

Mark J. Cintala
NASA / Johnson Space Center
Houston, Texas 77058
(713)244-5032/FAX(713)483-5347

Ronald P. Bernhard
Lockheed ESC
Houston, Texas 77058
(713)483-5018/FAX(713)483-5347

Thomas H. See
Lockheed - ESC
Houston, Texas 77058
(713)483-5027/FAX(713)483-5347

ABSTRACT

Approximately 20 m2 of protective thermal blankets, largely composed of Teflon, were retrieved from the Long Duration Exposure Facility (LDEF) after the spacecraft had spent ~5.7 years in space. Examination of these blankets revealed that they contained thousands of hypervelocity impact features ranging from micron-sized craters to penetration holes several millimeters in diameter. We conducted impact experiments in an effort to reproduce such features and to -- hopefully -- understand the relationships between projectile size and the resulting crater or penetration-hole diameter over a wide range of impact velocity. Such relationships are needed to derive the size- and mass-frequency distribution and flux of natural and man-made particles in low-Earth orbit.

Powder propellant and light-gas guns were used to launch soda-lime glass spheres of 3.175 mm (1/8") nominal diameter (Dp) into pure Teflon FEP targets at velocities ranging from 1 to 7 km/s. Target thickness (T) was varied over more than three orders of magnitude from infinite halfspace targets ($Dp/T < 0.1$) to very thin films ($Dp/T > 100$).

Cratering and penetration of massive Teflon targets is dominated by brittle failure and the development of extensive spall zones at the target's front and, if penetrated, the target's rear side. Mass removal by spallation at the back side of Teflon targets may be so severe that the absolute penetration-hole diameter (Dh) can become larger than that of a standard crater (Dc) at relative target thicknesses of $Dp/T = 0.6$-0.9. The crater diameter in infinite halfspace Teflon targets increases -- at otherwise constant impact conditions -- with encounter velocity by a factor of $V^{0.44}$. In contrast, the penetration-hole size in very thin foils ($Dp/T > 50$) is essentially unaffected by impact velocity. Penetrations at target thicknesses intermediate to these extremes will scale with variable exponents of V. Our experimental matrix is sufficiently systematic and complete, up to 7 km/s, to make reasonable recommendations for the velocity-scaling of Teflon craters and penetrations. We specifically suggest that cratering behavior and associated equations dominate all impacts in which the shock-pulse duration of the projectile (tp) is shorter than that of the target (tt). We also demonstrate that each penetration hole from space-retrieved surfaces may be assigned a unique projectile size, provided an impact velocity is known or assumed. This calibration seems superior to the traditional ballistic-limit approach.

This abstract was taken from a NASA Technical Publication of the same title. Interested readers are referred to this document for detailed results, discussions and photographic documentation (including the witness plates) of the ~90 experiments conducted in this study.

Hörz, F., Cintala, M.J., Bernhard, R.P., Cardenas, F., Davidson, W., Haynes, G., See, T.H., Winkler, J. and Knight, J. (1994) Cratering and Penetration Experiments in Teflon Targets at Velocities from 1 to 7 km/s, NASA TM-104-797, pp. 220.

DIMENSIONAL SCALING FOR IMPACT CRATERING AND PERFORATION

Alan J. Watts
POD Associates, Inc
2309 Renard Pl., SE, Suite 201
Albuquerque, NM 87106

Dale Atkinson
POD Associates, Inc
2309 Renard Pl., SE, Suite 201
Albuquerque, NM 87106

SUMMARY

POD Associates have revisited the issue of generic scaling laws able to adequately predict (within better than 20%) cratering in semi-infinite targets and perforations through finite thickness targets. The approach used was to apply physical logic for hydrodynamics in a consistent manner able to account for chunky-body impacts such that the only variables needed are those directly related to known material properties for both the impactor and target. The analyses were compared and verified versus CTH hydrodynamic code calculations and existing experimental data. Comparisons with previous scaling laws were also performed to identify which (if any) were good for generic purposes. This paper is a short synopsis of the full report (ref. 1) available through the NASA Langley Research Center, LDEF Science Office.

INTRODUCTION

The need for scaling laws exists because the options (*i.e.* experiments and/or computer simulations) are very expensive and time-consuming. Interpretation of the *many* LDEF/SOLAR MAX/other impacts cannot be done directly via either experiments or simulations. To derive the new scaling laws, POD's approach was: (1) use physical logic to determine expectations. (While this does not guarantee the *final* answer, it should indicate the correct form of the relationships); (2) Use the CTH impact hydrodynamics code (from Sandia National Laboratory, Albuquerque) to map out specific responses and determine sensitivities to parameter changes. (The CTH code was chosen because it is *"the"* code presently supported by DOD, and has been *"proven"* against many different

impact experiments); (3) Compare (1) and (2) with *existing* scaling laws and experiments to determine which (*if any*) are good fits to data, and are credible for impact conditions not readily accessible to experiments.

A "good" fit is one which obeys physics, has credibility, and requires *only* changes due to *known* material parameters. Accuracy need only be in the range of 10 - 20% for many cases. This allows an experimenter/code analyst to "home-in" on specific cases, as required.

POD's approach is primarily based on consideration of *momentum* and *stresses*. This approach assumes that, immediately following the short-lived pseudo one-dimensional (1-D) shock stress, the Bernoulli stress can be used as the "initial stress driver" for the remainder of the analyses. The logic is based on the concept of Bernoulli stress generated after a pulse reverberation through the projectile giving rise to an expanding (diverging) pulse in the target. The pulse contains fixed total *momentum*, but decreasing areal momentum, which induces hoop strains and stresses, which themselves decrease with radial distance. When the hoop stress drops to the local yield value, cratering stops. *Energy* is not directly invoked in the analysis. All energy solutions have the problem of needing to determine the correct *partition* between projectile, target, melting or vaporization, plastic flow and elastic waves.

POD's investigations mostly concentrated on impacts of aluminum into aluminum (both 6061-T6) and aluminum into Teflon, since these cases are representative of many of the LDEF cratering events.

CRATERING IN INFINITE TARGETS

For crater *diameters* (d_c), *the reverberation* pulse is assumed to be limited to one reverberation in the projectile (diameter d_p), since "later" momentum no longer contributes to the lateral push. Using this logic, coupled with dispersion of the pulse, we obtain

$$d_c/d_p = 1.0857(\rho_p/\rho_t)^{0.2857}(\rho_t/Y_t)^{0.2857}(c_t/c_p)^{0.2857}u_0^{0.5714}/(1+(\rho_p/\rho_t)^{1/2})^{0.5714} \quad [1]$$

where ρ is density, Y is yield strength, u_0 is normal impact speed, c is sound speed, and the subscripts apply for the projectile (p) or target (t). Note that the yield value is the static one, since we are describing the *terminal* phase of cratering.

For crater *depths* (P), the total projectile momentum is involved, but the effective shock speed is updated and a "cut-off" speed is defined, below which Bernoulli flow no longer occurs. From this we obtain

$$P/d_p = (1/4)(4/3)^{1/3}(\rho_p/\rho_t)^{1/3}(\rho_t/Y_t)^{1/3}\{(c_{0,t}+s(u_0-u_{t,crit})/(1+(\rho_t/\rho_p)^{1/2}))(u_0-u_{t,crit})\}^{1/3} \quad [2]$$

where $c_{0,t}$ is the low stress target sound speed, s is the Hugoniot term from the shock-speed versus

particle speed relationship, and $u_{t,crit}$ is the limit velocity needed to ensure Bernoulli flow, given by

$$u_{t,crit} = (2Y_t/\rho_t)^{1/2}(1+(\rho_t/\rho_p)^{1/2}) \quad [3]$$

Figures 1 and 2 indicate the results of equations 1 and 2 versus CTH data for the cases of Al into Al and Al into Teflon, respectively. For the Al/Al case the fit is within a few percent, while for the Al/Teflon case POD's predictions are about 18% low versus CTH across the entire impact velocity range considered. Figure 3 shows the comparison between POD's predictions and those of Cour-Palais (ref. 2) for an Al/Al impact. The two sets of predictions are seen to be quite close, indicating that the previous NASA use of the Cour-Palais predictions should be giving credible results.

PERFORATIONS IN FINITE TARGETS

The Ballistic Limit

We define the ballistic limit as the condition where a through-hole is just produced. The logic is based on *both* the creation of a front surface crater *and* the reflection of the diverging shock off the target rear surface. When the reflected shock (tensile) exceeds the tensile strength of the target at the "normal" depth of crater, perforation occurs. This logic gives a result which has *two* parts: one relating to crater depth and one relating to tensile spall. The result is one term dependent on *yield* strength and 2/3 power of impact speed, and one term dependent on *tensile* strength and approximately unit power of impact speed. The net result is a speed index $2/3 < n < 1.0$, as experimentally observed, and a need for *both* material strength terms. We obtain

$$T/d_p = (1/8)(4/3)^{1/3}(\rho_p/\rho_t)^{1/3}(\rho_t/Y_t)^{1/3}\{(c_{0,t}+s(u_0-u_{t,crit})/(1+(\rho_t/\rho_p)^{1/2}))(u_0-u_{t,crit})\}^{1/3}$$

$$+(1/4)\{\rho_p u_0^2/(2\sigma_s(1+(\rho_p/\rho_t)^{1/2})^2)\}^{1/n} \quad [4]$$

where T is the target thickness, n is an index describing the rate of decrease in compressive shock strength versus propagation distance. For aluminum $n \approx 2.0$, while for Teflon $n \approx 2.4$, based on data from the CTH calculations. The term σ_s is the *tensile* strength of the target. Thus the perforation ballistic limit requires both yield and tensile strengths. Figures 4 and 5 show comparisons between the new POD predictions and those of others for the cases of Al/Al and Al/Teflon impacts, respectively. It is seen that the most recent equation of McDonnell (ref. 3) gives very similar data to those of POD for the Al/Al case, but a somewhat larger variation for the Al/Teflon case.

Foils

A foil implies $T << d_p$, and for this case the pulse-time is limited by the transit across the foil and becomes $t = 2T/c_t$. Additionally, the index for stress decrease, n, becomes very large owing to the two free surfaces, the jetting, and the lip development. We obtain

$$d_c/d_p = (\rho_p/\rho_t)^{1/(n+1)}(\rho_t/Y_t)^{1/(n+1)}u_0^{2/(n+1)}(2T/d_p)^{1/(n+1)}/(1+(\rho_p/\rho_t)^{1/2})^{2/(n+1)} \quad [5]$$

for $n >> 2$ this implies $d_c/d_p \Rightarrow 1.0$, *regardless of material properties or impact speed.* This accords with experiment.

Intermediate Thickness Targets

To describe the intermediate case we assumed that the index n is itself a function of T/d_p. The simplest possibility chosen was

$$n = n_0(1+md_p/T) \quad [6]$$

where n_0 is the "infinite target" index. To equate d_c/d_p in both [1] and [5] we need $n = 2.5$ when $T = 2/3d_p$ which implies $m = 0.166$.

This approach gives a response very similar to that observed by Hörz (ref. 4). The asymptotic response for aluminum becomes

$$(d_c - d_p)/d_p = (3.0\ T/d_p)(\ln(A) - \ln(T/d_p)) \quad [7]$$

$$\text{where } A = 2\ (\rho_p/\rho_t)\ (\rho_t/Y_t)\ u_0^2\ /\ (1 + (\rho_p/\rho_t)^{1/2})^2 \quad [8]$$

This implies an almost *linear* response as $T \Rightarrow 0$, but the $\log(T/d_p)$ term gives a variable rate as T/d_p increases. The log(A) term also gives a very weak dependence on material properties and impact speed. This should be compared with results of Sawle (ref. 5), Maiden (ref. 6), and Brown (ref. 7) who suggest

$$(d_c - d_p)/d_p \propto (T/d_p)^n \quad [9]$$

where $n = 2/3$ (Sawle), or $n = 2/3$ (Maiden), or $n = 0.646$ (Brown). However, as noted by Herrmann (ref. 8), these various equations also contain impact velocity indexes which imply *very large* holes at high speeds, in contrast to experimental data. Figure 6 indicates the predictions of POD's equation 5, using the variable value of n from equation 6, for crater diameter versus the value of T/d_p, for an Al target foil. These predictions are compared with the data from Hörz for the

perforation *hole* size. The two groups of data track each other well.

SUPRALINEARITY

Experimentally, craters increase in size *faster* than the projectile does, all other factors constant. This phenomenon has been "explained" (by others) by either (a) shape changes during impact, or (b) strain-rate effects which increase the effective yield strength of the target. POD believes *neither* of these explanations works because:

(a) shape changes invalidate the concept of "chunky bodies" behaving like spheres, and POD's analysis also indicates that *exact shape* is not important.

(b) if strain-rate were important then we have a *velocity* dependence which is not included in the logic. Further, the strain-rate increase in yield occurs during the compressive shock only. The logic ignores stress-relaxation and the fact that the hysteretic reversal of stress does not suffer the same increase in yield since the release waves give much lower strain-rates. Only if cratering is a *direct* function of the shock front should strain-rate have a *direct* effect.

(c) POD's CTH calculations compared a large projectile versus small ones. *No supralinearity* was observed, despite different strain-rates. Further, there is *nothing* in either hydrodynamics, shape, or simple strain-rate that implies a "scale-length", which is necessary to explain supralinearity. To obtain a "length" we require the combination velocity/strain-rate, which thus gives a velocity dependence.

POD invoked the "Petch law" (ref. 9) which *does* invoke a "scale-length" and gives yield strength as a function of material grain size. Using this approach, POD demonstrated that the supralinear index is *not* constant, but merely appears to be over the projectile sizes commonly used for experiments.

The Petch law states

$$Y_t = Y_0 \, (1 + (\delta / d)^{1/2}) \qquad [10]$$

where Y_t is the observed strength, Y_0 is an intrinsic strength, d is the mean grain size and δ is a material-specific "size" parameter, given by

$$\delta = \pi \, G \, \gamma / Y_0^2 \qquad [11]$$

where G is the shear modulus and γ is the surface energy per area for opening cracks.

The result is to downgrade predictions by the factor

$$f = 1/(1 + (\delta / r_c)^{1/2})^{1/3} \qquad [12]$$

and this analysis implies that supralinearity is really a *small projectile down-scaling*, which essentially vanishes for projectiles larger than about 1.0 cm. Since *none* of the hydrocode simulations (done by anybody) include the Petch logic for material strength, it is not surprising that the codes *never* predict supralinearity. Figure 7 illustrates the behavior of equation 12, and indicates that for very small projectiles the supralinear exponent (slope of the line) approaches 1/6, while for large projectiles the exponent approaches zero. For projectiles in the range microns to millimeters, the mean exponent is very close to the Cour-Palais quote of 0.056, *i.e.*, $d_c/d_p \propto d_p^{0.056}$.

OBLIQUE IMPACTS

Because oblique impacts are 3-D, hydrodynamic code calculations are time-consuming. Thus POD performed limited numbers of such computations. Previous arguments have suggested that oblique impacts behave as if only the impact velocity component normal to the target surface were involved. This is supported by experiments.

Data show that until obliquities greater than about 60^0 are involved, the craters remain almost hemispherical. For larger obliquities the craters become obviously elongated in the downstream direction. Ricocheting of the projectile is observed at these higher obliquities.

POD's CTH calculations *confirm* the "cosine law", indicating that the crater depth and "lateral" crater diameter (i.e. perpendicular to the projectile plane of impact/ricochet) develop as if for the impact speed $u_0\cos\theta$, where θ is the angle between the impact velocity and the normal to the target surface.

POD's analysis indicates no contrary behavior. All of POD's equations remain valid provided the term u_0 is replaced everywhere by the term $u_0\cos\theta$.

POD's analysis also accounts for projectile ricochet. Such ricochets depend either on the ability of the projectile component of speed parallel to the target surface "out-running" the induced disturbance (this is the "stone bounce on water" logic), or on simple geometry arguments for the upper portions of the projectile to "pass over" the induced crater lips. The CTH results appear to be consistent with these arguments.

Because POD's analyses do *not* invoke energy for cratering there is no reason to expect a deviation from the cosine law even at very high impact speeds.

OTHER DATA COMPARISONS

POD has recently received details of work done by Wingate et al. (Los Alamos National Laboratory) (ref. 10), presented at the 1992 HVIS Symposium. The work involves Cu/Cu impacts, and compares four hydrodynamic code predictions. The codes are: EPIC, MESA, SPH and CALE, and experimental data is also compared. The following table lists the codes results and the POD predictions.

The calculations are for an impact at 6 km/s. The projectile diameter was d_p = 0.4747 cm (0.5 g). Properties for copper were:

$$\rho_p = \rho_t = 8.93 \text{ g/cm}^3,\ c_{0,t} = 3.94 \text{ Km/s},\ s = 1.49,\ Y_t = 2.4 \text{ Kbars}$$

and to compute our values POD used equation [1] for d_c, and [2] for P.

Results

quantity	experiment	EPIC	MESA	SPH	CALE	*POD*
P (cm)	1.4	1.8	1.59	1.73	1.51	*1.55*
d_c (cm)	2.54	2.4	2.8	2.6	2.44	*2.71*
P/d_c	0.55	0.75	0.57	0.67	0.62	*0.572*

We observe that POD's predictions are close to the experimental data. Also note that the variations in the code answers are themselves about 19% (for P), 17% (for d_c) and 32% (for P/d_c). The ratios for the POD values versus experiment are:

1.107 (for P), 1.07 (for d_c) and 1.04 (for P/d_c).

Part of Wingate's work was to explain supralinearity for small (micron size) projectiles. To do so he invoked strain-rate hardening and proposed that the effective yield strength of copper acted as if 5 times larger than normal, thus was set at 12 kbars. This increased yield value reduced the code predictions for crater *volume* by a factor of 4.1 (EPIC), 4.4 (MESA) and 3.3 (SPH). The POD prediction is *3.973* (Eqn $[1]^3$) for the same higher yield. Note that LANL did *not* actually use a strain-rate model, they merely increased the yield value in the "normal" model.

OTHER SCALING LAWS

POD has compared many existing scaling laws for cratering, which describe either crater depths and/or diameters. Essentially *none* of these scaling laws can be considered generic, since those few that fit data for aluminum do *not* fit the data for Teflon, or *vice versa*. As an example, although the Cour-Palais prediction is very good for an Al/Al impact (figure 3) it is less good for an Al/Teflon impact, as seen in figure 8.

POD has also compared existing equations for the ballistic limit condition. Of these, those recent ones by McDonnell give the best overall consistent fits for both aluminum and Teflon targets. The differences between McDonnell's recent versions are too small to justify a "best choice", since they all give good fits to CTH data and to POD's analysis, and to existing experimental data. However, McDonnell does not describe the condition of intermediate thickness targets.

POD's analyses and CTH calculations agree well with the experimental data of Hörz for cratering in infinite targets and the ballistic limit in finite targets. The analysis also indicates that the intermediate thickness case can be described, although POD has not yet finalized the results.

CONCLUSIONS

POD believes it has a "respectable handle" on scaling laws for cratering and perforations. Our equations fit results (computer and experimental) for targets of aluminum, Teflon and copper. We have indicated that the rules for crater diameter are *not* the same as for crater depth, and that truly hemispherical craters are a rarity rather than the rule.

POD's equations also adequately describe the ballistic limit condition for both aluminum and Teflon FEP targets. We have demonstrated that the condition really involves *two* terms, one describing crater depth and one describing the rear-surface generated spall. The response involves *both* yield strength and tensile strength, and the velocity index is between 2/3 and 1.0.

POD has demonstrated that for oblique impacts the "cosine rule" *does* apply. We have also indicated the rules for projectile ricochets.

POD has explained supralinearity by using the Petch law, and has concluded that this gives a *small-size downscaling*, and vanishes for projectiles larger than about 1 cm.

POD believes it would be worthwhile to study other metals, plastics and ceramics. Specifically, POD believes it is possible to formulate the responses for intermediate-thickness target perforations. This would strongly augment the experimental work of Hörz. The latter is *the only obvious manner in which perforations can be used to decipher impact projectile details.*

REFERENCES

1. *"Dimensional scaling for impact cratering and perforations"*, Watts et al., POD IRAD-93-001, 1993. Work performed under subcontract to Lockheed Engineering and Sciences Company under purchase order number 02N0171219, supported by the LDEF project office, and the LDEF M&D SIG (NASA Langley Research Center, and NASA Johnson Space Center).

2. Cour-Palais, B.G., Hypervelocity Impact Investigations and Meteoroid Shielding Experience Related to Apollo and Skylab, NASA CP-2360, pps. 247-275, 1985.

3. McDonnell, J.A.M. and Sullivan, K., Proceedings of the Workshop on Hypervelocity Impacts in Space, University of Kent at Canterbury, 1992, pp. 39-47.

4. Hörz, F. et al., Dimensionally Scaled Penetration Experiments to Extract Projectile Sizes from Space Exposed Surfaces, 1992 HyperVelocity Impact Symposium, Austin, TX, November 1992.

5. Sawle, D.R., Hypervelocity Impact in Thin Sheets and Semi-Infinite Targets at 15 km/s, AIAA Hyp. Vel. Imp. Conf., April/May 1969, Paper No. 69-378.

6. Maiden, C.J. et al., Investigation of Fundamental Mechanism of Damage to Thin Targets by Hypervelocity Projectiles, Final Report to U.S. Naval Research Laboratory, GM Research Laboratories, September, 1963.

7. Brown, M.L., Hypervelocity Impact in Thin Nickel Targets, Lockheed Electronics Company, 644D-40-64, August, 1970.

8. Herrmann, W. and Wilbeck, J., Review of Hypervelocity Penetration Theories, SANDIA REPORT, SAND-86-1884C, 1986.

9. Petch, N.J., The Cleavage Strength of Polycrystals, J. of Iron and Steel Institute, Vol. 174, pp 25-26, 1953.

10. Wingate, C.A., Stellingwerf R.F., Davidson R.F. and Burkett M.W., Models of High Velocity Impact Phenomena, 1992 Hypervelocity Impact Symposium, Austin, TX., Nov. 1992.

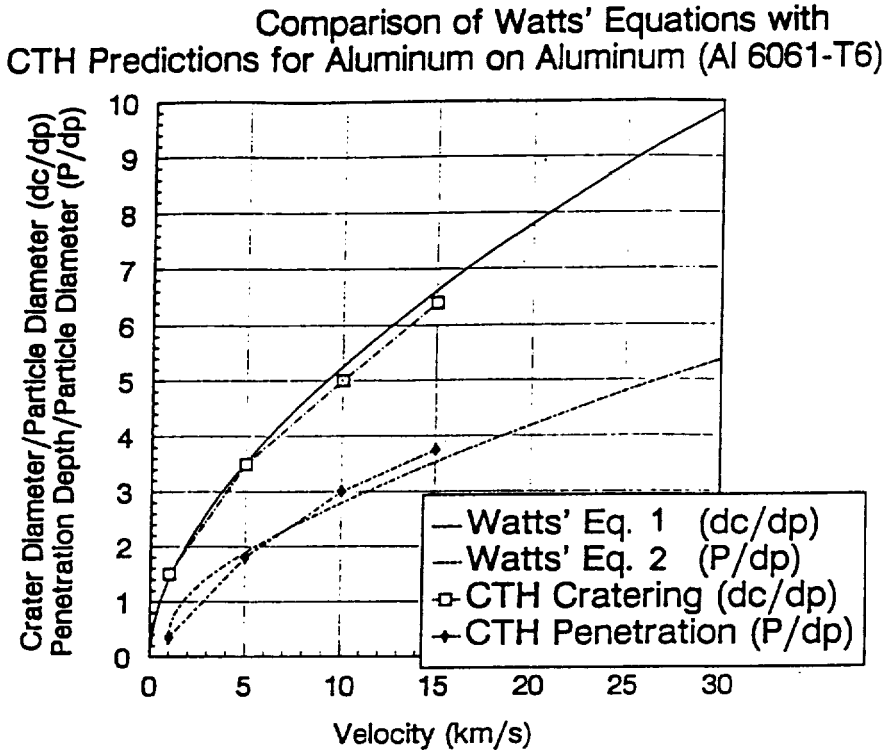

Figure 1

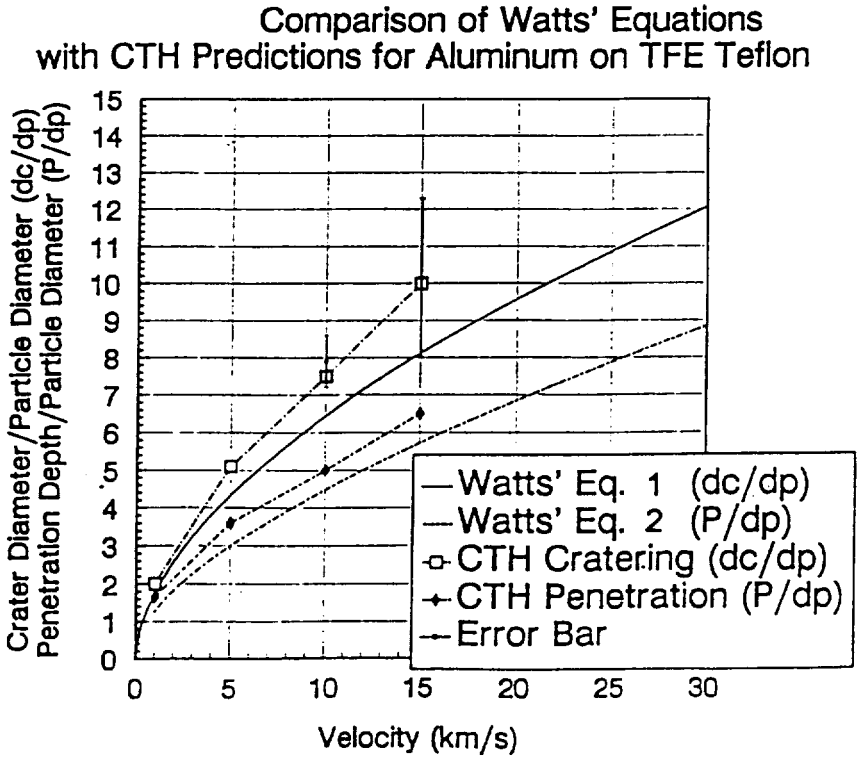

Figure 2

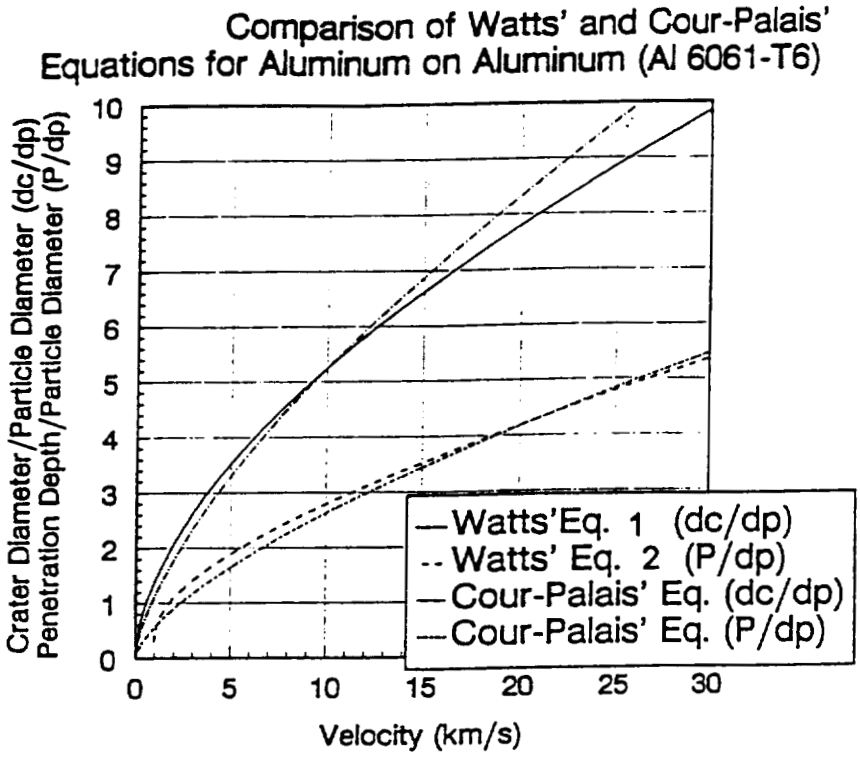

Figure 3

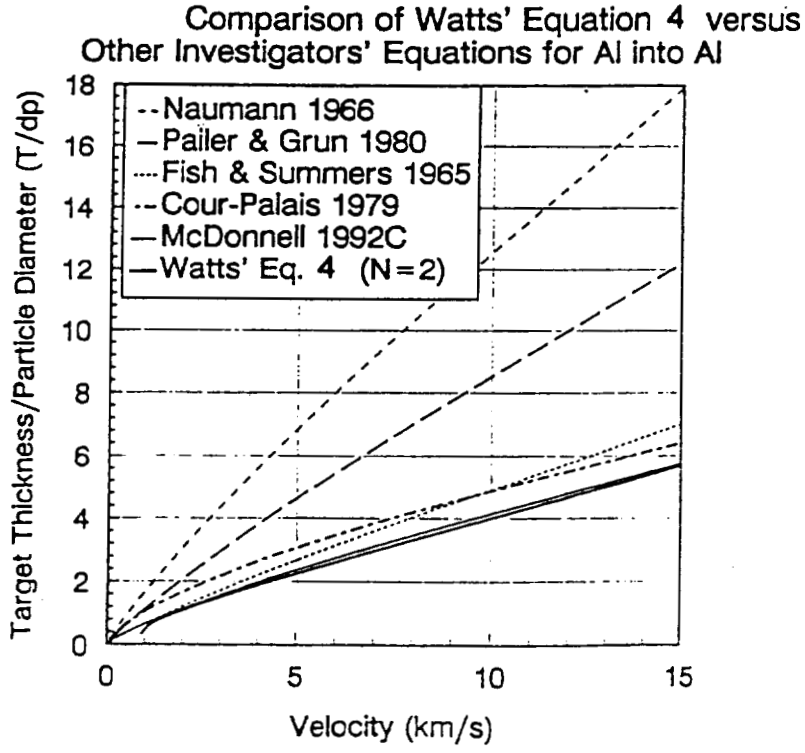

Figure 4

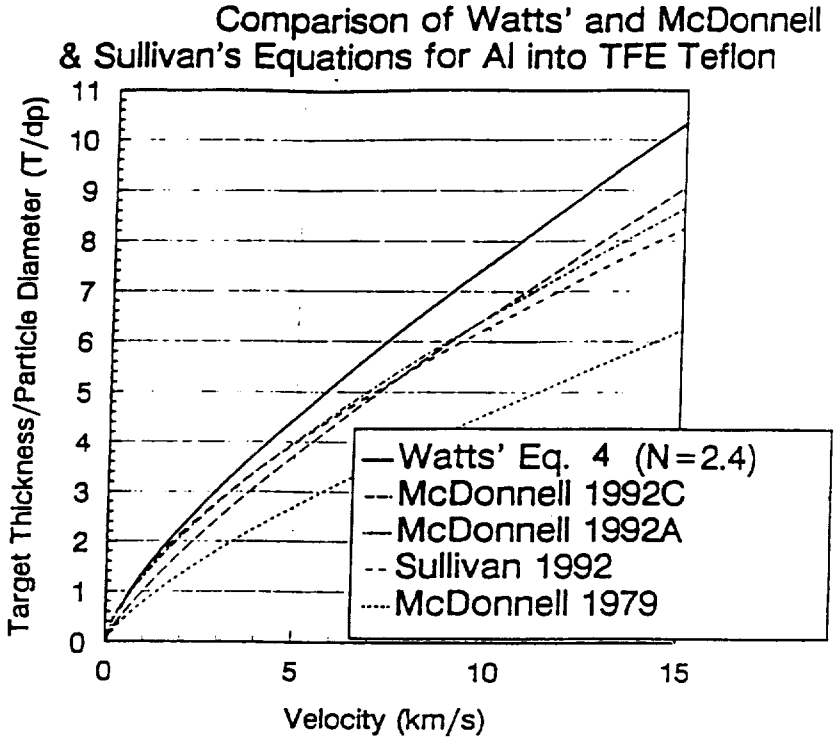

Figure 5

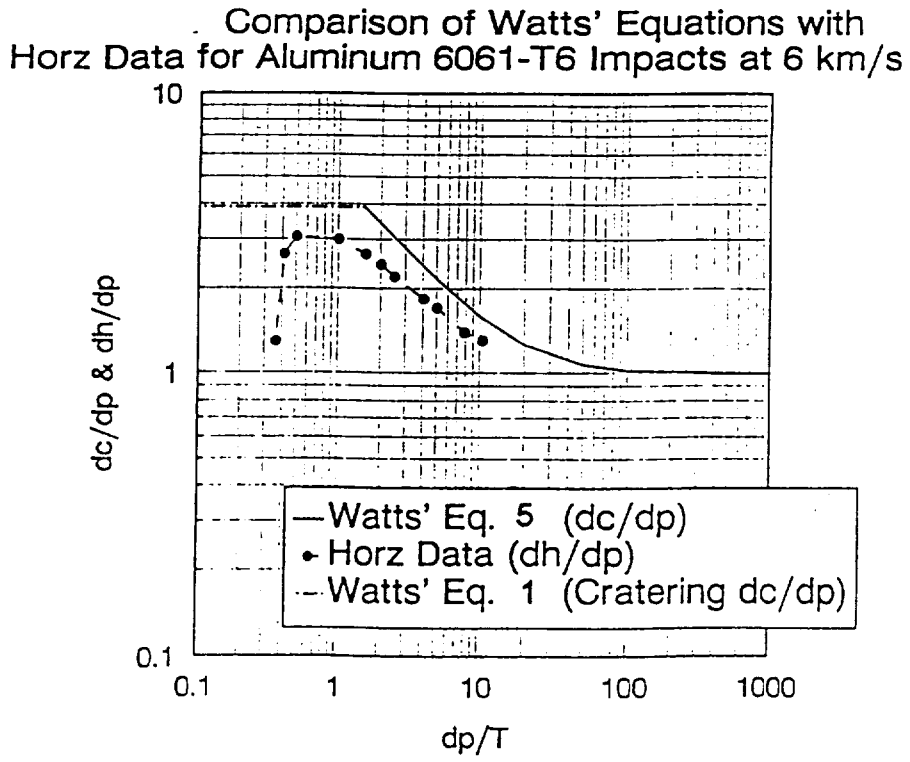

Figure 6

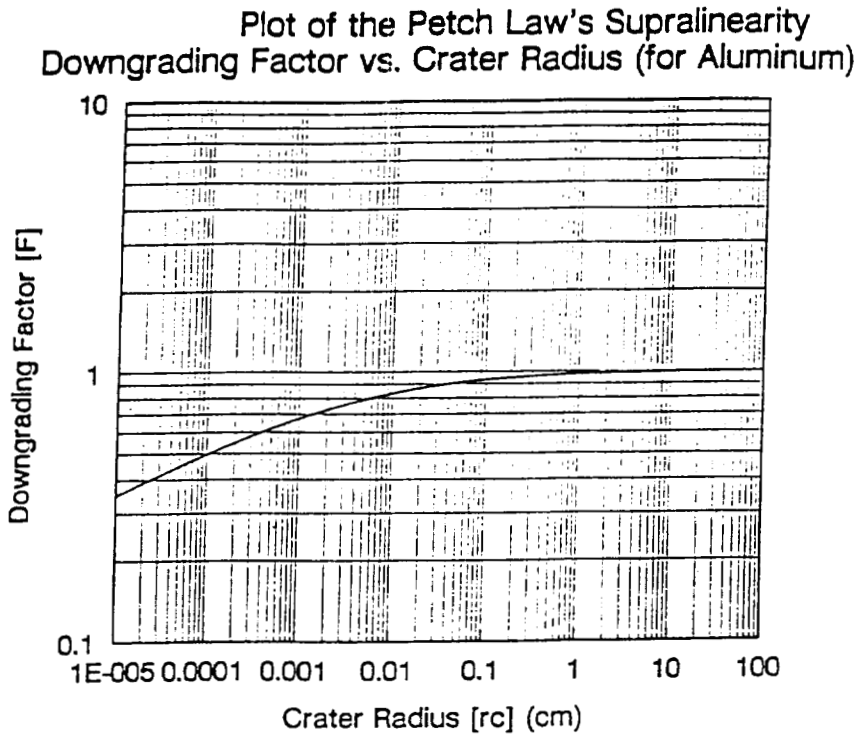

Figure 7

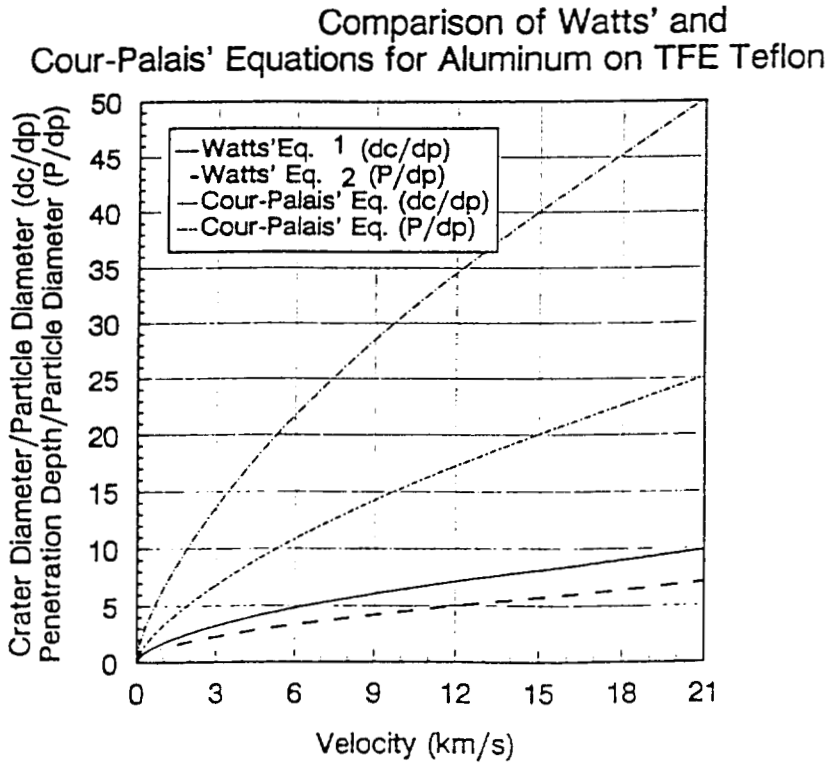

Figure 8

REPORT DOCUMENTATION PAGE

Form Approved
OMB No. 0704-0188

1. AGENCY USE ONLY *(Leave blank)*	2. REPORT DATE	3. REPORT TYPE AND DATES COVERED
	February 1995	Conference Publication

4. TITLE AND SUBTITLE

69 Months In Space:
Third LDEF Post-Retrieval Symposium

5. FUNDING NUMBERS

233-03-02-03

6. AUTHOR(S)

Arlene S. Levine, Editor

7. PERFORMING ORGANIZATION NAME(S) AND ADDRESS(ES)

NASA Langley Research Center
Hampton, VA 23681-0001

8. PERFORMING ORGANIZATION REPORT NUMBER

L-17430A

9. SPONSORING/MONITORING AGENCY NAME(S) AND ADDRESS(ES)

National Aeronautics and Space Administration
Washington, DC 20546-0001

10. SPONSORING/MONITORING AGENCY REPORT NUMBER

NASA CP-3275, Part 1

11. SUPPLEMENTARY NOTES

12a. DISTRIBUTION/AVAILABILITY STATEMENT

Unclassified—Unlimited

Subject Category 99

12b. DISTRIBUTION CODE

13. ABSTRACT *(Maximum 200 words)*

This volume is a compilation of papers presented at the Third Long Duration Exposure Facility (LDEF) Post-Retrieval Symposium. The papers represent the data analysis of the 57 experiments flown on the LDEF. The experiments include materials, coatings, thermal systems, power and propulsion, science (cosmic ray, interstellar gas, heavy ions, micrometeoroid, etc.), electronics, optics, and life science. In addition, papers on preliminary data analysis of EURECA, EOIM-3, and other spacecraft are included.

14. SUBJECT TERMS	15. NUMBER OF PAGES
Space Experiment	561
	16. PRICE CODE: A24

17. SECURITY CLASSIFICATION OF REPORT	18. SECURITY CLASSIFICATION OF THIS PAGE	19. SECURITY CLASSIFICATION OF ABSTRACT	20. LIMITATION OF ABSTRACT
Unclassified	Unclassified	Unclassified	

NSN 7540-01-280-5500

*U.S. GOVERNMENT PRINTING OFFICE: 1995-628-064-23070

Standard Form 298 (Rev. 2-89)
Prescribed by ANSI Std. Z39-18
298-102